Fluid Bed Coating and agglomeration: Scale-up and process optimisation

Hede, Peter Dybdahl

Publication date:
2009

Fluid bed coating and agglomeration: Scale-up and process optimisation

Ph.D. Thesis

Peter Dybdahl Hede

31st of August 2008

Novozymes A/S

Novozymes Bioprocess Academy

CHEC Research Centre
Department of Chemical and Biochemical Engineering
Technical University of Denmark

Preface

This thesis is submitted as partial fulfilment of the requirements for the Ph.D. degree at the Department of Chemical and Biochemical Engineering at the Technical University of Denmark (DTU). The work has been carried out in the period of September 2005 to August 2008 under the supervision of Professor Anker Degn Jensen at the Technical University of Denmark and Senior Science Manager Poul Bach at Novozymes A/S. The research work was performed mainly at the laboratory and pilot plant facilities at Novozymes A/S in Bagsværd, Denmark. The project was financially supported by the Novozymes Bioprocess Academy and the MP_2T Graduate School of Chemical Engineering at Technical University of Denmark.

First of all, I would like to express my sincere thanks to Anker and Poul for their encouragement, guidance and relevant criticism throughout the three years. I am grateful for the opportunity to carry out my project under their experienced and competent supervision. I have enjoyed the close scientific cooperation and appreciate the continuous support for my professional ambitions.

I also owe thanks to Marloes Brussen (TU Delft), Karin Madsen (DTU), Sidsel M. Andersen (DTU) and Bjarke L. Neidel (DTU) who all carried their bachelor or master projects partly under my supervision. Their project challenges and questions have helped me to get a deeper understanding of the research field. Further, I would like to thank the people at the Solid Products Development at Novozymes A/S for guidance and help with numerous practical problems.

Finally, I would like to thank Ann Dorrit for her support, great patience and for taking care of business at home during the last months of my project.

Vesterbro, August 2008

Peter Dybdahl Hede

Summary

Fluid bed coating is a flexible and versatile process commonly used in the manufacture of pharmaceutical and biotechnological products. Fluid beds have important advantages over other types of granulators including good heat and mass transfer, temperature homogeneity, mechanical simplicity and one-pot processing capabilities. The basic principle is to atomise a liquid into a bed of fluidised particles. The liquid spray typically consists of a solute which acts as a coating medium, and a solvent in which the solute is dissolved or dispersed. By contacting the core particles the liquid droplets spread and partly penetrate into the core pores. The warm fluidisation air evaporates the solvent, leaving a coating layer of solute on the particle surfaces. Particle growth can occur by either inter-particle agglomeration or by surface coating. Agglomeration occurs when liquid bridges of coating solution form between colliding particles. If the liquid bridge is strong enough to prevent subsequent particle separation, the liquid bridge solidifies resulting in a permanent agglomerate. In coating processes, agglomeration is generally unwanted and a number of other potential problems associated with the process include: spray drying loss of atomised coating droplets, attrition and breakage of the core particles and coating layer, deactivation of the active ingredient due to high temperature/humidity exposure and more. By constituting the boundaries these potential problems in all define the fluid bed coating process optimisation problem, and the engineering challenge is to navigate in between these often narrow borderlines.

Industrial enzyme products are often subjected to fluid bed coating processes because product handling is easier and the enzyme storage stability is better in a dry granule than in a liquid formulation. Furthermore, it is important that the enzyme products are produced with a constant high quality. Consequently, the choice of process conditions and formulation ingredients become critical and preferably rely on a detailed insight into the various phenomena and processes occurring during fluid bed coating.

The objectives of this thesis are to investigate particle- and process-related phenomena influencing the top-spray batch fluid bed coating process, primarily in terms of agglomeration tendency and coating layer properties such as mechanical strength and morphology. In continuation of this, the focus is on obtaining a fundamental understanding of fluid bed coating process scale-up. Taking its origin in industrial enzyme fluid bed coating processes, the research work is focussed on the two most common types of coating processes being coating with aqueous inorganic salt solutions (exemplified in terms of aqueous solutions of sodium sulphate) and coating with aqueous solutions of polymers (exemplified in terms of aqueous solutions of polyvinyl alcohol (PVA) with dispersed TiO_2 particles). Placebo coating experiments are carried out in three top-spray pilot-scale fluid beds ranging in capacity from a core particle bed load of 0.5 kg, 4 kg and 24 kg.

Initially, two statistical data-driven models are derived from a double unreplicated 2^{4-1} fractional factor design applied in order to investigate the influence of the fluidisation velocity, atomisation air pressure, coating solution dry-matter concentration and bed temperature on two response parameters being; agglomeration tendency and impact strength of salt coated sodium sulphate cores. The agglomeration model indicates decreasing agglomeration tendency with increasing coating solution dry-matter concentration and atomisation air pressure, whereas the impact strength model indicate increasing impact strength with increasing coating solution dry-matter concentration, atomisation air pressure and bed temperature. The observed impact strength tendencies are concluded to be closely associated with a high extent of coating solution droplet penetration into the Na_2SO_4 cores.

Furthermore, two simple scale-up principles are tested on the salt coating process being the Flux Number and the combined Relative Droplet Size/Drying Force principles. Neither of the two scale-up principles specifies all the variables involved in the process, and both of the scale-up principles are dependent on proper choices of e.g. the inlet fluidisation air temperature, which is an unfortunate feature. With qualified choices of certain process variables, however, it is demonstrated for both scale-up principles that it is possible to maintain a low tendency of agglomeration and match the particle size distribution across the three pilot-scale fluid beds. With the Flux Number approach this is, nevertheless, only achieved for a very slow coating process with significant spray drying loss of the coating solution. It is observed how two coating processes with identical Flux Number values may result in completely different agglomeration tendencies based on the choice of the variables constituting the Flux Number. This is concluded to result from the broad process variable guidelines provided by the inventors of the Flux Number leading to too many possible process variable combinations for the same Flux Number value. New boundaries are suggested in the present work that are narrower than the ones presented in the original patent, but even so, the Flux Number scale-up approach is concluded to be a too simple approach to be used as a generic scale-up principle. With the qualified choices for the variables constituting the Relative Droplet size and Drying Force parameters, results from similar salt coating experiments indicate that it is possible to keep the agglomeration tendency low and at the same time match the particle size distribution across the three pilot-scale fluid beds. For the scale-up in terms of the combined Relative Droplet Size/Drying Force principle, impact and attrition tests indicate that it is possible to produce granules with similar attrition and impact strength across fluid bed scale, and that the two types of properties are inversely related.

Following the experimental studies of the top-spray inorganic salt fluid bed coating process a lumped-region dynamic heat and mass transfer model is developed, enabling the calculation of the fluidisation air temperature and humidity as well as particle moisture contents and temperature. The model results are in good agreement with steady state experimental data for important variables such as the fluidisation air outlet temperature and humidity as well as the bed temperature. Simulations reveal that the three pilot-scale fluid beds are not significantly different with respect to steady state in-bed conditions. As long as the atomisation air pressure, liquid spray rate and fluidisation air velocity (in m/s) are all above certain values, similar inlet fluidisation air temperatures in the three scales will lead to similar low tendencies of agglomeration while the process intensity is maintained. This is because such process conditions give similar vertical temperature, humidity and Drying Force profiles again leading to similar particle liquid layer thicknesses which in turn cause similar tendency of agglomeration as verified using the viscous Stokes theory. Simulations of a 900 kg RICA-TEC production-scale fluid bed reveal that the vertical temperature and humidity gradients increase significantly with respect to the pilot-scales, meaning that the error of measuring a representative bed temperature at one location (as typically done industrially) becomes much larger. The previously tested simple scale-up principles are concluded not to be useful when transferring the coating process from pilot-scale into production-scale fluid beds. Furthermore, it is observed that if the inlet temperature is fixed across scale then the spray intensity must be decreased the larger the fluid bed scale in order to avoid agglomeration. This is a consequence of the poor mixing and longer particle circulation times the higher the fluidised bed is. For similar process intensity the coating process becomes increasingly sensitive towards the tendency of agglomeration the larger the fluid bed scale. It is concluded that scale-up of the top-spray fluid bed coating process should be done with the support from a mathematical model as the one developed. It hereby becomes possible to simulate and optimise the coating process individually at each scale.

The PVA/TiO_2 coating process is studied next in the pursuit of finding the causes why polymer and inorganic salt solutions cannot be processed under similar fluid bed process condition without resulting in significantly different agglomeration tendencies. Fluid bed coating experiments with different values of the Drying Force and the liquid spray rate indicate that the PVA/TiO_2 coating process is much more sensitive towards agglomeration under similar thermodynamic and spray operating conditions. Detailed studies show that such differences do not arise solely from differences in coating solution bulk viscosity or from differences in mean droplet diameters. Rather, the different behaviour results from differences in stickiness (tack) measured in terms of a probe tack tester developed for the purpose. Realising that the PVA/TiO_2 coating solution is a colloidal dispersion of TiO_2 particles this is made use of to suppress the tendency of agglomeration by substituting some of the PVA/TiO_2 with lubricant and plasticizer in the form of Neodol 23-6.5, and further reduce pH to a value far from the isoelectric point. In terms of this it is possible to arrive at an agglomeration tendency within range of the agglomeration tendency for a salt coating process processed under similar conditions.

For the polymer fluid bed coating process a tack Stokes number is introduced as a better measure of the agglomeration tendency in comparison with the traditional viscous Stokes theory. This new number is based on the work needed to reach maximum tack (above which breakage occurs) in the probe tack test instead of the viscous dissipation energy. The new tack Stokes number correlates well with observed levels of agglomeration, and as a promising feature, proportionality is observed between the agglomeration weight percentage and the new tack Stokes number. The reason for the better performance of the tack Stokes number is concluded to be influenced by the liquid layer thickness. It is argued that in the polymer fluid bed coating process the coating liquid layer is very thin and sticky, meaning that any agglomeration tendency is due to liquid surface phenomena rather than due to bulk viscous phenomena. Such surface phenomena are concluded to be well predicted by the developed probe tack test. Results from the polymer coating study illustrate that the optimisation of a fluid bed coating process should focus also on the coating solution formulation besides focussing on process-related variables.

Resumé (Summary in Danish)

Coating af partikler i et fluidiseret leje er en fleksibel og alsidig proces, der finder udbredt anvendelse i fremstillingen af farmaceutiske og bioteknologiske produkter. Fluidiseretleje-granulatorer har en række vigtige fordele i forhold til andre typer af granulatorer såsom gode varme- og masseovergangsegenskaber, temperaturhomogenitet, designsimplicitet og muligheden for at foretage flere typer af processer i det samme udstyr. Basalt set handler fluidiseretlejecoating om at forstøve en væske ned på et leje af fluidiserede partikler. Den væskeholdige forstøvning består typisk af et fastformigt stof, der udgør coatingsmediet, og et solvent, i hvilken det fastformige stof er opløst eller dispergeret. Ved kontakt mellem de våde dråber og partiklerne i lejet spredes dråberne ud på partikeloverfladerne og trænger delvist ind i partiklernes porer. Den varme fluidiseringsluft fordamper solventet, hvorved der gradvist dannes et coatingslag på hver partikeloverflade. De fluidiserede partikler kan vokse i størrelse enten pga. overfladecoating eller pga. partikel-partikel agglomerering. Agglomerering opstår, når våde væskebroer dannes mellem kolliderende partikler. Hvis denne væskebro er stærk nok til at modstå efterfølgende partikelseparation, vil væskebroen størkne og et permanent agglomerat hermed være dannet. I coatingsprocesser er agglomerering typisk uønsket, og en række andre problemer i processen inkluderer spraytørringstab af de forstøvede væskedråber, slitage og brud af partikler og af coatingslaget, deaktivering af den aktive komponent pga. høj leje-temperatur og/eller høj fugtighed i lejet etc. Disse potentielle problemer forbundet med coating i et fluidiseret leje udgør det samlede optimeringsproblem, og den ingeniørmæssige udfordring består i at navigere indenfor disse ofte snævre grænser.

Industrielle enzymprodukter involverer ofte coating i et fluidiseret leje, idet produkt-håndtering er lettere og enzymets opbevaringsstabilitet bedre i et tørt granulat end i en flydende formulering. Endvidere er det vigtigt, at enzymprodukter produceres med en konstant høj kvalitet. Som en konsekvens af dette er valg af proces- og formuleringsbetingelser særdeles vigtige, hvilket igen kræver detaljeret viden og indsigt i de mange forskelligartede fænomener, der optræder i en coatingsprocess i et fluidiseret leje.

Formålet med denne afhandling er at undersøge partikel- og procesrelaterede fænomener, der influerer coatingsprocesser med topforstøvning i et fluidiseret leje – dette primært med fokus på agglomereringstendens og egenskaber i coatingslaget såsom mekaniske egenskaber og morfologi. I fortsættelse af dette er fokus rettet mod at opnå en fundamental forståelse for opskalering af coatingsprocesser i fluidiserede lejer. Med udgangspunkt i industrielle enzymgranulater har forskningsarbejdet omdrejningspunkt i de to mest almindelige coatingsprocesser i fluidiseretleje: coating med vandige uorganiske saltopløsninger (eksemplificeret ved vandige opløsninger af natriumsulfat) og coating med vandige opløsninger af polymerer (eksemplificeret ved vandige opløsninger af polyvinylalkohol (PVA) med dispergerede TiO_2 partikler). Placebocoatingseksperimenter er udført i tre fluidiserede lejer med topforstøvning i pilotskala spændende i partikelkapacitet fra 0,5 kg, 4 kg og til 24 kg.

To statistiske datadrevne modeller er udledt fra et dobbelt ikke-gentaget 2^{4-1} fraktioneret faktordesign anvendt på saltcoatingsprocessen af natriumsulfatkerner for herigennem at undersøge indflydelsen af fluidiseringshastigheden, atomiseringsluftens dysetryk, coatings-opløsningens tørstofindhold og lejets temperatur på to responsparametre; agglomererings-tendens under coating og slagstyrke af de færdige granulater. Den udledte agglomererings-model indikerer faldende agglomereringstendens med stigende tørstofindhold af coatings-opløsningen såvel som med stigende dysetryk af atomiseringsluften. Tilsvarende indikerer

slagstyrkemodellen stigende slagstyrke med stigende tørstofindhold af coatingsopløsningen, dysetryk af atomiseringsluften samt temperaturen i lejet. De observerede slagstyrketendenser konkluderes at være tæt forbundne med høje grader af dråbeindtrængning ind i natrium-sulfatkernerne.

Endvidere testes to simple opskaleringsprincipper på saltcoatingsprocessen: Fluxtallet og det kombinerede relative dråbestørrelse/lejets tørringskraft. Ingen af de to principper specificerer alle variable involveret i processen, og begge principper er afhængige af behørige valg af eksempelvis fluidiseringsluftens indgangstemperatur, hvilket er upraktisk. Med kvalificerede valg af bestemte procesvariable demonstreres det dog for begge skaleringsprincipper, at det er muligt at opretholde en lav agglomereringsgrad og samtidig matche partikelstørrelses-fordelingen henover de tre udstyrsskalaer. Dette er dog for fluxtalsprincippet kun opnåeligt under en langsom coatingsprocess med et betydeligt spraytørringstab til følge. Det observeres, hvordan to coatingsprocesser med identiske fluxtal kan lede til markant forskellige agglomereringstendenser ud fra valget af de variable, der udgør fluxtallet. Dette konkluderes at stamme fra de meget brede variabelretningslinjer, som er givet af opfinderne af fluxtallet, hvilket leder til for mange mulige kombinationer af procesvariable for den samme værdi af fluxtallet. Nye og mere strikse retningslinjer foreslås i det nærværende arbejde, men på trods af dette konkluderes fluxtalsskaleringsprincippet at være en for simpel tilgang til coating i fluidiseretleje til at kunne anvendes som et generisk opskaleringsprincip. Med kvalificerede valg for de variable, der udgør den relative dråbestørrelse og lejets tørringskraft, demonstreres det for tilsvarende saltcoatingseksperimenter, at det er muligt at holde agglomererings-tendensen lav og på samme tid matche partikelstørrelsesfordelingen henover skala. For opskalering ved hjælp af det kombineret relative dråbstørrelse/lejets tørringskraftprincip vises det endvidere, at det er muligt at producere granulater med samme slid- og slagstyrke henover udstyrsskala, og at de to typer af mekaniske egenskaber er omvendt relaterede.

På baggrund af de eksperimentelle studier af coatingsprocessen med topforstøvning af uorganiske saltopløsninger udvikles en dynamisk varme- og masseovergangsmodel for det fluidiserede leje. Denne model gør det muligt at udregne fluidiseringsluftens temperatur og fugtindhold samt fugtindholdet på partiklerne og partiklernes temperatur. Resultater opnået med modellen viser god overensstemmelse mellem eksperimentelle ligevægtsdata for vigtige variable såsom fluidiseringsluftens udgangstemperatur og udgangsfugt samt lejets temperatur. Simuleringer afslører, at de tre fluidiserede lejer i pilotskala ikke er afgørende forskellige med hensyn til ligevægtsbetingelser inde i lejet. Så længe atomiseringsluftens dysetryk, coatingsopløsningens forstøvningshastighed og fluidiseringsluftens hastighed (i m/s) alle er over bestemte grænser, vil samme indgangstemperaturer for fluidiseringsluften i de tre skalaer lede til samme lave agglomereringstendenser, mens procesintensiteten bibeholdes henover skala. Dette skyldes, at sådanne betingelser giver tilsvarende samme vertikale temperatur-fugt- og tørringskraftsprofiler, hvilket igen leder til samme væskelags-tykkelse på partiklerne og derved til samme agglomereringstendenser som verificeret ved hjælp af den viskøse stokesteori. Simuleringer af et 900 kg RICA-TEC fluidiseret leje i produktionsskala afslører, at de vertikale temperatur- og fugtgradienter vokser markant i forhold til pilotskalaerne. Dette betyder, at fejlen ved at måle én repræsentativ temperatur på ét sted i lejet (som det typisk gøres i industrien) bliver væsentlig større. De førnævnte testede simple skaleringsprincipper konkluderes ikke at være brugbare, når coatingsprocessen skal overføres fra pilotskala og til produktionsskala. Endvidere observeres det, at hvis indgangstemperaturen på fluidiserings-luften fastholdes på samme niveau i hver skala, så skal forstøvningsintensiteten reduceres jo større skala, såfremt agglomerering skal undgås. Dette er en konsekvens af ringere opblanding og længere partikelcyklustider, desto højere det fluidiserede leje er. Dette illustrerer, at for

den samme procesintensitet bliver coatingsprocessen mere følsom overfor agglomerering, jo større skala det fluidiserede leje er i. Det konkluderes, at opskalering af den fluidiseretlejecoatingsproces med topforstøvning bør ske med hjælp fra en matematisk model som den, der præsenteres i nærværende arbejde. Ved brug af en sådan model bliver det herved muligt at simulere og optimere hver skala for sig.

PVA/TiO_2-coatingsprocessen studeres med fokus på at finde årsagerne til, at polymer- og saltopløsninger ikke kan coates under samme betingelser i et fluidiseret leje uden at forårsage signifikant forskellige agglomereringstendenser. Coatingseksperimenter udført under betingelser med forskellige tørringskraft- og forstøvningsniveauer indikerer, at PVA/TiO_2-coatingsprocessen er langt den mest følsomme overfor agglomerering under givne termodynamiske og forstøvningsmæssige forhold. Detaljerede studier viser, at sådanne forskelle mellem de to typer af coatingsopløsninger ikke alene skyldes forskelle i opløsningernes startviskositet eller forskelle i de gennemsnitlige dråbediametre. Forskellene skyldes i højere grad betydelige forskelle i klisterevne, hvilket måles ved hjælp af en speciel klisterevnetest udviklet i nærværende forskning. Det faktum, at PVA/TiO_2-opløsningen er et kolloidsystem, udnyttes til at undertrykke agglomereringstendensen, idet en del af opløsningens indhold af PVA/TiO_2 udskiftes med smøre- og blødgøringsmidlet Neodol 23-6,5 i kombination med, at pH sænkes til en værdi langt fra det isoelektriske punkt. Gennem denne modificering bliver det muligt at opnå en agglomereringstendens tæt på den, der fremkommer under en saltcoatingsprocess udført ved samme betingelser.

Til brug for polymercoatingsprocessen introduceres et klisterstokestal foreslået som en bedre indikation af agglomerering i forhold til det traditionelle viskøse stokestal. Dette nye tal er baseret på det arbejde, der kræves for at nå til maksimal vedhæftningsevne (målt i den førnævnte klisterevnetest), hvorimod det viskøse stokestal baserer sig på viskøs spredningsenergi. Det nye klisterstokestal korrelerer udmærket med de observerede grader af agglomerering, og en lovende detalje er, at der observeres proportionalitet mellem klisterstokestallet og agglomereringsgraden i vægtprocent. Årsagen til denne forbedring konkluderes at være influeret af væskelagstykkelsen på partiklerne under coating. På baggrund af en række forhold sandsynliggøres det, at coatingslagets tykkelse i en polymercoatingsproces er meget lille og samtidigt meget klistret, hvilket igen betyder, at en mulig agglomerering skyldes overfladefænomener på coatingslaget snarere end viskøse fænomener inde i selve væskelaget. Sådanne overfladefænomener konkluderes at kunne forudsiges med god præcision i den udviklede klisterevnetest. Resultater fra polymercoatingsprocessen illustrerer således, at optimeringen af en coatingsproces i et fluidiseret leje bør fokusere på coatingsopløsningens formulering såvel som på procesrelaterede forhold.

Publications from this research

1) Hede, P.D.: Towards *Mathesis Universalis:* Modern aspects of modelling batch fluid bed agglomeration and coating systems – a review, CHEC Report R0605, Department of Chemical Engineering, CHEC Research Centre, Technical University of Denmark, pp. 1 – 101.

2) Hede, P.D., Bach, P. and Jensen, A.D.: Small-scale top-spray fluid bed coating: Granule impact strength, agglomeration tendency and coating layer morphology, Powder Technology, Vol. 176, No. 2-3, pp. 156-167.

3) Hede, P.D., Bach, P. and Jensen, A.D.: Experimental Validation of Macro- and Micro-level Scaling Laws in Small- and Medium Scale Top-Spray Fluidised Bed Coaters; in: Bi, X., Berruti, F. and Pugsley, T. (Editors), Fluidization XII – New Horizons in Fluidization Engineering, Engineering Conferences International, British Columbia, Canada, May 2007, pp. 823-830, ISBN 978-0-918902-57-3.

4) Hede, P.D., Bach, P. and Jensen, A.D.: Validation of the Flux Number as scaling parameter for top-spray fluidised bed systems, Chemical Engineering Science, Vol. 63, No. 3, pp. 815-828.

5) Hede, P.D., Bach, P. and Jensen, A.D.: Top-spray fluid bed coating: Scale-up in terms of Relative Droplet size and Drying Force, Powder Technology, Vol. 184, No. 3, pp. 318-332.

6) Hede, P.D., Bach, P. and Jensen, A.D.: Two-fluid spray atomisation and pneumatic nozzles for fluid bed coating/agglomeration purposes: a review, Chemical Engineering Science, Vol. 63, No. 14, pp. 3821-3842.

7) Hede, P.D., Bach, P. and Jensen, A.D.: Fluidised bed coating with sodium sulphate and PVA/TiO_2. Part I: Review and agglomeration regime maps, Industrial & Engineering Chemical Research, awaiting publication – proof corrected version.

8) Hede, P.D., Bach, P. and Jensen, A.D.: Fluidised bed coating with sodium sulphate and PVA/TiO_2. Part II: Influence of coating solution viscosity, stickiness, pH and droplet diameter on agglomeration, Industrial & Engineering Chemical Research, awaiting publication – proof corrected version.

9) Hede, P.D., Bach, P. and Jensen, A.D.: Fluidised bed coating with sodium sulphate and PVA/TiO_2. Part III: The role of tackiness and the tack Stokes number, Industrial & Engineering Chemical Research, awaiting publication – proof corrected version.

10) Hede, P.D., Bach, P. and Jensen, A.D.: Batch top-spray fluid bed coating: Scale-up insight using dynamic heat and mass transfer modelling, Chemical Engineering Science, Vol. 64, No. 6, pp. 1293-1317.

Table of contents

Chapter 1. General introduction

Chapter introduction

The first chapter contains a general introduction to the Ph.D. thesis. The background and concepts of fluid bed coating is briefly presented followed by an outline of the present challenges and common problems associated with the process. The industrial use of fluid bed granulation processes is briefly touched, outlining the industrial process challenges and needs in light of enzyme containing particles. The research objectives of the thesis are presented and the chapter ends with a short presentation of the structure of the thesis.

1. General introduction

Fluid bed particle coating is a process where coatings are applied to particles. The basic principle is to atomise a liquid into a bed of fluidised particles. The liquid spray typically consists of a solute, which acts as a coating medium, and a solvent in which the solute is dissolved or dispersed. By contacting the core particles the liquid droplets spread and partly penetrate into the core pores. The warm fluidisation air evaporates the solvent, leaving a layer of solute on the surface of the particle. Particle growth can occur by either inter-particle agglomeration or surface layering, commonly known as *coating*. Agglomeration occurs when liquid bridges of coating solution form between colliding particles. If the liquid bridge is strong enough to prevent subsequent particle separation, the liquid bridge solidifies resulting in a permanent agglomerate. In coating processes, agglomeration is generally an unwanted phenomenon, but it may be desired in certain fluid bed processes. Fluid bed coating is explained in further detail in chapter two.

Fluid bed coating is a very flexible process being suitable for many types of cores (including crystals and particles with wide size distributions) and coating materials (i.e. water soluble coatings, suspensions, emulsions, molten waxes, fats etc.) (Jones, 1985 & 1994). The fluidised bed unit is a versatile equipment enabling different unit operations such as drying, cooling, coating or agglomeration to be carried out in the same vessel in a one-step process. Furthermore, the process facilitates some control of final granule properties such as size, bulk density, sphericity and mechanical strength (Ronsse, 2006).

1.1. Common problems encountered in fluid bed processing

With respect to fluidised bed coating, a multitude of problems and side-effects are often encountered of which particle agglomeration perhaps is the most troublesome from an industrial perspective. When wet particles collide during the coating process, a liquid bridge may be formed between them. Depending on the liquid bridge strength and the kinetic energy of the colliding particles, these bridges may persist beyond the point of solidification or drying, and consequently, dry permanent agglomerates are formed (Smith and Nienow, 1983 and Saleh et al., 1999). Depending on the process variables, granule growth due to agglomeration can accelerate beyond a point at which these larger agglomerates can no longer be fluidised. This phenomenon is termed *wet quenching* and should be avoided at all costs. To avoid the side-effect of agglomeration, process operators could increase the kinetic energy of

the fluidised particles, decrease the liquid spray rate or increase the drying capacity of the fluidisation air. However, these measures decrease the overall energy efficiency and increase production time (i.e. if the liquid spray rate is decreased) and hence production costs (Kage et al., 1998, Ronsse, 2006 and Dewettinck & Huyghebaert, 1999).

A second and sometimes serious problem is the issue of spray drying of the coating solution. The exhaust air of a fluid bed coating process is usually not saturated, and consequently premature droplet evaporation is likely to occur before the coating solution droplet adheres onto the core particle surface (Jones, 1985 and Hemati et al., 2003). Depending on the size and the density of the produced fines, the spray-dried coating material could be entrained with the fluidisation air and subsequently collected by the exhaust filter system. In case of heavier dry fines, the spray dried coating material remains in the fluidised bed and is either agglomerated or entrapped within the coating film, resulting in coating imperfections (Smith and Nienow, 1983). Furthermore, the droplets that successfully manage to impinge on the surface of the core particles may have increased viscosity at the moment of impingement due to the high degree of solvent evaporation. As a result, droplet spreading and film-forming abilities are impaired, resulting in improper or raspberry-like coatings characterised by a large number of pores (Link & Schlünder, 1997). Besides the reduced coating quality, spray drying losses increase production costs due to the loss in coating material and the increased processing time required to reach a certain degree of coating (i.e. a certain coating layer thickness) (Gouin, 2005 and Ronsse, 2006).

Premature droplet evaporation is the result of complex interactions between several factors including the evaporative capacity of the fluidisation air within the spraying region, the mean droplet travel distance and velocity, the droplet impingement efficiency and the droplet adhesion probability (Dewettinck & Huyghebaert, 1998 and Heinrich et al., 2003). One of the major factors in controlling the degree of spray drying losses is the reduction of the droplet path length, usually by positioning the nozzle at the surface of the expanded fluidised bed (or even within the fluidised particle bed) in case of top-spray coating processes (see chapter two) (Jones, 1994). Spray drying losses and agglomeration are two side effects occurring at opposite ends of the bed's drying capacity range, which implies that fluidised bed coating is often characterised by a narrow operational regime (Ronsse, 2006).

A third problem commonly encountered in fluid bed coating is attrition and breakage of the coating layers and core particles. The combined fragmentation of core particles and the crumbling of the coating layer by attrition is the result of interparticle and particle-to-wall collisions. Elutriation of the resulting dust debris gives rise to reduced process yields. Furthermore, dust-like particles easily agglomerate with the wet intact core particles, resulting in an end-product with altered properties (Guignon et al., 2002). Attrition depends on the kinetic energy of the particles and on the friability of both the core material and the coating. For example, crystalline materials are more prone to attrition compared to amorphous solids (Liu & Litster, 1993 and Guignon et al., 2003).

Besides the problems resulting from the aforementioned phenomena, a fourth common problem concerns the granule components. Elevated temperatures and humidities often have negative effects on the stability of active biological ingredients (such as enzymes) meaning that loss of product activity during fluid bed coating is a common problem. When applying fluid bed coating to such heat and/or moisture-sensitive products (being in the core and/or in the coating layer), the primary aim is often to keep the product temperature and particle moisture contents below certain threshold values. This schism often conflicts with the nature

of the coating process where liquid is sprayed onto particles and solvent evaporated at high temperatures. With products designed for controlled-release applications a further issue concerns the coating layer thickness. Narrow distributions of the coating layer thicknesses are often required, because small deviations typically alter the release properties (Watano et al., 1995 and Abe et al., 1998).

1.2. Industrial production of enzyme granular products

Originally, fluid bed particle coating was established in the pharmaceutical, food and cosmetic industries, which are able to compensate for the cost of the process by the high price of their final product (Teunou & Poncelet, 2002). Later, other biotech industries such as the enzyme industry began to make use of fluid bed coating processes in larger scales. In industries with high-grade products produced in small batches, the objective will often focus primarily on avoiding agglomeration during coating, and otherwise optimise the granule properties with little attention to the coating process itself. However, in industries with lower grades of bulk granular products produced in several tonnes per hour, other issue such as process intensity, spray drying loss, attrition and breakage may additionally become important issues. Although based on specially-designed high-grade gene-modified organisms, the enzyme industry is an example of an industry with much focus on production cost-cutting. Enzymes are biological catalysts in the form of globular proteins that accelerate chemical reactions, and they are used for many different purposes in a variety of industries. The largest user measured in quantity is the detergent industry followed by the dairy, brewing, baking and agricultural industry (Novozymes, 2004).

Now-a-days enzyme granules are being produced in large plants with coating capacities of several tonnes per hour. Being almost a bulk industry there is a constant pressure on costs and production capacity making all the common problems encountered in fluid bed coating processes relevant. Besides the low-cost requirements for the granulation materials, solid enzyme formulation is further limited by the fact that enzymes are sensitive biological products. The complex enzyme molecules typically lose their structure and thereby their catalytic activity when exposed to high temperature and/or moisture, setting certain boundaries for the fluid bed process conditions as well as for the post-process treatment. The fact that human exposure to enzymatic active dust can result in allergic reactions further sets harsh requirements with respect to granule processing. Industrial enzymes are usually produced by fermentation thereby being in liquid solution, but certain applications and customer traditions require solid enzyme products. Enzymes are formulated into solid products, mainly because the enzyme storage stability is better if the enzyme is in a dry state rather than in a liquid formulation. Enzymes are further incorporated into granules to make them both safer and more convenient to store and use in further mixing with other products such as e.g. detergent granules (Novozymes, 2004). There are several principles in which enzymes can be incorporated into a granule, but basically the enzyme is either incorporated into the granule core or coated onto a spherical filler core. Additional coating is in either case needed to enhance the mechanical properties, colour, density and to improve the storage stability as well as to secure proper release properties when the granule is used.

The most common types of fluid bed coating processes with respect to enzyme granules may be divided into two general categories: Coating with aqueous solutions of inorganic salts (with or without active ingredients) and coating with aqueous solutions of film-forming water-soluble polymers (with or without additional compounds). These types of coating processes have been treated in a number of industrial patents filed by some of the large

enzyme companies such as Genencor International/Danisco (Arnold et al., 1993, Dale et al., 1999 and Becker et al., 2005), Kao Corporation (Kiuchi et al., 1998), Novozymes (Markussen, 1986 & 2002 and Simonsen, 2002), Procter & Gamble (Foley et al., 2003) and Henkel (Paartz et al., 1998).

Salt coatings are typically added together with the enzyme or preferably between the enzyme core/layer and an outer polymer coating layer. The salt layer provides a protective layer towards moisture and bleach components when the enzyme granules are stored in a bleach containing detergent. In one of the first Genencor patents by Arnold et al. (1993) a chlorine scavenger layer such as ammonium sulphate was preferred as the ammonium ion is able to react with chlorine from detergent granules, thereby protecting the enzyme during storage by actively neutralising oxidants. However, due to possible smell of ammonia, modern enzyme granules typically use low-cost compounds as magnesium sulphate or sodium sulphate even though they do not function as chlorine scavengers. These compounds do, however, resemble similar water and H_2O_2 barrier properties, and, furthermore, help to reduce the formation of enzymatic-active dust (Markussen, 2002).

A polymer layer is typically added as the final outer layer in order to provide simultaneous benefits of low dust, colour appearance, moisture barrier properties and controlled release of the enzyme. Typically, water-soluble polymers are used and numerous polymers are commercially applied in enzyme granule coatings including most often polyvinyl alcohol (PVA), polyethylene glycol (PEG), methylcellulose (MC) and methylhydroxy-propyl cellulose (MHPC or HMPC). With only few exceptions, a range of other components are typically added to the aqueous polymer solution including plasticizers, lubricants and pigments functioning as anti-agglomerating agents (van Ee et al., 1997 and McGinity, 1997). More information about the polymer and salt coating processes may be found in chapter ten.

A typical enzyme granule has a diameter of 300 to 1200 µm with an average diameter around 500 µm and a coating layer thickness usually in the range of 5 to 20 µm (Novozymes, 2004 and Jørgensen, 2002). Figure 1.1 and 1.2 show some typical structures of commercial enzyme granules with both main types of coating layers. Whereas the Enzoguard® granule in figure 1.1 is made solely by successive fluid bed coatings on inactive sugar or starch cores, the enzyme-containing inner core in the Novozymes granule in figure 1.2 is made in a high shear mixer followed by successive fluid bed coatings.

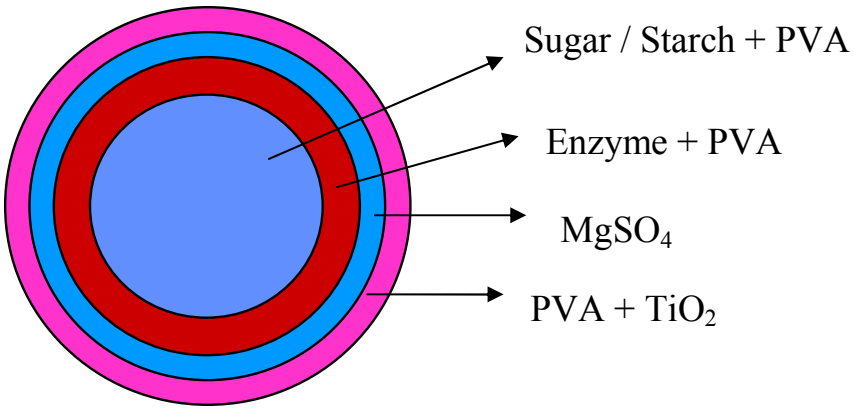

Figure 1.1: The structure of a commercial Danisco/Genencor Enzoguard® granule (Dale et al., 1999). Figure not to scale.

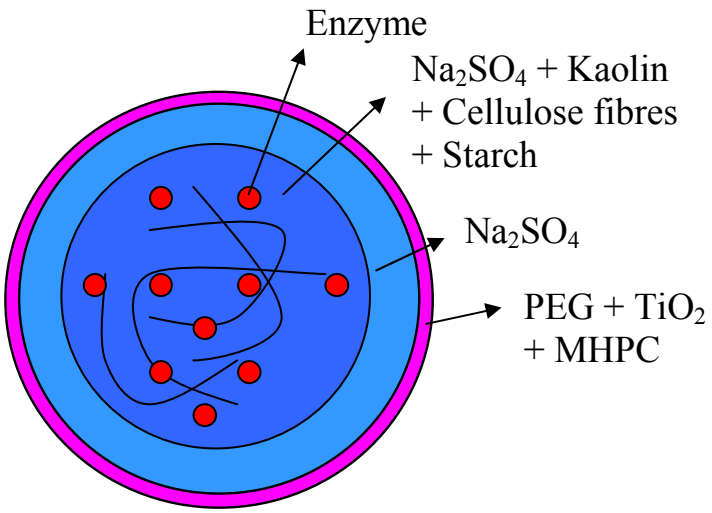

Figure 1.2: The structure of a commercial Novozymes granule (Simonsen, 2002 and Markussen, 1986 & 2002). Figure not to scale.

The enzyme content of commercial granules typically varies between 1 and 10 w/w%, meaning that the major part of an enzyme granule consists of inactive filler, binder and coating materials (Kringelum, 2002 and Härkonen, et al., 1993). The binder material is often a water-soluble polymer, but also starch is commonly used. Salts, clay, cellulose fibres, sugar, starch and other materials can be used as fillers in amounts of up to 50 w/w% (Härkonen, et al., 1993). Inactive filler cores usually consist of sugar, salts or starch (Jørgensen, 2002). A variety of materials can be used for coatings including gums, carbohydrates, celluloses, lipids, proteins, inorganic salts and polymers (Jackson & Lee, 1991). The coating material is generally dissolved in water at a low concentration prior to the coating process to form a coating solution of typically 0.5 to 30 w/w% (Teunou & Poncelet, 2002). Because of environmental concerns regarding the use of organic solvents, water is used extensively as solvent even though it might not be the optimal choice in a chemical or energy consumption sense (Rubino, 1999).

1.3. Fluid bed coating objectives and challenges in the enzyme industry

The engineering exercise in the enzyme industry is often to optimise the process and formulation conditions to the best possible trade-off between the desired target parameters. The general objectives in fluid bed coating processes are mainly focussed on the ability to be able to:

- Perform the coating process (at the unit-operation-level) in a fast (high-intensity), well-controlled (high-yield), reproducible and low-cost manner.
- Avoid/control the tendency of agglomeration during the coating process.
- Avoid/reduce premature coating solution droplet drying.
- Avoid/reduce attrition and breakage of the core particles and coating layers.
- Maintain as much of the original enzyme concentrate activity as possible during processing.
- Encapsulate the coated granules (at the particle-level) homogenously in order to obtain granules with even coating, good appearance, storage stability (long shelf life), mechanical properties and controlled-release/dissolution properties.

These objectives are not easily all met at once, and inevitably there is a trade-off between these performance indicators, because e.g. high yield, low production costs and short production times are only ideal optimums. The actual optimum will vary based on the product and its application. For example, the continuous focus on low-cost products will necessitate cheaper raw materials and higher product throughputs. This is likely to compromise some aspects of product quality.

Fluid bed coating has been slow to develop in the enzyme industry. This is not surprising given the economic constraints for low-cost ingredients and low-cost, high volume processing where every cent of additional cost per kilogram of product is important. This, however, means that only limited and application-specific information regarding specific fluid bed coating techniques, including optimum processing conditions, are available in the literature. To a large extent, process control of fluid bed systems is still empirically based. There is still a lack of quantitative understanding of the mechanisms in fluid bed coating, and one of the problems is the missing link between the particle-level (also known as the *micro-level*) and the unit-operation-level (also known as the *macro-level*) of the coating process, i.e. there is a limited understanding of how process changes at the unit-operation-level (e.g. a change in nozzle pressure or in fluidisation velocity) affect the coating system at the level of the individual particles (e.g. agglomeration tendency or coating layer morphology). This is mainly due to the fact that particle processing is a difficult unit-operation. To some extent, particles may be considered as a fourth state of matter as they are able to take on the behaviours of one or more of the other states. Depending on size, particles may e.g. develop cohesive strength and transfer shear stresses among the particles as a true solid. Likewise will most particles demonstrate significant compressibility like a gas and behave liquid-like when being fluidised. What further adds to the complexity of particle processing is the fact that the final granule properties are dependent on any of the events that the granule has ever experienced (Merrow, 2000 and Bell, 2005). Furthermore, the composition inside a fluid bed is heterogeneous as particle mixing is chaotic and non-uniform. This means that if a small element of the fluidised bed at an arbitrary point is considered, vital variables such as: fluidisation air temperature and humidity, particle temperature, particle moisture contents and particle size distribution remain unknown or difficult to measure. Fluid bed systems are thereby hard to understand and model, and thereby to fully characterise.

The gap in understanding between the unit-operation-level and the particle-level also become pronounced in a scale-up context. Proper scale-up from laboratory-scale to full production-scale is still the major industrial challenge. Often, the behaviour of large-scale fluid beds differs significantly from the lab-scale behaviour, which is an obstacle for the testing and development of industrial applications. One example is the faster rise of bubbles in large-scale fluid beds, which results in less exchange with the particle phase and poor particle mixing. Due to this scale dependence, the study of pilot-scale trials is often required as an intermediate step between lab- and production-scale. This additional step serves to avoid unexpected effects at the large-scale as direct scaling from lab-scale to industrial scale is still very risky.

With respect to fluid bed coating processes in the enzyme industry, the most important challenges may be summed up as:

- Be able to predict a-priori the tendency of agglomeration based on process and coating formulation conditions.

- Be able to predict a-priori the mechanical properties of the final coating layer based on process and coating formulation conditions.
- Be able to scale-up the fluid bed coating process correctly in order to maintain particle properties (especially a low agglomeration tendency and good mechanical properties) as well as match unit-operation-level variables such as process intensity and coating mass yield across scale.
- Develop a useful modelling approach that will make it possible to gain further insight into the fluid bed coating process preferably making it possible to simulate the process, and thereby to a lesser extent be dependent on experimental data.

1.4. Research objectives

The focus of this Ph.D. thesis is on the fluid bed coating process in terms of scale-up and process optimisation. The aim is to contribute to the fundamental understanding of the coating process hereby indentifying the important variables and parameters being involved. The main objectives of the research work are:

- Identification, characterisation and classification of particle- and process-related phenomena influencing fluid bed coating process up-scaling from small-scale to production-scale fluid beds. This is done with special focus on being able to avoid agglomeration, and at the same time be able to reproduce the particle size distribution and granule mechanical properties across scale during the salt coating process.

- Conduct a survey of available mathematical modelling methods (e.g. black-box models, Population Balance models and Discrete Element Models (DEM)) in order to explore the usefulness of such model approaches in the perspective of industrial fluid bed coating processes.

- Apply and study selected mathematical models and approaches by holding them up against experimental data thereby providing quantitative as well as qualitative experience and knowledge of their applicability and validity.

- Provide suggestions and general guidelines for fluid bed coating process optimisation and scale-up.

Through research in all of the above mentioned subjects the overall aim of the Ph.D. thesis is to achieve a better understanding - qualitatively as well as quantitatively - of the different phenomena influencing fluid bed coating processes. A combined experimental and theoretical approach to the investigations is taken, and although working solely with placebo enzyme granules, the research work has a clear connection to commercial enzyme granules. Emphasis is put on attaining results that may have academic interest, but also may be exploited industrially.

1.5. Outline of the thesis

The thesis consists of twelve consecutive chapters. Chapter two, three and four are literature studies treating, respectively; fluid bed coating and fluidisation fundamentals, granulation modelling approaches, and scale-up of the fluid bed granulation process. The experienced reader may consider to skip these chapters or simply to read the summaries at the end of each chapter.

Chapter five concerns the materials and equipment used in the research work, and chapter six to ten present experimental and modelling results from the conducted research. The five experimental chapters are based on the original manuscripts from scientific papers being either already published in scientific journals or currently under review. In order to get a quick overview of the research work, the reader may consider reading the original abstracts and conclusions at, respectively, the beginning and end of each of the five chapters. Chapter eleven contains the final overall conclusion of the thesis. The thesis ends in chapter twelve with a presentation of general engineering guidelines and considerations relevant for future process optimisation and scale-up. Some suggestions for future work are furthermore stated.

As there is no uniform agreement in the scientific literature it is necessary to clarify the use of certain terms in the present thesis. The term *particle* refers loosely to a solid material of uniform or non-uniform composition of a certain size. If the particles have sizes in the range of a few microns the term *powder* may additionally be used. The term *granule* is on the other hand used more firmly to characterise a particle that has undergone some sort of treatment so that is has a non-uniform composition, e.g. by consisting of different coating layers. The term is thereby used as a generic term for both coated particles and agglomerates. Likewise is *granulation* used throughout this thesis as a joint designation for both coating and agglomeration processes.

1.6. References

Abe, E., Yamada, N., Hirosue, H. and Nakamura, H. (1998) Coating mass distributions of seed particles in a tumbling fluidized bed coater, Powder Technology, No. 97, pp. 85-90.

Arnold, R.E., Becker, N.T., Boston, M.G., Mansikkamaki, A., and Wendt, D.J. (1993) Coated Enzyme Containing Granule, International patent WO 93/07263, Genencor International.

Becker, N.T., Flynn, M.J. and Gebert, M.S. (2005) Particle with substituted polyvinyl alcohol coating, United States Patent US 6,872,696, Genencor International Inc.

Bell, T.A. (2005) Challenges in the scale-up of particulate processes – an industrial perspective, Powder Technology, No. 150, pp. 60-71.

Dale, D.A., Gaertner, A.L., Park, G. and Becker, N.T. (1999) Coated enzyme-containing granule, United States Patent US 5,879,920, Genencor International Inc.

Dewettinck, K. and Huyghebaert, A. (1998) Top-spray fluidized bed coating: Effect of process variables on coating efficiency. Lebensmittel-Wissenschaft und Technologie, Vol. 31, pp. 568-575.

Dewettinck, K. and Huyghebaert, A. (1999) Fluidized bed coating in food technology. Trends in Food Science and Technology, Vol. 10, pp. 163-168.

Foley, P.R., Painter, J.D., Leyendecker, M.R., Sadlowski, E.S., Song, B.X. and Thien, J.H. (2003) Enzyme composite particles having an acidic barrier and a physical barrier coating, United States Patent US 6,656,898, The Procter & Gamble Company.

Gouin, S. (2005) Fluidized bed microencapsulation: Thermodynamics of aqueous and ethanolic coating processes. Journal of Microencapsulation, No. 22, pp. 829-839.

Guignon, B., Duquenoy, A., Dumoulin, E.D. (2002) Fluid bed encapsulation of particles: principles and practice. Drying Technology, No. 20, pp. 419-447.

Guignon, B., Regalado, E., Duquenoy, A., Dumoulin, E. (2003) Helping to choose operating parameters for a coating fluid bed process. Powder Technology, No. 130, pp. 193-198.

Härkönen, H. , Koskinen, M. , Linko, P. Siika-aho, M. and Poutanen, K. (1993) Granulation of Enzyme Powders in a Fluidized Bed Spray Granulator, Lebensmittel-Wissenschaft und Technologie, Vol. 26, pp. 235-241.

Heinrich, S., Blumschein, J., Henneberg, M., Ihlow, M., Peglow, M. and Mörl, L. (2003) Study of dynamic multi-dimensional temperature and concentration distributions in liquid sprayed fluidized beds. Chemical Engineering Science, Vol. 58, pp. 5135-5160.

Hemati, M., Cherif, R., Saleh, K. and Pont, V. (2003) Fluidized bed coating and granulation: influence of process-related variables and physicochemical properties on the growth kinetics. Powder Technology, No. 130, pp. 18-34.

Jackson, L.S and Lee, K. (1991) Microencapsulation and the Food Industry, Lebensmittel-Wissenschaft und Technologie, Vol. 24, pp. 289-297.

Jones, D.M. (1985) Factors to consider in fluid-bed processing. Pharmaceutical Technology, Vol. 9, pp. 50-62.

Jones, D. (1994) Air suspension coating for multiparticulates. Drug Development and Industrial Pharmacy, Vol. 20, pp. 3175-3206.

Jørgensen, K. (2002) Design of a Shear and Impact Resistant Enzyme Granule, M.Sc. Thesis, Department of Chemical Engineering, Technical University of Denmark.

Kage, H., Takahashi, T., Yoshida, T., Ogura, H., Matsuno, Y. (1998) The coating surface and agglomeration of seed particles in a fluidized bed coater. Advanced Powder Technology, Vol. 9, pp. 245-259.

Kiuchi, T., Kohtaro S., Sato, M., Kawamura, J. and Yamada, N. (1998) Enzyme-containing granulated substance and preparation process thereof, United States Patent US 5,851,975, Kao Corporation.

Kringelum, J. (2002) Measurement and modelling of water sorption kinetics of enzyme granules. M.Sc. Thesis, Department of Chemical Engineering, Technical University of Denmark.

Link, K.C. and Schlünder, E.-U. (1997) Fluidized bed spray granulation. Investigation of the coating process on a single sphere. Chemical Engineering and Processing, Vol. 36, pp. 443-457.

Liu, L.X. and Litster, J.D. (1993) Spouted bed seed coating: the effect of process variables on maximum coating rate and elutriation. Powder Technology, No. 74, pp. 215-230.

Markussen, E.K. (1986) Enzyme containing granulates suitable for use as detergent additives, European Patent EP 0 170 360 B1, Novo Industri A/S.

Markussen, E.K. (2002) Enzyme containing granule, United States Patent US 6,348,442, Novozymes A/S.

McGinity, J.W. (1997) Aqueous polymeric coatings for pharmaceutical dosage forms, Marcel Dekker Inc. New York, 2nd edition.

Merrow, E.W. (2000) Problems and progress in particle processing, Chemical Innovation, No. 1, pp. 35-41.

Novozymes (2004) Enzymes at work, Novozymes A/S.

Paatz, K., Rähse, W., Pichler, W., Upadek, H. and Kühne, N. (1998) Multi-enzyme granules, United States Patent US 5,846,798, Henkel Kommanditgesellscahft auf Aktien.

Ronsse, F. (2006) Modelling heat and mass transfer in fluidised bed coating processes, Ph.D. Thesis, Ghent University.

Rubino, O.P. (1999) Fluid-Bed Technology. Overview and Criteria for Process Selection, Pharmaceutical Technology, No. 23, pp. 104-117.

Saleh, K., Steinmetz, D. and Hemati, A. (2003) Experimental study and modeling of fluidized bed coating and agglomeration. Powder Technology, No. 130, pp. 116-123.

Simonsen, O. (2002) Lubricated Granules, International Patent WO 02/20746 A1, Novozymes A/S.

Smith, P.G. and Nienow, A.W. (1983) Particle growth mechanisms in fluidized-bed granulation. I. The effects of process variables. Chemical Engineering Science, Vol. 38, pp. 1223-1231.

Teunou, E. and Poncelet, D. (2002) Batch and continuous fluid bed coating – review and state of the art. Journal of Food Engineering, No. 53, pp. 325-340.

van Ee, J.H., Misset, O. and Baas, E.J. (1997) Enzymes in Detergency, Surfactant Science Series, Volume 69, Marcel Dekker, New York, 2nd Edition.

Watano, S., Sato, Y., Miyanami, K., Murakami, T., Nagami, N., Ito, Y., Kamata, T. and Oda, N. (1995) Scale-up of agitation fluidized bed-granulation. II. Effects of scale, airflow velocity and agitator rotational speed on granule size, size distribution, density and shape. Chemical and Pharmaceutical Bulletin, No. 43, pp. 1217-1220.

Chapter 2. Fluid bed coating and fluidisation fundamentals

Chapter introduction

Fundamentals of fluidisation and fluid bed coating are the subjects for chapter two. First, the working principle of fluid bed coating and types of fluid beds are introduced. Next the spraying of liquid using two-fluid nozzles is presented with focus of nozzle operations both in theory and practice. Finally, fluidisation of particles is presented by introducing both fundamental parameters and basic principles of heat and mass transfer in fluid beds. All of these subjects are prerequisites for understanding the nature of the fluid bed coating process. The subjects covered in this chapter are large scientific fields with many years of theoretical and practical development. This thesis does not allow an in-depth historical review. Instead it has been the aim to present relevant theories, which will form the background for the following chapters where more advanced theories and principles are treated.

The first part of the chapter is mainly based on the paper: *Two-fluid atomisation and pneumatic nozzles for fluid bed coating purposes: a review* (referred to as Hede et al., 2008c) published as a peer-reviewed scientific paper in the journal *Chemical Engineering Science*, Vol. 63, No.14, pp. 3821-3842, 2008, whereas the last part of the chapter is mainly based on the paper: *Batch top-spray fluid bed coating: Scale-up insight using dynamic heat and mass transfer modelling* published as a peer-reviewed scientific paper in the journal *Chemical Engineering Science*, Vol. 64, No.6, pp. 1293-1317, 2009 (referred to as Hede et al., 2008g). Both papers are authored by Peter Dybdahl Hede (Technical University of Denmark), Poul Bach (Novozymes A/S) and Anker D. Jensen (Technical University of Denmark).

2. Fluid bed coating and fluidisation fundamentals

Fluidised bed coating is often referred to as a one-step enclosed system as the elementary steps of the process occur in the same chamber. Fluidisation and mixing of the solid bulk are provided by an upward hot airflow causing the fluidised bed of particles. Each of the particles forming the bed will experience a vertical cyclic transport as the particles are lifted by the fluidisation air to a certain height, after which the particles lose velocity and fall back into the upward air stream (see figure 2.3). Fine droplets of coating liquid are simultaneously distributed by the nozzle and sprayed onto the particle bed. Typically, only a minor fraction of the particle bed is exposed to the spray meaning that each particle, during its vertical transport cycle, will experience a period of wetting (in the spray zone) and period of drying (outside the spray zone). With time this will result in a gradual deposition of coating material on the particle surface in the end leading to a complete encapsulation of the particle core in a shell-layer structure. This principle of fluid bed coating is visualised in figure 2.1.

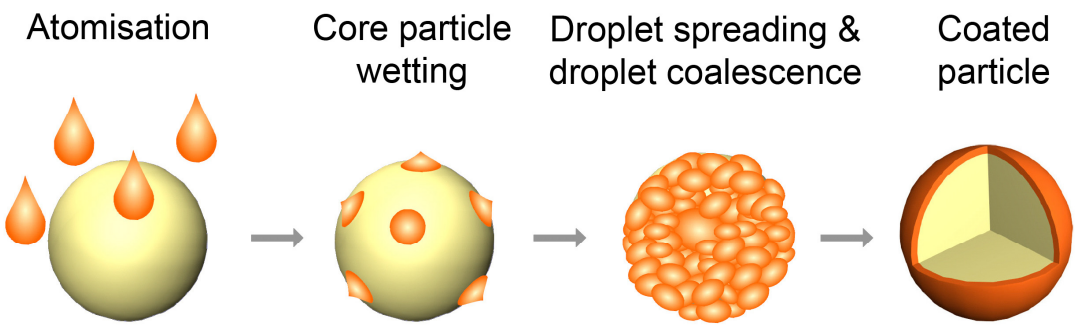

Figure 2.1: The principle of fluid bed coating (Glatt, 2008).

During the formation of the coating layer there is a certain probability that two wetted particles may collide. Upon collision a liquid bridge can be built between the particles. Depending on the properties of the droplet and fluidisation conditions among other things, this coalescence may either be temporary or permanent. If the liquid bridge is strong enough to resist the particle motion, the subsequent drying caused by the hot fluidisation air will turn the liquid bridge into a solid bridge, which typically is mechanically much stronger than the liquid bridge (Iveson et al., 2001a). In that case, an agglomerate is formed and more particles may be added as the agglomerate is wetted by new droplets. Agglomeration may continue until a point where growth is counteracted by breakage due to insufficient liquid bridge strength (Turchiuli et al., 2005 and Iveson et al., 2001a). Agglomeration is unwanted in a coating situation, but may be exploited in other fluid bed operations where typically particles of smaller or similar sizes to those of the droplets are agglomerated into larger granules. The principle of fluid bed agglomeration is visualised in figure 2.2.

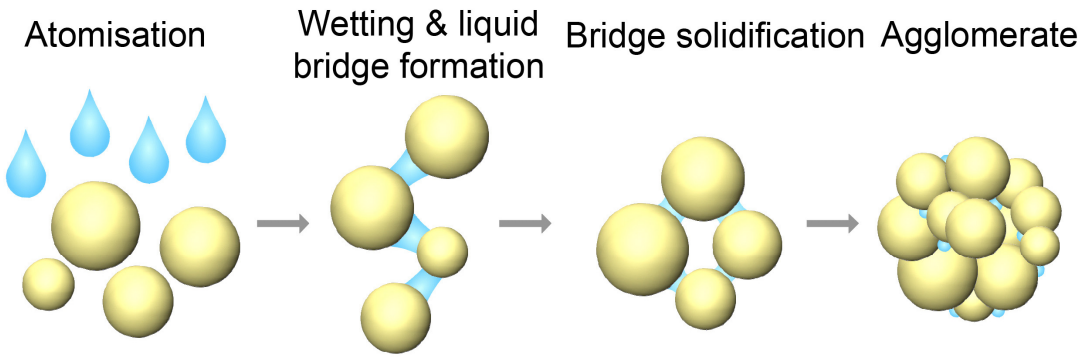

Figure 2.2: The principle of fluid bed agglomeration (Glatt, 2008).

Whether or not the fluid bed granulation process will result in agglomeration, such as in figure 2.2, or in a pure coating situation, such as in figure 2.1, depends on a variety of equipment design, operation and physical/chemical parameters and properties. Hede (2005) has listed more than 40 parameters that all, one way or the other, are involved in the outcome of the fluid bed granulation process. Knowledge about the nature of particle fluidisation as well as the production and behaviour of coating droplets are essential parts in the understanding of the underlying phenomena involved the process, and the complex way in which these numerous parameters interact. Before these subjects are presented, a brief introduction to fluid bed coating equipment will be given.

2.1. Types of fluid bed coating equipment

The concept of coating and/or agglomerating small particles is not limited to fluidisation of the particles. According to Salman et al. (2007), there are two other main types of wet-granulation equipment besides fluid beds being: tumbling granulators (drum or pan granulators) and high shear mixer granulators. This classification is based on the way the particles are agitated. In high shear mixing, the motion of particles is brought about by agitators rotating at low or high speed, ranging from 50 – 3000 revolutions per minute, on a vertical or horizontal axis (Rhodes, 1998). Due to the high mechanical impact on the material, high shear mixer granulators are typically used for sticky materials as they can spread viscous liquids and produce small high-density granules. When high shear mixing is used for coating purposes, the resulting granules consist of a matrix of the coating material rather than of an outer coating layer. In tumbling drum and pan granulators the particles undergo rolling motion in and out of the spray zone by continuously rotating the equipment. Whereas pan coating typically is a batch process, drum granulation may be operated continuously hereby becoming capable of handling large throughputs. The tumbling motion gives rise to a natural classification of the contents according to size, and problems with particle-size-dependent coating distribution is a typical problem with tumbling granulators. Tumbling granulators are typically used for bulk chemicals such as fertilizer and iron ore, as the principle gives product variances too large for the pharmaceutical and food industries. As neither the high shear mixer nor the tumbling granulators offer the same heating (drying) and cooling capabilities as the fluid bed, granules produced in either of the two equipments are often post-processed in a fluid bed. Further information about the alternative main types of granulation equipment may be found in Rhodes (1998) and Salman et al. (2007).

Fluid bed granulation is in many ways different from other types of granulators because the particles are set in motion by an upward flowing gas, which is also responsible for the coating solvent evaporation and heating of the particles. The advantages over the other types of granulators include good heat and mass transfer, temperature homogeneity, mechanical simplicity and the fact that all the stages of granulation (heating, coating, drying, cooling) can be performed in the same equipment, hereby saving time, particle transfer losses and labour costs (Summers & Aulton, 2002). Another advantage is that the particle size distribution of the final granules typically is more narrow and easier to control in fluid beds compared to other types of granulators. This means that granules can be tailor-made to a large extent (Salman et al., 2007).

Fluid beds used for agglomerating or coating are classified according to the nozzle position (top, bottom or side) and to the operating conditions (continuous or batch) (Guignon et al., 2002). Batch fluid bed granulators typically have a cylindrical or conical shape. Fluidisation air is distributed upwards through a bottom grid with an adequate distribution and size of holes. Small-scale fluid beds typically have only a single nozzle, but larger production–scale fluid beds can have more than a few dozen nozzles (Guignon et al., 2002). In general, there are four basic types of batch fluid bed granulation systems as sketched in figure 2.3.

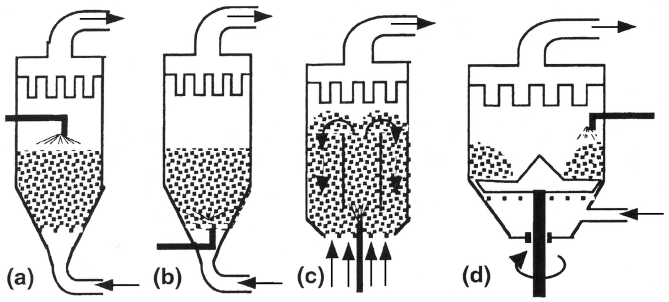

Figure 2.3: Different basic types of batch fluid beds: a) Top-spray, b) Bottom-spray, c) Wurster type, d) Rotor with tangential spray (Teunou & Poncelet, 2002).

Top-spraying is the oldest and simplest technique with the nozzle placed at the top of the chamber thus spraying counter-currently onto the fluidised particles. Particles as small as 100 μm have been coated in top-spray systems. However, controlling the distance the droplets travel before impacting the core particles is difficult due to the vigorous and random particle fluidisation (Jones, 1988a,b and Ronsse, 2006). Consequently, premature droplet evaporation can be severe leading potentially to spray drying loss of the coating solution. Generally, granules prepared by top-spray have a looser structure and are more porous than granules prepared from other types of fluid beds (Rubino, 1999). The top-spray system is still widely used for protective coatings and to a larger extent for agglomeration purposes, but for high-quality controlled-release coating it is now often replaced by bottom-spray or the Wurster type (Teunou & Poncelet, 2002).

The chance of collision between particles and liquid droplets are considerably increased with the use of the bottom-spray type. Introducing liquid from the bottom gives a shorter distance between the nozzle outlet and the particle bed, thereby reducing the risk of premature droplet drying. This leads in general to a larger coating efficiency. This type of fluid bed is very efficient for coating processes, but the risk of unwanted agglomeration during coating is higher than in a top-spray due to the higher concentration of wet particles in the spray zone (Teunou & Poncelet, 2002). Bottom-spray systems are seldom used without the hollow-cylinder insert known as the *Wurster-type* (Rubino, 1999).

Work by Wurster in the fifties led to an improvement of the bottom spray bed known as the *Wurster system*. By inserting a fixed hollow cylinder into the chamber, the circulation of the particles is better controlled and the drying rate increased, reducing the risk of agglomeration. The coating chamber contains an unbaffled, open-end cylinder known as the *partition*. Typically, the size of the gap between the partition and the air distributor plate is adjustable. Whereas the simple top-spray and bottom-spray typically have holes of similar sizes distributed equally over the distributor plate area, the inner section of the air distributor plate in the Wurster set-up, corresponding to the cross-sectional area of the partition projected onto the plate, is provided with large-diameter holes compared to the outer section of the plate. Consequently, a higher portion of the volumetric fluidisation airflow goes through the partition. Particles entering the central partition are hereby pneumatically transported through the partition (Jones, 1988a and Ronsse, 2006). Once the particles have exited the central partition they fall back along the outer section of the fluidisation chamber, where the fluidisation airflow rate is much lower due to the design of the air distributor plate. The particles hereby experience a cyclic pattern of movement. The contact between droplets and particles is established in the partition by placing the nozzle in the centre of the air distributor plate spraying concurrently to the particles (Ronsse, 2006). Originally designed to coat

pharmaceutical tablets, this fluid bed type is particularly suited for coating particles as small as 50 µm (Teunou & Poncelet, 2002). Compared to the top-spray fluid bed, the Wurster fluid bed produces coating films of greater uniformity and with fewer imperfections. Often very dense and homogenous coating films are made by Wurster coating. This is explained by the fact that the particle motion is controlled to a higher extent, i.e. the number of vertical cycles and the time spent during each passage through the spray zone, as opposed to the top-spray configuration where particle motions are more random and uncontrolled. Furthermore, droplets are deposited concurrently, assuring a minimum droplet travel distance and thereby an almost absence of premature droplet drying (Ronsse, 2006).

A fourth type of fluid bed is known as the *rotor system*. The chamber consists of a disc rotating in the bottom of the fluidisation chamber, and the coating solution is sprayed tangentially and concurrently from one of several nozzles. A narrow gap exists between the chamber wall and the rotating disc through which the fluidisation air is introduced. The particle motion pattern results from the combination of the lift force created by the upward flowing fluidisation air, gravity, and the friction force created by the rotating disc. The combination of rotation and bottom-up airflow provides specific particle properties such as a high degree of spherical shape and high density of the coated particles. This type of fluid bed system is mainly used for coating, although the coating quality is similar to that obtainable with the Wurster type (Teunou & Poncelet, 2002 and Jones, 1988b).

Batch fluid beds are used industrially in various scales ranging from bed load capacities of 0.1 kg up to several tonnes. Mainly due to high investment costs, the simplest top-spray design is still in use for modern granular products, and optimisation of the top-spray fluid bed coating process is still ongoing. In an attempt to automate the coating process, the ever-growing need to cut production costs and to increase the capacity throughput has prompted the design of continuous fluidised bed coating systems of which the horizontal design is the most common as shown in figure 2.4 (Rümpler & Jacob, 1998). Particles in this design are admitted to the chamber at one end from which they move slowly through the chamber until the particles exit at the other end. Some horizontal fluid beds for particle agglomeration are vibrating fluid beds with a conveying belt, whereas the particle transport is provided solely by fluidisation air in other designs (Teunou & Poncelet, 2002).

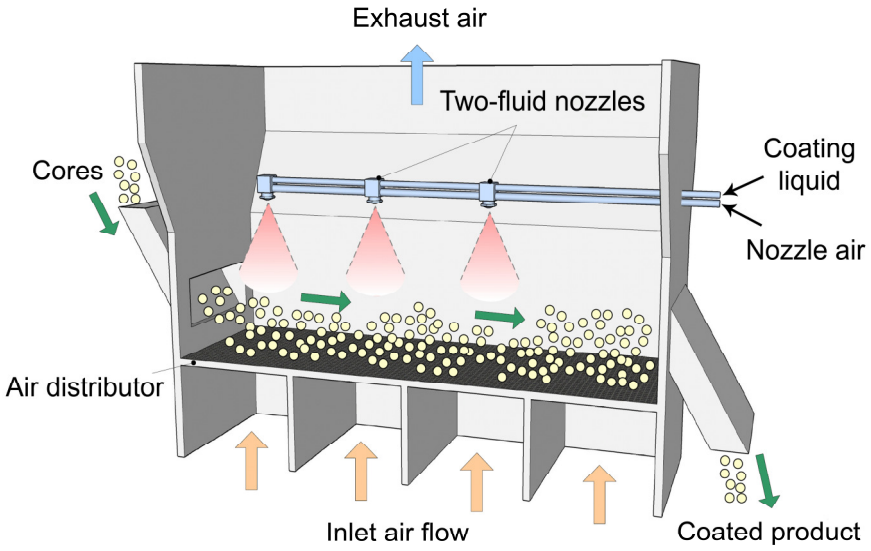

Figure 2.4: The principle of a horizontal continuous fluid bed coater (Based on Ronsse, 2006 and Rümpler & Jacob, 1998).

Compared to batch fluidised beds there is an additional difficulty of continuous fluidised bed coaters in terms of coating uniformity, and the fact that the coating layer thickness depends on the residence time of the particle in the bed. This problem is especially aggravating when dealing with polydisperse particles. Typically several meters of length are required to allow the necessary residence time to obtain a proper coating. To overcome some of this, vertical baffles are sometimes inserted into the fluidisation chamber to increase or to improve control of the particle residence time, and thus to reduce the required length of the horizontal fluidised bed (Teunou and Poncelet, 2002). The continuous fluid bed system may in principle be built into a single unit capable of heating, coating and afterwards drying the particles. It further offers the advantage of being able to successively coat particles with multiple coating materials in different zones in one continuous step. Continuous fluid bed operations require large throughputs, such as in the food and diary industries, in order to be economically feasible. For high-grade fluid bed granulated products in the biotech industries, batch fluid bed systems are still the preferred choice. Other issues concerning the use of continuous fluid bed systems have been reviewed by Teunou & Poncelelet (2002).

2.2. Two-fluid atomisation

Besides the position of the nozzle in the fluidisation chamber, the type of atomisation characteristic is a vital part for the fluid bed coating process. Atomisation is the principle of producing droplets by impacting a bulk liquid with high velocity gas. The mechanism is that a high velocity gas creates high frictional forces over a liquid surface causing liquid disintegration into droplets. Liquid disintegration in the presence of gaseous flow involves complex situations of liquid instability, but the overall process can be considered to occur in two phases. The first phase involves the tearing of the liquid into filaments and large droplets. The second phase completes the atomisation by further breaking these liquid forms into smaller and smaller droplets. The entire process is influenced by the magnitude of the liquid properties such as surface tension, density and viscosity, and the gaseous flow properties such as velocity and density (Spray Drying Systems Co., 2000). Gaseous media used in pneumatic nozzle atomisation in the context of fluid beds is most often air, but steam may also be used (Masters, 1972).

During atomisation a high relative velocity difference between liquid and air must be generated so that liquid is subjected to optimum frictional conditions. These conditions are generated by either expanding the air to sonic or super-sonic velocities prior to contacting the liquid, or by directing the airflow onto unstable thin liquid sheets formed within the nozzle. According to common nomenclature, the term *liquid sheet* is used both for a flat and for a thin cylindrical jet. (Lefebvre, 1989a). High velocity air can typically readily penetrate a low velocity liquid jet thereby causing the necessary turbulence and energy transfer to form a spray of narrow angle. However, at larger liquid feed rates even high velocity air cannot penetrate the thick liquid jets involved. In such case the connected jet of liquid is simply accelerated by the air so rapidly that the liquid acquires the air velocity, minimising the shear forces between liquid and air (Masters, 1972 and Schick, 2006). Atomisation is thus incomplete, and the result is a wide droplet size distribution. A high percentage of liquid remains in the center of the spray as a connected jet, and is ejected far into the particle bed, significantly increasing the chance of particle bed collapse due to the particle contact with partly or unatomised liquid. At such high liquid feed rates the liquid bulk must first be formed into thin sheets to assist liquid instability, effective air-liquid contact and break-down of liquid into ligament forms or individual droplets. Ineffective atomisation is the outcome

unless the sheet formation or liquid feed prefilming takes place even at extreme air velocities. The principle of the atomisation process may be seen from figure 2.5.

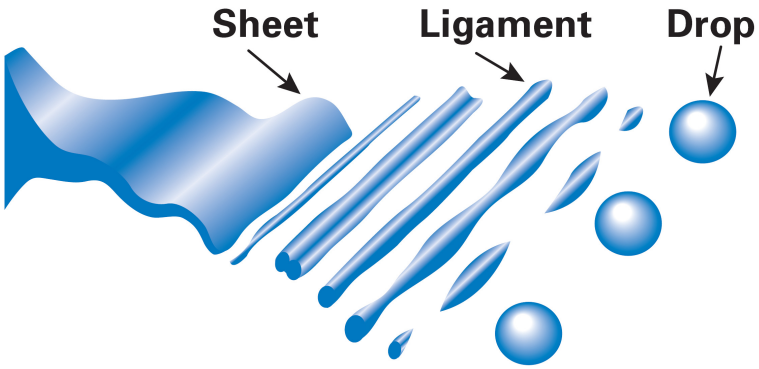

Figure 2.5: The process of atomisation begins by forcing liquid through a nozzle and directing an atomisation airflow onto it. In this process, the liquid is typically formed into liquid sheets that will break up into ligaments. These ligaments then break up further into very small "entities", which are usually called *drops*, *droplets* or *liquid particles* (Schick, 2006).

2.2.1. Two-fluid nozzle designs

There are various nozzle designs and sizes available to create optimum conditions of liquid-air contact for atomisation. The types of interest to fluid bed granulation fall into a category commonly known as *airblast atomisers* (Lefebvre, 1989a). For the most commonly used designs, the contact between liquid and gas phase takes place at the nozzle exit. This principle is known as *external mixing*. In other airblast designs, the liquid is injected into the high-velocity airstream in the form of one or more discrete jets. This principle is commonly known as *plain jet* or *internal mixing* atomisation (Ayres et al., 2001, Lefebvre, 1989a and Lefebvre, 1996). The design principles of internal and external two-fluid nozzles may be seen from figure 2.6.

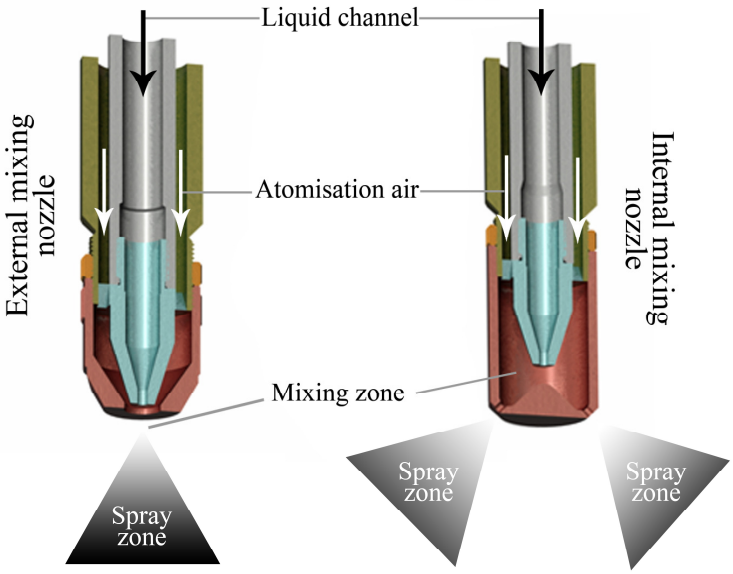

Figure 2.6: Examples of two-fluid nozzle designs. Left: Simple external mixing nozzle. Right: Simple internal mixing nozzle (based on Salman et al., 2007).

Both internal and external mixing nozzles can be prefilming nozzles. The principle behind prefilming nozzles is that the liquid is first spread out into a thin continuous sheet and then subjected to the atomising air. This is known to give the best control of the droplet size distribution (Masters, 1972). In general, the atomisation performance of such prefilming nozzles (being internal or external mixing), is superior to that of simple designs, but they are only really effective when both sides of the liquid sheet are exposed to the gas stream. This requirement gives complications in the physical design, which is one of the reasons why there are numerous prefilming nozzle designs available, but only few being used commercially (Niro, 2007).

There is some overlap with respect to performance for the internal and the external mixing two-fluid nozzles, and the choice between the two types is often based on several things. All two-fluid nozzles have either limited gas flow rates, high specific gas consumption, modest liquid capacities, a wide droplet size distribution or a combination of these limitations (Lefebvre, 1989a). Internal mixing nozzles require in general less air than external mixing nozzles in order to produce droplets with the same mean droplet diameter. This is due to a higher energy transfer between the air and the liquid as the atomisation takes place under pressure difference inside the mixing chamber, because the air and liquid pressures become equal first at the mixing chamber outlet (Hund, 1994). This is especially an advantage during nozzle scale-up where the required increase in gas-to-liquid flow rate with scale is much less than for external mixing nozzles (Lefebvre, 1989a,b). The downside is, however, that over time, the impact surface in the mixing zone becomes eroded and affects the spray droplet size pattern. The lifetime of an internal mixing nozzle can be very short if the liquid has solid impurities in it. Only few authors have used two-fluid nozzles with internal mixing in a fluid bed granulation context. In studies by Smith & Nienow (1982 & 1983) the nozzle was placed in the bottom of the bed and it was possible to avoid caking of the nozzle by spraying upwards, although collapse of the wet particle bed occurred at lower liquid feed rates compared to top-spraying. Other detailed fluid bed nozzle studies have been reviewed by Schaafsma (2000b).

Although internal mixing nozzles are still used for fluid bed purposes, external mixing nozzles enable greater control of atomisation by independent control of both liquid and air streams, and for that reason, external mixing nozzles are typically preferred for fluid bed processes in general. The external mixing nozzle has the liquid supply in the centre and the atomising air is supplied concentrically. This type requires more air, but the advantage is that it is possible to atomise a liquid that otherwise would have evaporated inside the mixing chamber of an internal mixing nozzle (Spray Drying Systems Co., 2000). Another advantage is that it is possible to vary the droplet size independently of the liquid flow. Scaling this principle to larger liquid and gas flows shows typically an increasing gas-to-liquid rate for a given mean droplet diameter (Gretzinger & Marshall, 1961 and Lefebvre, 1989a). In practice however, this is seldom a problem (Niro, 2007). Being a somewhat simpler principle than the internal mixing nozzle, the external nozzle is not as sensitive towards erosion and attrition. Even so, the simplest external mixing nozzle designs are often used commercially (Salman et al., 2007). An example of a typical external mixing nozzle design used in commercial fluid beds of different scales may be seen from figure 2.7. In this configuration the position of the air cap as well as the liquid and atomisation airflow velocities are the only variables that can be varied. Most designs offer additionally the possibility to replace the liquid insert with others of different liquid orifice diameters.

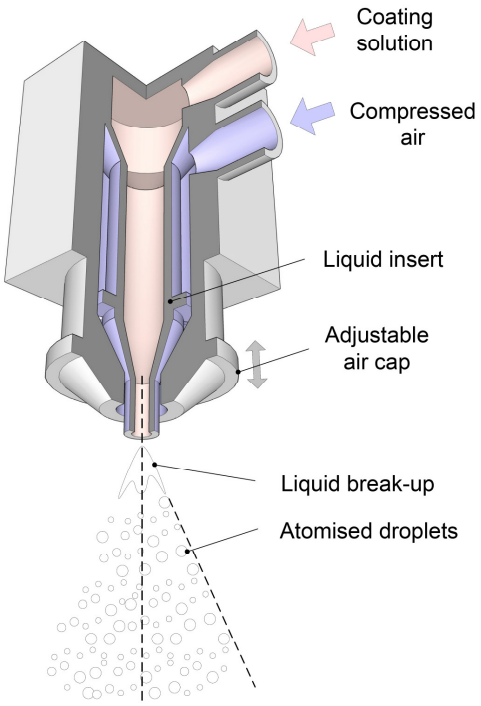

Figure 2.7: The principle of a simple external mixing nozzle design used in commercial fluid bed granulators (Ronsse, 2006).

2.2.2. Variables affecting the mean droplet size

The performance of a two-fluid nozzle is typically characterised and validated according to the mean droplet diameter. Two types of mean droplet diameters are commonly used, being the Sauter mean droplet diameter, d_{32}, and the volume median diameter, $d_{v0.5}$. The first is a means of expressing the fineness of a spray in terms of the droplet surface area produced by the spray, whereas the latter is a means of expressing the fineness of a spray in terms of droplet volume. The d_{32} is the diameter of a droplet having the same volume-to-surface area ratio as the total volume of all the droplets to the total surface area of all the droplets (Spray Drying Systems Co., 2000). Similarly, $d_{v0.5}$ is the volume median diameter being found by dividing the total spray volume in half (50% of the total volume will have droplets of larger diameters and 50% will have droplets of smaller diameters). Calculations using the latter method give more consideration to the larger droplet sizes (Rhodes, 1998). The mass median diameter, d_{mmd}, is defined analogously to $d_{v0.5}$, but on the basis of mass instead of volume.

Given the variety of nozzle designs and types, it may seem difficult to extract universal trends that can be used as a rule-of-thumb for any given nozzle. There are, however, a number of general and rough rules of thumb that are useful in understanding the factors that influence the mean droplet size. The mean droplet size and the uniformity of the droplet size distribution will in general vary based on several factors such as: characteristics and properties of the liquid, the nozzle design, the atomisation air and liquid flow rate through the nozzle and more (Schick, 2006 and Masters, 1972). A brief overview of some of the most important qualitative trends is presented below.

2.2.2.1. Design and operation

The liquid flow rate has a direct influence on droplet size. An increase in liquid flow rate will typically increase the mean droplet size and vice-versa (Schick, 2006 and Spray Drying Systems Co., 2000). The atomisation air pressure (i.e. the airflow rate) has in general an inverse effect on the mean droplet size. An increase in atomisation air pressure will typically reduce the mean droplet size whereas a reduction in pressure will increase the droplet size. Similarly, the spray angle (adjusted in terms of the air cap) has an inverse relationship effect on droplet size (a zero spray angle is parallel to the jet). An increase in spray angle will typically reduce the mean droplet size, and a reduction in spray angle will increase the mean droplet size (Schick, 2006 and Lefebvre, 1989a).

2.2.2.2. Liquid properties

The liquid properties of importance with respect to two-fluid atomisation are: viscosity, density and surface tension. An increase in viscosity will typically increase the Sauter mean droplet diameter, d_{32}, which is demonstrated in figure 2.8. Here d_{32} is plotted against viscosity for various levels of the atomisation air velocity (v_{air}) at a constant liquid flow rate in a prefilming external mixing airblast atomiser (Rizkalla & Lefebvre, 1975). If, however, the atomisation takes place into high ambient air pressure, the increase in d_{32} with increasing viscosity is somewhat larger than what is illustrated in figure 2.8 (Lefebvre, 1996).

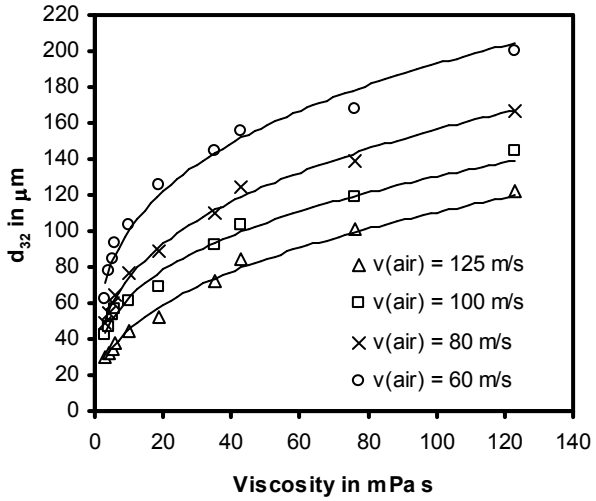

Figure 2.8: Variation in d_{32} with liquid viscosity for an external mixing prefilming airblast atomiser. T = 296 K, P = 1 bar, $\dot{m}_{liq}$ = 15 g/s, ρ_{liq} = 995 kg/m^3, γ_{liq} = 0.072 kg/s^2 (Data adapted from Rizkalla & Lefebvre, 1975 and Lefebvre, 1989a).

Further effects upon an increase in liquid viscosity are (Schick, 2006 and Lefebvre, 1989a):

- Decrease in liquid flow rate.
- Requirement of a higher minimum atomisation air pressure to maintain adequate spray angle/coverage.

Similarly, an increase in surface tension typically means an increase in d_{32}, which is illustrated in figure 2.9.

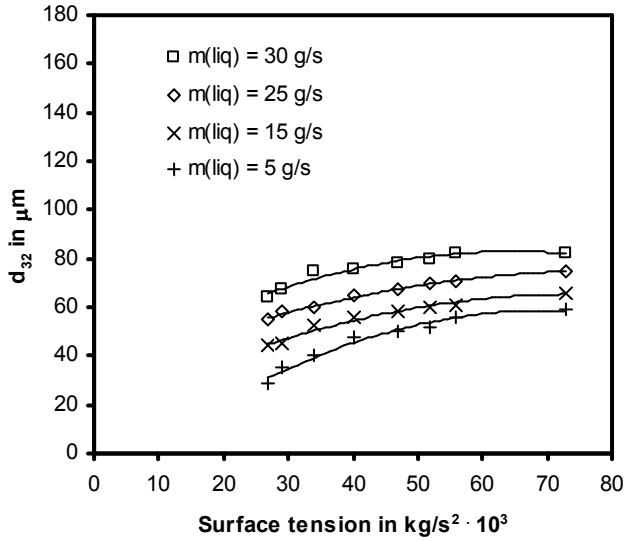

Figure 2.9: Variation in d_{32} with surface tension for an external mixing prefilming airblast atomiser. T = 296 K, P = 1 bar, v_{air} = 100 m/s, ρ_{liq} = 995 kg/m^3, η_{liq} = 1.2 mPa·s (Data adapted from Rizkalla & Lefebvre, 1975 and Lefebvre, 1989a).

Other effects of an increase in surface tension are (Schick, 2006 and Lefebvre, 1989a):

- Decreasing spray angle.
- Increase in the minimum operating atomisation air pressure at which atomisation takes place.

The effect on d_{32} upon an increase in either the surface tension or the viscosity is due to an increase in the amount of energy required to atomise the liquid. The result is fewer, but larger droplets (Lefebvre, 1989a).

Liquid density affects the droplet size in a complex manner. E.g. with prefilming atomisers, the distance to which the coherent liquid sheet extends downstream of the atomising lip increases with density, so that ligament formation occurs later and under conditions of lower relative velocity between the air and the liquid (at this increased distance, the velocity of the atomisation air has decreased). Furthermore, for any given flow rate, an increase in liquid density produces a more compact spray that is less exposed to the atomising action of the high-velocity air. These two effects combine to increase the mean droplet size. However, an increase in liquid density can also improve atomisation by reducing the thickness of the liquid sheet produced at the atomising lip in prefilming nozzles, and by increasing the relative velocity for plain jet nozzles. The net effect of these conflicting factors is that the influence of liquid density on d_{32} is fairly small as illustrated for a prefilming airblast atomiser in figure 2.10 (Lefebvre, 1989a and Rizkalla & Lefebvre, 1975).

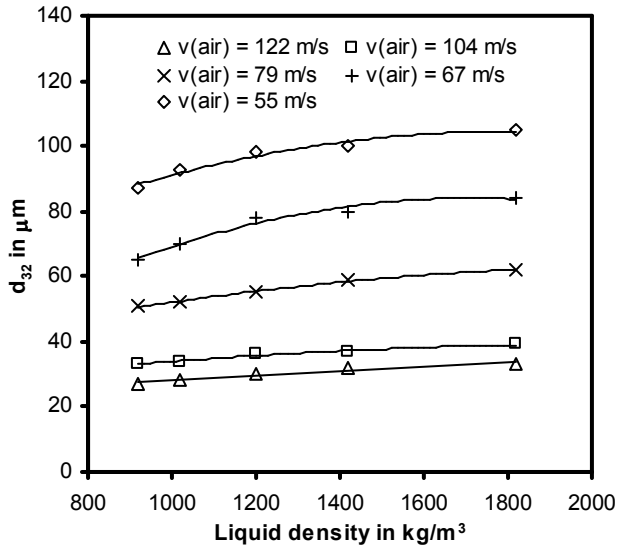

Figure 2.10: Variation in d_{32} with liquid density for an external mixing prefilming airblast atomiser. T = 296 K, $\dot{m}_{liq}$ = 15 g/s, P = 1 bar, γ_{liq} = 0.072 kg/s^2, η_{liq} = 1.2 mPa·s (Data adapted from Rizkalla & Lefebvre, 1975).

2.2.2.3. Atomisation air properties

Of all the factors influencing the mean droplet size, the atomisation air velocity is undoubtedly the most important. This trend becomes clear from inspection of figure 2.8 - 2.11. For low-viscosity liquids, d_{32} is roughly inversely proportional to the air velocity, which underlines the importance of a nozzle design which ensures that the liquid is exposed to the highest possible air velocity (Lefebvre, 1989a).

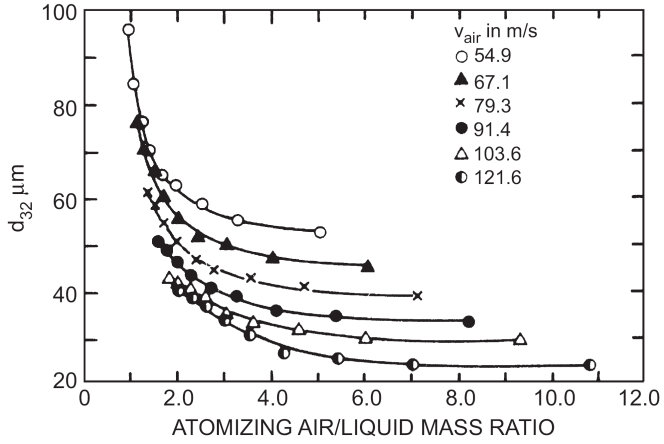

Figure 2.11: Variation in d_{32} with air/liquid mass ratio for a prefilming airblast atomiser. T = 296 K, P = 1 bar, γ_{liq} = 0.072 kg/s^2, ρ_{liq} = 995 kg/m^3, η_{liq} = 1.2 mPa·s (Lefebvre, 1980).

The effects of atomisation air pressure (used to accelerate the airflow thus being the gauge pressure) and temperature on d_{32} are illustrated in figure 2.12 and figure 2.13, respectively. These results taken together suggest that for prefilming nozzles, d_{32} is proportional to the air density to the power of -0.6 (Lefebvre, 1989a).

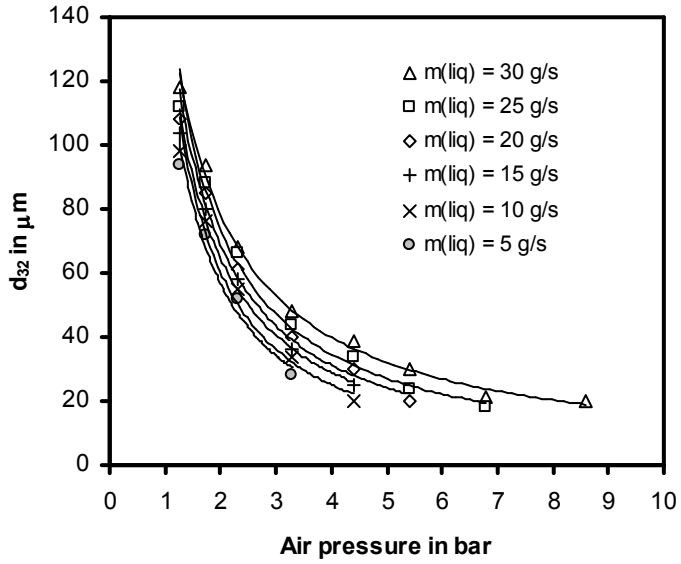

Figure 2.12: Variation in d_{32} with atomisation air (gauge) pressure for an external mixing prefilming airblast atomiser. T = 296 K, ρ_{liq} = 995 kg/m^3, γ_{liq} = 0.072 kg/s^2, η_{liq} = 1.2 mPa·s (Data adapted from Rizkalla & Lefebvre, 1975).

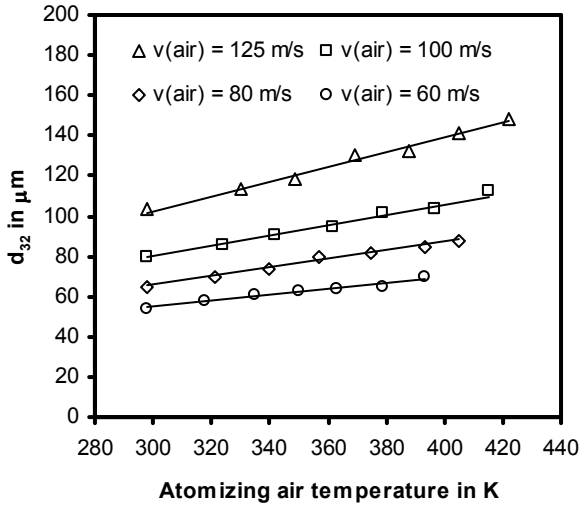

Figure 2.13: Variation in d_{32} with atomisation air temperature for an external mixing prefilming airblast atomiser. P = 1 bar, ρ_{liq} = 995 kg/m^3, γ_{liq} = 0.072 kg/s^2, η_{liq} = 1.2 mPa·s (Data adapted from Rizkalla & Lefebvre, 1975).

2.2.3. External mixing droplet size correlations

Measuring the mean droplet diameter produced from a given nozzle is a difficult exercise although different techniques are commercially available as presented by Schick (2006). In that perspective it is desirable to obtain a correlation that allows the prediction of the mean droplet diameter based on the nozzle design and operations. Literature on droplet size correlations is nevertheless sparse. Pneumatic two-fluid nozzles have received attention from many authors through the last 60 years, but the authors have often developed their own type of nozzle and developed an empirical correlation for the mean droplet size for this particular

nozzle. Droplet size correlations are often limited to a narrow parameter range, but nonetheless often cited without stating the associated parameter intervals or droplet size distributions. Here, only the most relevant equations are presented. For a thorough review of droplet size correlations, Lefebvre (1980) and Hede et al. (2008c) should be consulted.

In the work by Kim & Marshall (1971) studies were made on a simple convergent external mixing type of nozzle similar to the one presented in figure 2.7. Droplet size measurements were carried out on melts of wax mixtures over a range of liquid viscosities from 0.001 to 0.050 kg/m s, relative velocities from 75 to 393 m/s, air/liquid flow mass ratios of 0.06 to 40, liquid densities of 800 to 960 kg/m^3 and air densities of 0.93 to 2.4 kg/m^3 (all evaluated at the nozzle entrance prior to expansion). Based on experimental data, the empirical equation 2.1 was derived expressing the mass median diameter, d_{mmd}, in terms of nozzle dimensions and operating conditions. For more information concerning the range of validity for equation 2.1, Hede et al. (2008c) should be consulted.

$$d_{mmd} = \left[\frac{249 \cdot \gamma_{liq}^{0.41} \cdot \eta_{liq}^{0.32}}{(v_{rel}^2 \cdot \rho_{air})^{0.57} \cdot A_{annulus}^{0.36} \cdot \rho_{liq}^{0.16}} \right] + 1260 \cdot \left[\left(\frac{\eta_{liq}}{\gamma_{liq} \cdot \rho_{liq}} \right)^{0.17} \cdot \left(\frac{1}{v_{rel}^{0.54}} \right) \cdot \left(\frac{\dot{m}_{air}}{\dot{m}_{liq}} \right)^{m} \right] \tag{2.1}$$

where

$$m = -1 \text{ at } \left(\frac{\dot{m}_{air}}{\dot{m}_{liq}} \right) < 3 \text{ and } m = -0.5 \text{ at } \left(\frac{\dot{m}_{air}}{\dot{m}_{liq}} \right) > 3$$

and d_{mmd} is the mass median droplet diameter in μm and $A_{annulus}$ is the area of the air annulus in in^2. The units of η_{liq}, γ_{liq}, v_{rel} and ρ_{liq} are centipoise, dynes/cm, ft/sec, lb/ft^3, respectively. The discontinuity due to the parameter m is an unfortunate feature of equation 2.1 as the influence of the exact value of m for the prediction of d_{mmd} is significant. Furthermore, the correlation is applicable only to simple external mixing designs operating with Newtonian liquids. For comparison of data obtained with equation 2.1 with alternative correlations involving the Sauter mean diameter d_{32}, the following relation is suggested in accordance with Simmons (1976) (Kim & Marshall, 1971):

$$d_{32} = 0.83 \cdot d_{mmd} \tag{2.2}$$

Although determined empirically, equation 2.2 has proven to fit excellent with theoretical considerations concerning the Rosin-Rammler droplet size distribution, which will be presented in section 2.2.4.

In certain types of fluid bed granulation processes the coating/binder liquid is a suspension or a slurry rather than a solution. This is e.g. the case in polymer fluid bed coating processes where dry-matter in the form of e.g. TiO_2 particles is often added to the aqueous polymer solution in order to reduce the stickiness of the coating layer. In contrast to atomisation of pure liquids or homogenous solutions, atomisation of suspensions is a rather new field with only a few papers published so far. Schütz et al. (2004) recently published some numerical investigations with suspensions providing a mathematical-physical model capable of calculating the aerodynamically induced atomisation. The boundary conditions for this model

at the nozzle orifice were determined by CFD codes calculating the state variables inside the nozzle. The resulting d_{32} was determined by considering the nozzle geometry, operating conditions and fluid properties. Comparison of the experimental data from a simple hollow-cone nozzle with measured droplet sizes via laser diffraction showed good agreement, although model predictions are clearly limited by the necessary model assumptions. Following previous authors, some correlations for suspension droplet sizes produced from internal mixing two-fluid nozzles are published in Shirley & Truc (1987) and Glaser (1989). Only recently, Mulhem et al. (2003 & 2006) have published an empirical correlation for suspension droplet sizes generated by an external mixing two-fluid nozzle according to equation 2.3. Droplet size measurements were carried out on water, glycerol, various kaolin suspensions and CMC-water mixtures over a range of liquid viscosities from 0.001 to 0.080 kg/m·s, relative velocities less than 250 m/s, air/liquid flow mass ratios of 2 to 100, liquid densities of 1000 to 1130 kg/m^3 and atomisation air densities of 0.8 to 3 kg/m^3 (all evaluated at the nozzle entrance prior to expansion). For more information concerning the range of validity for equation 2.3, Hede et al. (2008c) should be consulted.

$$d_{32} = 0.21 \cdot d_{orifice} \cdot Oh^{0.0622} \cdot \left(We_{air} \cdot \frac{\dot{m}_{air}}{\dot{m}_{liq}} \right)^{-0.4} \tag{2.3}$$

where the ratio of the atomisation air dynamic pressure ($v_{air}^2 \cdot \rho_{air}$) to liquid capillary pressure ($\gamma_{liq}/d_{orifice}$) at the outset of the process is the gas-Weber number given by equation 2.4 (Walzel, 1993).

$$We_{air} = \frac{v_{air}^2 \cdot \rho_{air} \cdot d_{orifice}}{\gamma_{liq}} \tag{2.4}$$

and Oh is the so-called Ohnesorge number that relates surface tension and viscosity according to equation 2.5 (Lefebvre, 1989a).

$$Oh = \frac{\eta_{liq}}{\sqrt{\gamma_{liq} \rho_{liq} d_{orifice}}} \tag{2.5}$$

Equation 2.3 has shown good agreement with suspensions containing small particles with diameters in the range of 6 – 10 μm and for d_{32} values ranging from 5 – 100 μm. Apparently, the atomisation process is not affected significantly by the presence of the tested particles in the suspension, and equation 2.3 has shown adequate precision with pure water droplets (Mulhem et al., 2003). However, Mulhem et al. (2006) also showed that as the particles in the suspension increase in size up to the diameter of the liquid droplets, the solid particles and the liquid will become more and more separated. This is indicated by a bimodal droplet size distribution.

2.2.4. Droplet size distributions

Due to the heterogeneous nature of the atomisation process, the liquid threads and ligaments formed by the various mechanisms of jet and liquid sheet disintegration vary widely in diameter, and the resulting main droplets typically vary in size. Practical nozzles do therefore not produce sprays of uniform droplet size at any given operating condition. Instead the spray

may be regarded as a spectrum of droplet sizes distributed about some arbitrarily defined mean value (Lefebvre, 1989b). Thus, in addition to the mean droplet size, another parameter of importance in the definition of a spray is the distribution of droplet sizes. As no complete theory has yet been developed to describe the hydrodynamic and aerodynamic processes involved when jet and sheet disintegration occurs under normal atomisation conditions, a number of functions have been proposed. These are based on either probability or purely empirical considerations that allow the mathematical representation of measured droplet size distributions. Those include most importanly: normal, log-normal, Nukiyama-Tanasawa, Rosin-Rammler and upper-limit distributions (Lefebvre, 1989b and Nukiyama & Tanasawa, 1939 & 1940). Comparison of these distributions reveals that all of them have deficiencies of one kind or another. So far, no single distribution has emerged that has a clear advantage over the others. For any given application the best distribution function is obviously one that provides the best fit to the experimental data. The most widely used expression for droplet size distributions is one that was originally developed for particles being the Rosin-Rammler distribution given by equation 2.6.

$$1 - Q = \exp\left(-\frac{d_{dr}}{X}\right)^{q} \tag{2.6}$$

where Q is the fraction of the total volume (or total mass) contained in droplets of diameters less than d_{dr}, and X and q are constants. The Rosin-Rammler relationship thus describes the droplet size distribution in terms of two parameters X and q. The exponent q represents the spread of droplet sizes. The higher the value of q, the more uniform the spray becomes (Rosin & Rammler, 1933). Modern nozzles typically operate with q values in the range of 1.5 – 2.9 (Niro, 2007).

Although the Rosin-Rammler distribution assumes an infinite range of droplet sizes the distribution has a virtue of simplicity. Furthermore, it permits data to be extrapolated into the range of very fine droplets, where measurements are often difficult and least accurate. Another useful advantage of the Rosin-Rammler distribution is that all the representative droplet distribution diameters are uniquely related to each other via the distribution parameter q. This makes it possible to express certain spray properties in terms of the parameters q and thereby deduce one characteristic diameter from another if one of them is known. Lefebvre (1989b) and Chin & Lefebvre (1987) presented some of the most important expressions according to equation 2.7 – 2.11.

$$\frac{d_{v0.1}}{d_{mmd}} = (0.152)^{1/q} \tag{2.7}$$

where $d_{v0.1}$ is the droplet diameter such that 10 % of the total liquid volume is in droplets of smaller diameter.

$$\frac{d_{v0.5}}{d_{mmd}} = 1 \tag{2.8}$$

where $d_{v0.5}$ is the droplet diameter such that 50 % of the total liquid volume is in droplets of smaller diameter. Equation 2.8 is obvious as $d_{v0.5}$ is related to d_{mmd} via the liquid density.

$$\frac{d_{v0.9}}{d_{mmd}} = (3.322)^{1/q} \tag{2.9}$$

where $d_{v0.9}$ is the droplet diameter such that 90 % of the total liquid volume is in droplets of smaller diameter.

$$\frac{d_{v0.999}}{d_{mmd}} = (9.968)^{1/q} \tag{2.10}$$

where $d_{v0.999}$ is the droplet diameter such that 99.9 % of the total liquid volume is in droplets of smaller diameter.

$$\frac{d_{mmd}}{d_{32}} = (0.693)^{1/q}\ \Gamma(1-\frac{1}{q}) \tag{2.11}$$

where Γ is the gamma function known from mathematics as the extension of the factorial function to real and complex numbers. Interestingly, for sprays with a narrow size distribution, where q approaches a value of at least 2.5, equation 2.11 predicts a value of the d_{mmd}/d_{32} fraction close to 1.2 which is close to the result found experimentally by Kim & Marshall (1971) and Simmons (1976) in equation 2.2. The relationships in equation 2.7 and 2.9 – 2.11 are plotted as functions of the parameter q in figure 2.14.

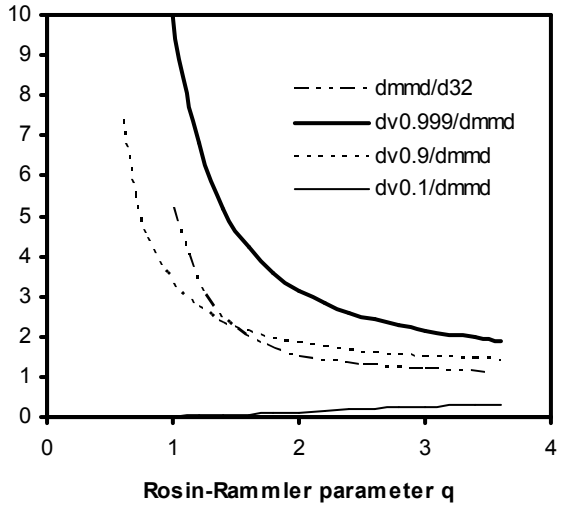

Figure 2.14: Relationship between the Rosin-Rammler distribution parameter q and various spray characteristics. Data obtained from equation 2.7 and 2.9-2.11.

From analysis of a considerable amount of droplet size data obtained with various nozzle types, Rizk & Lefebvre (1985) found that a better fit to the experimental data, especially for the larger droplet sizes, could be obtained by a modified Rosin-Rammler correlation according to equation 2.12.

$$1 - Q = \exp\left(-\frac{\ln d_d}{\ln X}\right)^q \tag{2.12}$$

These findings have, however, not been followed by other authors and a wide range of other statistical relationships have been suggested as reviewed by Lefebvre (1989a,b). Generally, little attention has been given in literature to the droplet size distribution in comparison with the mean droplet diameter. Although modern two-fluid nozzles have been designed to produce narrow droplet size distributions, it must be stressed that droplet size distributions are just as important for any practical nozzle application as are the mean droplet diameters (Schlick, 2007 and Spray Drying Systems Co., 2000).

2.3. Fluidisation fundamentals

Fluidisation occurs when a fluid (being gas, but applies in principle also to liquids) passes upwards through a bed of particles resulting in the particles assuming liquid-like properties (Rhodes, 1998 and Teunou & Poncelet, 2002). Due to frictional resistance, the pressure drop in the fluid increases with increasing fluid flow. At a certain point, where the upward drag force exerted by the fluid on the particles is equal to the apparent weight of the particles, the particles are lifted, and separation of the particles increase in all leading to fluidisation (Rhodes, 1998). This onset of fluidisation is known as the minimum fluidisation, and the corresponding velocity is called the *minimum fluidisation velocity*, v_{mf}. From this point, a further increase in gas velocity results in instabilities, where a part of the gas bypasses the rest of the bed in the form of bubbles. The fluidisation velocity, at which bubbles are first observed, is known as the *minimum bubbling velocity*, v_{mbu}. These bubbles tend to coalesce and thereby grow in size as they rise through the bed. The migration of these bubbles through the bed displaces the particles in a highly agitated fashion as the bubbles burst. For the fluidisation of certain types of particles, increasing the gas flow rate even further results in larger bubbles up to a point where the gas bubble diameter is equal to the chamber diameter. This result in a regime called *slugging fluidisation*. At a further increase in the gas velocity to a point close to the terminal velocity, the fluidisation behaviour drastically changes into what is known as *turbulent fluidisation*. This type of fluidisation is characterised by turbulent clusters of particles and gas voids of varying shape and size, as a distinct bubble phase is no longer present (Bi et al., 2000, Kunii & Levenspiel, 1991). At gas velocities equal to or beyond the terminal particle velocity the bed is entrained into a disperse or dilute phase, which gives rise to pneumatic transport out of the reactor. The different types of fluidisation regimes are visualised in figure 2.15.

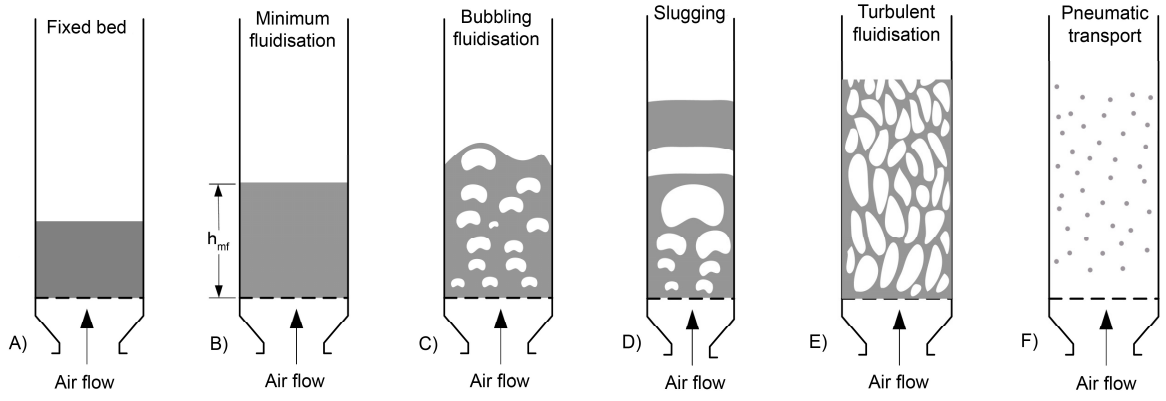

Figure 2.15: A schematic representation of different flow modes in a fluidised bed. a) Fixed bed, b) Bed at minimum fluidisation, c) Bubbling fluidised bed, d) Slugging bed, e) Turbulent fluidised bed, e) Pneumatic transport (based on Kunii & Levenspiel, 1991 and Ronsse, 2006).

2.3.1. Minimum fluidisation velocity

At a gas velocity at the onset of fluidisation, the drag force by the upward moving gas equals the weight of the particles. This gas velocity is known as the minimum fluidisation velocity. There are many empirical correlations available for the calculation of v_{mf} based on particle and fluidisation properties, as reviewed by Kunii & Levenspiel (1991). One of the standard equations is known as the *Ergun equation* suggested by Ergun (1952) according to:

$$v_{mf} = \frac{\eta_a}{\rho_a d_p}\left\{\left(\beta_{E1}^2 + \beta_{E2}\cdot Ar\right)^{1/2} - \beta_{E1}\right\} \tag{2.13}$$

where η_a is the gas viscosity, ρ_a the gas density, d_p the diameter of particles and β_{E1} and β_{E2} are the Ergun parameters depending on the particle sphericity and the bed voidage at incipient fluidisation, ε_{mf}. Ar is the Archimedes number (also sometimes referred to as the Galileo number) defined as (Kunii & Levenspiel, 1991):

$$Ar = \frac{d_p^3 \rho_a (\rho_p - \rho_a) g}{\eta_a^2} \tag{2.14}$$

where ρ_p is the particle density and g being gravity.

For particles above 100 μm the Ergun expression can be approximated by (Wen & Yu, 1966 and Teunou & Poncelet, 2002):

$$v_{mf} = \frac{\eta_a}{\rho_a d_p}\left\{\left(33.7^2 + 0.04084\cdot Ar\right)^{1/2} - 33.7\right\} \quad , \; d_p > 100\,\mu m \tag{2.15}$$

2.3.2. Terminal velocity

The terminal velocity, v_t, is the air velocity over which transportation by dragging or pneumatic conveying occurs. Above this high velocity the fluidisation will stop and the particles will be transported out of the bed. In a fluid bed context it is thereby desired to operate at a gas flow velocity between v_{mf} and v_t to avoid carryover of particles (Kunii & Levenspiel, 1991). Rules of thumb state that a proper fluidisation velocity should be found in the range of 0.2 to 0.5 times of v_t, and that v_t is at least ten times larger than v_{mf} (Niro, 1992). Kunii & Levenspiel (1991) suggest the following equation for the estimation of v_t:

$$v_t = \left[\frac{4\cdot d_p(\rho_p - \rho_a)g}{3\rho_a C_D}\right]^{1/2} \tag{2.16}$$

in which C_D is an experimentally determined drag coefficient for spherical particles given as (Kunii & Levenspiel, 1991):

$$C_D = \frac{24}{Re_p} + 3.3643\cdot Re_p^{-0.3471} + \frac{0.4607\cdot Re_p}{Re_p + 2682.5} \tag{2.17}$$

where Re_p is the particle Reynolds number defined as (Kunii & Levenspiel, 1991):

$$Re_p = \frac{\rho_a \cdot v_a \cdot d_p}{\eta_a} \tag{2.18}$$

where v_a is the velocity of the fluidisation gas.

For non-spherical particles, v_t may be found as (Kunii & Levenspiel, 1991):

$$v_t = v_t^* \cdot \left[\frac{\eta_a (\rho_p - \rho_a) g}{\rho_a{}^2} \right]^{1/3} \tag{2.19}$$

where v_t^* is the dimensionless terminal velocity approximated by (Kunii & Levenspiel, 1991):

$$v_t^* = \left[\frac{18}{(d_p^*)^2} + \frac{2.335 - 1.744 \cdot \psi_p}{(d_p^*)^{0.5}} \right]^{-1} \quad , \; 0.5 < \psi_p < 1 \tag{2.20}$$

where ψ_p is the particle shape factor (also known as the *particle sphericity*), which accounts for the non-spherical particle shape. The sphericity is defined as the surface of a sphere divided by the surface of an irregular particle both having the same volume (Kunii & Levenspiel, 1991). Thus a perfect sphere has $\psi_p = 1$. The parameter d_p^* is the dimensionless particle diameter determined by (Kunii & Levenspiel, 1991):

$$d_p^* = Ar^{1/3} \tag{2.21}$$

It can be seen from equation 2.13 and 2.14 that besides the gas properties, it is the size and density of the particles that determine the fluidisation velocity needed to obtain a homogenously fluidised bed. The larger and denser the particles are, the higher the fluidisation velocity must be to keep the particles fluidised (Guignon et al., 2002). During e.g. an agglomeration process, v_{mf} will increase as the granule diameter increases. As a result, the excess gas velocity, v_e, will decrease and so will the overall bed mixing (Schaafsma et al., 1999). The excess gas velocity, v_e, is the part of the fluidisation gas velocity above the minimum fluidisation velocity that is not necessary for fluidisation (Kunii & Levenspiel, 1991).

2.4. The Geldart classification of particles

Recognizing the importance of particle size and density on fluidisation properties, Geldart (1973) has found four overall fluidisation modes and determined a general particle classification chart. For any particle of known density ρ_p and mean particle diameter $\bar{d}_p$, the Geldart chart indicates the type of fluidisation behaviour to be expected (Kunii & Levenspiel, 1991). The Geldart chart can be seen in figure 2.16.

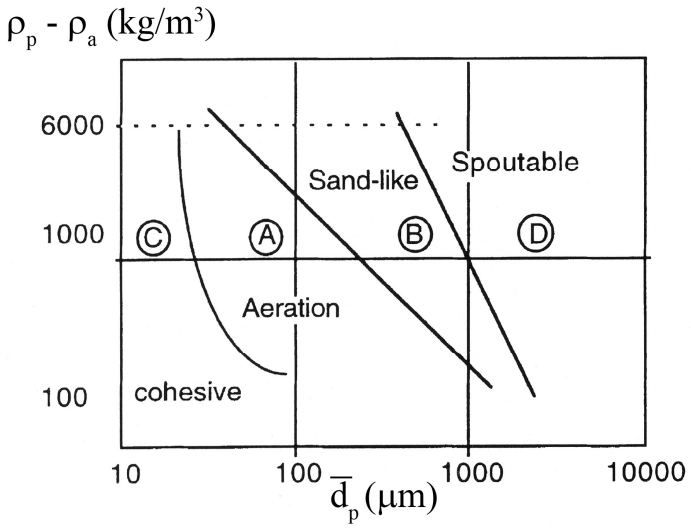

Figure 2.16: The Geldart classification of particles (Geldart, 1973 and Teunou & Poncelet, 2002).

The Geldart (1973) chart is one of the oldest classification schemes and other authors have suggested alternative schemes – e.g. a dimensionless Geldart classification scheme proposed by Rietema (1984). In spite of this, the original scheme by Geldart (1973) is well recognised and still widely used in all fields of particle technology. Often particles are simply referred to as "Geldart A particles" etc. in the literature. The chart has proven useful at fluidisation conditions up to ten times v_{mf} (Kunii & Levenspiel, 1991).

Geldart (1973) divides particles according to particle size and particle density into four different groups. From the smallest to the largest particles, the four groups are: C, A, B and D. The group C particles are cohesive or very fine powders, which are often difficult to fluidise. Here attempts of fluidisation will result in bubbles or channelling. At higher air velocities the particles will be carried out of the bed. Starch, flour and cement are typical examples of group C particles.

Materials having a small mean particle size and/or densities less than 1.4 g/cm^3 are placed in group A. Particles from this group fluidise well, and velocities higher than v_{mf}, but lower than the minimum bubbling velocity, v_{mbu}, will cause a homogenous expansion of the bed. At higher gas velocities bubbles will form, but the bubbles will be of limited size at all velocities up to v_t, where elutriation begins. All this helps to ensure both a large degree of mixing and a high extent of contact between the gas and particles, hence improving heat and mass transfer (Kunii & Levenspiel, 1991 and Geldart, 1973)

The group B particles are sandlike particles with mean particle diameters roughly between 40 and 500 μm and densities between 1.4 and 4 g/cm^3. The fluidisation mode of this type of particles is highly affected by the formation of gas bubbles in the bed, and group B particles typically fluidise well. The difference from group A particles is that the particle bed will only experience a limited expansion when the gas flow rises above v_{mf}. Furthermore, this regime has $v_{mbu} = v_{mf}$, which means that airflows larger than v_{mf} result in bubbles, and not in a more porous bed. These bubbles have no maximal size, and will continue to grow when the airflow rate is increased. This will cause large pressure fluctuations, and while the large bubbles may increase the mixing of the bed, the bubbles will not improve heat and mass transfer to any significant degree (Rhodes, 1998 and Abrahamsen & Geldart, 1980).

Particles from group D are large and/or dense particles and often difficult to fluidise. As the airflow rate required to fluidise group D particles is high, group D particles are not normally processed in conventional fluid beds (Kunii & Levenspiel, 1991 and Teunou & Poncelet, 2002). In this regime there is no upper limit to the size of the bubbles and high air velocities will easily result in very large slugs of gas (Rhodes, 1998). This will result in large pressure fluctuations with vertical distance and in all cause an inhomogeneous bed. As a result of this, Geldart D particles are typically handled in a spouted bed where a gas jet in the center creates a fountain of particles carried along from the bottom of the bed (Rhodes, 1998).

Although the division of particles into the four Geldart groups may seem unambiguous and rigid, it is important to note that at operating conditions far above ambient temperature and pressure, a particle may appear in a different group from that it occupies at ambient conditions. This is due to the effect of gas properties in form of ρ_a in the classification chart in figure 2.16. As far as fluid bed processing is concerned, changes in ρ_a with respect to ambient conditions often occur and this must therefore be taken into consideration when using the Geldart chart (Rhodes, 1998). Furthermore, agglomeration will also typically change the mean particle diameter significantly, meaning that the particles may change their Geldart group during processing.

2.5. Bubbling fluid beds

In many practical applications, the performance of fluidised beds depends on the bubbling behaviour, in which the understanding of the gas-solid contacting is important (Kunii & Levenspiel, 1991). The earliest and simplest view of the bubbling bed is that all gas in excess of v_{mf} (i.e. v_a-v_{mf}) passes through the bed as bubbles, while the particle emulsion remains at minimum fluidisation conditions. This theory is commonly known as the *two-phase theory* originally suggested by Toomey & Johnstone (1952) and later expanded by Davidson & Harrison (1963) and Kunii & Levenspiel (1991). Although numerous studies have later proved that fluidisation in general is somewhat more complex than what is described by this theory, the two phase model is still widely used due to its intuitive simplicity, elegance and its well-validated equations (Rhodes, 1998 and Kunii & Levenspiel, 1991).

2.5.1. Two-phase description of the bubbling fluid bed

The two-phase theory considers the bubbling fluidized bed to be composed of two phases: The bubbling phase (the gas bubbles) and the emulsion phase. The emulsion phase refers to the suspended solid particles and the interstitial gas volume between the fluidized particles. The theory states that the gas flow through the emulsion phase is equal to the minimum fluidisation gas flow rate as indicated by figure 2.17. Any gas in excess of the minimum fluidisation gas flow rate will bypass the emulsion phase as bubbles expressed according to equation 2.22.

$$\dot{V}_a = \underbrace{A_{plate} \cdot v_{mf}}_{\substack{\text{Gas flow through} \\ \text{the emulsion phase}}} + \underbrace{A_{plate} \cdot (v_a - v_{mf})}_{\substack{\text{Gas flow through} \\ \text{the bubble phase}}} \tag{2.22}$$

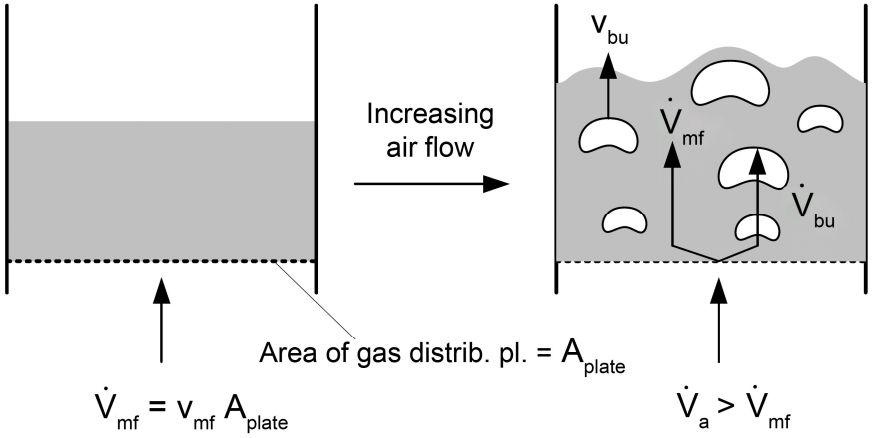

Figure 2.17: Gas flows inside the fluidised bed according to the two-phase theory (based on Ronsse, 2006 and Toomey & Johnstone, 1952).

In practice, the original two-phase theory overestimates the volume of gas passing through the bed as bubbles due to two prevailing effects in the gas flow pattern being; a significant gas flow through the bubbles and larger interstitial gas flow in the emulsion phase. Rhodes (1998) suggests in accordance with Peters et al. (1982) that equation 2.22 should be modified according to:

$$\dot{V}_a = \underbrace{A_{plate} \cdot v_{mf} + (1 - Y_{bu}) \cdot A_{plate} \cdot (v_a - v_{mf})}_{\text{Gas flow through the emulsion phase}} + \underbrace{Y_{bu} \cdot A_{plate} \cdot (v_a - v_{mf})}_{\text{Gas flow through the bubble phase}} \tag{2.23}$$

where Y_{bu} is a variable expressing the reduction in gas flow through the bubble phase. For Geldart A and Geldart B particles, Y_{bu} ranges between 0.8 - 1.0 and 0.6 - 0.8, respectively (Rhodes, 1998).

2.5.2. Gas bubble size

As observed by Rowe (1973), Davidson & Harrison (1963) and Kunii & Levenspiel (1991) among others, gas bubbles formed during fluidisation are not spherical, but rather hemispherical and vary greatly in size. This makes it difficult to characterise a mean bubble size, but for practical purposes a measure is often needed. It is common to define a spherical bubble diameter, d_{bu}, based on the volumetric size of the gas bubbles in the bed (Kunii & Levenspiel, 1991).

In fluid beds, having a rather small diameter ($h_{bed} > d_{bed}$), the diameter of the bubbles increases as they travel vertically through the bed due to bubble coalescence. To describe the relationship between bubble size and its position above the gas distributor, h_{bu}, the empirical Mori & Wen (1975) correlation is often used for Geldart B and D particles according to:

$$d_{bu} = d_{bu,max} - (d_{bu,max} - d_{bu,0}) \cdot \exp\left(\frac{-0.3 \cdot h_{bu}}{d_{bed}}\right)$$
$$\text{for} \begin{cases} d_{bed} \le 1.3\,\text{m}, & 0.05 \le v_{mf} \le 0.2\,\text{m/s} \\ 60 \le d_p \le 450\,\mu\text{m}, & v_a - v_{mf} \le 0.5\,\text{m/s} \end{cases} \tag{2.24}$$

where $d_{bu,0}$ is the initial diameter of the bubbles as they are formed at the air distributor plate. The parameter thus depends on the type of gas distribution plate. For standard perforated plate distributors, the initial bubble size under high gas flow rates may be approximated by equation 2.25, whereas other correlations for lower gas flow rates and other types of distributor plates may be found in Kunii & Levenspiel (1991):

$$d_{bu,0} = \frac{2.78}{g^{0.2}}\left(v_a - v_{mf}\right)^2 \tag{2.25}$$

The parameter $d_{bu,max}$ in equation 2.24 is the largest bubble diameter attainable, i.e. when all the gas bubbles coalesce to form a single bubble. According to Kunii & Levenspiel (1991) it may be estimated as:

$$d_{bu,max} = 0.65 \cdot \left[\frac{\pi}{4} \cdot d_{bed}^2 \left(v_a - v_{mf}\right)^2\right]^{0.4} \tag{2.26}$$

Another widely used correlation for Geldart B particles only, where the gas bubble diameter is correlated directly with the design of the distributor plate, is the correlation suggested by Darton et al. (1977):

$$d_{bu} = \frac{0.54}{g^{0.2}}(v_a - v_{mf})^{0.4}\left(h_{bu} + 4 \cdot \left(\frac{\pi \cdot (d_{bed}/2)^2}{N_{or}}\right)^{0.5}\right)^{0.8} \tag{2.27}$$

where N_{or} is the total number of perforations (orifices) in the distributor plate. The term $\pi \cdot (d_{bed}/2)^2 / N_{or}$ represents the distributor plate area per orifice. In case the distributor plate is porous, correlation 2.27 can be used by approximating $4 \cdot (\pi \cdot (d_{bed}/2)^2 / N_{or})^{0.5} \approx 0.03$ (Darton et al., 1977).

2.5.3. Gas bubble rise velocity

On the basis of the two-phase theory and experiments with single rising bubbles in a fluidised bed, Davidson & Harrison (1963) suggested that the rise velocity of a single bubble, in the absence of wall interactions, could be related to the bubble diameter according to:

$$v_{bu} = 0.711 \cdot (g \cdot d_{bu})^{0.5} \tag{2.28}$$

In the practical case with multiple rising bubbles, the drag force exerted by the bed on the individual bubbles is reduced compared to a single rising bubble, because the bubbles carry each other through the particle bed. In the case with multiple bubbles, equation 2.28 is modified according to (Davidson & Harrison, 1963):

$$v_{bu} = v_a - v_{mf} + 0.711 \cdot (g \cdot d_{bu})^{0.5} \tag{2.29}$$

Experimental investigations of equation 2.29 have shown that the equation cannot be used for all Geldart particle types at any particle diameter. In order to come up with an equation that

covers different particle sizes, Kunii & Levenspiel (1991) have proposed the following equation for Geldart B particles, based on data by Werther (1978):

$$v_{bu} = 1.6 \cdot ((v_a - v_{mf}) + 1.13 \cdot d_{bu}^{0.5}) \cdot d_{bed}^{1.35} + 0.711 \cdot (g \cdot d_{bu})^{0.5} \quad \text{for } d_{bed} \leq 1\,\text{m} \tag{2.30}$$

2.5.4. Particle bed expansion in bubbling fluid beds

Following the two-phase theory, the total voidage of a bubbling fluidised bed, ε_{bed}, consists of two parts; the voidage created by the bubble phase, ε_{bu}, and the voidage in the emulsion phase. According to Toomey & Johnstone (1952), for Geldart B and D particles, the voidage in the emulsion phase is equal to the bed voidage at minimum fluidisation giving:

$$\varepsilon_{bed} = \varepsilon_{bu} + (1 - \varepsilon_{bu}) \cdot \varepsilon_{mf} \quad \text{or} \quad (1 - \varepsilon_{bed}) = (1 - \varepsilon_{bu}) \cdot (1 - \varepsilon_{mf}) \tag{2.31}$$

The bubble voidage (fraction of bubbles), ε_{bu}, may be found according to (Toomey & Johnstone, 1952):

$$\varepsilon_{bu} = \begin{cases} \dfrac{\dot{V}_{bu}}{A_{bed} \cdot v_{bu}} = \dfrac{v_a - v_{mf}}{v_{bu}} \cong \dfrac{v_a - v_{mf}}{v_a - v_{mf} + 0.711 \cdot (g \cdot d_{bu})^{0.5}} & \text{for } v_{bu} \cong v_{mf}/\varepsilon_{mf} \\ \dfrac{\dot{V}_{bu}}{A_{bed} \cdot (v_{bu} + v_{mf})} = \dfrac{v_a - v_{mf}}{v_{bu} + v_{mf}} \cong \dfrac{v_a - v_{mf}}{v_a + 0.711 \cdot (g \cdot d_{bu})^{0.5}} & \text{for } v_{bu} \cong 5 \cdot v_{mf}/\varepsilon_{mf} \end{cases} \tag{2.32}$$

where A_{bed} is the bed surface area. The bed voidage at minimum fluidisation, ε_{mf}, may be found by the following equation suggested by Broadhurst & Becker (1975):

$$\varepsilon_{mf} = 0.586 \cdot \psi_p^{-0.72} \left(\frac{\eta_a^2}{\rho_a \cdot g \cdot (\rho_p - \rho_a) \cdot d_p^{\,3}} \right)^{0.029} \cdot \left(\frac{\rho_a}{\rho_p} \right)^{0.021}$$

$$\text{for} \begin{cases} 0.85 < \psi_p < 1 \\ 1 < \dfrac{\rho_a \cdot g \cdot (\rho_p - \rho_a) \cdot d_p^3}{\eta_a^2} < 10^5 \\ 500 < \dfrac{\rho_a}{\rho_p} < 50000 \end{cases} \tag{2.33}$$

2.5.5. Particle transport and particle circulation time

The existence of gas bubbles in the fluidised bed has a strong effect on the transport of particles. As a bubble travels vertically through the fluid bed, it drags a captive wake behind it, creating a mechanism for effective particle dispersion in bubbling beds. The gas phase of the bubble partly remains within the bubble, depending on the type of Geldart particles, although diffusion occurs within the emulsion phase at the bubble's surface, and part of the bubble's gas phase penetrates into the surrounding emulsion phase, creating a so-called *cloud* around the bubble (Kunii & Levenspiel, 1991). The structure of a rising bubble may be seen in figure 2.18.

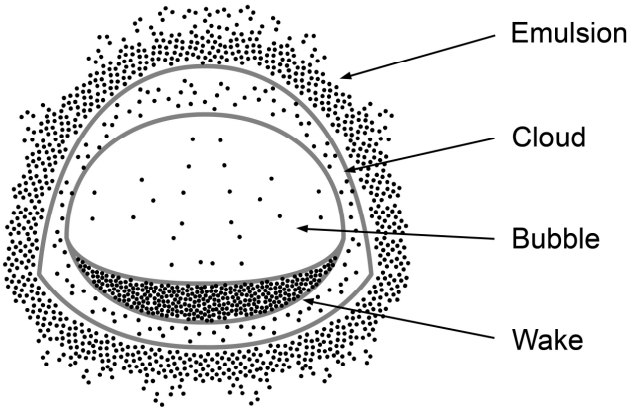

Figure 2.18: Structure of a rising bubble (Ronsse, 2006 based on Rowe, 1973).

Examinations by Rowe (1973) indicate that the upward fluidisation drift has a roughly conical shape with a volume of approximately 0.35 times the gas bubble volume, V_b, whereas the wake volume is approximately 0.25 times the bubble volume. Hence, each gas bubble displaces upwards a total volume of particles of approximately $0.6 \cdot V_b$. Figure 2.19 illustrates the different volumes as well as the different types of motion occurring during the rise of a bubble.

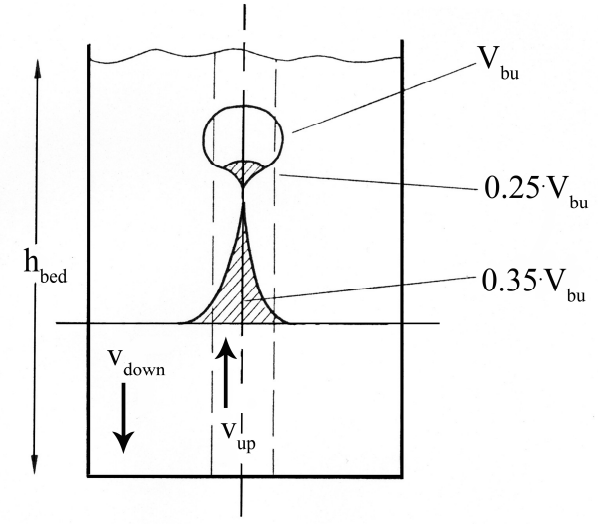

Figure 2.19: Model of particle movement due to the rise of a bubble in a bubbling fluidised bed (Based on Rowe, 1973).

Based on the equations for the bubble rise velocity, Rowe (1973) suggested a widely used equation for the calculation of the average particle circulation time, $\tau_{c,}$ during fluidisation at moderate gas velocities:

$$\tau_c = \frac{h_{mf}}{0.6 \cdot (v_a - v_{mf}) \cdot [1 - (v_a - v_{mf})/v_{bu}]} \tag{2.34}$$

According to Link & Schlünder (1997), τ_c should be less than a few seconds during a steady state coating process in order to keep the particle moisture contents low and hence reduce the chance of agglomeration. Abbott (2002) reports that the uniformity regarding size of coated

granules is highly affected by the value of τ_c in a batch fluid bed. If the average circulation time is too high, the number of time each particle will pass through the spray zone will vary from particle to particle. This will lead to significant variations in coating layer thicknesses and increase the chance of agglomeration even when the initial granule size distribution prior to coating is narrow (Teunou & Poncelet, 2002).

2.6. Basic principles of heat and mass transfer in fluid beds

Some of the clear advantages with fluid bed processing are the excellent heat and mass transfer potentials available, in particular the high transfer rate between the particles and the through-flowing fluidisation air (Kunii & Levenspiel, 1991). Heat may be transferred by three different mechanisms: conduction, convection and radiation, and in the context of fluid beds all three mechanisms are relevant. In the following subsections, a brief introduction to the basic principles of heat and mass transfer in fluid beds will be given. Only the general overall aspects are presented here as the specific equations are presented in association with the dynamic heat and mass transfer fluid bed model in chapter nine. For a thorough description of heat and mass transfer theory in fluid beds, literature such as Kunii & Levenspiel (1991) and Rohsenow et al. (1998) should be consulted.

2.6.1. Conductive heat transfer

The conduction mode of heat transfer involves energy transfer from regions of higher temperature to those with lower temperatures, but without any actual movement of material. The energy transfer occurs mainly through the contact of matter at a given point with adjacent matter. The rate of heat transfer by conduction can be described by Fouriers equation according to equation 2.35. Equation 2.35 is a general equation valid for gasses and solids as well as for liquids (Clement et al., 2004).

$$q_{cond} = -\lambda \cdot \nabla T \tag{2.35}$$

For one-dimensional conductive heat transfer, equation 2.35 becomes:

$$q_{cond} = -\lambda \cdot \frac{dT}{dx} \tag{2.36}$$

where λ is a proportionality factor known as the *thermal conductivity* being a material property and temperature dependent (Clement et al., 2004). The minus signs in equation 2.35 and 2.36 are added in order to have a positive heat transport from a warmer to a colder body (Dewettinck, 1997). Equation 2.36 may be solved for a rectangular, cylindrical or spherical coordinate system depending on the geometrical shape of the object being studied.

2.6.2. Convective heat transfer

Convective heat transfer is the major mode of heat transfer between the surface of a solid material and the surrounding fluid (being air or liquid). The rate of convective heat transfer depends on the properties of the fluid and the fluid flow characteristics (Dewettinck, 1997). When a fluid is directed along a smooth surface, a boundary layer is developed which is illustrated in figure 2.20.

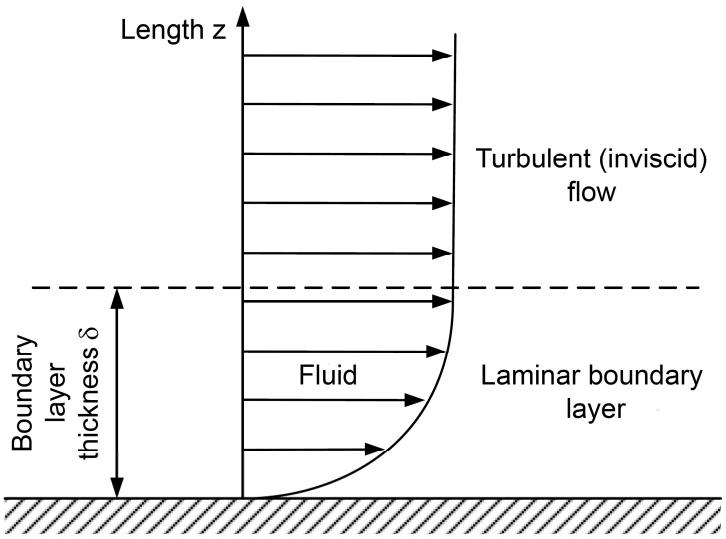

Figure 2.20: The laminar boundary layer for a forced laminar fluid flow flowing parallel to a solid surface (based on Ronsse, 2006 and Clement et al., 2004).

At great distances from the surface the fluid may be considered inviscid, as there are no temperature or velocity gradients (Clement et al., 2004). However, in the region closest to the surface, the viscous forces are dominant, creating a velocity gradient dv/dz normal to the surface. This region is called the *boundary layer* having a thickness of δ, which in the so-called *film model* is assumed to be very small compared to the diameter of the fluid bed chamber. This also means that the velocity and temperature in the core are almost identical to the mean value in the boundary layer (Clement et al., 2004). The fluid velocity is zero at the wall while the temperature is T_w meaning that when a surface is immersed in a fluid, the heat losses through the laminar boundary layer of thickness δ can be written according to equation 2.37 (following from Fourier's law and the assumptions in the film model).

$$q_{conv} = \frac{\lambda_a}{\delta}(T_a - T_w) \tag{2.37}$$

where λ_a is the thermal conductivity of the gas and T_a is the temperature of the gas phase (Ronsse, 2006). Equation 2.37 is only valid for forced turbulent flow. For other types of flow, the equation can still be used although the boundary layer thickness δ should be considered as the thickness of an equivalent rather than the real laminar boundary layer. The ratio between the thermal conductivity and the boundary layer thickness is known as the convective heat transfer coefficient, α_{heat}:

$$\alpha_{heat} = \frac{\lambda_a}{\delta} \tag{2.38}$$

Based on equation 2.38 a so-called *Nusselt number* may be derived according to equation 2.39. The Nusselt number is a dimensionless relationship that provides a basis for comparing the rate of convective heat loss from geometrically similar bodies immersed in a moving fluid.

$$Nu = \frac{\alpha_{heat} \cdot d_{body}}{\lambda_a} \tag{2.39}$$

The Nusselt number may thereby be defined as the ratio of the actual heat flux to the flux that would occur in a layer of motionless gas with thickness d_{body}, and with the same temperature difference across the gas layer (T_a - T_w) (Ronsse, 2006). Treating convective heat loss from fluid beds a distinction must be made between free (natural) and forced convection, as the empirical correlations typically have been derived for either of the two cases. A brief introduction to the two types of convection is presented below.

2.6.2.1. Free or natural convection

If the heat convection is caused only by temperature differences in the fluid resulting in a density gradient this is known as *free* or *natural convection* (Clement et al., 2004). For this type of heat transfer the Nusselt number may be described in general according to:

$$Nu = a \cdot (Gr \cdot Pr)^b \tag{2.40}$$

where a and b are constants depending on the geometry and the type of flow. For vertical cylinders and plates, values according to table 2-1 may be used:

Table 2-1: Values for the constants a and b for the calculation of the Nusselt number. Valid for vertical plates and cylinders (Rohsenow et al., 1998)

Gr·Pr	**a**	**b**
$< 10^4$ (laminar)	1.36	1/5
$10^4 < Ga \cdot Pr < 10^9$ (transition)	0.59	1/4
$> 10^9$ (turbulent)	0.13	1/3

In equation 2.40 there are two further dimensionless parameters – the Grashof number, Gr, which approximates the ratio of the buoyancy to viscous force acting on a fluid, and the Prandtl number, Pr, approximating the ratio of momentum diffusivity (kinematic viscosity) and thermal diffusivity. The two parameters are given by:

$$Gr = \frac{\beta_a \cdot g \cdot L^3 \cdot \rho_{film}^2 \cdot (T_w - T_e)}{\eta_{film}^2} \tag{2.41}$$

and

$$Pr = \frac{C_{p,film} \cdot \eta_{film}}{\lambda_{film}} \tag{2.42}$$

where L is a characteristic length of the body, C_p the specific heat capacity of the fluid and β_a is the thermal expansion coefficient of the fluidisation air being approximated as $3.0 \cdot 10^{-3}$ K^{-1}. All other physical properties in equation 2.41 and 2.42 should be evaluated at the film temperature being $T_{film} = (T_e + T_w)/2$, where T_e is the external air temperature. Hence, the subscript "film" in the parameters in the two equations (Ronsse, 2006 and Clement et al., 2004).

2.6.2.2. Forced convection

If the fluid motion is induced by a pump, a fan or a similar device, the convective heat transfer is termed *forced convection* (Rohsenow et al., 1998). The fluid flow past an immersed surface is related to the dimensionless Prandt and Reynolds number in forced convection. The Reynolds number is the ratio of the fluid's inertial force to viscous forces being defined as:

$$\mathrm{Re} = \frac{\rho_a \cdot v_a \cdot L}{\eta_a} \tag{2.43}$$

As in other areas of the heat transfer theory there are many proposed empirical correlations between the Nusselt number and the Prandtl and Reynolds number for forced convection. For the present work, especially two correlations are important:

For the calculation of the Nusselt number in vertical round pipes with turbulent flow and uniform temperature, the Dittus-Boelter equation may be used according to:

$$\mathrm{Nu} = 0.023 \cdot \mathrm{Re}^{0.8} \cdot \mathrm{Pr}^{0.4} \text{ valid for } \begin{cases} 0.7 < \mathrm{Pr} < 160 \\ \mathrm{Re} > 10000 \\ L_{tube}/d_{tube} > 10 \end{cases} \tag{2.44}$$

where L_{tube} is the length of the tube and d_{tube} the diameter of the tube. For flow past a single sphere with constant surface temperature an approximation of the Whitaker equation may be used to relate the Nusselt number to pertinent flow variables:

$$\mathrm{Nu}_p = 2 + \mathrm{Pr}^{2/5}(0.43 \cdot \mathrm{Re}_p^{1/2} + 0.06 \cdot \mathrm{Re}_p^{2/3})$$
$$\text{valid for } \begin{cases} 3.5 < \mathrm{Re}_p < 76000 \,,\, \mathrm{Re}_p = \dfrac{\rho_a \cdot v_a \cdot d_p}{\eta_a} \\ 0.71 < \mathrm{Pr} < 380 \,,\, \mathrm{Pr} = \dfrac{C_{p,a} \cdot \eta_a}{\lambda_a} \end{cases} \tag{2.45}$$

It is hereby assumed that the ratio between the viscosity of the bulk fluid to the viscosity of the fluid near the submerged surface is unity. This is a good approximation when dealing with small temperature differences between the surface, T_w, and the bulk fluid, T_a (Ronsse, 2006).

2.6.3. Radiative heat transfer

The third mode of heat transfer is radiation. Radiative heat transfer takes place between two surfaces due to the emission and later absorption of electromagnetic radiation. (Dewettinck, 1997). Contrary to conduction and convection, radiation requires no physical medium for its propagation. The energy emitted from a surface depends on the temperature and may be estimated in terms of the Stefan-Boltzmann law according to:

$$q_{rad} = \sigma \cdot A_{emis} \cdot \varepsilon \cdot T^4 \tag{2.46}$$

where A_{emis} is the area of the emissive surface, σ is the Stefan-Boltzmann constant being $5.669 \cdot 10^{-8}$ W m^{-2} K^{-4} and ε is the emissivity. When a body is exposed to thermal radiation a certain amount of the incoming energy is absorbed. The fraction of the incoming to the absorbed energy is the emissivity of the body. Hence, the emissivity describes the extent to which a surface is similar to a black body. In case of a perfect black body ε equals 1. Otherwise, ε ranges between 0 and 1.

In case of a single surface or body temperature T_w, the heat radiated into the surroundings, having a uniform temperature of T_e, may be estimated according to (Clement et al., 2004):

$$q_{rad} = \sigma \cdot A_{emis} \cdot \varepsilon \cdot (T_w^4 - T_e^4) \tag{2.47}$$

2.6.4. Heat and mass transfer analogy

Between the convective heat and convective mass transfer exists a close analogy caused by the fact that conduction and diffusion in a fluid are governed by practical laws of identical form. Similar to the Nusselt number for heat transfer, a dimensionless Sherwood number, representing the ratio of length scale to the diffusive boundary layer thickness, is defined according to (Ronsse, 2006 and Clement et al., 2004):

$$Sh = \frac{\alpha_{mass} \cdot d_{body}}{D_v} \tag{2.48}$$

where D_v is the molecular diffusion coefficient for water vapour in air and α_{mass} is the mass transfer coefficient.

While the Nusselt number for convection can be estimated using empirical correlations based on the Reynolds/Prandlt numbers or Grashof/Prandtl numbers in cases of free or natural convection, the Sherwoood number is likewise calculated using the same correlations, but based on dimensionless Reynolds and Schmidt numbers. Hence, as an example analogously to equation 2.45, the equivalent Whitaker equation for convective mass transfer, in case of e.g. evaporation from the surface of a sphere, is given by:

$$Sh_p = 2 + Sc^{2/5}(0.43 \cdot Re_p^{1/2} + 0.06 \cdot Re_p^{2/3}) \tag{2.49}$$

where the dimensionless Schmidt number, Sc, is the ratio of the momentum diffusivity (or viscosity) to the mass diffusivity given by:

$$Sc = \frac{\eta_a}{\rho_a \cdot D_v} \tag{2.50}$$

The particle Sherwood number is given by (Clement et al., 2004):

$$Sh_p = \frac{\alpha_{mass} \cdot d_p}{D_v} \tag{2.51}$$

2.7. Chapter summary

The chapter has outlined the fundamental principles of fluid bed granulation. Initially, the basic concepts of agglomeration and coating were presented. Although these concepts are fairly simple in principle, the complexity in terms of process control, arising from possible interactions from numerous parameters and properties, was briefly outlined. The importance of especially fluidisation and nozzle-related conditions was highlighted hereby motivating the subjects of the following sections in the chapter.

The types of fluid bed equipment were presented together with a brief presentation of other types of granulation equipment. The advantages of fluid beds over other types of granulators were emphasised including good heat and mass transfer, temperature homogeneity, mechanical simplicity and one-pot processing capabilities. Furthermore, the four basic types of batch fluid bed equipment were presented along with an introduction to the concepts of continuous fluid bed granulation. It was discussed how top-spray fluid beds are still in use industrially, although in terms of coating processes, the trend goes in the direction of more advanced bottom-spray batch fluid beds and to some extent into continuous fluid beds.

Two-fluid atomisation was introduced including fundamentals, nozzle designs and variables affecting the mean droplet size. A number of droplet size correlations were presented and the section ended with an introduction to droplet size distributions. The section clearly indicated the complexity of two-fluid atomisation, and how the droplets produced by such nozzles are affected by numerous properties concerning both the liquid and the atomising air.

The basic concepts of fluidisation were presented, and the fundamental parameters such as minimum fluidisation and terminal velocity were presented followed by the Geldart classification of particles and the two-phase description of the bubbling fluid bed. The two-phase theory is still widely used for its intuitive simplicity and its well-validated equations, although being a simple approach. Some of the most relevant equations were presented for the use in subsequent chapters. Finally, an introduction to the basic principles of heat and mass transfer was given. Heat transfer in terms of three mechanisms was presented being: conduction, convection and radiation. The section introduced some of the basic equations, and a close analogy to heat and mass transfer in other areas of chemical engineering was observed for the equations relevant for fluid beds. The analogy between heat and mass transfer was further briefly highlighted.

2.8. Table of symbols

Symbols		Unit
a	Constant in equation 2.40	Dimensionless
A_{bed}	Bed surface area	m^2
A_{emis}	Area of the emissive surface	m^2
$A_{annulus}$	Area of the air annulus	m^2 or in^2
A_{plate}	Area of the air distributor plate	m^2
Ar	Archimedes number	Dimensionless
b	Constant in equation 2.40	Dimensionless
C_p	Specific heat capacity	$J/(kg \cdot K)$
C_D	Drag coefficient	Dimensionless
d_{32}	The Sauter mean droplet diameter	μm

d_{bed}	Diameter of the particle bed	m
d_{body}	Characteristic diameter of a given body	m
d_{bu}	Gas bubble diameter	m
$d_{bu,0}$	Initial gas bubble diameter	m
$d_{bu,max}$	Largest gas bubble diameter attainable	m
d_{dr}	Mean droplet size	µm
d_{mmd}	Mass median droplet diameter	µm
d_p	Particle diameter	µm
d_p^*	Dimensionless particle diameter	Dimensionless
$\bar{d}_p$	Mean particle diameter	µm
$d_{orifice}$	Diameter of the liquid orifice at the nozzle exit	m
d_{tube}	Diameter of a given tube	m
$d_{v0.1}$	The droplet diameter such that 10 % of the total liquid volume is in droplets of smaller diameter.	µm
$d_{v0.5}$	Volume median diameter	µm
$d_{v0.9}$	The droplet diameter such that 90 % of the total liquid volume is in droplets of smaller diameter.	µm
$d_{v0.999}$	The droplet diameter such that 99.9 % of the total liquid volume is in droplets of smaller diameter.	µm
D_v	Molecular diffusion coefficient	m^2/s
g	Gravity	m/s^2
Gr	Grasshof number	Dimensionless
h_{bed}	Height of expanded particle bed	m
h_{bu}	Bubble position above the distributor plate	m
h_{mf}	Bed height at minimum fluidisation velocity	m
L	Characteristic length of a given body	m
L_{tube}	Length of a given tube	m
m	Exponent for equation 2.1	Dimensionless
$\dot{m}_{air}$	Mass rate of atomisation air	g/s
$\dot{m}_{liq}$	Mass rate of liquid	g/s
N_{or}	Total number of orifices in the distributor plate	Dimensionless
Nu	Nusselt number	Dimensionless
Nu_p	Particle Nusselt number	Dimensionless
Oh	Ohnesorge number	Dimensionless
P	Pressure	Pa
Pr	Prandtl number	Dimensionless
q	Rosin-Rammler parameter	Dimensionless
q_{cond}	Heat flux by conduction	$J/(s \cdot m^2)$
q_{conv}	Heat flux by convection	$J/(s \cdot m^2)$
q_{rad}	Heat flux by radiation	$J/(s \cdot m^2)$
Q	Fraction of the total volume contained in droplets of diameters less than d_{dr}	Dimensionless
Re	Reynolds number of gas phase	Dimensionless
Re_p	Particle Reynolds number	Dimensionless
Sc	Schmidt number	Dimensionless
Sh	Sherwood number	Dimensionless
Sh_p	Particle Sherwood number	Dimensionless
T	Temperature	K
T_a	Temperature of the gas phase	K

T_e	Temperature of the surroundings (externals)	K
T_w	Temperature of the chamber wall	K
v_a	Fluidisation air velocity	m/s
v_{air}	Atomisation air velocity	m/s
v_{bu}	Bubble rise velocity	m/s
v_e	Excess gas velocity	m/s
v_{liq}	Liquid velocity	m/s
v_{mbu}	Minimum bubbling velocity	m/s
v_{mf}	Minimum fluidisation velocity	m/s
v_{rel}	The difference between the nozzle atomisation air velocity and the liquid velocity at the nozzle exit	m/s or ft/s
v_t	Terminal velocity of a falling particle	m/s
v_t^*	Dimensionless terminal velocity of falling particle	Dimensionless
$\dot{V}_a$	Volumetric fluidisation air velocity	m^3/s
V_{bu}	Bubble volume	m^3
$\dot{V}_{bu}$	Volumetric fluidisation air velocity in the form of bubbles	m^3/s
$\dot{V}_{mf}$	Volumetric fluidisation air velocity needed to reach v_{mf}	m^3/s
We_{air}	Air Weber number	Dimensionless
X	Rosin-Rammler parameter	Dimensionless
Y_{bu}	Parameter expressing the reduction in gas flow through the bubble phase in equation 2.23	Dimensionless
z	Length coordinate	m

Greek

α_{heat}	Convective heat transfer coefficient	$J/(s \cdot m^2 \cdot K)$
α_{mass}	Mass transfer coefficient	m/s
β_a	Thermal expansion coefficient of the fluidisation air	K^{-1}
β_{E1}, β_{E2}	Ergun parameters	Dimensionless
γ_{liq}	Liquid surface tension	kg/s^2 or dynes/cm
Γ	Gamma function	Dimensionless
δ	Laminar boundary layer thickness	Dimensionless
ε	Emissivity	Dimensionless
ε_{bu}	Voidage created by the bubble phase	Dimensionless
ε_{bed}	Total voidage of a bubbling fluidised bed	Dimensionless
ε_{mf}	Bed voidage at minimum fluidisation	Dimensionless
η_a	Air viscosity	Centipoises
η_{liq}	Liquid viscosity	Centipoises
λ	Thermal conductivity	$J/(s \cdot m \cdot K)$
λ_a	Thermal conductivity of air	$J/(s \cdot m \cdot K)$
π	Pi	Dimensionless
ρ_a	Fluidisation air density	kg/m^3, g/cm^3 or lb/ft^3
ρ_{air}	Atomisation air density	kg/m^3, g/cm^3 or lb/ft^3
ρ_{liq}	Liquid density	kg/m^3, g/cm^3 or lb/ft^3
ρ_p	Particle density	kg/m^3
σ	Stefan-Boltzmann constant	$J/(s \cdot m^2 \cdot K^4)$
τ_c	Average particle circulation time	s
ψ_p	Particle sphericity	Dimensionless

2.9. References

Abrahamsen, A.R. and Geldart, D. (1980) Behaviour of Gas-Fluidized Beds of Fine Powders Part I. Homogeneous Expansion, Powder Technology, No. 26, pp. 35-46.

Abbott, A. (2002) Boundary Between Coating and Granulation, M.Sc. Thesis, Department of Chemical Engineering, The University of Queensland.

Ayres, D., Caldas, M., Semião, V. and da Graca Carvalho, M. (2001) Prediction of the droplet size and velocity joint distribution for sprays, Fuel, No. 80, pp. 383-394.

Bi, H.T., Ellis, N., Abba, I.A. and Grace, J.R. (2000) A state-of-the-art review of gas-solid turbulent fluidization. Chemical Engineering Science, Vol. 55, pp. 4789-4825.

Broadhurst, T.E. and Becker, H.A. (1975) Onset of Fluidization and Slugging in Beds of Uniform Particles, AIChE Journal, Vol. 21, No. 2, pp. 238-247.

Chin, J.S. and Lefebvre, A.H. (1987) Some comments on the characterization of drop-size distributions in sprays, ICLASS-85.

Clement, K.H., Fangel, P., Jensen, A.D. and Thomsen, K. (2004) Kemiske enhedsoperationer, Polyteknisk Forlag, 5th Edition.

Darton, R.C., LaNauze, D.C., Davidson, J.F. and Harrison, D. (1977) Bubble growth due to coalescence in fluidized beds. Transactions of the Institutions of Chemical Engineers, No. 55, pp. 274-280.

Davidson, J.F. and Harrison, D. (1963) Fluidised particles. Cambridge University Press.

Dewettinck, K. (1997) Fluidized bed coating in food technology: process and product quality, Ph.D. Thesis, Ghent University.

Ergun, S. (1952) Fluid flow through packed columns. Chemical Engineering Progress, No. 48, pp. 89–94.

Geldart, D. (1973) Types of Gas Fluidization, Powder Technology, No. 7, pp. 285-292.

Glaser, H.W. (1989) Das Zerstäuben von Suspensionen mit Ein- und Zweistoffdüsen, VDI Verlag, Düsseldorf.

Glatt (2008) Visit at the homepage www.glatt.com, May 2008.

Gretzinger, J. and Marshall, W.R. JR. (1961) Characteristics of Pneumatic Atomisation, AICHE Journal, Vol. 7, No. 2, pp. 312-318.

Guignon, B., Duquenoy, A. and Dumoulin, E.D. (2002) Fluid Bed Encapsulation of Particles: Principles and Practice, Drying Technology, No. 20, pp. 419-447.

Hede, P.D. (2005) Fluid bed coating and granulation, M.Sc. Thesis, Department of Chemical Engineering, Technical University of Denmark.

Hede, P.D., Bach, P. and Jensen, A.D. (2008c) Two-fluid spray atomisation and pneumatic nozzles for fluid bed coating/agglomeration purposes: a review, Chemical Engineering Science, Vol. 63, No. 14, pp. 3821-3842.

Hede, P.D., Bach, P. and Jensen, A.D. (2008g) Batch top-spray fluid bed coating: Scale-up insight using dynamic heat and mass transfer modelling, Chemical Engineering Science, Vol. 64, No. 6, pp. 1293-1317.

Hund, J. (1994) Ssshh! Internal mix atomization – the finishing industry's best kept secret, Wood & Wood Products, No. 1.

Iveson, S.M., Litster, D.L., Hapgood, K. and Ennis, B.J. (2001a) Nucleation, growth and breakage phenomena in agitated wet granulation processes: a review, Powder Technology, No. 117, pp. 3-39.

Jones D.M. (1988a) Air Suspension Coating. In: Swarbrick, J. and Boylan, J.C. (Eds.) Encyclopedia of pharmaceutical technology, Volume 1. Marcel Dekker, New York, p. 189-216.

Jones, D.M. (1988b) Controlling particle size and release properties – secondary processing techniques. In: Risch, S.J. and Reineccius, G.A. (Eds.) Flavor encapsulation, ACS Symposium Series 370. American Chemical Society, Washington DC, 158-175.

Kim, K.Y. and Marshall, W.R. (1971) Drop-Size Distributions from Pneumatic Atomisers, AIChE Journal, Vol. 17, No. 3, pp. 575-584.

Kunii, D. and Levenspiel, O. (1991) Fluidization Engineering, 2nd Edition, Butterworth-Heinemann, Stoneham.

Lefebvre, A.H. (1980) Airblast Atomization, Prog. Energy Combust. Sci., No. 6, pp. 233-261.

Lefebvre, A.H. (1989a) Atomisation and Sprays, Hemisphere Publishing Corporation, Washington D.C.

Lefebvre, A.H. (1989b) Properties of Sprays. Part. Part. Syst. Charact., No. 6, pp. 176-186.

Lefebvre, A.H. (1996) Some Recent Developments in Twin-Fluid Atomisation, Part. Part. Syst. Charact., No. 13, pp. 205-216.

Link, K.C. and Schlünder, E.U. (1997) Fluidized bed spray granulation. Investigation of the coating process on a single sphere, Chemical Engineering and Processing, No. 36, pp. 443-457.

Masters, K. (1972) Spray Drying, Leonard Hill Books, International Textbook Company Limited, London.

Mori, S. and Wen, C.Y. (1975) Estimation of bubble diameter in gaseous fluidized-beds, AIChE Journal, No. 21, pp. 109-115.

Mulhem, B., Fritsching, U. Schulte, G. and Bauckhage, B. (2003) Effect of solid particle characteristics on suspension atomization, Atomization and Sprays, No. 133, pp. 321–343.

Mulhem, B., Schulte, G. and Fritsching, U. (2006) Solid-liquid separation in suspension atomisation, Chemical Engineering Science, No. 61, pp. 2582-2589.

Niro (1992) Notes on Fluidized Beds, Niro Atomizer A/S.

Niro (2007) Narrowspan^{TM} Atomization – Powder Production with Narrow PSD, GEA Niro Powder Technology.

Nukiyama, S. and Tanasawa, Y. (1939) An experiment on atomisation of liquid – The effect of the properties of liquid on the size of drops, Trans. Soc. Mech. Engrs., Japan (JSME Journal), No. 18, Vol. 5, pp. 68–75.

Nukiyama, S. and Tanasawa, Y. (1940) An experiment on atomisation of liquid – the atomisation pattern of liquid by means of air stream. Trans. Soc. Mech. Engrs., Japan (JSME Journal), No. 22, Vol. 6, pp. 7–15.

Peters, M.H., Fan L.-S. and Sweeney, T.L. (1982) Reactant Dynamics in Catalytic Fluidized Bed Reactors with Flow Reversal of Gas in the Emulsion Phase, Chemical Engineering Science, Vol. 37, No. 4., pp. 553-565.

Rhodes, M. (1998) Introduction to Particle Technology, John Wiley & Sons Ltd., Chichester.

Rizk, N.K. & Lefebvre, A.H. (1985) Drop-size Distribution Characteristics of Spill-Return Atomizers, AIAA J. Propul. Power, Vol. 1, pp. 16 - 22.

Rizkalla, A.A. & Lefebvre, A.H. (1975) The Influence of Air and Liquid Properties on Airblast Atomisation, ASME Journal of Fluids Engineering, Vol. 97, No. 3, pp. 316-320.

Rohsenow, W.M., Hartnett, J.P. and Cho, Y.I. (1998) Handbook of heat transfer, McGraw-Hill, USA, 3rd Edition.

Rosin, P. & Rammler, E. (1933) The Laws Governing the Fineness of Powdered Coal, J. Inst. Fuel, No. 31, pp. 29-36.

Ronsse, F. (2006) Modelling heat and mass transfer in fluidised bed coating processes, Ph.D. Thesis, Ghent University.

Rowe, P.N. (1973) Estimation of solids circulation rate in a bubbling fluidised bed, Chemical Engineering Science, No. 28, pp. 979-980.

Rubino, O.P. (1999) Fluid-Bed Technology. Overview and Criteria for Process Selection, Pharmaceutical Technology, No. 23, pp. 104-117.

Rümpler, K. and Jacob, M. (1998) Continuous coating in fluidized bed, Food Marketing and Technology, No. 12, pp. 41-43.

Salman, A.D., Hounslow, M.J. and Seville, J.P.K. (2007) Handbook of Powder Technology, Granulation, Elsevier Publishing.

Schaafsma, S.H., Kossen, N.W.F., Mos, M.T., Blauw L. and Hoffman A.C. (1999) Effects and control of humidity and particle mixing in fluid-bed granulation, AIChE Journal, Vol. 45, No. 6, pp. 1202-1210.

Schaafsma, S.H. (2000b) Down-scaling of a fluidised bed agglomeration process, Ph.D. Thesis, University of Groningen.

Schick, R.J. (2006) Spray Technology Reference Guide: Understanding Drop Size, Spray Analysis and Research Services, Spray Drying Systems Co.

Schlick (2007) Series 940-943 Two-Substance Nozzles, Technical Information 16/01.

Schütz, S., Breitling, M. and Piesche, M. (2004) Atomization of Suspensions with Shear-Thinning Behavíor by Aerodynamic Wave Breakup, Chemical Engineering Technology, Vol. 27, No.6, pp. 619-624.

Shirley, C. T. and Truc, V. (1987) Atomization of coal-water slurry using twin-fluid jet atomizer, Fuel, No. 66, pp. 1596-1602.

Simmons, H.C. (1976) The Correlation of Drop-Size Distributions in Fuel Nozzle Sprays, Part 1: The Drop-Size/Volume-Fraction Distribution, ASME Paper 75.

Smith, P.G. and Nienow, A.W. (1982) On atomising a liquid into a gas fluidised bed, Chem. Eng. Science, Vol. 37, No.6, pp. 950-954.

Smith, P.G. and Nienow, A.W. (1983) Particle growth mechanisms in fluidised bed granulation. I. The effect of process variables, Chem. Eng. Science, Vol. 38, No. 8, pp. 1223-1231.

Spray Drying Systems Co. (2000) Engineer's guide to Spray Drying Technology.

Summers, M. and Aulton, M. (2002) Pharmaceutics. The Science of Dosage Form Design, 2nd Edition, Montford University, Churchill Livingstone, Leicester.

Teunou, E. and Poncelet, D. (2002) Batch and continuous fluid bed coating – review and state of the art, Journal of Food Engineering, No. 53, pp. 325-340.

Toomey, R.D. and Johnstone, H.P. (1952) Gaseous fluidization of solid particles, Chemical Engineering Progress, No. 48, pp. 220-226.

Turchiuli, C., Eloualia, Z., Mansouri, N.E. and Dumoulin, E. (2005) Fluidised bed agglomeration: Agglomerates shape and end-sue properties, Powder Technology, No. 157, pp. 168-175.

Walzel, P. (1993) Liquid atomisation, International Chemical Engineering, Vol. 33, No. 1, pp. 46-60.

Wen, .Y. and Yu, Y.H. (1966) A generalized method for predicting the minimum fluidization velocity. AIChE Journal, No. 12, pp. 610-612.

Werther, J. (1978) Scale-up of Fluidized Bed Reactors, German Chemical Engineering, No. 1, pp. 243-251.

Chapter 3. Modelling approaches to the fluid bed gran. process

Chapter introduction

The second part of the literature study introduces different modelling approaches of the fluid bed coating process. An important part of the Ph.D. thesis involves the conduction of a survey of available models to describe the process of fluid bed coating, and this survey is presented in the present chapter. Here the most relevant modelling approaches are introduced and evaluated in terms of their potentials as industrial tools for process control and optimisation. The chapter is meant as a brief introduction to the modelling approaches and principles, and the aim is to outline the present boundaries of the *Scientific Frontiers* of modelling fluid bed particle coating processes, rather than being a thorough historical review. Such reviews may be found elsewhere in e.g. Iveson et al. (2001a), Hangos & Cameron (2001), Cameron et al. (2005), Salman et al. (2007) and Hede (2006). However, when relevant for the understanding and for the comming chapters, theories and equations are presented in detail. The chapter is concluded with an evaluation of the model approaches in the perspective of industrial users.

The sections in chapter three are mainly based on the literature review: *Towards Mathesis Universalis: Modern aspects of modelling batch fluid bed agglomeration and coating systems – a review* (referred to as Hede, 2006) authored by Peter Dybdahl Hede (Technical University of Denmark).

3. Modelling approaches to the fluid bed granulation process

Fluid bed particle processing is a rapidly growing scientific field. Although the processing of particles in fluid beds as a unit operation is more than fifty years old, much of the quantitative understanding is yet to be developed (Pietsch, 2003). For long, process control of fluid bed systems has been empirically based, but within the last decade or so the quantitative understanding has been accelerating, and more than half of all available literature in the field of modelling fluid bed coating processes has been produced within the last ten to fifteen years (Scopus, 2008). The scientific development is currently in a phase of testing new and old modelling techniques and approaches. The final goal has nevertheless remained well-defined for many years: to be able to model coating systems as precisely as is needed in order to make it possible to optimise, control and design as well as predict the outcome of a process based on formulation, process and raw material parameters and properties.

There are several approaches to model the fluid bed coating process. Each principle has its own advantages and disadvantages. At one extreme are the fully-mechanistic models that seek to incorporate fundamental physics and chemistry at all length scales into integrated models. Such so-called *white-box* models have not yet been developed and validated with satisfying results due to the complexity and limited fundamental knowledge about the fluid bed coating process (Hangos & Cameron, 2001). At the other extreme are the fully empirical so-called *black-box* models that are built by fitting an arbitrary function to input-output data. (Cameron, 2005 and Hede, 2006). In between the black-box and white-box models are the so-called *grey-box* models that implement a certain degree of mechanistic process description, combined with empirical functions. The majority of the suggested fluid bed models fit into

this category (Ronsse, 2006). In the coming sections, the principles of some of the most used modelling approaches are presented.

3.1. Black-box modelling

Black-box models cover in principle all models where the fluid bed chamber is treated as a single perfectly well-mixed box. The term *black-box* refers to the fact that this model approach does not describe what is going on inside the fluid bed, but only considers in- and outlet streams. Early fluid bed coating models are typically black-box models consisting of a single heat and/or mass balance to describe the fluid bed coating process (Ronsse, 2006). Given the complexity of the fluid bed process, the black-box approach has often been chosen as a first rough model attempt. In general, such models seek to relate process and formulation parameters to either final granule product attributes or to coating process efficiencies, such as coating mass yield or agglomeration tendency. This is typically done in the simplest manner by balancing in- and outlet streams (Werner et al., 2007b).

Black-box models have the disadvantage of not taking fluidised bed behaviour into account as the gas and solid phases are assumed to be perfectly mixed, which is a rough assumption. As a consequence, black-box models are less suited to predict dynamic behaviours of the bed, and therefore they are commonly applied to predict only the steady state thermodynamic operation point (Ronsse, 2006). The characterisation of the solid phase in terms of a single set of variables, i.e. moisture contents and temperature, is in contradiction with experimental results, e.g. by Maronga & Wnukowski (1997a), where large gradients have been observed. Phenomena such as agglomeration and loss of the coating solution due to spray drying are furthermore difficult to integrate into black-box models (Cameron et al, 2005 and Ronsse, 2006).

In general, black-box models are considered to be a rough approach and not suitable for any fundamental understanding of the fluid bed coating process at the particle-level. Black-box models are, however, still being developed, as the models are simple enough to be implemented into simple process control software. Dewettinck et al. (1999) have e.g. developed a black-box thermodynamic model to calculate the steady-state thermodynamic operation point of a fluid bed coating process. Although the model treats the fluid bed as a single well-mixed system, convective and radiative heat losses along with vaporisation efficiency are included in the model. It was demonstrated by Dewettinck et al. (1999) that inclusions of such phenomena clearly improve the performance of the model.

More recently, Larsen et al. (2003) incorporated a dynamic black-box model into a process control strategy for aqueous film coating of pellets in a fluidised bed, while Gouin (2005) demonstrated a similar model for both aqueous and non-aqueous film coating processes. Other recent applications of black-box models in a process control context have been reviewed by Kerkhof (2000) and Ronsse (2006).

3.2. Statistical modelling

Statistical models are in principle also black-box models although the modelling procedure is slightly different. Statistical models are fully posteriori models meaning that they are solely built upon data after the experiments are done, and further, that statistic probability plays an important role in the formation of the models. Also known as *design of experiments* (DOE) or *factorial designs* the principle is widely used in experiments involving multiple factors in which it is necessary to study single as well as joint effects of the factors on one or several response parameters (Montgomery, 1997, Hede, 2005 and Ronsse, 2006).

A factorial experiment is an experiment where the design typically consists of two or more factors, each with discrete possible values known as *levels*, and where the experimental units take on all possible combinations of these levels across all of the factors. Such an experiment allows the study of the effect of each factor on the response variable, as well as the effects of interactions between factors on the response variable (Montgomery, 1997). For the majority of factorial designs, each factor has only two levels. If the number of experiments for a full factorial design is too high to be logistically feasible, a fractional factorial design may be done, in which some of the possible combinations (usually at least half) are omitted (Faure et al., 2001). This is also known as a *screening experiment* or *screening test*. In principle, a screening test will show the same tendencies as the full factorial design, although results from the screening test assume that certain high-order interactions are negligible. This is, nevertheless, most often the case in real-life experiments and screening tests are often used as a first quick and rough technique to sort out the most relevant factors (Montgomery, 1997).

In the most common types of experimental designs, a number of input variables (X_i) are selected among the process conditions and material properties (e.g. nozzle pressure, coating solution dry-matter contents, bed temperature etc.). A number of output variables are also selected (the Y_i parameters). In a fluid bed context usually the granule properties (e.g. agglomeration tendency, coating mass yield, coating layer quality etc.) are chosen. The goal is to determine a model for each Y_i (linear or not) as a function of each variable X_i and the interactions between the variables. Variables and interactions which do not contribute significantly to the model, i.e. do not affect the response to an extent that would unmistakingly not be confused with response noise, are withdrawn from the model (Faure et al., 2001). By comparison of the Y_i models, it is possible, using so-called *response surface methodology*, to optimize the different variables X_i to obtain a compromise between the results of the Y_i parameters desired.

The resulting models are obviously very dependent on the choice of the X_i parameters and the choice of the discrete test levels for each parameter. Selection of the input parameters is thereby not an easy task for a complex process as the fluid bed coating process. The nature of the factorial design makes the choice of input variables a potential problem in a fluid bed coating context. Ideally, the input variables should all be independent, and all input variables should exist in discrete levels. In the fluid bed coating process, where many phenomena and variables are interlinked, it is difficult to select independent input variables with sufficient relevance to be included into a model. This means that not all parameters involved in the coating process can be selected in the same test. In the fluid bed coating factorial design studies available in the literature, authors often choose to screen formulation as well as process parameters in the same test. Williams & Liu (2000) have e.g. chosen the coating liquid plasticizer level, fluidisation outlet temperature, spray rate and fluidisation velocity to be the factors to be analysed in order to reduce the drug release from a cellulose acetate

phthalate coating. Dewettinck & Huyghebaert (1998) have instead chosen to vary the nozzle pressure, inlet fluidisation air temperature, particle size and protein concentration in order to optimise the coating efficiency on weight basis.

Models derived from experimental data from one type of equipment are further very specific for the particular type of equipment, and statistical models are not normally used for other scales than the one the model was developed for. In a scale-up situation, the experimental work necessary to generate the first model has to be repeated in the larger scale equipment before the models can be compared. New optimums for the variables X_i have to be found, and they may be quite different from scale to scale, depending on the choice of the range studied for each X_i (Faure et al., 2001).

As with the thermodynamic black-box approach, the statistical modelling approach can be a powerful modelling tool if no detailed insight into the underlying physical principles is required. It may be time consuming, but it is simple and can lead to practical knowledge of the experimental domain studied (Faure et al., 2001). Consequently, the statistical models are relatively easy to implement into process control. If large amounts of process data are available or continuously being produced, the statistical models may be continuously updated and improved. Some examples of experimental designs for process control and/or optimization can be found in Wehrle et al. (1993), Ogawa et al. (1994), Vojnovic et al. (1995 & 1996), Miyamoto et al., (1997 & 1998), Dewettinck et al. (1999), Rambali et al. (2001), Hede (2005) and Hede et al. (2007a).

3.3. Particle-level modelling

Also known as the *micro-level*, the particle-level modelling approach treats the granulation process at the most detailed level, often in the perspective of one or two particles. This approach only seldom results in a model that can be used to control the process at the unit-operation scale, but rather leads to detailed models that treat isolated phenomena. Micro-level modelling is nevertheless a vital tool towards a complete engineering of the fluid bed coating process at all scales. If the particle-level mechanisms are not fully understood, a detailed modelling of the entire system at meso- or macro-scale does not have a fair chance of success. This section focuses on the particle-level modelling of some of the most important processes that may take place during fluid bed coating.

The fluid bed agglomeration process has in modern literature been described as a combination of three sets of separate processes: *Wetting and Nucleation*, *Consolidation and Coalescence*, and *Attrition and Breakage* (Iveson et al., 2001a). The principle of this approach can be seen in figure 3.1, where small particles are wetted by larger droplets hereby agglomerating into large granules. In a fluid bed coating context, the situation is slightly different as particles are typically wetted by smaller droplets to give a gradual coating layer build-up. In that perspective, it is more reasonable to divide the fluid bed coating process into similar three sets of separate processes being: *Wetting and possible droplet penetration into core particles*, *Coating and possible agglomeration*, and *Attrition and Breakage* according to figure 3.2.

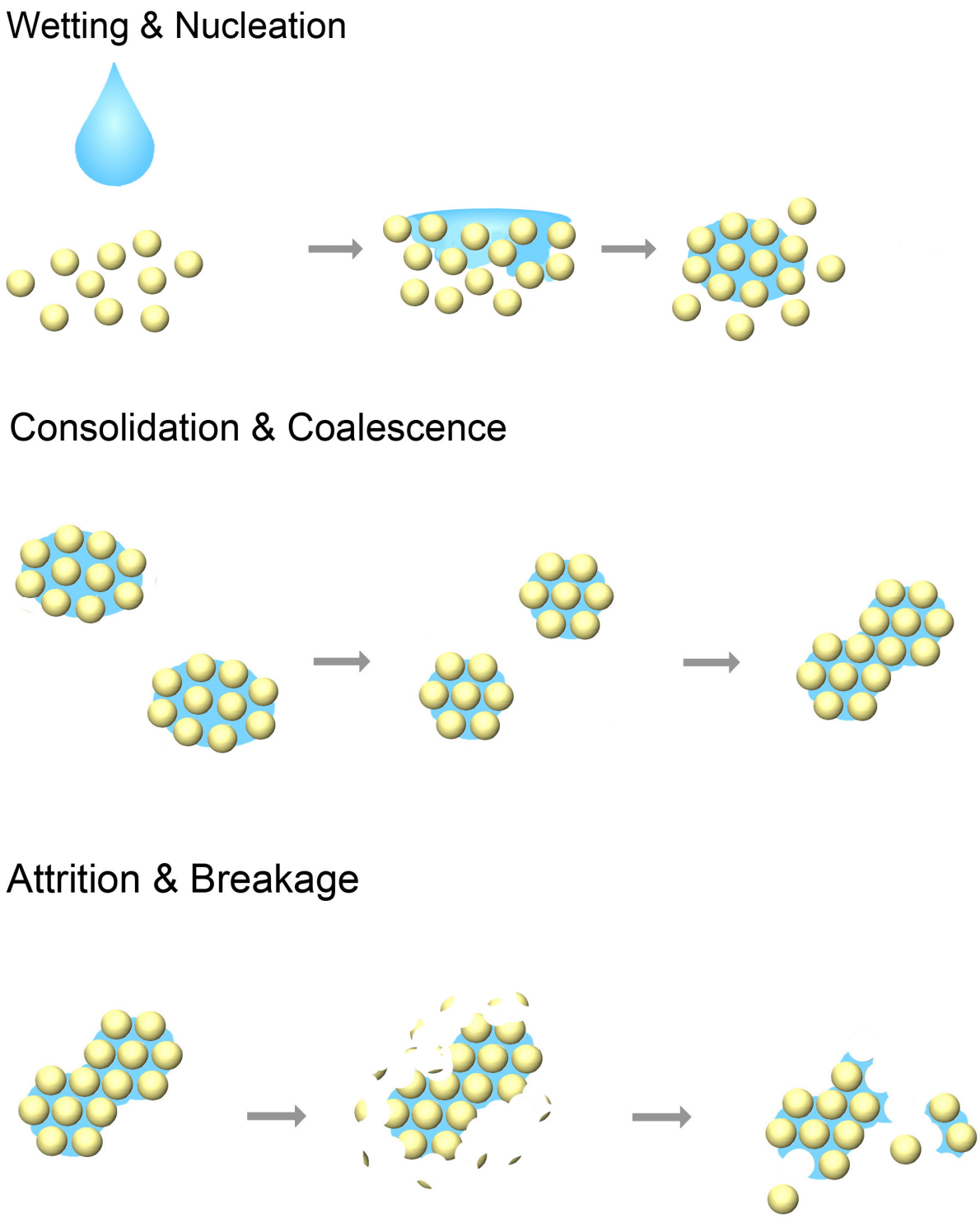

Figure 3.1: Modern description of the fluid bed agglomeration process at particle-level (Based on Iveson et al., 2001a,b).

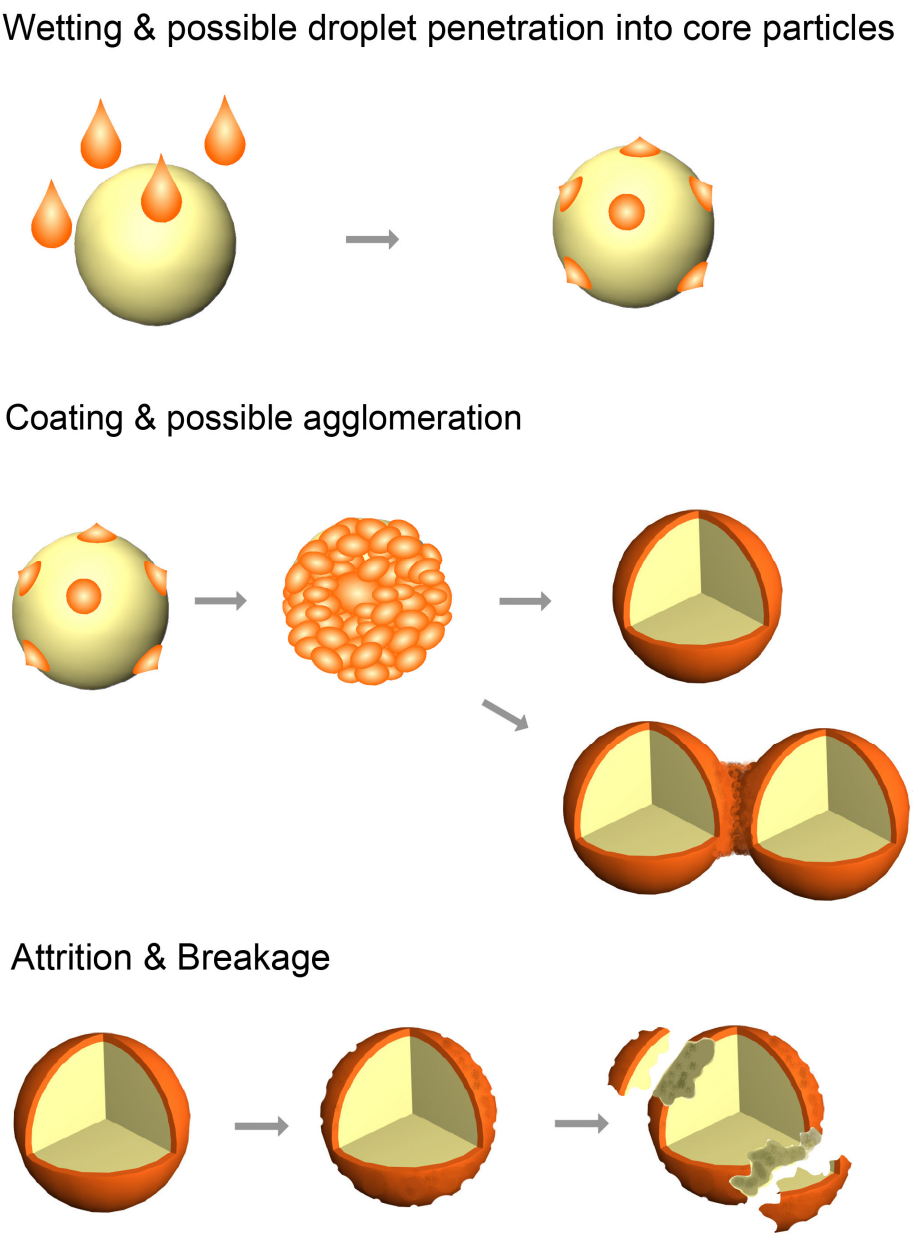

Figure 3.2: New description of the fluid bed coating process at particle-level.

By far, most of the available particle-level theory has treated the agglomeration situation of two small particles being wetted by a larger droplet. Even though fluid bed coated particles are not made by agglomeration, much of the developed theory behind the description of agglomeration has direct mechanistic parallels to the coating process. Agglomeration theory at particle-level has been treated recently in detail by Salman et al. (2007), Hede (2006) and Iveson et al. (2001a). Here only theory with interest to fluid bed coating will be presented.

3.3.1. Particle wetting, drying and possible penetration into core particles

The initial step in the fluid bed coating process is to bring the coating solution droplets into contact with the core particles. Initially, liquid droplets are formed at the nozzle outlet from which they fall and impact the particles visiting the spray zone. After the initial impact, the

droplets wet and possibly penetrate the core particles by capillary action. If a droplet is slow to penetrate the core particle, the droplet solvent may evaporate and the solid contents of the droplet will remain as a deposited coating layer on the core particle. If, on the other hand, it takes too long for the droplet to travel from the nozzle outlet to the particle, it may dry up before impact and become exhausted as a spray dried particle (Rubino, 1999 and Iveson et al., 2001a).

Whether or not the coating droplet wetting of the particle surface is energetically favourable is determined by thermodynamics, i.e. physical chemistry. Especially two aspects have been found to have major importance: firstly, the value of the contact angle between the solid particle and the liquid phase and secondly, the value of the spreading coefficient of the liquid phase over the solid phase (Iveson et al., 2001a). Both terms will be introduced below. Sufficient surface wetting and droplet spreading is necessary, since a non-wetting/non-spreading coating liquid will either not adhere to the particles or only cover a very small area, thereby restricting the formation of a complete coating shell (Tardos et al., 1997).

When a liquid droplet is placed in contact with a solid, three interfaces are present: The solid/liquid, the solid/vapour and the liquid/vapour interface. Each of these interfaces has their own interfacial energy, being γ_{sl}, γ_{sv} and γ_{lv}, respectively. The situation can be seen in figure 3.3. Even though this theory is developed for a plane solid surface there is a complete analogy to the wetting of spherical particles (Marmur et al., 1992). For a droplet that partially wets a solid, the total interfacial energy is at a minimum when the horizontal components of the interfacial tensions are in equilibrium. This situation can be described by the Young equation (Goodwin, 2004).

$$\gamma_{sv} = \gamma_{sl} + \gamma_{lv} \cdot \cos\theta \Leftrightarrow \gamma_{sv} - \gamma_{sl} = \gamma_{lv} \cdot \cos\theta \tag{3.1}$$

where θ is the contact angle in degrees. The contact angle depends on the composition of the coating solution and the physical properties of the core particle, especially roughness, porosity and affinity for the coating solution (Guignon et al., 2002).

The work of adhesion, W_A, is the work required to separate an interface into two separate surfaces (Goodwin, 2004), and for a solid/liquid interface it is given by the Dupré equation (Goodwin, 2004):

$$W_A = \gamma_{lv} + \gamma_{sv} - \gamma_{sl} \tag{3.2}$$

Combination of the Young and the Dupré equation gives:

$$W_A = \gamma_{lv}(1 + \cos\theta) \tag{3.3}$$

Thus by the combination, a relation between the work of adhesion and the contact angle is achieved. Equation 3.3 shows that if the contact angle is large (a large contact angle indicates poor wetting) the work of adhesion is small. With a low value of W_A the coating layer is expected to be loosely attached to the core particle resulting in poor mechanical properties of the coating layer. The direct connection between the solid-liquid contact angle and the properties of the final coated granule has been verified experimentally by Teipel & Mikonsaari (2004) among others (Iveson et al., 2001a).

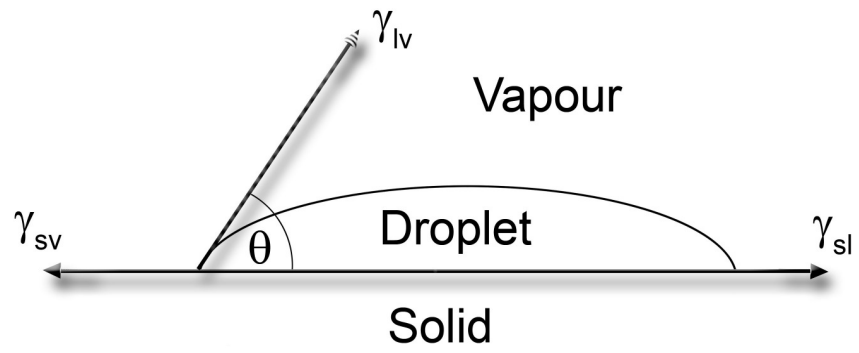

Figure 3.3: The three interfaces present when a liquid droplet is in contact with a solid phase (Based on Teipel & Mikonsaari, 2004).

In practice, the liquid-solid-vapour interface may not have sufficient time to reach its equilibrium state due to the interference from the agitation forces and drying occurring simultaneously in the fluid bed. Besides thermodynamics and wetting, there is also a potential chance that the liquid droplet may penetrate into the core particle depending on the surface porosity. Liquid penetration is driven by surface tension, contact angle and pore radius. The liquid will advance into the core particle by flowing into successively smaller pores (Hapgood et al., 2002). Prior to depletion of the liquid, the droplet has spread onto the bed surface. Denesuk et al. (1994) have showed that the spreading time, τ_s, is often far smaller than the time of droplet penetration (also known as the *time of depletion*), τ_{dpen}, indicating that as the droplet contacts the core surface, it will immediately spread to a semi-static configuration followed by a slower depletion process. Each of the time constants are viscosity dependent, but the ratio τ_s/τ_{dpen} has been proven not to depend on the liquid viscosity (Denesuk et al., 1994). The time it will take for a liquid droplet to spread, penetrate and saturate the pores of a core particle is thereby in practice solely dependent on the droplet penetration time (Schaafsma et al., 1998).

No models have yet been developed for the absorption of droplets into fluidised particles in motion, but a theory exists for the penetration of a single droplet into a porous surface. A first approach for the description of a theoretical droplet penetration time, τ_{dpen}, was suggested by Denesuk et al. (1993 & 1994) according to equation 3.4:

$$\tau_{dpen} = \frac{2V_{dr}^2}{\pi^2 \cdot \varepsilon_{pmsp}^2 \cdot r_{dr}^4 \cdot R_{pore}} \cdot \frac{\eta_{liq}}{\gamma_{lv} \cdot \cos\theta} \tag{3.4}$$

where V_{dr} is the total droplet volume, r_{dr} the radius of the droplet, ε_{pmsp} is the porous media surface porosity, γ_{lv} is the liquid surface tension, η_{liq} is the liquid viscosity, θ is the solid-liquid contact angle and R_{pore} is the effective pore radius based on the assumption of cylindrical parallel capillary pores in the porous solid structure given by the Kozeny approach:

$$R_{pore} = \frac{2 \cdot \varepsilon_{pmsp}}{(1 - \varepsilon_{pmsp}) \cdot s_0 \rho_p} \tag{3.5}$$

where s_0 is the particle specific surface area expressed in m^2/kg and ρ_p is the particle density (Denesuk et al., 1993).

In characterising and determining the wetting behaviour of a solid, the droplet penetration time is a widely used parameter as it contains both a thermodynamic and kinetic dependence. The thermodynamic wetting dependence is represented by ($\gamma_{lv} \cdot \cos\theta$) and the wetting kinetics by the viscosity η_{liq} and the pore radius R_{pore} (Iveson et al., 2001a). Hapgood et al. (2002) have showed that the Kozeny approach is only valid for low porosity solids with narrow pore size distributions. Pore radius and surface porosity values are typically determined experimentally with the given solid material in terms of e.g. mercury extrusion/intrusion experiments, and these values may be used instead of the Kozeny equation.

Several authors have observed the problem of droplets drying before impact, which is particularly prevalent in top-spray fluid bed arrangements where droplets travel counter-current to the fluidisation airflow (Link & Schlünder, 1997 and Werner et al., 2007a,b). Aronson and Tsaur (1993) noted from top-spray experiments that coating levels were significantly lower than the amount of coating material supplied to the system as a result of droplet pre-drying. However, because drying is occurring from the moment droplets are formed, some increase in droplet surface stickiness with drying is expected. This enhances the droplet–particle adherence and to some extent counteracts the glancing-off effect of pre-dried droplets. The simplest droplet drying problem is the evaporation of a pure liquid droplet in a quiescent gas stream. The drying time, τ_{evap}, can be estimated from equation 3.6 proposed by Marshall (1954).

$$\tau_{evap} = \frac{\rho_{dr} \cdot \Delta H_{vap} \cdot d_{dr}^2}{8 \cdot \lambda_a \cdot (T_a - T_{dr})} \tag{3.6}$$

where ρ_{dr} is the droplet density, ΔH_{vap} is the latent heat of vaporisation, d_{dr} is the droplet diameter, λ_a is the thermal conductivity of air, T_{dr} is the droplet surface temperature and T_a is the fluidisation air temperature.

As presented by Sloth (2007) slurries and coating solutions rarely show constant rate drying. Instead a falling rate period is usually observed from the outset of drying because transport of water to the surface of the drying substance is described in terms of diffusion, which can be regarded as the controlling mechanism in many drying processes (Sloth, 2007). Therefore, the time for a single droplet to dry was suggested by Crank (1956) to be estimated by the summation in equation 3.7 for diffusion in a solid, non-porous sphere with constant surface concentration.

$$\frac{W_t}{W_{eq}} = 1 - \frac{6}{\pi^2} \sum_{n=1}^{\infty} \frac{1}{n^2} \exp\left[- \frac{n^2 \cdot \pi^2 \cdot D_w \cdot t}{r_{dr,0}^2} \right] \tag{3.7}$$

where W_t and W_{eq} are the average moisture contents in kg H_2O/kg dry solid at time t and at equilibrium, respectively. The parameter $r_{dr,0}$ is the initial droplet radius and D_w is the constant binary diffusion coefficient.

Although equation 3.7 is limited by numerous assumptions including: non-shrinking system, uniform initial moisture distribution, negligible external resistance to moisture transfer, constant diffusion coefficient, unidirectional moisture movement and isothermal process conditions, it may provide a first estimate of the drying time (Werner et al., 2007b). In order to achieve a better estimate of the drying time, precise estimates of the concentration-dependent moisture diffusivities is needed. Unfortunately, only limited data are available on

the concentration dependent diffusivities for typical coating solutions, and their variation can be significant leading to some uncertainty in respect to drying time estimations (Adhikari, 2002 and Sloth, 2007).

On the particle-level, droplet drying time and droplet penetration time both have an important role regarding the morphology of the final coating layer, i.e. the appearance of the coating layer in respect to homogeneity and surface cracks etc. Studies by Link & Schlünder (1997) show that viscosity plays an important role, and that a high viscosity and short drying times often leads to raspberry-like coating layers with poor mechanical properties. Such raspberry-like coating layers are typically quite porous. If drying happens very fast, the coated layer dries first at the surface to form a shell-structure containing unvaporised solvent inside. As the solvent inside the solid shell starts to evaporate, the volume inside the shell will decrease causing shrinkage and cracking in the surface shell-structure.

Whether or not the coating layer forms crystals is of great importance. Besides influencing important properties, such as hygroscopicity and solubility, the mechanical properties of the coating layer is highly influenced by the extent of crystal formation. The formation of crystals will often lead to a stratified, porous and flaky coating layer with poor mechanical properties (Canselier, 1993). Guignon et al. (2002) report that the chance of a smooth and homogenous coating layer is improved if the core surface before coating is smooth and with few pores, although adhesion of the coating liquid is improved by surface roughness. Examples of SEM pictures of smooth, raspberry-like and crackled coatings can be seen in figure 3.4. Further issues on coating layer morphology may be found in a recent review by Werner et al. (2007a).

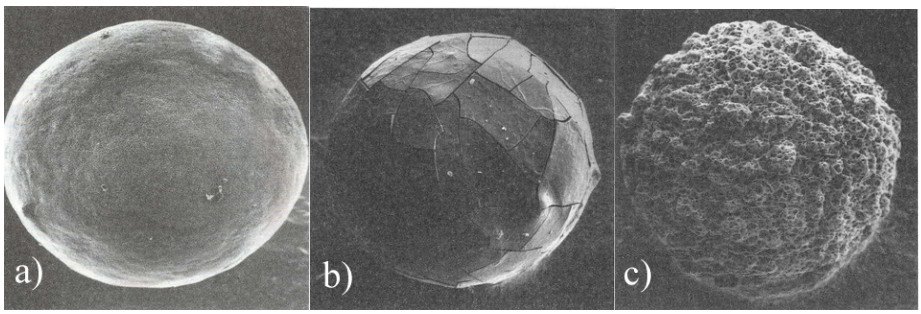

Figure 3.4: SEM pictures of coated single aluminium spheres having a diameter of 1.3 mm. a) Smooth coating by aqueous solution of lactose. b) Smooth coating with cracks by aqueous solution of PVP. c) Raspberry-like structure by aqueous solution of NaCl (Link & Schlünder, 1997).

Coating layer morphology and the time of droplet drying versus droplet penetration is closely related to droplet spreading, which is typically expressed in terms of a spreading coefficient. The spreading coefficient, λ_{ls}, is a measure of the tendency of a liquid and a solid combination to spread over each other, and indicates whether spreading is thermodynamically favourable or not. It is given by the difference between the work of adhesion and the work of cohesion according to (York & Rowe, 1994):

$$\lambda_{ls} = W_A - W_{CL} \tag{3.8}$$

The work of cohesion, W_C, is the work required to separate a unit cross-sectional area of a material from itself. For a solid $W_{CS} = 2\gamma_{sv}$, and for a liquid $W_{CL} = 2\gamma_{lv}$ (Iveson et al., 2001a). In a coating situation there are two possibilities in spreading between a particle and a liquid: the liquid may spread over the core particle and create a surface film; or the liquid and particle

may both have high works of cohesion. The solid-liquid interfacial area will then be minimised or nonexistent (Iveson et al., 2001a).

Spreading will occur spontaneously only when the spreading coefficient is positive. When λ_{ls} is positive, the liquid will spread and form a film over the particle surface, and liquid bridges may form between contacting particles. Particles being coated under conditions with a positive spreading coefficient have a higher chance of having homogenous coating layers. A positive spreading coefficient may be seen as a prerequisite of a successful coating process (Iveson et al., 2001a). Several investigations confirm that differences in final granule properties can be correlated with the spreading coefficient (Rowe, 1989 and Zajic & Buckton, 1990).

3.3.2. Particle growth modelling – Class I and Class II models

There are only few theoretical models available in the literature for predicting whether or not the collision of two wetted particles will either result in permanent agglomeration or in rebound. All models are associated with a number of assumptions and simplifications regarding the mechanical properties of the particles as well as the system in which the particles collide. Some of the first models were developed for predicting the sintering of fluidised beds used in the mining industry, but later models have been adapted to specifically describe the granulation process (Iveson et al., 2001a). Although being very different in nature, Iveson et al. (2001a) have divided the agglomeration models into two classes of which the distinct principles are sketched according to figure 3.5.

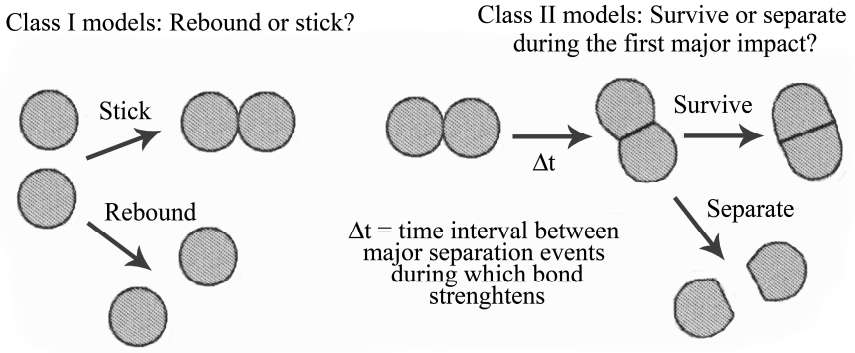

Figure 3.5: Schematic diagram of the two general classes of coalescence models: Class I models: Rebound or stick, Class II models: Survival or separation (based on Iveson, 2001).

Class I models assume that particles are free to move and that the elastic properties of the particle bodies are important. These models assume that initial coalescence occurs only if the kinetic energy of collision is entirely dissipated in the liquid layer. If not, the granules will rebound and move apart. Various combinations of energy dissipations have been considered by different authors including elastic losses, plastic deformation of the particles, viscous and capillary forces in the liquid layer and adhesion energies of the contact surfaces (Salman et al., 2007). In Class I models it is implicitly assumed that if the initial impact results in permanent agglomeration, none of the subsequent impacts will be able to break the two particles again. In other words this means that permanent agglomeration is assumed to occur whenever the two particles do not possess sufficient kinetic energy to rebound (Iveson et al., 2001a). It further implies that all collisions at near-zero velocities will result in permanent coalescence (Iveson, 2001).

Class II models on the other hand assume that elastic effects are negligible during the initial collision, usually because it is assumed that the granules are plastic in nature or physically constrained by surrounding granules. This leads to the simplification that all colliding granules are in contact for a finite time, Δt, during which a liquid bridge develops between them. Permanent agglomeration therefore occurs only if this liquid bridge is strong enough to resist subsequent collisions or shear forces. The strength of the binding bridge is assumed to be dependent on factors such as the initial amount of plastic deformation in the particle phase and the contact time of the two particles.

Due to the simplicity of both model classes, a lot of relevant criticism is associated with both views on agglomeration modelling. The coalescence criteria in Class I models are typically criticised for being unreasonable for most fluid bed granulation applications, because this class of models neglects the effect of subsequent collisions. Two granules which initially stick together in terms of a liquid bridge may in reality be so weakly held together that they would quickly break apart. It is also unreasonable to assume that agglomeration is controlled solely by the initial collision energy, when in many applications, the particles are constrained in contact with one another for significant lengths of time, as it occurs in the quiescent zones of a fluid bed. In these cases there is no single and uniform collision event. Instead the granules are constantly in contact with several others (Iveson, 2001). This means in other words that although non-rebound is a necessary condition for permanent agglomeration, it is not necessarily the only condition. Not only do the particles need to stick together when they first collide, but they must also form a bond strong enough to resist being broken by subsequent impacts in the fluid bed. This is not accounted for in Class I models thereby being an obvious limitation.

In all Class II models, only the first major separation event is considered and the magnitude of separation is usually approximated by some global average value. If the particle-particle bonding bridge survives this single event then it is considered to be a permanent agglomeration bond. However, in fluid beds the separation events may have a wide range of magnitudes and may further be distributed randomly in time. Therefore some criticisers (e.g. Iveson, 2001) state that it is inappropriate to model agglomeration by assuming a mean separation force, which occurs at regular intervals, and further; that the probability of the survival of a bonding bridge rather will depend on the history of impacts and the rate at which the binding bridges strengthens as they are kneaded together by a number of low-level impacts (Iveson, 2001).

Class II models have generally been developed and optimised for high collision force granulation equipment such as high shear mixing or drum granulation. In such high agitative equipment it is necessary to account for deformability of the granules during collision as well as the rupture forces. A number of different Class II coalescence models have been presented by e.g. Ouchiyama & Tanaka (1975) for drum granulation. In fluid beds, however, the agitative forces and thereby the particle collision velocities are smaller. This implies that deformation of the particles upon collision may often be neglected with good approximation. The assumptions associated with Class I models have indeed proven to be more realistic than those associated with Class II models, and the latter type is almost never applied with fluid bed systems (Teunou & Poncelet, 2002). Hence, only Class I models will be presented here.

3.3.2.1. Class I models: Agglomeration of non-deformable granules

Class I models treat the situation in which non-deformable particles collide and agglomerate. Under low-agitative conditions, as in the fluid bed, particles agglomerate by viscous dissipation in the surface liquid before contact with the core particle surfaces (Liu et al., 2000). As the two particles approach each other, first contact is made by the outer liquid coating layer. The liquid will subsequently be squeezed away from the space between the particles to the point where the two solid surfaces will touch. A solid rebound depends on the elasticity of the surface, characterized by a coefficient of restitution *e*. The particles will start to move apart and coating liquid will be sucked into the interparticle gap up to the point where a liquid bridge will form. This bridge will either break due to further movement in the bed or solidify leading to permanent agglomeration (Tardos et al., 1997). There is only a chance of permanent particle agglomeration if there is a liquid layer present at the surface of the colliding particles. This growth principle continues until insufficient liquid is available at the surface to bind new particles (Schaafsma et al., 1998). The relative amount of liquid present at that stage is called the *wetting saturation*, S_w, and it depends on the contact angle of the coating liquid and the pore structure of the core particle (Tardos et al., 1997). The wetting saturation reflects the wettability and spreading of the droplet on the particle surface, and it is often approximated by the liquid droplet volume at a given time divided by the pore volume of a particle, under the assumption that no droplet drying occurs (Schaafsma et al., 2000).

Ennis et al. (1991) have modelled the situation of agglomeration in a fluid bed by considering the impact of two solid non-deformable spheres each of which is covered by a thin viscous liquid layer of height h_{liq}. The simplified situation can be seen in figure 3.6.

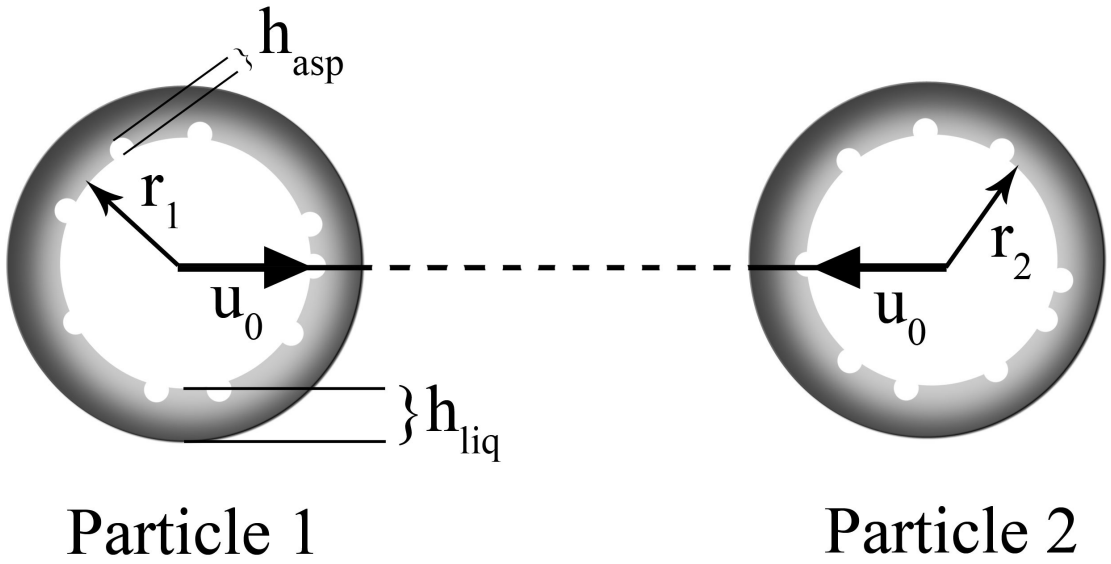

Figure 3.6: Schematic drawing of two colliding particles each of which is covered by a viscous liquid layer of thickness h_{liq} (Based on Ennis et al., 1991).

Being a typical Class I model, the model suggested by Ennis et al. (1991) assumes successful coalescence if the kinetic energy of impact is entirely dissipated by viscous dissipation in the liquid layer and only by elastic losses in the solid phase. The model predicts that collisions will result in permanent agglomeration when the viscous Stokes number (St_v) is less than a critical viscous Stokes number (St_v^*). The two numbers are given as (Ennis et al., 1991) (please refer to chapter ten for a full derivation):

$$St_v = \frac{8 \cdot \rho_g \cdot r_{harm} \cdot u_0}{9 \cdot \eta_{liq}} \tag{3.9}$$

and

$$St_v^* = \left(1 + \frac{1}{e}\right) \cdot \ln\left(\frac{h_{liq}}{h_{asp}}\right) \tag{3.10}$$

where η_{liq} is the coating solution viscosity, e is the coefficient of restitution, ρ_g is the granule density, h_{liq} is the thickness of the liquid surface layer, h_{asp} is the characteristic height of the particle surface asperities and r_{harm} is the harmonic mean granule radius of the two spheres given as (Iveson et al., 2001a):

$$r_{harm} = \frac{2 \cdot r_1 \cdot r_2}{r_1 + r_2} \tag{3.11}$$

u_0 is the initial collision velocity, which is not easily obtainable due to the chaotic pattern of motion for the particles in fluid beds. A rough estimate based on the bubble rise velocity, v_{bu}, has been presented by Ennis et al. (1991):

$$u_0 \approx \frac{12 \cdot v_{bu} \cdot r_{harm}}{d_{bu} \cdot \delta^2} \tag{3.12}$$

where d_{bu} is the gas bubble diameter and δ the dimensionless bubble space, defined as the axial fluid bed bubble spacing divided by the fluidisation gas bubble radius. Whereas the gas bubble diameter and spacing can be estimated by the dimensions of the air distributor plate, or found by experiments, the bubble rise velocity can be found according to the Davidson & Harrison (1963) formula in equation 2.29 (see chapter two).

The viscous Stokes number St_v can be seen as the ratio of kinetic energy to the viscous dissipation. During fluid bed batch granulation, St_v increases as the granules grow in size. This leads to three possible situations. The first so-called *non-inertial regime* occurs when $St_v << St_v^*$. All collisions result in successful agglomeration regardless of the size of the colliding granules, the granule kinetic energy or the coating liquid viscosity. As the granules grow larger the *inertial regime* occurs when $St_v \approx St_v^*$. The likelihood of agglomeration now depends on the size of the colliding granules and their kinetic energy, and liquid viscosity begins to play a role (Iveson et al., 2001a and Abbott, 2002). It can be seen from equation 3.9 and 3.11 that the collision between two small or one small and one large granule is more likely to succeed in permanent agglomeration than the collision between two large granules,

due to the size of r_{harm} and thereby the size of St_v versus St_v^*. This is a convenient way to understand why small particles agglomerate into larger ones (Tardos et al., 1997). Eventually, the system enters the *coating regime* when $St_v >> St_v^*$. Here all collisions between granules are unsuccessful in terms of agglomeration, and any further increase in the St_v will maintain the size of the granules (Iveson et al., 2001a and Tardos et al., 1997). The existence of the three regimes has been proved experimentally in different types of granulators (Ennis et al., 1991 and Achanta & Beimesch, 1998).

Agglomeration is promoted by a low value of St_v and a high value of St_v^*. For instance, increasing the granule liquid content will increase the liquid layer thickness, h_{liq}, which will increase St_v^* and hence increase the likelihood of successful agglomeration. The effect of the liquid viscosity is not easily predictable as an increase in the value of η_{liq} (lowering St_v) alters the coefficient of restitution *e* decreasing St_v^* as well (Iveson et al., 2001a).

Although St_v and St_v^* are important parameters in the prediction of agglomeration they are only valid for predicting the maximum size of granules which can coalesce. The parameters state nothing about the rate of agglomeration. Different authors have, nevertheless, showed that fast growth rates are attributed to the non-inertial regime while a slower growth is attributed to values of St_v close to St_v^*. With fast growth rates, systems tend to be collision limited (Ennis et al. 1991 and Cryer, 1999).

The model by Ennis et al. (1991) was a significant progress in the modelling of particle-level agglomeration in fluid beds, as it was the first model to consider dynamic affects such as viscous dissipation in the liquid layer. Results by e.g. Ennis et al. (1991), Achanta & Beimesch (1998) and Hede (2005) indeed showed that the agglomeration tendency is related to the relative sizes of St_v^* versus St_v . The model is, nevertheless, limited by its many assumptions being e.g. that there exists a uniform granule collision velocity or that capillary forces can be neglected in wet particle coalescence (Ennis et al., 1991). Ennis et al. (1991) justified neglecting capillary forces by arguing that the energy added during liquid bridge formation and particle approach is cancelled by the energy dissipated during particle separation and liquid bridge rupture. This is a rough assumption as the dynamic energy of the pendular bridge and the rupture energy are equal only if the collision has a coefficient of restitution equal to one, which is almost never the case (Liu et al., 2000). Especially the difficulty of determining a precise collision velocity, u_0, makes the viscous Stokes theory difficult to exploit fully in practice (Abbott, 2002). The theory does, however, give a rough number for the indication of the limit between no-agglomeration and successful agglomeration. In order to account for the effect of plastic deformation of the particles upon collision, Liu et al. (2000) have proposed an extension to the original Ennis et al. (1991) model. This model is, however, only relevant for high collision velocity granulator types as e.g. high shear mixers, and the extended model does not bring any improvement to the viscous Stokes theory with respect to fluid bed coating processes. Other and newer Class I models have been reviewed by Hede (2006), Iveson et al. (2001a) and Salman et al. (2007). However, the original Ennis et al. (1991) proposal is still the most used and most widely-accepted model when considering the particle-level approach of modelling agglomeration in fluid bed coating processes.

3.3.3. Breakage and attrition

The third and last type of process in the particle-level modelling approach concerns the growth limiting mechanisms. Two situations are typically considered being either the breakage of two particles held together by a liquid bridge or the situation where a coated particle, being partly or fully dry, loses some of its coating layer due to attrition and breakage. In literature, the two breakage phenomena are typically treated separately. Whereas dry granule breakage is often treated as a separate discipline, often without much attention to the process conditions, wet granule breakage is closely related to the liquid bridge properties. Both topics will be briefly presented below. For more information, Salman et al. (2007) and Reynolds et al. (2005) should be consulted.

3.3.3.1. Breakage of wet agglomerated particles

An agglomerate can exist in a number of different spatial structures depending on the liquid saturation. It is the amount of liquid as well as the humidity and temperature conditions in the bed that determines the degree of liquid saturation between the primary particles, which again determines the spatial structure of the final agglomerate (Jain, 2002). Such wet liquid bridges are obviously only temporary structures, and more permanent bonding between the primary particles is created by solid bridges formed as solvent evaporates from the bridges during further fluidisation. If the material of the particles is soluble in the coating liquid, crystalline bridges may be formed when the solvent evaporates. In some cases a finely ground solid binder material may be dispersed in the coating liquid thereby producing a cement-like solid binding bridge upon evaporation of the solvent (Rhodes, 1998). In any case, the initial forming of the liquid bridge is of primary importance regarding the properties and spatial structure of the final agglomerate, and it is almost always the case that the solid bridge will have the form of the liquid bridge (Summers & Aulton, 2001).

When particles agglomerate in fluid bed coating processes, the particles are typically held together by liquid bridges at their contact points known as the *pendular state*. This situation requires that the liquid saturation between the primary particles is low enough to let discrete binary bridges exist between the solid surfaces. Such a lens-shaped ring of liquid causes adhesion due to the surface tension forces of the air/liquid interface and the hydrostatic suction pressure in the liquid bridge (Summers & Aulton, 2001). Typical examples of agglomerates being bound by solidified pendular liquid bridges can be seen in figure 3.7 in which Na_2SO_4 cores agglomerated during coating with an aqueous Na_2SO_4/Dextrin solution in a fluid bed.

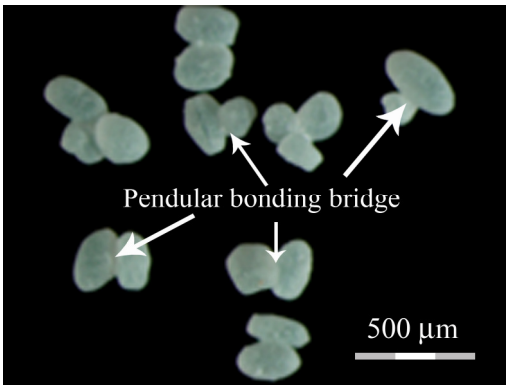

Figure 3.7: Examples of agglomerates being bound by pendular bonding bridges (Hede, 2005).

Liquid-bound granule strength is dominated by three types of forces being interparticle friction forces, static strength forces and dynamic strength forces (Salman et al., 2007 and Iveson et al., 2001a). The first two are interrelated as the static tensile force of the liquid bridge acts to pull particles together, and this normal force at particle contact activates friction. Static strength forces, as surface tension and capillary forces, are conservative forces in the sense that they always act to pull particles together in wetted systems. Frictional and viscous forces are dissipative as they always act against interparticle motion. The complex interaction of these different forces means that it is often difficult in practical situations to predict a-priori the effect of changing the coating solution composition in terms of agglomeration, unless the precise magnitude of each of these three types of forces is well-known (Iveson et al., 2002).

Simulations as well as experiments performed by Khan & Tardos (1997) indicate that liquid-bound agglomerates are often broken upon deformation in the liquid bridge by stretching under shear. They further showed that the stability of wet agglomerates is closely related to the Stokes deformation number, St_{def}, and that two regimes exist, involving high and low deformation characteristics based on the St_{def} number. Khan & Tardos (1997) defined the Stokes deformation number according to:

$$St_{def} = \frac{m_{aggl} \cdot u_0^2}{2 \cdot V_{aggl} \cdot \sigma(\dot{\gamma})} \tag{3.13}$$

in which m_{aggl} is the mass of the agglomerate, V_{aggl} the volume of the agglomerate and $\sigma(\dot{\gamma})$ is a specific characteristic stress in the agglomerate. In the most general case, this stress can be estimated according to the Herschel-Bulkley fluid model (generalised model of a non-Newtonian fluid) being:

$$\sigma(\dot{\gamma}) = \sigma_y + \eta_{app} \cdot \dot{\gamma}^{n_{fi}} \tag{3.14}$$

where σ_y is the yield strength, η_{app} is an apparent viscosity, n_{fi} the flow index and $\dot{\gamma}$ the shear rate (Tardos et al., 1997 and Fu et al., 2004). The Stokes deformation number defined in equation 3.13 increases with increasing particle size, and reaches at some point during granulation a critical value of St_{def}^* above which the agglomerates start to deform and eventually break. The critical Stokes deformation number is not as well-defined as the critical viscous Stokes number introduced by Ennis et al. (1991). This is due to the fact that, from a rheological point of view, particles bound by viscous liquid bridges form a complex system that exhibits both yield strength as well as non-Newtonian behaviour. Under the assumption that the agglomerate is a highly-concentrated slurry of the core particles in the coating liquid, the apparent viscosity η_{app} is negligible compared with the yield strength, meaning that $\sigma(\dot{\gamma}) \approx \sigma_y$. It is further assumed that the collision velocity, u_0, in fluid beds can be approximated according to:

$$u_0 \approx r_{aggl} \cdot \dot{\gamma} \tag{3.15}$$

where r_{aggl} is the radius of the agglomerate. These approximations lead altogether to a rough estimate of a theoretical expression for the critical Stokes deformation number according to:

$$St_{def}^{*} = \frac{m_{aggl} \cdot (r_{aggl}^{*} \cdot \dot{\gamma})^2}{2 \cdot V_{aggl} \cdot \sigma_y} \tag{3.16}$$

in which r_{aggl}^{*} is the critical radius of the agglomerate above which deformation and breakage occurs. Equation 3.16 thereby predicts an inverse linear relationship between the critical agglomerate radius and the shear rate, which in fact has been observed in simulations as well as in experiments by Tardos et al. (1997) and Khan & Tardos (1997).

There is generally very limited experimental work on breakage of wet agglomerates in fluid beds as most work focuses on drum granulation and high shear mixing (e.g. Fu et al., 2004 & 2005). In fact, the studies by Tardos et al. (1997) and Khan & Tardos (1997) are the only works so far specialised on fluid bed granulation. This is most likely due to the fact that the high intensity granulation types makes it much easier to estimate the average shear forces and the collision velocity based on equipment and process parameters.

3.3.3.2. Breakage and attrition of dry coated particles

A final coated granule typically consists of several different species combined in a heterogeneous way. In a physical sense a coated granule can be considered as a composite material (Iveson et al., 2001a and Bika et al., 2005). Given the heterogeneity of coated granules, it is not obvious that their mechanical properties can be described by the properties used for the description of metals, ceramics and other conventional solids. Dry granule deformation and destruction mechanisms are, however, fundamentally similar to those of other solids (Bika et al., 2001). As in other composite materials, the stress in a coated granule is transformed non-uniformly, meaning that it is concentrated in preferred paths, where some areas experience high stress loads and others little or no load. Other common characteristics are the distribution of defects (e.g. pores or grains) as well as internal and surface cracks that may dominate the macroscopic response to stress (Bika et al., 2001). These similarities imply that the description of failure in conventional solids can be applied to granules as well, and that granule strength is directly related to failure mechanisms (Scarlett et al. 2002). The mechanical properties of a dry granule may likewise be described crudely by the same set of properties used for characterising solids being: the Young´s modulus (modulus of elasticity), yield strength, tensile strength, ductility/brittleness, fracture toughness and hardness (Bika et al., 2001 & 2005).

The existence of cracks and the extent of crack propagation are of high importance in semi-brittle materials as granules. Several types of destruction can be traced back to the existence of cracks in the granule surface or in the core. A distinction between lateral and radial cracks has been made by Ghadiri & Zhang (2002). Radial cracks propagate radially from the surface to the inner of the granule, whereas lateral cracks propagate parallel to the granule surface.

The principle of a granule failing by radial crack propagation can be seen in figure 3.8. The tensile stress concentrates near the crack tip and is much higher than the applied stress, leading to local yielding near the crack tip. This zone is called the *process zone* or *damage* zone (Iveson et al., 2001a and Bika et al., 2001). The crack will thereby gradually propagate from the edge of the process zone to the interior of the granule, causing degradation of the granule's mechanical strength. The principle of lateral crack propagation is analogous, but the strength degradation only concerns the outer layer of the granule. Often radial and lateral cracks propagate simultaneously (Iveson et al., 2001a).

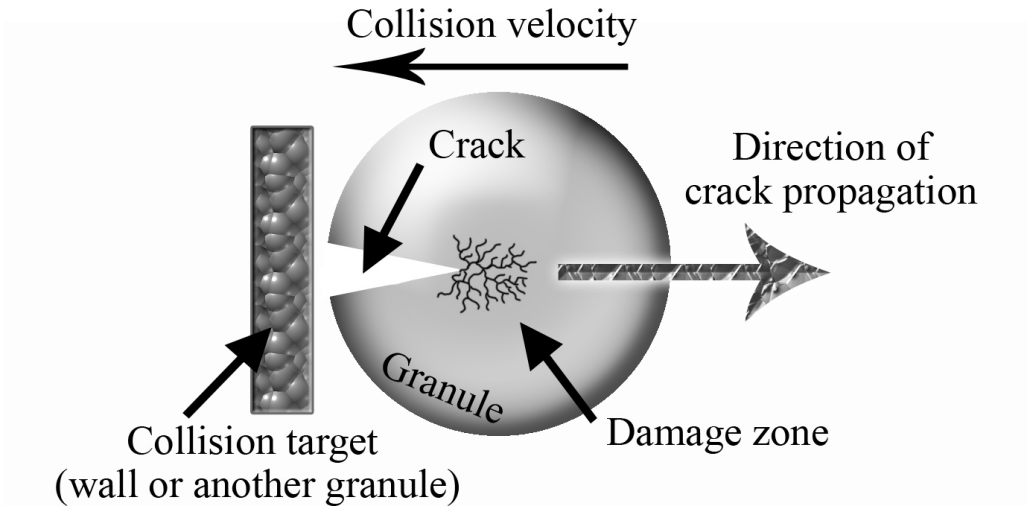

Figure 3.8: Fracture of a granule (semi-brittle) by radial crack propagation (based on Iveson et al., 2001a and Jørgensen et al., 2004).

The damage zone plays a large role in the mechanisms of dry granule breakage. The size of the damage zone with respect to the granule size, along with the main type of crack propagation, will determine the type of destruction. Granules with a small damage zone in comparison to the size of the granule will e.g. break by a brittle fracture mechanism. This mechanism is called *fragmentation* or *fracture* (Iveson et al., 2001a). Fracture of a granule is typically referred to in situations with major internal breakage due to the application of very large or repeated external forces head-on. Due to fracture, there is a drastic reduction in the granule size, and the resulting daughter particles are large compared to the original mother granule (Pitchumani et al., 2003). Fracture is the most severe kind of breakage because the original granule structure is completely destructed and the core is exposed to the surroundings (Jørgensen et al., 2004). For fracture to occur, the granule must be able to concentrate enough elastic energy to propagate single radial cracks throughout the granule structure. This is harder to accomplish as the size of the damage zone increases. Hence, fracture will only occur if the damage zone is significantly smaller than the granule size (Iveson et al., 2001a). Thornton et al. (2004) and Mishra & Thornton (2001) have showed that fracture is often associated with dense granules, whereas more porous and loosely packed granules destruct by other type of mechanisms.

Another type of fracture is chipping. If the granule is exposed to large external tangential forces instead of head-on, deep lateral cracks will propagate, and the surface area of the granules is damaged and some material is chipped off. Next to fracture, chipping is a severe type of damage. Due to chipping, the granule surface will become rougher, and exposure of the inner coating layers and even the granule core may occur, although the inner granule core structure is usually kept intact (Jørgensen et al., 2004 and Pitchumani et al., 2003). A formal classification of the different types of breakage mechanisms can be seen in table 3-1. The last two types are presented below.

Table 3-1: Formal classification of dry granule breakage mechanisms (Based on Beekman, 2000 and Pitchumani et al., 2003).

Force	Normal force	Tangential force
Small force (only local damage)	***Wear***	
	Attrition (by erosion, peeling or fatigue) 	Abrasion 
Large force (widespread damage)	***Fracture***	
	Fragmentation 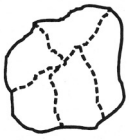	Chipping 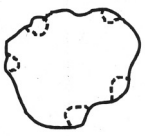

The damage zone is often of the order of the granule size, and fracture of granules and especially coated granules is rare (Ennis & Sunshine. 1993). Instead other types of destructive mechanisms occur. Wear is the overall term for gradual surface damage that merely peels off or polishes the granule leaving the original shape more or less unchanged (Pitchumani et al., 2003). Abrasion is wear caused by low magnitude tangential forces. The small tangential forces lead to polishing and rounding of the granules. This generates fine particles, and the mother granules become more and more spherical and smoother with time due to gradual loss of the coating layer (Jørgensen et al., 2004 and Pitchumani et al., 2003).

Propagation of lateral cracks, caused by low magnitude of head-on forces, is known as *attrition*. The forces acting on the granule result in the removal of sharp edges producing a more spherical granule. Beekman (2000) have subdivided the attrition phenomena into two subgroups: attrition by fatigue and attrition by erosion. Often impact forces cause attrition, and it is often observed that it takes many impact events before any damage of the granules can be observed. During the impact events, cracks propagate and finally lead to damage with an ever-increasing rate of loss of mass with time (Beekman, 2000). This type of attrition damage is called *fatigue*, and depending on the depth of the crack propagation, this may eventually lead to chipping or even fracture.

Erosion is the attrition mechanism occurring when a granule gradually loses mass mainly from the outside of the granule. Uneven parts of the granule surface are eroded, and the rate at which the granule loses mass is constant or decreasing with time (Beekman, 2000). When erosion only affects a specific surface layer it is called *peeling*. Initially, the rate of erosion will be constant, but it will decrease after the weak layer is removed. Peeling is often observed for granules that have a layered structure such as coated granules (Beekman, 2000 and Jørgensen et al., 2004).

In order to quantify the different breakage mechanisms, it is desirable to describe them by mechanical parameters such as the fracture toughness, K_c, and by mechanical properties that define deformability (Young´s modulus, E, yield strength, σ_y, and hardness, H). It is well-known that the type of breakage mechanism is also controlled by external factors such as fluidisation air temperature, nozzle pressure, impact velocity, type of load application (e.g. shear, tensile or compression impacts) and most importantly: loading rate and granule history (Bika et al., 2001). So far, the limited number of experiments allows only approximate

relations to be suggested. These relations are, however, an important step towards a quantitative prediction of the extent and type of breakage mechanism.

For estimations of the fractional volume removed by abrasive wear, $V_{abrasion}$, Iveson et al. (2001a) suggest in agreement with Bika et al. (2001) the following empirical relation:

$$V_{abrasion} \propto \frac{d_g \cdot v_{imp}^{n_{ab}} \cdot \rho_g}{K_c^{3/2} \cdot H^{1/2}} \tag{3.17}$$

where ρ_g is the granule density, d_g is the granule diameter, v_{imp} is the impact velocity and n_{ab} is a number ranging from 2.5 to 4. An unambiguous velocity dependence has not been determined yet due to severe problems in testing abrasive wear mechanisms without the influence of other types of destructive mechanisms. Instead another more widely proved relation for indentor analysis of abrasion has been suggested by Bika et al. (2001), based on fracture mechanics theory as well as experimental data fitting:

$$V_{abrasion} \propto \frac{d_g^{1/2} \cdot F^{5/4}}{A_{ind}^{1/4} \cdot K_c^{3/4} \cdot H^{1/2}} \tag{3.18}$$

where A_{ind} is the apparent area of indentor contact and F is the total applied indentor load.

It is worth noting that in both equation 3.17 and 3.18, $V_{abrasion}$ is inversely dependent on both the fracture toughness K_c and the hardness H. Several authors have proved these tendencies (Bika et al., 2001 and Ennis & Sunshine, 1993) although Mullier et al. (1991) suggest that $V_{abrasion}$ should depend on $1/K_c$ instead of $1/K_c^{3/4}$ in equation 3.18.

Attrition is the most studied of the four overall breakage phenomena possibly because it is the most observed mechanism in fluid bed processes. Another reason may be that experiments where granules are exposed to head-on forces by impact tests are easier to conduct than tangential force tests. Unfortunately, some attrition experiments show signs of surface deterioration by several of the other mechanisms simultaneously (Reynolds et al., 2005 and Bika et al., 2005). This is especially the case when large numbers of granules are tested together in bulk tests. It is therefore not always possible to determine the mechanisms individually, and often the observed breakage mechanism is simply referred to as attrition without further specification (Beekman, 2000). As indicated, the term *attrition* should only refer to wear by head-on forces, but the widespread use has resulted in the use of the term to describe all kinds of material losses from attrition by fatigue to fracture. Hence, the attrition relations presented below may also be applied for the description of fracture mechanisms (Bika et al., 2001).

Still there exists no unified description or method to assess, quantify or predict attrition, although several attempts have been made (Reynolds et al., 2005). Ghadiri & Zhang (2002) suggest the following relation for estimations of the fractional volume removed by attrition, $V_{attrition}$, according to:

$$V_{attrition} \propto \frac{\rho_g \cdot v_{imp}^2 \cdot d_g \cdot H}{K_c^2} \tag{3.19}$$

It is interesting to notice from equation 3.19 that the fractional loss is proportional to the impact kinetic energy $\rho_g \cdot v_{imp}^2$ and that it varies linearly with granule size d_g. The linearity between $\rho_g \cdot v_{imp}^2 \cdot d_g$ and $V_{attrition}$ complies fully with results found by Beekman et al. (2002) who showed a direct proportionality.

Comparing equation 3.17 with 3.19 indicates that impact attrition is more sensitive to fracture toughness K_c than abrasive wear. The velocity dependencies in both equations are in accordance with experimental evidence (Reynolds et al., 2005 and Bika et al., 2005). The higher the velocity, the more severe the type of breakage mechanism is, meaning that more material is lost. There is a general agreement in literature that breakage of dry granules increases with increasing impact velocity (Subero et al., 1999, Mishra & Thornton, 2001, Scarlett et al., 2002 and Jørgensen et al., 2004). At increased impact velocity, the primary breakage mechanism is changed from attrition/abrasion to chipping and finally fracture. In addition, it can be seen by comparison that the effect of hardness, H, on attrition is the opposite of that for abrasion. Hardness acts to concentrate stress for fracture during impact, and it seems plausible that the fractional volume of a granule removed by attrition depends linearly on the hardness (Iveson et al., 2001a). The dependence on hardness is, however, not unambiguous. Liu et al. (2003) have tested several polymer coatings and found that the degree of attrition increases (although not much) with decreased coating hardness, whereas Ghadiri & Zhang (2002) suggest a direct linear relationship between H and $V_{attrition}$.

In 1969 Gwyn et al. proposed an empirical model for the prediction of the weight fraction, $Y_{attrition}$, of a granule sample that has undergone attrition as a function of time t in a fluid bed. The parameter $Y_{attrition}$ thereby goes from zero at no attrition to the size of one at point where all the granules in the sample have undergone attrition. The empirical relation was found to be (Gwyn, 1969):

$$Y_{attrition} = Q \cdot t^{n_{Gwyn}} \tag{3.20}$$

where n_{Gwyn} is an empirical constant and Q is a constant depending on the initial granule size. Whereas Q represents the severity of attrition and the initial attritability of the granule, n_{Gwyn} concerns the change in attritability with time. Hence, the two parameters are descriptive of both the material properties and the attrition process (Neil & Brigdwater, 1999). Results by Neil & Brigdwater (1999) indicate that n_{Gwyn} could be split up into two parameters such that $n_{Gwyn} = \xi \cdot \phi_{attrition}$, where ξ is a term describing the rate of granule degradation, and $\phi_{attrition}$ is a material property of attrition. This expansion should help adapting the formula to different types of equipment and to take into account the different attrition rates in erosion and fatigue mechanisms. The Gwyn formula has been studied intensively, and it has been found to characterise the extent of attrition successfully in many types of equipment besides fluid beds (Beekman, 2000).

As is the case with the Gwyn formula, the previously presented relations are primarily found on the basis of homogenous granules with an isotropic structure. The case is somewhat more complicated when dealing with coated granules. Hence, the presented relations may only help to give a qualitative prediction of the effect of the different mechanical parameters. There are still extensive needs for empirical experience concerning the mechanical properties of coated dry granules. More information on breakage mechanisms and breakage measurements in different types of test equipment may be found in Beekman (2000) and Salman et al. (2007) as well as in a recent comprehensive review by Reynolds et al. (2005).

3.3.4. Summing up on the particle-level modelling approach

The particle-level modelling approach treats the fluid bed coating process at the most detailed level. Dividing the models into categories of: Wetting and possible droplet penetration into core particles, Coating and possible agglomeration, and Attrition and Breakage (of liquid bound agglomerates and final dry granules), a number of the most relevant models and equations have been presented. The level of detail in these models is typically high, but a number of inherent problems are associated with such detailed models. First of all, the models are typically derived from isolated studies and typically treat only a single phenomenon, while others are not considered. Often the theory at particle-level considers the situation where only two particles interact. Furthermore, a lot of simplifying assumptions are associated with the models, and a-priori knowledge is often needed in order to apply the equations quantitatively. Likewise, many of the parameters needed in the equations cannot be determined easily in practice, and if they can, the single value in the equation may in fact in reality consist of a wide distribution of values. That is e.g. the case with the particle collision velocity, u_0, for the viscous Stokes theory as presented. Hence, much of the particle-level theory cannot be applied readily for real granulating systems for other than qualitative purposes. This is due to the fact that the situation inside a fluid bed during processing is far more complex than what particle-level models account for. Particle-level modelling does, however, provide valuable information into the mechanisms of fluid bed coating. So far, particle-level modelling is a learning tool still being in a phase of gaining further insight into the coating process and testing new model suggestions. The challenge will be in the future to incorporate such detailed particle-level theory into macro- or meso-scale models that are capable of describing the entire complex granulation system with the numerous types of processes taking place simultaneously during fluid bed processing.

3.4. Modelling the granulation process using population balances

Since there are no two particles in a fluid bed coating process that have exactly the same properties (e.g. size, shape, porosity, coating liquid content etc.), all the properties associated with the particle phase should ideally be characterised by distributions and not by single values. The population balance model approach takes this into account by treating the chosen particle properties as distributions. A population balance equation is an equation in the number density and may be regarded as representing a number balance on particles of a particular state. (Ramkrishna, 2000 and Iveson, 2002). In other words, the population balance keeps track of the particle property distributions at any time during the process, and if being fully developed, describes all the changes in the particle property distribution due to the numerous possible process mechanisms that particles can undergo during fluid bed granulation. A description of a coating system by means of population balances is thereby a description in terms of a model of how the particle property distributions change with time (Ramkrishna, 2000 and Randolph & Larson, 1971 & 1988).

The particles in population balances are characterised by internal as well as external coordinates. The internal coordinates of the particle provide quantitative characteristics of the particle properties such as size, shape and porosity etc. (Cameron et al., 2005). Commonly, internal coordinates are defined in terms of a vector $\mathbf{x} \equiv (x_1, x_2, \ldots, x_z)$ in which z represents z different physical quantities associated with the particle. Each physical quantity is thereby formally given its own dimension in the **x** vector. The external coordinates denote and specify the location of the particles in physical space. Hence, the external coordinates denote the position vector inside the fluid bed in terms of Euclidean coordinates being rectangular,

cylindrical or spherical coordinates. The joint space of internal and external coordinates is commonly referred to as the *particle state space*. Fundamental to the formulation of population balances is the assumption that there exists a number density of particles at every point in the particle state space, and that the number of particles in any region of the particle state space is obtained by integrating the number density over the region desired. In a discrete region, the integration amounts to simply summing over the discrete state in the specific region (Ramkrishna, 2000).

Although the definitions of the internal coordinates and the particle state space allow, in principle, the derivation of a general multi-dimensional population balance, most previous work with population balances for fluid bed systems only considers one-dimensional balances in which only one internal parameter varies with time. Usually, either particle length (diameter or radius) or particle volume (alternatively particle mass) is taken as particle size. The discussion of whether particle length or particle volume should be taken as particle size depends on the dominant growth mechanism (Madsen & Andersen, 2006). Verkoeijen et al. (2002) recommend the use of volume as the particle size since this type of size is additive during agglomeration, and because volume is conserved if evolution of porosity between particles is disregarded (Cameron et al., 2005). Furthermore, volume is independent of the particle shape, which is fortunate in the perspective of particle agglomeration. Hence for the presentation of the population balances, particle volume is chosen as size. If particle size is chosen as the only internal coordinate, the population balance follows the change in the particle size distribution as granules break, grow by coating or agglomeration and enter or leave the control volume (Cryer, 1999). Written in words, the full population balance for a batch fluid bed may be expressed formally according to equation 3.21 (Salman et al., 2007). For more background on the nature of population balances, and for a full derivation of the balances for one or several internal coordinates, Ramkrishna (2000), Cameron et al. (2005) and Hede (2006) should be consulted.

The rate of change of numbers of particles in a size range =

The rate at which particles grow into that size range by coating

– The rate at which particles leave that size range by further coating

+ The rate at which particles are "born" in that size range by agglomeration of smaller particles (3.21)

– The rate at which particles "die" in that size range by agglomeration into larger size ranges

+ The rate at which particles are "born" from breakage of larger size ranges

– The rate at which particles in that size range "die" from breakage into smaller size ranges.

3.4.1. One-dimensional population balances for fluid bed batch systems

When particle volume is the only internal coordinate, the number density n(v, t) represents the particle-size distribution (PSD) where v is the particle volume and t is time. The one-dimensional population balance thus follows the change in particle-volume distribution with time. The number of particles, N_i, of a given size range from v_i to v_{i+1} is by definition given as:

$$N_i \equiv \int_{v_i}^{v_{i+1}} n(v,t) \cdot dv \tag{3.22}$$

Figure 3.9 shows the relation between density n and number N_i. The cumulative size distribution can be obtained from integration between the limits 0 to v, whereas the total particle number is found by integration of the entire size interval (Litster & Ennis, 2004).

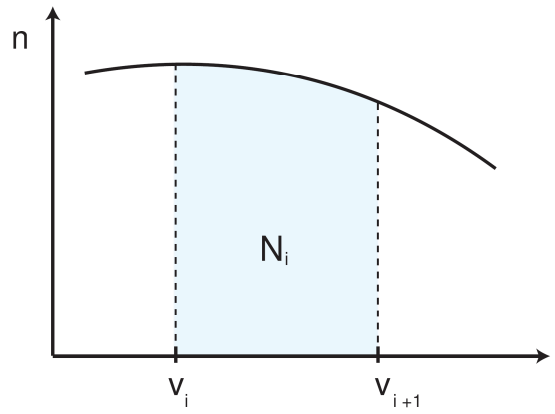

Figure 3.9: Sketch of the relation between the particle number N_i and number density n, where integration of n in a given interval will give the number of particles N_i in that particular interval (Madsen & Andersen, 2006).

During fluid bed granulation, the population of particles evolves with time. A control volume (or interval) from v to v + dv in an infinitesimal time interval is considered, where changes in the particle size distribution are due to different fluxes to and from the control volume. This results from mechanisms such as coating, agglomeration and breakage.

A one-dimensional population balance for a specific particle state, here being volume, can be set up similarly to other chemical reaction balances (Ramkrishna, 2000). The resulting population balance equation is a partial differential equation according to (Hulbert and Katz, 1964 and Ramkrishna, 2000):

$$\text{Accumulation} + \text{Output} - \text{Input} = \text{Net generation}$$

$$\underbrace{\frac{\partial n(v,t)}{\partial t}}_{\text{Number density}} + \underbrace{\frac{\partial}{\partial x}(G(v,t)\cdot n(v,t))}_{\text{Growth due to coating}} = \text{Birth} - \text{Death} \tag{3.23}$$

The first term in equation 3.23 corresponds to accumulation. The second term is the growth term where a particle grows with the coating growth rate G from or to the control volume. This corresponds to convective transport of the particles along the one-dimensional size axis. The net generation terms are the last two terms; Birth and Death. These are birth and death rate terms, which describe the appearance and disappearance of particles in the control volume caused by agglomeration and breakage (Hulbert & Katz, 1964, Litster et al., 1995 and Kumar & Ramkrishna, 1996a,b & 1997).

3.4.1.1. The agglomeration birth and death terms

The agglomeration rate term was proposed by Hulbert and Katz (1964) to be proportional to the number densities for two agglomerating particles, n(v − u, t) and n(u, t), and this birth rate expression has traditionally been represented according to:

$$\text{Birth of particles with volume v} = \frac{1}{2}\int_0^v \beta(v-u, u, t)\cdot n(v-u, t)\cdot n(u, t)\cdot du \qquad (3.24)$$

The agglomeration birth rate term thereby describes agglomeration of two particles of sizes u and v − u giving birth to a particle in size interval v. Solely binary collisions are assumed to occur (Adetayo & Ennis, 1997 and Ramkrishna, 2000). The probability for successfully producing an agglomerate of size v is β(v − u, u) in number^{-1}·time^{-1}. In the literature, β is often referred to as the *coalescence kernel* (Sastry, 1975). As the birth of particles of size v appears from agglomeration of particles of smaller sizes, all the sizes from 0 to v must be considered, and hence, integration between these limits is performed. The leading factor 1/2 ensures that every collision is only counted once (Hulbert and Katz, 1964 and Ramkrishna, 2000). Similarly, agglomeration of particles of size v and u results in death of a particle of size v, which gives the following death rate term (Hulbert and Katz, 1964 and Ramkrishna, 2000).

$$\text{Death of particles with volume v} = n(v, t)\int_0^\infty \beta(v, u, t)\cdot n(u, t)\cdot du \qquad (3.25)$$

in which the integral from 0 to ∞ ensures that the possibility that a particle of volume v agglomerates with any other particle with a volume ranging from 0 to infinity is accounted for.

In equation 3.24 and 3.25 the agglomeration frequency is expressed in terms of the single parameter β. This parameter obviously depends on a number of physical and statistical properties associated with the collision. The parameter β is the only mathematical term in the population balances that links the physical and process parameters with the statistical chance of successful agglomeration (Ding et al., 2006). In other words, the coalescence kernel governs the mathematical description of agglomeration, as the term can be seen as a pseudo rate constant for the agglomeration process. The choice of kernel can dramatically affect the rate of coalescence and thereby the shape of the predicted granule size distribution, especially in agglomeration processes (Cryer, 1999 and Madsen & Andersen, 2006).

Although some of the modern kernels have a generic first-principle foundation, all kernels are empirical or semi-empirical in nature, and have typically been suggested mainly based on experimental observations. Kernel expressions are often functions of particle size besides a number of fitted coefficients. These empirical coefficients are deduced from curve fitting from experimental data. Historically, much focus has been on the development of new kernels in order to be able to describe agglomeration processes under different conditions. One of the first suggestions by Kapur & Fuerstenau in 1969 suggested that β should simply be a constant β_0. Recent considerations by Cameron et al. (2005) and Liu & Litster (2002) indicate that the coalescence kernel is affected by two major factors being: the collision probability of the specified pair of particles, and the chance of successful permanent agglomeration or particle

rebound (Cameron et al., 2005). Whereas the first factor mainly depends on the particle sizes and fluidisation conditions, Liu et al. (2000) have found that the most important aspects affecting the chance of permanent agglomeration are: elastic-plastic properties of the particles, viscosity of the liquid layer, head on collision forces and the energy balance of the system. This has lead to a reappearance of the general coalescence kernel expression originally suggested by Sastry as late as in 1975, and it has again become common to subdivide the kernel expression into two parts according to:

$$\beta(v, u) = \beta_0 \cdot \beta^*(v, u) \tag{3.26}$$

where β_0 is the rate constant depending on the operating conditions of the fluid bed including liquid viscosity, particle moisture contents etc. The term $\beta^*(v, u)$ expresses the kernel dependence on the size of the agglomerating particles. It further determines the shape of the resulting particle size distribution (Liu and Litster, 2002 and Salman et al., 2007). Due to the complexity and limited knowledge of the forces affecting the particles inside the fluid bed, a form of the coalescence kernel based on physical properties of the particle materials has not yet been fully established. However, many empirical and theoretical expressions for the term $\beta^*(v, u)$ have been proposed in the literature, although these expressions generally have been sparsely validated. A historical summary of the development in coalescence kernel expressions may be found in Hede (2006) and Cameron et al. (2005).

3.4.1.2. The breakage birth and death terms

Although the influence of breakage on the number density function has often been neglected in low agitative systems as fluid beds, a general version of equation 3.23 must include terms that account for such phenomena. Modifications to equation 3.23 have been presented by Ramkrishna (2000) and Cameron et al. (2005) in order to include the birth of new particles in size class v due to breakage of particles from higher size classes, and the death of particles of size class v due to breakage into lower size classes.

In the derivation of the breakage birth and death terms it is assumed that the break-up of particles occurs independently of each other. Additionally, it is assumed that breakage occurs instantaneously implying that it occurs on a small time scale compared with the one used for observing the changes in particle population. Hulbert and Katz (1964) suggested an expression for the breakage birth rate term according to:

$$\text{Birth of particles with volume v} = \int_v^\infty \alpha(u,t) \cdot b(u,t) \cdot P(v \mid u, t) \cdot n(u,t) \cdot du \tag{3.27}$$

The term b(u, t) is the breakage function, which is the fraction of the population of particles breaking per unit time. The term is also known as the *selection function*. The number of particles of size u that breaks is $b(u, t) \cdot n(u, t)$. An expression for the number of particles resulting from breakage is obtained by multiplication with the average number of newly formed particles $\alpha(u, t)$ resulting from the breakage of a single particle of size u. The average number of newly formed particles depends on the mechanical properties of the particles and is frequently obtained from separate breakage studies. It obviously has a minimum value of two, but it is not restricted to be an integer as it is an average number.

The probability density function P(v | u, t) is the probability for particles of size u to break up and create a particle of the smaller size v at time t. Thus, multiplication with the probability density function gives the number of newly formed particles which have size v. Integration between limits v and ∞ is performed, because only breakage of particles larger than size v can produce particles of size v (Hulbert and Katz, 1964, Ramkrishna, 2000 and Cameron et al., 2005). The probability density function, representing the distribution of particle states for the fragments resulting from breakage, is often determined quantitatively from experimental studies. The function inherits certain properties from conservation laws, which must constrain the breakage process (Ramkrishna, 2000).

Correspondingly, the death rate term by breakage is the average number of particles of size v that breaks and, thus, disappears from size v (Ramkrishna, 2000 and Cameron et al., 2005). It is suggested by Hulbert and Katz (1964) to be expressed as:

$$\text{Death of particles with volume v} = b(v,t)\cdot n(v,t) \tag{3.28}$$

3.4.1.3. The general one-dimensional population balance equation

Accounting for size changes due to coating and agglomeration as well as breakage, the one-dimensional population balance in its full form may finally be expressed according to:

$$\underbrace{\frac{\partial n(v,t)}{\partial t}}_{\text{Number density}} + \underbrace{\frac{\partial}{\partial x}(G(v,t)\cdot n(v,t))}_{\text{Growth due to coating}} =$$

$$\underbrace{\frac{1}{2}\int_0^v \beta(v-u,u,t)\cdot n(v-u,t)\cdot n(u,t)\cdot du}_{\text{Birth due to agglomeration}} - \underbrace{n(v,t)\int_0^\infty \beta(v,u,t)\cdot n(u,t)\cdot du}_{\text{Death due to agglomeration}} \tag{3.29}$$

$$+\underbrace{\int_v^\infty \alpha(u,t)\cdot b(u,t)\cdot P(v\,|\,u,t)\cdot n(u,t)\cdot du}_{\text{Birth due to breakage}} - \underbrace{b(v,t)\cdot n(v,t)}_{\text{Death due to brekage}}$$

The resulting equation is a partial integro-differential equation for which a solution is not a trivial matter. Known analytical solutions are only available for special forms of the coalescence kernel with an assumed initial number density distribution (Hulburt & Katz, 1964 and Ramabhadran et al., 1976). Numerical solutions to partial integro-differential equations are nevertheless a topic on its own and numerous methods have been presented in literature.

The method of weighted residuals with global functions is one of the most popular methods to solve population balance equations (Ramkrishna, 1985). In this method, the solution is approximated by a linear combination of a series of chosen basis functions, whose unknown coefficients are determined by satisfying the population balance equation to define a residual. The idea of weighted residuals is to find the coefficients that force the residuals to be orthogonal to a chosen set of weighting functions (Hu et al., 2005). The method of moments is equivalent to the method of weighted residuals if the weighting functions are chosen to be polynomials (Randolph & Larson, 1971). Since polynomial weights are often a poor choice for population balances on semi-infinite intervals, and not all population balance equations can be reduced to moment equations, the method of moments is concluded by Hu et al. (2005) not to be advantageous. A further limitation of global functions is that they cannot always

capture the features of the solution, especially when there are abrupt changes and discontinuities in the solution (Madsen & Andersen, 2006).

A particular attractive approach that has evolved is to discretise the population balance equation into discrete, but contiguous size ranges, and then solve the discrete equations numerically (Batterham et al., 1981, Hounslow et al., 1988 and Kostoglou and Karabelas, 1994). The effectiveness of this approach lies in rapid solutions of selected properties of the population. In practical applications, certain properties of the particle population may be more important than others, either because they control product quality or because they are easier to measure for the purpose of process control (Ramkrishna, 2000). This method requires in principle a uniform particle distribution, which, however, is somewhat unrealistic for processes where agglomeration may occur, but more reasonable in coating-dominant processes. Kumar and Ramkrishna (1997) extended this method for solving population balance equations for breakage and agglomeration of particles. This extended method combines the features of the discretisation technique with the method of characteristics. Problems with numerical dispersion and stability are often issues associated with most existing discretisation techniques, and also with the method suggested by Kumar and Ramkrishna (1997) (Madsen & Andersen, 2006). A number of other solution techniques have been suggested in literature including: Sectional methods (Gelbart et al., 1980), orthogonal collocation and spline collocation on finite elements (Gelbard & Seinfeld, 1978) and collocation using Galerkin´s method (Nicmanis & Hounslow, 1998). Detailed reviews of previous work on solving population balance equations have been made by Kostoglou and Karabelas (1994), Vanni (2000), Lee (2001) and Salman et al. (2007).

Most of the existing solution methods are tailored to handle specific applications and lack generality (Hu et al., 2005). This means that the applicability and accuracy of the solution techniques vary with the different population balance models. As population balance modelling is a fairly new subject in the context of industrial fluid bed granulation, it is still not obvious which technique will be the most convenient to use. Recently, Madsen & Andersen (2006) studied the use of one-dimensional population balances in the context of fluid bed coating. They found that the discretisation techniques in terms of finite difference methods, including the original Hounslow et al. (1988) principle, produce unstable systems resulting in oscillating solutions. For a pure coating system, Madsen & Andersen (2006) developed a new discrete form of the population balance equation based on simple physical considerations. The method excels by automatically fulfilling the number and volume balances regardless of the form of the growth term. Unfortunately, a very fine discretization is required to obtain reasonable results.

3.4.1.4. The coating growth term

In the context of fluid bed coating, the agglomeration and breakage terms are less interesting compared to the coating growth term, G, which covers the convective growth. The general population balance includes this term, although most literature on fluid bed population balance modelling focus on agglomeration, and often assume the growth term to be constant or even completely neglects the term. Recent literature suggests that the growth term can be described as being dependent on time and particle size. Peglow et al. (2006) suggest the following growth term:

$$G(v,t) = \sigma(t) \cdot v^{k} \tag{3.30}$$

where σ(t) is a time-dependent coating rate and k is a proportionality constant. If the growth expression is independent of size, k = 0. In case the growth expression depends on the particle diameter, k = 1/3 and similarly, k will be equal to 2/3 or 1, if the growth expression depends on the surface or volume, respectively (Peglow et al., 2006). Liu and Litster (1993) suggest that particles having the same exposure time in the liquid spray zone will receive the same thickness of coating layer. This means for a well-mixed system that the growth expression can be regarded proportional to the surface area of the particles. The authors have applied this model on a coating process in a spouted bed and obtained good agreement with experimental data.

In the situation with population growth due to coating only, coating material is added to the particles while the number of particles remains constant. In such situations the general population balance equation may be reduced to a simple hyperbolic partial differential equation of the following form:

$$\underbrace{\frac{\partial n(v,t)}{\partial t}}_{\text{Number density}} = -\underbrace{\frac{\partial}{\partial v}(G(v,t)\cdot n(v,t))}_{\text{Growth due to coating}} \tag{3.31}$$

The population balance will be number conserving, as no mechanisms to create or destroy particles are included in the model. The particles will grow in size according to the form of G, and the total volume of the system will grow in time, since G according to the physics of this system will be positive. The solution to this differential equation is straightforward. For simple analytical expressions of G the equation is analytically solvable, but for more complex expressions of G a connection between volume and time can still be derived, which is possible to solve numerically. Solution techniques for pure growth as well as combined growth and agglomeration models have been reviewed by Ramabhadran et al. (1976) and lately by Madsen & Andersen (2006).

3.4.2. Summing up on the population balance modelling approach

With respect to the fluid bed granulation process, the majority of reported work has focused on the one-dimensional population balance model having size as the only internal coordinate. However, several other independent granule properties have been identified, and for some time known to strongly influence agglomeration (Iveson, 2002). These include internal coordinates as granule liquid content, porosity, pore saturation and granule shape etc. This strongly calls for an expansion into multi-dimensional balances as suggested by Iveson (2002). Although it is possible to formally set up multi-dimensional balances, no solution technique is yet capable of solving such mathematical problems. At the present time, where not all of the effects incorporated into such multi-dimensional models are fully understood, it is not likely that such models could be formulated mathematically in terms of all fundamental properties of the system (Iveson, 2002).

Although both particle coating and agglomeration occurs simultaneously in practice, the general form in equation 3.29 is almost never used as either the agglomeration or the coating population balance is solved and validated alone. This is likely to be due to mathematical problems rather than to physical considerations. As indicated from the works by Madsen & Andersen (2006) it is difficult to find a versatile solution technique for the general population balance with sufficient accuracy to handle coating-dominant as well as agglomeration-dominant situations. Even with the so-called *physical approach* solution technique, developed

by Madsen & Andersen (2006), the solution of the general equation requires computational times of more than 10^3 seconds.

Whereas the population balances may be used with reasonable accuracy in pure agglomeration processes, the use of population balance equations in coating processes is somewhat less attractive. This is due to the fact that the particle size distribution, compared to the initial particle diameters on which the population is founded, undergoes only small changes in a coating process compared to the significant changes in an agglomeration processes. This has two negative consequences in terms of population balance modelling: First of all, it is difficult to find a solution technique that can adequately account for such small size changes in a fast a reliable manner, and secondly, it is difficult to obtain valid experimental data due to the practical difficulties in measuring small changes in the particle size distribution using e.g. light scattering technique. This means in practice, that even though it becomes possible to model the coating process adequately in terms of a population balance, it may be extremely difficult to validate the model with experimental data.

Population balance modelling is typically criticised for the empirical influence of the coalescence kernel. Still the majority of applied population balance studies rely on semi- or fully empirical kernel expressions, although a lot of effort has been put into the development of new and mechanistic coalescence kernels. It is indeed a problematic feature of the population balance models, that even with the use of advanced mathematics, the model predictions are still highly dependent on an empirically-based parameter. However, for fluid bed coating processes with limited agglomeration, the influence of the choice of kernel expression has been shown by Madsen & Andersen (2006) to be rather small.

At the moment, the population balance models are used more as a learning tool to understand processes and mechanisms rather than being used as an optimisation tool. Population balance models have to some extent been used successfully to provide insight into the separate mechanisms by which particles grow. However, since particle characteristics, essential hydrodynamic parameters regarding liquid-solid contacting, particle mixing and agglomeration are lumped into the coalescence kernel, population balances cannot be applied for a-priori design and scale-up of fluid bed granulation processes (Goldschmidt et al., 2003). Still new papers are being published in which especially new and improved solution techniques are being suggested for the solution of one-dimensional balances. Much of this development has unfortunately been at the expense of proper model validation along with an advanced “mathemisation” of the population balances, and the field is to some extent moving further and further away from granulation physics and experimental data (Faure et al., 2001). With respect to fluid bed coating processes, a lot of effort is still needed before population balance modelling can be used for process control purposes, although first promising steps have been taken recently by Ronsse (2006) in combination with lumped-region modelling. At the moment, the capabilities of the population balance models as predictive tools do not compare in any reasonable way with other modelling approaches in terms of accuracy versus the effort to set-up and solve the models.

3.5. Hydrodynamic modelling of the fluid bed granulation process

Although fluidisation-related phenomena are known to be highly important for the coating process, none of the previously presented modelling approaches have taken this directly into account. Hydrodynamic modelling of fluid bed systems takes the starting point in the fluidisation behaviour and in advanced models includes the effect of fluidisation on each particle. Contrary to the population balances, the size population balance equation is not directly involved in hydrodynamic models. Instead the underlying possible particle rate processes, such as wetting, agglomeration, coating and breakage are directly simulated. Typically, a sample of particles within a control volume of the fluid bed is considered, and the initial conditions such as positions in a 3-D space, fluidisation velocities in three dimensions, internal stresses etc. are assigned for each particle. Each of the particle rate processes are simulated, and hence their internal coordinates are updated directly. A hydrodynamic modelling approach of fluid bed systems is a fairly new discipline that has developed in the last ten to fifteen years due to the enormous increase in computer processing power and algorithm development. It is nevertheless a difficult, but promising discipline being a prerequisite for continuum and discrete element modelling, which are both subjects to be presented in this section.

Hydrodynamics is fluid dynamics applied to liquids, and as the particle bed load is fluidised in the chamber during processing, *hydrodynamics* is often used as a term rather than the more general term *fluid dynamics*, being the sub discipline of fluid mechanics that studies fluids in motion. As with other typical fluid dynamic problems, a fluid bed hydrodynamic problem often involves the calculation of various properties for the fluidised particles such as velocity, porosity, density and temperature as function of space and time. The system consisting of the fluidised particles and the fluidisation gas is often treated as a two-phase gas-solid flow system (Goldschmidt, 2001 and Goldschmidt et al., 2003). A modern approach by Goldschmidt (2001) reduces this simplification by treating the fluid bed coating system as a multi-phase system, which allows a detailed hydrodynamic modelling of the top-spray fluid bed coating process. The description of such systems seeks in any case to account for the inherent complexity of dense gas-particle flows, which can be related to particle-particle and particle-wall interactions as well as gas-particle interactions (Goldschmidt, 2001). Hydrodynamic modelling is rarely combined with advanced mass transfer or chemical/physical reactions and equations, as first attempts by Samuelsberg & Hjertager (1996) strongly indicate the prior need for valid and well-proven hydrodynamic models.

On an overall scale, there are basically two types of hydrodynamic models being the Eulerian models (also known as *continuum models*) and the Lagrangian models commonly referred to as *Discrete Element Models* (DEM) (Goldschmidt, 2001 and Taghipour et al., 2005). Both types consider the gas phase as a continuum, but there are a number of differences in the modelling approaches and assumptions regarding the particle phase. The following sections will briefly introduce the basic principles and differences. For an in-depth treatment of fluid bed hydrodynamic modelling and granular dynamics of two-phase flows, Hoomans (1999) and Goldschmidt (2001) should be consulted.

3.5.1. Eulerian (continuum) models

In Eulerian models all phases are treated as interpenetrating phases, and the theory behind such models is basically an extension of the classical kinetic gas theory that takes non-ideal particle-particle collisions and gas-particle drag into account (Goldschmidt, 2001). In this

scheme, collections of particles are modelled using continuous medium mechanics, as the Navier-Stokes equations for the fluid phase are applied to the particle phase with little modification (Jain, 2002). The solid particles are generally considered to be identical having a representative diameter and density, meaning that the particle phase is volume averaged (Taghipour et al., 2005 and Depypere, 2005). The general idea in formulating such a multi-fluid model is to treat each phase as an interpenetrating continuum, and therefore to construct integral balances of continuity, momentum and energy for each phase with appropriate boundary conditions and jump conditions for the phase interfaces. As the continuum approximation for the solid phase has no equation of state, certain averaging techniques and assumptions are required to obtain a momentum balance for the solid phase (Pain et al., 2001).

Although constitutive relations according to the kinetic theory of particle flows have been incorporated into recent Eulerian models (e.g. Gidaspow et al., 2004 and Chiesa et al., 2005), pure continuum models for fluid bed granulation still suffer from the fact that the contact between fluid, particles and boundary surfaces is not considered explicitly with respect to particle inertia and the mechanical properties of the particles. This limits the ability of Eulerian multi-phase models to represent particle-particle and fluid-particle interactions adequately, thereby reducing the accuracy of the prediction of both the fluid and the particle dynamics (Fan et al., 2003 and Sun, 2002). This inaccuracy can be overcome by explicit calculations of the particle contact mechanics in a particle-scale reference frame using a Lagrangian approach as it will be presented below. Considering the limited required computational power and model complexity, the multi-fluid interpenetrating approach of the Eulerian granular multi-phase model is still a fast method to calculate flow fields, as it is well known from simple particle systems as spray-drying and conveying systems etc. (Sloth, 2007). From such studies, however, it is impossible to study the fluid bed dynamics at particle-level. A number of software codes have been developed commercially, as reviewed by Xia & Sun (2002), hereby simplifying the task of continuum modelling and simulation. Due to the obvious need for accounting precise particle-level properties into fluid bed coating hydrodynamic models, pure Eulerian models must be regarded as inappropriate even in an industrial context. Hydrodynamic fluid bed scaling attempts based on empty vessel considerations are often founded on Eulerian models (e.g. Krishna & van Baten, 2001 and Cooper & Coronella, 2005). However, the models often turn out to be inaccurate when particles are being processed. Recent attempts by e.g. Depypere (2005) and Lettieri et al. (2003) have quite clearly illustrated that future development in the field of hydrodynamic fluid bed process modelling should be concerned with Lagrangian principles rather than with Eulerian.

3.5.2. Lagrangian models – Discrete Element Methods

The Lagrangian approach may be seen as an extension of the Eulerian, since Lagrangian models describe the solid and the liquid phases at particle-level and the gas phase as a continuum. In the two-phase flow situation, the Newtonian equations of motion for each individual particle are solved with inclusion of the effects of particle collisions and forces acting on the particles by the gas (Goldschmidt, 2001). That is, Newton´s law of motion is simultaneously solved for a large number of particles either in a computational unit cell with periodic boundaries, or on a computational domain representing the entire fluid bed vessel or its subset. In general, the following equations are solved (Cameron et al., 2005 and Kafui & Thornton, 2008):

$$m_i \frac{d\mathbf{v}_i}{dt} = \mathbf{F}_i \tag{3.32}$$

and

$$I_i \frac{d\boldsymbol{\omega}_i}{dt} = \mathbf{T}_i \tag{3.33}$$

in which m_i is the particle mass, $\mathbf{v}_i$ is the linear velocity vector, t is time, I_i is the moment of inertia, $\boldsymbol{\omega}_i$ is the angular velocity vector, $\mathbf{T}_i$ is the net torque vector due to the tangential components of the contact forces and $\mathbf{F}_i$ is the net force vector acting on particle i. $\mathbf{F}_i$ is often written as the sum of three contributions according to (Cameron et al., 2005):

$$\mathbf{F}_i = \mathbf{F}_i^{\mathbf{H}} + \mathbf{F}_i^{\mathbf{P}} + \mathbf{F}_i^{\mathbf{E}} \tag{3.34}$$

where $\mathbf{F}^{\mathbf{H}}$ is the force due to fluid-particle interactions also known as the *drag force*, $\mathbf{F}^{\mathbf{P}}$ is the force due to particle-particle interactions during collisions, and $\mathbf{F}^{\mathbf{E}}$ is a force acting on the particle due to an external field being e.g. the gravitational field, $m_i \cdot g$. $\mathbf{F}^{\mathbf{E}}$ is sometimes completely ignored and $\mathbf{F}^{\mathbf{H}}$ is often estimated from empirical equations. In general, the numerous discrete element approaches involves different assumptions and expressions for the net force vector in equation 3.34 (Goldschmidt et al., 2004 and Kafui & Thornton, 2008).

Besides obviously being far more precise than the Eulerian models, such discrete particle models do not require additional closure equations for the suspended particle phase, since they compute the motion of every individual particle, taking collisions and external forces acting on the particles directly into account (Goldschmidt, 2001). The Lagrangian approach may roughly be divided into two groups based on the nature of the particle-particle interactions, being: the soft-particle and the hard-particle approach; both of which will be briefly introduced below.

3.5.2.1. Hard-particle models

In hard-sphere models the particles are assumed to interact through instantaneous, binary collisions. A sequence of collisions is processed one collision at the time in the order of occurrence (Hoomans, 1999, Hoomans et al., 2000 and Tsjui et al., 1993). Here the discrete elements represent both the primary particle and the agglomerates, in which case the identities of agglomerated elements are lost and a new larger element is created in their place (Cameron et al., 2005). Hard-sphere models are also referred to as *event driven models*, since a sequence of collisions is processed in which all particles are moved until the next collision occurs. Particle collision dynamics are described by collision laws, which account for energy dissipation due to non-ideal particle interaction by means of the empirical coefficients of normal and tangential restitution, and a coefficient of friction (Goldschmidt, 2001). The dissipative particle interactions in the particle phase make these systems significantly different from molecular systems where energy associated with collision is always conserved. This means that energy has to be continuously supplied to the particle system in order to keep the particles in motion. This can for instance be achieved by applying a shear rate through proper choices of boundary conditions as suggested by Campbell & Brennen (1985). It has recently become common to choose the collision particle partners and sequences based on the relative approach velocity (Hoomans et al., 1996 & 2000).

Based on work by Hoomans (1999), Goldschmidt (2001) and Goldschmidt et al. (2003) developed a hard-sphere discrete particle model for granulating fluidised beds, which captures the principles of basic two-dimensional hard-particle modelling well. This model computes the motion of every individual particle and droplet in the system considering the gas phase as a continuum. Particle-scale processes such as particle-particle collisions, droplet-particle coalescence and agglomeration are taken into account by simple closure models. Distinction is here made between three types of entities being: dry particles, wetted particles and droplets. All three types are assumed to be spherical, and encounters are detected as soon as contact occurs at a point on the line joining the centres of the two entities. In addition, six types of encounters are distinguished: Encounters among dry particles described by hard-sphere collision laws from mechanics; Droplet-droplet encounters described by hard-sphere collision laws as well, as they are assumed to be repulsive for atomised liquid droplets with a typical radius of 50 μm, colliding with small mutual differences; Encounters between droplets and dry or wetted particles; Encounters between dry or wetted particles and a chamber wall, described by hard-sphere collision laws; Encounters between droplet and walls, resulting in removal of the droplet from the simulation, and last; Encounters between a wetted particle and another particle, leading to either rebound described by hard-sphere collision laws or agglomeration. Which of the two latter situations that occurs depends on the odds of the particles hitting each other on a wet spot (Goldschmidt et al., 2003). It is further assumed that a new particle entity is formed at the position of the centre of mass of the original entities upon coalescence as it is sketched in figure 3.10.

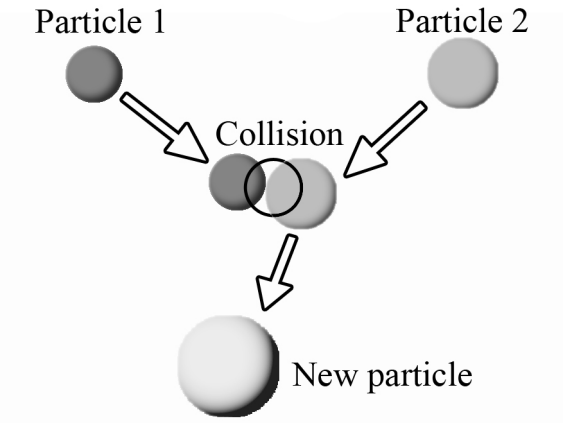

Figure 3.10: Repositioning and merging of particles upon agglomeration (Based on Goldschmidt et al., 2003).

Mass, momentum and volume of the new entities are conserved and transferred to the newly formed particle, where after the original entities are excluded from the simulation. In case of droplet impact with a particle, the area on the newly formed particle covered by liquid depends on the original particle size, the size of the droplet and a defined minimum liquid layer thickness as sketched in figure 3.11.

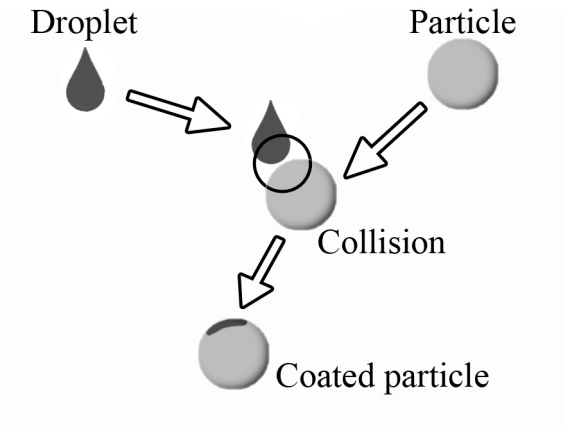

Figure 3.11: Liquid layer formation upon droplet-particle coalescence (Based on Goldschmidt et al., 2003).

In case of agglomeration, the wetted area available for subsequent agglomeration is reduced by the projected area of the smallest particle, in order to account for liquid bridge formation and the masking of the wetted surface, which cannot be reached anymore because the newly agglomerated particle is in the way. This is sketched in figure 3.12.

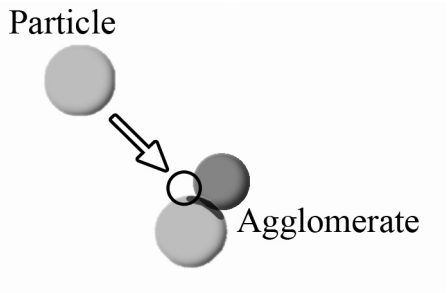

Figure 3.12: Masking of wetted surface for subsequent agglomeration (Based on Goldschmidt et al., 2003).

Although inclusion of liquid and gas inside the pores is taken into account for agglomerates containing more than three primary particles in the model by Goldschmidt et al. (2003), the model does, however, not account for non-spherical particles, droplet penetration into the cores or breakage of agglomerates, and is further limited by the two-dimensional geometry. Even so, simulations using the two-dimensional Goldschmidt model are only possible for 50,000 granules at the time, thereby being only comparable to experimental data from very small fluid beds. This clearly illustrates the need for more computational power, if the hard-particle principles should be used for any industrial purposes. It also indicates why the hard-particle approach has first been used within the last ten to fifteen years, although the principles were introduced originally in the late fifties.

In another recent study by Kafui & Thornton (2008), a full 3-D fluid bed granulation model was developed for Geldart group A particles. The model uses simple functional relationships to model the 3-D particle wetting in the conical spray zone. Agglomeration as well as breakage of agglomerates is also accounted for in the model. The strengthening of liquid bridges upon drying is likewise accounted for in terms of an increase in energy of adhesion with drying. With this model, Kafui & Thornton (2008) were capable of simulating 50,000 particles at the time providing qualitatively realistic particle size evolution trends. Although still in a proof-of-concept phase, this modelling concept is promising. However, even with the anticipated future increase in computer processing capacity, it will take many years before the

model can be applied with real fluid beds containing several millions of particles. Other recent attempts in hard-particle DEM modelling have been reviewed by Link et al. (2007).

3.5.2.2. Soft-particle models

The soft-particle approach differs from the hard-particle approach as it considers interparticle collisions as a continuous process that takes place over a finite time. Here the discrete elements strictly represent the primary particles, which maintain their identity even as they become part of larger agglomerates. In such models, agglomerate deformation during collision can be modelled, as the contact forces between the primary particles are calculated from a simple mechanical analogy involving a spring, a dashpot and a friction slider; i.e. the normal and tangential component of forces are expressed as the sum of forces due to the springs and dashpots, and the normal and tangential velocities are expressed in terms of the relative velocity prior to collision (Gera et al., 1998). The principle of the linear spring-dashpot model is sketched in figure 3.13. Such inter-particle bond models are particular suitable for the modelling of impact breakage of pre-existing agglomerates which undergo some sort of brittle fracture (Thornton & Cismocos, 1999). Another advantage is that information of the agglomerate morphology is obtained automatically from the simulation (Cameron et al., 2005). Hence, the majority of discrete element simulations of agglomerate strength use the soft-particle approach.

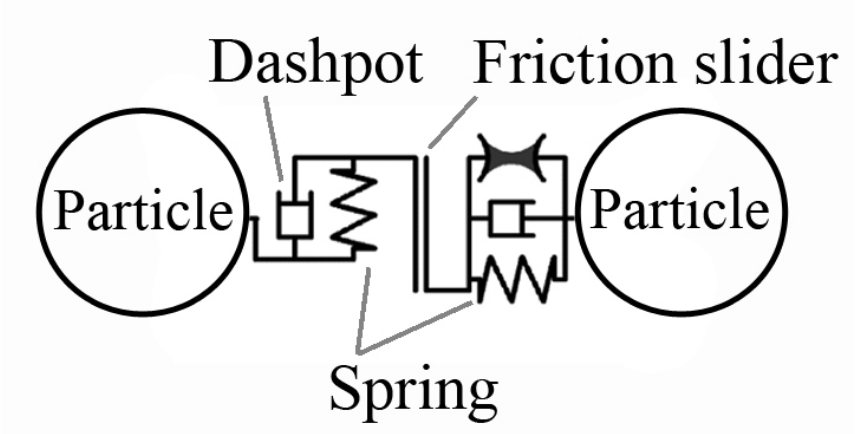

Figure 3.13: Contact force model for soft-particle modelling (Based on Gera et al., 1998).

In soft-particle simulations, the interactive forces exerted on each particle are computed as continuous functions of the distance between contiguous particles, and are based on physically realistic interaction laws. Soft-particle models are also referred to as *time driven models* as all particles are moved over a certain period of time where after the collision dynamics are computed from the particle overlaps. In case a particle is in contact with several other particles, the resulting contact force follows from the addition of the binary contributions (Goldschmidt, 2001). Compared to the hard-particle principle this approach is computationally intensive and requires even higher computational demands than hard-sphere simulations. However, the soft-particle approach does have the clear advantage that it provides information on the structure and dynamics of granular materials including details of positions, velocities, forces and energy partitions. In soft-particle simulations of agglomeration, agglomerates are modelled as assemblies of primary particles, which often are assumed to be spherical and elastic (Lian et al., 1998). In all, the soft-particle modelling approach is useful in the simulation of the deformation and breakage of agglomerates, but less interesting in a fluid bed coating context.

3.5.3. Summing up on the hydrodynamic modelling approach

Hydrodynamic modelling is a relatively new approach with respect to modelling fluid bed coating systems with only few papers published so far. As with the population balances most hydrodynamic granulation studies consider pure agglomeration studies. Effective modelling of solid-fluid flows requires methods for adequate characterisation of the discrete nature of the solid particle phase and a valid representation of the interaction between solids and fluids. Simple multi-phase models using the Eulerian method addresses the problem within a continuum framework. In continuum models, contact between fluids, particles and boundary surfaces is not considered explicitly with respect to particle inertia and mechanical properties. This limits the ability of continuum multi-phase models to adequately represent particle-particle and fluid-particle interactions, hereby reducing the accuracy of the prediction of both the fluid and the particle dynamics. Such models may give precise indications of empty-vessel fluidisation flows, but the representation of all phases simply as interpenetrating continuums is a too rough approach for the fluid bed coating process.

Since Lagrangian (DEM) models describe particle motions in detail, it is expected that these models show closer resemblance with experimental results than with the Eulerian models. However, a direct comparison between hard- or soft-particle models and experiments has not been made so far, mainly because of the limited number of particles that can be handled by the discrete element models. Further complications arise from the fact that a rigorous comparison can only be made if the discrete element models account for the full three-dimensional motion of the particles, as a two-dimensional modelling of the particle collision dynamics has proven to be too restrictive (Hoomans, 1999). This strongly increases the required number of particles and consequently the computational demands. Only recently 3-D studies are beginning to be published. The number of particles that can be accounted for in present models is a generic, but serious limiting factor in any of the discrete element models. Even with modern computers, present models cannot account for more than 10^6 particles in 2-D, which is several orders of magnitude lower than what is processed in industrial fluid beds. Even if the computational processing capacity continues to be roughly doubled each 18 month according to Moore´s law, it will take many years before commercial fluid beds can be fully modelled in terms of discrete element models. In terms of fluid bed coating processes, the hydrodynamic modelling approach is not yet matured sufficiently to be used for process control and scale-up tasks. As with the population balances, the results obtainable from present hydrodynamic modelling studies do not compare reasonably with the effort to set-up and solve the models.

3.6. Lumped-region modelling

As a trade-off between the level of detail, and the possibility of using the models for process control, another modelling approach has been suggested by Overturf & Reklaitis (1983), Maronga & Wnukowski (1997a,b), Temple & van Boxtel (1999), Heinrich & Mörl (1999), Freitas & Freire (2001), Heinrich et al. (2003), Larsen et al. (2003), Werther & Bruhns (2004), Ronsse (2006), Ronsse et al. (2007a,b) among others. At the heart of this approach is the discretisation in one, two or three dimensions of the fluidisation chamber into small so-called *control volumes* for which dynamic heat and mass transfer balances are set up and solved. For the most advanced models, physical parameters and properties are represented by distributions. In the less advanced models, the fluid bed is typically discretised in vertical direction only, assuming well-mixed behaviour inside each control volume. Typically, some of the control volumes are assigned to be coating control volumes, whereas others are drying

control volumes only. In all control volumes, fluidisation air humidity and temperature are typically the main parameters accounted for. Particles are in most models allowed to move between the control volumes with a certain rate related to the fluidisation velocity.

The strong focus on local temperature and humidity conditions as well as the distinction between coating and non-coating control volumes arise from a number of detailed fluid bed coating experiments carried out by different authors throughout the years as reviewed by Heinrich et al. (2003). The temperature and humidity inside the fluid bed are known from numerous studies to be the driving force behind the drying of the coating solution on the granule surface. When the bed temperature is too high there is little or no coating growth, because of rapid surface drying and premature spray-drying of the coating solution before impact (Guignon et al., 2002). On the other hand, if the humidity is too high and/or the temperature is too low, the bed is likely to collapse due to wet quenching (Maronga & Wnukowski, 1998). It is often a basic assumption in black-box models that all granules have the same temperature and moisture contents, and that for all granules, the coating and drying history are the same. Results by Maronga & Wnukowski (1998) indicate, however, that the temperature and humidity during the coating process in a top-spray fluid bed vary significantly with radial and especially vertical position. During the coating process, pockets of low temperature and high humidity are formed deep inside the bed, causing fluctuations in temperature of typically more than 10% on a °C scale. Based on these systematic fluctuations, the top-spray fluid bed is suggested to be formally divided into four zones, which can be seen in figure 3.14 (Maronga & Wnukowski, 1998).

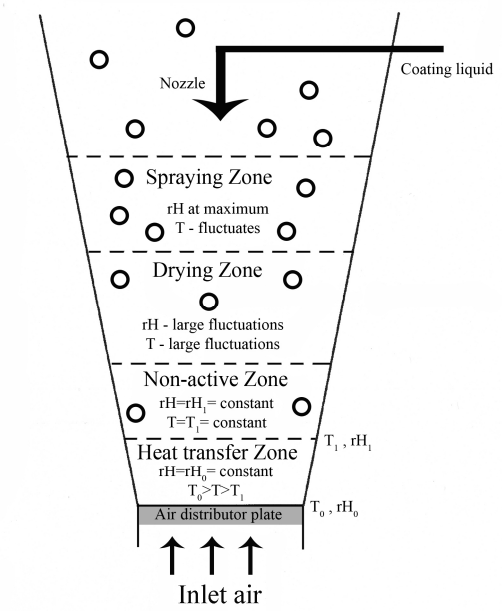

Figure 3.14: Zones in a top-spray fluid bed during steady state coating (Based on Maronga & Wnukowski, 1998). The sizes of the zones are not to scale.

As seen in figure 3.14, the highest humidity and the lowest temperature are situated closest to the bed surface in the spraying zone. The size and rate of particle transfer to this zone are important factors because particles are coated if and only if they visit this zone. Maronga & Wnukowski (1997b) reported that an increase in the size of the spraying zone decreases the variance of the coating distribution (Maronga & Wnukowski, 1997a,b). The highest temperature and humidity fluctuations are reached in the drying zone, although zones of low temperature and high humidity are not always correlated or identical. In the heat transfer zone

the conditions are close to those of the inlet air. Between the heat transfer zone and the drying zone exists a non-active zone, where neither temperature nor humidity change significantly (Maronga & Wnukowski, 1998). The minimisation of this zone may at first seem advantageous to the coating process in order to decrease the particle circulation time. Nevertheless, the non-active zone acts as a safeguard against the chance of wet quenching the bed. Hence, the fluid bed coating process has to be operated with a significant size of the non-active zone (Maronga & Wnukowski, 1997b).

The experimental results obtained by Maronga & Wnukowski (1997a,b & 1998) among others have formed the basis for a recent dynamic heat and mass transfer model suggested by Ronsse (2006) and Ronsse et al. (2007a,b). The model is capable of describing the temperature, humidity and coating mass concentration fields along the vertical z-axis of the coating process in a top-spray fluidised bed. This simple model approach fulfils the industrial needs for an intuitive model that captures only the most important phenomena during the coating process. At the same time the calculation times are short, and the results can be straightforwardly interpreted and used for direct comparison with experimental data. From comparison with experimental data, Ronsse et al. (2007a) concluded that the model is reliable in predicting the steady state thermodynamic behaviour of the fluid bed during coating.

As with the model suggested by Ronnse (2006) and Ronsse et al. (2007a,b) it is common to account for other properties besides the fluidisation air humidity and temperature. Additional properties such as particle water contents, particle surface temperature and reactor wall temperature can also be accounted for in lumped-region models. Even with the simple one-dimensional lumped-region models, the level of detail can be varied by including e.g. detailed hydrodynamics and liquid deposit mechanisms. However, detailed agglomeration theory is yet to be implemented into lumped-region models.

The fact that the lumped-region modelling approach is capable of simulating the whole fluid bed at practical time scales, at the same time including process conditions at the detailed level of choice, makes this approach interesting in a scale-up context, where the aim often is to compare different fluid bed scales and only to a lesser extent to be able describe the particles individually. In that sense, the proposed lumped-region models in literature are not the most advanced models in terms of mathematics and level of detail, but the modelling principle does offer the greatest versatility and could in principle be coupled with elements from all of the other presented modelling approaches.

3.7. Chapter summary – the modelling approaches and fluid bed coating

This chapter has introduced a number of the most relevant modelling approaches for the fluid bed coating process. Traditionally, many different modelling approaches have been suggested ranging from black-box models, and models based on statistical treatment of experimental data, to highly advanced multi-dimensional population balance models (PPB) and 3-D discrete element models (DEM) (Hede, 2006). In between is a range of particle-level models treating isolated phenomena in detail such as droplet wetting of core particles, liquid bridge breakage etc. The lumped-region modelling approach offer a versatile technique, where the fluid bed on macro-scale is subdivided into a series of well-mixed control volumes for which temperature and humidity balances are set up for each volume.

The choice of a proper modelling principle obviously depends on the interest and the purpose of the model. For a quick and rough estimate of the influence of different process or formulation parameters, the black-box and statistical model approach could be applied initially. If further insight is required, other approaches should be chosen. Particle-level models could serve as guidelines for how different parameters and properties affect the coating process in detail, but models at this scale cannot be used to predict the outcome at the unit-operation scale. As presented in this chapter, the effort of modelling the coating system in terms of advanced hydrodynamic and population balance models is not very likely to result in something useful, and in any case it will be difficult to validate the models with experimental data. In that sense, the lumped-region modelling approach appears to be the most versatile and obvious choice. Using this approach it is fairly simple to quickly set up a model that is capable of modelling the entire coating system at the detailed level of choice. A clear advantage with this approach is that the model can be continuously expanded to include further details, and elements from all the other modelling principles may be implemented into such lumped-region models. As a summary, table 3-2 presents the advantages and disadvantages concerning each of the presented modelling approaches.

Table 3-2: Summary of the advantages and disadvantages associated with the presented modelling approaches.

Modelling principle	Advantages	Disadvantages
Thermodynamic black-box modelling	A quick tool in the first phase of process optimisation and process control. Models are simple and thereby easy to set up and solve. Models are easily implemented into process control software. Models are easily validated with experimental data.	Gives no fundamental insight into the underlying physical principles of the process. The models are not often capable of describing the dynamic behaviour of a system – most often only steady state conditions may be predicted. A too simple approach to be used in a process design phase or for scale-up.
Statistical black-box modelling	The statistical analysis of the model data will ensure that only statistical valid data will be included into the model. Models are simple and thereby easy to set up and solve. Commercial software packages are available to help the data analysis. Models are easily implemented into process control software. Models are easily validated with experimental data. If data is constantly being produced the models may be continuously updated and improved.	Gives no fundamental insight into the underlying physical principles of the process. Models are very dependent on the choices of the input parameters and the choice of the discrete test levels. Models are equipment-specific and cannot usually be used for scale-up. Large factorial designs may require a large number of experiments making the modelling approach time-consuming.
Particle-level modelling	The modelling approach is the most detailed providing valuable information of the various phenomena taking place in fluid bed coating processes. Proper particle-level understanding is vital in any fluid bed modelling attempt, and particle-level models have significantly improved the insight into granulation processes.	Models are typically based on isolated studies far away from practical conditions in fluid beds. Models are difficult to implement into process-control routines or software. Particle-level models cannot stand alone in terms of predicting the outcome of a fluidised bed coating process.

Table 3-2: Summary of the advantages and disadvantages associated with the presented modelling approaches (continued).

Modelling principle	Advantages	Disadvantages
Population balance modelling	The representation of the particle-phase in terms of distributions instead of single values is a realistic way to describe the granulation system. The nature of population balances allows the possibility to include all relevant properties into a multi-dimensional population balance. Population balance models are capable of describing the granulation process dynamically.	A one-dimensional population balance is a too simple approach to model the granulation process. Other internal coordinates should be added, thereby moving from one-dimensional into multi-dimensional population balances. Solution techniques for multi-dimensional population balances are not yet established. Even with the one-dimensional balances, numerous problems, including instability and numerical dispersion, are common. Coalescence kernels are still semi or fully empirical, making population balance simulations to a large extent still dependent on experimental results.
Hydrodynamic modelling (Pure Eulerian)	A fast method to calculate flow fields at any fluid bed scale. Pure Eulerian models are far from being as process-time demanding as the other hydrodynamic techniques. A whole range of commercial programs are available, making the simulation coding part fairly straightforward.	Knowledge of the equation of state for the particles is needed a-priori. The study of particle-level fluid bed dynamics is impossible in terms of pure Eulerian models. Basically just an extension to the classical, and in many ways inaccurate, kinetic gas theory.
Hydrodynamic modelling (Hard-particle approach)	High precision of the particle dynamics as the Newtonian equations of motion for each individual particle are solved with inclusion of the effects of particle collisions and forces acting on the particles by the fluidisation air. A larger number of particles can be included into the hard-particle models than what is possible in soft-particle models.	Present models are only capable of accounting for about 50,000 granules at the time in 3-D, thereby making it difficult to compare simulations with experimental data. Particle morphology cannot be studied with the use of hard-particle models as agglomerates as well as single particles are commonly assumed perfectly spherical.
Hydrodynamic modelling (Soft-particle approach)	High precision of the particle dynamics as the Newtonian equations of motion for each individual particle are solved with inclusion of the effects of particle collisions and forces acting on the particles by the fluidisation air. Soft-particle simulation is a promising tool for studying the effect of changing some of the physical and chemical parameters involved in the granulation process. Especially breakage of pre-existing agglomerates is commonly studied at the particle-level using the soft-particle approach. Morphology is obtained automatically from soft-particle simulations.	Soft-particle simulations struggle with high computational processing demands. Commonly, only a few thousand particles can be simulated at the time. Soft-particle modelling is less interesting in a fluid bed coating process context, although the principle may be applied to study breakage phenomena of coated granules.

Table 3-2: Summary of the advantages and disadvantages associated with the presented modelling approaches (continued).

Modelling principle	Advantages	Disadvantages
Lumped-region modelling	The most versatile modelling principle. Elements from all the other modelling approaches may be implemented. Models are physically based on in- and outlet streams and heat and mass transfer balances. This makes the model fairly easy to validate with experimental data. Lumped-region modelling is interesting in a scale-up context as the physical dimensions of the fluid bed are easily integrated into the model.	Detailed agglomeration and coating mechanisms are not normally included into lumped-region models. As with the black-box models the modelling approach gives little particle-level insight into the underlying physical phenomena involved in the process. It is difficult to estimate the number of coating control volumes versus the total number of control volumes to be assigned for the model. Often rough empirical estimations are necessary.

3.8. Table of symbols

Symbols		Unit
a	Constant in equation 2.40	Dimensionless
A_{bed}	Bed surface area	m^2
A_{ind}	Apparent area of indentor contact	m^2
b(v, t)	Fraction of particles breaking per unit time	-
d_{bu}	Gas bubble diameter	m
d_g	Granule diameter	μm
D_w	Binary diffusion coefficient	m^2/s
e	Particle coefficient of restitution	Dimensionless
F	Total applied indentor load	N
$\mathbf{F}_i$	Net force vector acting on particle i	-
$\mathbf{F}_i^{\mathbf{H}}$	Drag force vector	-
$\mathbf{F}_i^{\mathbf{E}}$	Force vector accounting for external fields	-
$\mathbf{F}_i^{\mathbf{P}}$	Force vector accounting for particle-particle interactions	-
g	Gravity	m/s^2
G(v, t)	Coating growth rate	-
h_{asp}	Characteristic height of particle surface asperities	m
h_{liq}	Liquid layer thickness	m
ΔH_{vap}	Latent heat of vaporisation	J/kg
H	Hardness	N/m^2
I_i	Moment of inertia	-
k	Exponent in equation 3.30	-
K_c	Fracture toughness	$N/m^{3/2}$
m	Mass	kg
m_{aggl}	Agglomerate mass	kg
n	Summation number	Dimensionless
n_{ab}	Exponent in equation 3.17	Dimensionless
n_{fi}	Flow index	Dimensionless
n_{Gwyn}	The Gwyn relation exponent factor in equation 3.20	Dimensionless
n(v, t)	Number density	-
N_i	Number of particles	-
P(v | u, t)	Probability density function	-

Q	Proportionality factor	Dimensionless
r_1, r_2	Radius of granule 1 and 2, respectively	μm
r_{aggl}	Radius of an agglomerate	μm
r_{aggl}^*	Critical radius of an aggl. after which deformation occurs	μm
$r_{dr,0}$	Initial droplet radius	μm
r_{dr}	Droplet radius	μm
r_{harm}	Harmonic mean granule radius	μm
R_{pore}	Radius of parallel capillary pores in porous media	μm
s_0	Particle specific surface area	m^2/kg
St_{def}	Stokes deformation number	Dimensionless
St_{def}^*	Critical Stokes deformation number	Dimensionless
St_v	Viscous Stokes number	Dimensionless
St_v^*	Critical viscous Stokes number	Dimensionless
S_w	Wetting saturation	Dimensionless
t	Time	s
$\mathbf{T}_i$	Net torque vector	-
T_a	Fluidisation air temperature	K
T_{dr}	Droplet surface temperature	K
u	Particle size (volume) class	-
u_0	Initial granule collision velocity	m/s
v	Particle size (volume) class	-
$\mathbf{v}_i$	Velocity vector	-
v_{imp}	Impact velocity	m/s
v_{bu}	Bubble rise velocity	m/s
$V_{abrasion}$	Fractional volume removed by abrasive wear	m^3
$V_{attrition}$	Fractional volume removed by attrition	m^3
V_{aggl}	Agglomerate volume	m^3
V_{dr}	Droplet volume	m^3
W_A	Work of adhesion for an interface	N/m
W_C	Work of cohesion	N/m
W_{CS}	Work of cohesion for a solid	N/m
W_{CL}	Work of cohesion for a liquid	N/m
W_{eq}	Average moisture contents at equilibrium	kg H_2O/kg dry solid
W_t	Average moisture contents at time t	kg H_2O/kg dry solid
$\mathbf{x}$	Internal coordinate vector	-
X_i	Input variables	Dimensionless
$Y_{attrition}$	Weight fraction of a granule sample that has undergone attrition	Dimensionless
Y_i	Output variables	Dimensionless
z	Counting number	Dimensionless

Greek

$\alpha(u, t)$	Average number of new particles formed from break up	-
β	Coalescence kernel	-
β_0	Rate constant	-
$\beta^*(v, u)$	Coalescence kernel expression	-
$\dot{\gamma}$	Shear rate	s^{-1}
γ_{lv}	Interfacial tension between liquid and vapour	N/m

γ_{sv}	Interfacial tension between solid and vapour	N/m
γ_{sl}	Interfacial tension between solid and liquid	N/m
δ	Dimensionless bubble spacing	Dimensionless
ε_{pmsp}	Porous media surface porosity (void fraction)	%
η_{app}	Apparent viscosity	kg/m·s
η_{liq}	Coating solution viscosity	kg/m·s
θ	Contact angle	°
λ_a	Thermal conductivity of air	W /(m·K)
λ_{ls}	Spreading coefficient (liquid over solid)	N/m
ξ	Term describing the rate of granule degradation	Dimensionless
π	Pi	Dimensionless
ρ_{dr}	Droplet density	kg/m^3
ρ_g	Granule density	kg/m^3
ρ_p	Particle density	kg/m^3
$\sigma(\dot{\gamma})$	Characteristic stress in an agglomerate	N/m^2
σ_y	Yield stress/strength	N/m^2
$\sigma(t)$	Time-dependent coating rate	s^{-1}
τ_{dpen}	Droplet penetration time	s
τ_{evap}	Droplet evaporation time	s
$\phi_{attrition}$	Material property of attrition	Dimensionless
$\boldsymbol{\omega}_i$	Angular velocity vector	-

3.9. References

Abbott, A. (2002) Boundary Between Coating and Granulation, M.Sc. Thesis, Department of Chemical Engineering, The University of Queensland.

Achanta, S. and Beimesch, W.E., (1999) Process for making a low density detergent composition by controlled agglomeration in a fluidised bed dryer, Patent WO99/03964.

Adetayo, A.A. and Ennis, B.J. (1997) Unifying Approach to Modelling Granule Coalescence Mechanisms, AIChE Journal, No. 43, pp. 927-934.

Adhikari, B.P. (2002) Drying kinetics and stickiness studies of single drop of sugar and acid-rich solutions, Ph.D. Thesis, University of Queensland, Australia.

Aronson, M.P. and Tsaur, L. (1993) Spray coating and spray drying encapsulation with latex polymers, in. Blanshard, J.M.V. and Lillford, P.J. (Eds.) The Glassy State in Foods, Nottingham University Press, pp. 417-434.

Batterham, R.J., Hall, J.S. and Barton, G. (1981) Pelletizing Kinetics and Simulation of Full-Scale Balling Circuits, Proceedings 3rd International Symposium on Agglomeration, Nürnberg, Germany.

Beekman, W.J. (2000) Measurement of the Mechanical Strength of Granules, Ph.D. Thesis, Technical University of Delft.

Beekman, W.J., Meesters, G.M.H., Scarlett, B. and Becker, T. (2002) Measurement of Granule Attrition and Fatigue in a Vibrating Box, Particle System Characterisation, No. 19, pp. 5-11.

Bika, D.G., Gentzler, M. and Michaels, J.N. (2001) Mechanical properties of agglomerates, Powder Technology, No. 117, pp. 98-112.

Bika, D., Tardos, G.I., Panmai, S., Farber, L. and Michaels, J.N. (2005) Strength and morphology of solid bridges in dry granules of pharmaceutical powders, Powder Technology, No. 150, pp. 104-116.

Cameron, I.T., Wang, F.Y., Immanuel, C.D. and Stepanek, F. (2005) Process systems modelling and applications in granulation: A review, Chemical Engineering Science, Vol. 60, No. 14, pp. 3723-3750.

Campbell, C.S. and Brennen, C.E. (1985) Computer simulation of granular shear flows, Journal of Fluid Mechanics, No. 151, pp. 167-188.

Canselier, J.P. (1993) The effect of surfactants on crystallization phenomena, Journal of Dispersion Science Technology, No. 14, pp. 625-644.

Chiesa, M., Mathisen, V., Melheim, J.A. and Halvorsen, B. (2005) Numerical simulation of particulate flow by the Eulerian-Lagrangian and the Eulerian-Eulerian approach with application to a fluidized bed, Computers & Chemical Engineering, No. 29, pp. 291-304.

Cooper, S. and Coronella, C.J. (2005) CFD simulations of particle mixing in a binary fluidized bed, Powder Technology, No. 151, pp. 27-36.

Crank, J. (1956) The Mathematics of Diffusion, Oxford University Press, London.

Cryer S.A. (1999) Modelling Agglomeration Processes in Fluid-Bed Granulation, AIChE Journal, Vol. 45, No. 10, pp. 2069-2078.

Davidson, J.F. and Harrison, D. (1963) Fludized Particles, Cambridge University Press, New York.

Denesuk, M., Smith, G.L., Zelinski, B.J.J., Kreidl, N.J., and Uhlmann, D.R. (1993) Capillary Penetration of Liquid Droplets into Porous Materials, Journal of Colloid Interface Science, No. 158, pp. 114-120.

Denesuk, M., Zelinski, B.J.J., Kreidl, N.J., and Uhlmann, D.R. (1994) Dynamics of Incomplete Wetting on Porous Materials, Journal of Colloid Interface Science, No. 168, pp. 141-151.

Depypere, F. (2005) Characterisation of Fluidised Bed Coating and Microcapsule Quality: A Generic Approach, Ph.D. Thesis, University of Ghent.

Dewettinck, K. and Huyghebaert, A. (1998) Top-spray fluidized bed coating: Effect of process variables on coating efficiency. Lebensmittel-Wissenschaft und Technologie, No. 31, pp. 568-575.

Dewettinck, K., De Visscher, A., Deroo, L. and Huyghebaert, A. (1999) Modeling the steady-state thermodynamic operation point of top-spray fluidized bed processing, Journal of Food Engineering, No. 39, pp. 131-143.

Ding, A., Hounslow, M.J. and Biggs, C.A. (2006) Population balance modelling of activated sludge flocculation: Investigating the size dependence of aggregation, breakage and collision efficiency, Chemical Engineering Science, No. 61, pp. 63-74.

Ennis, B.J., Tardos, G. and Pfeffer, R. (1991) A microlevel-based characterization of granulation phenomena, Powder Technology, No. 65, pp. 257-272.

Ennis, B.J. and Sunshine, G. (1993) On Wear as a mechanism of granule attrition, Tribology International, Vol. 26, No. 5, pp. 319-327.

Fan, R., Marchisio, D.L. and Fox, R.O. (2003) Application of the Direct Quadrature Method of Moments to Polydisperse Gas-Solid Fluidized Beds, Preprint submitted to Elsevier Science.

Faure, A., York, P. and Rowe, R.C. (2001) Process control and scale-up of pharmaceutical wet granulation processes: a review, European Journal of Pharmaceutics and Biopharmaceutics, No. 52, pp. 269-277.

Freitas, L.A.P. and Freire, J.T. (2001) Heat transfer in a draft tube spouted bed with bottom solids feed, Powder Technology, Vol. 114, pp. 152–162.

Fu, J., Adams, M.J., Reynolds, G.K., Salman, A.D. and Hounslow, M.J. (2004) Impact deformation and rebound of wet granules, Powder Technology, No. 140, pp. 248-257.

Fu, J., Reynolds, G.K., Adams, M.J., Hounslow, M.J. and Salman, A.D. (2005) An experimental study of the impact breakage of wet granules, Chemical Engineering Science, No. 60, pp. 4005-4018.

Ghadiri, M. and Zhang, Z. (2002) Impact attrition of particulate solids. Part 1: A theoretical model of chipping, Chemical Engineering Science, No. 57, pp. 3659-3669.

Gelbard, F., Tambour, Y. and Seinfeld, J.H. (1980) Sectional representations for simulating aerosol dynamics, Colloid Interface Science, No. 76, pp. 541-556.

Gelbard, F., and Seinfeld, J.H. (1978) Numerical Solution of the Dynamic Equation for Particulate Systems, J. Comput. Phys., No. 28, pp. 357.

Gera, D., Gautam, M., Tsuji, Y., Kawaguchi, T. and Tanaka, T. (1998) Computer simulation of bubbles in large-particle fluidized beds, Powder Technology, No. 98, pp. 38-47.

Gidaspow, D., Jung, J.W. and Singh, R.K. (2004) Hydrodynamics of fluidization using kinetic theory: an emerging paradigm, Powder Technology, No 148, pp. 123-141.

Goldschmidt, M.J.V. (2001) Hydrodynamic Modelling of Fluidised Spray Granulation, Ph.D. Thesis, University of Twente.

Goldschmidt, M.J.V., Weijers, G.G.C., Boerefijn, R. and Kuipers, J.A.M. (2003) Discrete element modelling of fluidised bed spray granulation, Powder Technology, No. 138, pp. 39-45.

Goodwin, J. (2004) Colloids and Interfaces with Surfactants and Polymers – An Introduction, John Wiley & Sons Ltd., Chichester.

Gouin, S. (2005) Fluidized bed microencapsulation: Thermodynamics of aqueous and ethanolic coating processes, Journal of Microencapsulation, No. 8, pp. 829-839.

Guignon, B., Duquenoy, A. and Dumoulin, E.D. (2002) Fluid Bed Encapsulation of Particles: Principles and Practice, Drying Technology, No. 20, pp. 419-447.

Gwyn, J.E. (1969) On the Particle Size Distribution Function and the Attrition of Cracking Catalysts, AIChE Journal, Vol. 15, No.1, pp.35-39.

Hangos, K. and Cameron, I.T. (2001) Process Modelling and Model Analysis, Academic Press, London, UK.

Hapgood, K.P., Litster, J.D., Biggs, S.R. and Howes, T. (2002) Drop penetration into Porous Powder Beds, Journal of Colloid Interface Science, No. 253, pp. 353-366.

Hede, P.D. (2005) Fluid bed coating and granulation, M.Sc. Thesis, Department of Chemical Engineering, Technical University of Denmark.

Hede, P.D. (2006) Towards Mathesis Universalis: Modern aspects of modelling batch fluidised bed agglomeration and coating systems – a review, CHEC Report R0605, Department of Chemical Engineering, Technical University of Denmark, pp. 1-101.

Hede, P.D., Bach, P. and Jensen, A.D. (2007a) Small-scale top-spray fluidised bed coating: Granule impact strength, agglomeration tendency and coating layer morphology, Powder Technology, No. 176, pp. 156-167.

Heinrich, S., Blumschein, J., Henneberg, M., Ihlow, M., Peglow, M. and Mörl, L. (2003) Study of dynamic multi-dimensional temperature and concentration distributions in liquid-sprayed fluidized beds, Chemical Engineering Science, No. 58, pp. 5135-5160.

Heinrich, S. and Mörl, L. (1999) Fluidized bed spray granulation – a new model for the distribution of particle wetting and of temperature and concentration distribution, Chemical Engineering and Processing, No. 38, pp. 635-663.

Hjortsø, M.A. (2006) Population Balances in Biomedical Engineering – Segregation through the Distribution of Cell States, McGraw-Hill , NY.

Hoomans B.P.B. (1999) Granular dynamics of gas-solid two-phase flows, Ph.D. Thesis, University of Twente.

Hoomans B.P.B., Kuipers J.A.M., Briels W.J. and Van Swaaij W.P.M. (1996) Discrete particle simulation of bubble and slug formation in a two-dimensional gas-fluidised bed: a hard sphere approach, Chemical Engineering Science., No. 51, pp. 99-118.

Hoomans, B.P.B., Kuipers J.A.M. and Van Swaaij W.P.M. (2000) Granular dynamics simulation of segregation phenomena in bubbling gas-fluidised beds, Powder Technology, No. 109, pp. 41-48.

Hounslow, M. J., Ryall, R. L., and Marshall, V. R. (1988). A discretized population balance for nucleation, growth, and aggregation. AIChE Journal, Vol. 4, pp. 1821–1832.

Hu, Q., Rohani, S., and Jutan, A. (2005) New numerical method for solving the dynamic population balance equations. AIChE Journal, Vol. 51, No. 11, pp. 3000–3006.

Hulburt, H.M. and Katz, S. (1964) Some problems in particle technology – A statistical mechanical formulation, Chemical Engineering Science, No. 19, pp. 555-574.

Iveson, S.M. (2001) Granule coalescence modelling: including the effects of bond strengthening and distributed impact separation forces, Chemical Engineering Science, No. 56, pp. 2215-2220.

Iveson, S.M., Litster, D.L., Hapgood, K. and Ennis, B.J. (2001a) Nucleation, growth and breakage phenomena in agitated wet granulation processes: a review, Powder Technology, No. 117, pp. 3-39.

Iveson, S.M., Wauters, P.A.L., Forrest, S., Litster, J.D., Meesters G.M.H. and Scarlett, B. (2001b) Growth regime map for liquid-bound granules: further development and experimental validation, Powder Technology No. 117, pp. 83-87.

Iveson, S.M. (2002) Limitations of one-dimensional population balance models of wet granulation processes, Powder Technology, No. 124, pp. 219-229.

Jain, K. (2002) Discrete Characterization of Cohesion in Gas-Solid Flows, M.Sc. Thesis, School of Engineering, University of Pittsburgh.

Jørgensen, K., Bach, P. and Jensen, A.D. (2004) Impact and attrition shear breakage of enzyme granules and placebo particles-application to particle design and formulation, Powder Technology, No. 149, pp. 157-167.

Kafui, D.K. and Thornton, C. (2008) Fully-3D DEM simulation of fluidised spray granulation using an exploratory surface energy-based spray zone concept, Powder Technology, No. 184, pp. 177-188.

Kapur, P.C. and Fuerstenau, D.W. (1969) A Coalescence Model for Granulation, Industrial & Engineering Chemistry Process Design Development, No. 8, pp. 56-62.

Kerkhof, P.J.A.M. (2000) Some modelling aspects of (batch) fluid-bed drying of lifescience products, Chemical Engineering and Processing, No. 39, pp. 69-80.

Khan, I. and Tardos, G.I. (1997) Stability of wet agglomerates in granular shear flows, Journal of Fluid Mechanics, No. 347, pp. 347-368.

Kostoglou, M., and A. J. Karabelas (1994) Evaluation of Aero Order Methods for Simulating Particle Coagulation, J. Colloid Interface Sci., No. 163, pp. 420.

Krishna, R. and van Baten, J.M. (2001) Using CFD for scaling up gas-solid bubbling fluidised bed reactors with Geldart A powders, Chemical Engineering Science, No. 82, pp. 247-257.

Kumar, S. and Ramkrishna, D. (1996a) On the solution of population balance equations by discretization - I. A fixed pivot technique. Chemical Engineering Science, No. 51, pp. 1311–1332.

Kumar, S. and Ramkrishna, D. (1996b) On the solution of population balance equations by discretization - II. A moving pivot technique. Chemical Engineering Science, No. 51, pp. 1333–1342.

Kumar, S. and Ramkrishna, D. (1997) On the solution of population balance equations by discretization - III. Nucleation, growth and aggregation of particles. Chemical Engineering Science, No. 52, pp. 4659–4679.

Larsen, C.C., Sonnergaard, J.M., Bertelsen, P. and Holm. P. (2003) A new process control strategy for aqueous film coating of pellets in fluidised bed. European Journal of Pharmaceutical Sciences, No. 20, pp. 273-283.

Lee, M.H. (2001) A Survey of Numerical Solutions to the Coagulation Equation, J. Phys. A: Math. Gen., 34, 10219-10241.

Lettieri, P, Cammarata, L., Micale, G.D.M. and Yates, J. (2003) CFD simulations of gas fluidized beds using alternative Eulerian-Eulerian modelling approaches, International Journal of Chemical Reactor Engineering, No. 1, pp. 1-19.

Lian, G., Thornton, C and Adams, M.J. (1998) Discrete particle simulation of agglomerate impact coalescence, Chemical Engineering Science, No. 19, pp. 3381-3391.

Link, K.C. and Schlünder, E.U. (1997) Fluidized bed spray granulation. Investigation of the coating process on a single sphere, Chemical Engineering and Processing, No. 36, pp. 443-457.

Link, J.M., Godlieb, W., Deen, N.G. and Kuipers, J.A.M. (2007) Discrete element study of granulation in a spout-fluidized bed, Chemical Engineering Science, Vol. 62, pp. 195-207.

Litster, J.D., Smit, J. and Hounslow, M.J. (1995) Adjustable Discretized Population Balance for Growth and Aggregation, AIChE Journal, Vol. 41, No. 3, pp. 591-603.

Litster, J.D. and Ennis, B. (2004) The Science and Engineering of Granulation Processes, Kluwer Academic Publishers, Dordrecht.

Liu, L.X. and Litster, J.D. (1993) Coating mass distribution from a spouted bed seed coater: experimental and modelling studies, Powder Technology, No. 74, pp. 259-270.

Liu, L.X., Litster, J.D., Iveson, S.M. and Ennis, B.J. (2000) Coalescence of Deformable Granules in Wet Granulation Processes, AIChE Journal, Vol. 46, No. 3, pp. 529-539.

Liu, L.X., Golchert, D., Page, N.W., Page, D. and Litster, J.D. (2003) Strength and attrition resistance of agglomerates and particulate coatings, Powder Technology, No. 130, pp. 415-420.

Liu, L.X. and Litster, J.D. (2002) Population balance modelling of granulation with a physically based coalescence kernel, Chemical Engineering Science, No. 57, pp. 2183-2191.

Madsen, K., and Andersen, S.M. (2006) Population balance modelling of batch fluid bed granulation, M.Sc. Thesis, Department of Chemical Engineering, Technical University of Denmark, pp. 1-297.

Marmur, A., Schrader, M.E. and Loeb, G. (1992) Modern Approach to Wettability, Plenum Press, New York.

Maronga, S.J. and Wnukowski, P. (1997a) Establishing temperature and humidity profiles in fluidized bed particulate coating, Powder Technology, No. 94, pp. 181-185.

Maronga, S.J. and Wnukowski, P. (1997b) Modelling of the three-domain fluidized-bed particulate coating process, Chemical Engineering Science, No. 17, pp. 2915-2925.

Maronga, S.J. and Wnukowski, P. (1998) The use of humidity and temperature profiles in optimising the size of fluidized bed in a coating process, Chemical Engineering and Processing, No. 37, pp. 423-432.

Marshall, W.R. Jr. (1954) Atomization and Spray Drying, AIChE, New York.

Montgomery, D.C. (1997) Design and Analysis of Experiments, 4th Edition, John Wiley & Sons Inc., NY.

Mishra, B.K. and Thornton, C. (2001) Impact breakage of particle agglomerates, International Journal of Mineral Processing, No. 61, pp. 225-239.

Miyamoto, Y., Ogawa, S., Miyajima, M., Matsui, M., Sato, H., Takayama, K. and Nagai, T. (1997) An application of the computer optimization technique to wet granulation process involving explosive growth of particles, Int. J. Pharm., No. 149, pp. 25–36.

Miyamoto, Y., Ryu, A., Sugawara, S., Miyajima, M., Matsui, M., Takayama, K. and Nagai, T. (1998) Optimization of the granulation process for designing tablets, Chem. Pharm. Bull., No. 46, pp. 1432–1437.

Mullier, M.A., Seville, J.P.K. and Adams, M.J. (1991) The effect of agglomerate strength on attrition during processing, Powder Technology, No. 65, pp. 321-333.

Neil, A.U. and Bridgwater, J. (1999) Towards a parameter characterising attrition, Powder Technology, No. 106, pp. 37-44.

Nicmanis, M., and M. J. Hounslow (1998) Finite-Element Methods for Steady-State Population Balance Equations, AIChE Journal, Vol. 44, pp. 2258.

Ogawa, S., Kamijima, T., Miyamoto, Y., Miyajima, M., Sato, H., Takayama, K. and Nagai, T. (1994) A new attempt to solve the scale-up problem for granulation using response surface methodology, J. Pharm. Sci., No. 83, pp. 439–443.

Ouchiyama, N. and Tanaka, T. (1975) The probability of coalescence in granulation kinetics, Industrial & Engineering Chemistry Process Design Development, No. 14, pp. 286-289.

Overturf, B.W. and Reklaitis, G.V. (1983) Fluidized-Bed Reactor Model with Generalized Particle Balances, AIChE Journal, Vol. 29, No. 5, 1983.

Pain, C.C., Mansoorzadeh, S. and de Olivera, C.R.E. (2001) A study of bubbling and slugging fluidised beds using the two-fluid granular temperature model, International Journal of Multiphase Flow, No. 27, pp. 527-551.

Peglow, M., Kumar, J., Heinrich, S., Tsotsas, E., and Mörl, L. (2006) An Improved Discretized Tracer Mass Distribution of Hounslow et al. AIChE Journal, Vol. 52, No. 4, pp. 1326–1332.

Pietsch, W. (2003) An interdisciplinary approach to size enlargement by agglomeration, Powder Technology, No. 130, pp. 8-13.

Pitchumani, R., Meesters, G.M.H. and Scarlett, B. (2003) Breakage behaviour of enzyme granules in repeated impact test, Powder Technology, No. 130, pp. 421-427.

Rambali, B., Baert, L. and Massart, D.L. (2001) Using experimental design to optimise the process parameters in fluidised bed granulation on a semi-full scale, International Journal of Pharmaceutics, No. 220, pp. 149-160.

Ramkrishna, D. (2000) Population Balances – Theory and Applications to Particulate Systems in Engineering, Academic Press, London.

Randolph, A.D. and Larson, M.A. (1971) Theory of Particulate Processes – Analysis and Techniques of Continuous Crystallization, Academic Press, NY.

Randolph, A.D. and Larson, M.A. (1988) Theory of Particulate Processes – Analysis and Techniques of Continuous Crystallization, 2nd Edition, Academic Press, NY.

Ramabhadran, T. E., Peterson, T. W., and Seinfeld, J. H. (1976) Dynamics of aerosol coagulation and condensation. AIChE Journal, No. 22, pp. 840–851.

Ramkrishna, D. (1985) The status of population balances, Chemical Engineering, No. 3, pp. 49–95.

Ramkrishna, D. (2000) Population Balances – Theory and Applications to Particulate Systems in Engineering, Academic Press, London.

Reynolds, G.K., Fu, J.S., Cheong, Y.S., Hounslow, M.J. and Salman, A.D. (2005) Breakage in granulation: A review, Chemical Engineering Science, Vol. 60, pp. 3969-3992.

Rhodes, M. (1998) Introduction to Particle Technology, John Wiley & Sons Ltd., Chichester.

Ronsse, F. (2006) Modelling heat and mass transfer in fluidised bed coating processes, Ph.D. Thesis, Ghent University.

Ronsse, F., Pieters, J.G. and Dewettinck, K. (2007a) Combined population balance and thermodynamic modelling of the batch top-spray fluidised bed coating process. Part I – Model development and validation, Journal of Food Engineering, No. 78, pp. 296-307.

Ronsse, F., Pieters, J.G. and Dewettinck, K. (2007b) Combined population balance and thermodynamic modelling of the batch top-spray fluidised bed coating process. Part II – Model and process analysis, Journal of Food Engineering, No. 78, pp. 308-322.

Rowe, R.C. (1989) Binder-substrate interactions in granulation: a theoretical approach based on surface free energy and polarity, International Journal of Pharmaceutics, No. 52, pp. 149-154.

Rubino, O.P. (1999) Fluid-Bed Technology. Overview and Criteria for Process Selection, Pharmaceutical Technology, No. 23, pp. 104-117.

Salman, A.D., Hounslow, M.J. and Seville, J.P.K. (2007) Handbook of Powder Technology, Granulation, Elsevier Publishing.

Samuelsberg, A.E. and Hjertager, B.H. (1996) Computational fluid dynamic simulation of an oxy-chlorination reaction in a full-scale fluidized bed reactor, Proceedings of the 5th International Conference on Circulating Fluidized Beds, Beijing.

Sastry, K.V.S. (1975) Similarity Size Distribution of Agglomerates during their Growth by Coalescence in Granulation or Green Pelletization, International Journal of Mineral Processing, No. 2, pp. 187-203.

Scarlett, B., Beekman, W.J., Meesters, G.M.H. and Pitchumani, R. (2002) Particles – Their Strengths and Weaknesses, Key Engineering Materials, Vol. 230-232, pp. 203-212.

Schaafsma, S.H., Vonk, P., Segers, P. and Kossen, N.W.F. (1998) Description of agglomerate growth, Powder Technology, No. 97, pp 183-190.

Schaafsma, S.H., Vonk, P., and Kossen, N.W.F. (2000) Fluid bed agglomeration with a narrow droplet size distribution, International Journal of Pharmaceutics, No. 193, pp. 175-187.

Scopus (2008) Survey conducted via the homepage www.scopus.com, May 2008.

Sloth, J. (2007) Formation of Enzyme Containing Particles by Spray Drying, Ph.D. Thesis, Technical University of Denmark.

Subero, J., Ning, Z., Ghadiri, M. and Thornton, C. (1999) Effect of interface energy on the impact strength of agglomerates, Powder Technology, No. 105, pp. 66-73.

Summers, M. and Aulton, M. (2001) Pharmaceutics. The Science of Dosage Form Design, 2nd Edition, Montford University, Churchill Livingstone, Leicester, UK.

Sun, D-W. (2002) Computational fluid dynamics (CFD) – a design and analysis tool for the agri-food industry, Computers and Electronics in Agriculture, No. 34, pp. 1-3.

Taghipour, F., Ellis, N. and Wong, C. (2005) Experimental and computational study of gas-solid fluidized bed hydrodynamics, Chemical Engineering Science, No. 60, pp. 6857-6867.

Tardos, G.I., Khan, M.I. and Mort, P.R. (1997) Critical Parameters and Limiting Conditions in Binder Granulation of Fine Powders, Powder Technology, No. 94, pp. 245-258.

Teipel, U. and Mikonsaari, I. (2004) Determining Contact Angles of Powder by Liquid Penetration, Particle System Characterization, No. 21, pp. 255-260.

Temple, S.J. and van Boxtel, A.J.B. (1999) Modelling of Fluidized-bed Drying of Black Tea, J. Agric. Eng. Res., No. 74, pp. 203-212.

Thornton, C. and Ciomocos, M.T. (1999) Numerical simulations of agglomerate impact breakage, Powder Technology, No. 105, pp. 74-82.

Thornton, C., Ciomocos, M.T. and Adams, M.J. (2004) Numerical simulations of diametrical compression test on agglomerates, Powder Technology, No. 140, pp. 258-267.

Tsuji Y., Kawaguchi T. and Tanaka T. (1993) Discrete particle simulation of two-dimensional fluidized bed, Powder Technology, No. 77, pp. 79-87.

Vanni, M. (2000) Approximate Population Balance Equations for Aggregation-Breakage Processes, J. Colloid Interface Sci., No. 221, pp. 143.

Verkoeijen, D., Pouw, G.A., Meesters, G.M.H. and Scarlett, B. (2002) Population balances for particulate processes - a volume approach, Chemical Engineering Science, Vol. 57, No. 12, pp. 2287-2303.

Vojnovic, D., Moneghini, M. and Rubessa, F. (1995) Experimental design for a granulation process with “a priori” criteria, Drug Dev. Ind. Pharm., No. 21, pp. 823–831.

Vojnovic, D., Moneghini, M. and Chicco, D. (1996) Nonclassical experimental design applied in the optimization of a placebo granulate formulation in high-shear mixer, Drug Dev. Ind. Pharm., No. 22, pp. 997–1004.

Werner, S.R.L., Jones, J.R., Paterson, A.H.J., Archer, R.H. and Pearce, D.L. (2007a) Air-suspension particle coating in the food industry: Part I – state of the art, Powder Technology, Vol. 171, pp. 25-33.

Werner, S.R.L., Jones, J.R., Paterson, A.H.J., Archer, R.H. and Pearce, D.L. (2007b) Air-suspension particle coating in the food industry: Part II – micro-level process approach, Powder Technology, Vol. 171, pp. 34-45.

Wehrlé, P., Nobelis, P., Cuine, A. and Stamm, A. (1993) Scaling-up of wet granulation. A statistical methodology, Drug Dev. Ind. Pharm., No. 19, pp. 1983–1997.

Werther, J. and Bruhns, S. (2004) 3-D Modeling of Liquid Injection into Fluidized Beds, International Journal of Chemical Reactor Engineering, Vol. 2., Article A31.

Williams R.O. and Liu, J. (2000) Influence of processing and curing conditions on beads coated with an aqueous dispersion of cellulose acetate phthalate, European Journal of Pharmaceutics and Biopharmaceutics, No. 49, pp. 243-252.

Xia, B. and Sun D-W. (2002) Applications of computational fluid dynamics (CFD) in the food industry: a review, Computers and Electronics in Agriculture, No. 34, pp. 5-24.

York, P. and Rowe, R.C. (1994) Monitoring granulation size enlargement processes using mixer torque rheometry, First International Particle Technology Forum, Denver.

Zajic, L. and Buckton, G. (1990) The use of surface energy values to predict optimum binder selection for granulations, International Journal of Pharmaceutics, No. 59, pp. 155-164.

Chapter 4. Scale-up of fluid bed granulation processes

Chapter introduction

The last chapter of the literature study contains a survey of available theory concerning fluid bed scale-up. Initially, an outline of the scale-up objectives, challenges and difficulties are presented. With focus on macro- and micro-level scale-up approaches the chapter further goes through the most relevant scale-up theories and principles.

The chapter is adapted from *Towards Mathesis Universalis: Modern aspects of modelling batch fluid bed agglomerating and coating systems – a review* authored by Peter Dybdahl Hede (Technical University of Denmark). The review is referred to as Hede (2006).

4. Scale-up of fluid bed granulation processes

One of the areas of particle technology that has a special commercial interest is the principle of transferring a granulation process from one scale to another, thereby being able to produce granules at different scales with similar properties. Typically, the task goes in the direction of matching first of all the particle size distribution across scale, and secondly if possible, at the same time, to maintain a high-intensity process during scale-up. Other scale-up targets may include: match of morphology and colour as well as mechanical properties of the final coating layer etc. (van Ee et al., 1997). It is often difficult to find optimum conditions for all parameters at the same time, and scale-up is in practice a trade-off between the target parameters. In the pharmaceutical industry with high-grade products produced in small batches, scale-up will often focus primarily on optimising granule properties as the production costs are small compared to the value of the product. This gives little incentive to invest ressources into optimising the granulation process intensity. However, in industries with lower grades of bulk granular products produced in several tonnes per hour, process intensity may become a highly important scale-up parameter in addition to the beforementioned scale-up targets.

Although industrial needs for scaling down a process do occur from time to time, the typical industrial problem is far more often to scale up a process. Often product and process properties are optimised in small- and medium-scale pilot fluid beds and then transferred to much larger production-scale. The scale-up of a fluid bed granulation process requires decisions to be made at many levels, including: fixed parameters (e.g. nozzle design and fluidisation chamber dimensions), parameters related to the core material (such as composition, porosity, sphericity and more), coating solution (e.g. viscosity, surface tension, contact angle and more) and the type of fluidised bed, input parameters, operating conditions including spray and fluidisation conditions as well as processing time etc. With such a variety of interlinked parameters and properties, combined with a lack of quantitative understanding of the granulation process, it is obvious that scale-up of a fluidised bed granulation process is a challenging task (Hede et. al., 2008b). Unfortunately, in many cases, the design and variety of the equipment at different scales do not facilitate a straightforward scale-up, and often different important granule properties as well as the general granule quality are observed to change with scale (Leuenberger, 2003). It is often observed that the coating process gives the

best results the smaller the scale meaning that a lot of time is needed to adjust the production-scale equipment in order to produce granules with similar properties. In all, this makes the principles of scaling somewhat more of an art rather than science, and the scale-up of fluid bed processes is in fact still today a mix of physics, mathematics, experience, common sense and qualified guesses.

4.1. Scaling challenges

Disastrous scaling attempts of fluid bed processes from the early history of fluidisation clearly indicates that scaling of particle processes is far more difficult than the start-up and scaling of processes handling liquids (Squires, 1982). Modern industrial fluid bed granulation scaling involves a variety of issues including typically: problems with production site variances in the particle size distribution, proper coating liquid distribution at different scales, differences in agglomeration tendencies with scale etc. (Lödige, 2006). Still the majority of fluid bed equipment sold to the industry are standard units that are only slightly modified according to the specific granular product. Hence, chemical engineers working in the field of fluid bed granulation processes will often find that upscaling in many ways is more of an exercise in finding ways to adapt to the limitations given by the fluid bed chamber design, rather than designing the equipment to work properly with the given process. This is mainly due to the lack of quantitative understanding of the fluid bed coating process both at users and equipment designers, and this shortage becomes even more evident during scale-up. As a consequence of this, direct scale-up of fluid bed processes from lab-scale to production–scale is almost never done without including an intermediate pilot-scale step, where scale-up errors may be detected without loosing vast amounts of valuable products (van Ommen et al., 2006).

What complicates the scale-up situation is the fact that the fluid bed manufactures to some extent are conservative in their choice of principles and parameters for building up-scaled equipment. This means that the chamber design principles used to build the up-scaled process equipment not necessarily are the optimal choices (Lödige, 2006). As it has been emphasised by Leuenberger (1983), two systems are geometrically similar when the ratio of the linear dimensions of the small-scale and the scaled-up system are constant. Going from small-scale pilot fluid beds to production-scale, geometrical similarities almost never occur (Rambali et al., 2003). Typical examples of dimensions of commercial fluid beds may be seen from table 4-1 and figure 4.1.

Table 4.1: Dimensions and capacities of four commercial fluid beds at different scales.

Fluid bed parameters	**(Small pilot-scale) GEA Aeromatic-Fielder Strea-1**	**(Medium pilot-scale) Niro MP-1**	**(Large pilot-scale) GEA-Niro MP-2/3**	**(Production-scale) RICA-TEC/ Anhydro A/S**
Bed capacity	0.5 – 1 kg	3 – 4 kg	20 – 24 kg	800 – 900 kg
Length a	10 cm	17 cm	27 cm	140 cm
Length b	31 cm	48.5 cm	63 cm	279 cm
Length c	18 cm	93 cm	270 cm	339 cm
Length d	25 cm	29 cm	64 cm	280 cm

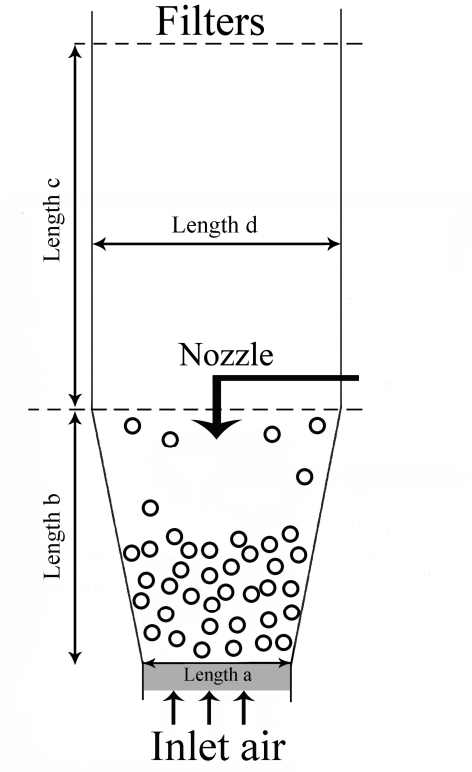

Figure 4.1: Sketch of the dimensions for four commercial fluid beds at different scales. Length dimensions corresponding to the symbols in the figure are stated in table 4-1.

The dimensions in figure 4.1 and table 4.1 reveal one of the classical problems with fluid bed process up-scaling, which indeed is related to the design of fluid bed equipment. Compared to small or medium pilot-scale equipment, the large pilot-scale and the production-scale equipment are much larger in vertical size while the horizontal dimensions are only slightly expanded. This means that the expanded particle bed height increases significantly with scale causing changes in hydrodynamics such as faster rise of bubbles again resulting in less particle exchange with the dense phase and thereby longer particle cycle times (Watano et al., 1995b and van Ommen et al., 2006). At the same time, similar types of external mixing nozzles with identical liquid orifice diameters are typically used for any of the fluid bed scales, and the need for the increased spray capacity in the large-scale is typically solved by simply adding more identical nozzles. The air and liquid volumetric flow rates through the nozzles are typically only slightly increased with scale, making it reasonable to believe that the spray zone remains close to similar in vertical extension (i.e. in absolute length), while the expanded bed height increases significantly with scale. This means that not only do the particle cycle time increases significantly with scale, also the time each particle spends in the spray zone is significantly decreased. This is likely to be part of the reason why granule properties often are observed to be different when produced at different scales. However, simulations and detailed experimental studies are needed in order to verify this.

What further complicates the scale-up situation is that different particle materials and particle sizes scale-up differently. Geldart B particles are e.g. far more difficult to scale-up compared to e.g. Geldart A particles, due to the differences in how the particles influence the bubbling fluidisation (Knowlton et al., 2005). A variety of other examples of scaling sophistries makes fluid bed scale-up a challenging task. Even with the strong need of a scientific approach to address scale-up systematically and scientifically, up-scaling of fluid bed processes has

traditionally not had much academic interest although being a common engineering exercise. As reviewed by Hede (2006) advances in scaling principles are often done in industry and typically only reach the public in the form of patents. Still much time is spent in industrial scaling on simple empirical trial and error experiments in order to optimise the scaled-up process, and often the primary goal of industrial scale-up is to try to avoid large mistakes and delays rather than finding the true causes for the unsuccessful attempts (Knowlton et al., 2005). The number of less than twenty scientific papers ever published in the field clearly indicates that fluid bed granulation scale-up until now has not been an area of much scientific interest or success. Recent scaling attempts do, however, indicate that it is possible to some extent to approach the scaling problems semi-quantitatively, as it will be presented in the following sections.

4.2. The levels of approaching scale-up

Scale-up principles presented in patents and in the scientific literature are mostly simple mathematical formulas or relations that are suggested to be kept constant across scale. Following the length of scale in the description of the fluid bed system as it was presented in chapter one, the scale-up principles may be divided into either micro- or macro-level scaling principles according to what focus of similarity the principle has. Overall, the goal of scale-up is to maintain identical product attributes (micro-scale) across the fluid bed scales (macro-scales), but it is not obvious at which level the starting point for the scale-up principle should be. Both types of scaling approaches are presented in the following sections.

4.2.1. The macro-level approach

Fluidised bed scaling principles at the macro-level have been studied intensively for fluidised catalytic cracking regenerators and bubbling fluidised beds for more than thirty years (Glicksman et al., 1993 and Schouten et al., 1996). Scale-up of granulation processes based on equipment parameters is referred to as the *macro-scale approach*. A typical macro-scale approach determines the desired conditions over a range of dimensionally similar unit operations typically using well-known dimensionless groups as Reynolds and Sherwood numbers (Mort, 2005 & 2008 and Knowlton et al., 2005). In addition, several other dimensioned parameters or parameter groups are used, including specific energy input, excess gas fluidisation velocity and absolute humidity in the outlet fluidisation air etc. These operation parameters typically affect multiple product transformations, and the challenge is to scale-up the equipment, being geometrically similar or not, in a way that maintains key product attributes, while at the same time achieving an industrially efficient operation (Mort, 2005).

Scale-up attempts based on the dimensionless parameters typically rely on analogies in the heat and mass transfer as well as in the hydrodynamic behaviour of the flow regimes in the fluidised beds, especially on proper description of the bubble hydrodynamics. A number of the classical hydrodynamic scaling expressions and so-called *scaling laws*, based on the superficial gas velocity and minimum fluidisation velocity, may be found for bubbling fluidised beds in Ellenberger & Krishna (1994) and Werther (1980). Horio et al. (1986) developed a rule of hydrodynamic similarity for a scale change of fluidised beds based on the governing equations of bubble and interstitial gas dynamics. They proposed that when geometrically similar scale-up is to be carried out, while maintaining hydrodynamic similarity, two conditions most be satisfied. The first condition assures a similarity of bubble coalescence in the two different fluid bed scales according to:

$$v_{a(s2)} - v_{mf(s2)} = \sqrt{L_{slr}} \cdot (v_{a(s1)} - v_{mf(s1)}) \tag{4.1}$$

in which $v_{a(s1)}$ and $v_{a(s1)}$ are the (superficial) fluidisation air velocity in bed scale 1 and 2, respectively, and $v_{mf(s1)}$ and $v_{mf(s1)}$ are the minimum fluidisation velocity in bed scale 1 and 2, respectively. The parameter L_{slr} is the scaling length ratio. Assuming that the bed height, h_{bed}, the vessel diameter, d_{vessel}, the air distribution plate diameter, $d_{air\ distrib\ pl.}$, as well as the diameters of the orifices in the air distributor plate, $d_{orifices}$, and other structural parameters are scaled in the same proportionality, L_{slr} is defined as (Horio et al., 1986):

$$L_{slr} \equiv \frac{h_{bed(s1)}}{h_{bed(s2)}} = \frac{d_{vessel(s1)}}{d_{vessel(s2)}} = \frac{d_{air\ distrib\ pl.(s1)}}{d_{air\ distrib\ pl.(s2)}} = \frac{d_{orifices(s1)}}{d_{orifices(s2)}} \tag{4.2}$$

If the second condition given by equation 4.3 is satisfied, this will assure similarities in bubble splitting and in the interstitial flow pattern (Horio et al., 1986):

$$v_{mf(s2)} = \sqrt{L_{slr}} \cdot v_{mf(s1)} \tag{4.3}$$

The scaling principles by Horio et al. (1986) have proved promising for Geldart B particles, when properties such as mass transfer and chemical reactions were to be maintained across fluid bed scales. Whether or not the scaling principle is valid for granulating fluid bed systems is yet to be proved.

Similar to the scaling parameters by Horio et al. (1986), Glicksman (1984 & 1988) proposed a full set of scaling relationships by non-dimensionalising the equations of motion, along with their boundary conditions, for the particle and the fluid phase in a fluid bed. Using the length from the air distributor plate to the fluidisation chamber exhaust exit, $L_{chamber}$, as a typical length dimension, the following relations were suggested to be kept constant during scaling:

$$\frac{v_a^2}{g \cdot L_{chamber}}, \quad \frac{\beta_{id} \cdot L_{chamber}}{\rho_p \cdot v_a}, \quad \frac{L_{chamber}}{d_{vessel}} \tag{4.4}$$

in which β_{id} is the coefficient of interphase drag (fluid-to-particle force) and g is the gravitational acceleration.

Other more advanced scaling parameters based on chaotic similarity theory have been proposed by Schouten et al. (1996). Being an empirical approach, the principle is based on the observation that the behaviour of a bubbling fluid bed is of chaotic nature. This degree of chaos is quantified by the Kolmogorov entropy, which is a measure of the rate of loss of information in the system (typically expressed in bits of information per second). The basic idea of the chaos scale-up methodology is that the rate of information loss should be kept similar across scale in order to ensure hydrodynamic similarity (Briongos & Guardiola, 2005). Experiments by vander Stappen (1996) demonstrated the usefulness of matching a measured chaotic similarity group, the so-called *similarity group*, at different fluid bed scales. This parameter group was suggested by van den Bleek & Schouten (1996) to be kept constant across scale, being expressed as (Sanderson & Rhodes, 2005):

$$\frac{S_{Kolmogorov} \cdot d_{bed}}{v_{mf}} \tag{4.5}$$

in which d_{bed} is the fluidised bed diameter and $S_{Kolmogorov}$ is the Kolmogorov entropy, which Schouten et al. (1996) derived an empirical equation for, according to:

$$S_{Kolmogorov} = 10.7 \cdot \left(\frac{v_a - v_{mf}}{v_{mf}} \right)^{0.4} \cdot \frac{d_{bed}^{1.2}}{h_s^{1.6}} \tag{4.6}$$

where h_s is the settled bed height. This Kolmogorov expression is purely empirical and based on experiments in small fluid beds making the predictive capacity of the scale-up principle limited. The scale-up principle is yet to be tested with commercial fluid beds scales.

Specifically for fluid bed granulation processes Turton & Cheng (2005) recently suggested a set of new scaling rules in which it is proposed that the following relative spray rate condition is satisfied during scaling:

$$\frac{\dot{V}_{liq(s1)}}{\dot{V}_{liq(s2)}} = \left[\frac{d_{vessel(s1)}}{d_{vessel(s2)}} \right]^2 \tag{4.7}$$

in which $\dot{V}_{liq(s1)}$ and $\dot{V}_{liq(s2)}$ are the volumetric spray rate of the coating solution in fluid bed scale 1 and 2, respectively. The scaling of the volumetric spray rate is suggested to be set proportional to the amount of fluidisation air introduced into the bed, which in turn will be proportional to the total bed area, assuming that the same (superficial) air velocity v_a is used during scale-up (Turton & Cheng, 2005).

Further, the relative coating time, t_{coat}, is suggested to be kept constant during scale-up according to (Turton & Cheng, 2005):

$$\frac{t_{coat(s2)}}{t_{coat(s1)}} = \frac{\dot{V}_{liq(s1)} \cdot m_{bed(s2)}}{\dot{V}_{liq(s2)} \cdot m_{bed(s1)}} \tag{4.8}$$

in which $m_{bed(s1)}$ and $m_{bed(s2)}$ are the bed loads in fluid bed scale 1 and 2, respectively. Inherent in these scaling rules are the assumptions that the bed fill levels are the same, the distributor plates in each fluid bed scale are geometrically similar, the fluidisation airflow rate is constant, and that the temperature and relative humidity of the inlet air are held constant during scale-up (Turton & Cheng, 2005).

The Flux Number by Akkermans et al. (1998) is a different macro-scale approach as the primary focus here is on particle density, gas velocities, spray area and coating solution distribution on an overall scale. The Flux Number combines these parameters into a single dimensionless parameter claimed to govern the overall possible outcome during wet-granulation in fluidised beds. The Flux Number is defined according to equation 4.9.

$$FN = \log\left[\frac{\rho_p \cdot v_e}{\dot{q}_{mliq}} \right] \tag{4.9}$$

where ρ_p is the particle density determined according to equation 4.10.

$$\rho_p = \frac{BD}{1-\varepsilon_{bed}} \tag{4.10}$$

in which BD is the bulk density of the particles and ε_{bed} is the bed porosity determined e.g. by mercury porosimetry. The parameter $\dot{q}_{mliq}$ is the mass spray flux in kg/(s·m^2) at a normalised distance D_0 from the nozzle outlet, and v_e is the excess gas velocity. Although the Flux Number is claimed by Boerefijn and Hounslow (2005) to be a commonly accepted suitable descriptor of the balance between the flux of solids in the spray zone and the spray flux that wets the solids, no experimental evidence has been presented in detail so far in the open literature. The practical use of the Flux Number as scale-up parameter is treated further in chapter seven.

Macro-level scaling principles, as the above presented, are in principle an overall way to address the scale-up situation, and they do not normally take interparticle forces in fluidised beds into account. They typically also omit any influence of the particle coefficient of restitution as well as the influence of particle frictional forces (Glicksman et al., 1993). What is even more critical is that most of the scaling principles completely neglect any influence from the sprayed liquid phase. This means that scaling principles developed for pure gas-solid systems, such as e.g. for fluidised bed combustors, cannot be applied alone for fluidised bed granulation processes, as the liquid phase is known to be of utmost importance for the control of the process (Teunou & Poncelet, 2002). A fluidised bed system involving all three phases of solid, liquid and gas is more complicated than a fluidised bed having only a solid and a gas phase. This makes most of the macro-level scaling laws somewhat inappropriate for granulation process scaling, and recent scale-up approaches tend to regard macro-scale scale-up as too inaccurate for successful scale-up of granulation processes in fluid beds. Thus, new principles for scale-up of granulating and coating fluidised beds must be used. Simple macro-level dimensionless numbers and scaling similarity parameters may, nevertheless, still be applied in order to estimate the different hydrodynamic regimes. Hence, the satisfaction of selected macro-level scaling laws may be seen as a prerequisite for further detailed micro-level scaling theory. A historical review of macro-level scale-up approaches for pure gas-solid fluid beds may be found in Glicksman et al. (1994).

4.2.2. The micro-level approach

The micro-scale approach on scale-up is based on defining the key transformations in an agglomeration or coating process on the scale of individual particles and liquid droplets (Salman et al., 2007). The match of detailed particle-level properties across scale is referred to as the *micro-level* scale-up approach. In that sense population balance models may be seen as a micro-level description as presented in chapter three. While the use of population balances may provide a useful micro-scale view of the agglomeration process, the complexity of this approach has proven to be too excessive for practical scale-up applications. So far no scaling attempts using population balance models have been reported (Mort, 2005 and Faure et al., 2001). Modern micro-level scaling approaches instead follow the description of the granulation process as a combination of the three sets of separate processes presented in chapter three, being for agglomeration processes: *Wetting and Nucleation*, *Consolidation and Coalescence*, and *Attrition and Breakage*, and for coating processes: *Wetting and possible droplet penetration into core particles*, *Coating and possible agglomeration*, and *Attrition and Breakage*. Often the scaling attempts seek to scale-up each of these processes separately.

The process of initial wetting of the particles appears to be the easiest component to scale-up. The spray droplet size and the droplet size distribution can be estimated or measured and controlled with adequate accuracy. This further means that the size of the spray zone is in principle relatively easy scaled as it depends mainly on the spray angle, nozzle pressure and the position of the nozzle above the fluidised bed (Faure et al., 2001). Results by Watano et al. (1995a) and considerations by Boerefijn & Hounslow (2005) indicate that the wetting zone conditions should be scaled-up to remain relatively constant. There is, nevertheless, no uniform agreement whether or not the mean droplet size should be kept constant across scale (Hapgood, 2000, Mehta 1988 and Rambali et al., 2003). Additionally, it is important to know how quickly the particle bed in the wetting zone is renewed in order to avoid agglomeration and overwetting. Detailed studies by Litster et al. (2001 & 2002) and Hapgood (2000) have integrated this knowledge by combining the volumetric liquid spray rate with the particle flux into an equipment independent parameter called the *dimensionless spray flux* Ψ_a:

$$\Psi_a = \frac{3 \cdot \dot{V}_{liq}}{2 \cdot \dot{A}_p \cdot d_{dr}} \tag{4.11}$$

where $\dot{A}_p$ is the particle flux through the spray zone, $\dot{V}_{liq}$ the volumetric spray rate of spherical droplets produced by the nozzle and d_{dr} is the mean droplet diameter. Litster (2003) suggests that the dimensionless spray flux is a parameter to be kept constant during scale-up. Based on values of the liquid droplet penetration time, τ_{dpen}, the dimensionless spray flux, Ψ_a, and the particle circulation time, τ_c, Litster et al. (2001) have proposed a widely cited nucleation regime map for scale-up of high-shear granulation processes. The works of Lister et al. (2001) and Hapgood (2000) clearly follow previously presented fluid bed scaling principles in which dimensionless numbers have been used as scaling parameters.

Although being developed for the high shear mixers and tumbling granulators, Hapgood (2000) claims that the spray flux may also be used for scale-up of fluid bed granulation systems. The problem of using the dimensionless spray flux in a fluid bed context is the estimation of the particle flux through the spray zone. Litster et al. (2001) assumed a two-dimensional flat spray area and estimated $\dot{A}_p$ as the particle velocity past the spray times the width of the particle bed being wetted. Neglecting the vertical spray zone depth is a rough assumption for fluid bed systems where the spray fan typically reaches a considerable distance into the particle bed. Similarly, the particle flux past the spray zone is of chaotic nature in a fluid bed and thus difficult to estimate. So far no useful description of the particle flux $\dot{A}_p$ has been provided for fluid bed systems, and the use of the dimensionless spray flux in terms of fluid bed upscaling is less likely to be successful.

Similar to the dimensionless spray flux, Mehta (1988) suggested to scale-up by the air distributor area in order to have a similar fluidisation profile and thereby a constant velocity (in m/s) through the air distributor plate across scale. Assuming a higher bed height in the large-scale this means that the drying capacity of the inlet air per kilogram of the particle bed will be relatively lower (at constant inlet fluidisation air conditions) in the large-scale compared to the small-scale fluid bed. In order to keep the evaporation of coating solution solvent constant, Mehta (1988) corrected the spray rate based on the fluidisation airflow rate and bed load. Furthermore, Mehta (1988) argued that the droplet size must be kept similar across scale, and they used an approximation for the scale-up of the spray rate by using the ratio of the cross-sectional area of the air distribution plates at the different scales.

Based on the results by Mehta (1988), Rambali et al. (2003) scaled up a fluid bed granulation process from small- (5 kg) to medium- (30 kg) and large-scale (120 kg) by looking at the effect of the particle bed moisture contents at the end of the spraying process together with the effect of droplet size on the granule size. The fluidisation airflow rate (in m/s) was kept constant in all three beds in order to have a constant airflow profile and to have approximately similar breaking forces on the granules. The droplet size was controlled in terms of a Relative Droplet size, RD, defined as the ratio of the coating liquid mass spray rate $\dot{m}_{spray}$ divided by the atomisation air mass flow rate through the nozzle $\dot{m}_{nozzle\ air}$ squared according to:

$$RD = \frac{\dot{m}_{spray}}{(\dot{m}_{nozzle\ air})^2} \tag{4.12}$$

In the scaling experiments by Rambali et al. (2003) it was observed that the effect of a change in Relative Droplet size was different for each fluid bed scale, but that the granulation process was successful in terms of matching the mean particle size by scaling up to the large-scale from the small-scale, considering only the Relative Droplet size. The practical use of the Relative Droplet size as scale-up parameter is treated further in chapter eight.

In the process of scaling particle agglomeration and wet granule breakage conditions, the use of the previously presented viscous Stokes numbers, St_v, and the Stokes deformation number, St_{def}, may be applied as rough guidelines for the type of operating regime with the given process conditions in the fluid bed. Problems in estimating especially the distribution of collision velocities, u_0, needed in both the St_v and St_{def} expressions, however, make these parameters difficult to exploit for practical scale-up purposes. So far, no detailed scaling attempts have used the viscous Stokes theory although initial attempts by Tardos et al. (1997) and parallel attempts by Watano et al. (1995a,b) appears to be promising.

4.2.3. The multi-scale approach – linking micro- and macro-level approaches

Although formally divided into micro- and macro-level approaches, successful scaling decisions obviously depend on proper choices of conditions at both levels, as decisions on the macro-scale influence micro-scale attributes and vice-versa. With advanced products as enzyme granules, experience by Lödige (2006) clearly indicates that during scale-up, focus should be on both levels. Likewise, if specific micro-level product attributes are known to be very important, then the scale-up decisions must focus on adapting the macro-level properties accordingly. Hence, combining the micro- and the macro-level approach must be considered important to achieve a practical scale-up strategy. Recently, Mort (2003 & 2005) has suggested a multi-scale approach by trying to develop a meso-scale linkage, hereby shortening the gap between the micro- and macro-level scaling principles. These considerations were made initially for high-shear granulators, but may apply for fluid beds as well. Realising that, in a practical scale-up context, it may not be useful or necessary to model the entire system at the micro-level, Mort (2003) argues that macro-level scale-up principles should be built with proper inclusion of the detailed micro-level theories. These purely theoretical considerations made by Mort (2003 & 2008) are, however, yet to be transformed into practical scale-up principles.

4.3. Summing up on scaling fluid bed granulation processes

In summary, the scale-up of a fluid bed granulation process requires decisions to be made at many levels. Decisions must be closely related to a large number of parameters including: fixed parameters, parameters related to the starting materials and the type of fluid bed, input parameters, operating conditions including spray and fluidisation conditions as well as processing time etc. With such a variety of interlinked parameters and properties combined with a lack of quantitative understanding of the granulation process, it is obvious that the scaling of a fluid bed granulation process is a difficult task. The present review clearly shows signs of a scientific field with much understanding yet to be explored. Although progress has been made towards a formal quantitative description, the scaling of granulation processes in fluid beds is still a mix of physics, mathematics, experience, common sense and qualified guesses.

The macro-level scaling rules appear to be the most developed, and the majority of published scientific papers have taken this approach to fluid bed granulation scale-up. This is obvious as such overall considerations are easiest to propose as well as to validate. A number of scaling rules and attempts of building dimensionless groups have been introduced, but at the present moment it is not obvious which of these that have the greatest chance of providing successful scale-up. A general disadvantages with the majority of macro-level scaling rules is that such approaches tend to neglect the influence of interparticle forces and other vital particle properties as well as the influence of the liquid phase. Hence, from a formal point of view it seems unlikely that such unit-operation-scale scaling rules will be adequate for granulation processes.

Micro-level scaling theory, on the other hand, is still in its childhood, and much validation with real granulation processes is needed before any scaling recommendations may be provided. The problems with the micro-level scaling parameters illustrate, from another point of view, that there is still a major work to be done in the fundamental particle-level understanding of the granulation process. There is no doubt that proper up-scaling is closely related to a fundamental understanding of the granulation process at the particle-level, and until quantitative understanding is achieved at all levels, fluid bed process scaling will most likely continue to be more of an art rather than science.

4.4. Tables of symbols

Symbols		Unit
$\dot{A}_p$	Particle flux through the spray zone	m^2/s
BD	Bulk density	kg/m^3
$d_{air\ distrib\ pl.}$	Air distribution plate diameter	m
d_{bed}	Fluidised bed diameter	m
d_{dr}	Mean droplet size	μm
$d_{orifices}$	Diameter of the orifices in the air distributor plate	mm
d_{vessel}	Fluid bed vessel diameter	m
D_0	Normalised distance	m
FN	Flux Number	Dimensionless
g	Gravity	m/s^2
h_{bed}	Expanded bed height	m
h_s	Settled bed height	m

$L_{chamber}$	Length from air distributor plate to exhaust exit	m
L_{slr}	Length scale ratio	Dimensionless
m_{bed}	Bed load	kg
$\dot{m}_{nozzle\ air}$	Atomisation air mass flow rate	kg/s
$\dot{m}_{spray}$	Coating solution mass spray rate	kg/s
$\dot{q}_{mliq}$	Mass spray flux	kg/(s·m^2)
RD	Relative Droplet size	s/kg or min/g
s1, s2	Scale 1 and 2, respectively	Dimensionless
$S_{Kolmogorov}$	Kolmogorov entropy	bits/s
t_{coat}	Coating time	s
v_a	Fluidisation air velocity	m/s
v_e	Excess gas velocity	m/s
v_{mf}	Minimum fluidisation velocity	m/s
$\dot{V}_{liq}$	Volumetric spray rate	m^3/s

Greek

β_{id}	Coefficient of interphase drag	Dimensionless
ε_{bed}	Bed porosity	%
ρ_p	Particle density	kg/m^3
τ_c	Average particle circulation time	s
τ_{dpen}	Droplet penetration time	s
Ψ_a	Dimensionless spray flux	Dimensionless

4.5. References

Akkermans, J.H.M., Edwards, M.F., Groot, A,T.J., Montanus, C.P.M., Van Pomeren, R.W.J. and Yuregir, K.R. (1998) Production of detergent granulates, Patent WO98/58046.

Boerefijn, R. and Hounslow, M.J. (2005) Studies of fluid bed granulation in an industrial R&D context, Chemical Engineering Science, No. 60, pp. 3879-3890.

Briongos, J.V. and Guardiola, J. (2005) New methodology for scaling hydrodynamic data from a 2D-fluidized bed, Chemical Engineering Science, No. 60, 5151-5163.

Ellenberger, J. and Krishna, R. (1994) A Unified Approach to the Scale-up of Gas-Solid Fluidized Bed and Gas-Liquid Bubble Column Reactors, Chemical Engineering Science, Vol. 49, No. 24B, pp. 5391-5411.

Faure, A., York, P. and Rowe, R.C. (2001) Process control and scale-up of pharmaceutical wet granulation processes: a review, European Journal of Pharmaceutics and Biopharmaceutics, No. 52, pp. 269-277.

Glicksman, L.R. (1984) Scaling Relationships For Fluidized Beds, Chemical Engineering Science, Vol. 39, No. 9, pp. 1373-1379.

Glicksman, L.R. (1988) Scaling relationships for fluidized beds, Chemical Engineering Science, Vol. 43, No. 6, pp. 1419-1421.

Glicksman, L.R., Hyre, M. and Woloshun, K. (1993) Simplified scaling relationships for fluidized beds, Powder Technology, No. 77, pp. 177-199.

Glicksman, L.R., Hyre, M.R. and Farrell, P.A. (1994) Dynamic Similarity in Fluidization, Int. J. Multiphase Flow, Vol. 20, Suppl., pp. 331-386.

Hapgood, K. (2000) Nucleation and binder dispersion in wet granulation, Ph.D. Thesis, University of Queensland.

Hede, P.D. (2006) Towards Mathesis Universalis: Modern aspects of modelling batch fluidised bed agglomeration and coating systems – a review, CHEC Report R0605, Department of Chemical Engineering, Technical University of Denmark, pp. 1-101.

Hede, P.D., Bach, P. and Jensen, A.D. (2008b) Top-spray fluidised bed coating: Scale-up in terms of relative droplet size and drying force, Powder Technology, Vol. 184, No. 3, pp. 318-332.

Horio, M., Nonaka, A., Sawa, Y. and Muchi, I. (1986) A New Similarity Rule for Fluidized Bed Scale-up, AIChE Journal, Vol. 32, No. 9, pp. 1466-1482.

Knowlton, T.M., Karri, S.B.R. and Issangya, A. (2005) Scale-up of fluidized-bed hydrodynamics, Powder Technology, No. 158, pp. 72-77.

Leuenberger, H. (1983) Scale-up of granulation processes with reference to process monitoring, Acta Pharmaceutical Technology, No. 29, pp. 274-280.

Leuenberger, H. (2003) Scale-up in the 4th dimension in the field of granulation and drying or how to avoid classical scale-up, Powder Technology, No. 130, pp. 225-230.

Litster, J.D., Hapgood, K.P., Michaels, J.N., Sims, A., Roberts, M., Kameneni, S.K. and Hsu, T. (2001) Liquid distribution in wet granulation: dimensionless spray flux, Powder Technology, No. 114, pp. 32-39.

Litster, J.D., Hapgood, K.P., Michaels, J.N., Sims, A., Roberts, M. and Kameneni, S.K. (2002) Scale-up of mixer granulators for effective liquid distribution, Powder Technology, No. 124, pp. 272-280.

Litster, J.D. (2003) Scaleup of wet granulation processes: Science not art, Powder Technology, No. 130, pp. 35-40.

Lödige (2006) High-shear scale-up meeting at Novozymes A/S by Horst Spittka from Lödige Process Technology, Novozymes A/S, Bagsværd, 17th of January 2006.

Mehta, A.M. (1988) Scale-up considerations in the fluid-bed process for controlled-release products, Pharmaceutical Technology, No. 12, pp. 46-52.

Mort, P.R. (2003) A multi-scale approach to modelling and simulation of particle formation and handling processes, Proceedings of the 4th International Conference for Conveying and Handling of Particulate Solids, Budapest, Hungary.

Mort, P.R. (2005) Scale-up of binder agglomeration processes, Powder Technology, No. 150, pp. 86-103.

Mort, P.R. (2008) Scale-up and Control of Binder Agglomeration Processes – Flow and Stress Fields, Powder Technology, accepted manuscript.

Rambali, B., Baert, L. and Massart, D.L. (2003) Scaling up of the fluidized bed granulation process, International Journal of Pharmaceutics, No. 252, 197-206.

Salman, A.D., Hounslow, M.J. and Seville, J.P.K. (2007) Handbook of Powder Technology, Granulation, Elsevier Publishing.

Sanderson, J. and Rhodes, M. (2005) Bubbling Fluidized Bed Scaling Laws: Evaluation at Large Scales, Particle Technology and Fluidization, Vol. 51, No. 10, pp. 2686-2694.

Schouten, J.C., Vander Stappen, M.L.M. and Van den Bleek, C.M. (1996) Scale-Up of Chaotic Fluidized Bed Hydrodynamics, Chemical Engineering Science, Vol. 51, No. 10, pp. 1991-2000.

Squires, A.M. (1982) Contribution toward a history of fluidization, Adapted from: Proceedings of the Joint Meeting of Chemical Engineering Society of China and American Institute of Chemical Engineers, Chemical Industry Pres, Beijing, pp. 322-353.

Tardos, G.I., Khan, M.I. and Mort, P.R. (1997) Critical Parameters and Limiting Conditions in Binder Granulation of Fine Powders, Powder Technology, No. 94, pp. 245-258.

Teunou, E. and Poncelet, D. (2002) Batch and continuous fluid bed coating – review and state of the art, Journal of Food Engineering, No. 53, pp. 325-340.

Turton, R. and Cheng, X.X. (2005) The scale-up of spray coating processes for granular solids and tablets, Powder Technology, No. 150, pp. 78-85.

van den Bleek, C.M. and Schouten, J.C. (1996) Deterministic chaos: a new tool in fluidized bed design and operation, The Chemical Engineering Journal, No. 53, pp. 75-87.

vander Stappen, M.L.M. (1996) Chaotic hydrodynamics of fluidized beds, Ph.D. Thesis, Technical University of Delft.

van Ee, J.H., Misset, O and Baas, E.J. (1997) Enzymes in Detergency, Surfactant Science Series, Volume 69, Marcel Dekker, New York.

Van Ommen, J.R., Teuling, M., Nijenhuis, J. and van Wachem, B.G.M. (2006) Computational validation of the scaling rules for fluidized beds, Powder Technology, No. 163, pp. 32-40.

Watano, S., Sato, Y., Miyanami, K., Murakami, T., Ito, Y., Kamata, T. and Oda, N. (1995a) Scale-Up of Agitation Fluidized Bed Granulation I. Preliminary Experimental Approach for Optimization of Process Variables, Chemical and Pharmaceutical Bulletin, No. 43, pp. 1212-1216.

Watano, S., Sato, Y., Miyanami, K., Murakami, T., Ito, Y., Kamata, T. and Oda, N. (1995b) Scale-Up of Agitation Fluidized Bed Granulation IV. Scale-Up Theory Based on the Kinetic Energy Similarity, Chemical and Pharmaceutical Bulletin, No. 43, pp. 1227-1230.

Werther, J. (1980) Modelling and Scale-up of Industrial Fluidized Bed Reactors, Chemical Engineering Science, No. 35, pp. 372-379.

Chapter 5. Equipment and materials

Chapter introduction

In chapter five, the materials and primary apparatus used in all the research experiments are presented in one place. Only equipment of primary importance for the conducted research will be introduced in detail, as the principles behind secondary standard support equipment is assumed to be known. What is presented in chapter five is essentially a compilation of the equipment parts adapted from the four papers being: *Small-scale top-spray fluid bed coating: Granule impact strength, agglomeration tendency and coating layer morphology* (referred to as Hede et al., 2007a), *Top-spray fluid bed coating: Scale-up in terms of Relative Droplet size and Drying Force* (referred to as Hede et al., 2008b), *Validation of the Flux Number as scaling parameter for top-sprayed fluid bed coating systems* (referred to as Hede et al., 2008a) and *Fluidised bed coating with sodium sulphate and PVA/TiO_2. Part I: Review and agglomeration regime maps* (referred to as Hede et al., 2008d). All four papers are authored by Peter Dybdahl Hede (Technical University of Denmark), Poul Bach (Novozymes A/S) and Anker D. Jensen (Technical University of Denmark).

5. Equipment and materials

The experimental part of the research work is focused on primarily fluid bed coating scale-up and process optimisation, and secondly on granule properties such as mechanical strength and morphology. Being a Ph.D. project with an industrial focus, the choice of materials and equipment has been aimed at resembling commercial enzyme granulation processes and conditions as much as possible. However, as there is a considerable health risk of working with enzymes, especially with enzyme-containing solids and dust, and as the amount of enzyme in industrial enzyme granules is usually only a few w/w%, the effect on e.g. agglomeration tendency or mechanical strength of mixing enzymes in the coating liquid is negligible. For safety reasons, the choice was therefore to work solely with placebo cores and coating solutions throughout the research. The results obtained from such placebo studies are, however, likely to apply for real enzyme granules and granulation processes as well. This has been verified by Neidel (2007) based on fluid bed coating experiments with placebo as well as with commercial protease granules.

5.1. Fluid bed equipment

All experimental work was carried out at the granulation pilot-plant and laboratories at Novozymes A/S in Bagsværd. The pilot facility disposes over a number of batch fluid beds at different scales ranging from laboratory table-top scale to large pilot-scale. From this equipment three fluid beds of different scales were selected in which all the research experiments were carried out. The capacity of these three fluid beds ranges from 0.5 kg to 24 kg. All three are top-spray fluid beds each having a single external mixing two-fluid nozzle.

In the statistical small-scale studies presented in chapter six, an outlet liquid orifice nozzle diameter of 0.8 mm was used, whereas for all other experiments a diameter of 1.2 mm was used for all scales. This was done in order to fix as many parameters as possible across scale hereby carefully choosing the three fluid bed set-ups to be as similar as possible. Likewise for all scales, the coating solution feed was led from an external heated reservoir at a constant temperature to the nozzle through an adjustable peristaltic tube pump. A sketch of the general set-up for each of the three fluid bed systems may be seen from figure 5.1. The physical dimensions of the three fluid bed scales may be seen from figure 5.2 and table 5-1. For all three fluid beds the fluidisation air inlet temperature and fluidisation velocity as well as the nozzle pressure was controlled independently via the fluid bed control interface. All other parameters had to be adjusted accordingly.

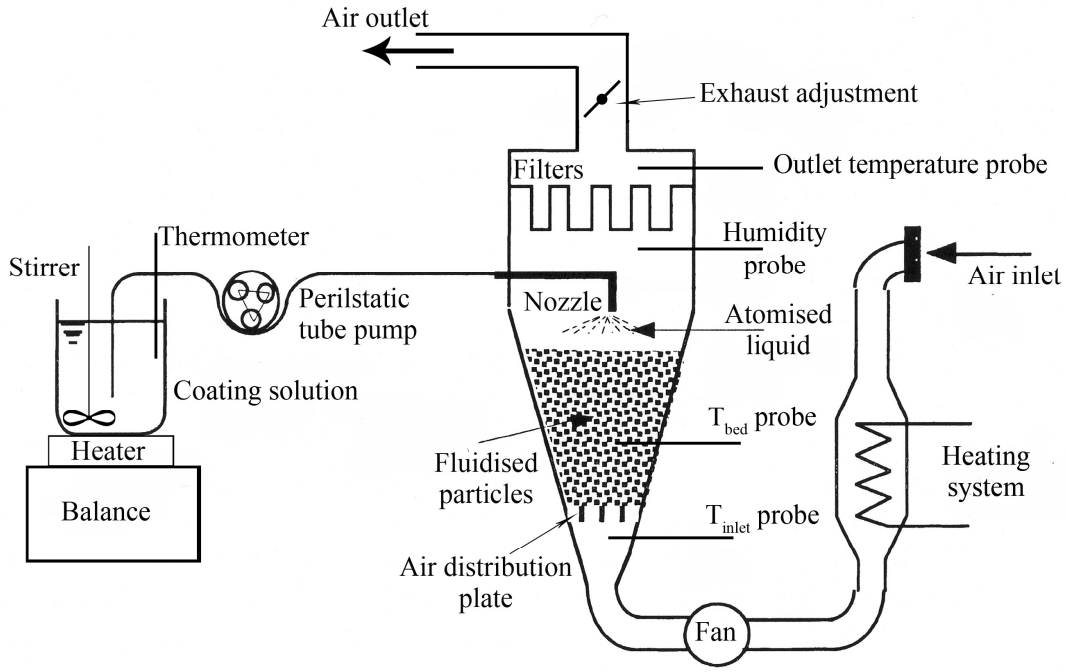

Figure 5.1: Formal sketch of the general top-spray set-up used for the three fluid bed scales in the research work.

Prior to coating, the core bed load was always heated until the relative humidity inside the fluidisation chamber was constant, typically ranging from 0.5 rH% to 3 rH% depending on weather conditions (none of the three fluid bed set-ups allowed humidity conditioning of the inlet fluidisation air). In each coating experiment the aim was to coat until the bed load had increased 20 w/w%, which a typical weight gain during a commercial coating process of enzyme granules. Such a weight gain will ensure that a reasonable coating layer (~ 5-10 µm) develops on the core particles. After coating, the bed load was kept fluidised at identical fluidisation velocity and inlet fluidisation temperature conditions in order to dry the coated granules. This was done until the relative humidity inside the chamber was identical to the conditions prior to coating. This drying phase typically lasted less than 10% of the total coating time meaning that the amount of debris caused by attrition in the drying phase was of negligible importance for the final particle size distribution. As a control the coated bed load was afterwards weighted in order to make sure that the bed load had gained about 20 w/w% in weight.

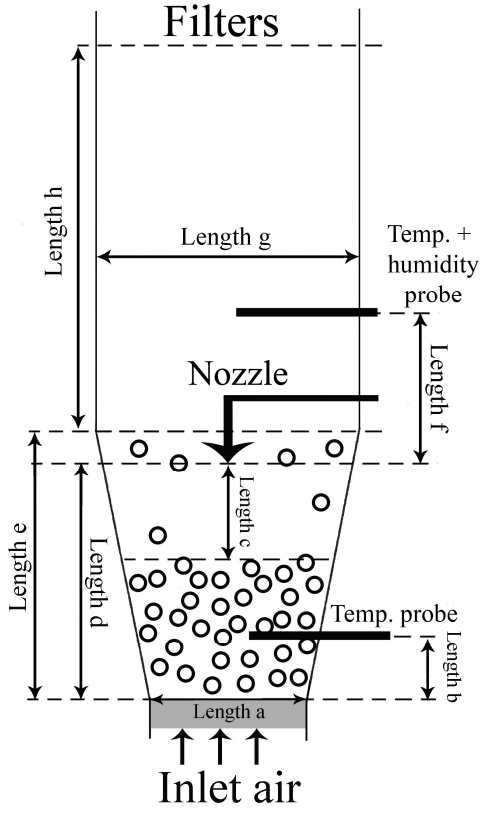

Figure 5.2: Sketch of the dimensions for the three commercial fluid beds used in the research work. Length dimensions corresponding to the symbols in the figure are stated in table 5-1.

Table 5-1: Detailed dimensions of the three commercial fluid bed set-ups used the research work.

Fluid bed parameters	(Small pilot-scale) GEA Aeromatic-Fielder Strea-1	(Medium pilot-scale) Niro MP-1	(Large pilot-scale) GEA-Niro MP-2/3
Length a	10 cm	17 cm	27 cm
Length b	10.5 cm	6 cm	11 cm
Length c	18 cm	32 cm	37 cm
Length d	27 cm	57.5 cm	81 cm
Length e	31 cm	48.5 cm	63 cm
Length f	15 cm	28 cm	82 cm
Length g	25 cm	29 cm	64 cm
Length h	18 cm	93 cm	270 cm

Although the working principles of the three fluid bed scales are the same, there are a number of minor details and specific conditions associated with each scale. The three scales are briefly presented below.

5.1.1. Small-scale fluid bed: Strea-1

The smallest of the three fluid bed scales is a modified table-top GEA Aeromatic-Fielder Strea-1 top-spray fluidised bed. The small-scale fluid bed offers in principle all the possibilities and functions of larger beds, and it can be used for drying, cooling, coating as well as agglomeration. It consists of a conical fluidisation chamber and a docking station. The chamber is made of stainless steel with a vessel volume of 12 L allowing the bed load to be between 0.5 kg and 1.0 kg depending on particle size and density. For the conducted research

experiments a bed load of 0.5 kg was chosen in order to allow sufficient versatility in terms of finding proper values for the volumetric fluidisation air velocity. The Strea-1 available at Novozymes is a top-spray version, but other variants of the Strea-1 can be arranged to bottom spray or Wurster design (GEA, 2005).

Modification to the original vessel design made it possible to insert a digital thermometer into the fluidisation chamber wall thereby enabling measurements of the bed temperature between the bottom air distributor plate and the nozzle outlet. In addition, a humidity measurement apparatus (Testo 645 Thermohygrometer with TopSafe probe measuring humidity highly accurately with a sensitivity of ±1 rH% in the range of 0.1 – 99.9 rH%) was inserted above the nozzle allowing the relative humidity in the fluidisation chamber to be measured. The vertical position of 15 cm from the nozzle outlet and a horizontal probe depth of 12 cm were carefully chosen in order not to let the humidity measurements be directly affected by the nozzle outlet.

For the statistical modelling experiments in chapter six, the standard Strea-1 reusable nylon filters were inserted at the top of the fluidisation chamber in order to prevent particles and spray-dried coating droplets from being exhausted. Although the back-flush option in the Strea-1 set-up was switched on, hereby flushing the filters every sixty seconds, the filters could not be cleaned sufficiently by the back-flush under some conditions. Hence, for the scale-up studies, the nylon filters were replaced by custom-made reusable stainless steel filters with a mesh orifice size of 25 µm. Also for these experiments the back-flush option in the Strea-1 set-up was switched on allowing the filters to be flushed every sixty seconds. A photo of the small-scale set-up can be seen from figure 5.3.

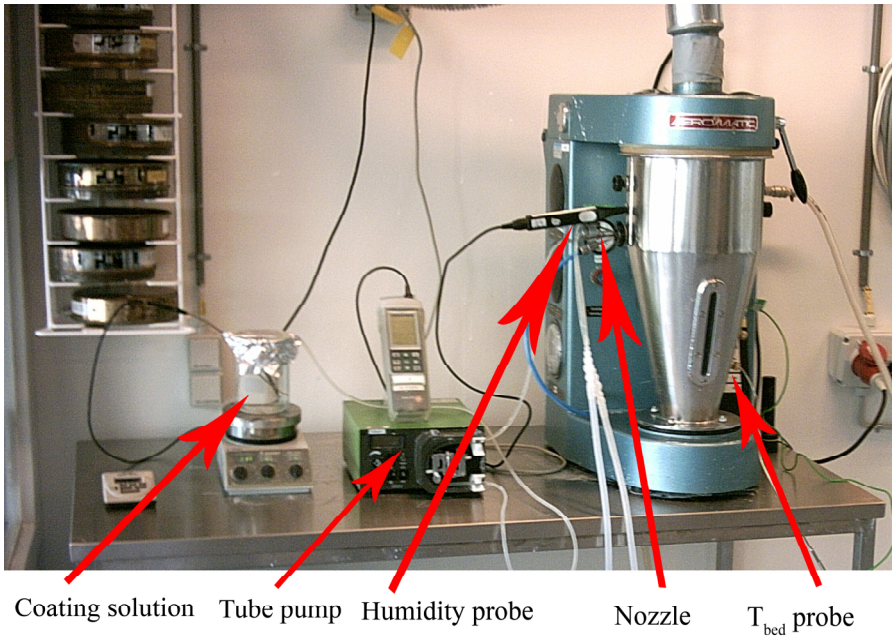

Figure 5.3: Picture of the small-scale Strea-1 set-up.

The air used for fluidisation is supplied from the surroundings by suction through filters at the back of the docking station. In the statistical modelling experiments presented in chapter six, both the nozzle itself and the nozzle air was heated, besides keeping the coating solution reservoir at 80 °C. An integrated heating jacket connected to a thermostated external water bath at 80 °C heated the nozzle itself, whereas the atomisation air (supplied from an external compressed air supply) was led through an external electrical heating cartridge at 80 °C

before reaching the nozzle. This was chosen in order to avoid clogging of the nozzle due to crystalisation of the solute inside the nozzle. It was later found that it is sufficient to keep the coating liquid feed heated during the coating process, and the additional nozzle and atomisation air heating was not applied for any of the following experiments. In all of the following experiments the coating solution reservoir was kept at a constant temperature of 60 °C.

5.1.2. Medium-scale fluid bed: MP-1

The medium-scale top-spray fluid bed is a standard Niro-Aeromatic Multiprocessor type MP-1. It has a stainless steel fluidisation chamber with a bottom plate diameter of 17.0 cm allowing a particle bed load of 4 kg to be fluidised, thereby being eight times larger in bed load capacity than the Strea-1. A picture of the MP-1 set-up can be seen in figure 5.4. As for the Strea-1 set-up, it was possible to measure the bed temperature between the bottom air distributor plate and the nozzle outlet. The Testo 645 Thermohygrometer was inserted 28 cm above the nozzle outlet at a horizontal depth of 14 cm allowing the relative humidity in the fluidisation chamber to be measured at a location similar to the Strea-1 set-up. The back-flush option in the MP-1 set-up was switched on allowing the filters to be flushed every sixty seconds in the same way as for the small-scale set-up.

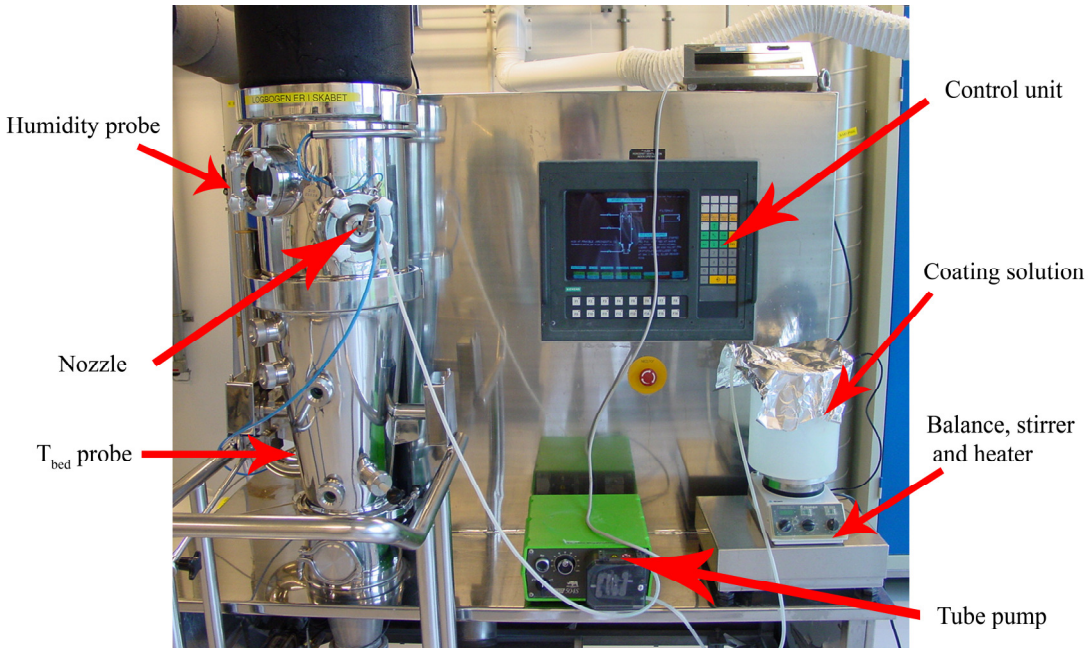

Figure 5.4: Picture of the medium-scale MP-1 set-up.

5.1.3. Large-scale fluid bed: MP-2/3

The large-scale fluid bed is a GEA Aeromatic-Fielder MP-2/3 capable of processing a particle bed load of 24 kg, thereby being six times larger in bed load capacity with respect to the MP-1 and 48 times with respect to the Strea-1 set-up. A picture of the MP-2/3 set-up can be seen in figure 5.5. As for the other fluid bed scales, it was possible to measure the bed temperature between the bottom air distributor plate and the nozzle outlet. The Testo 645 Thermo-hygrometer was inserted 82 cm above the nozzle outlet at a horizontal depth of 21 cm allowing the relative humidity in the fluidisation chamber to be measured at a location similar to the other fluid bed scales. The back-flush option in the MP-2/3 was set to be identical to the other set-ups.

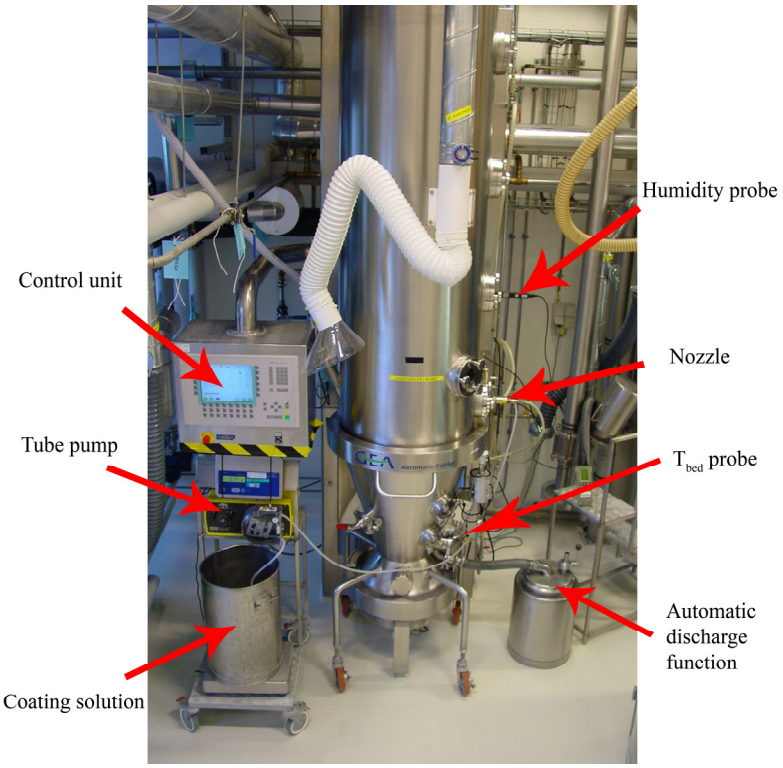

Figure 5.5: Picture of the large-scale MP-2/3 set-up.

5.2. Mechanical strength test equipment

For granular products produced in fluid beds especially two types of mechanical stresses are important for the product quality being impacts and attrition. Although impact strength and attrition resistance are not the only parameter for granule strength characterisation, they are probably the most important and may well be considered representative for the mechanical strength of a granule sample. Attrition takes place in the fluid bed during processing, and to some extent during pneumatic conveying and further processing. During fluidisation, the core and coated particles gradually lose mass as the outer layer is gradually eroded when the particles bump into each other and into the chamber walls as it was presented in chapter three. Granules are on the other hand exposed to numerous impacts due to post-process handling, transportation, packing and further mixing with e.g. detergents, which cause degradation and breakdown of the coating layer (Beekman, 2000, Jørgensen, 2002 and Jørgensen et al., 2004). Two types of mechanical strength test equipment were applied in selected studies in the present work in order to simulate granule attrition and the impacts that commercial granules are exposed to. Both types of equipment are presented below.

5.2.1. Pneumatic Impact Gun

The Pneumatic Impact Gun (PIG) is a specially designed device made at Genencor International Inc. for the purpose of bulk testing the impact strength of granules. The equipment has been built specially to simulate the impacts that coated enzyme granules experience during handling and further mixing with e.g. detergents etc. The equipment consists of a test box, a dust collection box, a sieve and a torque wrench, besides the gun itself. The impact gun itself consists basically of two cylindrical parts of which the outer part is fixed and the inner part is able to move in vertical direction hereby functioning as a piston. Figure 5.6 illustrates the principle of the PIG set-up.

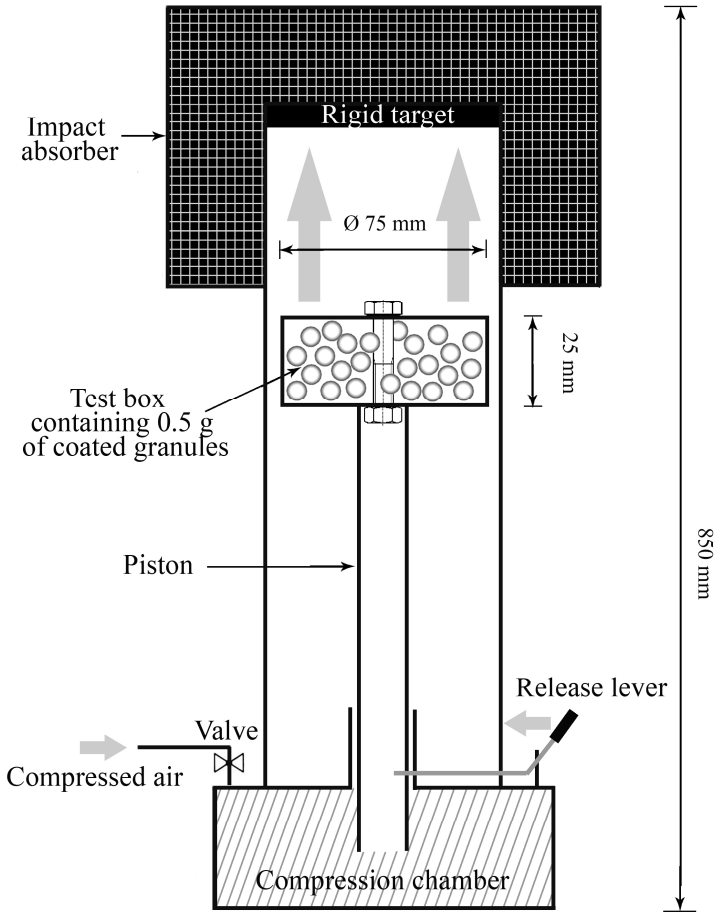

Figure 5.6: Schematic illustration of the Pneumatic Impact Gun.

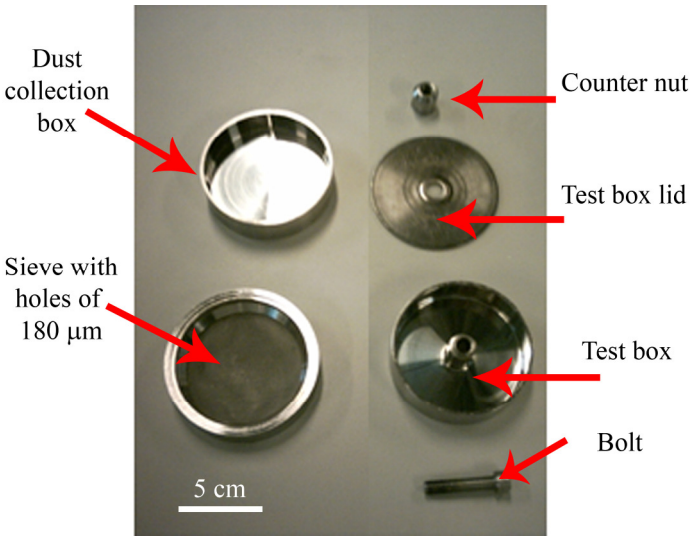

Figure 5.7: PIG test box, sieve and dust collection box.

Granule samples to be tested are placed in a closed stainless steel test box which is illustrated in figure 5.7. Initially in the test, the test box is loaded with the precisely weighed bulk granules sample of 0.5 g (m_{sample}) and the lit is fastened with the use a torque wrench. This is done in order to make sure that the bolt fastening the lit has the same torque in each experiment. Afterwards, the test box is placed on top of the piston connected to the

compression chamber. The piston is moved by compressed air built up in a compression chamber below the piston. The supply of compressed air comes from the laboratory compressed air system. By generating pressure, the piston with the test box on top will travel in a vertical direction until it impacts an absorber at the outer cylinder roof. The granules inside the test box will hereby experience an impact depending on the pressure used to lift the piston. The piston is locked at its lowest position until a release lever on the side of the compression chamber is pulled. A pressure gauge is connected to the compression chamber indicating the pressure build-up in the chamber. By adjusting the pressure in the compression chamber according to the pressure gauge, it is possible to maintain the same velocity of the test box during each impact test. A velocity of 10 m/s was selected according to Genencor standards (GI, 2003). For each coated granule sample the impacts are repeated ten times, and the box contents are afterwards sieved on an electrical shaker for one minute using a specially designed stainless steel sieve having mesh orifices with diameters of 180 μm. Based on microscopy analysis of coated particle size fractions below 180 μm it was observed that such minor fractions consisted of fractured daughter pieces and peeled-off coating layer parts, whereas size fractions above this level consisted primarily of coated granules. Hence, the demarcation of dust and coated particles seems reasonable in terms this sieve size. The amount of the created dust with diameters below 180 μm ($m_{dust\ created}$) is thereby considered an indication of the impact strength expressed as a breakage percentage $Y_{Breakage}$ according to equation 5.1.

$$Y_{Breakage} = \frac{m_{dust\ created}}{m_{sample}} \cdot 100\% \tag{5.1}$$

Instead of just choosing a fixed number of PIG tests for each granule batch and then find the average $Y_{Breakage}$ value, the number of PIG tests to be conducted was determined by the coefficient of variance. A coefficient of variance of 10 % was set as the maximum allowed value estimated as a reasonable low variance from prior tests. Hence, if for a given batch the coefficient of variance among the breakage percentages was below 10 %, an average value was found. Otherwise further PIG tests for the given batch were conducted until the coefficient of variance came below the maximum limit. A minimum of three PIG experiments were performed for each coated batch.

5.2.2. Spouted bed tester

Attrition tests were performed using a fluidised bed jet known as the *Unilever elutriation dust test* or simply *spouted bed attrition test* (see also e.g. Bentham et al., 2004, Boerefijn et al. 2000 or Forsythe & Hertwig, 1949). The principle is simply to fluidise a sample of coated granules with a specific gas velocity for a specific amount of time in a vertical cylindrical glass column. This column has an air distributor plate in the bottom with only a single orifice in the middle having a diameter of 1000 μm. The attrition in such a simplified mini fluid bed involves the entrainment of particles from the dense phase region near the tube walls into the dilute jet core. Once in this region, particles are accelerated by the gas jet and collide with each other as well as with the tube walls. The dust formed by attrition will then be elutriated and collected in an attached filter in the top of the glass column. The filters used in the present spouted bed attrition test are glass fibre filters designed to hold back dust debris with diameters above 1 μm. Figure 5.8 illustrates the schematic set-up of the spouted bed attrition test equipment.

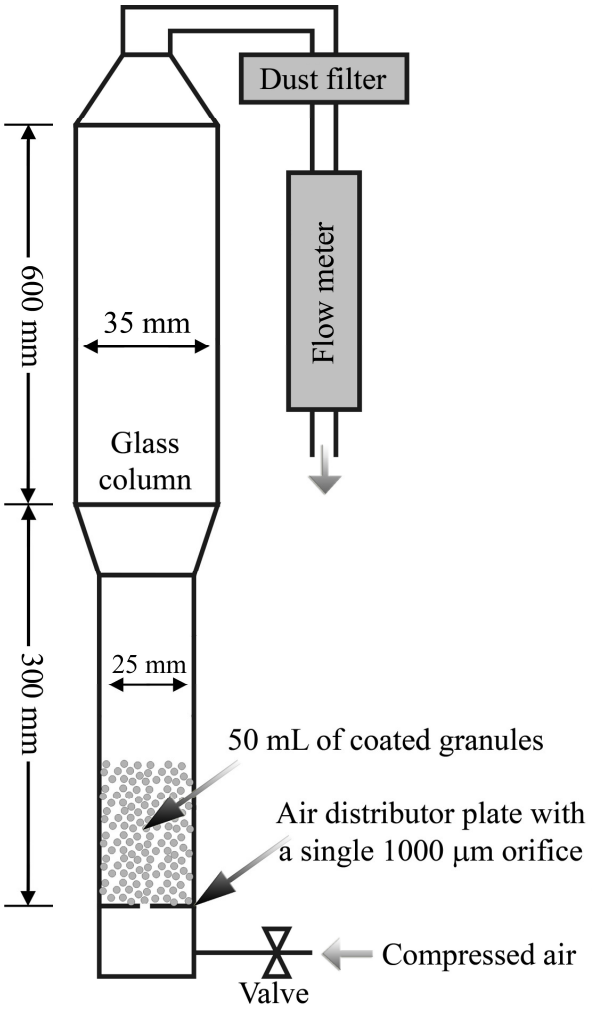

Figure 5.8: Schematic illustration of the spouted bed attrition test equipment.

In each attrition test run a sample of coated granules, corresponding to a volume of 50 mL, is weighted off and placed in the glass column. The precise mass of the new clean filter is determined and placed in the set-up. The airflow is turned on corresponding to a gas velocity through the single orifice of 245 m/s. This gives a fluidisation velocity in the upper column of 0.2 m/s thereby exceeding the terminal velocity for particles with diameters less than 50 μm (Boerefijn et al., 1998 and Zhang et al., 1998). Hence at these conditions, particles and debris with diameters less than 50 μm are caught in the filters and accounted as dust.

After 5 minutes of fluidisation the flow is stopped and the filter is weighted. The system is reassembled and fluidisation is continued for another 35 min. The filter is then weighted again and a quantitative attrition parameter $Y_{attrition}$ is determined for the granule sample according to equation 5.2.

$$Y_{Attrition} = \frac{m_{dust\ created}}{m_{sample}} \cdot 100\% \tag{5.2}$$

in which $m_{dust\ created}$ is determined according to equation 5.3.

$$m_{dust\ created} = m_{dust\ filter\ 40\ min} - m_{dust\ filter\ 5\ min} \tag{5.3}$$

Prior experience with the spouted bed equipment has shown that the dust caught in the filters during the first few minutes of fluidisation primarily results from spray dried coating droplets lossely attached to the outer coating layer and not from real attrition of the coating layer. In order not to let this interfere with the attrition test results, the amount of the created attrition dust was found from equation 5.3 thereby neglecting the first five minutes of dust caught in the filter.

Analogously to the PIG procedure, the number of attrition tests was determined by the coefficient of variance. A minimum number of three attrition tests were conducted for each coated granule batch, and a coefficient of variance of 20 % was set as the maximum allowed value estimated as a reasonable low variance from prior tests. Hence, if for a given batch the coefficient of variance among the attrition percentages from the attrition tests was below 20 %, an average value was calculated. Otherwise, further attrition tests were conducted until the value came below 20 %. A minimum of three attrition tests were performed for each coated batch.

5.3. Sieve

For the sieving analysis of coated granules, a Retsch Sieve Shaker AS 200 control was used with a sieve stack consisting of sieves with different mesh orifice diameters depending on the core particle size fraction used in the particular study. One example could be a stack consisting of sieves with mesh orifice diameters of 150 μm, 180 μm, 212 μm, 250 μm, 300 μm, 355 μm, 425 μm, 500 μm and 600 μm for the sieving analysis of coated particles with initial core diameters in the range of 180 - 350 μm. Sieving above and below the initial core particle span was always done in order to check for the level of debris and peeled-off coating layer as well as for agglomerates. A sample of 200 g from each coated batch was sieved for 3 minutes with an amplitude of 1.1 mm, and the weight of each fraction was determined with the AS 200 control interface using a connected Mettler balance.

Prior to the sieve analysis it was verified by microscope analysis which one of the sieves that was the one closest to the agglomeration cut-off value; i.e. if for instance it was observed that coated granules with diameters above 425 μm consisted of agglomerates, whereas particles below this limit were primarily single coated granules, this sieve mesh orifice diameter was set as the agglomeration limit. Based on this and the weight of each of the particle size fractions, the degree of agglomeration was determined for each batch according to equations similar to equation 5.4.

$$\text{Agglomeration \%} = \frac{\text{coated batch weight fraction with } d_p > 425\,\mu\text{m}}{\text{total coated batch weight}} \cdot 100\,\% \qquad (5.4)$$

In studies where mechanical strength tests were performed on coated granule samples, the samples were picked from a representative size range consisting of primarily coated granules and not of fines or agglomerates. In the present example this would mean that the obtained fraction of coated granules between 355 μm and 425 μm was the fraction to be tested in the mechanical strength tests.

5.4. Rheological equipment

Viscosity measurements were performed with a Physica MCR 301 Rheometer (Anton Paar, Austria) in which it was possible to measure the shear viscosity at different temperatures and shear rates. Viscosity measurements were carried out by the concentric coaxial cylinder principle in rotational tests with controlled shear rate. The stainless steel cup, in which the stainless steel cylinder rotated, was inserted into a Peltier C-PTD 200 thermocup connected to a circulating cooling/heating liquid.

Stickiness (tack) measurements were carried out in a TA.XT2i Texture Analyser (Stable Micro Systems, England). The particular texture analyser setup has been developed as part of the research work at Novozymes for the measurement of the adhesive failure energy and for simulation of the particle agglomeration bonding and unbonding process. With the apparatus, the strength of adhesive bonds can be determined under variation of the most important parameters such as contact pressure, contact time and rate of separation.

The contact probe is a standard Perspex 20 mm probe being an acrylic cylinder with sharp edges and a well-defined surface area. A specially designed stainless steel plate is applied for the coating liquid samples. For the liquid sample a cylinder-shaped hole with a diameter of 30 mm and a depth of exactly 200 μm was cut with a milling cutter into the stainless steel plate. A sketch of the texture analyser system may be seen from figure 5.9.

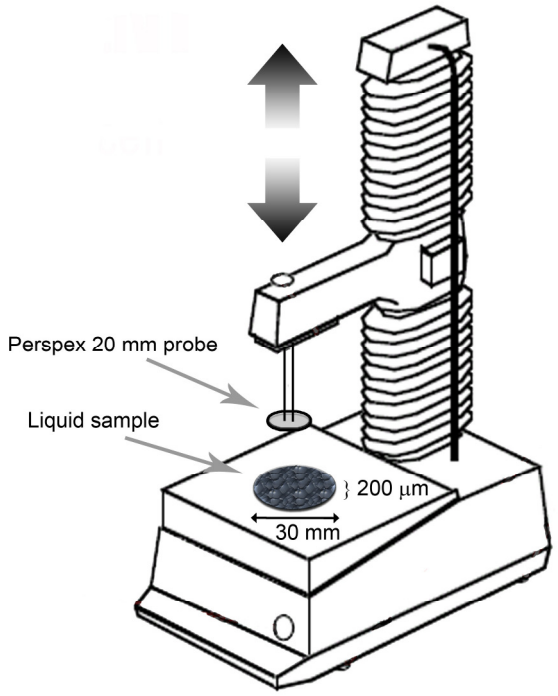

Figure 5.9: Sketch of the TA.XT2i Texture Analyser set-up.

In order to simulate the stickiness during evaporation of the aqueous coating solution solvent, a Steinel Type 3482 2000 watts electronically controlled heating fan was pointed towards the contact point between the texture analyser probe and the liquid sample, as it may be seen from figure 5.10. With the use of a thermometer it was possible to precisely adjust the heating fan in order to maintain a constant temperature of 35 ºC at the contact point.

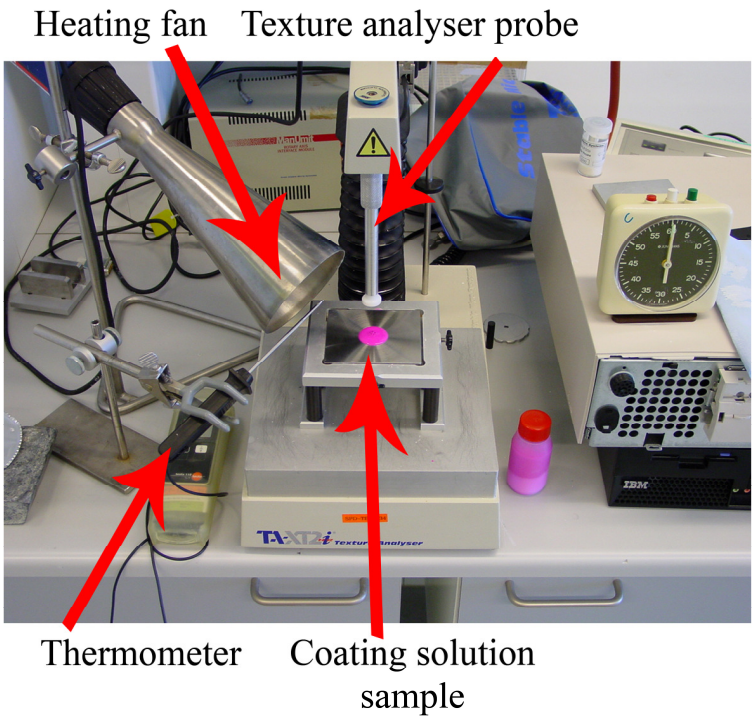

Figure 5.10: Picture of the TA.XT2i Texture Analyser set-up.

The chosen Texture Analyser settings make the probe advance towards the liquid sample at a velocity of 10.0 mm/s (Pre-Test Speed) until a 5 g trigger force is detected. The probe then begins fast to compress the liquid sample until it reaches a force of 50 g. This force is maintained for 0.05 sec to allow only brief contact between the probe and the sample, in order to assemble the short particle-particle contact time in a fluid bed. After this time, the probe then withdraws to a distance of 4 mm away from the sample at a constant speed of 10.0 mm/s (Post-Test Speed), during which the force required to separate the probe from the sample surface is recorded. The maximum force normalised with the probe area is taken as the measurement of stickiness.

The procedure for the Texture analyser is as follows: The coating solution (kept at 25 ºC) is injected into the reservoir on the stainless steel plate, and then the surface is carefully scraped off with a small glass plate to ensure uniform sample thickness. Now the sample is ready for the tack measurement. After the tack measurement the probe and sample plate are cleaned and a new sample is prepared. In the next test run, the heating fan is switched on for 30 s before a new tack measurement is made. This procedure with cleaning, preparation and measurements is repeated, each time adding 30 s to the heating time before sampling the tack with the probe, until the liquid sample is completely dried. Correlations between the time the heating fan is switched on, and the dry-matter contents of the liquid sample are obtained for each coating solution in terms of combined weight difference measurements and Karl Fisher titration using a 701 KF Titrino and a 703 Titrino stand (Metrohm AG, Switzerland). Initial twenty-times repetition measurements with a standard PVA/TiO_2 solution showed that the standard deviation for the stickiness test is 0.396 mN/mm^2. This indicates that differences in stickiness in the range of ± 0.792 mN/mm^2 are not statistically different.

5.5. Standard analysis equipment

A number of standard apparatus have been used for different kinds of simple analyses. The apparatus will not be presented here in detail as they are common standard techniques assumed to be well-known. This analysis equipment includes:

- Visual microscopy analysis with the use of an Olympus KL 1500 LCD microscope.
- Granule and coating solution water content determination with the use of a Metrohm A 701/703 Karl Fisher Titrino titrator.
- SEM pictures taken with a JEOL Scanning Electron Microscope.
- Pore size and porosity measurements with the use of a Micromeritics Autopore II 9220 mercury intrusion/extrusion porosimeter.
- Particle size distribution measurement with the use of a Malvern Mastersizer 2000.
- Measurements of pH with the use of a Radiometer MeterLab PHM210 digital pH meter.
- Measurement of contact angles between coating solutions and core materials obtained with the use of a DataPhysics Instruments OCA-20 video-based contact angle meter.
- Simple viscosity analysis of coating solutions at different temperatures with the use of a Rheotec Falling Ball KF10 viscometer.

5.6. Core materials

Two types of core materials were used for the coating experiments – non-porous glass ballotini cores (Potters Industries, UK) pre-sieved twice in the size range of 180 – 350 μm, and anhydrous sodium sulphate cores (Minera de Santa Marta - Spanish Mining Company, Spain) (CAS no. 7757-82-6) pre-sieved twice in the size range of 180 – 350 μm, 200 – 300 μm, or 400 – 500 μm depending on the study. Pure sodium sulphate has a density of 2680 kg/m^3 making the uncoated Na_2SO_4 cores a typical Geldart group B sandlike material with sphericities in the range of 0.86. The glass ballotini cores are almost perfect spheres and made of a special soda lime glass composition having a density of 2450 kg/m^3. Microscope pictures of both core materials may be seen in figure 5.11.

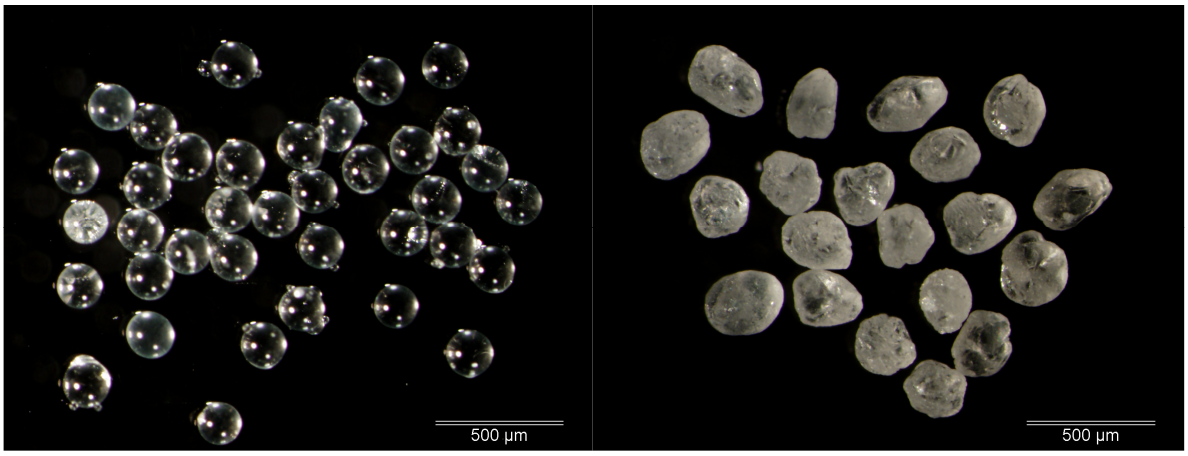

Figure 5.11: Core materials used in the coating experiments. Left) Uncoated glass ballotini cores. Right) Uncoated sodium sulphate cores (pictures obtained with an Olympus KL 1500 LCD microscope).

The moisture content of the uncoated sodium sulphate cores was determined to be less than 0.4 w/w% (inclusive crystal water – measured by determining the weight loss caused by exposing a particle sample of 500 g to 110 °C for 24 hours in a heating cupboard) and the average porosity of the cores was determined to 20.7 % using mercury intrusion/extrusion porosimetry. From this analysis it was further observed that the pore size distribution was narrow and unimodal having an average pore diameter of 1.29 µm. SEM analysis of the sodium sulphate cores showed mostly smooth core surfaces with few, but large pores.

5.7. Coating materials

A number of different coating materials and coating solution additives have been used in different studies in the research work. In the sodium sulphate coating experiments the grade of sodium sulphate for the coating layer is similar to that of the sodium sulphate core particles, although the material has been milled into fine dust in order to ease the solubility in water. Na_2SO_4 is soluble in hot water, but only partly soluble in cold water below 30 °C. This is due to the formation of hydrates of which Glauber salt is the most important. Glauber salt is the decahydrate $Na_2SO_4 \cdot 10\ H_2O$ (CAS no. 7723-73-3) and it is far from being as soluble as anhydrous Na_2SO_4. This means that if Na_2SO_4 is exposed to water at room temperature, Glauber salt will precipitate. The solubility of sodium sulphate increases sharply with temperature and reaches a maximum solubility of 28.1 g in 100 g H_2O at approximately 33 °C and decreases slowly beyond this temperature. At temperatures above 32 °C the formation of Glauber salt is negligible and formed precipitated Glauber salt will dissolve (Efunda, 2005).

Dextrin Avedex W80 (CAS no. 9004-53-9) from AVEBE is used as binder material in all sodium sulphate coating experiments in amounts of 1 w/w% of the amount of coating solution sodium sulphate contents. It is a cheap and white odourless potato based starch commonly used in industrial Novozymes coatings. It is highly soluble in water even at 20 °C and has a bulk density of around 800 kg/m^3 (Eklund, 2005).

Sodium carboxymethylcellulose (CMC) (CAS no. 9004-32-4) from Aqualon (Purity > 99.5 %) is used in selected experiments as a thickener in order to increase the viscosity of the coating solution. CMC is an odourless anionic water-soluble polymer derived from cellulose and widely used in a variety of pharmaceuticals, personal care and food products. It dissolves rapidly in cold as well as in hot water in concentrations up to 10 w/w% (Aqualon, 1998).

In selected droplet penetration and morphology studies, a number of colour additives have been added to the coating solutions in amounts of less than 0.1 w/w% of the coating solution dry-matter contents in order to be able to distinguish the coating layer from the white sodium sulphate cores. The most used colour additive is a triphenylmethane colour named Sicovit Patent Blue 85E131 (CAS no. 3536-49-0) provided by BASF. It is widely used in small amounts in cosmetics, food and drugs as colouring agent. It comes in dark blue powder form and precautions must be taken in order to avoid dust inhalation and prolonged exposure to skin (BASF, 2005). Patent blue is highly water soluble and well suited for spectroscopy analysis having a maximum absorbance in the visual region at 638 nm (Saujanya, 2005).

Another used colour additive is the insoluble pigment colour Colanyl Green GG 131 (CAS no. 1328-53-6). Colanyl Green is a cobber-containing chlorinated organic pigment colour widely used in production at Novozymes as colouring agent for commercial enzyme granules. It is dispersed at the producer into a highly viscous green paste. As it is known to cause allergic reactions, precautions must be taken in order to avoid skin contact as well as aerosol inhalation (ChemIndustry, 2005).

The polyvinyl alcohol (PVA) type (CAS no. 9002-89-5) used in the polymer coating experiments is Celanese Celvol E5/88 (Similar to Elvanol 51-05 or Celvol 205S used in studies by e.g. Hsu et al (2001) and Becker et al. (2005)) having a degree of hydrolysis of 88.5 ± 1.00 thereby being a partially hydrolysed PVA type. In a 4 w/w% solution, pH is 5.5 ± 1.00. The glass transition temperature T_g for this type of PVA is reported to be approximately 58 ºC (Celanese, 2005).

The primary alcohol ethoxylate under the Shell trademark Neodol 23-6.5 (CAS no. 70694-96-1) is used as a combined plasticizer, surfactant and lubricant in coating solutions as a substitute for a small amount of PVA/TiO_2. Neodol 23-6.5 is based on high purity C12-C13 primary alcohol ethoxylate with an average of approximately 6.5 moles of ethylene oxide per mole of alcohol. The density of Neodol 23-6.5 is 0.97 g/cm^3 at 40 ºC, and the viscosity at 40 ºC is 26.1 mPa·s (Shell Chemicals, 2005).

Titanium dioxide type 2044 (CAS no. 13463-67-7) from Kronos is used as filler and pigment in the PVA solutions. It has a specific gravity of 3.55 and a volume median particle diameter ($d_{v0,5}$) of 0.28 μm. This type of TiO_2 is a rutile pigment provided with a surface-treatment with aluminium and silicon compounds that ensures opacity and tint reducing properties in dispersions (Kronos, 1999).

Demineralised H_2O is used as coating solution solvent in all coating experiments.

5.8. Chapter summary

In chapter five the equipment and materials used in the experimental work of the conducted research have been presented. The three pilot-scale fluid beds were introduced being: a 0.5 kg small pilot-scale Strea-1, a 4 kg medium pilot-scale MP-1 and a 24 kg large pilot-scale MP-2/3. All three are single nozzle top-spray batch fluid beds with similar nozzle liquid orifice diameters. In all three set-ups it was possible to measure the inlet, bed and outlet temperature as well as the humidity in the outlet fluidisation air at a distance safely above the nozzle outlet.

Further, two types of mechanical strength test equipment were presented being the Pneumatic Impact Gun and the spouted bed attrition test equipment. The first has been used to simulate the impacts that commercial granules experience during post-granulation handling and further mixing etc., whereas the latter is a mini fluid bed, simulating the attrition of particles both during coating and during post-process treatment.

Lastly, coating and core materials were presented. In most of the studies, anhydrous sodium sulphate cores presieved in certain size ranges were used as core materials, while in a few selected studies spherical glass ballotini cores were used. Similarly, most of the coating experiments involved coating with aqueous solutions of sodium sulphate using Dextrin as binder material, whereas a single large study involved the use of polyvinyl alcohol coating solutions with dispersed TiO_2 particles functioning as anti-agglomerating agents, filler material and colour pigment.

5.9. Tables of symbols

Symbols		Unit
$d_{v0.5}$	Volume median diameter	μm
d_p	Particle diameter	μm
$m_{dust\ filter\ 5\ min}$	Amount of dust created after 5 min of attrition test	kg
$m_{dust\ filter\ 40\ min}$	Amount of dust created after 40 min of attrition test	kg
$m_{dust\ created}$	Amount of dust created by impact	kg
m_{sample}	Amount of sample	kg
T_{bed}	Particle bed temperature	K
T_g	Glass transition temperature	K
$Y_{Attrition}$	Attrition percentage parameter	Dimensionless
$Y_{Breakage}$	Breakage percentage parameter	Dimensionless

5.10. References

Aqualon (1998) Blanose Cellulose Gum – Physical and Chemical Properties, Hercules Aqualon.

BASF (2005) BASF Corporation United States. Visit at the homepage: www.basf.com, April 2005.

Becker, N.T., Flynn, M.J. and Gebert, M.S. (2005) Particle with substituted polyvinyl alcohol coating, Unisted States Patent US 6,872,696.

Beekman, W.J. (2000) Measurement of the Mechanical Strength of Granules, Ph.D. Thesis, Technische Universiteit Delft.

Bentham, A.C., Kwan, C.C., Borefijn, R. and Ghadiri, M. (2004) Fluidised-bed jet milling of pharmaceutical powders, Powder Technology, No. 141, pp. 233-238.

Boerefijn R., Zhang, S.-H. and Ghadiri, M. (1998) Analysis of ISO fluidized bed jet test for attrition of fluid cracking catalyst particles, from: Fan L.-S. and Knowlton, M. Fluidization IX, pp. 325-332, ECI Engineering Foundation, New York.

Boerefijn R., Gudde, N.J. and Ghadiri, M. (2000) A review of attrition of fluid cracking catalyst particles, Advanced Powder Technology: The International Journal of the Society of Powder Technology, Japan, Vol. 11, No. 2, pp. 145-174.

Celanese (2005) Celvol 205S Polyvinyl Alcohol Sales Specification, Celanese Chemicals. ChemIndustry (2005). Visit at the homepage: www.chemindustry.com, April 2005.

Efunda (2005) Engineering Fundamentals. Visit at the homepage: www.efunda.com, March 2005.

Eklund (2005) Email correspondence with Frank Eklund, AVEBE Sweden, March 2005.

Forsythe, W.L. and Hertwig, W.R. (1949) Attrition characteristics of fluid cracking catalysts – laboratory studies, Industrial Engineering Chemistry, No. 41, pp. 1200-1206.

GEA (2005) Aeromatic-Fielder Strea-1 brochure, Niro Pharma Systems, GEA Powder Technology Division.

GI (2003) Pneumatic Impact Gun – Equipment Manual, Genencor International Inc.

Hede, P.D., Bach, P. and Jensen, A.D. (2007a) Small-scale top-spray fluid bed coating: Granule impact strength, agglomeration tendency and coating layer morphology, Powder Technology, Vol. 176, No. 2-3, pp. 156-167.

Hede, P.D., Bach, P. and Jensen, A.D. (2008a) Validation of the Flux Number as scaling parameter for top-sprayed fluid bed coating systems, Chemical Engineering Science, Vol. 63, No. 3, pp. 815-828.

Hede, P.D., Bach, P. and Jensen, A.D. (2008b) Top-spray fluid bed coating: Scale-up in terms of relative droplet size and drying force, Powder Technology, Vol. 184, No. 3, pp. 318-332.

Hede, P.D., Bach, P. and Jensen, A.D. (2008d) Fluidised bed coating with sodium sulphate and PVA/TiO_2. Part I: Review and agglomeration regime maps, Industrial & Engineering Chemical Research, awaiting publication – proof corrected version.

Hsu, E.R., Gebert, M.S., Becker, N.T. and Gaertner, A.L. (2001) The Effects of Plasticizers and Titanium Dioxide on the Properties of Poly (Vinyl Alcohol) Coatings, Pharmaceutical Development and Technology, Vol. 6, No. 2, pp. 277-284.

Jørgensen, K. (2002) Design of a Shear and Impact Resistant Enzyme Granule, M.Sc. Thesis, Department of Chemical Engineering, Technical University of Denmark.

Jørgensen, K., Bach, P. and Jensen, A.D. (2004) Impact and attrition shear breakage of enzyme granules and placebo particles-application to particle design and formulation, Powder Technology, No. 149, pp. 157-167.

Kronos (1999) Kronos® 2044 titanium dioxide, information sheet, Kronos Europe.

Neidel, B. (2007) Water-soluble polymer fluid bed coatings, M.Sc. Thesis, Department of Chemical Engineering, CHEC Research Center, Technical University of Denmark, pp. 1-123.

Novozymes (2006) Internal attrition guidelines by Novozymes A/S, Bagsværd, Denmark.

Saujanya (2005) Manufactures & Exporters of Dyes, Dye intermediates and Chemicals, Ahmedabad, India. Visit at the homepage: www.saujanya.com, April 2005.

Shell Chemicals Europe (2005) NEODOL 23-6.5 Product specification sheet, pp. 1-2.

Zhang, S.-H., Boerefijn, R. and Ghadiri, M. (1998) The effect of orifice size on the breakage of fluid cracking catalyst particles in fluidised bed jets, from: Proceedings from Third World Congress on Particles Technology, Brighton, UK, 1998.

Chapter 6. Statistical black-box modelling in the small-scale FB

Chapter introduction

Chapter six is the first chapter presenting experimental work from the research. In this chapter the principles of statistical modelling are applied on coating experiments in the small-scale fluid bed. The agglomeration tendency and impact strength are selected as response parameters, and two models are derived and validated based on experimental data. The present chapter is published as a peer-reviewed scientific paper in the journal *Powder Technology*, volume 167, pp. 156-167, 2007. The paper is entitled *Small-scale top-spray fluid bed coating: Granule impact strength, agglomeration tendency and coating layer morphology* authored by Peter Dybdahl Hede (Technical University of Denmark), Poul Bach (Novozymes A/S) and Anker D. Jensen (Technical University of Denmark). The paper is referred to as Hede et al. (2007a).

The following sections are exact reproductions of the paper, although the sections concerning equipment and materials have been left out (please refer to chapter five). Furthermore, the format of the paper has been adapted to that of this thesis.

6. Small-scale top-spray fluid bed coating: Granule impact strength, agglomeration tendency and coating layer morphology

Abstract

The degree of agglomeration and impact strength of Na_2SO_4 cores (all in the size range of 200–300 μm) coated with aqueous solutions of sodium sulphate and Dextrin have been investigated as a function of several process and formulation variables. The coating process was performed in a modified small-scale GEA Aeromatic-Fielder Strea-1 top-spray fluidised bed, and the impact strength was tested in bulks using a Pneumatic Impact Gun, in which granule samples of 0.5 g were exposed to ten repeated impacts at 10 m/s. Using an unreplicated double 2^{4-1} fractional factor design, two regression models were derived from experimental data describing quantitatively the degree of agglomeration and impact strength, respectively. The agglomeration model suggests in accordance with previous studies that an increase in the nozzle pressure as well as in the coating solution dry-matter concentration decreases the tendency of agglomeration. The consistency between the agglomeration model and new experimental data is concluded to be satisfactory. The impact strength model indicates increasing impact strength with increasing nozzle pressure, coating solution dry-matter concentration and bed temperature. These tendencies may be influenced by the large extent of droplet penetration, as observed in additional coating droplet penetration and coating layer morphology studies in the present paper. The validation of the impact strength model shows that the model clearly follows overall experimental tendencies. The derivation of these statistical models may be seen as a first step towards the development of processes for production of unagglomerated coated enzyme granules with high mechanical strength, and contribute to an improved understanding of fluid bed coating processes and products.

6.1. Introduction

To improve handling and product properties, enzymes are often incorporated into granules which are commonly produced by fluidised bed processes. As presented in prior work by e.g. Härkonen et al. (1993) and Jørgensen et al. (2004), inert carrier particles in the fluidised bed are typically coated with a formulated enzyme concentrate sprayed onto the particles through nozzles. The use of conventional top-sprayed fluidised bed systems finds wide use in pharmaceutical and food coating operations in pilot-scale as well as in larger production-scale, as presented by Rubino (1999) and reviewed by Teunou & Poncelet (2002). The desired product is a product consisting of unagglomerated individual carrier particles each coated homogenously with a layer of the enzyme. If formulation or process conditions such as fluidisation velocity, bed temperature, humidity of the air, spray rate and droplet size etc., are incorrectly chosen, either excessive agglomeration or excessive spray drying of the spray feed will happen. In both cases a poor product quality and loss will be the result. In general, the optimum coating conditions with respect to product quality and capacity are close to the agglomeration conditions. Despite the wide use of fluidised bed processing, it is still not possible to predict this limit based on the formulation properties and the basic process conditions. Extensive experiments are needed in order to find the optimum process conditions and at the same time optimise the product properties.

Regarding product properties, the mechanical strength of the final coated granule is of vital importance. Due to handling, transportation, packing and further mixing with e.g. detergents, the enzyme granule is exposed to many types of mechanical stresses, causing degradation and breakdown of the coating layer (Jørgensen et al., 2004). This is unwanted not just for health and safety reasons, but also because of reduced enzyme storage stability. Especially impact strength is important regarding mechanical properties of granules made in fluidised beds. Consequently, it is desired to optimise the impact strength by adjustment of the formulation and process conditions.

It is the aim of this paper to address the tendency of agglomeration and impact strength quantitatively in terms of models built from statistical valid experimental data based on an unreplicated double 2^{4-1} fractional factor design. The influence of four parameters is screened in the present paper, being: the fluidisation velocity, the atomisation air pressure, the coating solution salt concentration and the bed temperature.

6.2. Experimental design, operating conditions and analysis of results

The process and formulation conditions for the model experiments may be seen in table 6-1. In accordance with coating guidelines presented in chapter five the core bed load was heated prior to coating until the relative humidity inside the fluidisation chamber was constant. In each coating operation the aim was to coat until the bed load had increased 20 w/w%, in order to make sure that a reasonable coating layer (~ 5-10 μm) had developed on the core particles. For all the experiments in this paper, the batch weight gain was in the range of 19.1 – 19.5 w/w% indicating little loss of core material as well as little loss of coating solution due to spray drying.

Table 6-1: General operating conditions in all model experiments.

Parameter	Operating conditions
Nozzle liquid orifice diameter	0.8 mm
Inlet fluidisation air temperature	80 °C
Temperature of the water bath heating the nozzle	80 °C
Atomisation air temperature	80 °C
Coating solution temperature	80 °C
Heating cartridge temperature	80 °C
Bed load	500 g
Desired weight gain of the core particle bed	20 w/w%
Amount of Dextrin in coating solution (of the amount of Na_2SO_4)	1 w/w%
Fluidisation velocity (v_a) (adjustable parameter)	To be varied (always at $T_{Strea-1\ inlet}$, 1 bar)
Nozzle pressure (Pn) (adjustable parameter)	To be varied
Coating solution salt concentration (Cs) (adjustable parameter)	To be varied
Bed temperature (Tb) (dependent parameter)	To be varied

An unreplicated double 2^{4-1} fractional factor design (Montgomery, 1997) was used to arrange the combinations of the four screened parameters (fluidisation velocity (v_a), atomisation air pressure (Pn), coating solution salt concentration (Cs) and bed temperature (Tb)). The design was double in the sense that for each factor combination, values of $Y_{Breakage}$ and Agglomeration% were determined according to equation 6.2 and 6.1, respectively.

$$\text{Agglomeration \%} = \frac{\text{coated batch weight fraction with } d_p > 355\,\mu m}{\text{total coated batch weight}} \cdot 100\,\% \qquad (6.1)$$

$$Y_{Breakage} = \frac{m_{dust\ created}}{m_{sample}} \cdot 100\% \qquad (6.2)$$

The principle of the 2^{4-1} design set-up can be seen in figure 6.1 and table 6-2. The coded and actual values of the investigated parameters are illustrated in table 6-3.

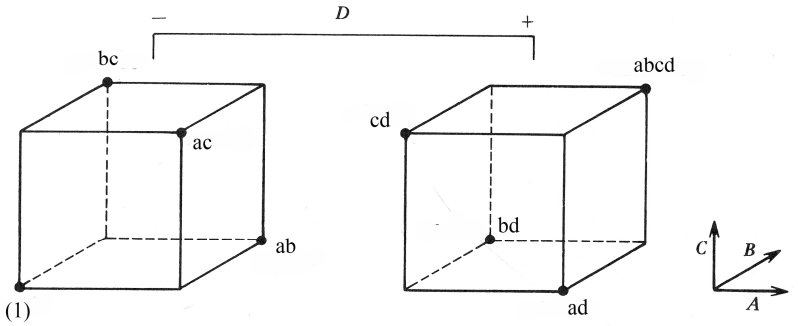

Figure 6.1: The formal set-up of the 2^{4-1} fractional factorial design (Montgomery, 1997).

Table 6-2: The formal set-up of the 2^{4-1} fractional factorial design (Montgomery, 1997).

	Basic 2^3 design			D = ABC	Treatment combination
Run	A	B	C		
1	-	-	-	-	(1)
2	+	-	-	+	ad
3	-	+	-	+	bd
4	+	+	-	-	ab
5	-	-	+	+	cd
6	+	-	+	-	ac
7	-	+	+	-	bc
8	+	+	+	+	abcd

Table 6-3: The four parameters and their high and low levels to be tested in the double unreplicated 2^{4-1} fractional factor design.

	Actual values		Coded values	
Factor	**Low**	**High**	**Low**	**High**
A (v_a)	1.35 m^3/min	1.77 m^3/min	-1	1
B (Pn)	1.5 bar	3.0 bar	-1	1
C (Cs)	10 w/w%	30 w/w%	-1	1
D (Tb)	45 °C	55 °C	-1	1

The Design-Expert® 6.0.6 software (Stat-Ease Corporation, US) was used to fit polynomials to the responses and to draw the normal plots. SAS JMP® 5.0.1 was used for further statistical treatment of the ANOVA (Analysis of Variance) data associated with the resulting models.

6.3. Results and discussion

6.3.1. Effect of screened process and formulation variables

The experimental parameter combinations as well as the impact strength and agglomeration percentage response values, corresponding to the eight fluid bed coating experiments, are summarised in table 6-4.

Table 6-4: Agglomeration percentage and breakage percentage responses for the eight model experiments in the double unreplicated 2^{4-1} fractional factor design.

Run	A	B	C	D	%Agglomeration (Response 1)	$Y_{Breakage}$ (Response 2)
1	-1	-1	-1	-1	83.1 %	14.7 %
2	1	-1	-1	1	89.8 %	12.7 %
3	-1	1	-1	1	0.5 %	10.8 %
4	1	1	-1	-1	1.9 %	13.9 %
5	-1	-1	1	1	12.1 %	8.4 %
6	1	-1	1	-1	13.7 %	12.4 %
7	-1	1	1	-1	1.4 %	8.8 %
8	1	1	1	1	1.9 %	4.5 %

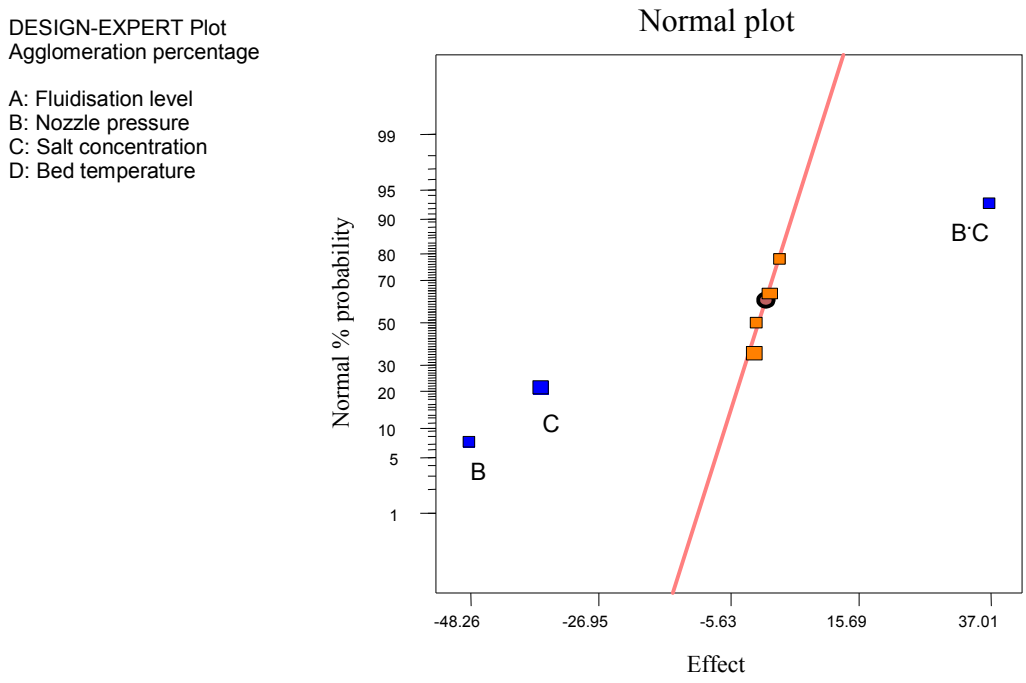

Figure 6.2: Normal plot of the agglomeration percentage responses.

First-order polynomials and first-order interaction terms were fitted to the response. From a normal plot of the agglomeration data in figure 6.2 it was seen that, for the given fractional factor design, only the nozzle pressure (B) and the coating solution salt concentration (C) and their first order joint term (B·C) were significant terms. In fact these three terms accounted for more than 99.7% ($R^2 = 0.9976$) of the variation of the data set. It thereby seems reasonable to base a regression model solely on these three terms. Consequently, the agglomeration percentage regression equation was obtained in coded units according to equation 6.3/6.4, and in real physical units according to equation 6.5.

$$\text{Agglomeration \%} = 25.55 - 24.13 \cdot X_B - 18.27 \cdot X_C + 18.50 \cdot X_B X_C \tag{6.3}$$

$$X_B = \frac{\text{Nozzle pressure in bar} - (1.5\text{ bar} + 3.0\text{ bar})/2}{(3.0\text{ bar} - 1.5\text{ bar})/2} \quad \text{and}$$

$$X_C = \frac{Na_2SO_4\text{ conc. in w/w\%} - (10\text{ w/w\%} + 30\text{ w/w\%})/2}{(30\text{ w/w\%} - 10\text{ w/w\%})/2} \tag{6.4}$$

$$\text{Agglomeration \%} = 245.5 - 81.5 \cdot \text{bar}^{-1} \cdot P_{nozzle} - 7.4 \cdot \text{w/w\%}^{-1} \cdot C_{Na_2SO_4} + 2.5 \cdot \text{bar}^{-1} \cdot \text{w/w\}}^{-1} \cdot P_{nozzle} \cdot C_{Na_2SO_4} \tag{6.5}$$

where $P_{nozzle} \in \{1.5\text{ bar};\ 3.0\text{ bar}\}$ and $C_{Na2SO4} \in \{10\text{ w/w\%};\ 30\text{ w/w\%}\}$.

According to the ANOVA statistics for the model as such, Prob > F was less than 0.0001. Although being very simple this model does in fact describe the experimental data quite well, as it can be seen from figure 6.3.

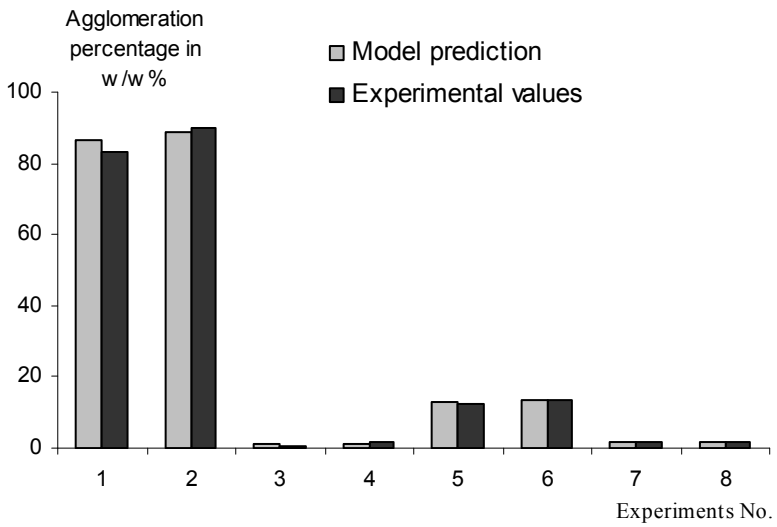

Figure 6.3: Model descriptions of agglomeration percentages versus the experimentally determined data.

According to equation 6.5 the lowest degree of agglomeration should result from conditions in which the nozzle pressure as well as the coating solution salt concentration are as high as possible. This seems reasonable since coating droplets produced at the nozzle outlet will decrease in size with increasing nozzle pressure (Guignon et al., 2002, Dewettinck, 1997 and Dewettinck et al., 1999). Smaller droplets, combined with the fact that there is less solvent in each droplet to be evaporated with increasing coating solution dry-matter contents, means all in all that the coating solution droplets will remain wet for shorter time, which again reduces the chance of agglomeration.

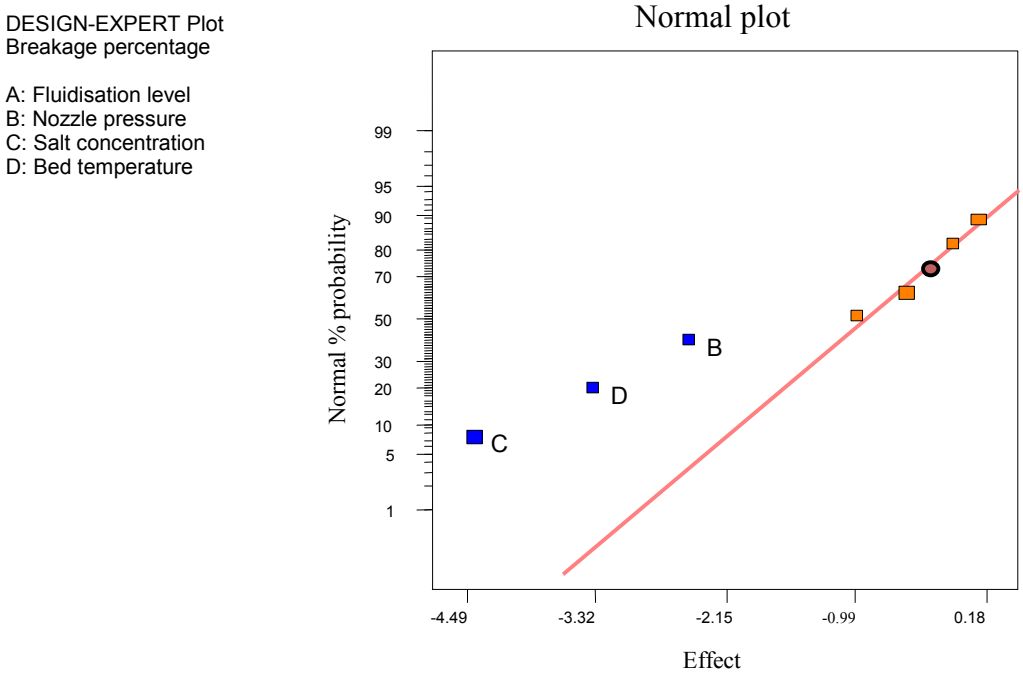

Figure 6.4: Normal plot of the impact strength responses.

Similar to the agglomeration model, an impact strength model was set up based on the data from table 6-4. This time, however, no interaction terms were found to have significant importance, as only the first-order terms of nozzle pressure (B), coating solution salt concentration (C) and the bed temperature (D) were the parameters to have significant importance regarding the impact strength. This can be seen from the normal plot in figure 6.4. These three terms accounted for around 94.6% ($R^2 = 0.9461$) of the variation of the data set. Analogously, the impact strength model in coded units was determined according to equation 6.6/6.7 and in real physical units according to equation 6.8.

$$Y_{Breakage} = 10.77 - 1.28 \cdot X_B - 2.24 \cdot X_C - 1.66 \cdot X_D \tag{6.6}$$

$$X_B = \frac{\text{Nozzle pressure in bar} - (1.5\text{ bar} + 3.0\text{ bar})/2}{(3.0\text{ bar} - 1.5\text{ bar})/2} \quad \text{and}$$

$$X_C = \frac{Na_2SO_4\text{ conc. in w/w\%} - (10\text{ w/w\%} + 30\text{ w/w\%})/2}{(30\text{ w/w\%} - 10\text{ w/w\%})/2} \quad \text{and} \tag{6.7}$$

$$X_D = \frac{\text{Bed temp. in °C} - (45\,°C + 55\,°C)/2}{(55\,°C - 45\,°C)/2}$$

$$Y_{Breakage} = 35.7 - 1.7 \cdot \text{bar}^{-1} \cdot P_{nozzle} - 0.2 \cdot \text{w/w\%}^{-1} \cdot C_{Na_2SO_4} - 0.3 \cdot °C^{-1} \cdot T_{bed} \tag{6.8}$$

where $P_{nozzle} \in \{1.5\text{ bar};\ 3.0\text{ bar}\}$, $C_{Na2SO4} \in \{10\text{ w/w\%};\ 30\text{ w/w\%}\}$ and $T_{bed} \in \{45\,°C;\ 55\,°C\}$.

For the model as such, ANOVA statistics stated that Prob > F was less than 0.0053. Again good fitting to the experimental data can be observed in figure 6.5 although the model is quite simple.

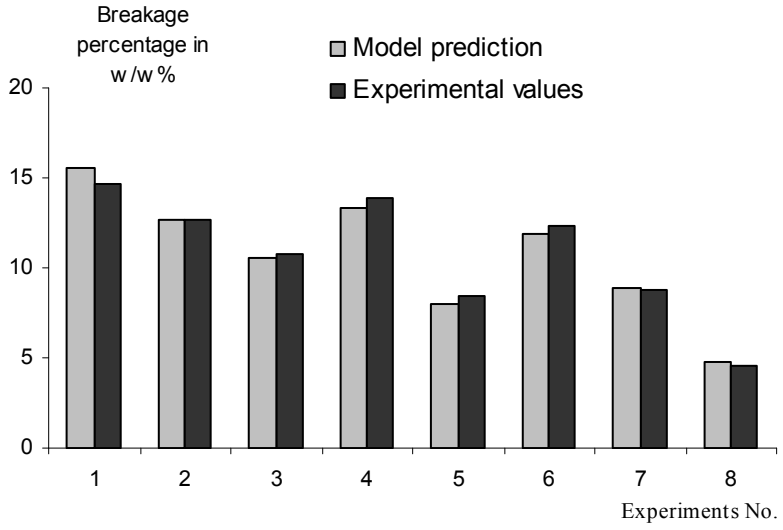

Figure 6.5: Model descriptions of $Y_{Breakage}$ values versus the experimentally determined data.

The impact strength model predictions seem interesting as the highest impact strength, according to equation 6.8, should be obtained under coating conditions where all three terms are as large as possible. Although not being directly comparable, results by Beekman (2000) and Jørgensen et al. (2004) indicate that high granule impact strength is often closely related to the morphology of the coating layer, as homogenous and smooth coating layers often tend to have the highest impact strength. According to studies by Link & Schlünder (1997) the smoothness of coated alumina spheres improves with dilution of, in their case, a $Ca(OH)_2$ coating solution. The present impact strength results are thereby somewhat in opposition to the previously reported tendencies. The situation in the present studies is, however, different as the sodium sulphate cores have far larger average pore diameters than the alumina spheres used by Link & Schlünder (1997). This was further investigated in morphology and droplet penetration studies.

6.3.2. Morphology and droplet penetration studies

In order to study the coating of a porous core particle in detail, a number of additional experiments were conducted where colour agents were added to the coating solution, and the coating operation was performed under process conditions according to table 6-5.

Table 6-5: Operating conditions in additional droplet penetration/morphology experiments.

Parameter	Operating conditions
Nozzle liquid orifice diameter	0.8 mm
Inlet fluidisation air temperature	80 °C
Temperature of the water bath heating the nozzle	80 °C
Atomisation air temperature	80 °C
Coating solution temperature	80 °C
Heating cartridge temperature	80 °C
Bed load	500 g
Desired weight gain of the core particle bed	20 w/w%
Amount of Dextrin in coating solution (of the amount of Na_2SO_4)	1 w/w%
Fluidisation velocity (v_a) (adjustable parameter)	Level 20 ~ 1.77 m^3/min (at $T_{Strea\text{-}1\ inlet}$, 1 bar)
Nozzle pressure (Pn) (adjustable parameter)	2 bar
Coating solution salt concentration (Cs) (adjustable parameter)	From 15 to 30 w/w%
Bed temperature (Tb) (dependent parameter)	50 °C

Visual microscopy analysis of the coated sodium sulphate cores was conducted. Figure 6.6A and 6.6B show cut-through examples of coated granules. It can be observed from these figures that the level of droplet penetration was significant as the coloured coating solution has penetrated far into the core material in both cases. Rough calculations of the droplet drying time using equation 3.6 and the time of droplet penetration using the equation 3.4 (see chapter three) (Denesuk et al., 1993 & 1994 and Hede, 2005) indicated in accordance with the visual microscopy analysis that the time of droplet penetration was a hundred to a thousand times faster than the coating droplet drying time under the given process conditions. The mean droplet diameter needed for both equations was found with the use of the semi-empirical equation 2.1 (see chapter two).

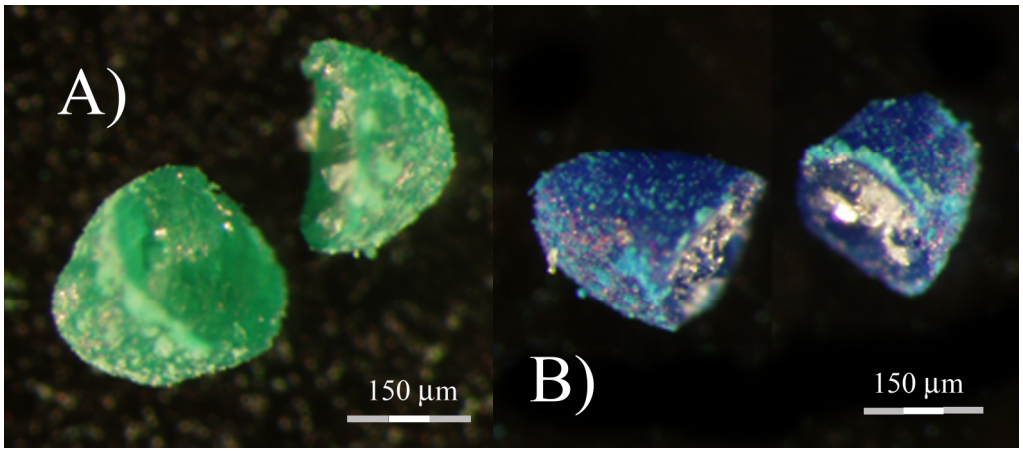

Figure 6.6: Microscope pictures of: A) Cut-through profile of a coated granule using Colanyl green colour. B) Cut-through profile of a coated granule using Patent blue colour.

According to equation 3.4, the time of droplet penetration is directly proportional to the coating liquid viscosity. Hence, it seems reasonable to expect that the level of droplet penetration decreases with increasing coating liquid viscosity. This was tested in a number of additional coating experiments in which Sicovit Patent blue (see chapter five) was used in amounts of 0.1 w/w% and sodium carboxymethylcellulose (CMC) was added to the coating solutions in different amounts as thickener in order to increase the viscosity. The data from these coating experiments can be seen in table 6-6, and corresponding examples of cut-through coloured coated granules can be seen in figure 6.7. In accordance with calculations, it was observed from visual microscopy analysis that the level of droplet penetration decreased with increasing coating liquid viscosity, and that the level of droplet penetration was negligible at conditions in which the coating liquid viscosity was increased to roughly 7000 mPa·s (Measured using a Rheotec Falling Ball KF10 viscometer at a temperature identical to the wet bulb temperature inside the fluidised bed during processing – such high viscosity solutions clearly exhibits non-Newtonian behaviour).

Table 6-6: Summary of important data from additional droplet penetration/morphology experiments.

Exp.	Coating solution salt conc. (Cs)	η_{liq} at 30 °C (wet bulb temp.)	d_{dr}	τ_{evap}	τ_{dpen}	Qualitative description of the degree of colour penetration	Aggl. %	$Y_{Breakage}$
γ4B	10 w/w%	1.0 mPa s (0 w/w% CMC)	11 µm	0.1 s	$6 \cdot 10^{-5}$ s	Deep droplet penetration. More than 3/4 of all the studied cut-through granules were all blue.	21.9 %	6.3 %
γ5A	10 w/w%	2.2 mPa s (1.3 w/w% CMC)	11 µm	0.1 s	$1 \cdot 10^{-4}$ s	Deep droplet penetration to the same extent as observed in batch γ4B.	86.9 %	0.6 %
γ5B	10 w/w%	22 mPa s (2.7 w/w% CMC)	19 µm	0.4 s	$4 \cdot 10^{-3}$ s	Considerable droplet penetration. The majority of the observed granule cores were blue while minor spots remained unaffected.	90.8 %	0.3 %
γ5C	10 w/w%	445 mPa s (5.2 w/w% CMC)	65 µm	4 s	1.0 s	Limited droplet penetration, as only parts of the granule cores were blue while other spots remained white and unaffected.	84.1 %	1.1 %
γ5D	30 w/w%	3.2 mPa s (0 w/w% CMC)	10 µm	0.1 s	$2 \cdot 10^{-4}$ s	Deep droplet penetration. All the observed cut-through granules were all blue, although not as dark blue as the granules from batch γ4B and γ5A.	12.1 %	3.3 %
γ5E	30 w/w%	4100 mPa s (2.7 w/w% CMC)	98 µm	10 s	21 s	Limited droplet penetration. Less than 1/4 of the studied cut-through granules had colour penetration into the inner half of the granule core.	83.0 %	0.7 %
γ5F	30 w/w%	7240 mPa s (5.2 w/w% CMC)	126 µm	16 s	60 s	No droplet penetration in any of the observed cut-through granules. The boundary between the coating layer and the granule core was well defined. The coating layer was roughly 10 µm thick.	75.1 %	0.8 %

An interesting thing to note from the results in table 6-6 is the significant increase in viscosity of the coating solution of more than ten times from experiment γ5C to γ5F and similar from γ5B to γ5E as only the amount of Na_2SO_4 in the coating solution was different. It seems that the increased Na_2SO_4 concentration has a salting-out effect on the CMC causing the significant increase in viscosity (Nakano et al., 1999). Visually there was a difference in solution appearance as well, as the 10 w/w% solutions were slightly dim whereas the 30 w/w% solutions were completely opaque.

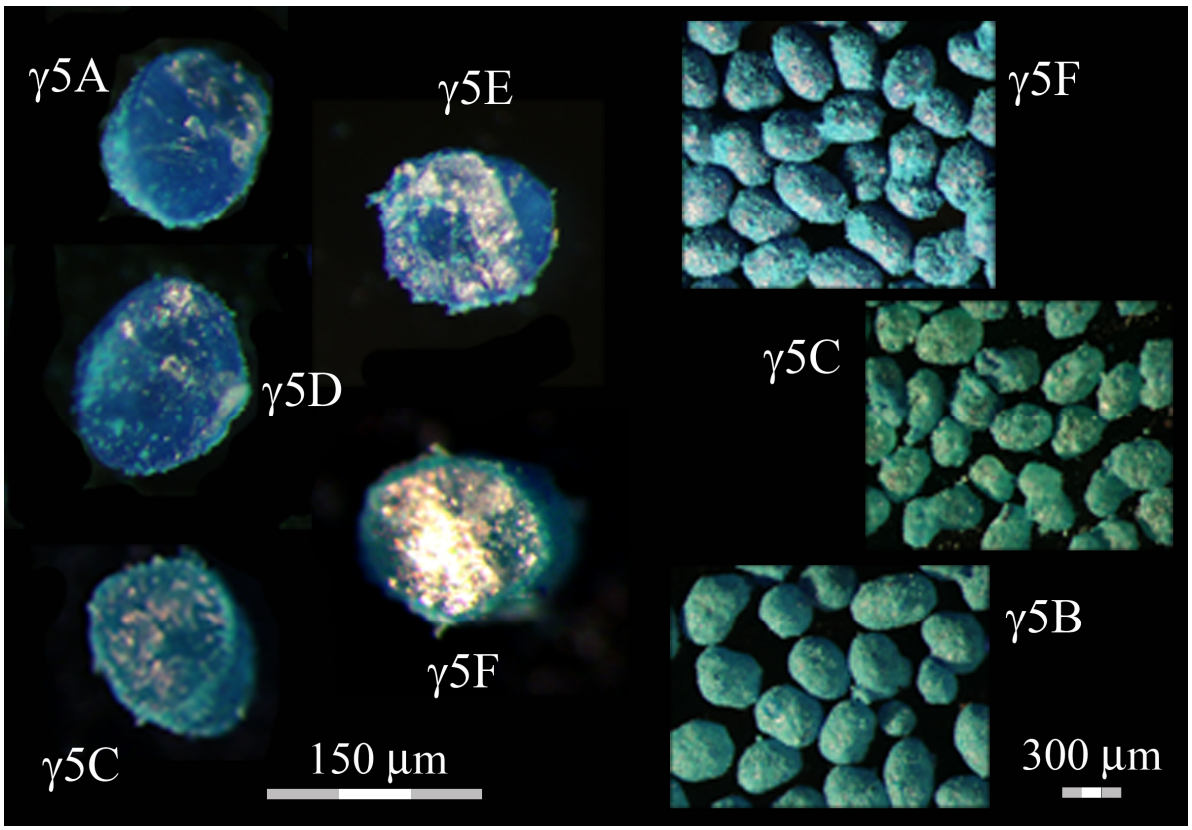

Figure 6.7: Examples of microscope pictures of coated granules and coated granule cut-through profiles. Reference number codes according to table 6-6.

From microscopy analysis of the coated granules in figure 6.7 it was observed that the coating surface morphology changes significantly with droplet viscosity. Whereas the coating layer is smooth and homogenous in batch γ5B with a low droplet viscosity, the surface layer becomes increasingly rough and raspberry-like when the droplet viscosity increases from batch γ5B to γ5C and further from batch γ5C to γ5F. These results are in full accordance with experiments by Link & Schlünder (1997) indicating that the viscosity-affecting dry-matter contents of the coating solution has a primary importance for the resulting roughness of the coating layer, independently of the porosity of the core material. This was investigated further in terms of SEM analyses.

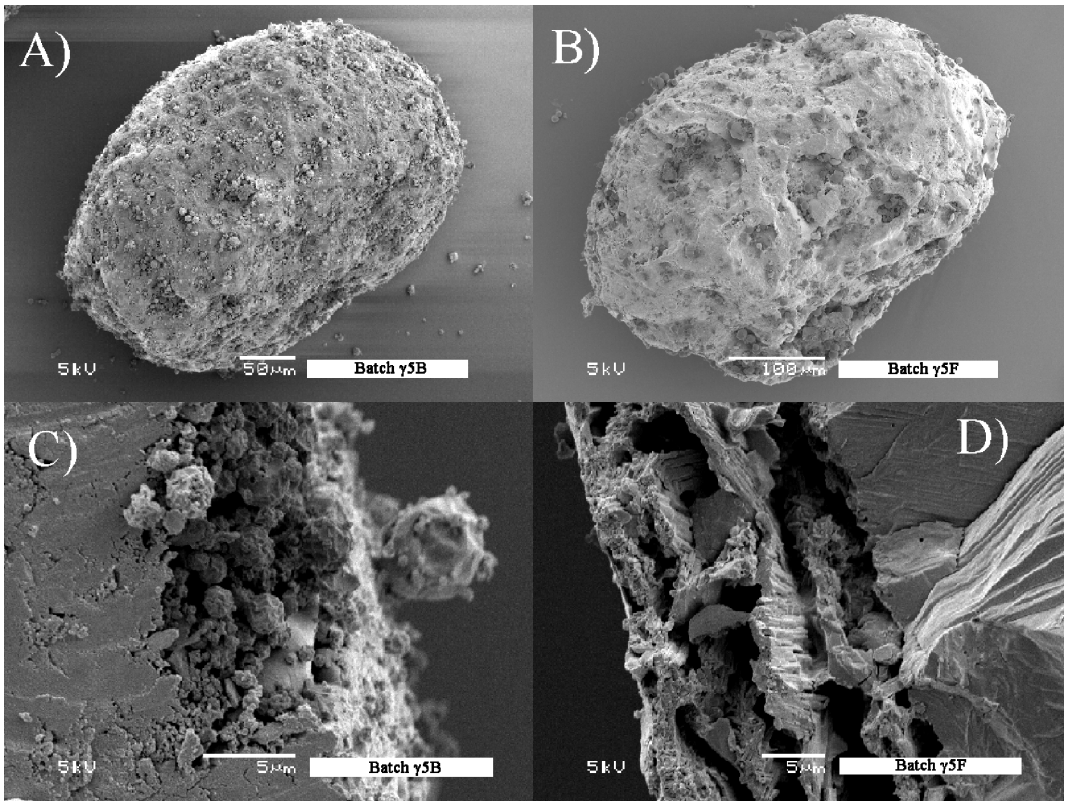

Figure 6.8: Examples of SEM pictures of: A) Coated granule from batch γ5B. B) Coated granule from batch γ5F. C) Cut-through edge profile of coated granule from batch γ5B. D) Cut-through edge profile of coated granule from batch γ5F.

Figure 6.8 shows SEM pictures of coated granules and cut-through edge profiles of coated granules from batch γ5B and γ5F. It can be seen by comparing figure 6.8A with figure 6.8B that although both coating layers are fluffy and covered with small spray-dried droplets, the increase in coating liquid viscosity from figure 6.8A to 6.8B makes the coating layer flaky, stratified and inhomogeneous. There is significant shrinkage in the coating layer in figure 6.8B as the coating liquid layer has dried first on the outer surface leaving the inner layer still wet. As the inner wet layer afterwards dries by the evaporation of remaining coating solution solvent, the inner coating layer is left as a highly porous cave-like structure, which eventually shrinks and cracks. This is further verified in figure 6.8D where a cut-through edge profile of the coating layer of a granule from batch γ5F is seen to be highly porous with a cave-like structure. These observations agree with experiments by Link & Schlünder (1997) and results by Keningley et al. (1997). The sharp distinction between core and coating material complies fully with the results in table 6-6 stating that for experiment γ5F, the time of droplet penetration is somewhat larger than the droplet drying time. Hence, as expected, the majority of the coating material remains at the core surface in figure 6.8D.

The coating layer is observed to float homogenously together in figure 6.8C showing a cut-through edge profile of a granule from batch γ5B. In accordance with the results in table 6-6, a considerable amount of the coating layer is observed to have penetrated into the core material, and the boundary between core and coating layer is not distinguishable. Comparing the core parts in figure 6.8C with 6.8D clearly indicates that the inner granule core structure is highly affected by the high degree of droplet penetration. In the case with a high degree of droplet penetration in figure 6.8C, the core structure is observed to be compressed and homogenous, whereas the original crystal core structure is clearly visible in figure 6.8D. All

in all the SEM pictures in figure 6.8 are hereby seen to be in agreement with the viscosity tendencies predicted by the τ_{evap} and τ_{dpen} calculations in table 6-6.

6.3.3. Further studies of agglomeration and granule impact strength

Besides making it possible to study the droplet penetration versus droplet drying time, the morphology/droplet penetration experiments also made it possible to study the impact strength and the degree of agglomeration as function of droplet viscosity. As seen in table 6-6, the agglomeration tendency clearly increases with increasing viscosity. Going e.g. from experiment γ4B to γ5A, the viscosity is only roughly doubled whereas the resulting agglomeration percentage increases significantly from 21.9 % to 86.9 %. This observation is in accordance with previous studies (e.g. by Abbott, 2002, Keningley et al., 1997 and Schaafsma et al., 1998) of the effect of viscosity changes on agglomeration, although none of the mentioned authors used as porous particles as in the present studies. As the viscosity increases, the coating solution droplets increase in size, thereby halting the droplet penetration, while at the same time the drying time increases. Besides resulting in wet coated surfaces for a longer time, the surface stickiness increases with viscosity thus providing improved adhesion between wet granules, all in all leading to increased risk of agglomeration as observed.

Studying the impact strength values for the seven experiments in table 6-6 reveals several interesting points: First of all it can be seen by comparing experiment γ4B with γ5D (in which no CMC has been added to the coating solution) that the impact strength increases with increasing salt concentration. In both cases the droplet penetration was significant. A reasonable theory is that the increased impact strength with increasing salt-concentration results from the formation of inner-pore salt bridges, as the droplets with a high salt concentration dry inside the capillary pores partly filling them out, hereby providing additional strength upon evaporation of the solvent. This may happen at a low salt concentration as well, but it is expected that the volume and strength of the inner-pore salt bridges increase with increasing salt concentration. This theory was partly supported by mercury intrusion/extrusion porosity analysis of coated granule samples from experiment γ4B and γ5D, as the average porosity of batch γ4B was determined to 19.2 %, whereas the average porosity of batch γ5D only was 18.7 % compared to the average porosity of 20.7 % for the uncoated cores. The measured decrease in porosity may thus originate from inner-pore salt bridges as suggested, although the decrease in porosity is small. Further detailed studies will have to be conducted before any definitive conclusion regarding the salt bridge theory can be verified.

It can furthermore be seen from table 6-6 that the addition of CMC has an advantageous effect on the impact strength, as the $Y_{Breakage}$ values are all very small in the batches where CMC has been added to the coating solution, compared to the $Y_{Breakage}$ values in experiment γ4B and γ5D as well as the $Y_{Breakage}$ values in table 6-4. The $Y_{Breakage}$ values in table 6-6 do, however, not decrease with increasing amount of CMC, as the values for experiment γ5A, γ5B, γ5C, γ5E and γ5F are not significantly different. Interestingly, this indicates that even though the coating layer is raspberry-like and rough due to high coating droplet viscosity, the impact strength may be even higher than for coated granules with smooth surfaces. Apparently, the CMC improves the impact strength. Perhaps the long cellulose chains of the CMC act as a reinforcing impact absorber, resulting in flexible and strong surfaces. This was nevertheless not tested separately.

The higher impact strengths at high coating liquid viscosity may also be explained by the fact that at high viscosity, the droplet drying times by far exceed the residence time in the fluidised bed drying zone estimated to roughly 0.2 s on an average using the semi-empirical equation 6.9, in which the applied fluidisation velocities in m/s were calculated at the chamber inlet using the chamber cross-section area of 10 cm (Link & Schlünder, 1997 and Hede, 2005). Hence, in e.g. experiment γ5F it is reasonable to believe that there was a significant moisture build-up in the Na_2SO_4 cores during coating. This was partly verified by the significantly longer post-spray drying time in batch γ5F of 21 min and 18 min in batch γ5C compared to a drying time of only 11 min in experiment γ5D and 12 min in batch γ4B. According to Link & Schlünder (1997) this will have a significant effect on the mechanical properties of the final coating layer. E.g. will the wettability and spreading of coating droplets on the core surfaces improve if the core material is slightly moisturised. Furthermore, the morphology of the final granule is highly influenced by the moisture contents as well, as it seems to improve the homogenisation of the coating layer if each new wet droplet impacts a surface still partially wet by older droplets not yet completely dried (Link & Schlünder, 1997).

$$\tau_{res,dry} \approx \tau_c = \frac{h_{mf}}{0.6 \cdot (v_a - v_{mf}) \cdot [1 - (v_a - v_{mf})/v_{bu}]} \text{ , at high fluidisation velocities} \qquad (6.9)$$

6.3.4. Model validation

The models in equation 6.5 and equation 6.8 were validated by comparing the model predictions of agglomeration tendency and impact strength with experimental data from eight new experiments with conditions according to table 6-7. These parameter combinations were chosen in order to make sure that the validation process would cover a relevant and wide range for each of the three parameters (nozzle pressure (Pn), coating solution salt concentration (Cs) and bed temperature (Tb)). As the fluidisation velocity was not a significant term in either of the two models, a value of 1.55 m^3/min was chosen for all experiments. The conditions in experiment δ1 and δ6 are both beyond the boundaries of the conditions used to derive the models. These conditions were added to the validation test in order to check the general applicability of the model equations. Except for the parameter variation according to table 6-7, all other process and formulation combinations were identical to the original conditions in table 6-1.

Table 6-7: Parameter combinations for the validation experiments.

Parameter to be varied	Exp. δ1	Exp. δ2	Exp. δ3	Exp. δ4	Exp. δ5	Exp. δ6	Exp. δ7	Exp. δ8
v_a	1.55 m^3/min	1.55 m^3/min	1.55 m^3/min	1.55 m^3/min	1.55 m^3/min	1.55 m^3/min	1.55 m^3/min	1.55 m^3/min
Pn	1.0 bar	1.5 bar	2.0 bar	2.5 bar	3.0 bar	4.0 bar	1.5 bar	3.0 bar
Cs	5 w/w%	10 w/w%	20 w/w%	25 w/w%	30 w/w%	40 w/w%	10 w/w%	30 w/w%
Tb	55 °C	55 °C	55 °C	55 °C	55 °C	55 °C	45 °C	45 °C

Figure 6.9A depicts the agglomeration model predictions compared to the experimental values from the validation series in table 6-7. It may be seen from this figure that in spite of some slight scattering, the model does predict the degree of agglomeration well, especially inside the original model parameter space. The situation is less successful regarding the impact strength model. It can be seen from figure 6.9B that the model predicts higher impact breakage values than the experimentally determined data in all eight experiments. One reason for this could be that the model lacks certain high-order parameter interaction terms. As mentioned previously, the model in equation 6.8 accounts for only 94.6 % of the non-

normality in the original $Y_{Breakage}$ data set in table 6-4. The remaining part may be due to high order parameter interactions, which cannot be identified from the 2^{4-1} fractional factor design. An important point to consider is, however, that the model follows the overall $Y_{Breakage}$ tendencies quite closely. The model predicts for instance that increasing the coating solution salt concentration and the nozzle pressure will decrease the $Y_{Breakage}$ values, and this is in fact what has been observed from the validation experiments. Satisfyingly, the model also follows the tendencies outside the model range as observed for experiment δ1 and δ6. That the lowest experimentally determined impact breakage values are associated with a high nozzle pressure, a high coating solution salt concentration and a high bed temperature is in full accordance with the model as well as the pore-salt-bridge theory discussed earlier.

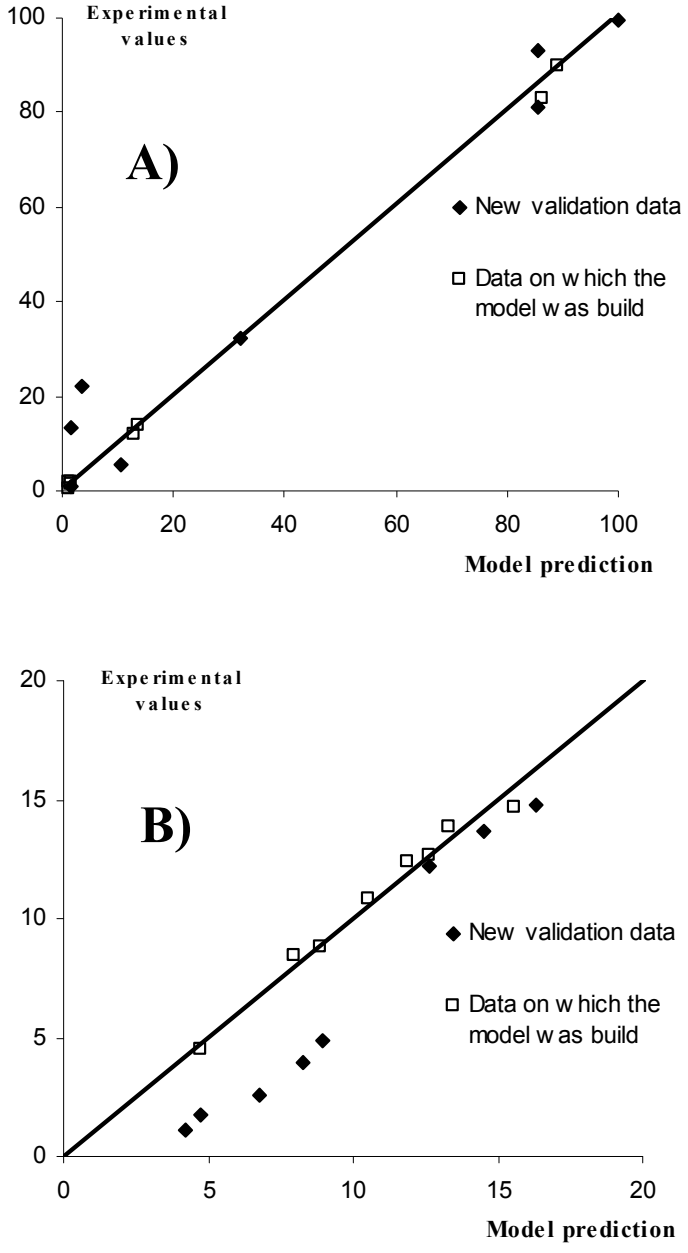

Figure 6.9: Model predictions versus the experimentally determined data from the new validation experiments. A) The agglomeration model. B) The impact breakage model.

6.4. Conclusion

Using an unreplicated 2^{4-1} fractional factor design the influence of the fluidisation velocity, nozzle pressure, coating solution dry-matter concentration and bed temperature on fluidised bed coating of Na_2SO_4 core particles was investigated. Based on data, regression models were derived being capable of quantitatively describing the degree of agglomeration and impact strength. In accordance with expectations, the agglomeration model indicated decreasing agglomeration tendency with increasing coating solution dry-matter concentration and atomisation air pressure. Model validations showed adequate precision inside the parameter space on which the model was derived.

The impact strength model indicated increasing impact strength with increasing coating solution dry-matter concentration, atomisation air pressure and bed temperature. The observed impact strength tendencies were concluded to be closely associated with the high extent of coating solution droplet penetration into the Na_2SO_4 cores. Additional experiments indicated that the coating solution droplet penetration is significant and that this droplet penetration has a significant importance regarding the morphology of the final coated granule. It appears hereby that the porosity of a core being coated has a significant, but not yet fully understood influence on the properties of the final coated granule. A reasonable theory is that penetrated coating droplets with high contents of dry-matter will form solid salt bridges inside the pores of the carrier particles upon drying, and that this will improve the impact stress resistance of the final coated granules. This theory was partly verified by porosity measurements indicating a decrease in final coated granule porosity with increasing coating solution dry-matter contents. The validation of the impact strength model was slightly less successful, as the model in all cases predicts higher impact breakage values than the new experimental data, although the model does follow overall impact strength tendencies closely.

From viscosity experiments it was observed that addition of sodium carboxymethylcellulose (CMC) to the coating solution has a beneficial influence on the impact strength and that the agglomeration tendency increases with increasing viscosity of the coating solution.

According to the derived models, there is no contradiction between high impact strength and low tendency of agglomeration. The models may be seen as a first step towards the design of fluidised bed coating processes leading to unagglomerated, coated enzyme granules with high mechanical strength.

6.5. Table of symbols

Symbols		Unit
C_{Na2SO4}(Cs)	Coating solution concentration of dissolved Na_2SO_4	w/w%
d_{dr}	Droplet diameter	µm
d_p	Particle diameter	µm
h_{mf}	Bed height at minimum fluidisation	m
$m_{dust\ created}$	Amount of dust created by impact	g
m_{sample}	Amount of sample	g
P_{nozzle} (Pn)	Atomisation air (nozzle) pressure	bar
T	Temperature	K
T_{bed} (Tb)	Particle bed temperature	K
v_a	Fluidisation velocity	m/s

v_{bu}	Bubble rise velocity for a fluidised bed	m/s
v_{mf}	Minimum fluidisation velocity	m/s
X	Coded parameter	Dimensionless
$Y_{Breakage}$	Breakage percentage parameter	Dimensionless

Greek

η_{liq}	Coating solution viscosity	mPa s
τ_c	Average particle circulation time	s
τ_{dpen}	Droplet penetration time	s
τ_{evap}	Droplet evaporation time	s
$\tau_{res,dry}$	Residence time in the primary drying zone	s

6.6. References

Abbott, A. (2002) Boundary Between Coating and Granulation, M.Sc. Thesis, Department of Chemical Engineering, The University of Queensland.

Beekman, W.J. (2000) Measurement of the Mechanical Strength of Granules, Ph.D. Thesis, Technische Universiteit Delft.

Denesuk, M., Smith, G.L., Zelinski, B.J.J., Kreidl, N.J., and Uhlmann, D.R. (1993) Capillary Penetration of Liquid Droplets into Porous Materials, Journal of Colloid Interface Science, No. 158, pp. 114-120.

Denesuk, M., Zelinski, B.J.J., Kreidl, N.J., and Uhlmann, D.R. (1994) Dynamics of Incomplete Wetting on Porous Materials, Journal of Colloid Interface Science, No. 168, pp. 141-151.

Dewettinck, K. (1997) Fluidized Bed Coating in Food Technology: Process and Product Quality, Ph.D. Thesis, University of Gent.

Dewettinck, K., Messens, W., Derro, L. and Huyghebaert, A. (1999) Agglomeration Tendency during Top-Spray Fluidized Bed Coating with Gelatin and Starch Hydrolysate, Lebensmittel-Wissenschaft and Technologie, No. 32, pp. 102-106.

Guignon, B., Duquenoy, A. and Dumoulin, E.D. (2002) Fluid Bed Encapsulation of Particles: Principles and Practice, Drying Technology, No. 20, pp. 419-447.

Hede, P.D. (2005) Fluid bed coating and granulation, M.Sc. Thesis, Department of Chemical Engineering, CHEC Research Center, Technical University of Denmark.

Hede, P.D., Bach, P. and Jensen, A.D. (2007a) Small-scale top-spray fluidised bed coating: Granule impact strength, agglomeration tendency and coating layer morphology, Powder Technology, No. 176, pp. 156-167.

Härkönen, H. , Koskinen, M. , Linko, P. Siika-aho, M. and Poutanen, K. (1993) Granulation of Enzyme Powders in a Fluidized Bed Spray Granulator, Lebensmittel-Wissenschaft und Technologie, Vol. 26, pp. 235-241.

Jørgensen, K., Bach, P. and Jensen, A.D. (2004) Impact and attrition shear breakage of enzyme granules and placebo particles-application to particle design and formulation, Powder Technology, No. 149, pp. 157-167.

Keningley, S.T., Knight, P.C. and Marson, A.D. (1997) An investigation into the effects of binder viscosity on agglomeration behaviour, Powder Technology, No. 91, pp. 95-103.

Link, K.C. and Schlünder, E.U. (1997) Fluidized bed spray granulation. Investigation of the coating process on a single sphere, Chemical Engineering and Processing, No. 36, pp. 443-457.

Montgomery, D.C. (1997) Design and Analysis of Experiments, 4th Edition, John Wiley & Sons Inc., NY.

Nakano, T., Yuasa, H. and Kanaya, Y. (1999) Suppression of Agglomeration in Fluidized Bed Coating. III. Hofmeister Series in Suppression of Particle Agglomeration. Pharmaceutical Research, No. 10, pp. 1616-1620.

Rubino, O.P. (1999) Fluid-Bed Technology. Overview and Criteria for Process Selection, Pharmaceutical Technology, No. 23, pp. 104-117.

Schaafsma, S.H., Vonk, P., Segers, P. and Kossen, N.W.F. (1998) Description of agglomerate growth, Powder Technology, No. 97, pp 183-190.

Teunou, E. and Poncelet, D. (2002) Batch and continuous fluid bed coating – review and state of the art, Journal of Food Engineering, No. 53, pp. 325-340.

Chapter 7. Scale-up validation of the Flux Number

Chapter introduction

Chapter seven takes the starting point in an existing fluid bed coating scale-up parameter being the Flux Number. In terms of conducted fluid bed coating experiments in three fluid bed scales, the Flux Number is validated as a scale-up principle with the aim of being able to predict and match the tendency of agglomeration across the three fluid bed scales. The present chapter is published as a peer-reviewed scientific paper in the journal *Chemical Engineering Science*, Vol. 63, No. 3, pp. 815-828, 2008. The paper is entitled *Validation of the Flux Number as scaling parameter for top-spray fluidised bed systems* authored by Peter Dybdahl Hede (Technical University of Denmark), Poul Bach (Novozymes A/S) and Anker D. Jensen (Technical University of Denmark). The paper is referred to as Hede et al. (2008a).

The following sections are exact reproductions of the paper, although the sections concerning equipment and materials have been left out (please refer to chapter five). Furthermore, the format of the paper has been adapted to that of this thesis.

7. Validation of the Flux Number as scaling parameter for top-spray fluidised bed systems

Abstract

Top-spray fluidised bed coating scale-up experiments have been performed in three scales in order to test and validate the Akkermans Flux Number as possible scale-up parameter. Coating operations were performed on low porosity sodium sulphate cores (180 - 350 μm) coated with aqueous solutions of Na_2SO_4 using Dextrin as binder in three top-spray fluidised bed scales, i.e. a small-scale (Type: GEA Aeromatic-Fielder Strea-1), medium-scale (Type: Niro MP-1) and large-scale (Type: GEA MP-2/3). Following the parameter guidelines adapted from the original patent description, the Flux Number was tested in the preferred range of 3.5 to 4.5 as well as with a value of 4.7 in a total of 24 experiments. The agglomeration tendency was observed to decrease with increasing Flux Number on an overall basis, but coating conditions with Flux Number values below 4.5 resulted in a complete collapse of the bed. Coating conditions with Flux Number values of 4.5 and 4.7 were, however, successful in terms of low agglomeration tendency and match of particle size fractions, but indicated in addition a strong influence of nozzle pressure. The present paper suggests even narrower boundaries for the Flux Number compared to the original patent descriptions, and adds further new guidelines for the successful scale-up of top-spray fluidised bed coating systems in terms of the Flux Number.

7.1. Introduction

Many types of biological ingredients are formulated into solid products by spraying the concentrate onto inactive filler cores in a fluidised bed. The desired product consists thereby of unagglomerated individual carrier particles each coated homogeneously with a layer of the active ingredient. If formulation or process conditions are incorrectly chosen, either excessive agglomeration or excessive spray drying of the feed may happen (van Ee et al., 1997). In both cases a poor product quality is achieved, and in any case, control of agglomeration is essential during scale-up.

Often product and process properties are optimised in small and medium pilot-scale fluidised beds and then transferred to production-scale. The scale-up of a fluidised bed granulation process requires decisions to be made at many levels, including: fixed parameters (e.g. nozzle type and fluidisation chamber dimensions), parameters related to the core material (such as porosity, sphericity and more), coating solution (e.g. viscosity, surface tension, contact angle and more) and the type of fluidised bed, input parameters, operating conditions including spray and fluidisation conditions as well as processing time etc. With such a variety of interlinked parameters and properties, combined with a lack of quantitative understanding of the granulation process, it is obvious that scale-up of a fluidised bed granulation process is a challenging task (Hede et. al., 2008b).

Fluidised bed scaling principles at the macro-scale level have been studied intensively for fluidised catalytic cracking regenerators and bubbling fluidised beds for more than thirty years (Glicksman et al., 1993 and Schouten et al., 1996). A typical macro-scale approach determines desired conditions over a range of dimensionally similar unit operations typically using well-known dimensionless groups such as the Froude number, the Reynolds number and the Power number (Mort, 2005 and Knowlton et al., 2005). In addition, several other dimensioned parameters or parameter groups are used, including specific energy input and excess gas fluidisation velocity etc. These operation parameters typically affect multiple product transformations, and the challenge is to scale-up the equipment in a way that maintains key product attributes while at the same time achieves an industrially efficient operation (Mort, 2005).

Scale-up attempts based on the dimensionless parameters rely typically on analogies in the hydrodynamic behaviour of the flow regimes in the fluidised beds, and especially on proper description of the bubble hydrodynamics. A number of the classical hydrodynamic scaling expressions and so-called *scaling laws*, based on the superficial gas velocity and minimum fluidisation velocity, may be found for bubbling fluidised beds in Ellenberger & Krishna (1994) and Werther (1980). Horio et al. (1986) developed a rule of hydrodynamic similarity for a scale change of fluidised beds based on the governing equations of bubble and interstitial gas dynamics. Similarly, Glicksman (1984 & 1988) proposed a full set of scaling relationships by non-dimensionalising the equations of motion for the particles and the fluid phase in a fluidised bed along with their boundary conditions, using the length from the air distributor plate to the fluid bed chamber exhaust exit, $L_{chamber}$, as a typical length dimension.

Macro-level scaling laws, as the above presented, do not normally take interparticle forces in fluidised beds into account. They also typically omit any influence of the particle coefficient of restitution as well as the influence of frictional forces (Glicksman et al., 1993). What is even more critical is that the scaling principles completely neglect any influence from the sprayed liquid phase. This means that scaling principles developed for pure gas-solid systems,

such as e.g. fluidised bed combustors, cannot be applied alone for fluidised bed coating or agglomeration processes, as the liquid phase is known to be of utmost importance for the control of the process. A fluidised bed system involving all three phases of solid, liquid and gas is more complicated than a fluidised bed having only a solid and a gas phase, and thus new principles for scale-up of agglomerating and coating fluidised beds must be used.

Scaling up of coating fluidised bed processes is a common industrial exercise and traditionally the field has not had much academic interest. As reviewed by Hede (2006) advances in scaling principles are often done in industry and typically only reach the public in the form of patents. Recent scientific papers by e.g. Rambali et al. (2003), Mehta (1988), Boerefijn & Hounslow (2005) and Hede et al. (2008b) indicate some progress in the field, although the scale-up procedures are somewhat different. Mort (2005) suggests that granulation process scale-up should focus on combined particle-level and unit-operation-level variables and parameters. Results by Hede et al. (2008b) (see also chapter eight) follow these trends by suggesting scale-up in terms of a Drying Force and a Relative Droplet parameter. These principles focus especially on temperature and humidity conditions as well as on nozzle conditions. Although promising there are also limitations to the application of these scale-up principles. The Flux Number by Akkermans et al. (1998) is a different approach as the primary focus here is on particle density, gas velocities, spray area and coating solution distribution on an overall scale. The Flux Number combines these parameters into a single dimensionless parameter claimed to govern the overall possible fluid bed granulation outcome. Based on the Flux Number, Boerefijn and Hounslow (2005) provided a domain-map for coating, agglomeration and wet-quenching regimes according to figure 7.1.

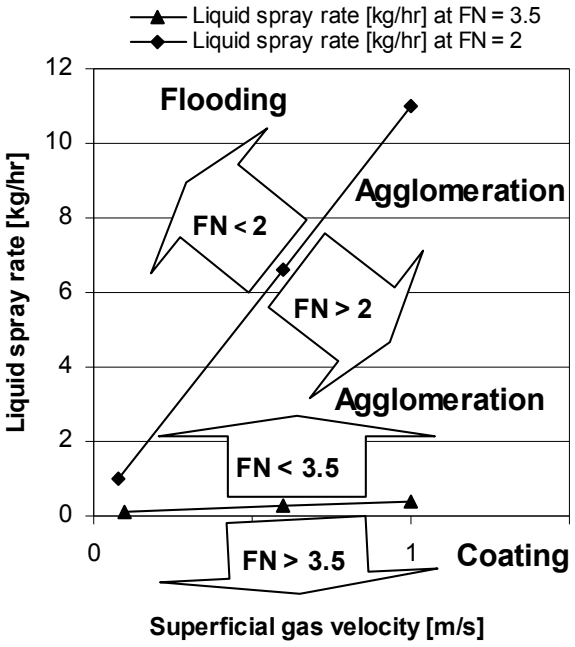

Figure 7.1: Domain-map for wet-quenching (flooding), agglomeration and coating regimes based on values of the Flux Number (FN) (Boerefijn & Hounslow, 2005).

Although the Flux Number is claimed by Boerefijn and Hounslow (2005) to be a commonly accepted suitable descriptor of the balance between the flux of solids in the spray zone and the spray flux that wets the solids, no experimental evidence has been presented in detail so far in the open literature. It is the aim of this paper to provide a systematic experimental validation of the Flux Number as scaling parameter for top-spray fluidised bed coating systems.

7.1.1. The dimensionless Flux Number

A series of International Patent Classifications by Unilever Research concerns the use of a Flux Number in the process of top-spray fluidised bed production of detergent granules. The Flux Number and the expressions for the associated parameters are adapted from Akkermans et al. (1998). The Flux Number is expressed according to equation 7.1.

$$FN = \log\left[\frac{\rho_p \cdot v_e}{\dot{q}_{mliq}}\right] \tag{7.1}$$

where ρ_p is the particle density determined according to equation 7.2.

$$\rho_p = \frac{BD}{1-\varepsilon_{bed}} \tag{7.2}$$

in which BD is the bulk density of the particles and ε_{bed} is the bed porosity determined by e.g. mercury porosimetry. The parameter $\dot{q}_{mliq}$ is the spray mass flux in kg/(s·m^2) at a normalised distance D_0 from the nozzle outlet, and v_e is the excess gas velocity in m/s determined simply as the difference between the (superficial) gas velocity v_a and the minimum fluidisation velocity v_{mf} as shown in equation 7.3.

$$v_e = v_a - v_{mf} \tag{7.3}$$

Preferably, v_a is determined at the position in the fluidisation chamber corresponding to the bed height h_{bed}. Similarly, the gas velocity at minimum fluidisation v_{mf} is measured at the height of the bed at minimum fluidisation, h_{mf}.

If a discernible bed is apparent then the bed height, h_{bed}, can be measured directly, but often it cannot easily be determined as the degree of turbulence in the cloud of fluidised particles is so high that no discernible bed is formed. This is often the case with bubbling fluidisation as is the case with the materials and particle sizes processed in the experiments in this paper. As an estimate when no discernible bed is formed, h_{bed} may be calculated from equation 7.4 (Akkermans et al., 1998).

$$h_{bed} = 1.67 \cdot h_{mf} \tag{7.4}$$

Having determined h_{bed} and h_{mf} it is possible to determine the so-called normalised length D_0 from the expression in equation 7.5. D_0 thereby has the units of meters although being referred to in the original Akkermans et al. (1998) patent description as a *normalised* length.

$$D_0 = h_{nozzle} - h_{bed} \tag{7.5}$$

where h_{nozzle} is the height of the spray nozzle above the bottom of the fluidisation chamber. If D_0 is 15 cm or less, then D_0 is taken as 15 cm for purposes of determining the contact area A. This is because for practical purposes it has been found that the mean penetration of the spray for a nozzle situated below or within the cloud of solids is about 15 cm. The contact area A is the contact area wetted by the spray in a horizontal plane situated at D_0 below the nozzle. The value of A must be determined in terms of experiments or by simple calculations based on

known spray angles. In the present paper, the contact area A was found by first determining the nozzle outlet spray angle by photo analysis at the given nozzle pressure, and then simply calculate the wetted area at the distance of D_0 assuming full-cone spray characteristics. The contact area A is used to determine the liquid mass spray flux $\dot{q}_{mliq}$ according to equation 7.6.

$$\dot{q}_{mliq} = \frac{Q_{mliq}}{A} \tag{7.6}$$

where Q_{mliq} represents the mass flow of liquid applied.

According to the invention by Akkermans et al. (1998), the value of FN must be such that FN is at a value above 2 and preferably at least 3 for a major proportion of the process time (at least 30 %, but preferably around 95 %). FN should never exceed a value of 6 and preferably not exceed 4.5. According to the patent description, v_a should be preferably in the range of 0.8 – 1.2 m/s and $\dot{q}_{mliq}$ at least 0.15 kg/(s·m)^2, preferably in the range of 0.20 – 1.5 kg/(s·m)^2.

A Procter & Gamble patent by Wasserman et al. (2000) states, in accordance with Akkermans et al. (1998), that the fluidised bed operation conditions should be such that FN preferably is from 3.5 to 5. In addition to the Flux Number specification, the patent by Wasserman et al. (2000) states that coating conditions should be met in order for the viscous Stokes number St_v to be greater than 10, more preferably in the range of 100 – 1000. The viscous Stokes number is a measure of the likelihood of agglomeration in an equipment such as the fluidised bed, and the number is defined analogously to the original viscous Stokes number by Ennis et al. (1991) (assuming that the particle collision velocity, u_0, can be approximated by the excess gas velocity, v_e) according to equation 7.7 (Wasserman et al., 2000 and Achanta & Beimesch, 1998).

$$St_v = \frac{4 \cdot \rho_g \cdot d_p \cdot v_e}{9 \cdot \eta_{liq}} \tag{7.7}$$

where η_{liq} is the coating solution viscosity, ρ_g is the granule density, d_p is the mean particle diameter and v_e is the excess gas velocity. More fundamental information about the viscous Stokes number may be found Ennis et al. (1991) and Iveson et al. (2001) whereas a full derivation of equation 7.7 may be found in chapter ten (see also chapter three). A Procter & Gamble patent by Achanta & Beimesch (1998) further explains the usefulness of the viscous Stokes number in the context of producing detergent granules, stating that St_v should be less than 1 in order for the fluidised bed system to start to agglomerate.

7.2. Experimental

Sodium sulphate cores pre-sieved twice in the size range of 180 – 350 μm were used as core material. The sodium sulphate cores were coated with aqueous solutions of sodium sulphate in the amount of 15 w/w% using 1 w/w% (of the amount of sodium sulphate) Dextrin as binder. Demineralised water was used as solvent (see also chapter five).

It was verified by microscope analysis of the different fractions that coated granules with diameters above 425 μm consisted of agglomerates whereas particles below this limit were primarily single coated granules. Thus, this sieve orifice diameter was set as the

agglomeration limit, and based on the weight of each of the fractions an agglomeration percentage was determined for each batch according to equation 7.8 (see also chapter five).

$$\text{Agglomeration \%} = \frac{\text{coated batch weight fraction with } d_p > 425\,\mu m}{\text{total coated batch weight}} \cdot 100\,\% \qquad (7.8)$$

7.2.1. Scaling procedure

In order to test the applicability of the Flux Number, a number of choices had to be made prior to the coating experiments. Being a dimensionless logarithmic relationship, small changes in the Flux Number correspond to large changes in vital process parameter values. Furthermore, a given Flux Number value allow in principle (although obviously not in practice) an infinity of different values for v_e and $\dot{q}_{mliq}$ to be chosen, indicating that a given Flux Number value does not give the exact fluidised bed operation conditions unambiguously. Results by Hede et al. (2007a), obtained with the small-scale fluidised bed with the same type of core materials and coating solution, indicate that the actual fluidisation velocity has a minor influence on agglomeration above a certain value, compared to the nozzle conditions which are of importance for the overall agglomeration tendency, irrespectively of the exact values. Thus, the choice of the excess gas velocity is most likely not as important as the choice of the liquid mass flux for the given Flux Number. The guidelines for the parameters constituting the Flux Number provided by the Akkermans et al. (1998) patent are unfortunately quite vague allowing e.g. the value for $\dot{q}_{mliq}$ to range preferably between 0.20 – 1.5 kg/(s·m)^2. This vagueness could be intentional, intended to widen the coverage and applicability of the Flux Number. This is unfortunate in terms of testing the scale-up parameter, but may be an advantage regarding the patent coverage. The guidelines for v_a were, however, the narrowest and this was the starting point for the scale-up tests in the present paper. According to section 7.1.1 the value for v_a in m/s should preferably be chosen in the range of 0.8 – 1.2 m/s, which is well within the range where the exact value is of minor importance regarding agglomeration in the small-scale fluid bed (Hede, et al., 2007a). Hence as a starting point, the value for v_a was chosen to be 1.0 m/s at the bed height h_{bed} in all three fluidised bed set-ups. Having fixed the value for v_a this also fixed the value for v_e as the value for v_{mf} for a mean particle diameter of 300 μm was determined to be 0.07 m/s with the use of equation 2.15 (see chapter two) (Kunii & Levenspiel, 1991 and Teunou & Poncelet, 2002). The choice of this excess gas velocity, together with the coating formulation properties, resulted in a viscous Stokes number being close to 900 and thereby safely within the preferred range of 10 – 1000, hereby following additionally the guidelines from the Achanta & Beimesch (1998) and Wasserman et al. (2000) patents for successful coating operations.

It should be noted that even though the fluidisation conditions are chosen such that the superficial gas velocity v_a at the bed height is 1.0 m/s in all three fluidised beds, this does not mean that the superficial gas velocity is identical at the air distribution plate in the bottom of the three beds. This is due to the fact that the three fluidised beds are not dimensionally consistent. As indicated from the sketch of the dimensions of the three beds in figure 5.2 (see chapter five), the three fluidisation chambers are quite different in shape and dimensions. The fluidised beds are thereby not dimensionally consistent according to the rules by Leuenberger (1983 & 2003) stating that systems are similar when the ratio of the linear dimensions of the small-scale and the upscaled system are constant. This is a typical issue with different commercial fluidised bed scales as there is no uniform agreement on how to design the fluidisation vessels. Dimensionally consistency is, however, not a requirement for the use or

validation of the Flux Number as the parameter seeks to overcome these issues by focusing on process-related parameters. Having v_a at the bed height at 1.0 m/s corresponds to gas velocities just above the air distribution plate of 2.9 m/s in the small-scale, 2.2 m/s in the medium-scale and 3.2 m/s in the large-scale. The volumetric fluidisation flow rate necessary to maintain v_a at the bed height at 1.0 m/s requires 82 Nm^3/hr in the small-scale, 137 Nm^3/hr in the medium-scale and 651 Nm^3/hr in the large-scale.

Having determined the value for v_e the next step was to find a value for the particle density ρ_p. Following the guidelines presented in section 7.1.1 the bulk density was determined to 1428 kg/m^3 by pouring the uncoated core particles into a container with a well-defined known volume. The surface of the solids in the container was levelled by careful scraping-away the excess material with a metal slid at right angles to the surface of the solids and to the rim of the container. The solids in the container were then weighted, and the weighted mass was divided by the internal volume of the container to give the bulk density of the particles according to the patent description (Akkermans et al., 1998). The resulting bed porosity ε_{bed} has been determined previously by Hede (2005) to be close to 0.37 with Micromeritics Autopore II intrusion/extrusion mercury porosimetry thereby giving an apparent density of 2266 kg/m^3 according to equation 7.2.

Having determined the apparent particle density and fixed a level for the superficial gas velocity, the only parameter that would have to be changed according to the different Flux Number values is the liquid mass flux $\dot{q}_{mliq}$. As mentioned earlier, the liquid mass flux is the mass flow of liquid applied per unit contact area where the contact area A is measured at the so-called normalised nozzle-to-bed distance D_0. However, the contact area at D_0 is not a constant property even though the fluidisation velocity and thereby D_0 is. This is due to the fact that with nozzle pressure, the spray angle from the two-fluid nozzle changes. For the medium-scale fluidised bed e.g., the spray angle is roughly 14º at a nozzle pressure of 3 bar whereas the spray angle is roughly 21º at a nozzle pressure of 1 bar. This means that the value for A (and thereby obviously the required liquid mass flux $\dot{q}_{mliq}$ for a given Flux Number) is strongly dependent on the nozzle pressure. Unfortunately, the Akkermans et al. (1998) patent does not give any specific information about the operating conditions for the nozzles. The patent only emphasises that the value of the Sauter mean droplet diameter, d_{32}, of the coating solution should preferably not be greater than the value of the d_{32} of that fraction of the total solid starting material which has a particle diameter ranging from 20 μm to 200 μm. The patent further loosely states that the d_{32} should preferably be between 20 μm and 200 μm. The first condition was easily met with the given fluidised bed equipment and the particle size distribution of the sodium sulphate core processed, but the second condition with the droplet size interval was only achievable in the medium- and large-scale as droplets much above 10 μm tend to overwet the bed in the small-scale, resulting in complete collapse of the bed.

With the use of equation 2.1 (see chapter two) Sauter mean droplet diameters were estimated to be between 4 and 10 μm for the small-scale, between 9 and 43 μm for the medium-scale and between 15 and 99 μm for the large-scale depending on the nozzle pressure and the liquid feed rates. As mentioned earlier, the spray angle changes with nozzle pressure, but what is more important regarding the droplet size is that the gas flow rate through the nozzle changes as well with nozzle pressure. For the three nozzles used in the present study an almost linear dependence between the nozzle pressure in bar and the atomisation airflow in m^3/hr was observed (see also chapter eight). All other conditions being the same, if the nozzle pressure

increases so does the atomisation airflow rate through the nozzle, meaning that the mean droplet size decreases.

In order to test the sensitivity of the Flux Number with respect to values of $\dot{q}_{mliq}$, two nozzle pressures were chosen for each fluidised bed scale being 1 bar and 3 bar. For each nozzle pressure and for each type of fluidised bed equipment, a contact area A was determined in terms of experiments for the given nozzle pressure at the distance of D_0 as explained earlier. As it may be seen from table 7-1, the contact area is quite dependent on the nozzle pressure.

Table 7-1: Overview of the determined values of the contact area A at D_0 for the two tested nozzle pressures. The values for D_0 were determined with the use of experimental observations of h_{bed} and measurement of h_{nozzle} in combination with the correlations presented in section 7.1.1.

Fluidised bed scale	Normalised nozzle-to-bed distance D_0 in cm	Nozzle pressure	Contact area A in cm^2
Strea-1 (Small-scale)	14.5 cm (set to 15 cm according to patent guidelines)	1 bar	28.3
		3 bar	19.6
MP-1 (Medium-scale)	32.3 cm	1 bar	130.8
		3 bar	51.3
MP-2/3 (Large-scale)	32.6 cm	1 bar	283.4
		3 bar	153.9

Having determined the values for A for all three fluidised bed scales, the only parameter that will change with the choice of Flux Number and nozzle pressure is the mass flow of liquid applied Q_{mliq} which is the value that the tube pump feeding the nozzle will be set at.

Although temperature is not a property directly associated with the Flux Number or the viscous Stokes number, a long history of published fluidised bed coating results clearly show that the bed temperature during coating has a primary importance regarding the tendency of agglomeration (e.g. Schæfer & Wørts, 1978). Even a minor change in bed temperature of a few degrees may have a significant effect on the agglomeration tendency (Hede, 2005). Akkermans et al. (1998), nevertheless, state only in very general terms that the bed temperature should be between ambient temperature and 60 ºC. However, the experience with the given fluidised bed equipment, core particles and coating solution is that at temperatures below 50 ºC the bed tend to agglomerate easily, and hence, the choice in the present studies was to aim at a bed temperature of 55 ºC in all coating experiments regardless of the choice of Flux Number, nozzle pressure and mass flow of coating liquid. The choice of this bed temperature ought to limit the bed temperature effect towards agglomeration. Having fixed the bed temperature and the fluidisation velocity through the bed throughout the experiments, the only independent parameter for each single experiment was the inlet air temperature which is the only parameter that cannot be determined prior to the experiments. The advantages of running the fluid bed process in terms of an adjustable inlet air temperature and choosing all other process parameters a-priori were presented in detail in Hede et al. (2008b).

In order to test the Flux Number, a number of 24 coating experiments were planned. Throughout the experiments the coating solution formulation was kept constant thereby giving a constant viscous Stokes number in the range of 900. Furthermore, the superficial gas velocity v_a at h_{bed} was kept constant at 1.0 m/s and the bed temperature was maintained at 55 ºC throughout each coating operation. The Flux Number was tested for each fluidised bed scale in four levels at values of 3.5, 4.0, 4.5 and 4.7, and each Flux Number condition was carried out two times – once with a nozzle pressure of 1 bar and once with a nozzle pressure of 3 bar.

In accordance with coating guidelines presented in chapter five the core bed load was heated prior to coating until the relative humidity inside the fluidisation chamber was constant. In each coating operation the aim was to coat until the bed load had increased 20 w/w%, in order to make sure that a reasonable coating layer (~ 5-10 μm) had developed on the core particles. For all the experiments in this paper, the actual batch weight gain may be seen from table 7-2.

7.3. Results and discussion

Issues concerning reproducibility of data with the same type of fluidised bed equipment and core materials were treated in detail by Hede et al. (2008b) (see chapter eight). It was observed how the standard deviation from the Retsch Sieve Shaker AS 200 equipment was 0.82 % in terms of the agglomeration percentage thereby indicating as a common rule of thumb that different batches having agglomeration percentages in the range of ± 1.64 % are not statistically different. From detailed analysis of the three fluidised bed scales it was further observed in the paper by Hede et al. (2008b) how statistically sound reproducible data could be produced and how a χ^2 tests could be used to determine how well the different particle size classes were reproduced across scale (Hede et al., 2008b).

7.3.1. Matching the agglomeration percentages and particle size fractions across scale

Following the overall plan for the scaling experiments the coating experiments were planned and carried out according to table 7-2. As large-scale experiments are time-consuming and require large amounts of core materials, experiments were carried out first in the small- and medium-scale. If the given conditions resulted in wet-quenching and a complete collapse of the bed in the small- and medium-scale these process conditions were not tested in the large-scale. The experiments were conducted in a four week period under similar weather conditions with room temperatures around 23 ºC and room humidity values in the range of 35 - 42 rH%. Table 7-2 presents the results from the scaling trials.

There are several important things to note from the results in table 7-2. First of all it was observed that Flux Number conditions at 3.5 and 4.0 were in all cases unsuccessful as the bed collapsed within the first few minutes of the coating process. For the Flux Number value of 3.5 the bed collapsed irrespectively of the nozzle pressure clearly indicating that the required spray rate at this Flux Number is far too high for the coating process. This is even though the values for $\dot{q}_{mliq}$ were in the lower end of the preferred range. At a Flux Number of 4.0 the bed collapsed in the medium-scale for nozzle pressures of 1 and 3 bar in scaling attempt C and D, whereas collapse was the case for the large- and small-scale with nozzle pressures of 1 bar. Only in two experiments X4 and Z4 the bed did not collapse although the agglomeration tendencies in both cases were close to 100 %. Even though the patents by Wasserman et al. (2000) and Akkermans et al. (1998) state that the preferred range for the Flux Number includes values as low as 3.5 this cannot be verified by the results in the present work.

Table 7-2: Results from the Flux Number scaling attempts.

Fluid bed equipment	Scaling attempt	Exp. code	Flux Number	Nozzle pressure	Required Q_{mliq}	Aggl. percentage	Coating time	Coating time per kg core load	Comment
Strea-1 (small-scale)	A	X1	3.5	1 bar	113.1 g/min	100 w/w%	N/A	N/A	The bed collapsed due to overwetting within the first few minutes of the coating process. At the time of collapse the humidity inside the fluidisation chamber exceeded 50 rH%. Actual batch weight gain: N/A.
	B	X2	3.5	3 bar	78.5 g/min	100 w/w%	N/A	N/A	The bed collapsed due to overwetting within the first few minutes of the coating process. Actual batch weight gain: N/A.
	C	X3	4.0	1 bar	35.8 g/min	100 w/w%	N/A	N/A	The bed collapsed within the first ten minutes of the coating process. Actual batch weight gain: N/A.
	D	X4	4.0	3 bar	24.8 g/min	93.8 w/w%	0:31 (hr:min)	62 min/kg	Large bubble fluidisation was observed. A steady coating state was never reached. Actual batch weight gain: N/A.
	E	X5	4.5	1 bar	11.3 g/min	24.5 w/w%	1:02 (hr:min)	124 min/kg	There was observed some build-up of particles adhered to the nozzle during coating. Actual batch weight gain: 17.1 w/w%.
	F	X6	4.5	3 bar	7.9 g/min	0.2 w/w%	1:20 (hr:min)	160 min/kg	Good fluidisation conditions. No particle-adhesion to the nozzle. Less than 10 w/w% loss of coating solution due to spray drying. Actual batch weight gain: 19.3 w/w%.
	G	X7	4.7	1 bar	7.1 g/min	35.9 w/w%	1:37 (hr:min)	194 min/kg	Good fluidisation conditions, but ~ 35 w/w% loss of coating feed due to spray drying loss. Actual batch weight gain: 17.4 w/w%.
	H	X8	4.7	3 bar	5.0 g/min	0.1 w/w%	2:19 (hr:min)	278 min/kg	Good fluidisation conditions, but ~ 15 w/w% loss of coating feed due to spray drying loss. Actual batch weight gain: 19.1 w/w%.

Table 7-2: Results from the Flux Number scaling attempts (continued).

Fluid bed equipment	Scaling attempt	Exp. code	Flux Number	Nozzle pressure	Required Q_{mliq}	Aggl. percentage	Coating time	Coating time per kg core load	Comment
MP-1 (medium-scale)	A	Y1	3.5	1 bar	523.2 g/min	100 w/w%	N/A	N/A	The bed collapsed due to overwetting within the first few minutes of the coating process. Actual batch weight gain: N/A.
	B	Y2	3.5	3 bar	205.4 g/min	100 w/w%	N/A	N/A	The bed collapsed due to overwetting within the first few minutes of the coating process. Actual batch weight gain: N/A.
	C	Y3	4.0	1 bar	165.5 g/min	100 w/w%	N/A	N/A	The bed collapsed within the first few minutes of the coating process. Actual batch weight gain: N/A.
	D	Y4	4.0	3 bar	64.9 g/min	100 w/w%	N/A	N/A	The bed collapsed within the first ten minutes of the coating process. Actual batch weight gain: N/A.
	E	Y5	4.5	1 bar	52.3 g/min	62.3 w/w%	1:31 (hr:min)	23 min/kg	The inside of the fluidisation chamber and the nozzle was graduately covered with wet particles during the coating process.
	F	Y6	4.5	3 bar	20.5 g/min	0.1 w/w%	4:26 (hr:min)	67 min/kg	Good fluidisation conditions. No particle-adhesion to the nozzle. Less than 10 w/w% loss of coating solution due to spray drying. Actual batch weight gain: 19.4 w/w%.
	G	Y7	4.7	1 bar	33.0 g/min	37.0 w/w%	2:39 (hr:min)	40 min/kg	Good fluidisation conditions, but ~ 50 w/w% loss of coating feed due to spray drying loss. Actual batch weight gain: 16.4 w/w%.
	H	Y8	4.7	3 bar	13.0 g/min	0.1 w/w%	6:31 (hr:min)	98 min/kg	Good fluidisation conditions, but 25 w/w% loss of coating feed due to spray drying loss. Actual batch weight gain: 18.9 w/w%.

Table 7-2: Results from the Flux Number scaling attempts (continued).

Fluid bed equipment	Scaling attempt	Exp. code	Flux Number	Nozzle pressure	Required Q_{miq}	Aggl. percentage	Coating time	Coating time per kg core load	Comment
MP-2/3 (Large-scale)	A	Z1	3.5	1 bar	1133.5 g/min	N/A	N/A	N/A	The coating experiment was not conducted as the small- and medium-scale experiments were unsuccessful.
	B	Z2	3.5	3 bar	615.4 g/min	N/A	N/A	N/A	The coating experiment was not conducted as the small- and medium-scale experiments were unsuccessful.
	C	Z3	4.0	1 bar	358.5 g/min	N/A	N/A	N/A	The coating experiment was not conducted as the small- and medium-scale experiments were unsuccessful.
	D	Z4	4.0	3 bar	194.6 g/min	97.8 w/w%	2:43 (hr:min)	7 min/kg	Large bubble fluidisation was observed. Actual batch weight gain: 19.3 w/w%.
	E	Z5	4.5	1 bar	113.4 g/min	4.4 w/w%	4:25 (hr:min)	11 min/kg	Minor tendency of particle adhesion to the nozzle, but no coverage of the chamber walls. Adequate fluidisation conditions. Actual batch weight gain: 19.5 w/w%.
	F	Z6	4.5	3 bar	61.5 g/min	0.7 w/w%	8: 41 (hr:min)	22 min/kg	Good fluidisation conditions. No particle-adhesion to the nozzle. Less than 15 w/w% loss of coating solution due to spray drying. Actual batch weight gain: 19.2 w/w%.
	G	Z7	4.7	1 bar	71.5 g/min	37.9 w/w%	6:52 (hr:min)	17 min/kg	Good fluidisation conditions, but ~ 30 w/w% loss of coating feed due to spray drying loss. Some build-up of particles on the nozzle and at the chamber walls. Actual batch weight gain: 18.9 w/w%.
	H	Z8	4.7	3 bar	38.8 g/min	0.1 w/w%	12:57 (hr:min)	32 min/kg	Good fluidisation conditions, but 35 w/w% loss of coating feed due to spray drying loss. Actual batch weight gain: 18.7 w/w%.

The effect of nozzle pressure within experiments having identical Flux Number was clearly observed for the experiments with Flux Numbers of 4.5. Whereas for e.g. experiment X5 and X6 the only difference is the nozzle pressure and thereby the liquid spray rate, the effect on agglomeration tendency is unambiguously detected; the agglomeration tendency increases with decreasing nozzle pressure irrespectively of the fluidised bed scale and the fact that the Flux Number is fixed. This tendency is also observed with the experiments having a Flux Number of 4.7.

Qualitatively the observed agglomeration tendencies in table 7-2 do indeed follow the domain map in figure 7.1 indicating that the agglomeration tendency decreases with increasing Flux Number. In the scaling attempts A, B, C and D having the smallest Flux Numbers the agglomeration tendencies are the largest. There is, however, a deviation from this overall tendency. Although some scattering in the agglomeration tendencies within the scaling attempt E, the trends are the opposite of the domain map. Whereas the tendency of agglomeration ought to decreases with increasing Flux Number this tendency is not observed when scaling attempt E and G is compared. There is statistically significant difference between the agglomeration tendencies in the following experiments: X5 and X7 as well as between Z5 and Z7. These observations clearly indicate that there are more important factors involved in agglomeration tendency than what is predicted by the domain map, and further that nozzle pressure is a factor of primary importance when it comes to the prediction of agglomeration tendency in terms of the Flux Number.

In the pursuit of reproducing the agglomeration tendency across scale it is observed from table 7-2 that only three scaling attempts are successful. The agglomeration tendencies for the three different batches within scaling attempt F, G and H are all within the ± 1.64 % range indicating that the agglomeration tendencies are not statistically different. This means in other words that the fixed coating conditions in these three times three experiments have resulted in similar agglomeration tendency across the scales.

As discussed in the paper by Hede et al. (2008b) the reproducibility of the agglomeration percentage within the ± 1.64 % interval does not necessarily indicate that the particle size distribution also is reproduced, as the different size classes do not necessarily have to be identical in order to achieve a similar agglomeration percentage. If the Flux Number should have any practical usefulness as a scaling parameter, the particle size fractions should also be reproduced across scale in addition to the agglomeration percentages. In order to check for the reproducibility of the particle size fractions within each Flux Number coating condition a χ^2 test was performed for all nine particle size classes (in case any of the size fractions were in the range of 0.01 w/w %, the size class was pooled into the next size class, as χ^2 tests on very small intervals may lead to false conclusions). This was obviously only done for the Flux Number conditions that did not cause a complete collapse of the bed. The results may be seen from table 7-3.

Table 7-3. P-values from a χ^2 test resulting from a comparative test of the three times nine particle fractions within each scaling attempt.

Scaling attempt	P-value from χ^2 test
E (experiments X5, Y5, Z5)	< 0.01
F (experiments X6, Y6, Z6)	0.26
G (experiments X7, Y7, Z7)	0.09
H (experiments X8, Y8, Z8)	0.59

From table 7-3 it is observed how the P-values from the χ^2 tests are above the 0.05 limit for scaling attempt F, G and H indicating that, on a 95% confidence level, the nine particle size fractions were matched across scale for all three scaling attempts. The particle size fractions were not matched in scaling attempt E, but this was also expected from the large deviations in agglomeration tendency as observed in table 7-2. By far the best match of particle size fractions was achieved in the scaling attempt F and H where there is almost no agglomeration tendency at all. This may also be visualised in a Rosin-Rammler-Bennet-Sperling-plot (RRSB-plot), as may be seen from figure 7.5, showing the particle size fractions from scaling attempt H. The RRSB-plot is a common way to describe the sum distribution Q3 as a function of different particle sizes in a mixture.

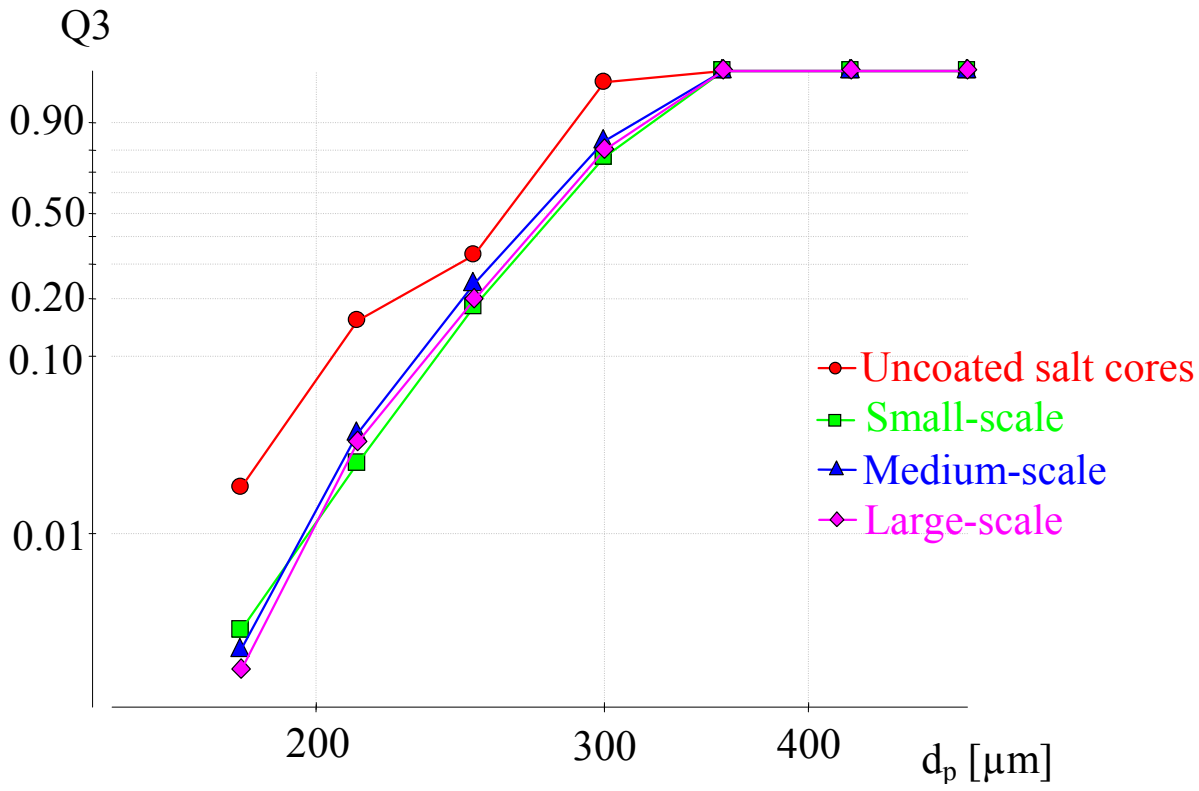

Figure 7.5: RRSB-plot (Rosin-Rammler-Bennet-Sperling) of particle size fractions from scaling attempt H. On the x-axis are the particle diameters and on the y-axis is the particle sum distribution Q3 in relation to particle volume.

Adequate matching is also observed in scaling attempt G and visualised in figure 7.6 where the particle size fractions are matched in spite of the agglomeration tendencies being around 37 %. One thing is to be able to match agglomeration tendencies and particle size fractions under coating conditions where no agglomeration occurs. This should seem somewhat straightforward compared to the match of significant agglomeration tendencies, which is another and far more complicated exercise. Hence, it seems reasonable that the P-values are the largest for the scaling attempts F and H. The most significant achievement is, however, that the P-value for scaling attempt G lies above the 0.05 level. For the process parameter conditions in the three scaling attempts F, G and H it is thereby reasonable to conclude that it is indeed possible to scale-up successfully in terms of the Flux Number.

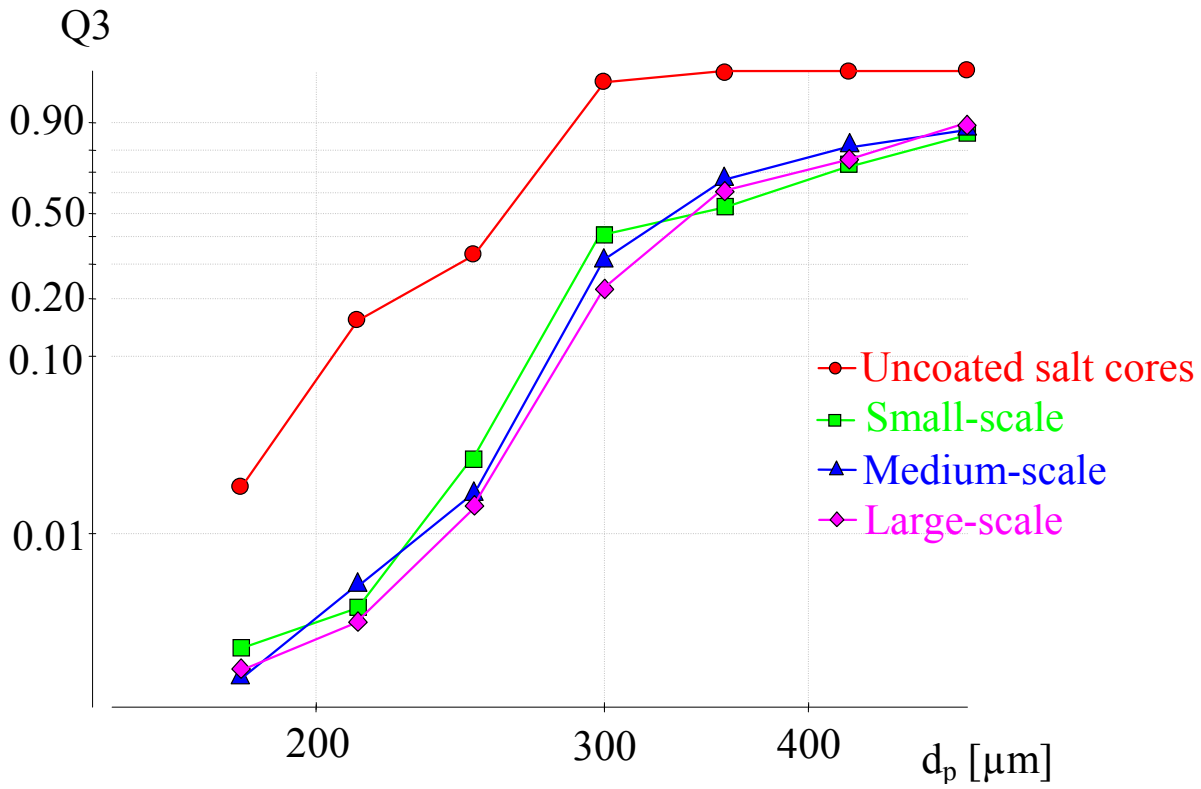

Figure 7.6: RRSB-plot (Rosin-Rammler-Bennet-Sperling) of particle size fractions from scaling attempt G. On the x-axis are the particle diameters and on the y-axis is the particle sum distribution Q3 in relation to particle volume.

7.3.2. Discussion of the Flux Number and scaling results

The Flux Number is an interesting parameter for scale-up purposes as it focuses on parameters known to have primary importance for the agglomeration tendency during the fluidised bed coating process. As reviewed by Hede (2005) and Iveson et al. (2001) control of the liquid distribution is essential for the tendency of agglomeration, and it makes sense to let the spray rate be a primary parameter in a scale-up relation. Likewise, it is common knowledge that the fluidisation velocity has a primary importance with respect to agglomeration. In that sense it seems reasonable to let the fluidisation velocity be a part of a scaling relationship. Whether or not the apparent density of the particle bed is important enough to be included in a scaling parameter may be discussed, but it does make the Flux Number a dimensionless parameter.

The Flux Number is not an easily applicable parameter as it requires some detailed a-priori knowledge of the fluidisation chamber dimensions, bed height at different fluidisation conditions and more. Many of these parameters will also vary with the given types of core materials and coating solution formulation, and may eventually have to be determined each time these conditions change. Even if these parameters and properties have been determined, other choices will have to be made as well regarding the values for the parameters constituting the Flux Number. Although the original patent description by Akkermans et al. (1998) indicates some wide ranges for the parameters, the results in this work show that these ranges may not be useful in general. The values for the mass spray flux $\dot{q}_{mliq}$ tested in this paper have all been either below or in the lowest part of the value range suggested in the

patent description. Even so, the agglomeration tendency was observed to be heavy for some cases although all other parameters were in the midst of the suggested range.

Other additions to the Flux Number in form of the viscous Stokes number suggested by Wasserman et al. (2000) and Achanta & Beimesch (1998) have proven not to be sufficient to control the tendency of agglomeration. The presents results have indicated that maintaining the viscous Stokes number even far above the value of 1 does not ensure successful coating conditions with limited agglomeration. There are several possible reasons why a single overall viscous Stokes number based on the excess gas velocity cannot alone (i.e. without also including a critical viscous Stokes number) be used for determining the boundaries for agglomeration as simply as it is claimed by Wasserman et al. (2000). Assuming that the particle collision velocity is simply equal to the excess gas velocity is first of all a rough assumption. As demonstrated by Ennis et al. (1991) the collision velocity depends also on the colliding particle radii as well as on bubbling fluidisation characteristics such as bubble diameter and dimensionless bubble space etc (see chapter three). Furthermore, the viscous Stokes number uses only one excess gas velocity value whereas there is a whole range of excess gas velocities in the conical fluidisation chambers used in the present studies. Similarly, the viscous Stokes number requires only one particle diameter even though there is a whole particle size distribution being processed. All of these issues are not accounted for in equation 7.7, and in all they constitute plausible reasons why the viscous Stokes number simplification suggested by Wasserman et al. (2000) does not bring any further control of the coating system in combination with the Flux Number.

The results in the present study show interestingly that the nozzle pressure has a strong influence on the tendency of agglomeration irrespectively of the Flux Number value. The largest agglomeration tendencies were observed with the lowest nozzle pressures in accordance with other studies by Hede et al. (2007a). As may be estimated from equation 2.1 (see chapter two) a high nozzle pressure combined with a low coating solution mass feed rate means smaller droplets. As it was seen from the determinations of spray area A, a nozzle pressure of 1 bar has a significantly larger spray area than a nozzle pressure of 3 bar. Furthermore, a low nozzle pressure means less extent of droplet penetration vertically into the bed which has importance regarding the degree of possible droplet spray drying. It was observed from the results in table 7-2 how the loss of coating solution due to spray drying increased with decreasing nozzle pressure. Irrespectively of this, as a consequence of equation 7.6, maintaining a similar Flux Number and thereby a similar value for the mass spray flux $\dot{q}_{mliq}$ means that at a low nozzle pressure, more liquid will have to be introduced through the nozzle per time due to larger spray area. These conditions mean all in all that larger droplets are produced faster at the nozzle, and even though a relative large amount of these droplets are spray dried, those who actually reach the core surfaces are large in volume meaning that the coated particles are wet for a longer time in all increasing the chance of agglomeration. These tendencies have been proven by several authors elsewhere (e.g. Schæfer & Wørts, 1977). The nozzle pressure tendencies observed in the present studies clearly illustrate an important weakness associated with the Flux Number: Even though two coating conditions have identical Flux Numbers the tendency of agglomeration is strongly influenced by the choice of nozzle pressure. The results in this paper strongly call for a further specification of the nozzle pressure in association with the Flux Number. So far it seems as if 3 bar for the tested nozzle types is the reasonable nozzle pressure in order to limit agglomeration, but further studies have to be conducted in order to determine a generic suitable range.

The fact that the experimental validation shows even narrower Flux Number boundaries of around 4.5 to 4.7 for a successful coating regime compared to the patent descriptions indicates first of all that there is more to the principles of scaling the coating process than what is accounted for in the Flux Number. Secondly, it highlights the need for proper validation and specification of the value ranges for the parameters constituting the Flux Number. Testing the Flux Number in high-end levels of 4.5 and 4.7 also indicates that it is relatively easy to perform a coating operation without the tendency of agglomeration: If agglomeration is a problem the solution is simply to increase the Flux Number. This will decrease the liquid feed rate to the nozzle and if this is not sufficient, the nozzle pressure may additionally be increased to produce smaller droplets. There are, however, two major problems with this procedure. Firstly, as observed with the present experiments, the coating time is prolonged by this procedure. As observed from the comparison of scaling attempt E to H, the coating time increases significantly with increasing Flux Number. Coating operations lasting e.g. almost 9 and 13 hours in experiment Z6 and Z8, respectively, are not desirable in practice. A second problem with high Flux Numbers is the high degree of spray drying loss of the liquid feed. At conservative coating conditions a large fraction of the coating solution droplets dry up before reaching the core particle surfaces. This means that larger quantities of the coating solution is required, but also give rise to problems concerning the properties of the coated core particles. It is well-known from previous studies (Beekman, 2000 and Hede, 2005) that partly dried-up droplets result in porous and flaky coating layers that exhibit poor mechanical properties when exposed to impact and attrition. Hence, there are indeed many reasons for not simply increasing the Flux Number in order to avoid agglomeration.

There is a long history in the field of dimensionless parameters from e.g. chemical reactor engineering, and it is indeed understandable to aim at finding dimensionless parameters that may describe the coating process in simple terms. The present results have, however, shown that for granulation processes it is difficult to establish a simple dimensionless parameter that involves all relevant properties and parameters.

7.4. Conclusion

The paper has experimentally tested the dimensionless Flux Number on a standard top-spray fluidised bed sodium sulphate coating process on placebo enzyme sodium sulphate cores (180 – 350 μm) as a possible scaling parameter suggested to be kept constant across scale. The Flux Number was tested in four discrete levels of 3.5, 4.0, 4.5 and 4.7 testing the influence of nozzle pressures of 1 bar and 3 bar for each Flux Number value. Systematic studies of fluidised bed coating processes have been carried out in three fluidised bed scales testing the tendency of agglomeration and the match of particle size fraction across scale.

On an overall level only, successful scale-up of top-spray fluidised bed coated particles by 48 times in weight from the small-scale over medium-scale to the large-scale fluidised bed has been achieved for Flux Number conditions of 4.5 and 4.7. For the Flux Number values of 4.7 the scaling up was successful irrespectively of the nozzle pressure whereas only the high-nozzle pressure condition was successful for a Flux Number of 4.5. For these Flux Number values in general the agglomeration tendency decreased with increasing Flux Number and increasing nozzle pressure. For all other Flux Number conditions the bed collapsed due to overwetting within the first minutes of the coating process.

The present studies clearly indicate the limitations of the Flux Number as scaling parameter. It is indeed possible to successfully scale-up in terms of the Flux Number, but only within a narrow range and only with detailed knowledge of the value range for the parameters constituting the Flux Number. On the basis of the present study, the following guidelines are suggested when using the Flux Number for fluidised bed coating scale-up purposes:

- Coating conditions with limited or no agglomeration requires Flux Numbers in the range of 4.5 – 4.7. Higher Flux Numbers prolong the coating time unnecessarily and give problems with high spray drying losses of the coating solution. The lower end of this narrow Flux Number range is within a practical range regarding the time of coating, the coating solution spray rate and more.

- Two values of the nozzle pressure were tested (1 and 3 bar) indicating that a high nozzle pressure is preferable in the tested sodium sulphate coating process.

- Viscous Stokes numbers values in the range of 100 – 1000 may be a prerequisite for successful coating operations, but still excessive agglomeration may occur.

- Values for the mass spray flux $\dot{q}_{mliq}$ may well be chosen below a value of 0.15 kg/(s·m)^2 – preferably in the range of 0.05 kg/(s·m)^2 to 0.08 kg/s·m^2 for the tested sodium sulphate coating process.

- Product temperatures in the range of 55 ºC are preferable for the tested sodium sulphate coating process, whereas product temperatures below 50 ºC lead to agglomeration with the Flux Number values tested in this study. Maintaining the product temperature should be done by adjustment of the inlet fluidisation air temperature. All other process conditions should be chosen a-priori and kept fixed throughout the process.

7.5. Table of symbols

Symbols		Unit
A	Contact (spray) area at the distance of D_0	m^2
BD	Bulk density of the particles	kg/m^3
d_{32}	Sauter mean droplet diameter	m
d_p	Mean particle diameter	m
D_0	Normalised distance	m
h_{bed}	Bed height	m
h_{mf}	Bed height at minimum fluidisation velocity	m
h_{nozzle}	The height of the spray nozzle above the bottom of the fluidisation chamber	m
FN	Flux Number	Dimensionless
$L_{chamber}$	Length from the air distributor plate to the fluidisation chamber exhaust exit	m
$\dot{q}_{mliq}$	Mass spray flux	kg/(s·m^2)
Q_{mliq}	The mass flow of liquid applied	kg/s
St_v	Viscous Stokes number	Dimensionless
u_0	Initial granule collision velocity	m/s

v_{mf}	Minimum fluidisation velocity	m/s
v_e	Excess gas velocity	m/s
v_a	Fluidisation (superficial) gas velocity	m/s

Greek

ε_{bed}	Bed porosity	Dimensionless
η_{liq}	Coating solution viscosity	kg/m·s
ρ_g	Granule density	kg/m^3
ρ_p	Particle density	kg/m^3

7.6. References

Achanta, S. and Beimesch, W.E., (1999) Process for making a low density detergent composition by controlled agglomeration in a fluidised bed dryer, Patent WO99/03964.

Akkermans, J.H.M., Edwards, M.F., Groot, A,T.J., Montanus, C.P.M., Van Pomeren, R.W.J. and Yuregir, K.R. (1998) Production of detergent granulates, Patent WO98/58046.

Beekman, W.J. (2000) Measurement of the Mechanical Strength of Granules, Ph.D. Thesis, Technische Universiteit Delft.

Boerefijn, R. and Hounslow, M.J. (2005) Studies of fluidised bed granulation in an industrial R&D context, Chemical Engineering Science, Vol. 60, pp. 3879-3890.

Ellenberger, J. and Krishna, R. (1994) A Unified Approach to the Scale-up of Gas-Solid Fluidized Bed and Gas-Liquid Bubble Column Reactors, Chemical Engineering Science, Vol. 49, No. 24B, pp. 5391-5411.

Ennis, B.J., Tardos, G. and Pfeffer, R. (1991) A microlevel-based characterization of granulation phenomena, Powder Technology, No. 65, pp. 257-272.

Glicksman, L.R. (1984) Scaling Relationships For Fluidized Beds, Chemical Engineering Science, Vol. 39, No. 9, pp. 1373-1379.

Glicksman, L.R. (1988) Scaling relationships for fluidized beds, Chemical Engineering Science, Vol. 43, No. 6, pp. 1419-1421.

Glicksman, L.R., Hyre, M. and Woloshun, K. (1993) Simplified scaling relationships for fluidized beds, Powder Technology, No. 77, pp. 177-199.

Hede, P.D. (2005) Fluidised bed coating and granulation, M.Sc. Thesis, Department of Chemical Engineering, CHEC Research Center, Technical University of Denmark, pp. 1-227.

Hede, P.D. (2006) Towards Mathesis Universalis: Modern aspects of modelling batch fluidised bed agglomeration and coating systems – a review, CHEC Report R0605, Department of Chemical Engineering, Technical University of Denmark, pp. 1-101.

Hede, P.D., Bach, P. and Jensen, A.D. (2007a) Small-scale top-spray fluidised bed coating: Granule impact strength, agglomeration tendency and coating layer morphology, Powder Technology, No. 176, pp. 156-167.

Hede, P.D., Bach, P. and Jensen, A.D. (2008a) Validation of the Flux Number as scaling parameter for top-sprayed fluid bed coating systems, Chemical Engineering Science, Vol. 63, No. 3, pp. 815-828.

Hede, P.D., Bach, P. and Jensen, A.D. (2008b) Top-spray fluidised bed coating: Scale-up in terms of relative droplet size and drying force, Powder Technology, Vol. 184, No. 3, pp. 318-332.

Horio, M., Nonaka, A., Sawa, Y. and Muchi, I. (1986) A New Similarity Rule for Fluidized Bed Scale-up, AIChE Journal, Vol. 32, No. 9, pp. 1466-1482.

Iveson, S.M., Litster, D.L., Hapgood, K. and Ennis, B.J. (2001) Nucleation, growth and breakage phenomena in agitated wet granulation processes: a review, Powder Technology, No. 117, pp. 3-39.

Knowlton, T.M., Karri, S.B.R. and Issangya, A. (2005) Scale-up of fluidized-bed hydrodynamics, Powder Technology, No. 158, pp. 72-77.

Kunii, D. and Levenspiel, O. (1991) Fluidization Engineering, 2nd Edition, Butterworth-Heinemann, Stoneham.

Leuenberger, H. (1983) Scale-up of granulation processes with reference to process monitoring, Acta Pharmaceutical Technology, No. 29, pp. 274-280.

Leuenberger, H. (2003) Scale-up in the 4th dimension in the field of granulation and drying or how to avoid classical scale-up, Powder Technology, No. 130, pp. 225-230.

Mehta, A.M. (1988) Scale-up considerations in the fluid-bed process for controlled-release products, Pharmaceutical Technology, No. 12, pp. 46-52.

Mort, P.R. (2005) Scale-up of binder agglomeration processes, Powder Technology, No. 150, pp. 86-103.

Rambali, B., Baert, L. and Massart, D.L. (2003) Scaling up of the fluidized bed granulation process, International Journal of Pharmaceutics, No. 252, pp. 197-206.

Schouten, J.C., Van der Stappen, M.L.M. and van den Bleek, C.M. (1996) Scale-Up of Chaotic Fluidized Bed Hydrodynamics, Chemical Engineering Science, Vol. 51, No. 10, pp. 1991-2000.

Schæfer, T. and Wørts, O. (1977) Control of fluidized bed granulation. II. Estimation of droplet size of atomised binder solutions, Archives of Pharmaceutical and Chemical Science, 5th Edition, pp. 178-193.

Schæfer, T. and Wørts, O. (1978) Control of fluidized bed granulation. III. Effects of inlet air temperature and liquid flow rate on granule size and size distribution. Control of moisture content of granules in the drying phase. Archives of Pharmaceutical and Chemical Science, 6th Edition, pp. 1-13.

Teunou, E. and Poncelet, D. (2002) Batch and continuous fluidised bed coating – review and state of the art, Journal of Food Engineering, No. 53, pp. 325-340.

van Ee, J.H., Misset, O and Baas, E.J. (1997) Enzymes in Detergency, Surfactant Science Series, Volume 69, Marcel Dekker, New York.

Wasserman, M.I., Ridyard, M.W., Capeci, S.W., Beimesch, W.E. & Mort, P.R. (2000) Process for coating detergent granules in a fluidized bed, Patent WO00/78912A1.

Werther, J. (1980) Modelling and Scale-up of Industrial Fluidized Bed Reactors, Chemical Engineering Science, No. 35, pp. 372-379.

Chapter 8. Scale-up using Relative Droplet size & Drying Force

Chapter introduction

Chapter eight introduces a novel scale-up principle in which two parameters are kept constant across three pilot fluid bed scales. The two parameters are the Drying Force (concerning fluidisation air temperature and humidity) and the Relative Droplet size (concerning nozzle liquid and atomisation air mass flows). This scale-up principle is introduced and validated with the aim of being able to match the tendency of agglomeration and particle size fractions as well as to match the coated granule impact and attrition strength across three pilot-scale fluid beds. The present chapter is published as a peer-reviewed scientific paper in the journal *Powder Technology*, volume 184, No. 3, pp. 318-332, 2008. The paper is entitled *Top-spray fluid bed coating: Scale-up in terms of relative droplet size and drying force* authored by Peter Dybdahl Hede (Technical University of Denmark), Poul Bach (Novozymes A/S) and Anker D. Jensen (Technical University of Denmark). The paper is referred to as Hede et al. (2008b).

The following sections are exact reproductions of the paper, although the sections concerning equipment and materials have been left out (please refer to chapter five). Furthermore, the format of the paper has been adapted to that of this thesis.

8. Top-spray fluid bed coating: Scale-up in terms of Relative Droplet size and Drying Force

Abstract

Top-spray fluid bed coating scale-up experiments have been performed in three scales in order to test the validity of two parameters as possible scaling parameters: the Drying Force and the Relative Droplet size. The aim was to be able to reproduce the degree of agglomeration, particle size fractions as well as the mechanical properties of the coated granules across scale. Two types of placebo enzyme granule cores were tested being non-porous glass ballotini cores (180 - 350 μm) and low porosity sodium sulphate cores (180 - 350 μm). Both types of core materials were coated with aqueous solutions of Na_2SO_4 using Dextrin as binder. Coating experiments were repeated for various Drying Force and Relative Droplet size values in three top-spray fluid bed scales being a small-scale (Type: GEA Aeromatic-Fielder Strea-1), medium-scale (Type: Niro MP-1) and large-scale (Type: GEA MP-2/3). The tendency of agglomeration was assessed in terms of particle size fractions larger than 425 μm determined by sieve analysis. Results indicated that the particle size distribution may be reproduced across scale with statistical valid precision by keeping the Drying Force and the Relative Droplet size constant across scale. It is also shown that neither of the two parameters alone may be used for successful scale-up. Morphology and microscope studies indicated that the coating layers are homogenous and have similar structures across scale only when both the Drying Force and the Relative Droplet size were fixed. Impact and attrition tests indicated that it is possible to produce granules with similar attrition and impact strength across scale, and that the two types of mechanical properties are inversely related.

8.1. Introduction

In the production of solid enzyme products, coating of the enzyme formulation onto inactive filler cores in fluid beds is a common process. The desired product consists of unagglomerated individual carrier particles each coated homogeneously with a layer of an enzyme-containing matrix. If formulation or process conditions are incorrectly chosen, either excessive agglomeration or excessive spray drying of the feed may happen. In both cases a poor product quality is achieved, and in any case, control of agglomeration is essential during scale-up. Often product and process properties are optimised in small and medium pilot-scale fluid beds and then transferred to production-scale. The scale-up of a fluid bed granulation process requires decisions to be made at many levels. Scaling decisions must be closely related to a large number of parameters including: apparatus related (e.g. nozzle type and fluidisation chamber dimensions), parameters related to the core material (such as porosity, mechanical properties and more), coating solution (e.g. viscosity, surface tension, contact angle and more) and the type of fluid bed, input parameters, operating conditions including spray and fluidisation conditions as well as processing time etc. With such a variety of interlinked parameters and properties, combined with a lack of quantitative understanding of the coating process, it is obvious that scale-up of a fluid bed granulation process is a challenging task.

A number of different scaling laws and principles have previously been suggested; in principle on either the unit-operation (macro) scale or on the particle-level (micro) scale. Recent work on scale-up of top-spray fluid bed granulation processes (e.g. by Mehta, 1988 and Rambali et al., 2003) indicate successful scale-up of agglomeration processes from small-scale fluid bed to large-scale fluid bed in terms of the so-called Relative Droplet size, defined as the liquid spray rate in g/min divided by the airflow through the nozzle in g/min squared according to equation 8.1. In the granulation experiments by Rambali et al. (2003) with corn starch and lactose monohydrate cores (mesh 200 μm) using an aqueous HPMC binder solution it was observed that the effect on mean granule size of the change in Relative Droplet size was different for each fluid bed scale, but that the granulation process was successful by scaling up to the large-scale bed from small-scale, considering only the Relative Droplet size. In their studies, the scale-up was restricted only to granule size having a target mean granule size of 400 μm, and other important granule properties such as porosity and flowability were not taken into account. Studies by Hede (2005) indicate that besides nozzle conditions the relative humidity as well as the temperature inside the fluidisation chamber during coating are important properties with respect to agglomeration. Both properties may be combined into a single parameter, the Drying Force, suggested to be kept constant during scale-up. In terms of fixed values of the Drying Force and the Relative Droplet size a range of vital process parameters are implicitly given. Hence, there is reason to believe that these two parameters are capable of controlling the tendency of agglomeration during fluid bed processing. The present paper aims at testing those two parameters as possible scaling parameters – alone as well as in combination – in a fluid bed coating context. The scale-up targets are to be able to reproduce the tendency of agglomeration, the entire particle size distribution as well as the mechanical properties of the coated granules across scale in terms of fixed values of the Drying Force and the Relative Droplet size. Match of these three properties across scale are vital for industrial fluid bed processes and products and are often subject to numerous trial-and-error attempts in industry.

8.2. Experimental

Sodium sulphate cores pre-sieved twice in the size range of 180 – 350 μm were used as core material. The sodium sulphate cores were coated with aqueous solutions of sodium sulphate in the amount of 15 w/w% using 1 w/w% (of the amount of sodium sulphate) Dextrin as binder. Demineralised water was used as solvent. Patent blue was added to the coating solution used in selected droplet penetration studies (see also chapter five).

Similar to the experiments in chapter seven, it was verified by microscope analysis of the different fractions that coated granules with diameters above 425 μm consisted of agglomerates whereas particles below this limit were primarily single coated granules. Thus, this sieve orifice diameter was set as the agglomeration limit, and based on the weight of each of the fractions the degree of agglomeration was determined for each batch according to equation 7.8 (see chapter seven).

The obtained fraction of coated granules between 355 μm and 425 μm was the fraction to be tested in the impact and attrition strength test equipment. Values for $Y_{Attrition}$ and $Y_{Breakage}$ were obtained with the use of equation 5.2 and 5.1, respectively (see chapter five).

8.2.1. Scaling parameters and scaling procedure

Based on the results by Mehta (1988), Rambali et al. (2003) scaled up a fluidised agglomeration process from small-scale (bed load: 5 kg) to medium- (bed load: 30 kg) and large-scale (bed load: 120 kg) by looking at the effect of the particle bed moisture contents during and at the end of the spraying process, and the effect of coating solution droplet size on the granule size. The fluidisation flow rate in m/s at the air distributor plate was kept constant in all their experiments in order to have approximately similar breaking forces on the granules. For the small- and medium-scale the same nozzle (liquid orifice diameter of 1.8 mm) was used whereas a three-head nozzle (liquid orifice diameters of 3 x 3.0 mm) was used for the large-scale fluid bed. The droplet size was controlled in terms of a Relative Droplet size, RD, defined as the ratio of the coating solution mass spray rate $\dot{m}_{spray}$ divided by the atomisation air mass flow rate through the nozzle $\dot{m}_{nozzle\ air}$ squared according to equation 8.1.

$$RD = \frac{\dot{m}_{spray}}{(\dot{m}_{nozzle\ air})^2} \tag{8.1}$$

The idea of RD is to maintain a similar droplet size across scale and the value of RD is only unambiguous if both the nozzle pressure and the liquid feed rate are chosen. Rambali et al. (2003) claim that the Düsen-Schlick manufacturer of two-fluid nozzles have found that the droplet size is proportional to the ratio in equation 8.1. This is in agreement with Masters (1972) suggesting that the mean spray droplet size d_{dr} produced by pneumatic two-fluid nozzles follows the general relation in equation 8.2.

$$d_{dr} = \frac{A}{(v_{rel}^2 \cdot \rho_{air})^{\alpha}} + B \cdot \left(\frac{\dot{m}_{nozzle\ air}}{\dot{m}_{spray}} \right)^{\beta} \tag{8.2}$$

where v_{rel} is the relative velocity between air and liquid at the nozzle outlet and ρ_{air} is the atomisation air density. The exponents α and β are functions of nozzle design and A and B are constants involving both nozzle design and liquid properties. The general relationship in equation 8.2 indicates that the relation in equation 8.1 has some influence towards the mean droplet size, although the exponent of 2 in the denominator in equation 8.1 is yet to be explained.

Results by Hede (2005) indicate that a so-called Drying Force parameter (DF) is closely related to the tendency of agglomeration during fluid bed coating. The Drying Force combines the bed temperature and outlet relative humidity (assumed equal to the average bed relative humidity as it is measured in the three fluid bed set-ups at some short distance above the nozzle outlet within the dispersed phase) during steady state coating conditions according to equation 8.3, hereby indicating the fluidisation air moisture evaporation force.

$$DF = P_{sat} \cdot \left(1 - \frac{\text{Bed rH\%}}{100\,\text{rH\%}}\right) \approx P_{sat} \cdot \left(1 - \frac{\text{Outlet rH\%}}{100\,\text{rH\%}}\right) \tag{8.3}$$

where P_{sat} is the saturated vapour pressure at the dry bulb bed temperature.

In order to test the scalability in terms of the Drying Force, different levels of the bed temperature were chosen and fixed. The humidity of the inlet air could not be controlled in any of the three fluid bed set-ups, but they were all recorded and no significant variation was observed. Equation 8.3 indicates furthermore, that the Drying Force is less sensitive to the relative humidity than to the bed temperature. Thus, it was possible to maintain the Drying Force at almost distinct levels without being able to precisely control the humidity of the inlet air.

The fluidisation velocity in m/s was kept constant at 3.3 m/s at a height in the fluidisation chamber just above the bottom plate through all experiments and across scale, in order to try to maintain a similar granule collision velocity as well as a similar level of attrition across scale. All three types of fluid beds have a conical fluidisation chamber shape, but the wall angles, bottom plate and other length dimensions are not dimensionally consistent going from small- to medium- and large-scale (see chapter five). A fluidisation velocity just above the bottom plate at 3.3 m/s corresponds to 93 Nm^3/hr in the Strea-1 set-up, 270 Nm^3/hr in the MP-1 and 680 Nm^3/hr in the MP-2/3 set-up.

In the present studies, the Relative Droplet size was kept constant during scale-up as the nozzle pressure was kept constant at two distinct levels (1 bar or 3 bar) in each scale and the liquid feed rate to the nozzle controlled and fixed at the tube pump in order to maintain a constant Relative Droplet size across scale. Even though the nozzle liquid orifice diameter of 1.2 mm and the nozzle pressure were identical in all three scales, the atomisation airflow in g/min were not identical as the nozzle air annulus orifices were different for each type of nozzle. This means in other words that for fixed values of the Relative Droplet size the nozzle liquid feed flow in g/min and the nozzle airflows in g/min were different for each fluid bed scale. Initial experiments had to be conducted in order to determine the airflow through the nozzle for different nozzle pressures without connecting the liquid feed. This was done by connecting a simple household gas-meter to the nozzle outlet and then measure the airflow rate versus the nozzle pressure. The Relative Droplet size was kept constant across scale as follows: Knowing the airflow rate through the given nozzle at a given nozzle pressure, the value of the Relative Droplet size from the small-scale fluid bed was kept constant during up-

scaling by calculating the liquid feed rate in g/min necessary to achieve an identical Relative Droplet size in the medium- and large-scale. The tube pump was thereby adjusted and fixed at this value throughout the coating experiment. With the given choice of Drying Force value and the choice of bed temperature, only the inlet fluidisation air temperature was changed in each experiment in order to match the Drying Force and the Relative Droplet size across scale.

In accordance with coating guidelines presented in chapter five the core bed load was heated prior to coating until the relative humidity inside the fluidisation chamber was constant. In each coating operation the aim was to coat until the bed load had increased 20 w/w%, in order to make sure that a reasonable coating layer (~ 5-10 μm) had developed on the core particles. For all the experiments in this paper, the batch weight gain was in the range of 18.7 w/w% - 19.5 w/w% indicating little loss of core material as well as little loss of coating solution due to spray drying.

8.3. Results and Discussion

8.3.1. Reproducibility of data

Quantitative data analysis requires certainty of reproducibility of data as well as knowledge of equipment variances. Several reproducibility issues have been treated in the present paper. First of all, the reproducibility of size fraction data from the sieve analysis was adressed. Ten samples from a representative coated batch were sieved separately in order to determine a standard deviation for the Retsch Sieve Shaker AS 200 control equipment (see also chapter five). In terms of the agglomeration percentage, it was seen that the standard deviation was 0.82 % thereby indicating that different batches having agglomeration percentages in the range of ± 1.64 % are not statistically different.

The reproducibility of data from the three different fluid bed scales was tested by performing two experiments with identical process and formulation conditions for each of the three fluid bed scales. As it may be seen from table 8-1, the agglomeration percentage is well repeated within all three fluid bed types.

Table 8-1: Verification of the reproducibility of data from the three different fluid bed scales. The bed temperature was maintained at 55 ºC and the nozzle pressure was kept at 1 bar in all experiments. Sodium sulphate cores (180 – 350 μm) were used in all experiments and the coating solution was the standard 15 w/w % Na_2SO_4 solution with 1 w/w% Dextrin as binder.

Fluid bed scale	Experiment 1	Experiment 2	P-value from the χ^2 test
Strea-1 (Small-scale)	Aggl % = 49.0 %	Aggl % = 49.8 %	0.21
MP-1 (Medium-scale)	Aggl % = 41.3 %	Aggl % = 40.7 %	0.92
MP-2/3 (Large-scale)	Aggl % = 35.9 %	Aggl % = 37.1	0.16

Formally, the reproducibility of the agglomeration percentage within the ± 1.64 % interval does not necessarily indicate that the particle size distribution also is reproduced, as the different size classes do not necessarily have to be identical in order to achieve a similar agglomeration percentage. In order to check this, a χ^2 test was performed for all nine size classes in the two identical experiments for each scale (in case any of the size fractions were in the range of 0.01 w/w %, the size class was pooled into the next size class, as χ^2 tests on very small intervals may lead to false conclusions). The χ^2 test is used throughout the paper as it is a simple and widely used test for statistical significant analysis of categorical data as the sieve fractions.

As observed from table 8-1, all the P-values are far above 0.05 (corresponding to a 95 % confidence interval) indicating that the six different particle size distributions are well reproduced in pairs. The conclusion from these first experiments is that, with identical process and formulation conditions, it is possible to reproduce data in all three scales with sufficient accuracy to perform statistical quantitative analysis and comparison of the data.

8.3.2. Matching the agglomeration percentages and particle size fractions across scale

In order to test the applicability of the Drying Force and Relative Droplet size as scaling parameters, a campaign of different fluid bed coating experiments was set up. An overview of the different experiments may be seen from table 8-2.

Table 8-2: Overview of the scaling experiments.

Fluid bed equipment	Experiment code	Core material	Bed temp. (target)	Nozzle pressure
Strea-1 (small-scale)	S1	Na_2SO_4	55 ºC	3 bar
	S2	Glass ballotini	55 ºC	3 bar
	S3	Na_2SO_4	55 ºC	1 bar
	S4	Na_2SO_4	50 ºC	3 bar
	S5	Na_2SO_4	45 ºC	3 bar
	S7	Glass ballotini	55 ºC	1 bar
MP-1 (medium-scale)	M1	Na_2SO_4	55 ºC	3 bar
	M2	Glass ballotini	55 ºC	3 bar
	M3	Na_2SO_4	55 ºC	1 bar
	M4	Na_2SO_4	50 ºC	3 bar
	M5	Na_2SO_4	45 ºC	3 bar
	M7	Glass ballotini	55 ºC	1 bar
MP-2/3 (Large-scale)	L1	Na_2SO_4	55 ºC	3 bar
	L2	Glass ballotini	55 ºC	3 bar
	L3	Na_2SO_4	55 ºC	1 bar
	L4	Na_2SO_4	50 ºC	3 bar
	L5	Na_2SO_4	45 ºC	3 bar
	L7	Glass ballotini	55 ºC	1 bar

The conditions for the eighteen coating experiments (six in each fluid bed scale) in table 8-2 were carefully chosen in order to test the influence of the various parameters involved in the fluid bed coating process including the influence of the Drying Force, the Relative Droplet size and the type of core material. The experiments were conducted in a six week period under similar weather conditions with room temperatures around 23 ºC and room humidities in the range of 35 - 39 rH%.

Important to note is that the coating time increased with scale. Whereas the coating time in the small-scale took about 30 minutes (drying phase ~ 4 - 5 minutes) and about 1 hour and 30 minutes in the medium-scale (drying phase ~ 5 - 8 minutes), the coating time in the large scale took about 3 hours and 30 minutes (drying phase ~ 9 - 15 minutes). Seen in respect to the difference in core material bed load with scale this means that the coating time is roughly 60 minutes per kg core material in the small-scale, 23 min/kg in the medium-scale and 9 min/kg in the large scale. These coating conditions are in the intense end of the usual range for all three scales.

As the absolute coating process times are so different according to the fluid bed scale, a phenomenon such as attrition is an important phenomenon to consider regarding the match of particle size distribution across fluid bed scale. Formally, it seems to be important whether the

particles are coated in 30 minutes or in 3 hours. However, the level of attrition is not in any way linearly dependent on time. Results by Hede (2005) have shown that rather than a linear relationship between the amount of attrition and processing time, there is a power-law relationship (the so-called Gwyn relationship presented first by Gwyn (1969) – see chapter three). This means that the majority of the debris caused by attrition is produced in the first phase of fluidisation, and thereby that the total amount of debris is not significantly affected by a prolonged processing time. At the fluidisation velocities used in the present studies the majority of debris is produced within the first 15 minutes of fluidisation. Hence, concerning the level of attrition it is of minor practical importance whether the coating process time lasts 30 minutes or 3 hours and 30 minutes.

A schematic overview of the resulting agglomeration percentages and levels of corresponding Drying Forces and Relative Droplet sizes may be seen from table 8-3. Note that the rightmost column shows P-values from χ^2 tests performed on the three sets of sieve fractions within the same scaling attempt.

There are many interesting things to extract from the results in table 8-3. Going horizontally in table 8-3, the Drying Force as well as the Relative Droplet size are maintained whereas either one or both of these parameters are changed going in the vertical direction. Comparing scaling attempt A, D and E, in which only the Relative Droplet size has been kept constant, it becomes evident that there is a relation between the Drying Force and the agglomeration tendency, but also that the relation is not in any way linear. E.g., the Drying Force has been reduced from around 12 kPa in attempt A to around 8.5 kPa in attempt D whereas the agglomeration percentages are not statistically significant different. When further reducing the Drying Force to around 6 kPa, the agglomeration tendency increases significantly. These tendencies are qualitatively reasonable since a higher agglomeration tendency is expected with decreasing Drying Force due to slower drying rate. With decreasing Drying Force the coating droplets will dry slower leaving the coating layer wet for a longer time on the core surfaces, hereby increasing the chance of liquid bridge building between particles, again resulting in solid bridge formation upon evaporation of the solvent and thereby permanent agglomeration.

The influence of the Relative Droplet size on the agglomeration tendency may be observed from the comparison of scaling attempt A and C. Going from attempt A to C, the Relative Droplet size is roughly increased seven times whereas the agglomeration tendency is increased more than thirty-five times. This tendency seems qualitatively reasonable. With the increased Relative Droplet size, the actual droplet size is increased as well, although not as much as seven times as it will be discussed in a coming section. With increased droplet diameter under similar Drying Force conditions, the larger droplets will remain wet for a longer time thereby increasing the chance of liquid bridge building between particles and thereby the chance of agglomeration.

Comparing the agglomeration tendencies within each scale in attempt A, D and E as well as in attempt A and C indicates that granulation process control in terms of either Drying Force alone or Relative Droplet size alone is not a successful choice, as the agglomeration tendency within each scale cannot be maintained in terms of fixing either of these parameters alone. Next is to determine whether or not a combination of the Relative Droplet size and the Drying Force may be applied for successful scale-up.

Table 8-3: Overview of results from the six scaling attempts in terms of Relative Droplet size (RD) in min/gram and Drying Force (DF) in kPa. The P-values in the rightmost column arise from a χ^2 test of the three sets of sieved fractions within the same scaling attempt. Scaling attempt B and F were carried out with glass ballotini cores whereas the other scaling attempts were done with sodium sulphate cores.

Scaling attempt	T_{bed}	P_{nozzle}	Strea-1 (small-scale)		MP-1 (medium-scale)		MP-2/3 (Large-scale)		P-value from χ^2 test
A	55 °C	3 bar	Exp. S1	Aggl % = 0.1	Exp. M1	Aggl % = 1.3	Exp. L1	Aggl % = 1.5	0.07
			RD = $3.5 \cdot 10^{-3}$	DF = 12.2	RD = $3.5 \cdot 10^{-3}$	DF = 12.0	Rd. = $3.5 \cdot 10^{-3}$	Df. = 12.5	
B	55 °C	3 bar	Exp. S2	Aggl % = 0.2	Exp. M2	Aggl % = 0.2	Exp. L2	Aggl % = 0.2	0.59
			RD = $3.5 \cdot 10^{-3}$	DF = 11.6	RD = $3.5 \cdot 10^{-3}$	DF = 12.1	Rd. = $3.5 \cdot 10^{-3}$	Df. = 11.8	
C	55 °C	1 bar	Exp. S3	Aggl % = 49.8	Exp. M3	Aggl % = 41.2	Exp. L3	Aggl % = 35.9	0.02
			RD = $24.5 \cdot 10^{-3}$	DF = 10.9	RD = $24.5 \cdot 10^{-3}$	DF = 12.0	Rd. = $24.5 \cdot 10^{-3}$	Df. = 12.0	
D	50 °C	3 bar	Exp. S4	Aggl % = 0.2	Exp. M4	Aggl % = 1.5	Exp. L4	Aggl % = 0.9	0.14
			RD = $3.5 \cdot 10^{-3}$	DF = 8.4	RD = $3.5 \cdot 10^{-3}$	DF = 8.9	Rd. = $3.5 \cdot 10^{-3}$	Df. = 8.6	
E	45 °C	3 bar	Exp. S5	Aggl % = 33.6	Exp. M5	Aggl % = 7.2	Exp. L5	Aggl % = 13.1	< 0.01
			RD = $3.5 \cdot 10^{-3}$	DF = 5.5	RD = $3.5 \cdot 10^{-3}$	DF = 6.4	Rd. = $3.5 \cdot 10^{-3}$	Df. = 6.8	
F	55 °C	1 bar	Exp. S7	Aggl % = 49.5	Exp. M7	Aggl % = 48.4	Exp. L7	Aggl % = 48.3	0.48
			RD = $24.5 \cdot 10^{-3}$	DF = 11.7	RD = $24.5 \cdot 10^{-3}$	DF = 11.9	Rd. = $24.5 \cdot 10^{-3}$	Df. = 11.8	

Comparing the agglomeration tendencies from the six scaling attempts, and the corresponding P-values from the χ^2 tests, indicates that successful scale-up is achieved in scaling attempt A, B, D and F all having agglomeration percentages far inside the ± 1.64 % range within each scaling attempt, and furthermore all having P-values above 0.05. This means that not only are the cut-off values corresponding to the agglomeration percentages matched across three scales, but, in addition, the different particle size fractions are identical on a 95 % confidence level. An example of how well the particle size classes are matched across scale may be seen from figure 8.1 showing a Rosin-Rammler-Sperling-Bennet plot of the particle size fractions from scaling attempt D. Interestingly, the best results are found with the glass ballotini core experiments in scaling attempt B and F. Here the tendency of agglomeration is closely reproduced across scale, and the P-values are far above 0.05 indicating high reproducibility of the particle size fractions. The glass ballotini cores may in many ways be seen as the ideal core material. Besides being almost perfectly spherical, glass ballotini cores are furthermore non-porous and so an issue such as droplet penetration is not likely to interfere with the tendency of agglomeration in the same complex manner as it may be the case with sodium sulphate cores. The comparison of scaling attempt A with B and attempt C with F indicate, however, that the agglomeration tendency is fairly similar on an overall level whether the core material is sodium sulphate or glass ballotini. The somewhat smaller agglomeration tendencies in the medium- and large-scale experiments in attempt C compared to attempt F may indicate that possible droplet penetration into the sodium sulphate cores could result in decreased tendency of agglomeration in accordance with other experiments by Hede (2005).

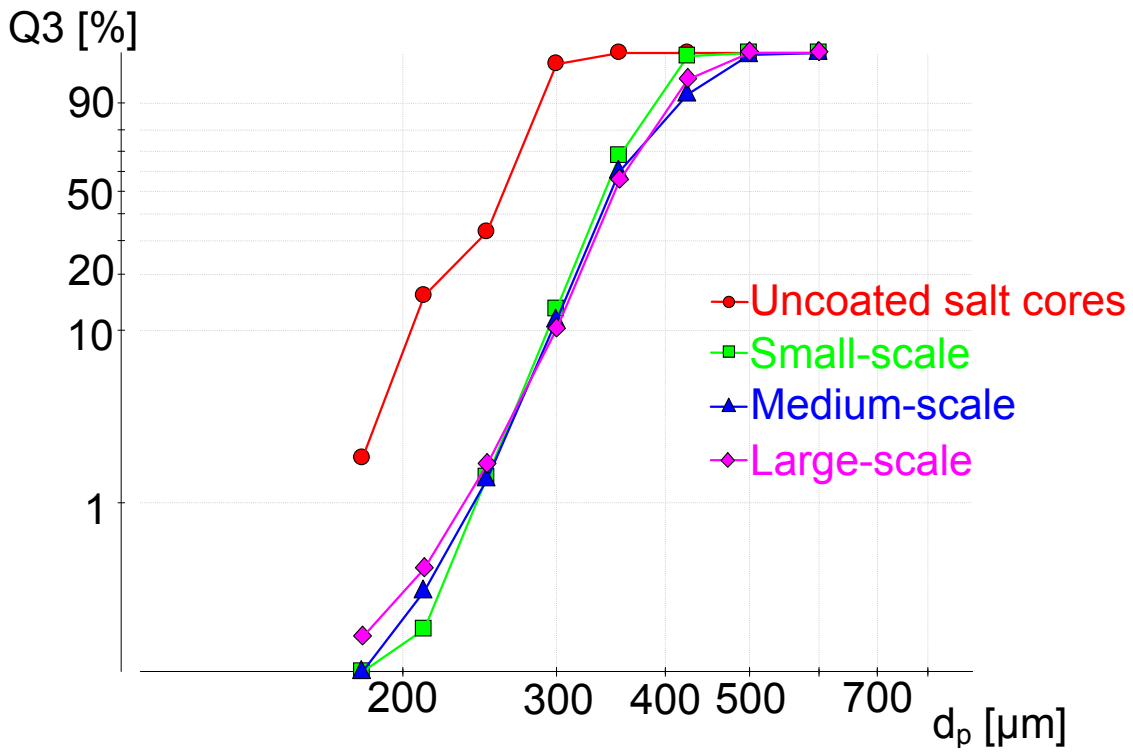

Figure 8.1: RRSB-plot (Rosin-Rammler-Sperling-Bennet) of particle size fractions from scaling attempt D. On the x-axis are the particle diameters and on the y-axis is the particle sum distribution Q3 in relation to particle volume.

The scaling attempts C and E are statistically unsuccessful as the agglomeration percentages are beyond the ± 1.64 % range. Likewise are the P-values from the χ^2 tests below the 0.05 limit although scaling attempt C is not far away with a P-value of 0.02. The scaling attempts

C and E are characterised by having a combination of a high Relative Droplet size and high Drying Force, and a combination of a low Drying Force and low Relative Droplet size, respectively, which means that the experiments could be in the extreme ends of the plausible range of the Drying Force and Relative Droplet size parameters. This could explain why these two scaling attempts are not successful while the others are.

8.3.3. Morphology and droplet penetration studies

Although maintaining the particle size distribution across scale is essential for most practical applications of fluid bed coating processes, issues such as the coating layer morphology and appearance may also have a significant importance regarding the final product properties. Morphology of the coating layer may not necessarily be identical just because the agglomeration tendency and particle size fractions are, and this may again strongly affect the mechanical properties of the granules as observed previously by Beekman (2000) and Hede et al. (2007a) among others. In order to test this, selected coated granule batches from all three scales were examined in optical microscope (Olympus KL 1500 LCD) and further by SEM (JEOL Scanning Electron Microscope).

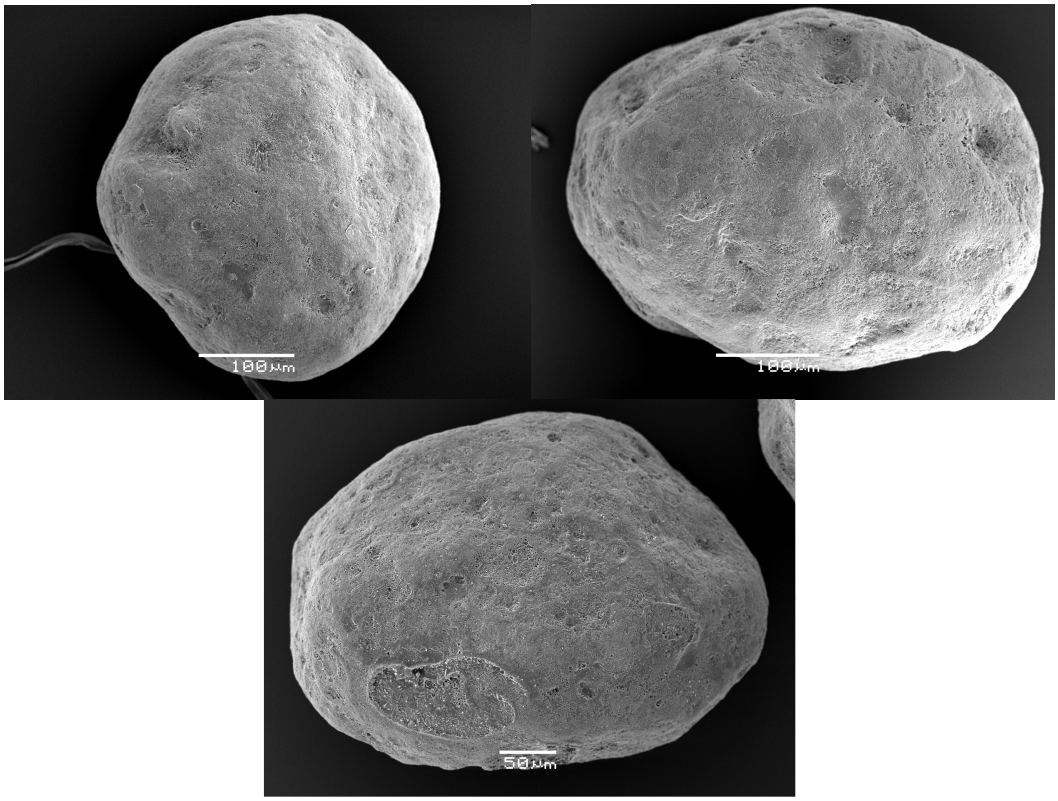

Figure 8.2: SEM pictures from scaling attempt A. Above left) Sodium sulphate core coated in small-scale. Above right) Sodium sulphate core coated in medium-scale. Below) Sodium sulphate core coated in large-scale.

An example of SEM pictures of sodium sulphate cores coated in three different fluid bed scales from the same scaling attempt A may be seen in figure 8.2. As observed, the morphology of the coating layer is relatively homogenous in all three cases and there is no significant difference in smoothness among the three batches. The coating layer structure of granules from the medium-scale batch M1 from the same scaling attempt A was furthermore examined in a number of cut-through profiles in SEM. As seen from a typical profile in figure 8.3, there are primarily amorphous regions in the coating layer with some crystalline regions.

The coating layer is well attached to the core structure and it is difficult to distinguish between the coating layer and the core. Good adhesion of the coating layer often implies good coating layer mechanical properties, which are almost always desirable for practical applications of coated granules (Beekman, 2000).

The process conditions used to coat the three granules in figure 8.2 and the granule in figure 8.3 have a high Drying Force and low Relative Droplet size. This indicates that the bed temperature was high and the average coating solution droplet diameter small during coating. That a high nozzle pressure and a high bed temperature lead to a strong and homogenous coating layer structure is in full accordance with previous fluid bed coating experiments performed by Hede et al. (2007a). Although one might have expected that large droplets and low bed temperature would be optimal conditions for the coating droplets to merge homogenously together on the core surface, there is now sufficient evidence to state that this is not likely to always be the case. Instead, it seems more optimal in terms of morphology to coat each particle with many small droplets that dry fast enough to produce an amorphous coating layer structure. These tendencies, however, have only been observed so far for relative dilute coating solutions with dry-matter contents not exceeding 15 w/w%. Probably, with such low dry-matter contents, a certain re-dissolution of the outer coating layer takes place upon impact with new droplets and this seems to have a beneficial effect on the compactness and homogeneity of the final coating morphology.

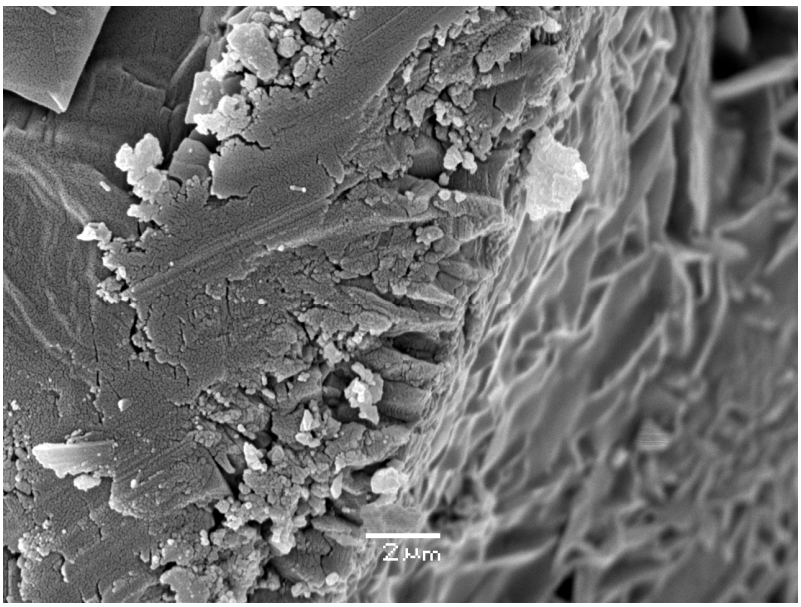

Figure 8.3: A typical cut-through profile of a coated sodium sulphate core from batch M1.

The effect of the Relative Droplet size and thereby the actual average droplet size on morphology was further studied by comparison of SEM pictures from experiment M2 and M7, in which only the Relative Droplet size was changed in medium-scale glass ballotini core experiments. As observed from figure 8.4, the effect of increasing the Relative Droplet size seven times, which corresponds to an increase in the Sauter mean droplet diameter (d_{32}) from roughly 8 µm to 21 µm estimated with the use of equation 2.1 (see chapter two), is quite clear. Although both granules have relatively smooth coating surfaces, the droplet footprints are significantly larger on the lowest photo. Apparently, the large droplets have not had sufficient time to merge homogenously together before complete drying. This slightly uneven coating may very well result in poor mechanical properties with possible chance of chipping off flakes of the coating layer upon granule impact. This is further investigated in section 8.3.4.

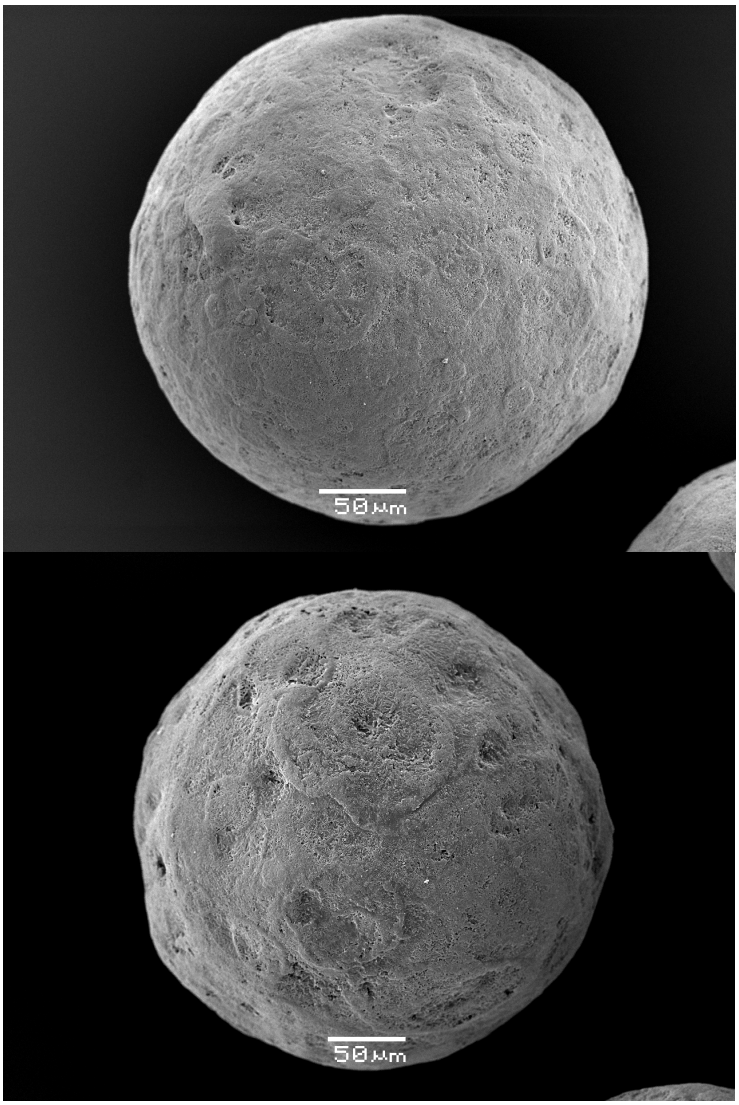

Figure 8.4: Effect of RD and actual average droplet size on coating layer morphology. Top) Coated glass ballotini core from experiment M2. Bottom) Coated glass ballotini core from experiment M7.

The influence of droplet penetration for the mechanical strength and morphology of a coating layer was observed by Hede et al. (2007a). In the present studies, cut-through samples of coated granules from scaling attempt A, C and E was examined in optical microscope. Although the conditions, under which the granules from these three scaling attempts were processed, are quite different, the level of droplet penetration was significant and similar in all cases. Typical cut-through pictures from batch S4 and M5 may be seen in figure 8.5. As observed, the blue colour from the coating solution has penetrated almost equally all through the otherwise white sodium sulphate core. As the composition of the coating liquid solution is similar throughout the experiments, the similar level of droplet penetration is in accordance with expectations (Hede, 2006). Results by Hede (2005) indicate that it is the viscosity of the coating solution that has the primary influence on droplet penetration, whereas parameters such as droplet size and bed temperature only play secondary roles in that respect.

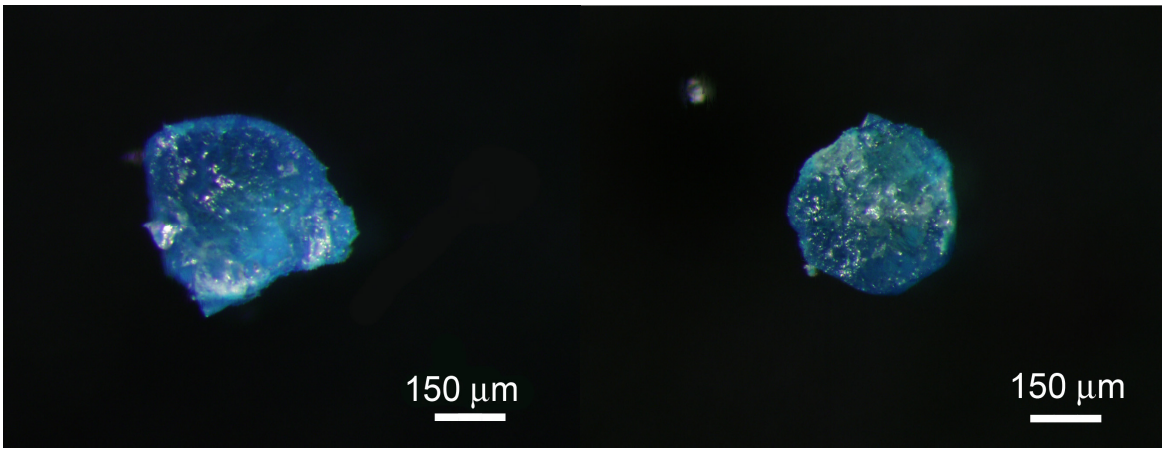

Figure 8.5: Cut-through samples of: Left) Coated sodium sulphate cores from experiment S4. Right) Coated sodium sulphate cores from experiment M5.

8.3.4. Impact and attrition strength test results

Mechanical strength tests in the form of impact and attrition tests were carried out for all the 18 batches according to the principles in section 5.2 (see chapter five). A schematic overview of the resulting impact strength and attrition results from the 18 batches may be seen from table 8-4. Note that the two rightmost columns show P-values from χ^2 tests performed on the three sets of attrition and PIG data, respectively, within the same scaling attempt. The choice to use χ^2 tests to determine whether or not the attrition and impact strength were repeated across scale was necessary due to the large spread in the values in table 8-4. As the strength values are widespread it is not possible to simply find a statistically sound standard deviation and to use this to determine how well the strength results are matched across scale, as was done statistically with the agglomeration data.

Table 8-4: Overview of the mechanical strength test results from the six scaling attempts. Scaling attempt B and F were carried out with glass ballotini cores whereas the other scaling attempts were done with sodium sulphate cores.

Scaling attempt	T_{bed} in °C	P_{nozzle} in bar	Strea-1 (small-scale)		MP-1 (medium-scale)		MP-2/3 (Large-scale)		P-value from χ^2 test of attrition tests	P-value from χ^2 test of PIG tests
			$Y_{Attrition}$	$Y_{Breakage}$	$Y_{Attrition}$	$Y_{Breakage}$	$Y_{Attrition}$	$Y_{Breakage}$		
A	55	3	0.06 %	4.6 %	0.04 %	14.2 %	0.09 %	11.1 %	0.12	< 0.01
B	55	3	0.20 %	7.6 %	1.26 %	8.1%	2.13 %	7.9 %	< 0.01	0.19
C	55	1	0.16 %	6.1 %	0.08 %	9.4 %	0.14 %	7.8 %	0.03	0.06
D	50	3	0.03 %	4.3 %	0.08%	10.5%	0.05%	8.3 %	0.09	0.01
E	45	3	0.05 %	6.5 %	0.07 %	10.1 %	0.15 %	11.0 %	< 0.01	0.02
F	55	1	0.40 %	5.9 %	3.38 %	7.1 %	5.85 %	6.3 %	< 0.01	0.14

Analysing the impact strength and attrition strength results separately in table 8-4 reveals several interesting things. It may be observed from table 8-4 that in only two scaling attempts A and D the attrition values are well matched across scale on a 95 % confidence level, as the P-values both exceed 0.05. These two scaling attempts have both used sodium sulphate cores as core material, and these two batches were the only ones with this core material that were

also successful in terms of matching the agglomeration tendency and particle size fraction in table 8-3. It is interesting that the successful match of attrition strength in scaling attempt A and D are associated with some of the lowest attrition values in table 8-4. This is most likely no coincidence. It is reasonable to expect that if two batches have granules highly resistant to attrition it will be much easier to match the amount of dust created compared to two batches that contains a higher proportion of weak granules. This is due to the fact that just a small portion of weak granules may unpredictably create relative large amounts of dust decreasing the chance of repeatable results.

Interestingly, the two scaling attempts B and F are unsuccessful regarding attrition. By far the worst attrition strength in table 8-4 is observed for the glass ballotini cores. As these cores are non-porous the coating droplets have no possibility to penetrate into the core structure and to build a cohesive structure to the same extent as with the sodium sulphate cores. Furthermore, it is reasonable to believe that the sodium sulphate coating attaches worse to glass ballotini cores than to sodium sulphate cores. This is likely to cause the poor attrition strength for these batches as is observed from table 8-4. As with scaling attempts B and F, the other scaling attempts C and E are unsuccessful towards the match of attrition strength. There is, however, one important overall tendency to extract from the scaling attempts B, C, E and F: It seems as if the attrition strength decreases with increasing scale meaning that the strongest granules are produced in the smallest scale. In a scale-up perspective this is an important discovery.

Regarding the match of impact strength across scale the tendencies in table 8-4 are somewhat the opposite of the attrition tendencies. It may be seen from the P-values in the right-most column in table 8-4 that the impact strength tendencies were matched well in scaling attempt B, C and F whereas all the other scaling attempts were unsuccessful in that respect. As discussed earlier those three scaling attempts B, C and F all failed in the attempt to reproduce attrition strength across scale. Two of these scaling attempts have used glass ballotini cores and so it seems as if the impact breakage mechanisms are more well-defined and thereby easier to reproduce if the core materials are glass ballotini cores instead of sodium sulphate cores. Although being in the high end of the observed impact strength tendencies, the breakage percentages for the scaling attempts B and F are not significantly larger than the breakage percentages observed for the sodium sulphate cores. In fact the impact strengths of the granules in scaling attempt F are among the best. Another interesting thing to note from table 8-4 is that in general the particles with the poorest impact strength are produced in the medium-scale whereas the coated granules with the best impact strength are produced in the small-scale. This means in all that granules coated in the small-scale fluid bed have the best attrition as well as the best impact strength.

Overall, the results in table 8-4 reveal an interesting general point, namely that good impact strength properties often mean poor attrition properties. The table also reveals that within a given fluid bed scale, a low agglomeration tendency gives granules with poor impact strength, but with good attrition properties although the tendency is not unambiguous. This may also be observed from figure 8.6 showing the measured $Y_{attrition}$ values versus the measured $Y_{breakage}$ values. Especially if the values for the small-scale fluid bed are left out a reciprocal tendency appears. Attrition mechanisms and failure due to impacts are in nature different, and from a theoretical point of view it seems reasonable that the two types of properties are inversely related. Whereas attrition often occurs as a result of gradual small-force wear (e.g. erosion, peeling or simply fatigue), fragmentation or chipping of the coating layer due to impacts on the other hand often occur at once and as a widespread damage phenomena (Beekman, 2000 and Pitchumani et al., 2003). This means that if a granule should be resistant to attrition,

surface cracks in the coating layer should not be able to propagate. This requires a dense homogenous coating layer as has been observed in the SEM pictures for the coated sodium sulphate cores. By correlating the observations from the SEM pictures with the attrition results in table 8-4, it seems reasonable to state that the attrition strength resistance increases with increasing homogeneity of the coating layer surface.

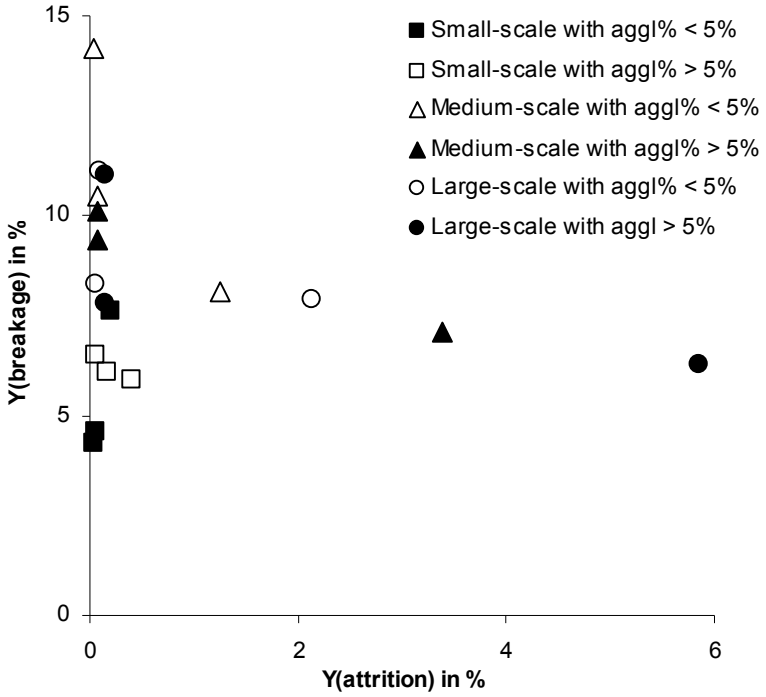

Figure 8.6: Graph showing the measured $Y_{attrition}$ values versus the measured $Y_{breakage}$ values.

High impact strength resistance is somewhat different from attrition strength resistance as it requires a hindrance of crack propagation not just in the coating layer, but also in the granule bulk phase. As the glass ballotini cores are denser and mechanically stronger compared to sodium sulphate cores, it is reasonable to expect a higher resistance towards crack propagation in the glass core structure than with the sodium sulphate cores. In accordance with this, the best impact strength tendencies are observed with the coated glass ballotini cores. Most likely more of the coating layer itself is removed upon impact compared to the coated sodium sulphate cores, due to a lower force of cohesion between the glass cores and coating layer as discussed earlier, but as the core structure remains relatively unaffected by the impacts, smaller amounts of fines is created on a weight basis. Thus a better impact strength value is observed for the coated glass ballotini cores, although this in reality does not necessarily mean that less of the coating layer is removed upon impact.

8.4. Conclusion

On an overall level, successful up-scaling of top-spray fluid bed coated particles by 48 times in weight from the small-scale over medium-scale to the large-scale fluid bed has been achieved. The tendency of agglomeration and particle size distribution were repeated across scale. Although two of the six scaling attempts were statistically unsuccessful with respect to agglomeration tendency, and clearly illustrates the limitations of the Drying Force and Relative Droplet size as universal scaling parameters, the scaling results presented in this paper are promising in terms of maintaining particle size fractions across scale. The best

results were achieved with non-porous highly spherical glass ballotini cores, but also statistically sound scale-up results were achieved with commercial sodium sulphate cores.

Studies of coated granules by SEM and by visual microscopy showed similar coating morphology across scale when the Drying Force and the Relative Droplet size were kept constant. Impact and attrition strength tests showed some scattering in the tendencies. The best impact strength tendencies were observed with the coated glass ballotini cores, whereas the best attrition strength values were observed with sodium sulphate cores coated under conditions with high bed temperature and high nozzle pressure. It was observed how high impact strength is often inversely related to high attrition strength.

The results presented in this paper suggest that two parameters should be kept constant during scale-up: A Drying Force parameter combining bed temperature with humidity conditions inside the fluidisation chamber during steady state coating conditions, and a Relative Droplet size parameter relating the liquid nozzle feed rate to the nozzle atomisation airflow. The present scale-up attempts thereby focus on nozzle conditions as well as on temperature and humidity conditions during steady state coating – all properties known to be of major importance regarding agglomeration tendency and coating layer properties. The paper further propose that nozzle conditions are fixed throughout the coating process and that conditions inside the fluidisation chamber are adjusted only in terms of the inlet air temperature.

Scale-up in terms of combined Drying Force and Relative Droplet size is a new proposal involving both the particle-level and the unit-operation scale perspective on fluid bed coating. The principles presented in this paper provide simple engineering principles for scale-up of fluid bed coating processes.

8.5. Table of symbols

Symbols		Unit
A	Constant	Dimensionless
B	Constant	Dimensionless
d_{32}	The Sauter mean droplet diameter	µm
d_{dr}	Droplet diameter	µm
DF	Drying Force	kPa
$\dot{m}_{nozzle\ air}$	Atomisation air mass flow rate	kg/s
$\dot{m}_{spray}$	Coating solution mass spray rate	kg/s
P_{sat}	Saturated vapour pressure	Pa
RD	Relative Droplet size	s/kg or min/g
v_{rel}	The difference between the nozzle atomisation air velocity and the liquid velocity at the nozzle outlet	m/s
$Y_{Attrition}$	Attrition percentage parameter	Dimensionless
$Y_{Breakage}$	Breakage percentage parameter	Dimensionless
Greek		
α	Function of nozzle design	Dimensionless
β	Function of nozzle design	Dimensionless
ρ_{air}	Atomisation air density	kg/m^3

8.6. References

Beekman, W.J. (2000) Measurement of the Mechanical Strength of Granules, Ph.D. Thesis, Technische Universiteit Delft.

Gwyn, J.E. (1969) On the Particle Size Distribution Function and the Attrition of Cracking Catalysts, AIChE Journal, Vol. 15, No.1.

Hapgood, K. (2000) Nucleation and binder dispersion in wet granulation, Ph.D. Thesis, University of Queensland.

Hede, P.D. (2005) Fluid bed coating and granulation, M.Sc. Thesis, Department of Chemical Engineering, CHEC Research Center, Technical University of Denmark.

Hede, P.D. (2006) Towards Mathesis Universalis: Modern aspects of modelling batch fluid bed agglomeration and coating systems –a review, Department of Chemical Engineering, Technical University of Denmark, pp. 1-101.

Hede, P.D., Bach, P. and Jensen, A.D. (2007a) Small-scale top-spray fluidised bed coating: Granule impact strength, agglomeration tendency and coating layer morphology, Powder Technology, No. 176, pp. 156-167.

Hede, P.D., Bach, P. and Jensen, A.D. (2008b) Top-spray fluidised bed coating: Scale-up in terms of Relative Droplet size and Drying Force, Powder Technology, No. 184, pp. 318-332.

Litster, J.D., Hapgood, K.P., Michaels, J.N., Sims, A., Roberts, M. and Kameneni, S.K. (2002) Scale-up of mixer granulators for effective liquid distribution, Powder Technology, No. 124, pp. 272-280.

Litster, J.D. (2003) Scaleup of wet granulation processes: Science not art, Powder Technology, No. 130, pp. 35-40.

Mehta, A.M. (1988) Scale-up considerations in the fluid-bed process for controlled-release products, Pharmaceutical Technology, No. 12, pp. 46-52.

Pitchumani, R., Meesters, G.M.H. and Scarlett, B. (2003) Breakage behaviour of enzyme granules in repeated impact test, Powder Technology, No. 130, pp. 421-427.

Rambali, B., Baert, L. and Massart, D.L. (2003) Scaling up of the fluidized bed granulation process, International Journal of Pharmaceutics, No. 252, 197-206.

Chapter 9. Heat and mass transfer modelling of fluid bed coating

Chapter introduction

Chapter nine concerns the scale-up of the top-spray salt coating process in terms of a dynamic heat and mass transfer lumped-region model being set up and implemented into Matlab. On the basis of selected experiments from chapter six to eight, model simulations are performed in order to validate the model and to obtain detailed scale-up insight. Furthermore, simulations of a 900 kg production-scale fluid bed are made and valuable conclusions regarding scale-up in general are drawn.

The present chapter is published as a peer-reviewed scientific paper in the journal *Chemical Engineering Science*, Vol. 64, No.6, pp. 1293-1317, 2009 and is entitled: *Batch top-spray fluid bed coating: Scale-up insight using dynamic heat and mass transfer modelling* authored by Peter Dybdahl Hede (Technical University of Denmark), Poul Bach (Novozymes A/S) and Anker D. Jensen (Technical University of Denmark). The paper is referred to as Hede et al. (2008g). The following sections are exact reproductions of the published paper, although the format has been adapted to that of this thesis.

9. Batch top-spray fluid bed coating: Scale-up insight using dynamic heat and mass transfer modelling

Abstract

A mathematical model was developed for batch top-spray fluid bed coating processes based on Ronsse et al. (2007a,b). The model is based on one-dimensional discretisation of the fluid bed into a number of well-mixed control volumes. In each control volume, dynamic heat and mass balances were set up allowing the simulation of the contents of water vapour, water on core particles and deposited coating mass as well as fluidisation gas, particle and chamber wall temperature. The model was used to test different scale-up principles by comparing simulation results with experimental temperature and humidity data obtained from inorganic salt coating of placebo cores in three pilot fluid bed scales being a 0.5 kg small-scale (GEA Aeromatic-Fielder Strea-1), 4 kg medium-scale (GEA Niro MP-1) and 24 kg large-scale (GEA MP-2/3). Results show good agreement between simulated and experimental outlet fluidisation air temperature and humidity as well as bed temperature data. Simulations reveal that vertical temperature and humidity gradients increase significantly with increasing scale and that in fluid beds as the simulated 900 kg (RICA-TEC Anhydro) production-scale, the gradients become too large to use the simple combined Drying Force/Relative Droplet size scale-up approach without also increasing the inlet fluidisation air temperature significantly. Instead, scale-up in terms of combinations of the viscous Stokes theory with simulated particle liquid layer profiles (obtained with the model) is suggested. In this way, the given fluid bed scale may be optimised in terms of low agglomeration tendency for a given process intensity across scale.

9.1. Introduction

In the chemical and pharmaceutical industry sensitive biological solid products, such as enzyme containing granules, are often produced by coating the active ingredient onto inactive filler cores in fluid beds. The desired product thereby consists of unagglomerated individual carrier particles each coated homogeneously with a layer of the active ingredient. Besides being able to maintain and protect the activity of the active ingredient, process optimisation often goes in the direction of finding correct formulation and process conditions in order to balance between excessive agglomeration and excessive spray drying of the feed (van Ee et al., 1997). If either of the phenomena is dominant, a poor product quality is achieved. In any case, control of agglomeration is essential during scale-up and this is known to be closely connected to the humidity and temperature inside the fluidisation chamber during the process (Hede et al., 2008b). For the sake of activity of the active ingredient, control of the humidity and temperature throughout the coating process is likewise of utmost importance (van Ee et al., 1997).

In industry, product and process properties are typically optimised in small- and medium-scale pilot fluid beds and then transferred to production-scale. The scale-up of a fluid bed granulation process requires decisions to be made at many levels, including: fixed parameters (e.g. nozzle and fluidisation chamber dimensions), parameters related to the core material (such as price, composition, porosity, sphericity and more), coating solution (e.g. viscosity, work of adhesion and more) and the type of fluid bed, input parameters, operating conditions including spray and fluidisation conditions as well as processing time etc. With such a variety of interlinked parameters and properties, combined with a lack of quantitative understanding of the granulation process, it is obvious that scale-up of a fluid bed granulation process is a challenging task (Hede et. al., 2008a,b).

Up-scaling of fluid bed processes is a common industrial engineering exercise and up to now the field has not had much academic interest. Typically, the task goes in the direction of matching first of all the particle size distribution across scale and, secondly, if possible at the same time, to maintain a high-intensity process during scale-up. Other scale-up targets include morphology and appearance as well as mechanical properties of the final coating layer (van Ee et al., 1997). As reviewed by Hede (2006) advances in scaling principles are often done in industry and typically only reach the public in the form of patents. Recent papers by e.g. Rambali et al. (2003), Boerefijn & Hounslow (2005) and Hede et al. (2008a,b) indicate some progress in the field although the scale-up procedures are somewhat different. Mort (2005) suggests that scale-up of wet-granulation processes should focus on combined particle-level and unit-operation-level properties and variables. Hede et al. (2008b) followed these trends by suggesting scale-up in terms of a combined Drying Force and a Relative Droplet parameter explained in detail later (see equation 9.2 and 9.3). These principles focus especially on temperature and humidity conditions as well as on nozzle conditions. However, there are also limitations to the application of these scale-up principles in terms of keeping the agglomeration tendency as low as possible at maximum process intensity. The Flux Number (see equation 9.4) suggested by Akkermans et al. (1998) is a different approach as the primary focus here is the balance between the particle flux in the spray zone and the liquid spray flux that wets the solids. The validation of the Flux Number by Hede et al. (2008a) indicate that it does not perform as good, with respect to agglomeration tendency, as the principles by Hede et al. (2008b) in the context of coating placebo cores with inorganic salt solutions. Nevertheless, neither of these simple scale-up principles provides detailed insight into the processes and conditions inside the bed. It is believed that temperature and humidity profiles

play an important role, but it is difficult to obtain detailed experimental insight into how these variables distribute vertically through the bed. Typically, the bed temperature is measured at one location only and the adjustment of the inlet fluidisation air temperature is based on this single measurement. It is hereby assumed that the measured temperature is representative for the entire bed which is not necessarily the case.

It is the aim of this paper to investigate the scale-up of top-spray fluid bed coating processes. Selected experimental data from previous (scale-up) studies by Hede et al. (2008a,b) are chosen, and simulations are performed in order to be able to explain the agglomeration outcome for these experiments. Simulations are done in terms of a thermodynamic heat and mass transfer model by which it becomes possible to obtain steady state temperature and humidity profiles as well as particle moisture profiles vertically through the bed. Viscous Stokes theory is applied in order to link the simulation and experimental data with a mechanistic particle-level agglomeration model.

9.2. Model

Results by Maronga & Wnukowski (1998) indicate that the temperature and humidity during the coating process in a top-spray fluid bed vary significantly with radial and especially vertical position. During the coating process, pockets of low temperature and high humidity are formed deep inside the bed, causing temperature fluctuations. Based on these systematic fluctuations, the top-spray fluid bed is suggested to be formally divided into four zones, which can be seen in figure 9.1 (Maronga & Wnukowski, 1998).

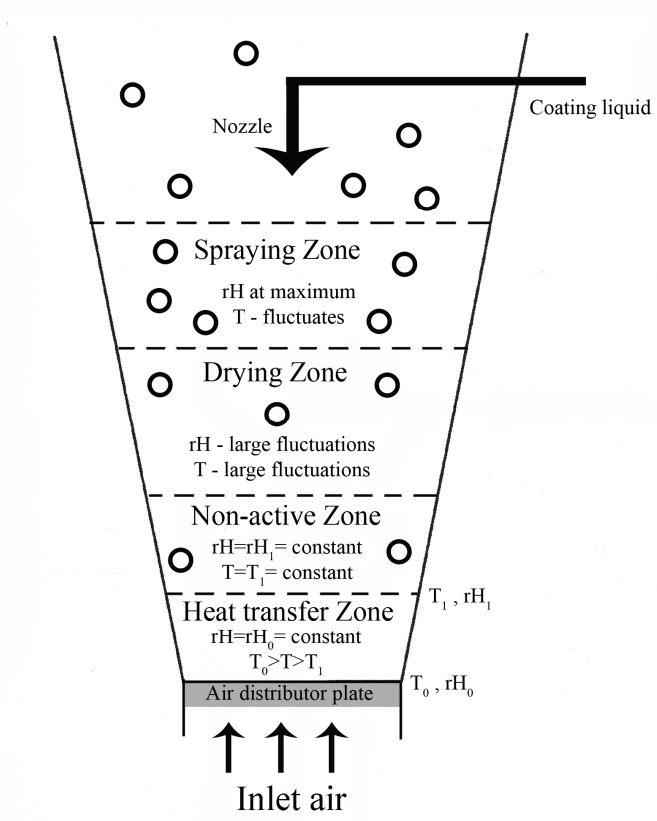

Figure 9.1: Zones in a top-spray fluid bed during steady state coating (Based on Maronga & Wnukowski, 1998). The sizes of the zones are not to scale.

The experimental results obtained by Maronga & Wnukowski (1997b) among others have formed the basis for a recent dynamic heat and mass transfer model suggested by Ronsse (2006) and Ronsse et al. (2007a,b). The model is capable of describing the temperature, humidity and coating mass concentration fields along the vertical axis of the coating process in a top-spray fluidised bed. This simple model approach fulfils the industrial needs for an intuitive model that captures only the most important phenomena during the coating process at the same time allowing short calculation times and results that can be straightforwardly interpreted and used for direct comparison with experimental data.

The model being set up and tested in the present paper is essentially the same model as presented by Ronsse et al. (2007a). The model is based on one-dimensional vertical discretisation of the fluid bed into a number of well-mixed control volumes. In each control volume, dynamic heat and mass balances are set up allowing the simulation of the contents of water vapour, water on core particles and deposited coating mass as well as fluidisation gas, particle and chamber wall temperature. The model furthermore accounts for heat losses to the external environment. However, the original Ronsse model was not developed in a scale-up context and we have carefully reviewed, modified and slightly expanded the model in order to be better able to predict process changes at different fluid bed scales. The model tested in the present paper is presented in its full form in appendix A and the associated assumptions are presented in the section below.

9.2.1. Model assumptions

Being a one-dimensional model, the basic principle is to divide the fluidised bed vertically into n control volumes from the bottom air distributor plate and up to the nozzle outlet, each having the same height of $h_{S,i} = h_{FB}/n$. Most fluid beds have frustum shapes where the diameter is smallest at the bottom plate and largest at the spray zone, which obviously affects the fluidisation air velocity in m/s in vertical direction. In a model perspective, this means that the upper and lower diameters are different for each control volume which is accounted for in the present model. The control volumes are numbered from 1 to n where the first control volume is nearest the fluidisation air distributor plate.

It is assumed that the droplets containing the coating solution have only a limited penetration depth into the bed, and consequently, that particle-droplet contact takes place only in a certain upper part of the volume of the fluidised bed (Maronga & Wnukowski, 1997a). Therefore, two types of control volumes are assumed to exist being non-coating and coating control volumes. Numbering the coating control volumes with the integer c means that out of n control volumes in total, c are coating control volumes and n-c are non-coating control volumes. It is assumed that each coating control volume receives a fraction $\dot{M}_c/c$ of the coating liquid. It is furthermore assumed that all of the sprayed coating solution is collected on the particles without premature droplet evaporation, and that the liquid is uniformly deposited on all particles in each coating control volume. A schematic representation of the model principle can be seen from figure 9.2.

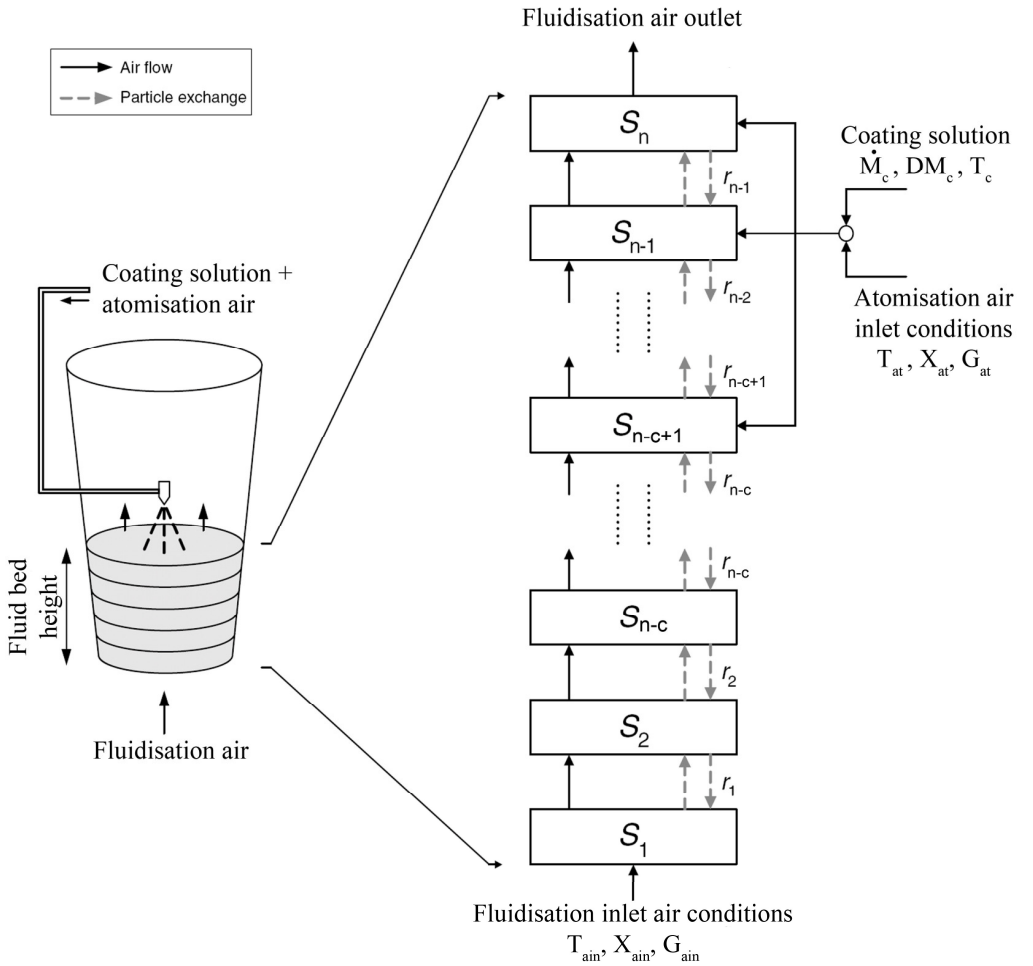

Figure 9.2: Schematic representation of the overall model principle (Based on Ronsse et al., 2007a).

A number of other assumptions are made being:

- Particles and air in each control volume (being coating or non-coating) are perfectly mixed. This means that the temperature and moisture content is the same for all particles in a control volume. It further implies that moisture and temperature is instantaneously exchanged when particles and air enter a new control volume.

- All particles have the same diameter d_p.

- Both the size of each control volume and the number of particles contained in each control volume are constant at all times.

- The weight of the coating mass added to each particle is small compared to the weight of the particle itself. Consequently, the weight of each individual particle is assumed constant throughout the process. Similarly, the thickness of the deposited coating film is small compared to the particle diameter, therefore the particle diameter is assumed to be constant. The coating deposition is assumed not to affect fluidisation properties.

- Particles are mechanically strong; there is neither attrition nor agglomeration. This means that neither coating material nor core material can be exhausted during the process.

- The air exhaust is at atmospheric pressure. The pressure drop across the fluidised bed is small compared to the overall atmospheric pressure. Consequently, the drying process is assumed to take place at constant atmospheric pressure.

- The atomisation air specific heat capacity, $C_{p,at}$, and the moist air specific heat capacities from two adjacent control volumes, $C_{p,a,i}$ and $C_{p,a,i-1}$, are assumed to be independent of temperature and assumed for a given control volume to be represented by $C_{p,a,i}$.

- Considering the diameter range of both droplets ($0 \leq d_{dr} \leq 50$ μm) and particles (100 μm $\leq d_p \leq$ 500 μm) the following conditions may be assumed according to Ronsse (2006):

$$Bi_p = \frac{\alpha_p \cdot d_p}{\lambda_p} << 0.1 \text{ and } Bi_{dr} = \frac{\alpha_{dr} \cdot d_{dr}}{\lambda_{dr}} << 0.1$$

  As a consequence of the small Biot numbers, the internal heat transfer in both the particles and the droplets are negligible compared to the convective heat transfer resistance at the particle surface. Hence, it is assumed that each droplet and each particle are isothermal and can be represented as having a single uniform temperature.

Another basic assumption is that the rate at which particles are transferred from control volume S_i towards its neighbouring control volume S_{i+1} (or S_{i-1}) equals the particle transfer rate from S_{i+1} (or S_{i-1}) towards S_i. The rate at which particles are exchanged is expressed by r, as the fraction of the particle population exchanged between neighbouring control volumes S_i and S_{i+1} per time unit. Estimating a reasonable value for r over all of the control volume boundaries is not an easy task. Ronsse et al. (2007a) estimated for a Glatt GPCG-1 fluid bed values between 0.81 and 1.82 s^{-1} based on experiments performed by Mostoufi & Chaouki (2001). For simplicity, Ronsse et al. (2007a) chose a fixed value of 1.4 s^{-1} irrespectively of fluidisation conditions. Alternatively, the exchange rate r may be calculated from theoretical considerations based on the average particle circulation time τ_c for which an estimation has been proposed by Rowe (1972) for bubbling fluid beds according to equation 9.1:

$$r = \frac{1}{\tau_c} = \frac{0.6 \cdot (v_a - v_{mf}) \cdot (1 - (v_a - v_{mf})/v_{bu})}{h_{mf}} \tag{9.1}$$

In the present study, the choice was to let r vary as a function of the fluidisation conditions according to equation 9.1, instead of fixing a single value for r for all simulations. The value for v_a was always chosen to be the value in the middle of the fluidisation chamber. It was assumed that the exchange rate was constant across all control volumes, and h_{mf} values were estimated from guidelines presented by Hede et al. (2008a). These values can be seen in table 9-1. For the tested fluidisation conditions in the three fluid bed scales tested, r values ranged between 2.26 s^{-1} and 2.70 s^{-1} for the small-scale, between 1.47 s^{-1} and 2.83 s^{-1} for the medium-scale and between 1.01 s^{-1} and 1.09 s^{-1} for the large scale. It seems reasonable that the r values are largest the smaller the fluid bed scale, as the average time of circulation τ_c is known to increase with scale (Rowe, 1972).

9.3. Model validation

9.3.1. Experimental validation set-up

Model validation data were obtained with commercial top-spray fluid beds in three pilot scales being a small-scale GEA Aeromatic-Fielder Strea-1, a medium-scale Niro-Aeromatic Multiprocessor type MP-1 and a large-scale GEA Aeromatic-Fielder MP-2/3. Set-up details and the principles of operation for these three fluid beds have been treated in detail elsewhere (Hede et al., 2007a & 2008a,b) (see also chapter five). Figure 9.3 shows a sketch of the physical dimensions of the fluid beds and table 9-1 summarises the important process conditions under which the validation experiments were carried out. Other process and physical parameters kept constant during all simulations may be seen in appendix B.

In all three experimental fluid bed set-ups a Testo 645 Thermohygrometer (combined humidity and temperature probe) was located just above the nozzle measuring the outlet fluidisation gas relative humidity and temperature. The uncertainty of the Thermohygrometer was ± 1 rH%, ± 1 ºC, while the uncertainties of the other temperature probes were ± 2 ºC.

Table 9-1: Process- and model-related parameters for the present study.

Process parameter	**Small-scale Strea-1**	**Medium-scale MP-1**	**Large-scale MP-2/3**
Type of nozzle	External mixing two-fluid	External mixing two-fluid	External mixing two-fluid
Liquid orifice diameter	1.2 mm	1.2 mm	1.2 mm
Fluidisation velocity (Simulation of the Flux Number exp.)	82 Nm^3/hr ~ 1.0 m/s at the top of the expanded bed height ~ r = 2.26 s^{-1}	137 Nm^3/hr ~ 1.0 m/s at the top of the expanded bed height ~ r = 1.47 s^{-1}	651 Nm^3/hr ~ 1.0 m/s at the top of the expanded bed height ~ r = 1.01 s^{-1}
Fluidisation velocity (Simulation of the DF/RD number exp.)	93 Nm^3/hr ~ 3.3 m/s 4 cm above the air distributor plate ~ r = 2.58 s^{-1}	270 Nm^3/hr ~ 3.3 m/s 4 cm above the air distributor plate ~ r = 1.98 s^{-1}	680 Nm^3/hr ~ 3.3 m/s 4 cm above the air distributor plate ~ r = 1.09 s^{-1}
Bed height at minimum fluidisation (h_{mf})	6 cm	13 cm	26 cm
Initial core bed load	0.5 kg	4 kg	24 kg
Diameter of the orifices in the air distributor plate	3 mm	3 mm	Stainless steel wire frame with mesh orifices of 90 µm ~ Porous air distr. plate
Number of orifices in the air distributor plate	92	260	
Coating solution dry-matter contents	10 – 30 w/w%	15 w/w%	15 w/w%
FB dimensions			
Length a	10 cm	17 cm	27 cm
Length b	10.5 cm	6 cm	11 cm
Length c	18 cm (at 3 bar)	32 cm (at 3 bar)	37 cm (at 3 bar)
Length d	27 cm	57.5 cm	81 cm
Length e	31 cm	48.5 cm	63 cm
Length f	15 cm	28 cm	82 cm
Length g	25 cm	29 cm	64 cm
Length h	18 cm	93 cm	270 cm
Model-related parameters			
Total number of control volumes	18 ~ $h_{S,i}$ = 1.5 cm	38 ~ $h_{S,i}$ = 1.5 cm	54 ~ $h_{S,i}$ = 1.5 cm
Number of coating control volumes	12 (P_{nozzle} = 3 bar) 9 (P_{nozzle} = 1 bar)	21 (P_{nozzle} = 3 bar) 15 (P_{nozzle} = 1 bar)	25 (P_{nozzle} = 3 bar) 18 (P_{nozzle} = 1 bar)
Bed temperature measurement corresponds to control volume number:	7	4	7

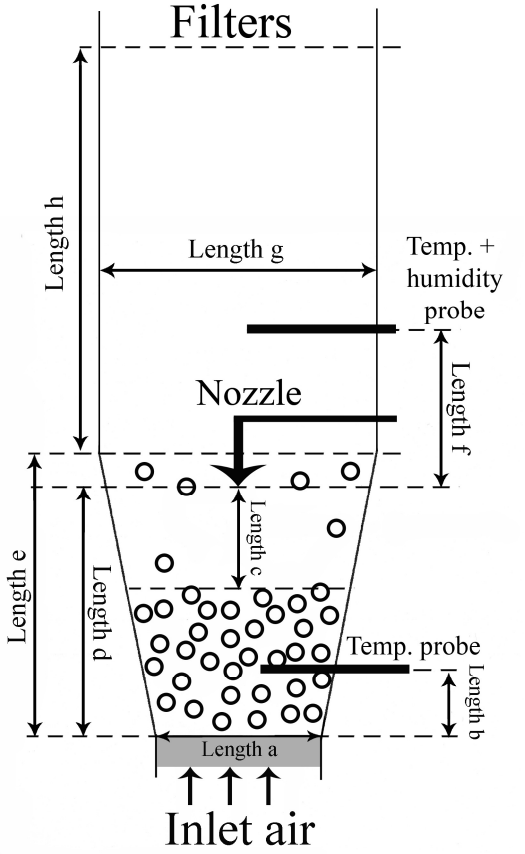

Figure 9.3: Sketch of the fluid bed dimensions for the three fluid bed scales. Length dimensions corresponding to the symbols in the figure are stated in table 9-1.

Choosing a control volume height of $h_{S,i}$ = 1.5 cm for all three fluid beds ensured a sufficient high number of control volumes without extending the computational time unnecessarily. Initially, simulations for the small-scale fluid bed showed that the results depended on the number of control volumes up to roughly n = 14. A number of 18 control volumes for the small-scale fluid bed thus ensured simulation results being independent of the number of control volumes. As a consequence of the choice of $h_{S,i}$, the other fluid bed scales were assigned a larger number of control volumes than the small-scale, and problems with the result-dependence of n were not observed for these scales.

Assigning the right number of control volumes to be coating control volumes is likely to be important with respect to the comparison of the simulated bed temperatures with the experimentally determined values. The outlet conditions should obviously be less affected by the assignment. In simulations by Ronsse (2006) a fixed value of c/n = 0.125 was chosen based on considerations for that particular fluid bed scale made by Dewettinck (1997). Based on detailed temperature and humidity studies, Maronga & Wnukowski (1997a,b & 1998) however concluded that the spray zone in practice often is significantly larger, especially for small fluid beds. In the present paper, estimations of the c/n ratio were made based on experimental observations from empty vessel nozzle operations combined with spray fan depth estimations made during coating experiments. Although empirical, these estimations do not conflict with results by Maronga & Wnukowski (1997a,b & 1998) and it would be in contradiction with observations to assign a single c/n value for all three scales. The estimated c/n values range from 0.66 for the small-scale to 0.46 for the large-scale at a nozzle pressure of 3 bar, and correspondingly, from 0.50 to 0.33 at a nozzle pressure of 1 bar. Notably, the

decreasing ratio of c/n with increasing scale illustrate a general latent problem with fluid bed coating scale-up being that the spray zone characteristics are not kept constant during scale-up. This is discussed further in section 9.4.2.

Hede et al. (2008a,b) concluded that the best practical principle to run a fluid bed coating process in general is by fixing nozzle conditions a-priori (i.e. fixing both the coating solution and atomisation air mass flow rates), choosing a level for the bed temperature and maintain these conditions throughout the coating process by adjusting initially in the process only the inlet fluidisation air temperature in order to reach the target bed temperature. All other process conditions, including the fluidisation velocity, should be fixed and chosen a-priori. These principles of operation were chosen for all validation experiments in the present paper. In all cases, the experimental conditions obtained under steady state were the ones to be compared with the simulation results.

9.3.1.1. Materials

Sodium sulphate cores pre-sieved twice in the size range of 180 – 350 μm were used as core material (see also chapter five). The sodium sulphate cores were coated with aqueous solutions of sodium sulphate in the amount of 10 - 30 w/w% using 1 w/w% (of the amount of sodium sulphate) Dextrin as binder. Demineralised water was used as solvent. More information about the salt coating process may be found in Hede et al. (2008d,e,f) (see chapter ten).

9.3.2. Calculation procedure

The model consists of six times n coupled ordinary differential equations (ODE´s): One equation for each of the six main variables to be calculated for each control volume S_i as a function of time. The six main variables are the deposited coating mass, $Y_{p,i}$, the particle surface temperature, $T_{p,i}$, the particle water contents, $W_{p,i}$, the gas phase temperature, $T_{a,i}$, the gas phase water contents (absolute humidity), $X_{a,i}$, and the control volume wall temperature, $T_{w,i}$. A number of the parameters and properties in these ODE´s are functions of one of more of the six parameters and they are calculated in a number of functions. The connections between the independent and the dependent variables are thus complex, and it not possible to obtain an analytical solution to the system of ODE´s. Thus a numerical solution procedure is required.

The numerical solution is aided by implementing the ODE system in Matlab version 2007a (The MathWorks Inc., US) using the ode15s standard Matlab solver (see also Shampine & Reichelt, 1997). When allowing Matlab to choose its own value for the step size, Δt, and setting the error value to 10^{-6}, a typical simulation example from $t_0 = 0$ to $t_{end} = 800$ s in the medium-scale fluid bed with 38 control volumes, whereof 21 are coating control volumes, takes roughly 15 minutes to complete on a 1.86 GHz, 512 MB of RAM, Pentium M (two single-core 32-bit x86 microprocessors).

9.3.3. First validation of steady state data – matching the outlet and product temperature as well as the outlet humidity in three pilot-scale fluid beds

For the validation of the model, steady state simulation results were compared with the measured values of the outlet fluidisation air temperature and outlet relative humidity. This was done for 35 fluid bed experiments in total in three fluid bed scales. The data was adapted from Hede et al. (2007a & 2008a,b,d). Assuming that the outlet conditions are equal to the conditions in the last upper control volume, it was possible to compare the simulated temperature and humidity with the experimentally determined values for a broad range of different process conditions, ranging from high to low process-intensity. Depending on the process intensity, the difference between the bed temperature and the outlet temperature typically ranged between 2 and 8 ºC. The experimentally measured outlet temperatures and humidities are compared to the values obtained from the simulations in as shown in figure 9.5 and 9.6, respectively.

In addition, the model predictions of the bed temperature were compared to experimental data at the location where the temperature probe was located, as shown in figure 9.4. As observed from table 9-1, these locations are different from fluid bed scale to fluid bed scale thus giving valuable indication of the performance of the model.

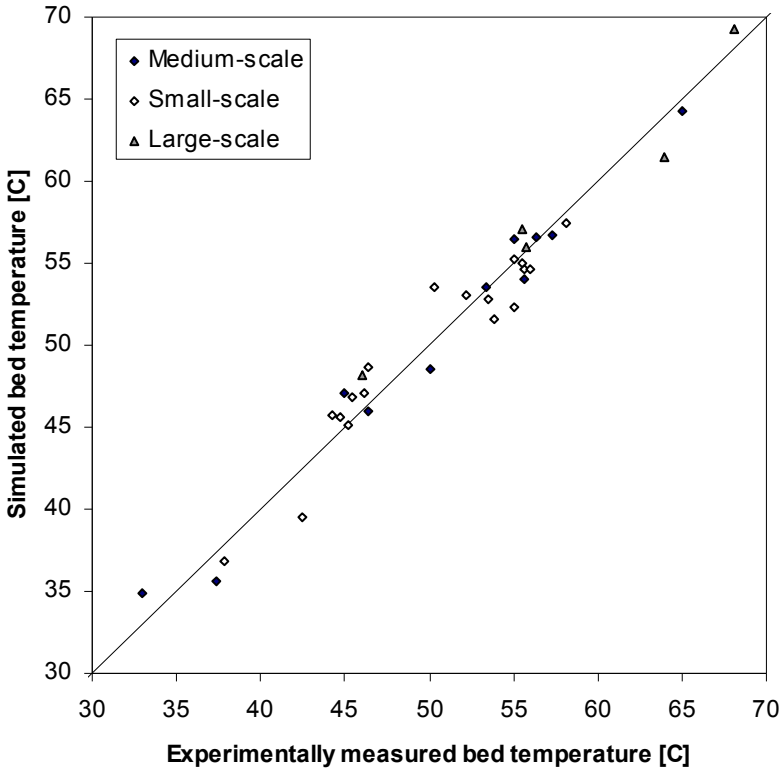

Figure 9.4: Simulated versus experimentally measured steady state bed temperatures.

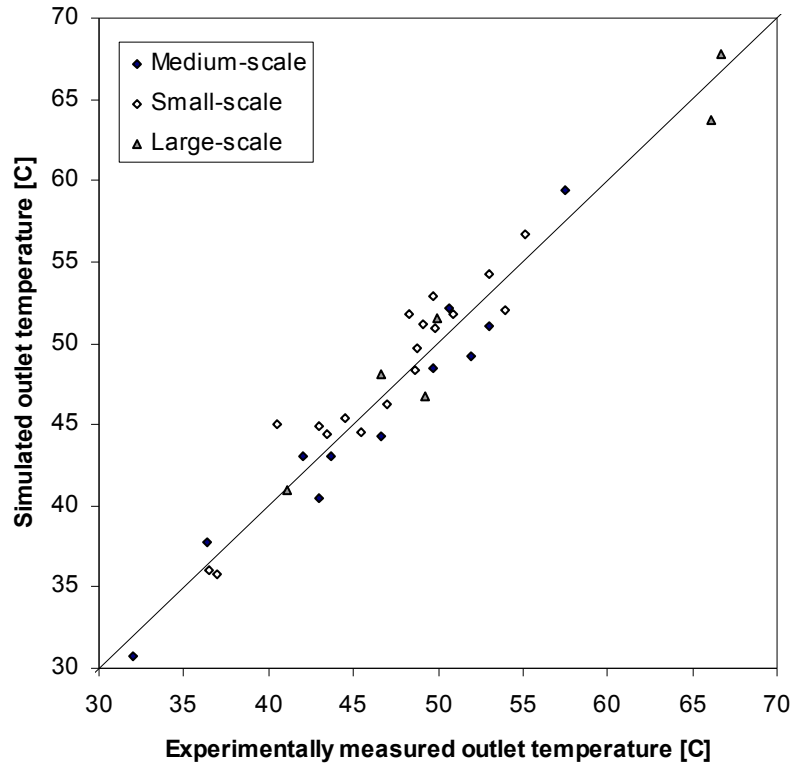

Figure 9.5: Simulated versus experimentally measured steady state outlet temperatures.

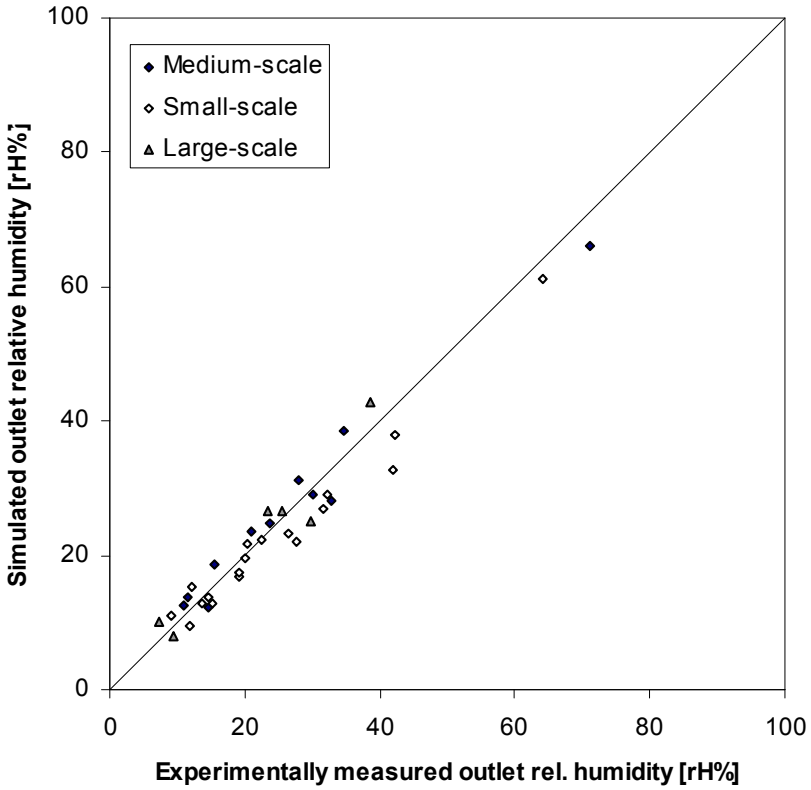

Figure 9.6: Simulated versus experimentally measured steady state outlet relative humidity values.

Figure 9.4 – 9.6 show in general a good agreement between model and experimental values for all three variables. Although some scattering is observed in all three plots, the data points distribute equally well on both sides along the straight line for the entire intervals, indicating that no systematic errors are apparent. This illustrates that the basic thermodynamics, including heat loss, is well accounted for in the model.

The best fit between model and experimental results is observed for the bed temperatures in figure 9.4. The bed temperature probes are for all three scales located deep within the bed at a safe distance from the spray zone. Being close to the bottom inlet and away from the assigned coating control volumes, the chance of cumulated calculation error, e.g. due to the simplicity of the heat loss terms in the model versus the actual heat loss, is thus small in the calculation of the fluidisation air temperature in the control volumes, which are used in the comparison with measured bed temperatures. In light of the chance of cumulated errors in vertical direction, the relations in figure 9.5 and 9.6 between model and experimentally measured outlet conditions are satisfactory.

It is furthermore observed from figure 9.4-9.6 that the model is capable of predicting conditions equally well ranging from high- to low-process-intensity coating operations giving credit to the model. In addition, the model performs observably just as well with the small- and medium-scale as with the large-scale, making it reasonable to use the model in a scale-up context.

9.3.3.1. Dynamic behaviour

A typical start-up situation in the medium-scale was selected with conditions according to table 9-2 in order to test the dynamic behaviour of the model. Before the nozzle is switched on, the particles are normally heated by the fluidisation air at an inlet temperature close to what is believed to be the correct inlet temperature for the spray phase. The heating process is typically maintained until the system reaches steady state where the outlet relative humidity is usually only a few rH% and the bed and outlet temperatures are close to that of the inlet temperature.

Table 9-2: Conditions for comparison of experimental data with simulation results in terms of the time needed to reach steady state in the medium-scale fluid bed.

Process conditions	Values
Initial particle moisture contents	$4 \cdot 10^{-3}$ kg water/kg core (experimentally measured)
External air temperature	23.6 ºC
External air humidity	35.7 rH% (at 23.6 ºC) ~ $6.5 \cdot 10^{-3}$ kg H_2O/kg dry air
Initial fluidisation chamber temperature ($T_{w,i}$)	23.6 ºC
Inlet fluidisation air temperature ($T_{a,in}$)	80 ºC
Fluidisation air velocity	270 Nm^3/hr ~ r = 1.98 s^{-1}
Inlet fluidisation air humidity	2.2 rH% (at 80 ºC) ~ $6.5 \cdot 10^{-3}$ kg H_2O/kg dry air
Bed load	4.0 kg

For the medium-scale fluid bed set-up, the inlet air is supplied from an external steam-based heating source, which also supplies other equipment. The temperature control is maintained by a thermostat which has some delay in response. This means in reality that it will take some time for the inlet air to adjust to the set point. Such phenomena are observed for all three fluid bed scales. For the present coating experiment, the inlet temperature was recorded and observed to develop according to figure 9.7. As observed from figure 9.7, it takes roughly 100 seconds before the inlet temperature reaches the set point at 80 ºC and another 350 seconds before the oscillation damps out. If the model is to be used for dynamic studies such non-ideal phenomena must be accounted for. An exponential function was thus fitted to the measured inlet fluidisation air temperature data and implemented into the model for simulations up to 500 seconds of process time.

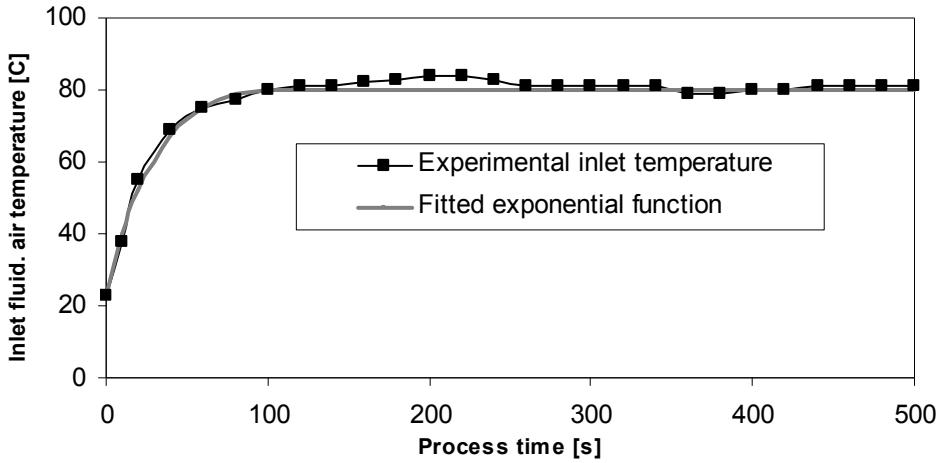

Figure 9.7: The inlet fluidisation air temperature as a function of process/simulation time.

By measuring the outlet and bed temperature as well as the outlet relative humidity each 20 seconds during start-up, it was possible to compare the measured values with those obtained from simulations under identical process conditions. The simulated data were obtained as follows: Initially the particles and fluidisation vessel were set to room conditions according to table 9-2. Setting all control volumes to non-coating control volumes, the model was set to run until steady state which corresponds to the initial heating up of the particles prior to the spray phase. Comparison with experimentally measured points can be seen from figure 9.8a-c.

Starting with figure 9.8a, it is observed that the curve for the simulated bed temperature follows the experimental data closely all the way up to steady state. For both the simulation and the experiment, it takes roughly 200 seconds to reach steady state. The tendency of reaching steady state at roughly 200 seconds is also observed for the outlet conditions in figure 9.8b and 9.8c. However, in these two figures the experimental data is observed to lack slightly behind the simulation results in the first 200 seconds although the deviations are close to the temperature and humidity probe uncertainty. Especially the humidity probe is known to have some seconds of response delay which could account for some of the deviation at the steepest gradients in figure 9.8b. In all, the test has showed that the model is indeed capable of predicting the dynamic thermodynamic behaviour during fluid bed processing, as the model predicts the three important variables well at any given time of operation.

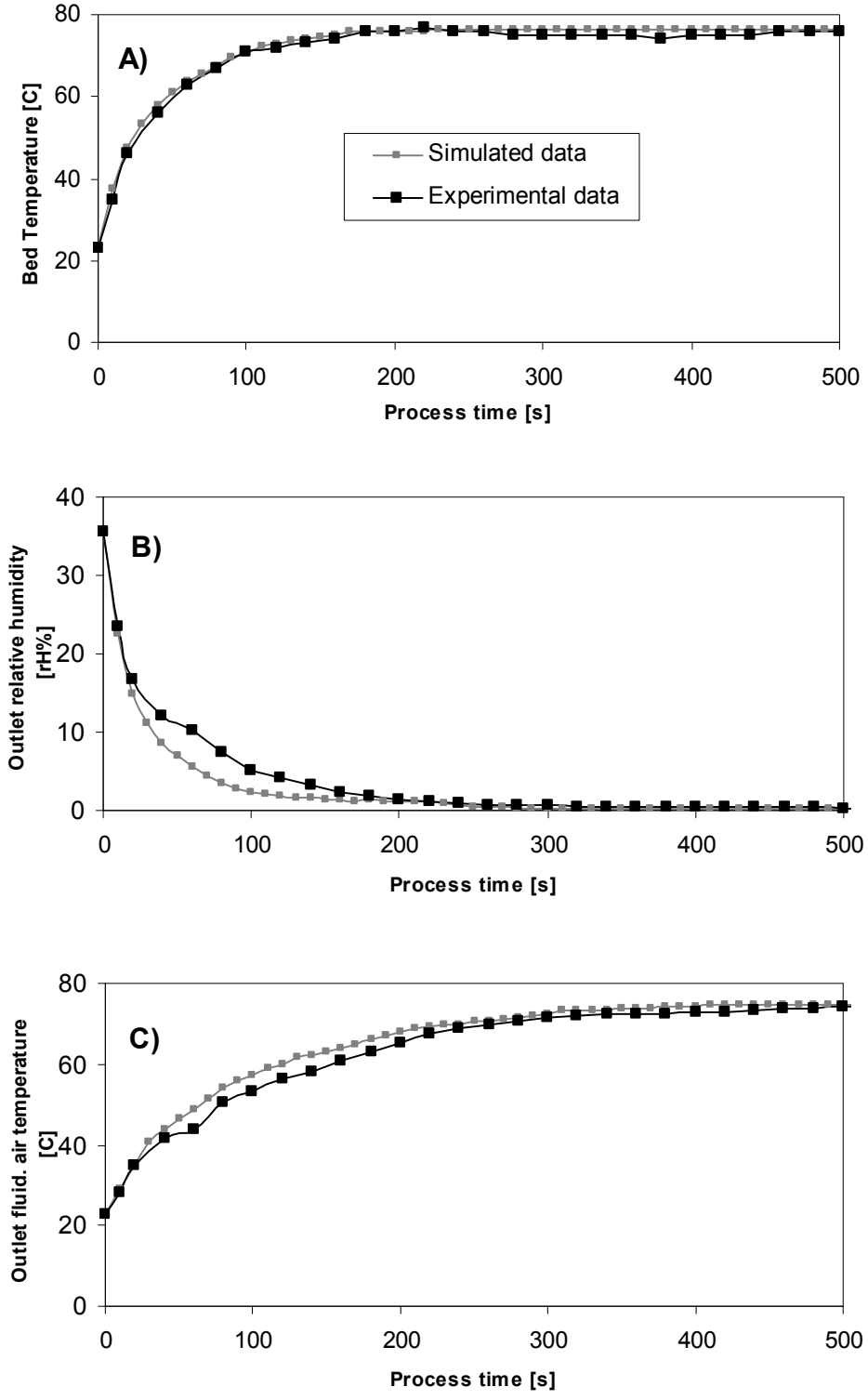

Figure 9.8: Comparison of experimental and simulated data as a function of process/simulation time: A) Bed temperature, B) Outlet relative humidity, C) Outlet temperature.

9.4. Scale-up simulations

The principles, advantages and disadvantages of scaling up the top-spray fluid bed inorganic salt coating process in terms of the combined Relative Droplet size (RD) and Drying Force (DF) have been thoroughly presented in a number of papers (Hede et al., 2008b, Rambali et al. 2003 and Mehta et al., 1988). Likewise, a number of papers have treated the scale-up using the Flux Number (Hede et al., 2008a and Boerefijn & Hounslow, 2005). The conclusions obtained from these experimental scale-up studies indicate that product temperature and humidity are vital parameters for the result of the coating process.

Both scale-up principles have shown to be capable of producing coated granules with statistically similar low degree of agglomeration across the three fluid bed scales used in the present paper. It is important to note that none of the two scale-up principles automatically fix all process conditions for the coating process. The scale-up principles rather give certain possibilities for some process parameters once others are chosen. This means in principle that other levels of agglomeration could have been observed by Hede et al. (2008a,b) for identical FN and RD/DF values. Furthermore, both scale-up principles need experiments to be carried out in order to determine the correct setting for the inlet fluidisation air temperature. That is, both the DF/RD and the FN approach have an independent parameter being the inlet fluidisation air temperature which cannot be determined a-priori from the DF/RD or the FN expressions, but needs to be found by adjustment in the coating process start-up phase in order to reach the required target bed temperature. Similarly, both scale-up principles are focused primarily on being able to reproduce the particle size distribution across scale and thereby avoid agglomeration. Although also important in a commercial framework, the two scale-up principles focus, however, to a lesser extent on process intensity. The two scale-up principles will be briefly introduced below, hereby illustrating how process conditions for the coating experiments were obtained with the scale-up parameters.

Based on the results by Mehta (1988), Rambali et al. (2003) scaled up a fluidised agglomeration process from small-scale (bed load: 5 kg) to medium- (bed load: 30 kg) and large-scale (bed load: 120 kg) by looking at the effect of the particle bed moisture contents during and at the end of the spraying process and the effect of coating solution droplet size on the granule size. The fluidisation flow rate in m/s at the air distributor plate was kept constant in all their experiments in order to have approximately similar breaking forces on the granules. For the small- and medium-scale the same nozzle (liquid orifice diameter of 1.8 mm) was used whereas a three-head nozzle (liquid orifice diameters of 3 x 3.0 mm) was used for the large-scale fluid bed. The droplet size was controlled in terms of a Relative Droplet size, RD, defined as the ratio of the coating solution mass spray rate $\dot{m}_{spray}$ divided by the mass airflow rate through the nozzle $\dot{m}_{nozzle\ air}$ squared according to equation 9.2.

$$RD = \frac{\dot{m}_{spray}}{(\dot{m}_{nozzle\ air})^2} \tag{9.2}$$

The idea of RD is to maintain a similar droplet size across scale and the value of RD is only unambiguous if both the nozzle pressure and the liquid feed rate are chosen. A further discussion of the Relative Droplet size may be found in Hede et al. (2008b).

Hede et al (2008b) further suggested that the bed temperature and outlet relative humidity (assumed equal to the average bed relative humidity – see chapter eight) during steady state coating conditions were combined into a so-called Drying Force parameter (DF), according to equation 9.3, indicating the fluidisation air moisture evaporation force.

$$DF = P_{sat} \cdot \left(1 - \frac{\text{Outlet rH\%}}{100\ \text{rH\%}}\right) \tag{9.3}$$

where P_{sat} is the saturated pressure at the dry bulb bed temperature. Results by Hede et al (2008b) showed that scale-up in terms of fixed values of both the Drying Force and the Relative Droplet size could lead to similar agglomeration tendencies as well as similar granule mechanical properties across the three pilot fluid bed scales used in the present paper.

Likewise, a number of papers have treated scale-up using the Flux Number (Hede et al., 2008a and Boerefijn & Hounslow, 2005). The Flux Number and the expressions for the associated parameters were suggested in a Unilever patent by Akkermans et al. (1998). The Flux Number is expressed according to equation 9.4.

$$FN = \log\left[\frac{\rho_p \cdot v_e}{\dot{q}_{mliq}}\right] \tag{9.4}$$

where ρ_p is the particle density determined according to equation 9.5.

$$\rho_p = \frac{BD}{1 - \varepsilon_{bed}} \tag{9.5}$$

in which BD is the bulk density of the core particles and ε_{bed} is the bed porosity determined by e.g. mercury porosimetry according to guidelines provided by Akkermans et al. (1998). The parameter $\dot{q}_{mliq}$ is the spray mass flux in kg/(s·m^2) at a normalised distance D_0 from the nozzle outlet, and v_e is the excess gas velocity in m/s. D_0 is determined according to equation 9.6.

$$D_0 = h_{nozzle} - h_{bed} \tag{9.6}$$

where h_{nozzle} is the height of the spray nozzle above the bottom of the fluidisation chamber and height h_{bed} is the expanded bed height (see also chapter seven).

One example of a scale-up attempt across the three fluid bed scales with low and statistical similar agglomeration tendencies obtained under high-intensity coating conditions may be seen from the first row in table 9-3, adapted from Hede et al. (2008b). Using this successful scaling attempt as benchmark, an unsuccessful scaling attempt of similar coating time using the Flux Number scale-up principle was adapted from Hede et al. (2008a). The data from the Flux Number scaling attempt may be seen from the last row in table 9-3.

Table 9-3: Scale-up data adapted from Hede et al. (2008a,b).

Scaling conditions	Strea-1 (small-scale)	MP-1 (medium-scale)	MP-2/3 (Large-scale)
Scale-up in terms of combined Relative Droplet size (RD) and Drying Force (DF)	RD = 3.5 $\cdot 10^{-3}$ min/g, P_{nozzle} = 3 bar DF = 12.2 kPa (T_{bed} = 55 ºC) T_{inlet} = 74 ºC 93 Nm^3/hr	RD = 3.5 $\cdot 10^{-3}$ min/g, P_{nozzle} = 3 bar DF = 12.0 kPa (T_{bed} = 54 ºC) T_{inlet} = 78 ºC 270 Nm^3/hr	RD = 3.5 $\cdot 10^{-3}$ min/g, P_{nozzle} = 3 bar DF = 12.5 kPa (T_{bed} = 56 ºC) T_{inlet} = 79 ºC 680 Nm^3/hr
	Results: Aggl. = 0.1 w/w% Process time: 0:37 Outlet abs. hum. = 15.9 g H_2O/kg dry air	Results: Aggl. = 1.3 w/w% Process time: 1:28 Outlet abs. hum. = 18.3 g H_2O/kg dry air	Results: Aggl. = 1.5 w/w% Process time: 3:46 Outlet abs. hum. = 19.1 g H_2O/kg dry air
Scale-up in terms of the Flux Number (FN)	FN = 4.5, P_{nozzle} = 1 bar T_{bed} = 55 ºC T_{inlet} = 75 ºC, 82 Nm^3/hr	FN = 4.5, P_{nozzle} = 1 bar T_{bed} = 55 ºC T_{inlet} = 97 ºC, 137 Nm^3/hr	FN = 4.5, P_{nozzle} = 1 bar T_{bed} = 55 ºC T_{inlet} = 74 ºC, 651 Nm^3/hr
	Results: Aggl. = 24.5 w/w% Process time: 1.02 Outlet abs. hum. = 16.1 g H_2O/kg dry air	Results: Aggl. = 62.3 w/w% Process time: 1:31 Outlet abs. hum. = 25.9 g H_2O/kg dry air	Results: Aggl. = 4.4 w/w% Process time: 4:25 Outlet abs. hum. = 17.6 g H_2O/kg dry air

Comparing the data in table 9-3 from experiments at the same scale, the resulting agglomeration tendencies are far from being similar, and a similar low tendency of agglomeration across the scales was not achieved in the Flux Number scale-up attempt. This results from the selection of the parameters for the two scaling principles and does not necessarily indicate that one of the scale-up principles is superior to the other. Hede et al. (2008a) argue that a low nozzle pressure of 1 bar causes a larger two-dimensional spray area at the distance of D_0 than at higher pressures, and that this, as a consequence of the choice of the definition of the Flux Number and hereby the parameter choices made by Hede et al. (2008a), dictates a high coating solution spray rate and a poor atomisation, which in all causes critically high *local* particle moisture contents combined with a low temperature of the fluidisation air in the spray zone. Furthermore, at a nozzle pressure of 1 bar the vertical extension of the spray zone is likely to be smaller than at 3 bar. So far it has not been possible to validate these suggested explanations. Simulations using the present model, however, make it possible to study local temperatures and humidity conditions in detail.

Initially, the conditions from the successful scaling attempt in terms of the combined Relative Droplet size and the Drying Force have been simulated. Steady state fluidisation air temperature and relative humidity profiles as well as Drying Force profiles for the three fluid bed scales may be seen from figure 9.9 – 9.11.

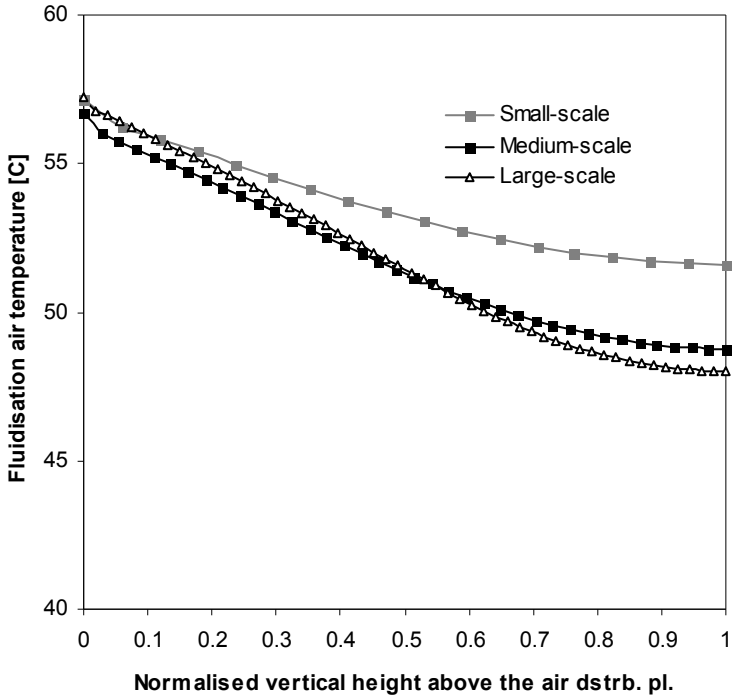

Figure 9.9: Steady state fluidisation air temperature profiles for the three fluid bed scales. RD = 3.5 ·10^{-3} min/g, DF = 12.0 – 12.5 kPa, P_{nozzle} = 3 bar. Other model parameters according to table 9-1 and 9-3.

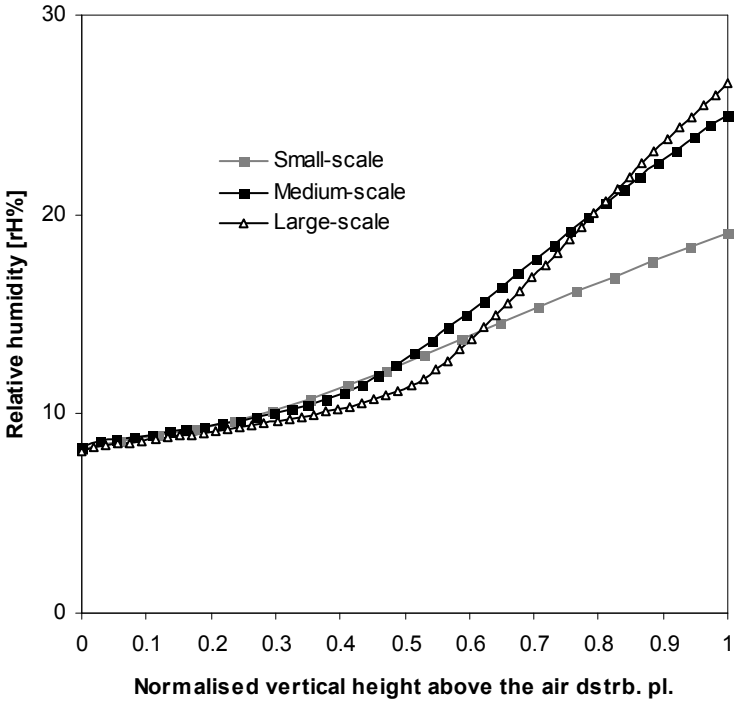

Figure 9.10: Steady state fluidisation air relative humidity profiles for the three fluid bed scales. RD = 3.5 ·10^{-3} min/g, DF = 12.0 – 12.5 kPa, P_{nozzle} = 3 bar. Other model parameters according to table 9-1 and 9-3.

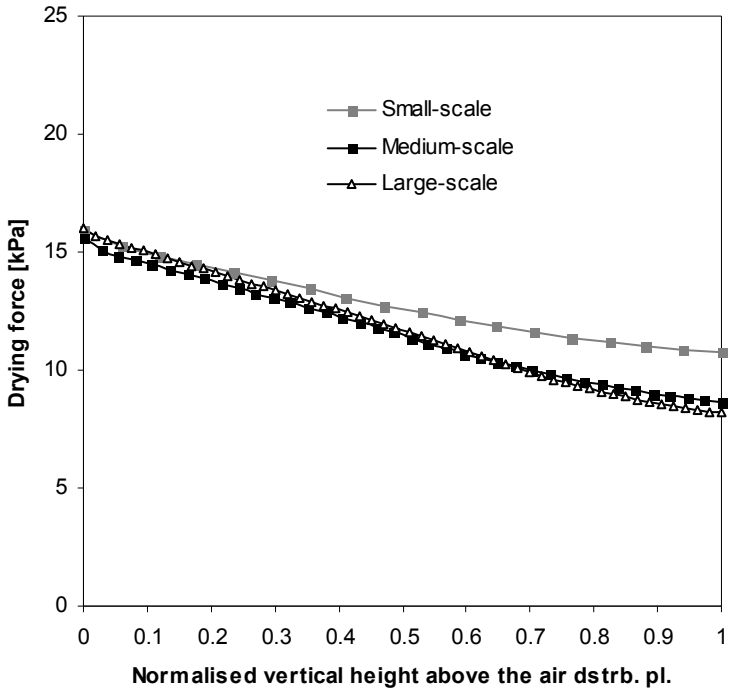

Figure 9.11: Steady state Drying Force profiles for the three fluid bed scales. RD = 3.5 ·10^{-3} min/g , DF = 12.0 - 12.5 kPa, P_{nozzle} = 3 bar. Other model parameters according to table 9-1 and 9-3.

From the comparison of the temperature and the relative humidity profiles in figure 9.9 and 9.10 several points are revealed. In accordance with the principle of which the coating operations were carried out, it is observed for all three scales that the fluidisation air temperatures are close to 55 ºC in the control volume where the bed temperature probe physically is located (see table 9-1). Taking the outlet relative humidity as the relative humidity value at normalised length of 1 in figure 9.10 this indicates that the overall Drying Force values were close to 12 kPa during scale-up, which is in accordance with the data in table 9-3. It appears that the temperature in the spray zone is slightly higher in the small-scale fluid bed than for the medium- and large-scale which are quite similar. Regarding the humidity profiles, it appears that the largest relative humidity gradients are observed for the large-scale followed by the medium- and small-scale. Based on the temperature and the relative humidity profiles it becomes clear that there is a greater homogeneity the smaller the fluid bed scale indicating that the particle mixing is significantly better the smaller the scale and more importantly, that the spray zone constitutes a larger percentage of the total expanded bed height (the c/n fraction is greater the smaller the fluid bed size).

The keypoint of the scale-up approach in figure 9.9 – 9.11 was to maintain a constant Drying Force across scale. As presented by Hede et al. (2008b) this was done in terms of the measured outlet humidity and the measured bed temperature at one location. Hence, the scale-up principle was based on a single (overall) Drying Force value, and it was therefore not on beforehand certain that the Drying Force profiles would be similar across scale on a detailed level. Even so, it appears from figure 9.11 that there is a great similarity in the Drying Force profiles for all three scales in particular for the first half of the chamber height. Similar tendencies have been observed for simulations with other RD/DF values across the three fluid bed scales. It is likely that this homogeneity and similarity in the Drying Force profiles across scale is part of the reason why the scale-up approach was successful regarding the production of particles with similar low tendency of agglomeration and similar attrition strength of the

coating layer. This becomes evident in the comparison with the Flux Number scale-up approach. Similar to the profiles in figure 9.9 – 9.11, profiles for the Flux Number scaling attempt can be seen in figure 9.12 – 9.14.

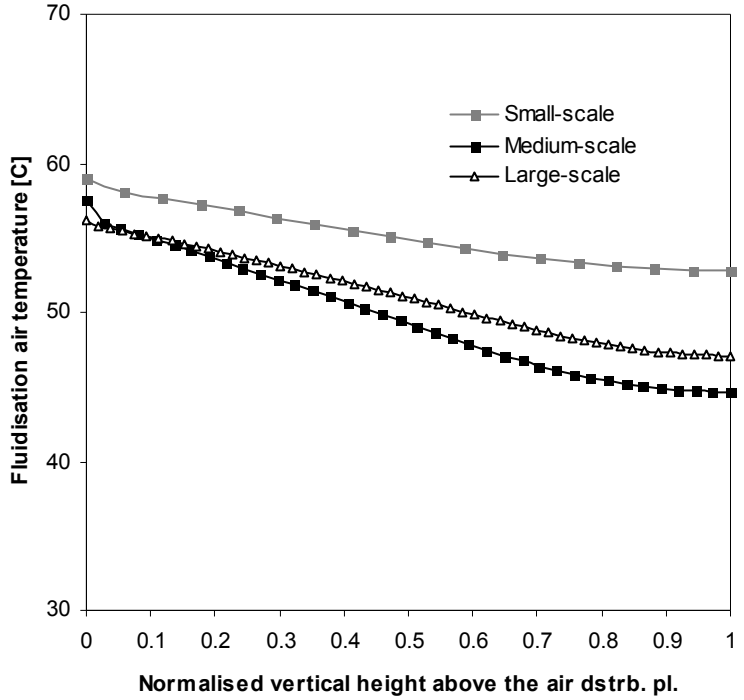

Figure 9.12: Steady state fluidisation air temperature profiles for the three fluid bed scales. FN = 4.5, P_{nozzle} = 1 bar. Other model parameters according to table 9-1 and 9-3.

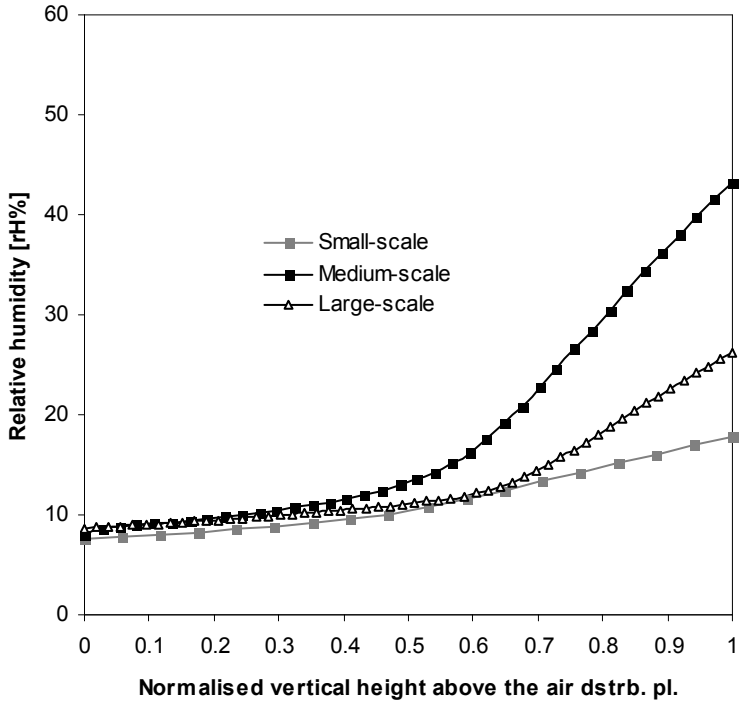

Figure 9.13: Steady state fluidisation air relative humidity profiles for the three fluid bed scales. FN = 4.5, P_{nozzle} = 1 bar. Other model parameters according to table 9-1 and 9-3.

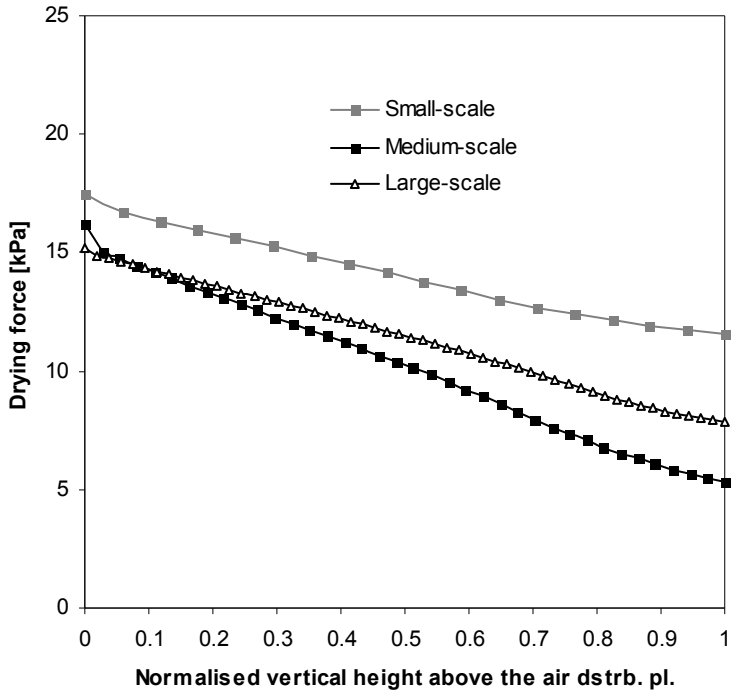

Figure 9.14: Steady state Drying Force profiles for the three fluid bed scales. FN = 4.5, P_{nozzle} = 1 bar. Other model parameters according to table 9-1 and 9-3.

In comparison to the profiles in figure 9.9 – 9.11, it is clearly observed from figure 9.12 – 9.14 how the temperature and humidity profiles vary from scale to scale, but also how different the Drying Force profiles are with identical Flux Number. Whereas the Drying Force ranges between 12 and 18 kPa in the small-scale, the range is 5-16 kPa in the medium-scale and 8-15 kPa in the large-scale. This means that particles in all scales and especially in the medium-scale are exposed to a dramatic temperature and moisture change during their drying-wetting cycle. With these simulation results in mind, it is not surprising to observe from table 9-3 that the far largest agglomeration tendency was observed in the medium-scale.

The comparison of the RD/DF and FN scale-up experiments should be evaluated in terms of the conditions under which the experiments were carried out (see table 9-3). The fluidisation air inlet temperatures were close to identical in the RD/DF experiments and the fluidisation velocities were also higher than for the FN experiments. It is thus not surprising to observe lower agglomeration tendencies for these experiments. Compared to the RD/DF experiments, the fluidisation velocities were lower in the FN experiments (as a consequence of the FN patent guidelines proposed by Akkermans et al. (1998)) although the liquid spray rates were similar and the spray zones shorter in vertical extension due to lower nozzle pressures. Especially for the medium-scale the fluidisation velocity was almost halved increasing the particle circulation time, which meant that the inlet air temperature had to be as high as 97 ºC in order to maintain the product temperature at 55 ºC. This leads to high humidity and temperature gradients and local zones with low temperature and high fluidisation air humidity which are known to cause severe agglomeration. Low temperature and high humidity leads to a low Drying Force causing slower drying, more moist particles and increased chance of agglomeration (Hede, 2005,2006). The comparison of the scale-up experiments clearly shows that it is difficult to compare the scale-up principles in terms of temperature and humidity profiles without also including a comparison of the selection of vital parameters such as fluidisation air inlet temperature, nozzle pressure and fluidisation air velocity. What is needed is a combination of the model with a fundamental agglomeration model. The advantages of

this will become evident when combining the model simulations of the particle moisture contents with the viscous Stokes theory in the next section.

9.4.1. Application of the viscous Stokes theory

The comparisons of the Drying Force profiles in figure 9.11 and 9.14 with the measured agglomeration percentages in table 9-3 indicate that zones of low temperature and high humidity increase the tendency of agglomeration. It is well-known that a low Drying Force results in a low drying capacity and thereby moist particles. The correlation between the particle moisture contents and the resulting agglomeration percentages in table 9-3 may be checked in terms of the present model, as one of the six calculated variables in each control volume is the particle moisture contents in kg H_2O/kg core. Figure 9.15 shows the steady state particle water content profiles from the two scale-up series.

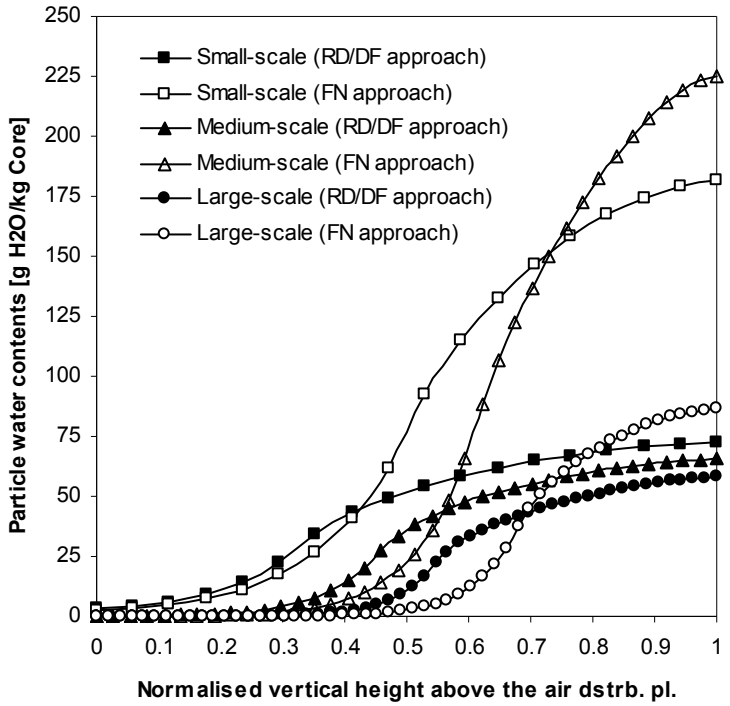

Figure 9.15: Steady state particle water content profiles for the three fluid bed scales. RD/DF approach: RD = 3.5 ·10^{-3} min/g , DF = 12.5 kPa, P_{nozzle} = 3 bar. FN approach: FN = 4.5, P_{nozzle} = 1 bar. Other model parameters according to table 9-1 and 9-3.

Comparison of the FN approach profiles in figure 9.15 with the agglomeration tendencies in table 9-3 clearly reveals that there is a close relation between the observed agglomeration percentages and the particle water contents in the spray zone. The agglomeration percentages in table 9-3 distribute according to the spray zone level of particle moisture contents observed in figure 9.15. Similarly for the RD/DF approach curves in figure 9.15, the curves reach close to similar levels of particle moisture contents in the spray zone, corresponding to the similar agglomeration tendencies in table 9-3, which again are at levels much smaller than what is observed for the FN approach. The results obtained in figure 9.15 follow closely the trends observed from the Drying Force profiles meaning that similar Drying Force profiles (obtained under conditions with similar Relative Droplet size) will ensure similar particle moisture content profiles, and possibly similar tendencies of agglomeration. This will become evident from the inclusion of the viscous Stokes theory presented below.

It is well known from numerous studies that the tendency of agglomeration increases with increasing particle moisture contents (Iveson et al., 2001). These observations have led to an agglomeration model suggested originally by Ennis et al. (1991). The model assumes permanent agglomeration to occur if the kinetic energy of impact is entirely dissipated by viscous dissipation in the liquid layer and only elastic losses in the solid phase. The model predicts that collisions will result in permanent agglomeration when the viscous Stokes number (St_v) is less than a critical viscous Stokes number (St_v^*). The two numbers are given as (Ennis et al., 1991) (see also chapter three):

$$St_v = \frac{8 \cdot \rho_g \cdot r_{harm} \cdot u_0}{9 \cdot \eta_{liq}} \tag{9.7}$$

and

$$St_v^* = \left(1 + \frac{1}{e}\right) \cdot \ln\left(\frac{h_{liq}}{h_{asp}}\right) \tag{9.8}$$

where η_{liq} is the coating solution viscosity, e is the coefficient of restitution, ρ_g is the granule density, h_{liq} is the thickness of the liquid surface layer, h_{asp} is the characteristic height of the particle surface asperities and r_{harm} is the harmonic mean granule radius of the two particles given as (Iveson et al., 2001):

$$r_{harm} = \frac{2 \cdot r_1 \cdot r_2}{r_1 + r_2} \tag{9.9}$$

u_0 is the initial collision velocity which is not easily obtainable due to the chaotic pattern of motion for the particles in fluid beds. A rough estimate based on the bubble rise velocity, v_{bu}, has been presented by Ennis et al. (1991):

$$u_0 \approx \frac{12 \cdot v_{bu} \cdot r_{harm}}{d_{bu} \cdot \delta^2} \tag{9.10}$$

where d_{bu} is the gas bubble diameter and δ the dimensionless bubble space defined as the axial fluid bed bubble spacing divided by the fluidisation gas bubble radius. Whereas the gas bubble diameter and spacing can be estimated by the dimensions of the air distributor plate, or found by experiments, the bubble rise velocity can be found according to the Davidson & Harrison (1963) formula (see also chapter two):

$$v_{bu} = v_a - v_{mf} + 0.711 \cdot (g \cdot d_{bu})^{0.5} \tag{9.11}$$

The fact that the present model assumes an equal number of particles (each having the same diameter) in each control volume at a given time makes it possible to calculate the liquid layer thickness on the core particle surfaces. Although the uncoated sodium sulphate cores are porous, it is reasonable to assume that the pores have been fully filled early in the process, and thereby that all the particle moisture contents at steady state is present at the core particle surfaces only. Such an assumption is reasonable based on previous droplet penetration studies made by Hede et al. (2007a) and Hede (2005).

With the use of the parameters in table 9-4 the liquid coating layer thicknesses are calculated for each control volume according to the moisture contents in figure 9.15. These liquid thickness profiles are depicted in figure 9.16. Likewise are the viscous Stokes number, St_v, and the critical viscous Stokes number, St_v^*, calculated for each control volume. The value of the difference between St_v and St_v^* indicates the chance of agglomeration and the different regimes have been added to figure 9.16. The boundaries of these regimes are obviously dependent on the value of St_v. As parameters such as the gas bubble diameter, d_{bu}, and the dimensionless bubble space, δ, change with vertical distance from the air distribution plate, the estimate of the initial collision velocity, u_0, (and thereby the value of St_v) is different from control volume to control volume and, in addition, different from each of the six experiments in figure 9.16. This means that no uniform single line may be drawn in figure 9.16 for the $St_v = St_v^*$ condition, but rather that this condition is indicated by a regime. As observed from figure 9.16 the regime is nevertheless quite narrow as the differences between the St_v values have limited practical influence on the $St_v - St_v^*$ values.

Table 9-4: Parameters for the viscous Stokes analyses.

Parameter	Values
Gravity (g)	9.82 m/s^2
Coefficient of restitution (*e*)	0.8
Characteristic length scales of surface asperities (h_{asp})	1 μm
Granule density (ρ_g)	2600 kg/m^3
Coating solution viscosity (η_{liq})	3.5 mPa s
Coating solution density (ρ_{liq})	1.1 kg/m^3

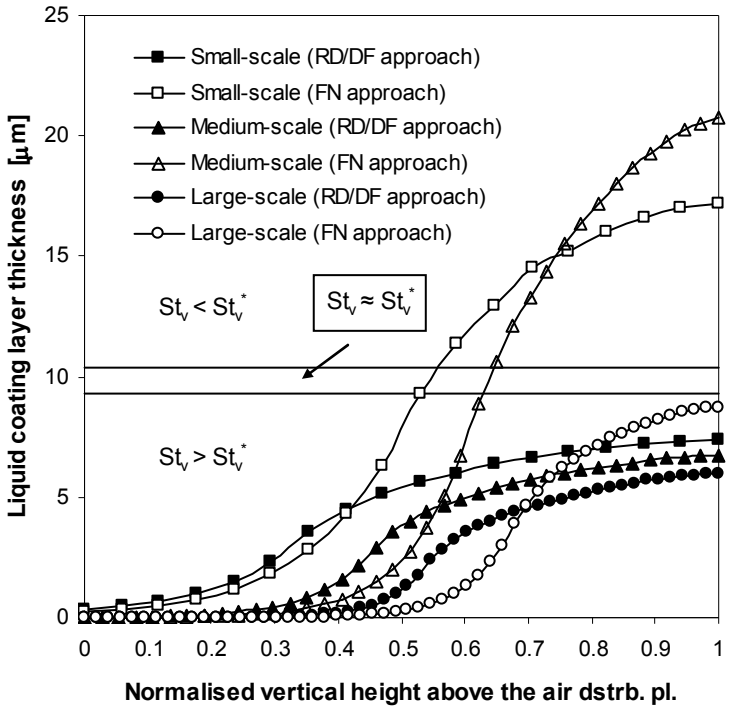

Figure 9.16: Steady state coating liquid thickness profiles for the three fluid bed scales. RD/DF approach: RD = 3.5 ·10^{-3} min/g , DF = 12.5 kPa, P_{nozzle} = 3 bar. FN approach: FN = 4.5, P_{nozzle} = 1 bar. Other model parameters according to table 9-1, 9-3 and table 9-4.

The addition of the regimes based on the viscous Stokes theory in figure 9.16 provides a quantitative basis for the previous conclusions regarding the effect of the particle water contents on agglomeration. A clear relation is observed in figure 9.16 between the agglomeration tendencies in table 9-3 and the curve shapes. Whereas the three experiments in the RD/DF scale-up attempt, with agglomeration percentages close to zero, are located solely in the coating regime ($St_v > St_v^*$), the curves for the experiments in the small- and medium-scale from the FN scale-up attempt cross the $St_v = St_v^*$ boundary into the agglomeration regime ($St_v < St_v^*$), just as was expected from the results in table 9-3.

9.4.2. Sensitivity analysis

In a series of detailed sensitivity analyses Ronsse et al. (2007b) and Ronsse (2006) concluded that the most important properties with respect to the position of the steady state conditions of the fluid bed coating process are the fluidisation air inlet temperature and the volumetric fluidisation velocity. Ronsse et al. (2007b) also concluded that an increase in the relative size of the spray zone or an increase of the particle exchange rate had a narrowing effect of the overall coating mass distribution. Results further indicated that the outlet conditions were not affected by a change in the c/n ratio or a change in the value for r. Similar observations were observed in this study. More interesting is the effect on particle moisture content profiles as a function of the choice of r and c/n, which is investigated in the present sensitivity analysis. For the sensitivity analysis, the medium-scale fluid bed was selected and the model parameters for the sensitivity analysis can be seen from table 9-5. In all the experiments for the sensitivity analysis, the volumetric fluidisation air velocity was fixed at 270 Nm^3/hr and the r value was varied without the use of the correlation in equation 9.1.

Table 9-5: Model parameters for the sensitivity analyses.

Process conditions	Values
Initial particle moisture content	$4 \cdot 10^{-3}$ kg water/kg core
External air temperature	20.0 ºC
External air humidity	35 rH% (at 20.0 ºC) ~ $5.1 \cdot 10^{-3}$ kg H_2O/kg dry air
Inlet fluidisation air temperature ($T_{a,in}$)	80 ºC
Fluidisation air velocity	270 Nm^3/hr
Inlet fluidisation air humidity	1.7 rH% (at 80 ºC) ~ $5.1 \cdot 10^{-3}$ kg H_2O/kg dry air
Bed load	4.0 kg
P_{nozzle}	3 bar
Coating solution spray rate	3 kg/h
Coating volume fraction (c/n ratio in % of total bed volume)	10.5-100 %
Particle exchange rate (r parameter)	0.5 – 3.0 s^{-1}

Initially a value of r = 2 s^{-1} was selected and fixed while the c/n ratio was varied. Figure 9.17 shows how the particle moisture content profiles vary as a function of the c/n fraction.

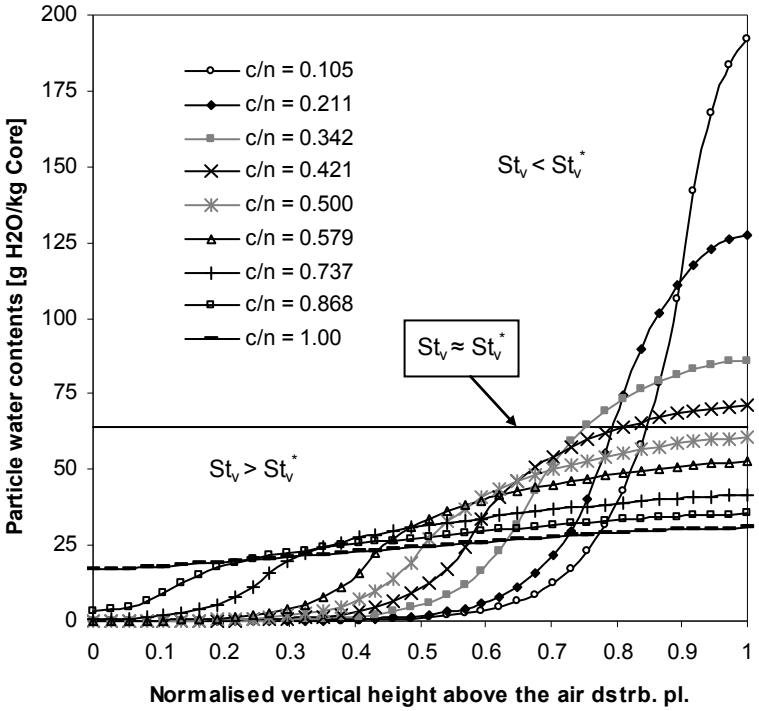

Figure 9.17: Steady state particle moisture content force profiles as functions of the coating volume fraction, c/n, for the medium-scale pilot fluid bed.

It can be observed from figure 9.17 that there is a significant effect of the c/n value on the resulting particle moisture content profile. As the number of coating control volumes decreases, the particle moisture gradients increase significantly. The disadvantages of operating the fluid bed coating process with a small spray zone are clearly observed from figure 9.17 as the liquid is concentrated close to the nozzle leading to high particle moisture values and possible agglomeration. It appears, however, that beyond a c/n value of about 42 % there is only minor effects of increasing the number of coating control volumes any further. This value is slightly scale-dependent as the same effect is observed for increasing c/n fractions the larger the fluid bed scale. In terms of the viscous Stokes theory, the $St_v = St_v^*$ boundary is reached for the medium-scale at a particle water content of 64 g H_2O/kg core for the given conditions, meaning that, in order to avoid agglomeration, the spray zone should take up roughly 50 % or more of the total expanded bed volume. This requirement is easily met in the small and medium pilot-scale fluid beds, but not in the larger fluid bed scales.

In order to test the influence of the particle exchange rate r for a given fixed fluidisation velocity, the c/n value was fixed at 55.3 % (~ 21 out of 38 control volumes were assigned to coating control volumes which corresponds to a nozzle pressure of 3 bar – see table 9-1) while the r value was varied between 0.5 and 3.0. All other conditions were chosen from table 9-4. Figure 9.18 shows the variation in the particle moisture profiles as functions of the r value.

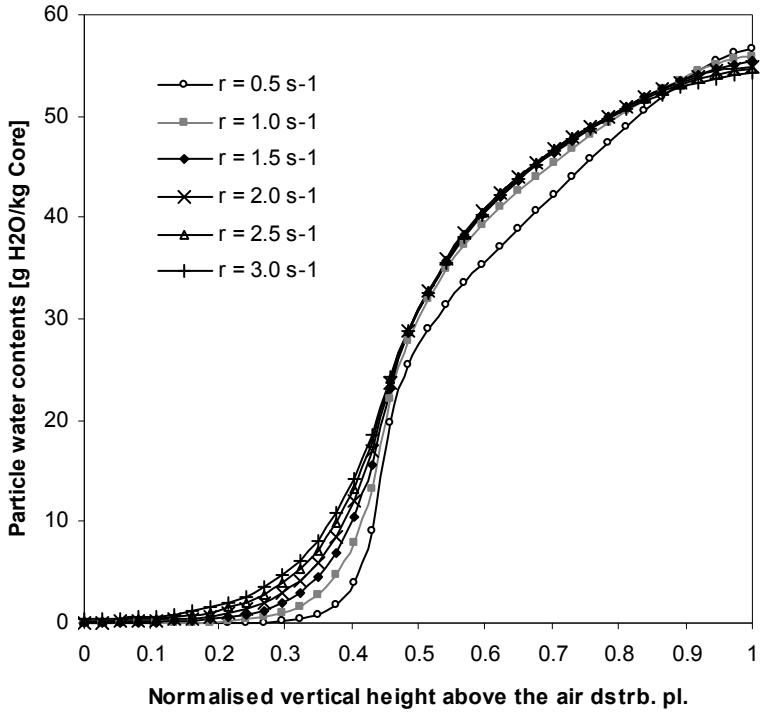

Figure 9.18: Steady state particle moisture content force profiles as functions of the particle exchange rate, r, for the medium-scale pilot fluid bed.

Contrary to figure 9.17, the effect of the particle exchange rate value on the particle moisture content profiles is observed from figure 9.18 to be rather small. Apparently, the moisture content in and near the spray zone is less affected by the value of r while the moisture content near the air distributor plate is slightly affected. If however a c/n value of 0.42 or less is chosen, the effect of r have been observed to be increasingly significant with decreasing c/n value. In conclusion, this indicates that as long as the spray zone is of considerable size (i.e. probably larger than 50 % of the total expanded bed volume), the exact value of r is less important for the particle moisture content, but as the spray zone decreases in size, the particle circulation time becomes increasingly important. It is reasonable to relate the r parameter to the fluidisation velocity as the vertical particle transport in a fluid bed is known to be closely related to the bubble rise velocity for Geldart B particles, as the ones being simulated in the present study. In that perspective, the use of equation 9.1 seems to be a reasonable choice.

9.4.3. Scale-up into a production-scale fluid bed

The present scale-up study did not allow experiments with production-scale fluid beds, but the model was used to simulate the conditions in a RICA-TEC (Anhydro A/S, Denmark) multi-nozzle production-scale top-spray fluid bed. Initial simulations of the production-scale revealed much larger temperature and humidity gradient vertically through the bed than was observed with the pilot-scale fluid beds. This means that the measured bed temperature at a single location is representative for the gas phase temperature at other positions in the chamber to a much lesser extent. Irrespectively of the vertical position, the bed temperature probe is positioned, the measurement will be far away from being representative. These observations reveal that scale-up into production-scale in terms of a single fixed overall Drying Force value is associated with greater uncertainty than scale-up between pilot-scale fluid beds, where vertical temperature homogeneity is larger.

Following the combination of the viscous Stokes theory with the particle moisture content profiles obtained with the model, the task was to obtain conditions for the production-scale in which the coating liquid layer thickness profile stays just below the $St_v = St_v^*$ boundary. According to the RD/DF scale-up attempt by Hede et al. (2008b) in table 9-3 the fluidisation velocity was chosen to be 3.3 m/s 4 cm above the air distributor plate for all three pilot-scale fluid beds. This ensured a reasonable high fluidisation air velocity of roughly 0.5 m/s at the top of the freeboard. The production-scale fluid bed is, however, designed physically different, meaning that the chamber cross-section expansion is not as large as in the pilot-scale fluid beds. A choice of 3.3 m/s close to the air distributor plate requires 18280 Nm^3/hr of fluidisation air (and leads to a gas velocity as high as 0.8 m/s at the top of the freeboard), which is beyond the actual capacity of the equipment. Instead a velocity of 11080 Nm^3/hr was chosen, giving 0.5 m/s at the top of the freeboard. The average particle circulation time in the production-scale was calculated to 3.5 s with the use of equation 9.1. Although the particle circulation time distribution especially in large fluid bed scales is often observed to be quite broad with values ranging from a few seconds and up to about 20 s, estimated on the basis of Positron Emission Particle Tracking (PEPT) experiments performed by Stein et al. (2002) among others, an average value of 3.5 s is in accordance with estimations made by Ronsse (2006) and Mostoufi & Chaouki (2001). For the simulation of the production-scale, an average particle circulation time was hereby chosen to be 3.5 s thereby giving a particle exchange rate of 0.28 s^{-1}.

Following the RD/DF scale-up principle in table 9-3 by Hede et al. (2008b), the Relative Droplet size was initially kept fixed at RD = $3.5 \cdot 10^{-3}$min/g (~ liquid spray rate = 221 kg/h) and other conditions selected according to table 9-6. Under these conditions it was necessary to increase the inlet fluidisation air temperature to 95 ºC in order to keep out of the agglomeration regime. This is more than 15 ºC higher than what was needed in the pilot-scale RD/DF experiments, in order to obtain liquid layer profiles below the $St_v = St_v^*$ boundary. This resulted in an outlet absolute humidity of 25.8 g H_2O/kg dry air hereby indicating that scale-up in terms of combined RD/DF dictates increasing process intensity in order to stay out of the agglomeration regime when going into production-scale.

In industrial fluid bed coating processes such a high increase in inlet fluidisation air temperature from pilot-scale to production-scale would often not be feasible in practice due to a possible damage of the active ingredient in the granule core or coating layer. Granule properties such as appearances and morphology will probably also be affected by an increase in the inlet fluidisation air temperature. In order to maximize the process intensity, the inlet temperature in pilot-scale would probably be chosen to be as high as possible, meaning that the inlet temperature in production-scale could not be increased beyond that of the pilot-scale. From the pilot-scale RD/DF experiments in table 9-3 it was observed how the inlet temperatures were close to each other ranging from 74 ºC to 79 ºC, while the bed temperatures were close to 55 ºC. Assuming that 79 ºC is the maximum inlet temperature that could be allowed before the granule or coating components would be destroyed, simulations are performed in order to find the maximum spray intensity these conditions could allow while still being just below of the $St_v = St_v^*$ boundary. Dimensions and process conditions for the simulation in the production-scale may be seen from table 9-6.

Table 9-6: Process- and model-related parameters for the production-scale scale-up study. Fluid bed dimensions correspond to figure 9.3.

Process parameter	**Production-scale RICA-TEC (Anhydro A/S)**
Type of nozzle	External mixing two-fluid, 3 lances with 3 nozzle each (a total of 9 nozzles)
Nozzle pressure	3 bar
Liquid orifice diameters	1.2 mm
Inlet fluidisation air temperature	79 ºC
Fluidisation velocity	11080 Nm^3/hr ~ 0.5 m/s at the top of the freeboard
Particle exchange rate	$r = 0.28\ s^{-1}$
Coating feed reservoir temperature	60 ºC
Initial core bed load	900 kg
Coating solution dry-matter contents	15 w/w%
External air temperature	20.0 ºC
External air humidity	35 rH% (at 20.0 ºC) ~ $5.1 \cdot 10^{-3}$ kg H_2O/kg dry air
FB dimensions	
Length a	140 cm
Length b	30 cm
Length c	69 cm (at 3 bar)
Length d	174 cm
Length e	279 cm
Length f	-
Length g	280 cm
Length h	339 cm
Model-related parameters	
Total number of control volumes	116 ~ $h_{S,i} = 1.5$ cm
Number of coating control volumes	46 ($P_{nozzle} = 3$ bar)
Bed temperature measurement corresponds to control volume number:	20

With the conditions in table 9-6 a number of simulations were performed in order to adjust the coating solution spray rate so that the particle liquid coating layer thickness profiles remained solely in the coating regime. An example where the profile touches the coating/agglomeration regime boundary in the upper part of the spray zone can be seen in figure 9.19. The curve indicates that the coating process would have had a low level of agglomeration. This is nevertheless achieved for a liquid spray rate of 108 kg/h giving a RD value as low as

$5.2 \cdot 10^{-5}$ min/g. Such a low spray rate would mean that it would take more than eleven hours to coat the 900 kg with a 20 w/w% salt layer, which is unacceptably long in practice.

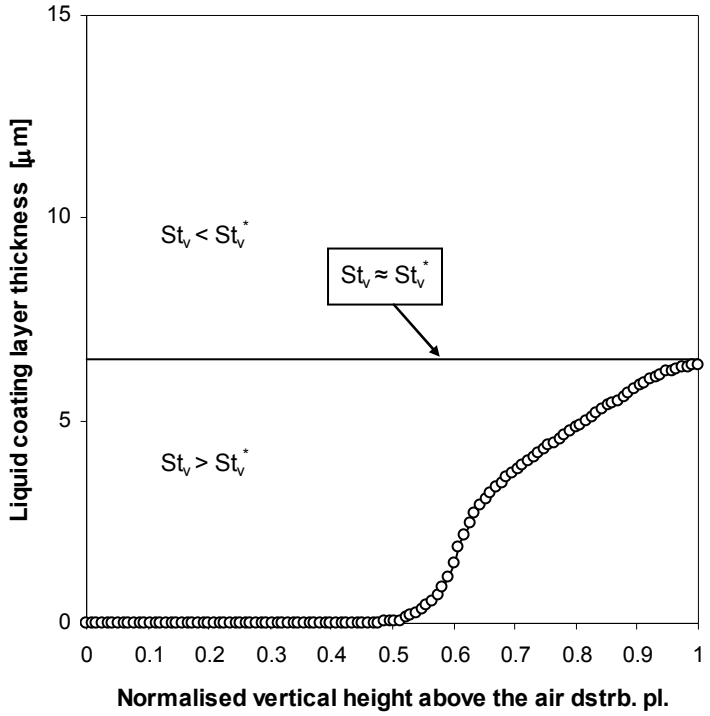

Figure 9.19: Steady state coating liquid thickness profiles for the production-scale fluid bed. RD = 5.2 ·10^{-5} min/g, P_{nozzle} = 3 bar. Other model parameters according to table 9-6.

The simulation with the conditions in table 9-6 and a spray rate of 108 kg/h gives an outlet absolute humidity of 15.4 g H_2O/kg dry air. Compared to the outlet absolute humidity values in table 9-3 ranging between 16 - 19 g H_2O/kg dry air, this indicates that the process intensity needs to be slightly smaller for the production-scale at similar inlet fluidisation air temperature in order to avoid agglomeration. Furthermore, as indicated from the RD/DF curves in figure 9.16, none of these three pilot-scale experiments came as close to the $St_v = St_v^*$ boundary as the production-scale in figure 9.19. This means that the RD/DF experiments in table 9-3 could have been optimised further to run at slightly higher spray intensity before starting to agglomerate. If the liquid spray rate is optimised in terms of the model with fixed inlet fluidisation air temperatures of 79 ºC, similar to the principle applied in figure 9.19, the outlet absolute humidity values for the pilot-scale fluid beds would range between 19 and 21 g H_2O/kg dry air with the larger outlet humidity values the smaller the fluid bed scale. Hence, the difference between the optimal pilot-scale and the production-scale process intensity without agglomeration is in reality somewhat larger for fixed inlet temperatures. The fact that the differences in process intensity are not significantly larger between the pilot- and production-scale is due to the counter-acting fact that the heat loss from the fluidisation vessel to the surroundings relative to the bed load is smaller the larger the fluid bed scale.

In comparison to the three pilot-scale fluid beds having bed temperatures ranging from 54 - 57 ºC at similar conditions, a bed temperature of 69 ºC was simulated for the production-scale at the location of the temperature probe. This is partly a consequence of the design of the large fluid bed where the distance from the nozzle outlet to the air distributor plate increases significantly with scale, while the bed temperature measurement is measured at a

similar vertical height across scale. Furthermore, the increased expanded bed height in the production-scale significantly increases the average particle circulation time and broadens the circulation time distribution hereby reducing the overall mixing, leading to large temperature and fluidisation air humidity gradients. Figure 9.20 and 9.21 presents the steady state fluidisation air temperature/relative humidity and Drying Force profiles, respectively.

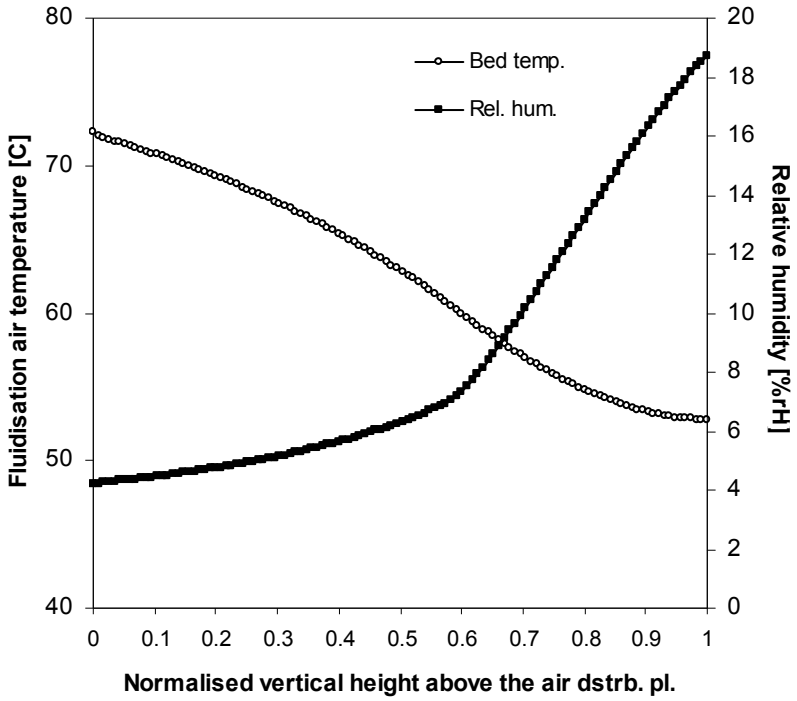

Figure 9.20: Steady state fluidisation air temperature and humidity profiles for the production-scale fluid bed. RD = 5.2 ·10^{-5} min/g, P_{nozzle} = 3 bar. Other model parameters according to table 9-6.

As observed from figure 9.20 there is a much larger temperature gradient than what was observed for the pilot-scale fluid beds in figure 9.9. From the fluidisation air inlet the temperature drops more than 20 ºC, while the relative humidity at the same time increases up to a level similar to figure 9.10 even though the RD value is far below the values for the experiments in figure 9.10. The overall Drying Force (calculated with the use of equation 9.3) is about 24 kPa, which is far from the values of 12 kPa for the three pilot-scales in table 9-3. This is due to the large temperature gradients in the production-scale fluid bed. In terms of Drying Force, this also has an effect as it can be observed from figure 9.21 showing the steady state Drying Force profile for the production-scale.

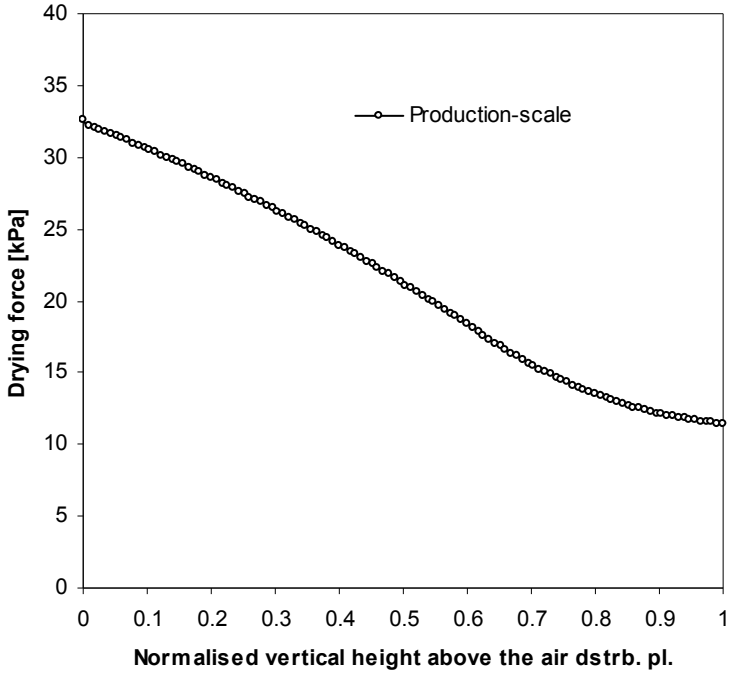

Figure 9.21: Steady state Drying Force profile for the production-scale fluid bed. RD = 5.2 ·10^{-5} min/g, P_{nozzle} = 3 bar. Other model parameters according to table 9-6.

The simulations of the production-scale fluid bed have revealed a classical problem with fluid bed coating process upscaling, which is related to the typical design of fluid bed equipment. Compared to pilot-scale equipment, production-scale equipment is typically much larger in vertical size, while the horizontal dimension is only slightly expanded. This means, among many things, that the expanded particle bed height increases significantly with scale. Typically, similar types of external mixing nozzles are used for any fluid bed scale, and the need for increasing spray capacity in the large scale is solved by adding more identical nozzles. As a consequence of this, even with increasing nozzle airflow rate in production-scale fluid bed equipment, the droplet penetration depth is not increased accordingly to the increased expanded particle bed height. In all, this means that while the spray zone remains close to similar in extension, the expanded bed height increases significantly with scale, causing large temperature and humidity gradients vertically across the bed as well as longer drying-wetting cycles for each particle. This is expected to result in accelerated agglomeration tendencies and different coating layer properties, as reported elsewhere (Werner et al., 2007a,b).

It was observed for the RD/DF pilot-scale experiments that similar high fluidisation velocities (in m/s) combined with close to similar fluidisation air inlet temperatures result in similar tendency of agglomeration, hereby indicating that these fluid bed scales do not behave significantly different with respect to coating behaviour as long as the nozzle pressure is not too low. These simple principles, however, cannot be followed into production-scale as the average particle circulation time significantly increases when going from pilot fluid bed scales to production-scale. This is another consequence of the design of large fluid beds, and comparison of the average particle exchange rates from the different scales reveals that the particle circulation time is roughly seven times larger in the production-scale compared to the small pilot-scale. This means that a much higher inlet and product fluidisation air temperature for a given spray rate is needed for the production-scale in order keep conditions in the spray zone outside the agglomeration regime.

As observed from table 9-6 the c/n ratio is less than 40 % which is where the value of r begins to play a role, as it was presented in the sensitivity analysis. As an indication of this, simulations revealed that the production-scale fluid bed required a simulation time of roughly 400 seconds to reach steady state for all properties, contrary to the pilot-scale fluid beds that required only a few hundred seconds to reach steady state. Besides affecting agglomeration tendency, a low average particle circulation time is likely to affect important properties not considered in the present study such as the quality of coating in terms of morphology and mechanical properties among other things. To overcome such fluid bed design problems the use of models as the one presented in this paper are useful tools in the optimisation of each fluid bed scale to produce unagglomerated coated granules at the same time having a high-intensity process.

9.5. Conclusion

A dynamic heat and mass transfer model for the top-spray batch fluid bed coating process was presented, enabling the calculation of the fluidisation air temperature and humidity as well as particle moisture contents. The model proved good agreement with steady state experimental data for important variables such as the outlet temperature and humidity as well as the product temperature.

The model was applied to study how changing scale influences the in-bed process conditions from an up-scaling point of view. To illustrate successful as well as unsuccessful fluid bed coating process scale-up, experimental data across three pilot-scale fluid beds were selected for model comparison from two papers by Hede et al. (2008a,b). Detailed simulations revealed that the three pilot-scales are not significantly different with respect to steady state in-bed conditions, and as long as the atomisation air pressure, coating solution spray rate and fluidisation air velocity (in m/s) are all above certain values, similar inlet fluidisation air temperatures will lead to similar low tendencies of agglomeration while the process intensity is maintained. This is because such process conditions give similar vertical temperature, humidity and Drying Force profiles again leading to similar particle liquid layer thicknesses, which in turn causes similar tendency of agglomeration as verified using the viscous Stokes theory.

When scaling up to production-scale the temperature and humidity gradients increase significantly, meaning that the error of measuring the bed temperature at one location becomes much larger. It hereby becomes erroneous to define and fix an overall Drying Force value. The Relative Droplet size may apparently be fixed across scale during scale-up, just as it was observed by Rambali et al. (2003), but this requires a significant increase in the inlet fluidisation air temperature in order to keep out of the agglomeration regime. If the inlet temperature is fixed across scale, due to product-activity considerations etc., then the spray intensity must be decreased the larger the fluid bed scale in order to avoid agglomeration. This results in a decreasing outlet absolute humidity and is a consequence of the poor mixing and longer particle circulation times the higher the fluidised bed is. This illustrates that for similar process intensity, the coating process becomes increasingly sensitive towards the tendency of agglomeration the larger the fluid bed scale.

In general, when optimal conditions are to be found for any fluid bed scale, combination of the viscous Stokes theory and particle liquid layer thickness profiles obtained from simulations appears to be a strong tool. Although requiring a heat and mass transfer model, as the one presented in this paper, this optimisation principle is scientifically valid as it is based

on thermodynamics and a generic first-principle model as the viscous Stokes theory. Contrary to the FN or DF/RD approach, this scale-up principle does not have any independent variables (such as the inlet fluidisation air temperature) and all fluid bed process settings can be determined a-priori at any scale.

In all, the dynamic thermodynamic modelling and simulations have provided valuable insight into the top-spray fluid bed coating process. The simplicity, accuracy and versatility of the developed fluid bed coating model makes it a promising simulation tool in future scale-up studies, as well as for the study of response of the system to a change in the process conditions. The scale-up conclusions may be summed up as:

- For each fluid bed scale the nozzle pressure has a great influence in terms of the vertical extension of the spray zone (besides an influence on the mean droplet size and the droplet size distribution). The larger the nozzle pressure, the further into the fluidised particle bed the droplets reach. In order to avoid high local particle moisture contents, the spray zone should ideally take up more than 50 % of the expanded bed height. This is normally achieved in small pilot-scale fluid beds, but not in larger scales. In order to achieve better coating processes in large scale, it is suggested to decrease the distance between the air distributor plate and the nozzle outlet or perhaps insert nozzles at difference vertical positions in the chamber, hereby expanding the vertical extension of the spray zone. Adjusting the fluidisation velocity accordingly should ideally ensure similar particle circulation time across scale.

- The representation of the bed temperature in terms of a single temperature probe located near the air distribution plate may be representative for the temperatures at other locations only in pilot-scale fluid beds. Due to the large increase in expanded particle bed height with increasing scale and the resulting large temperature gradients, such single point temperature measurements are not representative for the temperature at other locations in production-scale fluid beds. Even if the temperature probe is inserted closer to the nozzle outlet, the measurement error would still remain higher than for smaller fluid bed scales. It is suggested not to base process control alone on single-point bed temperature measurements in production-scale fluid beds.

- Agglomeration tendency during coating with salt solutions is closely related to the particle liquid layer profile. The spray rate per kg bed mass and the inlet temperature may be chosen differently from scale to scale, still resulting in a similar low tendency of agglomeration, as long as the vertical particle liquid layer profile through the bed stays below a certain limit determined by the viscous Stokes theory. In scale-up of the fluid bed salt coating process into production-scale it is suggested to use lumped-region models (as the one presented in this paper) in order to combine particle liquid layer simulation results with generic particle-level agglomeration models as the viscous Stokes theory.

9.6. Appendix A. Model equations

A.1. Particle balance on a single control volume

As a result of the model assumptions, the population balance for the particles in control volume S_i may be written according to equation A.1. The unit on both side of equation A.1 is number of particles per second.

$$\underbrace{\frac{dN_i}{dt}}_{\substack{\text{Rate of change in}\\ \text{number of particles}\\ \text{in control volume } S_i}} = \underbrace{r \cdot N_{bed}}_{\substack{\text{Particles entering from}\\ \text{control volume } S_{i-1}}} + \underbrace{r \cdot N_{bed}}_{\substack{\text{Particles entering from}\\ \text{control volume } S_{i+1}}} - \underbrace{r \cdot N_{bed}}_{\substack{\text{Particles leaving to}\\ \text{control volume } S_{i+1}}} - \underbrace{r \cdot N_{bed}}_{\substack{\text{Particles leaving to}\\ \text{control volume } S_{i-1}}} = 0 \qquad \text{(A.1)}$$

A.2. Moisture (water) balance of the particles

A.2.1. In a non-coating control volume

In each non-coating control volume, the balance of moisture on the surface of the core particles is governed by the amount of water introduced by the particles entering S_i from S_{i-1} and S_{i+1}, the amount of water removed by the particles leaving S_i to S_{i-1} and S_{i+1} as well as the water evaporated from or condensed on the particle surfaces according to equation A.2. The unit on both side of equation A.2 is kg H_2O per second.

$$\underbrace{M_p N_i \frac{dW_{p,i}}{dt}}_{\substack{\text{Rate of change in water}\\ \text{contents on particle surfaces}\\ \text{in control volume } S_i}} = \underbrace{M_p \cdot N_{bed} \cdot W_{p,i-1} \cdot r}_{\substack{\text{Mass of water from wet particles}\\ \text{entering from control volume } S_{i-1}}} + \underbrace{M_p \cdot N_{bed} \cdot W_{p,i+1} \cdot r}_{\substack{\text{Mass of water from wet particles}\\ \text{entering from control volume } S_{i+1}}} - \underbrace{M_p \cdot N_{bed} \cdot W_{p,i} \cdot r}_{\substack{\text{Mass of water from wet particles}\\ \text{leaving to control volume } S_{i+1}}} - \underbrace{M_p \cdot N_{bed} \cdot W_{p,i} \cdot r}_{\substack{\text{Mass of water from wet particles}\\ \text{leaving to control volume } S_{i-1}}} - \underbrace{R_{D,i} \cdot M_p \cdot N_i}_{\substack{\text{Mass of water from wetted particles}\\ \text{disappearing due to evaporation}}} \qquad \text{(A.2)}$$

For $1 \le i \le n - c$

A.2.2. In a coating control volume

In a coating control volume, the introduction of coating solution needs to be taken into account, resulting in equation A.3.

$$\underbrace{M_p N_i \frac{dW_{p,i}}{dt}}_{\text{Rate of change in water contents on particle surfaces in control volume } S_i} = \underbrace{M_p \cdot N_{bed} \cdot W_{p,i-1} \cdot r}_{\text{Mass of water from wet particles entering from control volume } S_{i-1}} + \underbrace{M_p \cdot N_{bed} \cdot W_{p,i+1} \cdot r}_{\text{Mass of water from wet particles entering from control volume } S_{i+1}} - \underbrace{R_{D,i} \cdot M_p \cdot N_i}_{\text{Mass of water from wetted particles disappearing due to evaporation}}$$

$$- \underbrace{M_p \cdot N_{bed} \cdot W_{p,i} \cdot r}_{\text{Mass of water from wet particles leaving to control volume } S_{i+1}} - \underbrace{M_p \cdot N_{bed} \cdot W_{p,i} \cdot r}_{\text{Mass of water from wet particles leaving to control volume } S_{i-1}} + \underbrace{\frac{1}{c}(1 - DM_c) \cdot \dot{M}_c}_{\text{Mass of water coming from the coating solution droplets}} \qquad \text{(A.3)}$$

For $n - c < i \leq n$

In the model, it is assumed that the coating solution is uniformly divided over all coating control volumes c. Hence the term 1/c in equation A.3.

A.3. Moisture (water) balance in the gas phase

A.3.1. In a non-coating control volume

The change in air moisture in a non-coating control volume S_i is determined by the incoming moisture in the process air from S_{i-1}, the moisture in the process air leaving towards S_{i+1} and the amount of water coming from evaporated water on the particle surfaces. Because the volume fraction of the bed, in which the atomisation air is homogeneously mixed, is unknown, it is further assumed that the sprayed coating solution and the atomisation air are divided over the same fraction of the fluidised bed being the upper c control volumes. Hence, the air moisture balance may be written according to equation A.4. The unit on both side of equation A.4 is kg H_2O per second.

$$\underbrace{M_{a,i} \frac{dX_{a,i}}{dt}}_{\text{Rate of change in water contents in the gas phase in control volume } S_i} = \underbrace{G_a \cdot X_{a,i-1}}_{\text{Mass of water from the fluidisation air entering from control volume } S_{i-1}} - \underbrace{G_a \cdot X_{a,i}}_{\text{Mass of water from the fluidisation air leaving to control volume } S_{i+1}} + \underbrace{R_{D,i} \cdot M_p \cdot N_i}_{\text{Mass of water entering the gas phase from particle surface drying}} \qquad \text{(A.4)}$$

For $1 \leq i \leq n - c$

where $M_{a,i} = V_i \cdot \rho_{a,i} \cdot \varepsilon_i$ and ε_i is the fraction of the control volume S_i that is not occupied by particles.

A.3.2. In a coating control volume

Similar to equation A.4, equation A.5 expresses the water balance for the coating control volumes.

$$\underbrace{M_{a,i}\frac{dX_{a,i}}{dt}}_{\substack{\text{Rate of change in water contents}\\ \text{in the gas phase in control volume } S_i}} = \underbrace{(G_a + \frac{i-(n-c)-1}{c}\cdot G_{at})\cdot X_{a,i-1}}_{\substack{\text{Mass of water from the cummulated fluidisation/}\\ \text{atomisation air entering from control volume } S_{i-1}}} - \underbrace{(G_a + \frac{i-(n-c)}{c}\cdot G_{at})\cdot X_{a,i}}_{\substack{\text{Mass of water from the cummulated fluidisation/}\\ \text{atomisation air leaving to control volume } S_{i+1}}}$$

$$+ \underbrace{\frac{1}{c}G_{at}\cdot X_{at}}_{\substack{\text{Mass of water from the}\\ \text{atomisation air entering}\\ \text{control volume } S_i}} + \underbrace{R_{D,i}\cdot M_p\cdot N_i}_{\substack{\text{Mass of water entering the gas phase}\\ \text{from particle surface drying}}} \qquad (A.5)$$

For $n - c < i \le n$

A.4. Coating mass balance of the particles

A.4.1. In a non-coating control volume

Particles are assumed only to receive coating if they are in coating control volumes. Hence, for the non-coating control volume, the coating mass balance is simply:

$$\underbrace{M_p N_i \frac{dY_{p,i}}{dt}}_{\substack{\text{Rate of change in coating}\\ \text{mass in control volume } S_i}} = 0 \qquad (A.6)$$

For $1 \le i \le n - c$

A.4.2. In a coating control volume

According to the assumptions, all particles located inside a single coating control volume receive an equal amount of coating mass. Hence, the equation for the coating mass balance is given by equation A.7.

$$\underbrace{M_p N_i \frac{dY_{p,i}}{dt}}_{\substack{\text{Rate of change in coating}\\ \text{mass in control volume } S_i}} = \underbrace{\frac{1}{c}\cdot DM_c\cdot \dot{M}_c}_{\substack{\text{Mass of water coming from}\\ \text{the coating solution droplets}}} \qquad (A.7)$$

For $n - c < i \le n$

A.5. Energy balance of the particles

A.5.1. In a non-coating control volume

The enthalpy balance of the particles within any control volume S_i depends on the enthalpy of the particles entering and leaving S_i, the convective heat transfer between the air and the particles, the latent heat of evaporation of water on the particle surface and the heat losses through the shell of the reactor. The unit in equation A.8 is in J/s.

$$\underbrace{N_i \cdot M_p \cdot C_{p,p} \frac{dT_{p,i}}{dt}}_{\substack{\text{Enthalpy exhange rate}\\ \text{in control volume } S_i}} = \underbrace{M_p \cdot N_{bed} \cdot C_{p,p} \cdot r \cdot (T_{p,i+1} - T_{ref})}_{\substack{\text{Enthalpy from particles entering}\\ \text{from control volume } S_{i+1}}} + \underbrace{M_p \cdot N_{bed} \cdot C_{p,p} \cdot r \cdot (T_{p,i-1} - T_{ref})}_{\substack{\text{Enthalpy from particles entering}\\ \text{from control volume } S_{i-1}}}$$

$$- \underbrace{M_p \cdot N_{bed} \cdot C_{p,p} \cdot r \cdot (T_{p,i} - T_{ref})}_{\substack{\text{Enthalpy from particles leaving}\\ \text{to control volume } S_{i+1}}} - \underbrace{M_p \cdot N_{bed} \cdot C_{p,p} \cdot r \cdot (T_{p,i} - T_{ref})}_{\substack{\text{Enthalpy from particles leaving}\\ \text{to control volume } S_{i-1}}}$$

$$+ \underbrace{\alpha_{p,i} \cdot N_i \cdot A_p \cdot (T_{a,i} - T_{p,i})}_{\substack{\text{Heat from convective heat}\\ \text{transfer from fluidisation air to particles}}} - \underbrace{R_{D,i} \cdot N_i \cdot M_p \cdot Q_{lat,i}}_{\substack{\text{Latent heat needed for}\\ \text{the drying of particles}}} - \underbrace{\Phi_{loss,p,i}}_{\substack{\text{Heat loss to surroundings}\\ \text{(particle-to-wall heat transfer)}}}$$

$\Rightarrow$

$$\underbrace{N_i \cdot M_p \cdot C_{p,p} \frac{dT_{p,i}}{dt}}_{\substack{\text{Enthalpy exhange rate}\\ \text{in control volume } S_i}} = \underbrace{M_p \cdot N_{bed} \cdot C_{p,p} \cdot r \cdot (T_{p,i+1} - T_{p,i})}_{\substack{\text{Netto enthalpy from particles entering}\\ \text{from control volume } S_{i+1}}} + \underbrace{M_p \cdot N_{bed} \cdot C_{p,p} \cdot r \cdot (T_{p,i-1} - T_{p,i})}_{\substack{\text{Netto enthalpy from particles entering}\\ \text{from control volume } S_{i-1}}}$$

$$+ \underbrace{\alpha_{p,i} \cdot N_i \cdot A_p \cdot (T_{a,i} - T_{p,i})}_{\substack{\text{Heat from convective heat}\\ \text{transfer from fluidisation air to particles}}} - \underbrace{R_{D,i} \cdot N_i \cdot M_p \cdot Q_{lat,i}}_{\substack{\text{Latent heat needed for}\\ \text{the drying of particles}}}$$

$$- \underbrace{\Phi_{loss,p,i}}_{\substack{\text{Heat loss to surroundings}\\ \text{(particle-to-wall heat transfer)}}} \qquad \text{(A.8)}$$

For $1 \le i \le n - c$

In equation A.8, A_p is the total surface of one particle in control volume S_i and $Q_{lat,i}$ is the latent heat of vaporisation for pure water approximated by equation A.9.

$$Q_{lat,i} = 10^3 \left(2500.6 - 2.364356 \cdot \left(T_{p,i} - 273.15\right)\right) \qquad \text{(A.9)}$$

A.5.2. In a coating control volume

Analogously to equation A.8 with the addition of a coating related term, the enthalpy balance for the particle phase in a coating control volume can be expressed in terms of equation A.10. Since the diameter of the sprayed droplets is generally between 10 and 40 µm (Lefebvre, 1989), it is assumed that the droplets, travelling from the nozzle towards the particle surface, reach the wet bulb temperature (T_{wb}) before colliding with the particle surface.

$$\underbrace{N_i \cdot M_p \cdot C_{p,p} \frac{dT_{p,i}}{dt}}_{\text{Particle enthalpy exhange rate in control volume } S_i} = \underbrace{M_p \cdot N_{bed} \cdot C_{p,p} \cdot r \cdot (T_{p,i+1} - T_{ref})}_{\text{Enthalpy from particles entering from control volume } S_{i+1}} + \underbrace{M_p \cdot N_{bed} \cdot C_{p,p} \cdot r \cdot (T_{p,i-1} - T_{ref})}_{\text{Enthalpy from particles entering from control volume } S_{i-1}}$$
$$- \underbrace{M_p \cdot N_{bed} \cdot C_{p,p} \cdot r \cdot (T_{p,i} - T_{ref})}_{\text{Enthalpy from particles leaving to control volume } S_{i+1}} - \underbrace{M_p \cdot N_{bed} \cdot C_{p,p} \cdot r \cdot (T_{p,i} - T_{ref})}_{\text{Enthalpy from particles leaving to control volume } S_{i-1}}$$
$$+ \underbrace{\alpha_{p,i} \cdot N_i \cdot A_p \cdot (T_{a,i} - T_{p,i})}_{\text{Heat from convective heat transfer from fluidisation air to particles}} - \underbrace{R_{D,i} \cdot N_i \cdot M_p \cdot Q_{lat,i}}_{\text{Latent heat from the drying of particles}}$$
$$+ \underbrace{\frac{1}{c}\dot{M}_c \cdot C_{p,c} \cdot (T_{wb,i} - T_{ref})}_{\text{Enthalpy comming from droplets entering } S_i \text{ with the wet bulb temperature}} - \underbrace{\frac{1}{c}\dot{M}_c \cdot C_{p,c} \cdot (T_{p,i} - T_{ref})}_{\text{Enthalpy needed to heat the droplets up to particle temperature}}$$
$$- \underbrace{\Phi_{loss,p,i}}_{\text{Heat loss to surroundings (particle-to-wall heat transfer)}} \qquad \text{(A.10)}$$

$\Rightarrow$

$$\underbrace{N_i \cdot M_p \cdot C_{p,p} \frac{dT_{p,i}}{dt}}_{\text{Particle enthalpy exhange rate in control volume } S_i} = \underbrace{M_p \cdot N_{bed} \cdot C_{p,p} \cdot r \cdot (T_{p,i+1} - T_{p,i})}_{\text{Netto enthalpy from particles entering from control volume } S_{i+1}} + \underbrace{M_p \cdot N_{bed} \cdot C_{p,p} \cdot r \cdot (T_{p,i-1} - T_{p,i})}_{\text{Netto enthalpy from particles entering from control volume } S_{i-1}}$$
$$+ \underbrace{\alpha_{p,i} \cdot N_i \cdot A_p \cdot (T_{a,i} - T_{p,i})}_{\text{Heat from convective heat transfer from fluidisation air to particles}} - \underbrace{R_{D,i} \cdot N_i \cdot M_p \cdot Q_{lat,i}}_{\text{Latent heat from the drying of particles}}$$
$$- \underbrace{\frac{1}{c}\dot{M}_c \cdot C_{p,c} \cdot (T_{p,i} - T_{wb,i})}_{\text{Enthalpy needed to heat the droplets up to the particle temperature}} - \underbrace{\Phi_{loss,p,i}}_{\text{Heat loss to surroundings (particle-to-wall heat transfer)}}$$

For $n - c < i \leq n$

A.6. Energy balance of the gas phase

A.6.1. In a non-coating control volume

The equation for the enthalpy balance of the gas phase within each control volume S_i is given by the enthalpy of the air entering from S_{i-1} and the enthalpy leaving to S_{i+1}, the enthalpy of the atomisation air, the heat transferred between the gas phase and the droplet phase, the heat transferred between the gas phase and the particles in S_i. The unit in equation A.11 is in J/s.

$$\underbrace{M_{a,i} \cdot C_{p,a,i} \frac{dT_{a,i}}{dt}}_{\text{Enthalpy exhange rate in control volume } S_i} = \underbrace{G_a \cdot C_{p,a,i} \cdot (T_{a,i-1} - T_{ref})}_{\text{Enthalpy from fluidisation air entering from control volume } S_{i-1}} - \underbrace{G_a \cdot C_{p,a,i} \cdot (T_{a,i} - T_{ref})}_{\text{Enthalpy from droplets leaving to control volume } S_{i+1}}$$

$$- \underbrace{\alpha_{p,i} \cdot N_i \cdot A_p \cdot (T_{a,i} - T_{p,i})}_{\text{Heat from convective heat transfer from fluidisation air to particles}}$$

$$- \underbrace{R_{D,i} \cdot N_i \cdot M_p \cdot C_{p,v,i} \cdot (T_{a,i} - T_{ref})}_{\text{Enthalpy required to heat the vapour up to gas temp.}}$$

$$+ \underbrace{R_{D,i} \cdot N_i \cdot M_p \cdot C_{p,v,i} \cdot (T_{p,i} - T_{ref})}_{\text{Enthalpy from the generated steam}}$$

$$- \underbrace{\Phi_{loss,a,i}}_{\text{Heat loss to surroundings (gas-to-wall heat transfer)}}$$

$$\Rightarrow \tag{A.11}$$

$$\underbrace{M_{a,i} \cdot C_{p,a,i} \frac{dT_{a,i}}{dt}}_{\text{Enthalpy exhange rate in control volume } S_i} = \underbrace{G_a \cdot C_{p,a,i} \cdot (T_{a,i-1} - T_{a,i})}_{\text{Netto enthalpy contribution from fluidisation air}}$$

$$- \underbrace{\alpha_{p,i} \cdot N_i \cdot A_p \cdot (T_{a,i} - T_{p,i})}_{\text{Heat from convective heat transfer from fluidisation air to particles}}$$

$$- \underbrace{R_{D,i} \cdot N_i \cdot M_p \cdot C_{p,v,i} \cdot (T_{a,i} - T_{p,i})}_{\text{Enthalpy required to evaporate water and heat the vapour up to gas temp.}}$$

$$- \underbrace{\Phi_{loss,a,i}}_{\text{Heat loss to surroundings (gas-to-wall heat transfer)}}$$

For $1 \le i \le n - c$

A.6.2. In a coating control volume

$$\underbrace{M_{a,i}\cdot C_{p,a,i}\frac{dT_{a,i}}{dt}}_{\text{Enthalpy exhange rate in control volume } S_i} = \underbrace{(G_a + \frac{i-(n-c)-1}{c}\cdot G_{at})\cdot C_{p,a,i}\cdot(T_{a,i-1}-T_{ref})}_{\text{Enthalpy from cummulated fluidisation/atomisation air entering from control volume } S_{i-1}}$$

$$- \underbrace{(G_a + \frac{i-(n-c)}{c}\cdot G_{at})\cdot C_{p,a,i}\cdot(T_{a,i}-T_{ref})}_{\text{Enthalpy from cummulated fluidisation/atomisation air leaving to control volume } S_{i+1}}$$

$$+ \underbrace{\frac{1}{c}\cdot G_{at}\cdot C_{p,a,i}\cdot(T_{at,i}-T_{ref})}_{\text{Enthalpy from atomisation air entering } S_i}$$

$$- \underbrace{\alpha_{p,i}\cdot N_i\cdot A_p\cdot(T_{a,i}-T_{p,i})}_{\text{Heat from convective heat transfer from fluidisation air to particles}} - \underbrace{R_{D,i}\cdot N_i\cdot M_p\cdot C_{p,v,i}\cdot(T_{a,i}-T_{ref})}_{\text{Enthalpy required to heat the vapour up to gas temp.}}$$

$$+ \underbrace{R_{D,i}\cdot N_i\cdot M_p\cdot C_{p,v,i}\cdot(T_{p,i}-T_{ref})}_{\text{Enthalpy from the generated steam}} - \underbrace{\Phi_{loss,a,i}}_{\text{Heat loss to surroundings (gas-to-wall heat transfer)}}$$

$\Rightarrow$

$$\underbrace{M_{a,i}\cdot C_{p,a,i}\frac{dT_{a,i}}{dt}}_{\text{Enthalpy exhange rate in control volume } S_i} = \underbrace{G_a\cdot C_{p,a,i}\cdot(T_{a,i-1}-T_{a,i})}_{\text{Enthalpy from fluidisation air}} \tag{A.12}$$

$$+ \underbrace{\frac{i-(n-c)}{c}\cdot G_{at}\cdot C_{p,a,i}\cdot(T_{a,i-1}-T_{a,i})}_{\text{Enthalpy from cummulated atomisation air}}$$

$$+ \underbrace{\frac{1}{c}\cdot G_{at}\cdot C_{p,a,i}\cdot(T_{at,i}-T_{a,i-1})}_{\text{Enthalpy from atomisation air entering } S_i}$$

$$- \underbrace{\alpha_{p,i}\cdot N_i\cdot A_p\cdot(T_{a,i}-T_{p,i})}_{\text{Heat from convective heat transfer from fluidisation air to particles}}$$

$$- \underbrace{R_{D,i}\cdot N_i\cdot M_p\cdot C_{p,v,i}\cdot(T_{a,i}-T_{p,i})}_{\text{Enthalpy required to evaporate water and heat the vapour up to gas temp.}}$$

$$- \underbrace{\Phi_{loss,a,i}}_{\text{Heat loss to surroundings (gas-to-wall heat transfer)}}$$

For $n - c < i \leq n$

The parameter $C_{p,a,i}$ is the specific heat of moist air in S_i. It is calculated using the following equation:

$$C_{p,a,i} = C_{p,dry\ air} + X_{a,i}\cdot C_{p,v} \tag{A.13}$$

where $C_{p,dry\ air}$ is the specific heat of dry air being 1000 J/(kg·K) and $C_{p,v}$ is the specific heat capacity of vapour being 1850 J/(kg·K).

A.7. Determining the model parameters

For the application of the model equations is it necessary to find expressions for the model parameters. The applied equations are presented in the following section.

A.7.1. Gas/solid heat and mass transfer

The convective heat transfer coefficient between the particles and the gas phase $\alpha_{p,i}$ can be approximated using the Whitaker equation according to equation A.14.

$$\mathrm{Nu}_{p,i} = 2 + \mathrm{Pr}_i^{2/5}\left(0.43 \cdot \mathrm{Re}_{p,i}^{1/2} + 0.06 \cdot \mathrm{Re}_{p,i}^{2/3}\right)$$
$$\text{for} \begin{cases} 3.5 < \mathrm{Re}_{p,i} < 76000\,,\ \mathrm{Re}_{p,i} = \dfrac{\rho_{a,i} \cdot v_{a,i} \cdot d_p}{\eta_{a,i}} \\ 0.71 < \mathrm{Pr}_i < 380\,,\ \mathrm{Pr}_i = \dfrac{C_{p,a,i} \cdot \eta_{a,i}}{\lambda_{a,i}} \end{cases} \tag{A.14}$$

The Nusselt number provides a basis for comparing the rates of convective heat loss from geometrically similar bodies immersed in a moving fluid. The thermal conductivity of the fluidisation air λ_a is required to calculate the Nusselt number, and the following equation was obtained by regression analysis by Ronsse (2006) based on data adapted from Janna (2000).

$$\lambda_{a,i} = 1.5207 \cdot 10^{-11} \cdot T_{a,i}^{\ 3} - 4.8574 \cdot 10^{-8} \cdot T_{a,i}^{\ 2} + 1.0184 \cdot 10^{-4} T_{a,i} - 3.9333 \cdot 10^{-4}$$
$$\text{where } T_{a,i} \text{ is in K} \tag{A.15}$$

Further, the viscosity of air in kg/(m·s) is calculated using the following equation:

$$\eta_{a,i}(T_{a,i}) = 10^{-6} \frac{1.458 \cdot T_{a,i}^{\ 3/2}}{T_{a,i} + 110.4} \text{ where } T_{a,i} \text{ is in K} \tag{A.16}$$

For the calculation of the Sc and Re numbers, the density of moist air $\rho_{a,i}$ is calculated using the ideal gas law simply as:

$$\rho_{a,i} = \frac{P_i(1 + X_{a,i})}{T_{a,i} \cdot R_g \cdot \left(\dfrac{1}{MW_a} + \dfrac{X_{a,i}}{MW_w}\right)}$$
$$\text{where } T_{a,i} \text{ is in K, } MW_a = 0.028966 \text{ kg/mol,} \tag{A.17}$$
$$MW_w = 0.018015 \text{ kg/mol and } R_g = 8.314472 \frac{m^3 \cdot Pa}{K \cdot mol}$$

The Nusselt number is given as:

$$\mathrm{Nu}_{p,i} = \frac{\alpha_{p,i} \cdot d_p}{\lambda_{a,i}} \tag{A.18}$$

In the model equations, the drying rate $R_{D,i}$ is expressed as mass unit of water evaporated per mass unit of core particles per time. The drying rate is related to the vapour concentration gradient across the boundary layer according to equation A.19.

$$R_{D,i} = \frac{\alpha'_{p,i} \cdot A_p \cdot \left(\frac{W_{p,i}}{|W_{p,i}| + a_{Langmuir}} \right) \cdot \left(P_{v,p,i} - P_{v,a,i} \right)}{M_p \cdot (R_g / MW_v) \cdot (T_{a,i} + T_{p,i})/2} \tag{A.19}$$

In equation A.19 the parenthesis containing $a_{Langmuir}$ is added to the drying rate term in order to avoid steep gradients in situations where the particle water contents approaches zero. The Langmuir expression has thus been added in order to make the simulations more stable by avoiding 0. order drying, which the Matlab ode solvers have difficulties to overcome. The parameter has nothing to do with the thermodynamic end result, but influences the $W_{p,i}(t)$ curve shape only. A value of 0.05 has been selected for the simulation in the present paper. Other values have been tested, but a value of 0.05 gives the best curve shape. The term $P_{v,p,i}$ is the vapour pressure at the particle surface and $P_{v,a,i}$ is the vapour pressure in the gas phase. $P_{v,p,i}$ is a function of the particle surface temperature and can be approximated through the following equation assuming that the boundary gas layer at the surface of a wetted particle is saturated (Campbell, 1977 and Ronsse et al., 2007b).

$$P_{v,p,i}(T_p) \approx P_{v,sat}(T_p) = 10^3 \cdot \exp(52.57633 - 6790.4985 \cdot \frac{1}{T_p} - 5.02808 \cdot \ln(T_p)) \tag{A.20}$$

where the temperature is in K and $P_{v,p,i}$ is in Pa

The term $(T_{a,i} + T_{p,i})/2$ corresponds to the film temperature and the parameter R_g/MW_v is the specific gas constant for water vapour being 461.9 J/(kg·K).

The vapour pressure in the fluidisation air is calculated as:

$$P_{v,a,i} = \left(\frac{rH\%}{100\%} \right) \cdot P_{v,a,i}(T_{a,i}) = \frac{P_i \cdot X_{a,i}}{\left(\frac{MW_w}{MW_a} + X_{a,i} \right)} \tag{A.21}$$

The mass transfer coefficient $\alpha'_{p,i}$ is calculated through an approximation in terms of the dimensionless Sherwood number for which the calculation is analogous to the calculation of the Nusselt number in equation A.14.

$$Sh_{p,i} = 2 + Sc_i^{2/5}(0.43 \cdot Re_{p,i}^{1/2} + 0.06 \cdot Re_{p,i}^{2/3}) \tag{A.22}$$

where the dimensionless Schmidt number, Sc, is the ratio of the momentum diffusivity (or viscosity) to mass diffusivity given by:

$$Sc_i = \frac{\eta_{a,i}}{\rho_{a,i} \cdot D_{v,i}} \tag{A.23}$$

where $D_{v,i}$ is the molecular diffusion coefficient for water vapour in air being approximated by:

$$D_{v,i} = 24.2 \cdot 10^{-6} \left(\frac{T_{a,i}}{293.15} \right)^{1.75} \left(\frac{10^5}{P_i} \right) \quad \text{(A.24)}$$

where the temperature is in K and P is in Pa

where the control volume pressure P_i is approximated by atmospheric pressure. Thus, P_i in equation A.24 is 101325 Pa.

The Sherwood number is given as:

$$Sh_{p,i} = \frac{\alpha'_{p,i} \cdot d_p}{D_{v,i}} \quad \text{(A.25)}$$

where $D_{v,i}$ is the molecular diffusion coefficient for water vapour in air being approximated in the same manner as for the Sc number according to equation A.24.

The wet bulb temperature is estimated on the basis of the given fluidisation air temperature and humidity using equation A.26 and A.27. Initially the vapour pressure at dew point P_{v_dp} is calculated according to:

$$P_{v\_dp} = \frac{\%\ \text{relative humidity}}{100\ \text{rH\%}} \cdot P_{sat}(T_a) \quad \text{(A.26)}$$

The vapour pressure at dewpoint is also equal to (cheresources.com, 2008):

$$P_{v\_dp} = P_{v,sat}(T_{wb}) - \frac{(P_{atm} - P_{sat}(T_{wb})) \cdot (T_{db} - T_{wb})}{1555.56 - 0.722 \cdot T_{wb}} \quad \text{(A.27)}$$

where P_{sat} in found analogously to equation A.20 as:

$$P_{v,sat}(T_{wb}) = 10^3 \cdot \exp(52.57633 - 6790.4985 \cdot \frac{1}{T_{wb}} - 5.02808 \cdot \ln(T_{wb})) \quad \text{(A.28)}$$

where the temperature is in K and P is in Pa

Conversion between absolute and relative humidity is done in terms of the following formulas realising that (Clement et al., 2004):

$$\frac{P_{actual}}{P_{ambient}} = \frac{X_a}{X_a + \frac{18.02\ \text{g/mol}}{28.85\ \text{g/mol}}} \quad \text{(A.29)}$$

where $P_{ambient}$ is assumed 101325 Pa. The relative humidity is found according to:

$$rH\% = \frac{P_{actual} \cdot 100\%}{P_{v,sat}} \tag{A.30}$$

A.8. Wall element heat balance and heat losses

To quantify the overall heat losses in each control volume S_i, the reactor shell is modelled into different elements or control volumes according to figure A1.

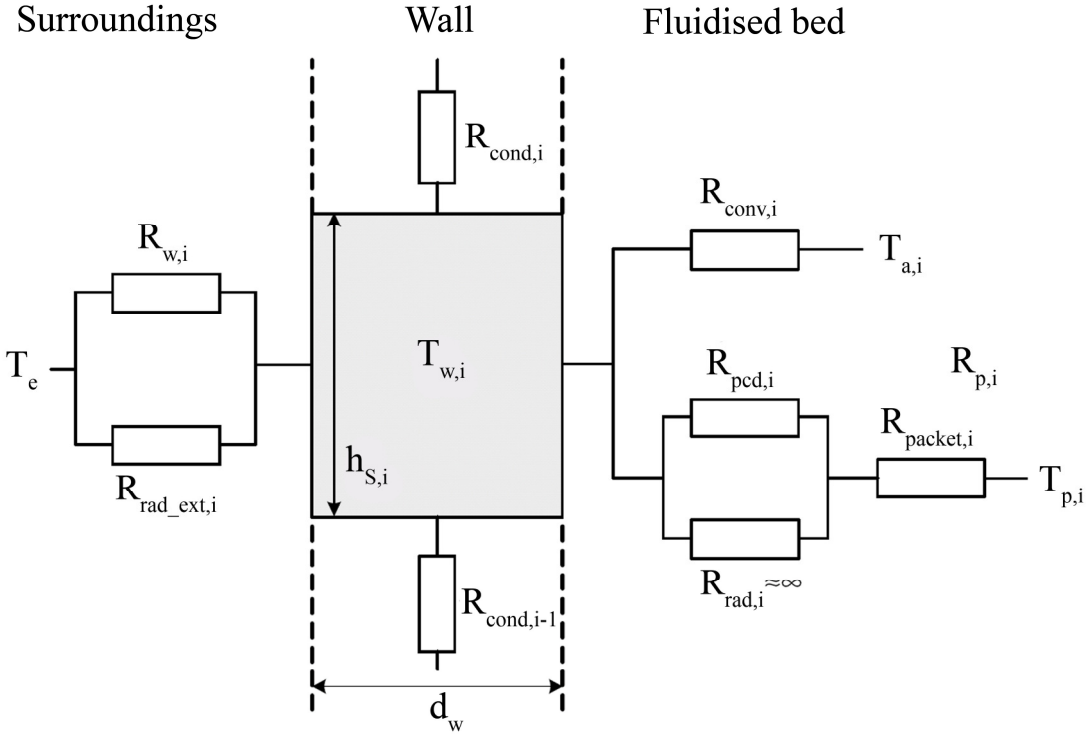

Figure A1: Schematic representation of the heat losses in a single control volume S_i. Based on Ronnse et al. (2007a)

The number of wall elements equals the number of fluidised bed control volumes. In modelling the temperature of the wall element, a number of in- and output heat terms were considered. The different terms are presented below.

A.8.1. Bed to inner wall heat transfer

In a bubbling fluidised bed some of the rising bubbles sweep past the inner reactor wall thereby washing away the particles located there and bringing fresh particles into direct contact with the surface. These groups of particles, which are continuously being swept away along the inner reactor wall, are denoted as emulsion packets. To take into account the coexistence of bubbles and particle emulsion packets in bubbling fluidised beds, the thermal resistance from the bed to the vertical and submerged surface in the bed (i.e. the inner wall), is denoted R_i (having units of $m^2 \cdot K/W$), and for control volume S_i given by:

$$\frac{1}{R_i} = \frac{\delta_w}{R_{conv,i}} + \frac{(1-\delta_w)}{R_{p,i}} \tag{A.31}$$

where δ_w is the bubble voidage at the submerged surface given as (using the Davidson & Harrison (1963) approach - see also chapter two):

$$\delta_w = \frac{\dot{V}_{bu}}{A_{bed} \cdot v_{bu}} = \frac{v_a - v_{mf}}{v_{bu}} \cong \frac{v_a - v_{mf}}{v_a - v_{mf} + 0.711 \cdot (g \cdot d_{bu})^{0.5}} \tag{A.32}$$

where A_{bed} is the bed surface area, v_{bu} is the bubble velocity in m/s, v_{mf} the minimum fluidisation velocity and d_{bu} is the gas bubble diameter for Geldart group B particles given by (Rhodes, 1998):

$$d_{bu} = \frac{0.54}{g^{0.2}} \left(v_{a,i} - v_{mf}\right)^{0.4} \left(h_{bu} + 4 \cdot \left(\frac{\pi \cdot (d_{plate}/2)^2}{N_{or}} \right)^{0.5} \right)^{0.8} \tag{A.33}$$

where g is gravity and h_{bu} is the bubble position above the air distributor plate, having a diameter of d_{plate}. N_{or} is the total number of perforations (plate orifices) in the gas distributor plate. In case the air distributor plate is not a perforated plate, but rather a porous plate, such as a stainless steel wire frame, the term $4 \cdot (\pi \cdot (d_{plate}/2)^2 / N_{or})^{0.5} \approx 0.03$. The gas velocity at minimum fluidisation is found by an approximation of the Ergun equation for particles with diameters above 100 μm (Teunou & Poncelet, 2002) as:

$$v_{mf} = \frac{\eta_{a,i}}{\rho_{a,i} d_p} \left\{ \left(33.7^2 + 0.04084 \cdot Ar\right)^{1/2} - 33.7 \right\} \quad , \; d_p > 100\,\mu m \tag{A.34}$$

where Ar is the Archimedes number defined as (Kunii & Levenspiel, 1991):

$$Ar = \frac{d_p^3 \rho_{a,i} (\rho_p - \rho_{a,i}) g}{\eta_{a,i}^2} \tag{A.35}$$

and $v_{a,i}$ is found simply as:

$$v_{a,i} = \frac{G_{a,i}}{\rho_a \cdot \frac{\pi}{4} \cdot \bar{d}_{S,i}^{\,2}} \tag{A.36}$$

A.8.2. Particles to inner wall heat transfer

The heat transfer from the particles to the inner reactor wall $R_{p,i}$ can be further divided into two serially connected heat transfers being the heat transfer by the emulsion packets and heat transfer through the combination of the wall-particle contact point and the thin gas layer surrounding the wall-particle contact point. The latter is composed of conductive and radiative heat transfer as given by:

$$R_{p,i} = \left(\frac{1}{R_{pcd,i}} + \frac{1}{R_{rad,i}} \right)^{-1} + R_{packet,i} \tag{A.37}$$

where R_{pcd} is the heat transfer resistance through the particle-vertical surface contact point and the surrounding thin gas layer, R_{rad} is the radiative heat transfer and R_{packet} is the heat transfer resistance due to the presence of emulsion packets. According to Kunii & Levenspiel (1991) the radiative heat transfer can be neglected when the temperature is lower than 400 ºC, which is the case for commercial fluid bed coaters. As a result, equation A.37 is approximated as:

$$R_{p,i} = R_{pcd,i} + R_{packet,i} \tag{A.38}$$

The heat transfer through the contact point between the particle and the vertical surface R_{pcd} can be calculated as:

$$\frac{1}{R_{pcd,i}} = \frac{2 \cdot \lambda_{aw,i}}{d_p} + \kappa_w \cdot C_{p,a,i} \cdot \rho_{a,i} \cdot v_{a,i} \tag{A.39}$$

where κ_w is the wall mixing constant assumed to be 0.05 according to Kunii & Levenspiel (1991). The thermal conductivity for stagnant gas in the vicinity of the submerged vertical surface $\lambda_{aw,i}$ can be estimated according to equation A.40:

$$\lambda_{aw,i} = \varepsilon_{mf,w} \cdot \lambda_{a,i} + (1 - \varepsilon_{mf,w}) \cdot \lambda_p \cdot \left[\frac{1}{\tau_w \cdot (\lambda_p / \lambda_{a,i}) + 1/3} \right] \tag{A.40}$$

where τ_w is the ratio of effective thickness of gas film around a contact point to particle diameter for contact between particle and surface. According to data adapted from Kunii & Levenspiel (1991), τ_w may be approximated as:

$$\tau_w = 0.3361 \cdot \left(\lambda_p / \lambda_{a,i}\right)^{-0.1862} \text{ for } 1 \le \left(\lambda_p / \lambda_{a,i}\right) \le 10^4 \tag{A.41}$$

In equation A.40 the variable $\varepsilon_{mf,w}$ is the bed voidage at the submerged vertical surface and at minimum fluidisation gas velocity. This parameter is assumed to be equal to the overall bed voidage at minimum fluidisation, and thus:

$$\varepsilon_{mf,w} \cong \varepsilon_{mf} \tag{A.42}$$

Considering thermal diffusion through an emulsion packet and assuming that the properties of the emulsion are equal to those at minimum fluidisation, R_{packet} can be calculated as:

$$\frac{1}{R_{packet,i}} = \frac{2}{\sqrt{\pi}} \cdot \left(\frac{\lambda_{amark,i} \cdot \rho_p \cdot (1 - \varepsilon_{mf}) \cdot C_{p,p} \cdot f_{bu,w}}{1 - \delta_w} \right)^{0.5} \tag{A.43}$$

where $f_{bu,w}$ is the bubble frequency at the vertical surface. Generally, it is assumed to be equal to the overall bubble frequency in the bed f_{bu}. The bubble frequency can be estimated on the basis of the volumetric flow rate of the fluidisation gas and the bubble size as:

$$f_{bu} = \frac{G_a}{\frac{\pi}{6} \cdot d_{bu}^{\ 3}} \tag{A.44}$$

For the use in equation A.40, ε_{mf} is calculated as (using the Broadhurst & Becker equation):

$$\varepsilon_{mf} = 0.586 \cdot \psi_p^{\ -0.72} \left(\frac{\eta_{a,i}^{\ 2}}{\rho_{a,i} \cdot g \cdot (\rho_p - \rho_{a,i}) \cdot d_p^{\ 3}} \right)^{0.029} \cdot \left(\frac{\rho_{a,i}}{\rho_p} \right)^{0.021} \tag{A.45}$$

where ψ_p is the particle sphericity (see also chapter two).

$\lambda_{amark,i}$ is the thermal conductivity for stagnant gas in the bed and is approximated as:

$$\lambda_{amark,i} = \varepsilon_{mf} \cdot \lambda_{a,i} + (1 - \varepsilon_{mf}) \cdot \lambda_p \cdot \left[\frac{1}{\tau_{mark} \cdot (\lambda_p / \lambda_{a,i}) + 2/3} \right] \tag{A.46}$$

where τ_{mark} is the ratio of effective thickness of gas film around a contact point to particle diameter for contact between adjacent particles. According to data adapted from Kunii & Levenspiel (1991), τ_{mark} may be approximated as:

$$\tau_{mark} = 0.3116 \cdot \left(\lambda_p / \lambda_{a,i} \right)^{-0.2174} \text{ for } 1 \le \left(\lambda_p / \lambda_{a,i} \right) \le 10^4 \tag{A.47}$$

A.8.3. Bubbles to inner wall heat transfer

In equation A.31, the term $\delta_w/R_{conv,i}$ describes the heat transfer resistance between the gas bubbles and the inner reactor wall. The heat transfer through convection at a submerged surface in the fluidised bed depends on the geometry of the heat transfer surface. However, as an approximation, $R_{conv,i}$ was calculated through the Nusselts number for forced convection in a vertical tube according to the Dittus-Boelter equation for fluids in turbulent flow (Ronsse, 2006):

$$Nu_{w,i} = 0.023 \cdot Re_{w,i}^{\ 0.8} \cdot Pr_i^{\ 0.4} \tag{A.48}$$

where

$$Nu_{w,i} = \frac{\alpha_{w,i} \cdot d_{s,i}}{\lambda_{a,i}} \tag{A.49}$$

and

$$\begin{aligned} Re_{w,i} &= \frac{\rho_{a,i} \cdot v_{a,i} \cdot d_{s,i}}{\eta_{a,i}} \\ Pr_i &= \frac{C_{p,a,i} \cdot \eta_{a,i}}{\lambda_{a,i}} \end{aligned} \tag{A.50}$$

Thus:

$$R_{conv,i} = \frac{1}{\alpha_{w,i}} = \frac{d_{s,i}}{Nu_{w,i} \cdot \lambda_{a,i}} \tag{A.51}$$

A.8.4. Heat transfer along the reactor wall

Because of the relatively small heat transfer resistance of the reactor wall (it is stainless steel) compared to the heat transfer resistance from the bed towards the wall and from the wall towards the environment, the wall element is considered to have a single temperature $T_{w,i}$. Due to the geometric nature of the wall element ($h_{S,i} >> d_w$), vertical heat conduction to or from adjacent wall element is also taken into account, meaning that:

$$R_{cond,i} = \frac{h_{S,i} + h_{S,i+1}}{2 \cdot \lambda_w} \tag{A.52}$$

A.8.5. Heat transfer from the wall towards the environment

This heat transfer towards the environment is composed of convective and radiative heat transfer. The convective heat transfer is approximated by calculating the Nusselt number of a vertical cylinder with height h_{bed} (corresponding to natural or free convection):

$$Nu_e = 0.59 \cdot (Gr_e \cdot Pr_e)^{0.25} \text{ when } 10^4 < Gr_e \cdot Pr_e < 10^9$$

where

$$Gr_e = \frac{\beta_a \cdot g \cdot (d_{S,i})^3 \cdot \rho_{film,i}^{\ 2} \cdot (T_{w,i} - T_e)}{\eta_{film,i}^{\ 2}}$$

and

$$Pr_e = \frac{C_{p,film,i} \cdot \eta_{film,i}}{\lambda_{film,i}} \tag{A.53}$$

and

$$Nu_e = \frac{\alpha_{film} \cdot d_{S,i}}{\lambda_{film,i}}$$

where β_a is the thermal expansion coefficient of the fluidisation air being approximated as $3.0 \cdot 10^{-3}$ K^{-1}. All other physical properties in equation A.53 should be evaluated at the film temperature being $T_{film} = (T_e + T_w)/2$, where T_e is the external air temperature. Hence the subscript "film" in the parameters in equation A.53.

Thus:

$$R_{w,i} = \frac{1}{\alpha_{film}} = \frac{d_{s,i}}{Nu_e \cdot \lambda_{film,i}} \tag{A.54}$$

The radiative heat loss is calculated by:

$$Q_{rad,i} = \sigma \cdot \theta_w \cdot A_{w,i} \cdot (T_{w,i}^{\ 4} - T_e^{\ 4}) \tag{A.55}$$

where $A_{w,i}$ is the wall area in control volume S_i (it is assumed throughout the model that the outer and inner area of the control volume is the same), σ is the Stefan-Boltzmann constant being equal to $5.669 \cdot 10^{-8}$ W m^{-2} K^{-4}, and θ_w is the emissivity which is used to describe the extent to which a surface behaves similar to a blackbody ($\theta_w = 1$). A black body is an ideal surface which emits the maximum possible energy at a given wavelength and temperature. For the present fluid bed model, a value of $\theta_w = 0.28$ is chosen, corresponding to emittance for far-infra-red radiation for stainless steel (omega.com, 2008).

A.8.6. Total heat transfer balance towards environment

By combining all described heat transfer terms, the total energy balance for the reactor wall may be written as:

$$C_{p,w} \cdot M_{w,i} \cdot \frac{dT_{w,i}}{dt} = \begin{bmatrix} \text{heat inputs from bed} \\ \text{and adjacent wall elements} \end{bmatrix} - \begin{bmatrix} \text{heat output to environment} \\ \text{and adjacent wall elements} \end{bmatrix} \tag{A.56}$$

where the mass of the reactor element $M_{w,i}$ is calculated as:

$$M_{w,i} = \pi \cdot d_{S,i} \cdot d_w \cdot h_{S,i} \cdot \rho_w \tag{A.57}$$

where $d_{S,i}$ is the inner (bottom) diameter of the control volume S_i, d_w is the reactor wall thickness, $h_{S,i}$ is the height of the wall element and ρ_w is the specific density of the reactor wall material. The reactor wall control volume can be observed in figure A2.

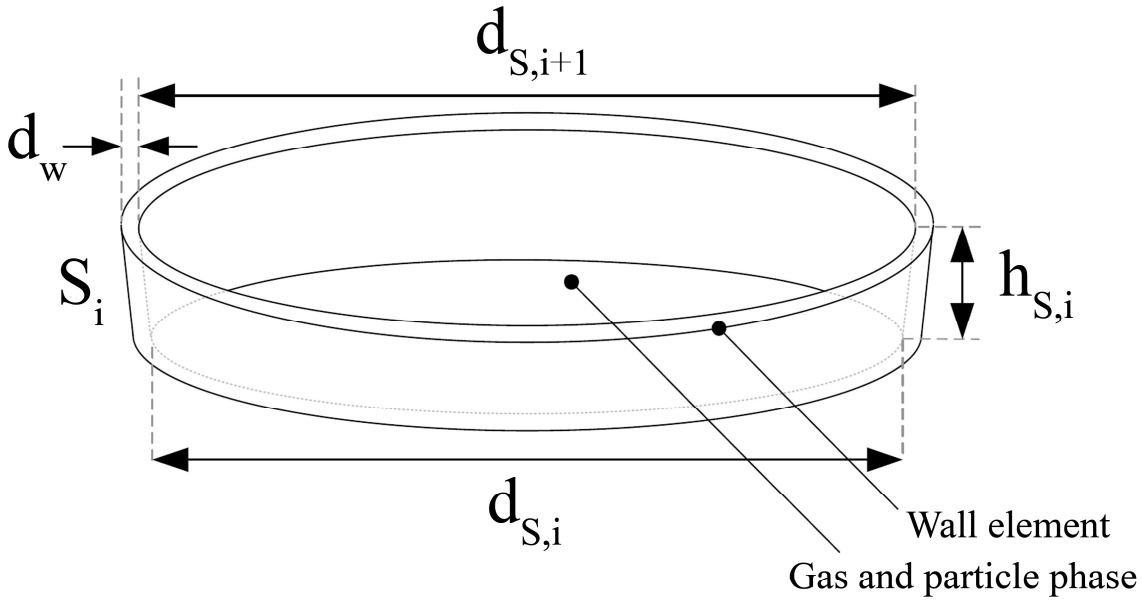

Figure A2: Schematic representation of the reactor wall control volume.

In terms of symbols, equation A.56 becomes:

$$\underbrace{C_{p,w}\cdot\rho_w\cdot A_{w,i}\cdot d_w\cdot\frac{dT_{w,i}}{dt}}_{\text{Enthalpy exchange rate at the wall in control volume } S_i}=\underbrace{\frac{A_{w,i}\cdot\delta_w\cdot(T_{a,i}-T_{w,i})}{R_{conv,i}}}_{\text{Convective heat from gas bubbles}}+\underbrace{\frac{A_{w,i}\cdot(1-\delta_w)\cdot(T_{p,i}-T_{w,i})}{R_{p,i}}}_{\text{Convective heat from particles}}$$

$$-\underbrace{\sigma\cdot\theta_w\cdot A_{w,i}(T_{w,i}^{\,4}-T_e^{\,4})}_{\text{Radiative heat transfer from wall to surroundings}}-\underbrace{\frac{A_{w,i}}{R_{w,i}}(T_{w,i}-T_e)}_{\text{Convective heat transfer from wall to surroundings}} \qquad \text{(A.58)}$$

$$+\underbrace{\frac{\pi\cdot d_{S,i}\cdot d_w}{R_{cond,i-1}}(T_{w,i-1}-T_{w,i})}_{\text{Conductive heat from } S_{i-1}}-\underbrace{\frac{\pi\cdot d_{S,i}\cdot d_w}{R_{cond,i}}(T_{w,i}-T_{w,i+1})}_{\text{Conductive heat leaving to } S_{i+1}}$$

In the heat and mass balance equations, the heat transfer from the fluidised bed towards the inner reactor wall is divided into two parts being the particles-to-wall heat transfer $\Phi_{loss,p,i}$ and gas-to-wall heat transfer $\Phi_{loss,a,i}$. These two heat transfer contributions correspond to the first two terms on the right-hand side in equation A.58 according to:

$$\Phi_{loss,a,i}=\frac{A_{w,i}\cdot\delta_w\cdot(T_{a,i}-T_{w,i})}{R_{conv,i}}$$

$$\Phi_{loss,p,i}=\frac{A_{w,i}\cdot(1-\delta_w)\cdot(T_{p,i}-T_{w,i})}{R_{p,i}} \qquad \text{(A.59)}$$

9.7. Appendix B. Parameter constants used in the simulations

All the parameters listed below were kept constant throughout all simulations irrespectively of the fluid bed scale.

Parameter	Symbol	Values used in the simulations
Langmuir coefficient	$a_{Langmuir}$	0.05 (Dimensionless)
Reactor wall thickness	d_w	0.003 m
Reactor wall thermal conductivity	λ_w	14.6 W /(m · K)
Reactor wall emittance	θ_w	0.28 (Dimensionless)
Reactor wall specific heat capacity	$C_{p,w}$	500 J/(kg · K)
Reactor wall density	ρ_w	7850 kg/m^3
Wall mixing constant	κ_w	0.05 (Dimensionless)
Stefan-Boltzmann constant	σ	$5.669 \cdot 10^{-8}$ W/(m^2 · K^4)
Particle diameter	d_p	$250 \cdot 10^{-6}$ m
Particle sphericity	ψ_p	0.86 (Dimensionless)
Particle density	ρ_p	2600 kg/m^3
Particle specific heat capacity	$C_{p,p}$	837 J/(kg · K)
Specific heat of dry air	$C_{p,dry\ air}$	1000 J/(kg · K)
Particle thermal conductivity	λ_p	0.8 W /(m · K)
Specific heat capacity of water	$C_{p,H2O}$	4181.3 J/(kg · K)
Specific heat capacity of cores	$C_{p,Core}$	902.537 J/(kg · K)
Specific heat capacity of vapour	$C_{p,v}$	1850 J/(kg · K)
Coating solution temperature	T_c	333.15 K
Atomisation air temperature	T_{at}	293.15 K
Absolute humidity of nozzle air	X_{at}	$2.87 \cdot 10^{-4}$ kg water/ kg dry air
External air temperature	T_e	298.15 K
External atmospheric pressure	P_e	$1.01 \cdot 10^5$ Pa
Gravity	g	9.82 m/s^2
Thermal expansion coefficient of the fluidisation air	β_a	$3.0 \cdot 10^{-3}$ K^{-1}

9.8. Table of symbols

Symbols		Unit
$a_{Langmuir}$	Langmuir coefficient	Dimensionless
A	Constant	Dimensionless
A_p	Surface area of a single particle	m^2
Ar	Archimedes number	Dimensionless
$A_{w,i}$	Total wall area in S_i	m^2
B	Constant	Dimensionless
BD	Bulk density of the powder	kg/m^3
Bi_{dr}	Droplet Biot number	Dimensionless
Bi_p	Particle Biot number	Dimensionless
c	Number of coating control volumes	Dimensionless
$C_{p,a,i}$	Moist air specific heat capacity in S_i	J/(kg·K)
$C_{p,c}$	Coating solution specific heat capacity	J/(kg·K)
$C_{p,Core}$	Specific heat capacity of cores	J/(kg·K)
$C_{p,dry\ air}$	Specific heat capacity of dry air	J/(kg·K)
$C_{p,H2O}$	Specific heat capacity of water	J/(kg·K)
$C_{p,p}$	Particle specific heat capacity	J/(kg·K)
$C_{p,v}$	Specific heat capacity of vapour	J/(kg·K)
$C_{p,w}$	Reactor wall specific heat capacity	J/(kg·K)
d_{bottom}	Reactor bottom diameter	m
d_{bu}	Gas bubble diameter	m
d_{dr}	Droplet diameter	m
d_p	Particle diameter	m
d_{plate}	Diameter of gas distributor plate	m
d_{top}	Reactor top diameter	m
d_w	Reactor wall thickness	m
D_0	Normalised distance	m
DF	Drying Force	kPa
$D_{v,i}$	Molecular diffusion coefficient for vapour	m^2/s
DM_c	Coating solution dry-matter content	kg dry-matter/kg solution
e	Particle coefficient of restitution	Dimensionless
f_{bu}	Bubble frequency	1/s
$f_{bu,w}$	Bubble frequency at the vertical surface	1/s
FN	Flux Number	Dimensionless
g	Gravity	m/s^2
G_a	Fluidisation dry air mass flow rate	kg/s
G_{at}	Atomisation dry air mass flow rate	kg/s
Gr	Grasshof number	Dimensionless
h_{asp}	Characteristic height of particle surface asperities	m
h_{bed}	Bed height	m
h_{bu}	Vertical bubble position above the distributor plate	m
h_{FB}	Fluid bed height	m
h_{liq}	Liquid layer height	m
h_{nozzle}	The height of the spray nozzle above the bottom of the fluidisation chamber	m
$h_{S,i}$	Height of control volume S_i	m
i	Index	Dimensionless

$\dot{m}_{nozzle\,air}$	Atomisation air mass flow rate	kg/s
$\dot{m}_{spray}$	Coating liquid mass spray rate	kg/s
$\dot{M}_c$	Mass flow rate of coating solution	kg/s
$M_{a,i}$	Mass of fluidisation air in S_i	kg
M_{bed}	Overall bed mass	kg
$M_{dr,i}$	Mass of droplets in control volume i	kg
M_p	Mass of a single particle	kg
MW_a	Molecular weight of fluidisation air	kg/mol
MW_w	Molecular weight of water	kg/mol
n	Total number of control volumes	Dimensionless
N_i	Number of particles in control volume S_i	Dimensionless
N_{bed}	Total number of particles in the system	Dimensionless
N_{or}	Total number of perforations in the gas distributor plate	Dimensionless
N_{sim}	Number of simulated particles	Dimensionless
Nu	Nusselt number	Dimensionless
$P_{ambient}$	Ambient pressure	Pa
P_{atm}	Atmospheric pressure	Pa
P_{at}	Atomisation air pressure	Pa
P_e	External atmospheric pressure	Pa
P_i	Pressure in S_i	Pa
P_{nozzle}	Nozzle pressure	Pa or bar
P_{v_dp}	Vapour pressure at dew point	Pa
$P_{v,a,i}$	Vapour pressure in gas phase in S_i	Pa
$P_{v,p,i}$	Vapour pressure at particle surface in S_i	Pa
$P_{v,sat}$	Saturated vapour pressure	Pa
Pr_i	Prandtl number in S_i	Dimensionless
$\dot{q}_{mliq}$	Spray mass flux	kg/(s·m^2)
$Q_{lat,i}$	Latent heat in S_i	J/g
$Q_{rad,i}$	Radiative heat loss	J
r_1, r_2	Radius of granule 1 and 2, respectively	µm
r	Particle exchange rate	1/s
r_{harm}	Harmonic mean granule radius	m
RD	Relative Droplet size	min/g
R_i	Thermal heat transfer resistance from the bed to a vertical submerged surface in the bed in S_i	(m^2·K)/W
$R_{cond,i}$	Thermal heat transfer resistance from vertical heat conduction coming from an adjacent wall element S_{i-1}	(m^2·K)/W
$R_{conv,i}$	Thermal heat transfer resistance from convection from fluidisation gas to chamber wall in S_i	(m^2·K)/W
$R_{D,i}$	Drying rate in S_i	kg water / (kg core · s)
R_g	Gas constant	m^3·Pa/(K · mol)
$R_{rad\_ext,i}$	Thermal radiative heat transfer resistance in the surroundings	(m^2·K)/W
$R_{pcd,i}$	Thermal heat transfer resistance through the particle-vertical surface contact point and the surrounding thin gas layer in S_i	(m^2·K)/W

$R_{p,i}$	Thermal heat transfer resistance from the particles to chamber wall in S_i	$(m^2 \cdot K)/W$
$R_{packet,i}$	Thermal heat transfer resistance due to the presence of emulsion packets in S_i	$(m^2 \cdot K)/W$
$R_{rad,i}$	Thermal radiative heat transfer resistance in S_i	$(m^2 \cdot K)/W$
Re	Reynolds number of gas phase in S_i	Dimensionless
$Re_{p,i}$	Particle Reynolds number in S_i	Dimensionless
R_w	Thermal heat transfer resistance from the wall to surroundings	$(m^2 \cdot K)/W$
S_i	The i´th control volume	Dimensionless
Sc_i	Schmidt number	Dimensionless
$Sh_{p,i}$	Particle Sherwood number	Dimensionless
St_v	Viscous Stokes number	Dimensionless
St_v^*	Critical viscous Stokes number	Dimensionless
t	Time	s
t_0	Simulation start time	s
t_{end}	Simulation end time	s
t_{sim}	Simulated time	s
t_{heat}	Time of heating stage	s
t_{spray}	Spraying time	s
u_0	Initial granule collision velocity	m/s
$T_{a,i}$	Fluidisation air temperature in S_i	K
T_{bed}	Bed temperature	K
$T_{a,in}$	Inlet fluidisation temperature	K
T_{at}	Atomisation air temperature	K
T_c	Coating solution temperature	K
T_{db}	Dry bulb temperature	K
T_e	Temperature of the surroundings (externals)	K
$T_{p,i}$	Particle temperature in S_i	K
T_{ref}	Reference temperature (arbitrarily chosen)	K
$T_{wb,i}$	Wetbulb temperature in S_i	K
$v_{a,i}$	Fluidisation air velocity in S_i	m/s
v_{mf}	Minimum fluidisation velocity	m/s
v_{bu}	Bubble rise velocity	m/s
v_e	Excess gas velocity	m/s
v_{rel}	The difference between the atomisation air velocity and the liquid velocity at the nozzle outlet	m/s
V_i	Volume of S_i	m^3
V_{bed}	Bed volume	m^3
$W_{p,i}$	Particle water content in S_i	kg water / (kg core)
$X_{a,i}$	Absolute air humidity in S_i	kg water/ kg dry air
$X_{a,in}$	Inlet fluidisation air absolute humidity	kg water/ kg dry air
X_{a_sat}	Fluidisation air absolute humidity at saturation	kg water/ kg dry air
X_{at}	Absolute humidity of nozzle air	kg water/ kg dry air
Y_i	Collected coating mass	kg dry-matter / kg core
$Y_{p,i}$	Coating mass deposited in S_i	kg dry-matter/ kg core

Greek

α_{dr}	Droplet convective heat transfer coefficient	W /(m^2·K)
$\alpha_{p,i}$	Particle convective heat transfer coefficient in S_i	W /(m^2·K)
$\alpha'_{p,i}$	Mass transfer coefficient in S_i	m/s
β_a	Thermal expansion coefficient of the fluidisation air	K^{-1}
δ	Dimensionless bubble spacing	Dimensionless
δ_w	Bubble voidage at the submerged surface	Dimensionless
Δt	Simulation time step	s
ε_i	Bed voidage in S_i (volume not occupied by particles)	Dimensionless
ε_{bed}	Bed porosity	Dimensionless
ε_{mf}	Bed voidage at minimum fluidisation	Dimensionless
$\varepsilon_{mf,w}$	Bed voidage at the submerged vertical surface at minimum fluidisation	Dimensionless
ε_{wall}	Reactor wall emittance for far-infrared radiation	Dimensionless
$\eta_{a,i}$	Fluidisation air viscosity in S_i	Pa·s
η_{liq}	Coating solution viscosity	kg/m s
θ_w	Reactor wall emittance	Dimensionless
κ_w	Wall mixing constant	Dimensionless
$\lambda_{a,i}$	Fluidisation air thermal conductivity in S_i	W /(m·K)
$\lambda_{aw,i}$	Thermal conductivity for stagnant gas in the vicinity of the submerged vertical surface in S_i	W /(m·K)
$\lambda_{amark,i}$	Thermal conductivity for stagnant gas in the bed in S_i	W /(m·K)
λ_p	Particle thermal conductivity	W /(m·K)
λ_w	Reactor wall thermal conductivity	W /(m·K)
$\rho_{a,i}$	Fluidisation air density in S_i	kg/m^3
ρ_g	Granule density	kg/m^3
ρ_{liq}	Coating solution density	kg/m^3
ρ_p	Particle density	kg/m^3
ρ_w	Reactor wall density	kg/m^3
σ	Stefan-Boltzmann constant	W/(m^2·K^4)
τ_{mark}	Equivalent gas film thickness of the gas film around the adjacent particle-particle contact point (compared to the particle diameter)	Dimensionless
τ_w	Equivalent gas film thickness of the gas film around the surface-particle contact point (compared to the particle diameter)	Dimensionless
$\Phi_{loss,a,i}$	Fluidisation air heat loss (air-to-wall heat transfer)	J/s
$\Phi_{loss,p,i}$	Particle loss (particle-to-wall heat transfer)	J/s
ψ_p	Particle sphericity	Dimensionless

9.9. References

Akkermans, J.H.M., Edwards, M.F., Groot, A,T.J., Montanus, C.P.M., Van Pomeren, R.W.J. and Yuregir, K.R. (1998) Production of detergent granulates, Patent WO98/58046.

Boerefijn, R. and Hounslow, M.J. (2005) Studies of fluid bed granulation in an industrial R&D context, Chemical Engineering Science, No. 60, pp. 3879-3890.

Campbell, G.S. (1977) An introduction to environmental biophysics, Springer-Verlag, NY.

Cheresources.com. Visit at the homepage cheresources.com, March 2008.

Clement, K.H., Fangel, P., Jensen, A.D. and Thomsen, K. (2004) Kemiske enhedsoperationer, Polyteknisk Forlag, 5. Edition.

Davidson, J.F. and Harrison, D. (1963): Fluidised Particles, Cambridge University Press, New York.

Dewettinck, K. (1997) Fluidized Bed Coating in Food Technology: Process and Product Quality, Ph.D. Thesis, University of Ghent.

Ennis, B.J., Tardos, G. and Pfeffer, R. (1991) A microlevel-based characterization of granulation phenomena, Powder Technology, No. 65, pp. 257-272.

Guignon, B., Duquenoy, A. and Dumoulin, E.D. (2002) Fluid Bed Encapsulation of Particles: Principles and Practice, Drying Technology, No. 20, pp. 419-447.

Hede, P.D. (2005) Fluidised bed coating and granulation, M.Sc. Thesis, Department of Chemical Engineering, CHEC Research Center, Technical University of Denmark, pp.1-227.

Hede, P.D. (2006) Towards Mathesis Universalis: Modern aspects of modelling batch fluidised bed agglomeration and coating systems – a review, CHEC Report R0605, Department of Chemical Engineering, Technical University of Denmark, pp. 1-101.

Hede, P.D., Bach, P. and Jensen, A.D. (2007a) Small-scale top-spray fluidised bed coating: Granule impact strength, agglomeration tendency and coating layer morphology, Powder Technology, No. 176, pp. 156-167.

Hede, P.D., Bach, P. and Jensen, A.D. (2008a) Validation of the Flux Number as scaling parameter for top-spray fluid bed systems, Chemical Engineering Science, No. 63, pp. 815-828.

Hede, P.D., Bach, P. and Jensen, A.D. (2008b) Top-spray fluidised bed coating: Scale-up in terms of Relative Droplet size and Drying Force, Powder Technology, No. 184, pp. 318-332.

Hede, P.D., Bach, P. and Jensen, A.D. (2008c) Two-fluid spray atomisation and pneumatic nozzles for fluid bed coating/agglomeration purposes: a review, Chemical Engineering Science, Vol. 63, No. 14, pp. 3821-3842.

Hede, P.D., Bach, P. and Jensen, A.D. (2008d) Fluidised bed coating with sodium sulphate and PVA/TiO_2. Part I: Review and agglomeration regime maps, Industrial & Engineering Chemical Research, awaiting publication – proof corrected version.

Hede, P.D., Bach, P. and Jensen, A.D. (2008e) Fluidised bed coating with sodium sulphate and PVA/TiO_2. Part II: Influence of coating solution viscosity, stickiness, pH and droplet diameter on agglomeration, Industrial & Engineering Chemical Research, awaiting publication – proof corrected version.

Hede, P.D., Bach, P. and Jensen, A.D. (2008f) Fluidised bed coating with sodium sulphate and PVA/TiO_2. Part III: The role of tackiness and the tack Stokes number, Industrial & Engineering Chemical Research, awaiting publication – proof corrected version.

Heinrich, S., Blumschein, J., Henneberg, M., Ihlow, M., Peglow, M. and Mörl, L. (2003) Study of dynamic multi-dimensional temperature and concentration distributions in liquid-sprayed fluidized beds, Chemical Engineering Science, No. 58, pp. 5135-5160.

Heinrich, S. and Mörl, L. (1999) Fluidized bed spray granulation – a new model for the distribution of particle wetting and of temperature and concentration distribution, Chemical Engineering and Processing, No. 38, pp. 635-663.

Iveson, S.M., Litster, D.L., Hapgood, K. and Ennis, B.J. (2001) Nucleation, growth and breakage phenomena in agitated wet granulation processes: a review, Powder Technology, No. 117, pp. 3-39.

Janna, W.S. (2000) Engineering Heat Transfer, 2nd Edition, Boca Raton: CRC Press N.Y., pp. 1-683

Kerkhof, P.J.A.M. (2000) Some modelling aspects of (batch) fluid-bed drying of lifescience products, Chemical Engineering and Processing, No. 39, pp. 69-80.

Kunii, D. and Levenspiel, O. (1991): Fluidization Engineering, 2nd Edition, Butterworth-Heinemann, Stoneham.

Larsen, C.C., Sonnergaard, J.M., Bertelsen, P. and Holm, P. (2003) A new process control strategy for aqueous film coating of pellets in fluidised bed, European Journal of Pharmaceutical Sciences, No. 20, pp. 273-283.

Lefebvre, A.H. (1989) Atomisation and Sprays, Hemisphere Publishing Corporation, Washington D.C.

Masters, K. (1972) Spray Drying – An Introduction to Principles Operational Practice and Applications, Leonard Hill Books, London.

Maronga, S.J. and Wnukowski, P. (1997a) Establishing temperature and humidity profiles in fluidized bed particulate coating, Powder Technology, No. 94, pp. 181-185.

Maronga, S.J. and Wnukowski, P. (1997b) Modelling of the three-domain fluidized-bed particulate coating process, Chemical Engineering Science, No. 17, pp. 2915-2925.

Maronga, S.J. and Wnukowski, P. (1998) The use of humidity and temperature profiles in optimising the size of fluidized bed in a coating process, Chemical Engineering and Processing, No. 37, pp. 423-432.

Mehta, A.M. (1988) Scale-up considerations in the fluid-bed process for controlled-release products, Pharmaceutical Technology, No. 12, pp. 46-52.

Mort, P.R. (2005) Scale-up of binder agglomeration processes, Powder Technology, No. 150, pp. 86-103.

Mostoufi & Chaouki (2001) Local solid mixing drag coefficient in fluidized beds, Powder Technology, No. 114, pp. 23-31.

Omega.com (2008) Visit at the website www.omega.com, February 2008.

Overturf, B.W. and Reklaitis, G.V. (1983) Fluidized-Bed Reactor Model with Generalized Particle Balances, AIChE Journal, Vol. 29, No. 5, 1983.

Rambali, B., Baert, L. and Massart, D.L. (2003). Scaling up of the fluidized bed granulation process, International Journal of Pharmaceutics, No. 252, pp. 197-206.

Rhodes, M (1998) Introduction to Particle Technology, John Wiley & Sons Ltd., Chichester.

Ronsse, F. (2006) Modelling heat and mass transfer in fluidised bed coating processes, Ph.D. Thesis, Ghent University.

Ronsse, F., Pieters, J.G. and Dewettinck, K. (2007a) Combined population balance and thermodynamic modelling of the batch top-spray fluidised bed coating process. Part I – Model development and validation, Journal of Food Engineering, No. 78, pp. 296-307.

Ronsse, F., Pieters, J.G. and Dewettinck, K. (2007b) Combined population balance and thermodynamic modelling of the batch top-spray fluidised bed coating process. Part II – Model and process analysis, Journal of Food Engineering, No. 78, pp. 308-322.

Rowe, P.N. (1972) Estimation of solids circulation rate in bubbling fluidised bed, Chemical Engineering Science, No. 28, pp. 979-980.

Shampine, L.F. and Reichelt, M.W. (1997) The Matlab ODE Suite, SIAM Journal of Scientific Computation, Vol. 18, No. 1, pp. 1-22.

Sloth, J. (2004) Opstilling og verificering af en tørringskinetisk model for monodisperse dråber i en spraytørrer, M.Sc. Thesis, Department of Chemical Engineering, Technical University of Denmark.

Stein, M., Ding, Y.L. and Seville, J.P.K. (2002) Experimental verification of the scaling relationships for bubbling gas-fluidised beds using the PEPT technique, Chemical Engineering Science, No. 57, pp. 3649-3658.

Temple, S.J. and van Boxtel, A.J.B. (1999) Modelling of Fluidized-bed Drying of Black Tea, Journal of Agricultural Engineering Research, No. 74, pp. 203-212.

Teunou, E. and Poncelet, D. (2002) Batch and continuous fluid bed coating – review and state of the art, Journal of Food Engineering, No. 53, pp. 325-340.

van Ee, J.H., Misset, O and Baas, E.J. (1997) Enzymes in Detergency, Surfactant Science Series, Volume 69, Marcel Dekker, New York.

Werner, S.R.L., Jones, J.R., Paterson A.H.J., Archer, R.H. and Pearce, D.L. (2007a) Air-suspension particle coating in the food industry: Part I — state of the art, Powder Technology, No. 171, pp. 25-33.

Werner, S.R.L., Jones, J.R., Paterson A.H.J., Archer, R.H. and Pearce, D.L. (2007b) Air-suspension particle coating in the food industry: Part II — micro-level process approach, Powder Technology, No. 171, pp. 34-35.

Werther, J. and Bruhns, S. (2004) 3-D Modeling of Liquid Injection into Fluidized Beds, International Journal of Chemical Reactor Engineering, Vol. 2, Article A31, pp. 1-35.

Chapter 10. Fluid bed coating with PVA/TiO_2 solutions

Chapter introduction

Chapter ten provides a comparative study of inorganic salt and polymer fluid bed coating processes. The focus is on differences and similarities in processing and operations. Polymer coating processes are more difficult to carry out in practice than inorganic salt coating processes, although it is not obvious what causes these differences. Studies focusing on Drying Force, coating solution bulk viscosity, mean droplet diameter, colloidal phenomena and stickiness are carried out, and results lead into a proposal of a new Tack Stokes number suggested to be a better measure of the agglomeration tendency than the original viscous Stokes number for polymer coating processes under certain conditions.

The present chapter is submitted to the journal *Industrial & Engineering Chemistry Research* as three separate papers. The papers are currently awaiting publication and are entitled, respectively: *Fluidised bed coating with sodium sulphate and PVA/TiO_2. Part I: Review and agglomeration regime maps*; *Fluidised bed coating with sodium sulphate and PVA/TiO_2. Part II: Influence of coating solution viscosity, stickiness, pH and droplet diameter on agglomeration*; *Fluidised bed coating with sodium sulphate and PVA/TiO_2. Part III: The role of tackiness and the tack Stokes number*. All three papers are authored by Peter Dybdahl Hede (Technical University of Denmark), Poul Bach (Novozymes A/S) and Anker D. Jensen (Technical University of Denmark). The papers are referred to as: Hede et al. (2008d), Hede et al. (2008e) and Hede et al. (2008f), respectively. The following sections are reproductions of the proof corrected papers, although the papers have been written together to form a single chapter. Furthermore, sections concerning equipment and materials have been left out (please refer to chapter five).

10. Fluidised bed particle coating with sodium sulphate or PVA/TiO_2 solutions: Differences and similarities in processing and operations

Abstract

The present paper addresses fluid bed coating of placebo enzyme granules (i.e. sodium sulphate cores, size range of 400 – 500 μm) by two types of aqueous coating solutions being sodium sulphate and PVA/TiO_2. The coating experiments were conducted in a medium-scale top-spray Niro MP-1 fluid bed, and a number of rheological experiments were performed on the coating formulations to support the interpretation of the fluid bed coating results. Results show that the agglomeration tendency is always less for the salt coating process than for the polymer coating process under similar process conditions, due to differences in stickiness (and not because of differences in bulk viscosities or mean droplet diameters), but also that it is possible to optimise the PVA/TiO_2 coating formulation and process in order to achieve a low tendency of agglomeration similar to the salt coating process. The best results for the PVA/TiO_2 solution are obtained by substituting the PVA/TiO_2 in equal amounts with Neodol 23-6.5, and further reduce the pH value in the coating solution to pH = 4. With the coating liquid layer thicknesses encountered during these fluid bed coating processes, it appears as if agglomeration is governed primarily by liquid surface phenomena rather than solely by

viscous phenomena. A modification to the original viscous Stokes number is suggested in the present paper defining the Stokes number in terms of the work needed to reach maximum tack instead of the viscous dissipation energy. The new tack Stokes number correlates well with observed levels of agglomeration from fluid bed coating experiments, and as a promising feature, proportionality is observed between the agglomeration weight percentages and the differences between the new tack Stokes number and a critical tack Stokes number.

10.1. Introduction

In the industrial production of granules in the enzyme and pharmaceutical industry, particles are commonly coated with one or several different layers in a fluidised bed. A spray-coated granule is thereby typically structured in a series of concentric layers in an onion-like fashion (van Ee et al., 1997). Coating layers typically serve a number of functions depending on the end-use of the granules. For enzyme-containing granules, the coating may contain the enzyme itself or may be used to protect the enzyme-containing core by improving the enzyme resistance to degradation or inactivation by components, such as oxygen or bleach components, from the surrounding detergent matrix, which are capable of oxidising or otherwise inactivating the enzyme (Markussen, 2002). Furthermore, the coating layer may have controlled-release properties upon introduction of the granule into an aqueous medium, or provide a barrier against ambient moisture to enhance the storage stability of the enzyme granule and reduce the possibility of microbial growth within the granule (Arnold et al., 1993). The ability of a coating to serve as a barrier to protect the enzyme is thereby related to the permeability of the protective coating, primarily by water and H_2O_2. In addition, the coatings also prevent the enzyme granules from generating dust when they are handled. This is important since enzymes are proteins that have the potential of inducing allergenic response when humans are exposed to aerosols of enzymatic active dust. The ability of a coating to prevent an enzyme granule from releasing dust is closely related to its mechanical properties of which attrition and impact strength are of primary importance (Beekman, 2000).

The most common types of fluid bed coating processes, with respect to enzyme granules, may be divided into two general categories: The coating with aqueous solutions of inorganic salts (with or without active ingredients) and the coating with aqueous solutions of film-forming water-soluble polymers (with or without additional compounds). These types of coating processes have been treated in a number of industrial patents that have been filed by some of the large enzyme companies such as Genencor International/Danisco (Arnold et al., 1993, Dale et al., 1999 and Becker et al., 2005), Kao Corporation (Kiuchi et al., 1998), Novozymes (Markussen, 1986 & 2002 and Simonsen, 2002), Procter & Gamble (Foley et al., 2003) and Henkel (Paartz et al., 1998). Schematic representations of typical commercial enzyme granules with both types of layers can be seen from figure 10.1 and figure 10.2. Figure 10.1 shows the structure of a commercial Genencor Enzoguard® granule. The core consists of a rounded sugar or starch particle with partially hydrolysed polyvinyl alcohol (PVA) as a thin outer layer. Atop that layer are three additional layers, where the inner layer consists of an enzyme mixed with fully hydrolysed PVA, the middle layer is magnesium (or sodium) sulphate, and the outer layer consists of a mixture of partially hydrolysed PVA, titanium dioxide and surfactant/lubricant/plasticizer. All layers are sprayed successively onto the core in a fluid bed (Dale et al., 1999). Figure 10.2 shows the structure of a commercial Novozymes TK granule. The granulation process is based on a combination of mixer and fluid bed technology, where the active granulate is built around an inert carrier core, which is produced in a high-shear mixer. Enzyme and functional layers are added onto the core in successive steps. First, the enzyme is added by absorption of concentrate into the carrier core in a high-

shear mixer. Additional concentrate then is added by spraying in a fluid bed to attain the specified product activity. Next, the granule is coated in a fluid bed with a layer of sodium sulphate (optionally, binders and titanium dioxide are added to the salt layer). The granule is finally equipped with an outer film coating that consists of a mixture of methylhydroxy-propylcellulose (MHPC) and polyethyleneglycol (PEG) for perfecting the dust control. An additional layer of PEG4000 may be added as a lubricant (Markussen, 2002 and Simonsen, 2002).

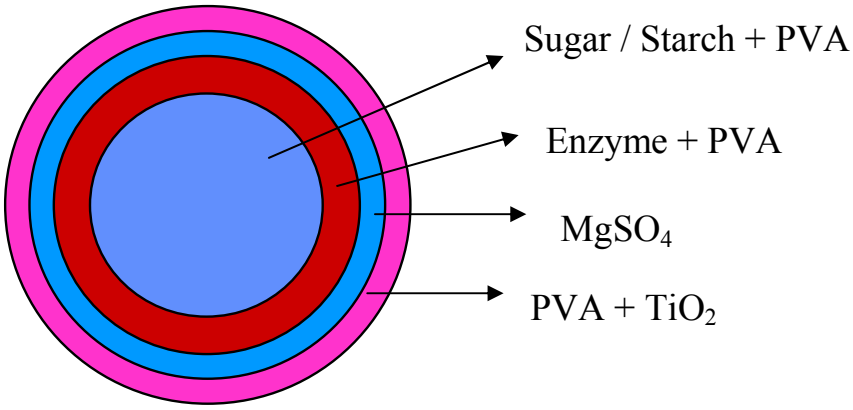

Figure 10.1: The structure of a commercial Danisco/Genencor Enzoguard® granule (Dale et al., 1999). Figure not to scale.

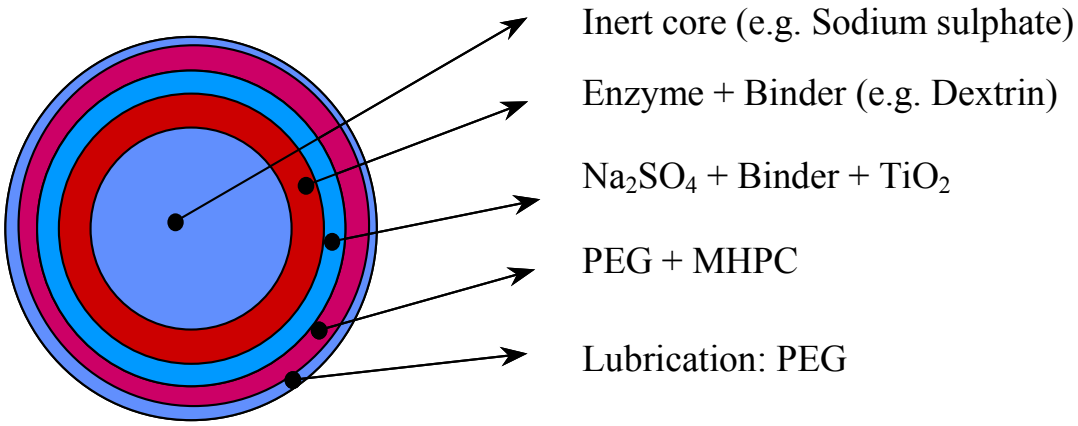

Figure 10.2: The build-up of a commercial Novozymes TK granule (Markussen, 2002 and Simonsen, 2002). Figure not to scale.

Although the principles behind the coating process of inorganic salts and polymer solutions are the same, screening studies by Neidel (2007) clearly show that the coating process of polymer solutions is far more difficult in terms of process control. This was the general observation within a broad range of tested coating solution formulations. It is not obvious what causes these differences in processing, and it is thereby not obvious which process or formulation conditions that could be kept similar or what conditions that should be chosen differently and to what extent. Phenomena such as agglomeration during coating, loss of coating solution due to spray drying loss etc. are notoriously far more outspoken with polymer coating than with the inorganic salt coating process (Neidel, 2007). In addition, results reported by Chu et al. (2006 & 2007) indicate that different colloidal phenomena in the polymer solutions also play a role in the coating process. Finding optimum coating conditions where the coating process can be conducted in a reasonable time without agglomeration or spray drying loss of the coating feed, for any of the two coating processes, is thus not an easy

task. Only limited fundamental research in the open literature has so far been reported in this field as previous work is done mostly in industry and often is protected in patents. It is the aim of this paper to highlight and suggest explanations for the similarities and differences in coating with inorganic salt solutions and polymer solutions in top-spray fluid beds. Initially, the different coating ingredients are discussed together with prior coating experiences.

10.2. Review of inorganic salt and polymer fluid bed coatings

10.2.1. Salt coatings

Salt coatings are typically added together with the enzyme or preferably between the enzyme core/layer and an outer polymer coating layer. The salt layer provides a protective layer toward bleach components when the enzyme granule is stored in a bleach-containing detergent. In one of the first Genencor patents by Arnold et al. (1993) a chlorine scavenger layer such as ammonium sulphate was preferred as the ammonium ion is able to react with chlorine from detergent granules, thereby protecting the enzyme during storage by actively neutralising oxidants. However, because of the possible smell of ammonia, newer enzyme granules typically use low-cost compounds as magnesium sulphate or sodium sulphate even though they do not function as chlorine scavengers. However, these compounds do resemble similar water and H_2O_2 barrier properties and, furthermore, help to reduce enzymatic dust problems when the granules are used (Markussen, 2002).

In recent publications by Hede et al. (2007a & 2008a,b) fluid bed coating processes with sodium salt solutions were treated in detail in the context of fundamentals and scale-up issues. Results are promising regarding control of the process, at the same time, being able to produce salt-coated granules with high mechanical strength and a low tendency for agglomeration during processing. Results indicate that nozzle conditions especially play an important role in the outcome of the process, and that the temperature and humidity conditions inside the bed during coating have primary importance regarding agglomeration. Hede et al (2008b) suggested that the bed temperature and bed humidity during steady state coating conditions were combined into a so-called Drying Force parameter, according to equation 8.3 (please refer to chapter eight) indicating the fluidisation air moisture evaporation force. The advantages of the Drying Force parameter in a scale-up context was emphasised in the work by Hede et al. (2008b). The paper by Hede et al. (2008b) further argues in favour of fluid bed process operation in terms of fixed nozzle conditions and fluidisation velocity throughout the coating process with the conditions inside the fluidisation chamber being adjusted only in terms of the inlet fluidisation air temperature.

10.2.2. Polymer film coatings

A polymer layer is typically added as the final outer layer to provide simultaneous benefits of low dust, as well as good colour appearance and moisture barrier properties and controlled release of the enzyme. Film coating of granules with water-insoluble substances is usually based on organic solutions of the film-forming material or on aqueous colloidal dispersions of polymer particles (Abletshauser et al., 1993). Typically, however, water-soluble polymers are used, and numerous polymers are used commercially for enzyme granule coatings, including most often, polyvinyl alcohol (PVA), polyethylene glycol (PEG), methylcellulose (MC) and methylhydroxy-propyl cellulose (MHPC or HMPC). With only a few exceptions, a range of other components are typically added to the aqueous polymer solution including plasticizers, lubricants, pigments as anti-agglomerating agents van Ee et al., 1997 and McGinity, 1997).

10.2.2.1. PVA

Polyvinyl alcohol (PVA) is used in a variety of pharmaceutical and drug delivery applications such as active component jellies, protein-based pharmaceuticals and sustained release oral dosage forms etc. (McGinity, 1997). PVA has in recent years been used for many pharmaceutical formulations due to its low cost as well as good barrier and tensile properties. As a component of tablet coating formulations intended for products such as e.g. food supplement tablets, PVA protects the active ingredients from moisture, oxygen, and other environmental components, while simultaneously masking their taste and odour. It allows for easy handling of finished products and facilitates ingestion and swallowing. The viscosity of PVA allows for the application of the polymer in tablets, capsules and other forms to which film coatings are typically applied at relatively high solids contents (Hsu et al., 2001 and McGinity, 1997). A repeat unit structure of PVA can be seen from figure 10.3.

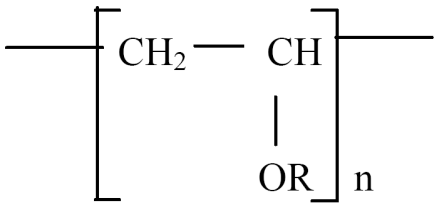

where R = H or $COCH_3$

Figure 10.3: The chemical repeat unit structure of partially hydrolysed polyvinyl alcohol (Saxena, 2004).

In the context of commercial enzyme granules, PVA is used for outer as well as inner coatings of the enzyme granules, where PVA serves as a barrier to protect the enzyme from exposure to harsh chemicals that may be present in the final product in which the enzyme is used. PVA has been proven to be a very effective coating component for detergent enzyme granules. PVA is particularly useful because it simultaneously provides a coating with reduced permeability to moisture and oxidants, a strong and attrition-resistant coating, and a coating that is readily soluble in water and detergent solutions in both cold and hot water. It is also sufficiently water-soluble to be prepared in aqueous coating solutions and sprayed onto enzyme-containing granules at a reasonable rate (Hsu et al., 2001 and Dale et al., 1999). It is soluble in water, and typically a 5 w/w% solution of polyvinyl alcohol exhibits a pH in the range of 5.0 to 6.5. PVA has a melting point of 180°C to 190°C, and the polymer further has the advantage of being non-toxic, hydrophilic and relatively easy to handle (Saxena, 2004). It is an odourless and tasteless, translucent, white or cream coloured compound that typically is manufactured in granular form (Celanese, 2005).

PVA is commercially available in a wide range of molecular weights and varying degree of hydrolysis from the polymer acetate precursor, making it possible to control the relative solubility and physical properties of the polymer coating, which again can be optimised to balance factors such as the ease of coating, dissolution rate of the granule, attrition resistance, and permeability of the granule to moisture and oxidants (Saxena, 2004 and Hsu et al., 2001). Suitable PVA types for an outer enzyme granule coating layers include typically partially to fully hydrolysed PVA having a low viscosity in the range of 5 – 15 cP in a 4 w/w% aqueous solution (Arnold et al., 1993).

Additional advantages of PVA include the facts that it can readily be plasticized with water, glycerol, PEG and other polyhydric compounds, and that it is compatible with pigments and fillers such as titanium dioxide, talc and carbonates among others (Saxena, 2004). For coating purposes, PVA is often dissolved in aqueous solutions, together with dispersed inert filler particles such as TiO_2, in order to help reducing the tendency of agglomeration as well as to make the granules appear white. PVA solutions also may be coloured with different kinds of dye colours (Jordan & Taylor, 2002).

10.2.2.2. Tackiness and work of adhesion of polymer solutions

Coating formulations consisting of water-soluble polymeric film-formers such as PVA are known to be inherently tacky (sticky) in nature and spontaneously adhere to many materials on contact, readily forming adhesive joints with no need for primary chemical bonding (Chau & Swei, 2004). The tack problem is especially troublesome in the coating of small particles, as their tendency to agglomerate is known to increase significantly with coating solution stickiness (Wan & Lai, 1992a). Most film-forming polymers become tacky during their drying phase, which is believed to be the major cause of undesired particle agglomeration during the fluid bed coating process (Wan & Lei, 1992b). Although the coating solution spray rate, bed temperature and moisture have been identified as critical parameters in the prevention of agglomeration (Hede, 2005 & 2006) it is sometimes not possible with troublesome coating solutions to use these operating parameters alone in controlling the extent of agglomeration. For coating applications, a low tackiness is generally desirable. A polymer formulation with a low tackiness generally shows a lesser tendency for film coating defects and results in an easier coating process and reduced processing time (Wesseling et al., 1999).

The mechanisms behind the stickiness of polymers in solution are not yet fully understood. It is believed that mainly viscoelastic effects and fibrillation of the adhesive are responsible for a large energy dissipation and strong adhesion and tackiness (Creton & Leibler, 1996, Russell & Kim, 1999, Roos et al., 2002). Chemically, stickiness of PVA is believed to be closely related to the conformation of the polymer chains. While being in solution, the polymer chains normally do not touch each other very often and slide over each other quite easily. Thus, PVA solutions are quite flexible and able to get into the microscopic cracks and crevices in the core particle surface. Upon solvent evaporation, the polymer chains will get closer, and, depending on the length of the chains, they will hook in the surface cracks and adhere well to the surface in mechanical interlocking mechanisms (Adhikari et al., 2001). The result is a sticky surface ready for agglomeration. This theory is supported by various experiments, indicating that there is a strong connection between tack and the contact with rough surfaces. In the presence of asperities on the solid surface, the actual area of contact is always less than the nominal area. This is because the polymer solution sinks into the surface valleys. Results by Hui et al. (2000) support previous findings by Creton & Leibler (1996) indicating that this true contact area depends on both the applied load and the time of contact between the adhesive and the adherent. As for other pressure sensitive adhesives (an adhesive that retains tack after solvent evaporation, so that it can be bonded by simple hand pressure), PVA needs a certain pressure to cohere, meaning that a certain force is necessary for two objects covered with PVA to stick together. Clamping is believed to be necessary in order for the PVA chains to twine into each other. After the PVA chains have been forced to coil into each other, they will leave a strong network upon solvent evaporation. This network is believed to cause the good cohesion properties of PVA and may be part of the explanation for the agglomeration tendency of wet PVA coated particles (Rajsharad & Kamble, 2006).

In the literature, a distinction is often made between adhesion studies and tackiness studies although these properties, indeed, are related. Adhesion is the work required to separate a unit-cross sectional area of two materials and it is governed by mechanical interlocking, wetting and electrostatic and chemical forces (Adhikari et al., 2001). From a mechanical point of view, the strength of an adhesive joint can be characterised by the work of detachment per unit area of interface A_{con}, which is given by the following equation (Zosel, 1985):

$$W_{adhesion} = \frac{1}{A_{con}} \cdot \int F \cdot v_{sep} \cdot dt \qquad (10.1)$$

where v_{sep} is the rate of separation and F is the tensile force during the unbonding process. This fracture energy per unit area of interface (also known as the *intrinsic adhesive failure energy*) is a measure for the adhesive bond energy (Zosel, 1985). From a theoretical point of view, work of adhesion is interesting because it can be related to well-known physical and chemical parameters such as contact angle, surface tensions and spreading coefficient, with the latter being the difference between work of adhesion and work of cohesion (York & Rowe, 1994) (see also chapter three). Furthermore, work of adhesion may be combined with solubility theory such as the Hansen or Hildebrand solubility parameters giving a theoretical possibility for the a-priori prediction of work of adhesion (Rowe, 1988). Considerable research has been conducted in an attempt to correlate the physical properties of polymer binder and coating solutions with subsequent granule and tablet properties, but often with limited success (Okhamafe & York, 1985, Johnson & Zograf, 1985, Rowe, 1988 & 1989, Parker et al., 1990, Felton & McGinity, 1997, Tüske et al., 2005). Experimental work has been somewhat inconclusive in demonstrating any quantitative relationship between surface energetics of the coating solution and the solid substrate and the resulting adhesive strength. One reason for this, which is a general problem faced in studying film adhesion, is the difficulty in accounting for the effect of bulk film properties on the adhesion measurement. Further problems often occur when static surface energetics are to be compared to the dynamic interactions that are occuring during granulation. Correlations between measured values for work of adhesion with those predicted from theory require optimum or fully developed interfacial contact between the adhesive and the adherent, which almost never takes place during granulation. Measured adhesion energies are often observed to be several orders of magnitude larger than the predicted thermodynamic work of adhesion (Creton & Leiber, 1996). In that respect, work of adhesion theory must be regarded as less interesting for dynamic particle processes such as the fluid bed coating process, as the interface interactions here are so fast that dynamics and possible imperfect interfacial contact also must be taken into account. More on polymer adhesion and measurement techniques for adhesion may be found in the thorough review by Michalski et al. (1997).

Tack or tackiness is the main property of pressure-sensitive adhesives and is defined as the ability of an adhesive to develop interactions under short contact time with a substrate under light pressure and during short contact time. Contrary to the work of adhesion, tack is not a material parameter that can be theoretically related to fundamental physical/chemical parameters. Because tack is evaluated by the maximum energy (stress) required to propagate an interfacial fracture, it is strongly dependent on the interfacial adhesion strength between the adhesive and adherent, but also on the energy dissipated in the polymer during separation, through viscoelastic losses and fibrillation phenomena etc. (Smitthipong et al., 2004 and Roos et al., 2002). Both viscoelasticity and the wetting of the adherent by the adhesive are of particular importance during the bond formation (Adhikari et al., 2001), and it is generally observed that tack is dependent on surface roughness and increases with contact time, contact

force and separation rate, as it has been demonstrated in results by Zosel (1985) and Hui et al. (2000). Tack is connected with the glass transition of the adhesive and is related to the corresponding compliance just above the glass transition temperature range, which itself is determined by the entanglement network of the polymer (Bartenev et al., 1969 and Phillips et al., 2007). The glass transition temperature is the temperature below which the physical properties of amorphous materials such as polymers vary in a manner similar to those of a solid phase (glassy state), and above which amorphous materials behave like liquids (rubbery state). Above T_g, the secondary non-covalent bonds between the polymer chains become weak in comparison to thermal motion and the polymer becomes rubbery and capable of elastic or plastic deformation without fracture (Goodwin, 2004).

The fact that tackiness cannot be unambiguously related to well-known physical parameters means that many types of equipment for the measurement of tackiness have been developed, as reviewed by Christensen (1998) and Gay (2002). These methods of expressing tack are useful in many practical cases, but the physical meaning of these values is not necessarily clear. The values determined by any tack tester are relative values under fixed conditions and do not necessarily compare with values determined under different conditions with other determining methods. The most popular method is in general the *Probe tack test*, as the Texture analyser set-up used in the present study (please refer to chapter five), in which the butt end of a cylindrical probe is brought into contact with the liquid sample at a specified load and time, and then removed at a specific rate. Several detailed stickiness studies have used this method previously (Zosel, 1985 and Werner et al., 2007). Probe tack tests for coating solutions have been reported by Chopra & Tawashi (1982, 1984 & 1985) and Wan & Lai (1992a,b). The probe tack test provides two measures of tack being the work spent in debonding the probe from the adhesive and the maximum tensile force achieved during the debonding step. Usually only the maximum tensile force is considered as a measure of tack, although this $F_{max(tack)}$ parameter is qualitatively different in nature from other measures of tack because it cannot be expressed as an integral of force or tension over time, distance or strain. It is unclear how $F_{max(tack)}$ depends on the rheological response of the adhesive during debonding, but it is certainly not as strongly influenced by the ability of the adhesive to dissipate energy during the debonding step as are the various other measures of tack. Thus, $F_{max(tack)}$ may be a better measure of the quality of the bond between adhesive and substrate in a fluid bed with fast interface interactions, than any other commonly employed measures of tack (Christensen, 1998). The Probe tack test with measurement of $F_{max(tack)}$ is thus the test principle selected to simulate the stickiness of the coating solutions in the present paper. A thorough review of mechanisms and test methods for stickiness determination may be found in Adhikari et al. (2001).

10.2.2.3. Viscous Stokes theory

Realising the importance of liquid layer properties for the tendency of agglomeration the viscous Stokes theory has been suggested by Ennis et al. (1991) as a way to express the likelihood of permanent coalescence between two spherical particles each covered equally with a liquid layer. The outcome of the collision of the two particles covered with a liquid layer of height h_{liq} is determined by the ratio of the initial kinetic energy of the system (relative to the center of mass) and the energy dissipated from the viscous force in the liquid bridge. This can be expressed analytically by the definition of the viscous Stokes number according to equation 10.2 (Ennis et al., 1991) (please refer also to chapter three).

$$St_v = \frac{\text{Initial kinetic energy}}{\text{Dissipated viscous energy in the liquid bridge}} = \frac{½ \cdot m_{harm} \cdot (2u_0)^2}{2 \cdot F_{vis} \cdot h_{liq}} \tag{10.2}$$

where F_{vis} is the viscous force due to the liquid bridge defined according to:

$$F_{vis} = \frac{3\pi \cdot \eta_{liq} \cdot r_{harm}{}^2 \cdot u_0}{2 \cdot h_{liq}} \tag{10.3}$$

and the reduced mass and radius between two different particles is given by:

$$r_{harm} = \frac{2 \cdot r_1 \cdot r_2}{r_1 + r_2} \tag{10.4}$$

and

$$m_{harm} = \frac{2 \cdot m_1 \cdot m_2}{m_1 + m_2} \tag{10.5}$$

The parameter η_{liq} is some time-average coating solution viscosity of the granulation process and u_0 is the initial collision velocity (please refer to chapter three).

Based on simple energy considerations, the viscous Stokes theory shows that if the viscous Stokes number is smaller than a critical value St_v^*, collision between particles result in permanent agglomeration. If $St_v >> St_v^*$ particles will rebound because the total incoming energy is larger than the one dissipated during collision (Tardos, 2005). The critical viscous Stokes number is given by (Ennis et al., 1991):

$$St_v^* = \left(1 + \frac{1}{e}\right) \cdot \ln\left(\frac{h_{liq}}{h_{asp}}\right) \tag{10.6}$$

where h_{asp} is the characteristic height of the particle surface asperities and *e* is the coefficient of restitution (Ennis et al., 1991). The viscous Stokes number and the critical viscous Stokes number are both derived in the appendix in section 10.8 as this was not done in the paper by Ennis et al. (1991).

Although focusing on liquid viscosity rather than tack or work of adhesion, the viscous Stokes theory does account for the influence of surface asperities i.e. if the parameter h_{asp} increases (due to increased roughness of the core particle surface) the critical viscous Stokes number will decrease allowing a smaller range of St_v values for permanent agglomeration. Analogously, an increased liquid layer (increasing h_{liq} values) results in larger St_v^* values meaning that more particles will agglomerate. More information about the viscous Stokes theory may be found in Ennis et al. (1991), Tardos et al. (1997) and Tardos (2005).

10.2.3. Plasticizers

Plasticizers are usually high-boiling organic solvents that are used to impact the flexibility of otherwise hard or brittle polymers. They are typically added to aqueous colloidal polymer dispersions to reduce the minimum film formation temperature (Wesseling et al., 1999). The effects of plasticizers on mechanical properties and permeability of polymers are well-known. Plasticizers generally cause a reduction in the cohesive intermolecular forces along the polymer chains, resulting in various changes in the polymer properties such as a reduction in tensile strength, while the elongation and flexibility are increased. Furthermore, the glass transition temperature is typically significantly reduced with the addition of plasticizer (McGinity, 1997). What takes place is that small molecules of plasticizer embed themselves between the polymer chains, increasing the spacing and free volume, and allowing them to move past one another even at lower temperatures. The decrease in the glass transition temperature of a polymeric film, as the plasticizer concentration increases, is a common measure of the plasticizer effectiveness. The degree of plasticization of the polymer is dependent to a large extent on the amount of plasticizer with respect to the polymer, and the interaction between the plasticizer and the polymer. For a plasticizer to be effective, it must be able to diffuse into and interact with the polymer and have minimal or no tendency for migration or exudation from the polymer (McGinity, 1997).

On the negative side of adding plasticizers to a polymer solution is that the water permeability typically is increased. This effect is due to the interaction of the plasticizer with the polymer molecules. The interactions decrease the intermolecular forces along the polymer chains, reducing internal hydrogen bonding while increasing intermolecular spacing. Furthermore, the addition of plasticizers in an attempt to reduce the minimum film formation temperature is known to increase the stickiness of the coating solution due to softening of the polymer (Wesseling et al., 1999).

Plasticizers do not necessarily need to be soluble in the solvent used for dissolving the polymer. For plasticizers that are soluble in the solvent phase, these can be added directly to the mixture or may be dissolved first in the solvent prior to addition of the polymer. Otherwise proper suspension is required (McGinity, 1997). Examples of commonly used plasticizers are: polyols such as glycerol, propylene glycol, polyethylene glycol (PEG), urea, triethyl citrate or dibutyl or dimethyl phthalate (McGinity, 1997).

10.2.4. Lubricants

With the term “lubricant” is usually understood any non-aqueous compound or mixture of compounds, which forms a liquid at 25 ºC and 1 bar, reduces the particle surface friction, lubricates the surface of the granule, decreases static electricity and/or reduces friability of the granules (Dale et al., 1999). Lubricants are thereby added to the coating solution in order to reduce the relative friction coefficient between the coated granules, thereby functioning at the outer granule surface at the particle-level contrary to the plasticizers that work at the intermolecular-level. Such thin layers of liquid on each individual granule reduce the frictional forces that might otherwise cause the granules to break. Lubricants can also play a related role in improving the coating process by reducing the stickiness of the coating layer, thus serving as an anti-agglomerating agent. However, the fundamental understanding of the mechanisms behind this effect is not complete (Hsu et al., 2001). Some plasticizers such as selected liquid alcohols of alkenes or alkenes with a carbon atom chain length between 9 and 15 also have a particle-level lubricating effects besides being a plasticizer and surfactant, but

in general the preferred lubricants are different from the preferred plasticizers. Suggested lubricating agents for commercial use include preferably fatty acids and plant, animal and minerals oils as well as silicone oils. However, other compounds or mixtures forming low viscosity non-aqueous liquids at 25 ºC may also in principle be used (Simonsen, 2002). Preferably, the lubricant is also a surfactant, reducing the surface tension of the coating solution hereby improving the coating solution wetting of the core particles.

One advantage of using lubricants having a low viscosity is that they are considerably easier to apply as a thin layer in small amounts on a granule surface, and that a homogenous distribution of the small amounts of lubricant on the entire granule surface is facilitated by a low viscosity. When using lubricants having a relative high viscosity, the lubricant tend to adhere inhomogenously to the granule surface in the form of sticky lumps. Hence, such types are not typically used for coating purposes due to increased risk of particle agglomeration. Commercial lubricants such as Neodol 23-6.5 and Softanol 50 have viscosities in the range of 20 – 40 mPa·s at 25 ºC (Simonsen, 2002 and Dale et al., 1999).

10.2.5. Pigments

Insoluble ingredients may be included in the coating formulation for a variety of reasons. Sometimes pigments are simply used as a filler to reduce the percentage of the amount of other more costly components in the film composition (Jordan & Taylor, 2002). Another important application is to use pigments to help reduce agglomeration or stickiness of coated particles during processing. Following the principles described in section 10.2.2.2. the filler particles act as granule surface asperities and thus help to reduce that actual contact area, lowering the chance of permanent particle-particle bonding. Suitable anti-agglomeration agents include fine insoluble materials such as talc, TiO_2, clays, amorphous silica, magnesium stearate and kaolin. In general, the anti-agglomerating agent should be inert with respect to the active ingredient (e.g. the enzyme) and preferably not affect the granule properties in a negative manner. Surface and morphology properties including the hydrophilicity of insoluble filler particles are known to be important factors that contribute to the properties of the final polymer film. Likewise has the concentration of pigment material a strong influence on the final mechanical and barrier properties of the film (McGinity, 1997). Application of insoluble materials in the film coating composition may not be used uncritically since adding pigments to a polymer film coating composition typically decreases the tensile strength, meaning that a weaker film is obtained as the amount of pigments in the film coating increases (Jordan & Taylor, 2002).

Pigments also act as colouring agents. In the sense of appearance for the granule end-users it is often desired to produce granules with homogenous colour. Often white is the preferred colour and such pigments are typically finely divided whiteners such as titanium dioxide or calcium carbonate. Preferably, such pigments are low residue pigments upon dissolution (Arnold et al., 1993 and Lehtola et al., 1995). Titanium dioxide is preferred in commercial enzyme granules because of its brightness and very high refractive index. TiO_2 particles added in a PVA solution further have the advantage of producing a film with high gloss, good light diffusion properties and uniform dimensions (Chu et al., 2007). TiO_2 is a cheap non-toxic all-use white pigment well-known from food and cosmetic products.

10.2.6. Rheology and colloidal phenomena in the PVA/TiO_2 system

Contrary to a sodium sulphate solution, a typical polymer solution with dispersed filler particles as the PVA/TiO_2 solution constitutes a colloidal system in which the TiO_2 particles are dispersed among the PVA chains in the aqueous solvent. The interactions between these components could possibly have an influence on the observed agglomeration tendencies. Such interactions are complex, however, and the behaviour of suspensions in the presence of polymers has been studied for many years due to the numerous applications of the processes occurring in such systems. Adding polymers to suspensions in order to control colloidal dispersion has been the subject of extensive research because of its importance in industrial applications (Chu et al., 2007). From these studies, valuable information about the PVA/TiO_2 systems may be obtained.

Several authors have studied the rheological behaviour of suspensions of inorganic particles in polymer solutions. Suspensions such as the PVA/TiO_2 generally behave as Newtonian liquids at low particle volume fraction, but become non-Newtonian at high particle concentration, exhibiting shear-thinning/shear-thickening and yield stress etc. (Chang et al., 1992 and Otsubo, 1986). Changing the suspension pH affects the particle surface charges, and hence the rheological behaviour. Particles in suspension experience various inter-particle forces, and the stability of a uniformly dispersed suspension is determined by the relative magnitude of various interparticle forces such as Brownian, van der Waals, electrostatic and hydrodynamic forces (Liang et al., 2005). Particles tend to aggregate when the van der Waal force of attraction is larger than the electrostatic and/or repulsive force. In that case the suspension is not stable. On the other hand, a well-dispersed suspension can be obtained when the repulsive force is greater than the attractive force. Suspensions generally exhibit shear-thinning characteristics and sometimes yield stress depending on the particle concentration near the iso-electric point. Newtonian behaviour prevails when pH is remote from the iso-electric point (Chu et al., 2007).

The surface of uncoated TiO_2 particles has surface hydroxyl groups. At high pH, these groups can ionise to give O^- groups and at low pH the lone pair on the oxygen can hold a proton to give OH_2^+ groups. The reactions of the amphoteric surface are given by the following reaction scheme (Goodwin, 2004 and Chu et al., 2007):

$$\text{Surface TiOH}_2^+ \xleftarrow{H_3O^+} \text{Surface TiOH} \xrightarrow{OH^-} \text{Surface TiO}^- + H_2O$$

Hence, the TiO_2 surface not only shows a variation in the magnitude of the surface charge with pH, but also a variation in the sign. At a certain pH value, the charge can be reduced to zero and the pH, at which this occurs, is termed the *isoelectric point* (Goodwin, 2004). For suspensions containing polymer, the phenomenon of polymer adsorption on particle surfaces in suspension has been theoretically verified and widely used for the creation of stable suspensions. When PVA is adsorbed on the surfaces of TiO_2 it generates a steric stabilisation repulsive force which aids the stabilisation of the suspension system. The active sites on the particle surface, at which the polymer chains are attached, are known as *attachment points*. According to the reaction scheme above, increasing pH results in a decrease of $TiOH_2^+$ and an increase of TiO^-, whereas TiOH tends to increase initially and then decrease. Since the adsorption of PVA on TiO_2 is primarily due to hydrogen bonding, the amount of PVA adsorbed on the TiO_2 surfaces increases significantly as pH increases. For 15 w/w% TiO_2 in 2.5 w/w% PVA suspensions, Chu et al. (2007) have determined the adsorption to increase from 0.024 g PVA/g TiO_2 to 0.080 g PVA/g TiO_2 as the suspension pH increases from 4 to

10. The increased adsorption is suggested by Chu et al. (2007) to be due to the differences in polymer chain conformations under different solvent environments causing the adsorbed macromolecules to form network structures on the particles surface.

To understand the mechanism of polymer adsorption on solid particle surfaces, it is important to consider the role of the functional groups present in the polymer. The main functional group in PVA is the hydroxyl group, but due to the presence of a small residual of non-hydrolysed acetate groups after polymerisation, the adsorption of PVA on the TiO_2 surface is greatly influenced by the acetate groups for partially or intermediately hydrolysed PVA. Since the affinity of the acetate group with TiO_2 is greater than the hydroxyl group, more segments of PVA chains will be attached to the particle surfaces the lower the degree of hydrolysation in the PVA, resulting in a more flat conformation. However, PVA with a higher degree of hydrolysis contains less acetate groups, and the adsorbed segments form loops and tails arranged perpendicularly on the particle surface. This allows more TiO_2 surface area available for polymer adsorption, meaning that in all more PVA is adsorbed on TiO_2 surfaces the higher the degree of hydrolysis (Sairam et al., 2006 and Chu et al., 2007).

The change in the coating solution characteristics upon a change in pH goes beyond the effect in viscosity. Also the surface tension is affected. As pH changes from acidic to basic, an increasing number of PVA macromolecules are adsorbed on the TiO_2 surfaces, resulting in a higher surface tension. This has been experimentally verified by Chu et al. (2007). With time, however, sedimentation occurred at high pH in the PVA/TiO_2 solutions tested by Chu et al. (2007). Chu et al. (2007) measured an isoelectric point of pH = 9.2 for a 15 w/w% TiO_2/ 2.5 w/w% PVA suspension (compared to an isoelectric point of 3.5 for a pure TiO_2 dispersion reported by Goodwin (2004)) and observed how the suspended particles started to agglomerate when pH approached the neighbourhood of the isoelectric point. Although the amount of PVA adsorbed on the TiO_2 surfaces is relatively large at pH ≈ 10, the concentration of TiO_2 in the continuous phase is actually lower than at lower pH due to the sedimentation of flocs. In general, Chu et al. (2007) found that dilute PVA/TiO_2 suspensions at pH close to the isoelectric point is not ideal for coating purposes. Chu et al. (2007) found that the surface tension increases with increasing degree of hydrolysis, but decreases with increasing molecular weight of PVA. At the same time, the amount of PVA adsorbed on the TiO_2 surface increases with increasing degree of hydrolysis and molecular weight.

Chibowski (1986) has studied the kinetics of the PVA adsorption on TiO_2 particles at different pH values for 0.05 w/w% PVA solutions. He observed that the adsorption of PVA on the TiO_2 particles is fast, irrespectively of the pH value of the solution. At pH = 10 the time necessary for the establishment of the equilibrium state is longer than at pH = 4 due to the difference in adsorption density. The adsorption density of PVA in g/m^2 TiO_2 surface area increases slightly when the pH value of the suspension increases due to the change of surface properties of TiO_2 and change of hydration of the surface groups as presented earlier. Chibowski & Szcypa (1984) and Chibowski (1986) observed, however, that the rate of PVA adsorption on TiO_2 is in general not considerably affected by the surface charge of TiO_2. The electrostatic interactions are thereby concluded to be unimportant in the mechanism of polymer adsorption on TiO_2 particles.

The mechanism of adsorption of PVA on inorganic particles has been further investigated by Killmann et al. (1988). Their results clearly indicated that the amount of adsorbed PVA is strongly dependent on the molecular weight and the number of acetate groups of PVA, resulting in different adsorption layer thicknesses. The adsorption force was observed to

increase with increasing degree of hydrolysis of PVA in accordance with Chu et al. (2007) and Chibowski (1986). The presence of the hydrophilic acetate groups also affect the conformation of polymer chains adsorbed on the particle surface (Killmann et al., 1988). The adsorption mechanisms of PVA on different types of particles are also different. For example, the amount of PVA adsorbed on TiO_2 particles increases with the suspension pH as the thickness of the double layer surrounding the TiO_2 particle is determined mainly by the molecular weight and the number of acetate groups of PVA. By contrast, the affinity of PVA and SiO_2 particles is strong at low pH, but weak at high pH. That is, the quantity of PVA adsorbed on the silica surface decreases with increasing pH (Boisvert et al., 2003). Since the adsorption of non-ionic polymers such as PVA takes place due to hydrogen bonding with the silanol group on the silica surface, the adsorption is favourably under low pH. Several other papers also report the importance of pH on the adsorption of non-ionic polymers on metallic oxide particles as reviewed by Chu et al. (2007). Most of the studies reported have focused on the adsorption mechanisms, but very little research has been done on the effect of the surface tension of the suspension.

Although there is a general agreement that much of the behaviour of PVA/TiO_2 suspensions is due to the adsorption of PVA on the surface of the TiO_2 particles, there is no general theory describing the adsorption of macromolecular compounds from the electrolyte solutions. The studies of the effect of polymers on colloid stability show that the flocculation and stabilisation processes depend on the amount of polymer adsorbed (Chu et al., 2007). The other factors affecting the colloid system behaviour are the pH value of the solution, the surface properties of the TiO_2 solid particles, the type of PVA and the ionic composition of the liquid phase, i.e. the presence of foreign ionic species. All of the above mentioned factors affect the magnitude of polymer adsorption and the polymer configuration on the solid TiO_2 particle surface (Chibowski, 1986).

Despite the numerous studies on the adsorption and rheological behaviour of adding PVA in inorganic suspensions, very little information is available on the coating behaviour of these polymer suspensions. Studies by Chu et al. (2007) indicated that the coating window is enlarged with the addition of inorganic particles such as TiO_2 and SiO_2 in PVA solutions, which is in agreement with the patent by Arnold et al. (1993).

10.3. Experimental

Coating experiments were carried out on sodium sulphate cores sieved in the range of 400-500 μm (see also chapter five). It was verified by microscope analysis of the different fractions that coated granules with diameters above 710 μm consisted of agglomerates, whereas particles below this limit were primarily single coated granules. Thus, this mesh orifice diameter was set as the agglomeration limit, and based on the weight of each of the fractions, an agglomeration percentage was determined for each batch according to equation 10.7 (see also chapter five).

$$\text{Agglomeration \%} = \frac{\text{coated batch weight fraction with } d_p > 710\,\mu\text{m}}{\text{total coated batch weight}} \cdot 100\,\% \qquad (10.7)$$

Issues concerning reproducibility of data with the same type of fluidised bed equipment and core materials were treated in detail by Hede et al. (2008b). Analogously to the works by Hede et al. (2008b) it was observed in the present study how the standard deviation from the Retsch Sieve Shaker AS 200 equipment for the given core materials was 0.44 w/w % in terms

of the agglomeration percentage, thereby indicating as a common rule of thumb that different batches having agglomeration percentages within the range of ± 0.88 w/w % are not statistically different.

10.3.1. Preparation of the coating solutions

The sodium sulphate coating solutions were prepared by pouring the Dextrin and the crushed sodium sulphate into the vortex of cold water. The solutions were afterwards heated up to 60 ºC in order to avoid any precipitation of Glauber salt (see chapter five). Stirring was kept at all times during the coating process and the temperature of the coating solutions was always kept at 60 ºC.

Preparation of the PVA solutions was a more complex exercise. The most critical step in effectively dissolving PVA is to completely disperse the PVA granules in water. Since the surface of the PVA granules will swell very quickly and clump together, it is very important to control the agitation as well as the temperature of the dispersion. Initially, the pigment material TiO_2 was added into the vortex of cold water at temperatures below 25 ºC. While stirring was maintained, the PVA granules were added slowly into the vortex. Cold water below 25 ºC is important to allow good dispersion before PVA swelling. If PVA is added into hot water the particles swell rapidly and clump together before complete dissolution can be achieved. Once the PVA granules were well dispersed in cool water, stirring was kept on for ½ hour before any other ingredients were added. Next the dispersion was carefully heated by ramping up to 85 ºC and keeping this temperature for further two hours. Afterwards, the coating solution was cooled down and kept at a constant temperature of 60 ºC during the coating process.

10.3.2. Coating solutions

According to the preparation guidelines presented in the previous section seven different aqueous coating solutions were prepared in order to allow the proper testing of the theories presented in the following section 10.4. The composition of the seven different coating solutions used for the studies in the present paper can be seen from table 10-1. In each coating experiment (all carried out in the top-spray medium-scale Niro MP-1 fluid bed) the aim was to coat until the bed load had increased 20 w/w%. This was done in order to make sure that a reasonable coating layer (~ 5-10 μm) had developed on the core particles (see also chapter five). The use of PVA and TiO_2 in equal amounts in experiments A – F (experiment E is solution A being five times diluted) follows suggestions by Arnold et al. (1993) and Becker et al. (2005). In experiment D and F, some of the PVA and TiO_2 are replaced by Neodol 23-6.5. The advantages of using plasticizers and lubricants in polymer coating solutions have been previously presented. Neodol 23-6.5 is used commercially and included in several Danisco/Genencor patents (e.g. Dale et al., 1999 and Arnold et al., 1993). The advantage of Neodol 23-6.5 is that it functions both as lubricant, plasticizer and surfactant (Arnold et al., 1993). Arnold et al. (1993) suggest that the lubricant should replace up to 30% of the polymer or pigment, but recent studies by Hsu et al. (2001) indicate that the best coatings are obtained with Neodol 23-6.5 replacements between 10 and 20 w/w%, in order to have the best plasticizing effects. In solution D and F Neodol 23-6.5 constitutes 10 w/w% of the coating solution dry-matter contents replacing both PVA and TiO_2 in equal amounts hereby following the newest guidelines.

Table 10-1: The seven different coating solution formulations tested in the present paper. The solvent was pure demineralised water in all coating solutions.

Solution number	Composition in w/w%	pH in the coating solution
A	10 w/w% PVA 10 w/w% TiO_2	Measured to pH = 7.0
B	10 w/w% PVA 10 w/w% TiO_2	Adjusted to pH = 4.0 using 1 M HNO_3
C	10 w/w% PVA 10 w/w% TiO_2	Adjusted to pH = 10.0 using 1 M NaOH
D	9 w/w% PVA 9 w/w% TiO_2 2 w/w% Neodol 23-6.5	Measured to pH = 7.0
E	2 w/w% PVA 2 w/w% TiO_2	Measured to pH = 7.2
F	9 w/w% PVA 9 w/w% TiO_2 2 w/w% Neodol 23-6.5	Adjusted to pH = 4.0 using 1 M HNO_3
G	15 w/w% Na_2SO_4 1 w/w% Dextrin (of the amount of Na_2SO_4)	Measured to pH = 7.1

10.4. Testing possible causes for differences in processing

Previous experience with sodium sulphate coatings (Hede, 2005 and Hede et al. 2007a & 2008a,b) and initial trials with PVA coatings by Neidel (2007), provided the basis for detailed studies of a number of possible reasons why the two types of coating solutions behave differently with respect to agglomeration. Industrially, there are several quality parameters that could be chosen for the comparison of the outcome of the two types of coating processes. In this paper the main focus was to find reasons for differences regarding agglomeration tendency during the coating process. First the theoretical background for the studies is emphasised.

10.4.1. The Drying Force and the liquid spray rate

As presented in Hede et al. (2008b), fixing the Drying Force as well as a spray related parameter, named the Relative Droplet size, made it possible to match the agglomeration tendency as well as the particle size distribution of the final coated granules across three pilot fluid bed scales in the salt coating process, where sodium sulphate cores were coated with coating solution G. Fixing nozzle conditions and the Drying Force gives adequate control over the salt coating process, as there is a clear relation between the nozzle conditions and Drying Force on one hand, and the agglomeration tendency on the other (see also chapter eight). Being a tool for the control of the salt coating process, it seems possible that fixing the same parameters will also lead to regimes of successful coating with no or little tendency of agglomeration for PVA/TiO_2 solutions. It is, however, difficult to estimate in advance if the PVA/TiO_2 coating process will respond to the changes in Drying Force and spray rate in a similar manner as the salt coating process. Therefore, as a start, 24 coating experiments were carried out for each of the coating solutions A and G for Drying Force values in a broad range between 3 and 19 kPa and for spray rates in a broad range between 8 and 160 g/min. This initial screening study is aimed at providing a first basis for how the two types of coating solutions behave in a relevant range of temperature/humidity and spray rate conditions.

10.4.2. Bulk viscosity, stickiness and the influence of the mean droplet diameter

When the coating solutions are being prepared, significant differences in bulk coating solution viscosities are observed. Whereas the sodium sulphate solution appears to have a viscosity close to pure water, the PVA/TiO_2 solution is far more viscous. Viscosity of the coating solution is believed to play an important role regarding the tendency of agglomeration, coating layer morphology and more (Hede, 2005 and Schæfer & Wørts, 1977). In addition, viscosity is known to affect the mean droplet diameter produced at the nozzle, and thereby also phenomena such as droplet penetration into the cores and droplet drying time (Hede, 2005). It is thereby likely that these apparent differences in bulk viscosities could be part of the reason for the observed differences in agglomeration tendency.

An important consequence of the difference in coating solution bulk viscosities is the differences in stickiness as the droplets dry on the particle surface. As the coating solution droplets dry upon evaporation of the aqueous solvent, the viscosity and stickiness increase. Upon solvent evaporation PVA solutions are known to be sticky and for that reason PVA is used in many commercial glues often simply with water as solvent. It is known to have good adhesion properties to objects upon complete drying and leaves a non-sticky film layer, although PVA glue is known to become sticky again on contact with moist surfaces or under humid conditions. Although there is no uniform agreement on how the PVA glue works, its stickiness is believed to be closely related to the polymer chains as discussed in section 10.2.2.2. (Rajsharad & Kamble, 2006).

It is reasonable to believe that the viscosity and stickiness are phenomena closely related as presented in section 10.2.2.2. It is possible that the viscosity of the PVA/TiO_2 solution will increase to a higher level than the viscosity of the sodium sulphate solution upon evaporation of the solvent, and that this increase in viscosity increases the coating stickiness and thus the tendency of agglomeration. It seems thereby obvious to test the influence of the coating solution bulk viscosity and the development in stickiness upon solvent evaporation. For this purpose three coating solutions were selected for rheological characterisation as well as for fluid bed coating experiments. The three coating solutions were solution A, E and G. Three coating experiments were performed for each coating solution for three sets of Drying Force/spray rate conditions according to table 10-2.

Table 10-2. Coating experiments for the test of the influence of coating solution bulk viscosity.

	Series 1	**Series 2**	**Series 3**
Solution A 10 w/w% PVA 10 w/w% TiO_2 pH = 7.0	Drying Force = 18 kPa Spray rate = 24 g/min	Drying Force = 18 kPa Spray rate = 90 g/min	Drying Force = 18 kPa Spray rate = 120 g/min
Solution E 2 w/w% PVA 2 w/w% TiO_2 pH = 7.2	Drying Force = 18 kPa Spray rate = 24 g/min	Drying Force = 18 kPa Spray rate = 90 g/min	Drying Force = 18 kPa Spray rate = 120 g/min
Solution G 15 w/w% Na_2SO_4 1 w/w% Dextrin pH = 7.1	Drying Force = 18 kPa Spray rate = 24 g/min	Drying Force = 18 kPa Spray rate = 90 g/min	Drying Force = 18 kPa Spray rate = 120 g/min

It is well known from detailed two-fluid nozzle studies that the liquid viscosity plays an important role regarding the resulting mean droplet diameter (Hede et al., 2008c). The mean droplet diameter is important for the coating process for several reasons (Schæfer and Wørts,

1977). First of all, the droplet diameter influences the droplet drying time. There is roughly a log-log linear dependence between the droplet diameter and the droplet drying time (Hinds, 1999). With increasing droplet diameter, and thereby increasing droplet drying time, the coated particles will be wet and sticky for a longer time thereby increasing the chance of agglomeration. Furthermore, the droplet diameter influences other important phenomena such as the time of droplet penetration into the core particle and the morphology of the final coating layer (Hede, 2005). Hence, there are indeed many reasons to believe that a careful control of the droplet diameter may be crucial with respect to control of agglomeration. Knowing that the bulk viscosity of the coating solutions A and G are significantly different, this means that for identical spray rates at identical nozzle pressures, the resulting mean droplet diameters are likewise different. This could be part of the reason for the observed differences in agglomeration tendency between the coating formulations. Following the studies of bulk viscosities and stickiness, it seems reasonable to perform detailed studies of the influence of the mean droplet diameter.

From the review of two-fluid nozzles for coating purposes in fluid beds by Hede et al. (2008c) it becomes clear that the determination and a-priori prediction of the mean droplet diameter produced in external mixing nozzles, as the one used in the present fluid bed set-up, is not an easy task. Direct measurement techniques often give different results. There are, nevertheless, a variety of correlations that may be used to estimate the mean droplet diameter from the coating solution properties and the nozzle dimensions and process conditions. Not all correlations can be used for the coating solutions and atomisation conditions in the present study, but the expression in equation 2.3 (please refer to chapter two) proposed by Mulhem et al. (2003 & 2006) was shown to give precise estimations of the mean droplet diameter for coating solutions similar to those used in the present study. Hence, this equation is used in the present study to estimate the droplets produced by the PVA/TiO_2 suspensions and the sodium sulphate solutions. Knowing the dimensions of the applied two-fluid nozzle and the corresponding atomisation air mass flow rate as well as the coating solution properties, made it possible to adjust the liquid flow rate in order to produce similar mean droplet diameters for solution A and solution G. In order to test the influence of the mean droplet diameter six experiments were performed according to table 10-3.

Table 10-3. Coating experiments for the test of the influence of the mean droplet diameter. Values for the d_{32} were calculated using equation 2.3 (please refer to chapter two).

	Series 1	**Series 2**	**Series 3**
Solution A 10 w/w% PVA 10 w/w% TiO_2 pH = 7.0	Drying Force = 18 kPa Spray rate = 24 g/min Mean droplet diameter = 11.3 µm	Drying Force = 18 kPa Spray rate = 19 g/min Mean droplet diameter = 8.0 µm	Drying Force = 18 kPa Spray rate = 14 g/min Mean droplet diameter = 5.2 µm
Solution G 15 w/w% Na_2SO_4 1 w/w% Dextrin pH = 7.1	Drying Force = 18 kPa Spray rate = 62 g/min Mean droplet diameter = 11.2 µm	Drying Force = 18 kPa Spray rate = 50 g/min Mean droplet diameter = 8.0 µm	Drying Force = 18 kPa Spray rate = 37 g/min Mean droplet diameter = 5.2 µm

10.4.3. pH, colloidal phenomena and additives

In terms of the previous experience with the colloidal phenomena in the PVA /TiO_2 system presented in section 10.2.6., it seems reasonable to test the influence of pH in the PVA/TiO_2 system on the tendency of agglomeration. In order to test this, three coating solutions were selected for rheological characterisation and for fluid bed coating experiments. The three

coating solutions were solution A, B and C. Two coating experiments were performed for each coating solution for two sets of Drying Force/spray rate conditions according to table 10-4.

Table 10-4. Coating experiments for the test of the influence of pH in the PVA/TiO_2 solution.

	Series 1	**Series 2**
Solution A 10 w/w% PVA 10 w/w% TiO_2 pH = 7.0	Drying Force = 18 kPa Spray rate = 24 g/min	Drying Force = 18 kPa Spray rate = 14 g/min
Solution B 10 w/w% PVA 10 w/w% TiO_2 pH = 4.0	Drying Force = 18 kPa Spray rate = 24 g/min	Drying Force = 18 kPa Spray rate = 14 g/min
Solution C 10 w/w% PVA 10 w/w% TiO_2 pH = 10.0	Drying Force = 18 kPa Spray rate = 24 g/min	Drying Force = 18 kPa Spray rate = 14 g/min

There are reasons to believe that the introduction of Neodol 23-6.5 will reduce the tendency of agglomeration in comparison to the original PVA/TiO_2 solution under similar process conditions. According to the manufacturer, Shell Chemicals Europe (2005), Neodol 23-6.5 is not charged and it will thereby most likely be less sensitive to changes in pH. This also indicates that Neodol 23-6.5 should be chemically stable at acidic pH values although this has not yet been tested properly. Nor have the lubricating and plasticizing effects for Neodol 23-6.5 at acidic pH been tested, but there is no reason to believe that Neodol 23-6.5 should function differently at pH = 4 than under conditions with pH = 7. Hence, it is believed that if a low pH value is beneficial in terms of reduced agglomeration tendency for the pure PVA/TiO_2 system, this will also be the case for a PVA/TiO_2/Neodol 23-6.5 system. In that sense it seems reasonable to study the influence of substituting PVA/TiO_2 with an additive and see how this substitution will work under acidic conditions. For this purpose three coating solutions were selected for rheological characterisation as well as for fluid bed coating experiments. The three coating solutions were solution A, D and F. Two coating experiments were performed for each coating solution for two sets of Drying Force/spray rate conditions according to table 10-5.

Table 10-5. Coating experiments for the test of the influence of additives and pH in the PVA/TiO_2 system.

	Series 1	**Series 2**
Solution A 10 w/w% PVA 10 w/w% TiO_2 pH = 7.0	Drying Force = 18 kPa Spray rate = 24 g/min	Drying Force = 18 kPa Spray rate = 14 g/min
Solution D 9 w/w% PVA 9 w/w% TiO_2 2 w/w% Neodol 23-6.5 pH = 7.0	Drying Force = 18 kPa Spray rate = 24 g/min	Drying Force = 18 kPa Spray rate = 14 g/min
Solution F 9 w/w% PVA 9 w/w% TiO_2 2 w/w% Neodol 23-6.5 pH = 4.0	Drying Force = 18 kPa Spray rate = 24 g/min	Drying Force = 18 kPa Spray rate = 14 g/min

10.5. Results and discussion

Following the structure of section 10.4, the results and discussion section is divided into subsections each treating its own study.

10.5.1. Testing the influence of the Drying Force and the liquid spray rate

In accordance with the guidelines for the first study, 24 coating experiments with solution A and 24 coating experiments with solution G were carried out for different values of the Drying Force and spray rate in g/min (always at an atomisation air pressure of 3 bar). For each batch the weight gain was determined after coating. For all the experiments in the test of the Drying Force versus agglomeration tendency, the weight gain varied between 18.6 and 19.7 w/w% meaning that the spray drying losses in the experiments were quite small. All the resulting agglomeration tendencies for the sodium sulphate coating experiments (determined with the use of equation 10.7) were plotted in terms of their spray rate and Drying Force coordinates according to figure 10.4.

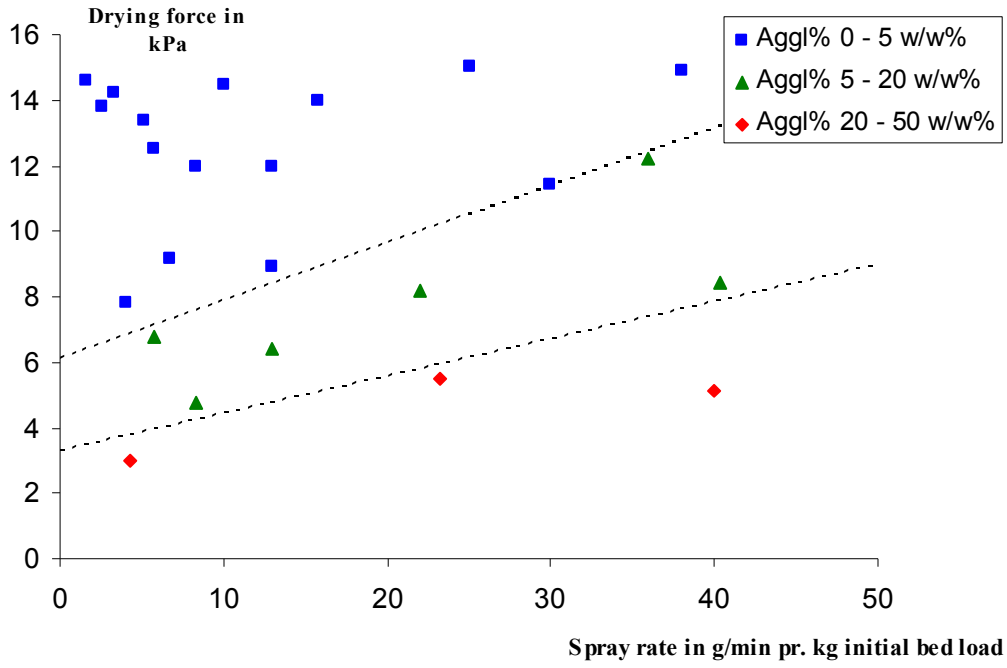

Figure 10.4: Agglomeration regime map for the salt coating process (with solution G) in the medium-scale fluid bed. The dashed lines indicate the demarcation between the different agglomeration regimes.

As observed from figure 10.4, the agglomeration tendencies are distributed in distinct bands. In accordance with results by Hede et al. (2008b) the agglomeration tendency is observed to increase as the Drying Force decreases. With decreasing Drying Force the coated particles are wet for a longer time thus increasing the likelihood of agglomeration. Likewise is the agglomeration tendency observed to increase for increasing spray rate at identical Drying Force, which is reasonable because at increasing spray rate, more particles will be wet locally in the bed thus increasing the chance of agglomeration as observed. Of interest in figure 10.4 is the fact that there is a wide range of Drying Force and spray rate values for which the agglomeration tendency is small.

A similar plot for the PVA/TiO_2 coating process in figure 10.5 indicates several interesting points. A first look reveals that the demarcations between the agglomeration categories are somewhat different from figure 10.4. Further, it can be observed that it was not possible to get below an agglomeration limit of 10 w/w% in any of the 24 experiments. The agglomeration tendency in figure 10.4 was observed to decrease when the Drying Force increased irrespectively of the spray rate, but in figure 10.5 the agglomeration tendency seems to be low only in a narrow regime surrounded by agglomeration tendencies in the range of 20 – 50 w/w %. A plausible reason for this could be that at Drying Force values close to and above 16 kPa, the bed temperature during steady state coating was approaching the glass transition temperature for PVA, which is approximately 58 ºC for the used type of PVA. At a temperature above T_g, the PVA is soft and can be easily deformed, which most likely increases the stickiness of the coating layer. It is thus not surprising to observe an increasing agglomeration tendency for the PVA/TiO_2 solution as the Drying Force increases beyond a certain boundary.

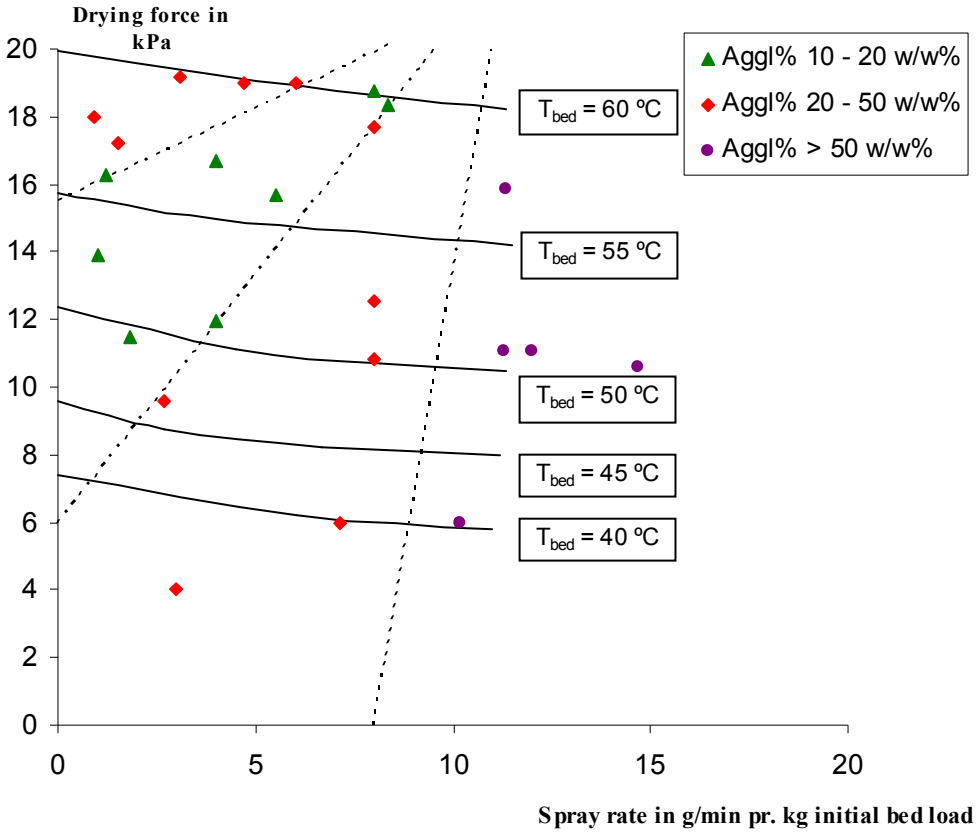

Figure 10.5: Agglomeration regime map for the PVA/TiO_2 coating process (with solution A) in the medium-scale fluid bed. The dashed lines indicate the demarcation between the different agglomeration regimes. Iso-bed-temperature lines are added in order to indicate at which bed temperatures the experiments were processed.

It is clear from the comparison of figure 10.4 and figure 10.5 that the tendency of agglomeration for the two types of coating solutions is not the same for identical value of the Drying Force and the spray rate. The two coating processes do not respond in a similar manner towards changes in the Drying Force and the spray conditions, and within the tested range for the PVA/TiO_2 solution, it has not been possible to find coating conditions leading to agglomeration percentages below 10 w/w%. Hence, it may be concluded that similar spray and similar Drying Force conditions do not lead to similar agglomeration tendency for the two

types of coating processes. The results from the test have indicated, however, that the agglomeration tendency for both types of processes distribute into regimes based on the spray rate and Drying Force.

10.5.2. Testing the influence of bulk viscosity, stickiness and mean droplet diameter

Prior to the test of the influence of the bulk viscosity, the coating solutions were initially characterised with respect to rheological properties, and detailed viscosity measurements were made for each of the three coating solutions in terms of both varying the shear rate and the temperature. In figure 10.6 the viscosities of the coating solutions have been determined as a function of shear rate at a constant temperature of 25 ºC. It becomes obvious from the curves in figure 10.6 that there are major differences between solution A and solution G with respect to rheological behaviour. Solution A being the PVA/TiO_2 solution, exhibits non-Newtonian behaviour as the viscosity clearly decreases with increasing shear rate. Furthermore, solution A has roughly a 20-30 times higher viscosity than the two other solutions. Newtonian behaviour is in contrary observed for solutions E and solution G up to a shear rate of 200 1/s at which possible eddy flow regimes occur in the rheometer. Solution E is the five times diluted solution A, and thus the graph in figure 10.6 shows that it is possible to have a PVA/TiO_2 and a sodium sulphate solution with similar bulk viscosities, when the PVA/TiO_2 solution is sufficiently diluted.

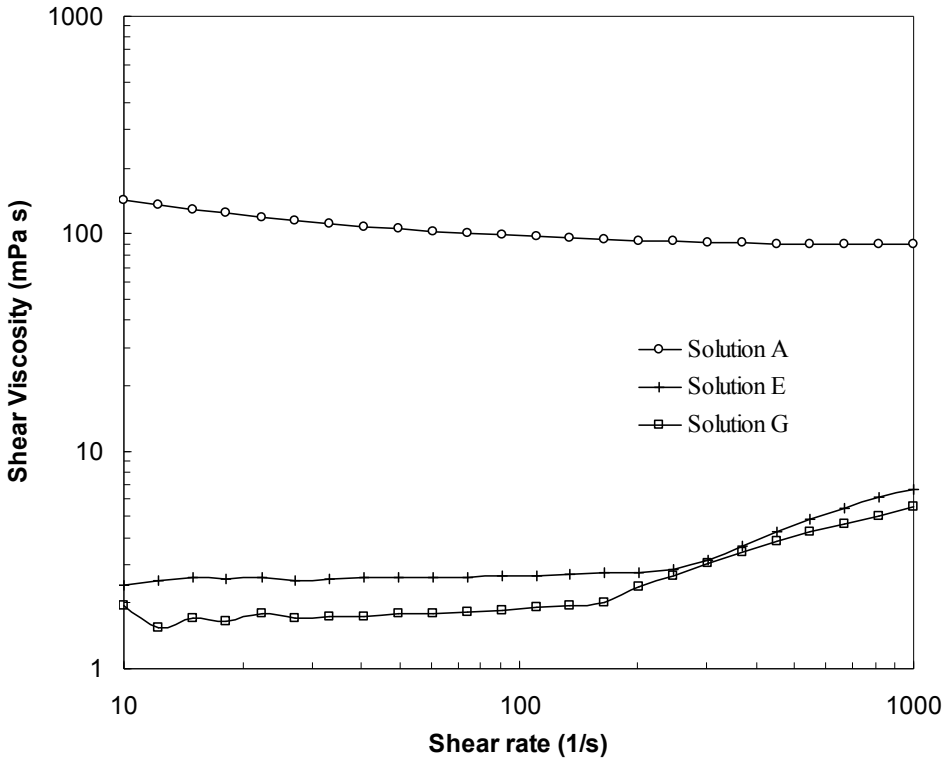

Figure 10.6: Viscosity curves of the solutions A, E and G as a function of shear rate at a constant temperature of 25 ºC.

Similar differences in viscosities can be observed from figure 10.7 where the viscosity as a function of temperature was determined for the three solutions for a constant shear rate of 1000 1/s. For solution A a dramatic decrease is observed with the viscosity being more than halved going from a solution temperature of 25 ºC to 70 ºC. The viscosity dependencies on

temperature for the diluted solution E and for the sodium sulphate solution are fairly small in comparison.

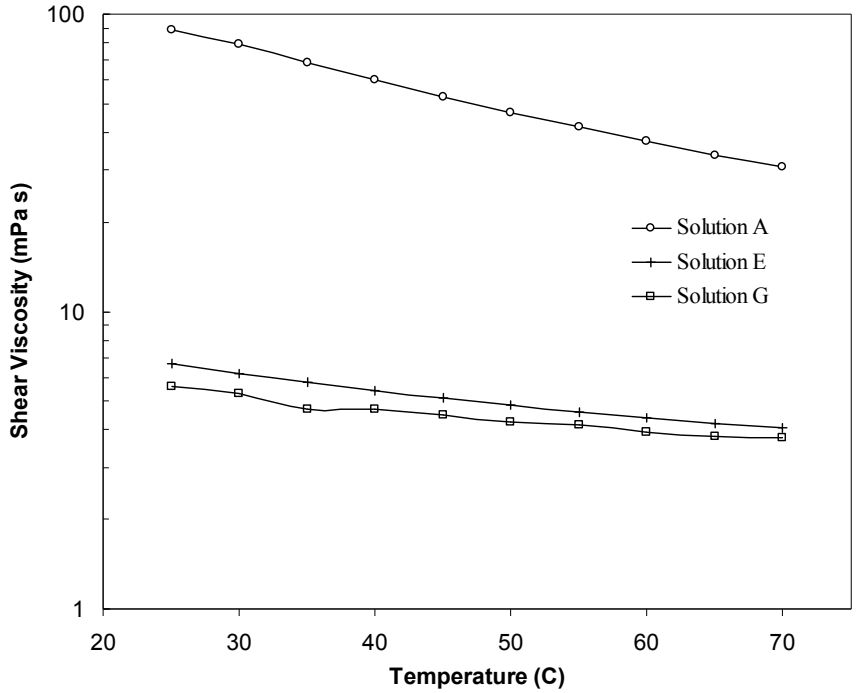

Figure 10.7: Viscosity curves of the solutions A, E and G as a function of temperature at a constant shear rate of 1000 1/s.

For the test of the influence of coating solution bulk viscosity, coating experiments were carried out in accordance with table 10-2. For each batch the weight gain was determined after the coating process. For all the experiments the weight gain varied between 19.1 and 19.7 w/w% meaning that the spray drying losses in the experiment were quite small. The corresponding agglomeration tendencies for all nine experiments (determined with the use of equation 10.7) may be observed from table 10-6.

Table 10-6. Results for the coating experiments for the test of the coating solution bulk viscosity. The viscosities were adapted from figure 10.7 at a temperature of 60 ºC.

	Series 1	**Series 2**	**Series 3**
Solution A 10 w/w% PVA 10 w/w% TiO_2 pH = 7.0	η_{bulk} = 46.7 mPa·s Drying Force = 18 kPa Spray rate = 24 g/min Aggl% = 19.1 w/w%	η_{bulk} = 46.7 mPa·s Drying Force = 18 kPa Spray rate = 90 g/min Aggl% = 81.7 w/w%	η_{bulk} = 46.7 mPa·s Drying Force = 18 kPa Spray rate = 120 g/min Aggl% = 91.1 w/w%
Solution E 2 w/w% PVA 2 w/w% TiO_2 pH = 7.2	η_{bulk} = 4.8 mPa·s Drying Force = 18 kPa Spray rate = 24 g/min Aggl% = 17.8 w/w%	η_{bulk} = 4.8 mPa·s Drying Force = 18 kPa Spray rate = 90 g/min Aggl% = 74.4 w/w%	η_{bulk} = 4.8 mPa·s Drying Force = 18 kPa Spray rate = 120 g/min Aggl% = 88.1 w/w%
Solution G 15 w/w% Na_2SO_4 1 w/w% Dextrin pH = 7.1	η_{bulk} = 4.3 mPa·s Drying Force = 18 kPa Spray rate = 24 g/min Aggl% = 0.9 w/w%	η_{bulk} = 4.3 mPa·s Drying Force = 18 kPa Spray rate = 90 g/min Aggl% = 1.3 w/w%	η_{bulk} = 4.3 mPa·s Drying Force = 18 kPa Spray rate = 120 g/min Aggl% = 1.5 w/w%

First of all it may be observed from table 10-6 that for solution G and solution A the resulting agglomeration tendencies are nicely within the regimes predicted by figure 10.4 and figure 10.5 respectively, adding further validity to the regimes maps. Of further interest from the results in table 10-6 are the differences between the resulting agglomeration tendencies for solution A and E, and solution E and G. Even though solution E and solution G have similar coating solution bulk viscosities, the resulting agglomeration tendencies are far from being similar even though the coating process conditions indeed were similar. In fact the agglomeration tendencies observed for the three experiments with solution E are close to the agglomeration tendencies observed for solution A, although not being statistically similar. The observed agglomeration tendencies are only slightly smaller for coating solution A than for coating solution E. Hence, regarding agglomeration tendency there is no obvious advantageous effect of diluting the PVA/TiO_2 solutions. The disadvantage is more outspoken for the processing point of view as the coating time for solution E is five times the time for solution A, in order to apply the same dry-matter content on the particle core bed. One plausible explanation for the similar agglomeration tendencies with solution E and A could be that, even though the diluted droplets from coating solution E have a lower initial bulk viscosity, they will eventually reach the properties of the droplets of solution A as the solvent evaporates. This was studied in Texture analyser tests studying the stickiness for the three solutions. Figure 10.8 shows the stickiness as a function of the dry-matter contents for the three solutions.

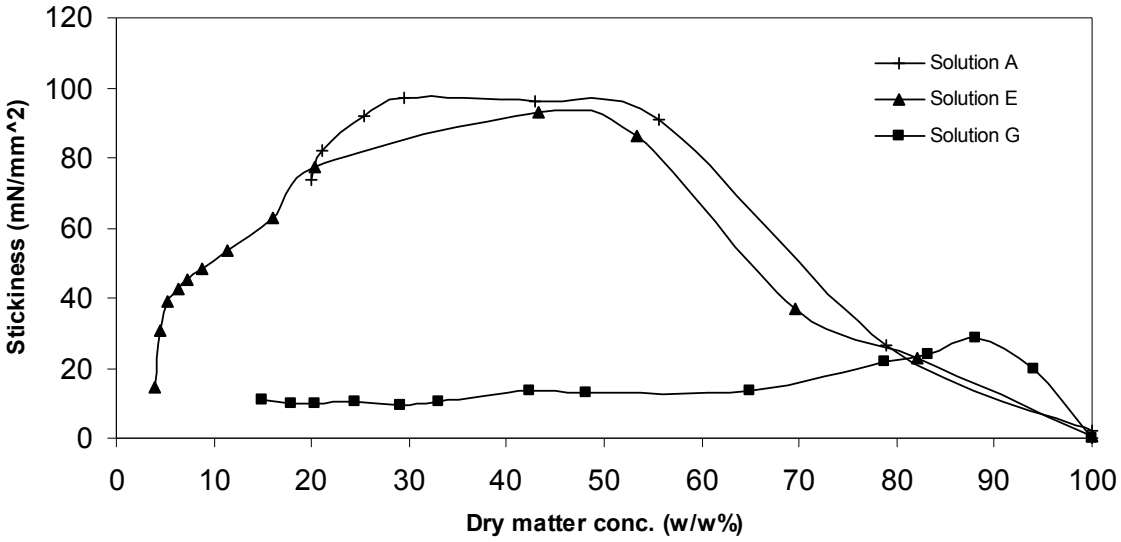

Figure 10.8: Stickiness as a function of dry-matter contents in the coating solution for solution A, E and G.

As observed in figure 10.8 the stickiness curves for solution A and solution E peak at almost the same value of ~ 95 mN/mm^2 and, furthermore, closely follow each other. This means that even though solution E has a solute concentration five times lower than solution A, the stickiness upon evaporation of the aqueous solvent will eventually reach an almost identical value for the two solutions. There are thus, no advantages of diluting the PVA/TiO_2 solution from a stickiness point of view. Figure 10.8 reveals that even though the stickiness of solution E and solution G are similar initially, the developments in stickiness upon solvent evaporation are quite different. For comparison with the PVA/TiO_2 solutions, the stickiness of the sodium solution G peaks several magnitudes lower at a maximum stickiness of ~ 30 mN/mm^2. Interestingly, the peak in stickiness for solution G is at dry-matter contents of roughly

90 w/w% in a narrow peak, whereas the stickiness peaks for a broader range of dry-matter contents ranging from roughly 30 – 55 w/w% for the PVA/TiO_2 solutions. This means that the stickiness of a sodium sulphate coating solution in general is significantly lower than for the PVA/TiO_2 solution, which is a plausible reason for the observed differences in agglomeration tendencies among the three solutions.

One parameter that influences agglomeration is the stickiness of a coating solution with respect to the dry-matter contents. Another parameter is the time required to evaporate all coating solution solvent and thereby reach 100 w/w% dry-matter contents. Figure 10.9 shows the stickiness as a function of time the heating fan was switched on, and figure 10.10 shows the dry-matter contents in the coating solution as a function of the time the heating fan was switched on. As observed from these two figures, solution A with the highest initial dry-matter contents requires the shortest time to reach complete drying, although the stickiness remains high during the drying phase. The sample with solution A has no measurable stickiness after 250 seconds of drying, whereas it takes almost 700 seconds before solution G is completely dried even though the dry-matter concentration between solution A and solution G differs only 5 w/w%. It is obviously questionable whether or not this drying time can be compared to the actual drying time in a fluid bed, but there is reason to believe that the drying times in figure 10.9 and figure 10.10 indeed are representative of what is taking place during fluid bed processing. As expected, figure 10.9 and figure 10.10 show that it takes the longest time to reach complete drying of solution E having initially a dry-matter contents five times lower than solution A.

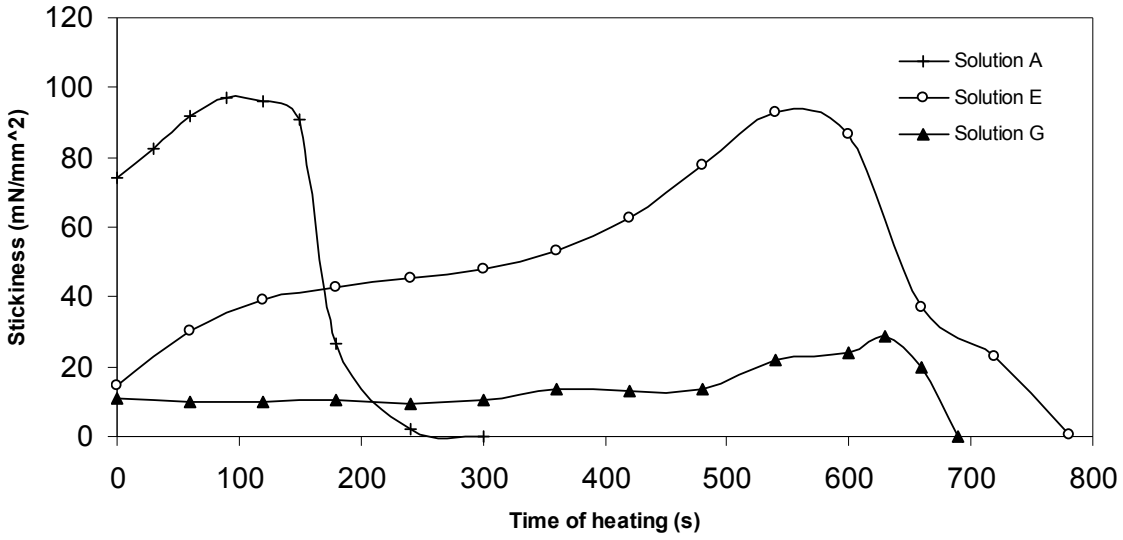

Figure 10.9: Stickiness as a function of the time the heating fan was switched on for solution A, E and G.

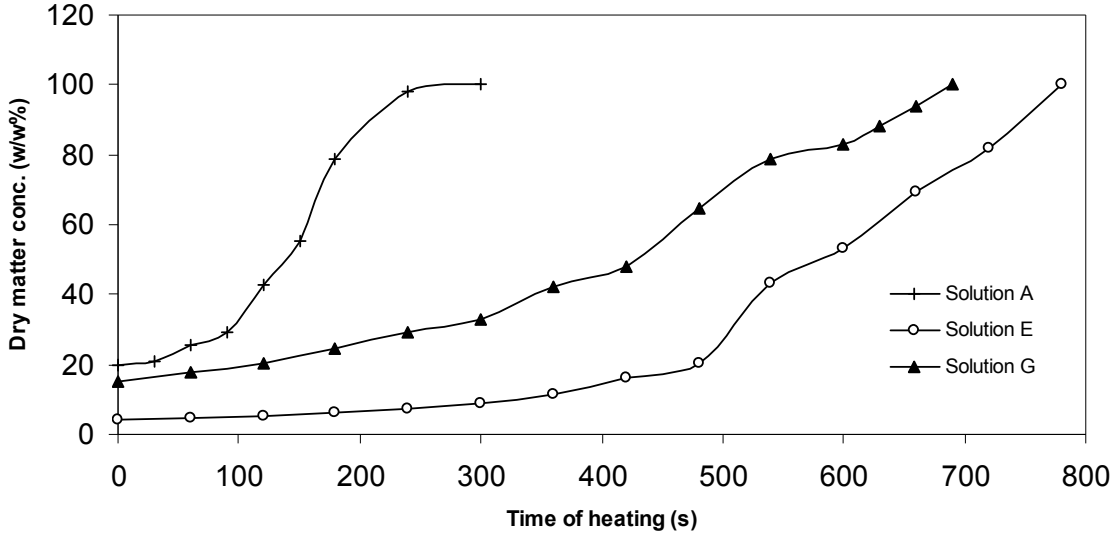

Figure 10.10: Dry-matter contents in the solution as a function of the time the heating fan was switched on for solution A, E and G.

The bulk viscosity is known to be of primary importance regarding the level of droplet penetration into the core particle as observed by Hede (2005). It was observed in studies by Hede (2005) how the droplet penetration decreased as the bulk viscosity of a sodium sulphate solution increased due to addition of sodium carboxymethylcellulose. Thus, it is expected that if there is any significant droplet penetration in the present study, the level will be larger for particles coated with coating solution E than for particles coated with solution A. From cut-through profiles in figure 10.11 it becomes clear that the levels of droplet penetration indeed are significantly different for coating solution A and E. For the granule in figure 10.11 coated with solution E, the coated granule is red all the way through the granule. This indicates that the coating solution has penetrated far into the original core. For the granule coated with solution A only a modest penetration is observed as the inner core has remained unaffected by the coating process. Interestingly, for both granules coated with PVA/TiO_2, the boundary between the coating layer and the core structure can be easily distinguished as a white/pale red shell layer. This indicates that upon impact with the coating droplet, the majority of PVA/TiO_2 remains on the outside of the core, whereas the aqueous solvent containing the pigment colour is drained into the pores of the core. For the granule coated with solution G, the blue colour has penetrated far into the core structure indicating a deep droplet penetration. For the salt coating, the boundary between the coating layer and the original core structure cannot easily be distinguished. These observations are in agreement with previous studies by Hede et al. (2007a & 2008b).

The data obtained in the test of the influence of the bulk viscosity have revealed several important things. First of all, the hypothesis suggesting similar tendency of agglomeration when similar coating solution bulk viscosity, cannot be confirmed. Even if the bulk viscosities of the PVA/TiO_2 solution and the sodium sulphate solution are arranged to be identical, the resulting agglomeration tendencies are far from being similar. It may furthermore be concluded from the data, that there is no beneficial effect regarding the dilution of the PVA/TiO_2 coating solution. On the contrary, by diluting the PVA/TiO_2 solution the stickiness eventually goes through the same magnitudes of stickiness of a more concentrated PVA/TiO_2 solution upon evaporation of the solvent, resulting in a similar agglomeration tendency.

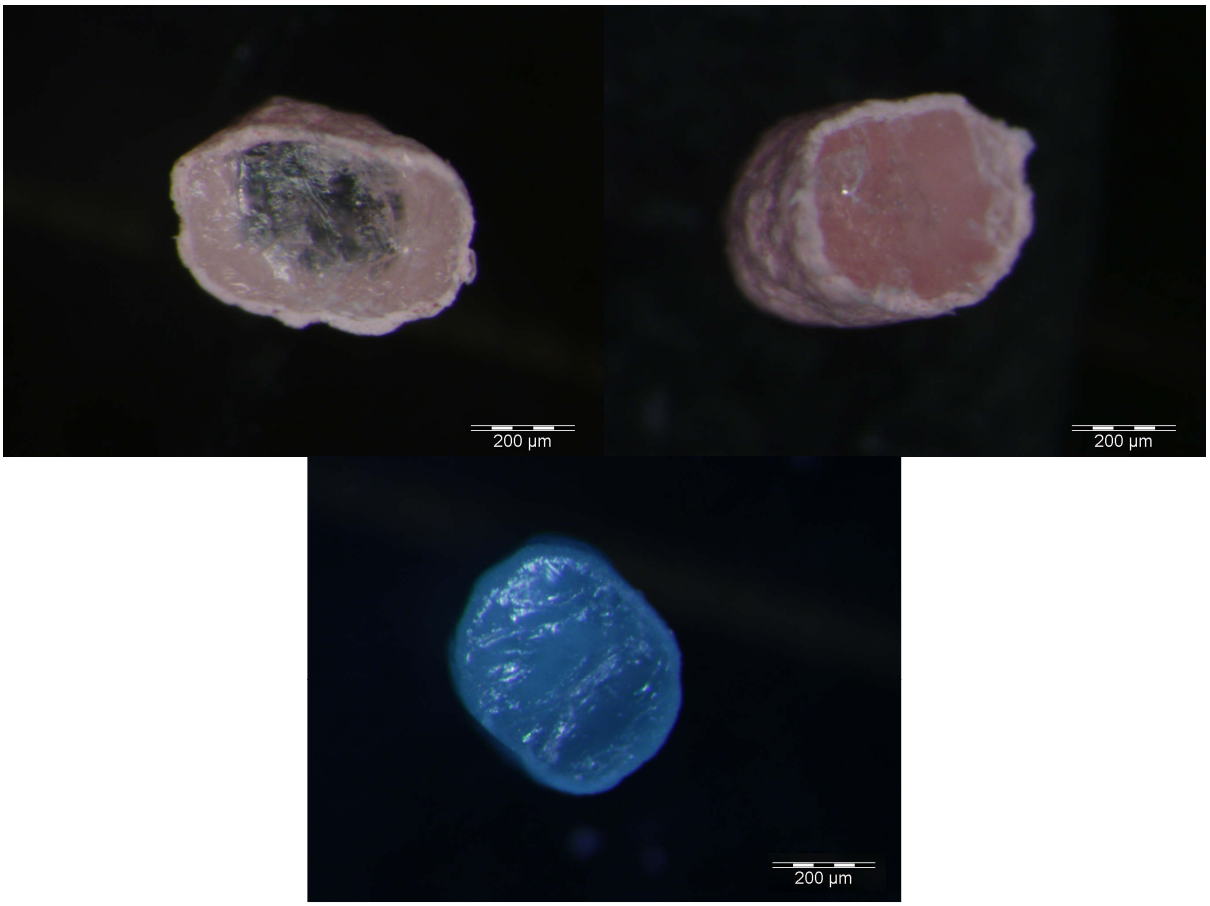

Figure 10.11: Cut-through profiles of granules coated under conditions with a Drying Force of 18 kPa and a spray rate of 24 g/min. Upper left: Coating solution A. Upper right: Coating solution E. Bottom: Coating solution G. Visual microscopy analyses were performed using an Olympus KL 1500 LCD microscope.

Coating experiments to test the influence of the mean droplet diameter were carried out in accordance with table 10-3. For each batch the weight gain was determined after coating. For all the experiments the weight gain varied between 18.8 and 19.5 w/w% indicating that the spray drying losses in the experiment were quite small. For both coating solutions, the spray drying losses were highest in the third series where the mean droplet diameters were the smallest. The corresponding agglomeration tendencies for all six experiments (determined with the use of equation 10.7) may be observed from table 10-7.

Table 10-7. Results for the coating experiments for the test of the influence of the mean droplet diameter. Values for the d_{32} were calculated using equation 2.3 (see chapter two).

	Series 1	**Series 2**	**Series 3**
Solution A 10 w/w% PVA 10 w/w% TiO_2 pH = 7.0	d_{32} = 11.3 µm Drying Force = 18 kPa Spray rate = 24 g/min Aggl% = 18.7 w/w%	d_{32} = 8.0 µm Drying Force = 18 kPa Spray rate = 19 g/min Aggl% = 16.4 w/w%	d_{32} = 5.2 µm Drying Force = 18 kPa Spray rate = 14 g/min Aggl% = 13.7 w/w%
Solution G 15 w/w% Na_2SO_4 1 w/w% Dextrin pH = 7.1	d_{32} = 11.2 µm Drying Force = 18 kPa Spray rate = 62 g/min Aggl% = 0.7 w/w%	d_{32} = 8.0 µm Drying Force = 18 kPa Spray rate = 50 g/min Aggl% = 0.8 w/w%	d_{32} = 5.2 µm Drying Force = 18 kPa Spray rate = 37 g/min Aggl% = 0.2 w/w%

First of all it may be seen from the results in table 10-7 that even though the droplet diameters are identical, the resulting agglomeration tendencies are significantly different for coating solution A and G, irrespectively of the mean droplet diameter levels. The agglomeration tendencies are statistically similar in the three experiments with coating solution G, as the three agglomeration percentages are within the ± 0.88 % range. The situation is different for the experiments with coating solution A as there are significant differences between the agglomeration percentages. In accordance with expectations, the agglomeration tendency decreases with decreasing mean droplet diameter.

Studies of cut-through profiles of granules coated with the same coating solution, but with a different mean droplet diameter, did not reveal any significant differences with respect to droplet penetration for both of the two solutions. However, the outer coating layer morphology was affected by the mean droplet diameter. As observed from figure 10.12, the coating layer becomes increasingly rough and raspberry-like as the mean droplet diameter increases. This tendency was most pronounced for coating solution A, as no significant differences in coating layer morphology were observed for granules coated with solution G. These findings clearly support previous results by Hede et al. (2008b), Neidel (2007) and Waldie (1991) stating that the mean droplet diameter is an important parameter regarding the final coating layer morphology. Apparently, under identical process conditions, this effect is most pronounced for polymer coatings.

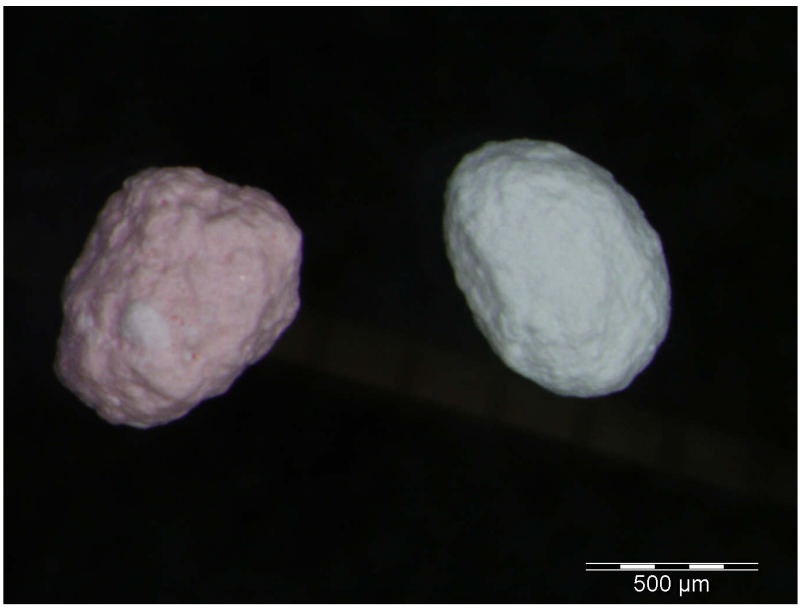

Figure 10.12: Microscope pictures of particles coated with coating solution A. Left: Red coated granule from series 1 (spray rate 24 g/min ~ d_{32} = 11.3 µm). Right: White coated granule from series 3 (spray rate 14 g/min ~ d_{32} = 5.2 µm). Visual microscopy analysis was performed using an Olympus KL 1500 LCD microscope.

In conclusion the results have shown that similar mean droplet diameters for solution A and solution G do clearly not result in similar agglomeration tendencies. It was, however, observed how the tendency of agglomeration in fact could be reduced by reducing the mean droplet diameter, although the reduction was only limited for solution A and not even statistically significant for solution G having agglomeration percentages close to zero in all three experiments. For solution A, the reduction of the mean droplet diameter did, furthermore, lead to coated particles with a smoother coating layer, which in addition most likely give granules with improved mechanical properties. One problem with the reduction of the mean droplet diameter is, nevertheless, that spray drying losses may increase (depending

on the nozzle position and the drying conditions), and if the droplet diameter is reduced simply by reducing the liquid feed rate, the coating time will increase with decreasing mean droplet diameter.

10.5.3. Testing the influence of pH, colloidal phenomena and additives

For the test of the influence of pH in the PVA/TiO_2 system, the coating solutions were initially characterised with respect to rheological properties, and viscosity measurements were made for each of the three solutions in terms of both varying the shear rate and the temperature, similarly to the second study. In figure 10.13 the viscosities of the coating solutions have been determined as a function of shear rate at a constant temperature of 25 ºC. It may be observed that all three solutions exhibit non-Newtonian behaviour as the viscosities all decrease with increasing shear rate. The largest decrease with shear rate is observed for solution C having the highest pH value. A general trend in figure 10.13 is that the viscosity decreases with decreasing pH. Going from solution C (pH = 10) to solution B (pH = 4) the viscosity is more than halved. The tendencies of the curves in figure 10.13 comply fully with the tendencies of the PVA/TiO_2 viscosity curves determined by Chu et al. (2007), although Chu et al. (2007) studied a more dilute 15 w/w% TiO_2/2.5 w/w% PVA suspension.

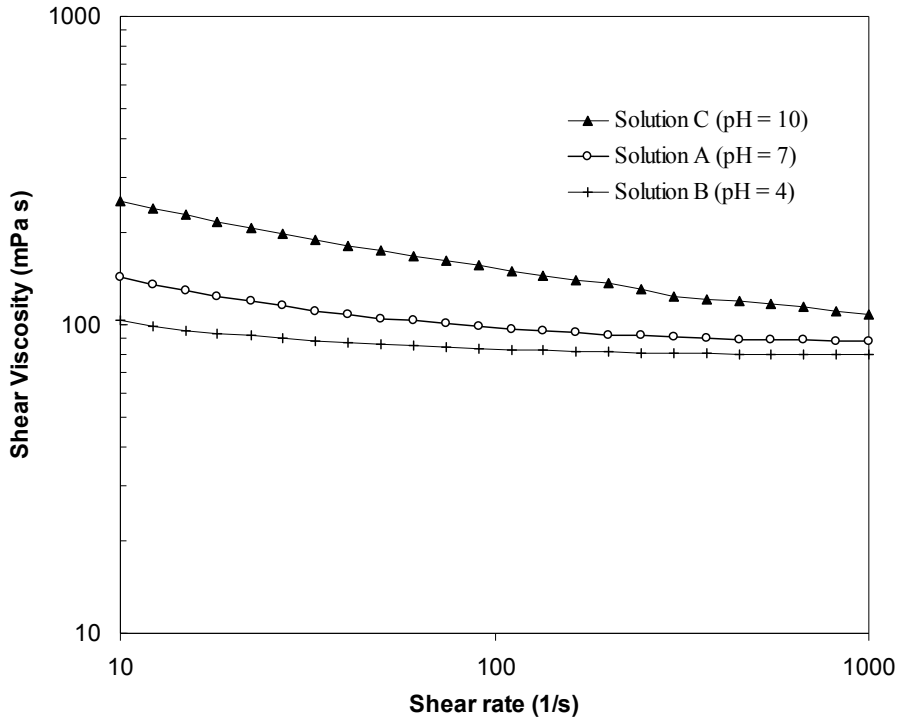

Figure 10.13: Viscosity curves of the solutions A, B and C as a function of shear rate at a constant temperature of 25 ºC.

Similar differences in viscosities can be observed from figure 10.14 where the viscosity as a function of temperature was determined for the three solutions at a constant shear rate of 1000 1/s. For these three solutions, a dramatic decrease is observed with the viscosity being more than four times lower going from a solution temperature of 25 ºC to 70 ºC.

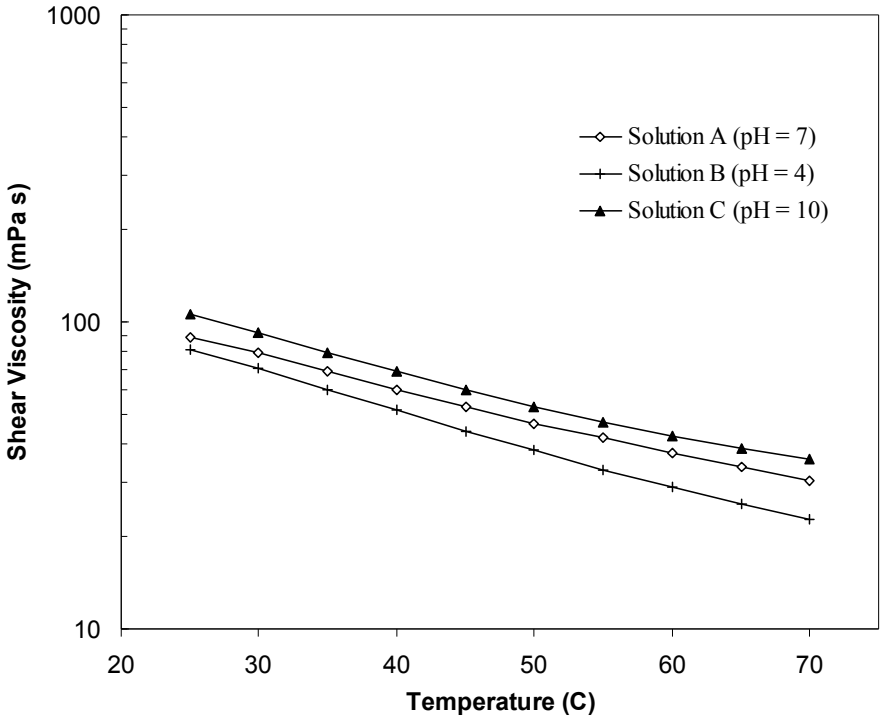

Figure 10.14: Viscosity curves of the solutions A, B and C as a function of temperature at a constant shear rate of 1000 1/s.

The results from the second study indicated that the bulk viscosity properties cannot directly be correlated with the tendency of agglomeration. Texture analyser studies of the stickiness for the three solutions A, B and C reveal in addition, that the magnitude of difference in bulk viscosity cannot directly be correlated with the difference in stickiness. Comparison of figure 10.15, 10.16 and 10.17 indicates that solution C exhibits both the largest stickiness and the longest time to reach complete evaporation. Figure 10.15 reveals that the lowest stickiness is found for solution B, having the lowest pH value, followed by solution A having a higher peak stickiness for a broader range of dry-matter contents. The decline in stickiness for solution B is the most pronounced, and the effect in stickiness upon reducing pH is clearly observed from figure 10.15. A possible reason for the reduced stickiness at pH = 4 is that, at this pH level far way from the isoelectric point, the TiO_2 particles are well distributed among the PVA chains and thus function more effectively as anti-stickiness agents. Although only a minor difference between solution A and solution B in figure 10.16 in terms of stickiness, it can be observed from figure 10.17 that it takes roughly 50 seconds longer to reach complete drying of solution B and C compared to solution A. The actual stickiness in these 50 seconds is, however, fairly low for solution B, but relatively large for solution C, as observed from figure 10.16. It may thereby be concluded that there is a statistical significant effect of reducing pH in the PVA/TiO_2 system in terms of stickiness. What is left to investigate is whether or not this effect can be correlated with any differences in agglomeration tendency, but before this is tested, the dependence between stickiness and viscosity is studied.

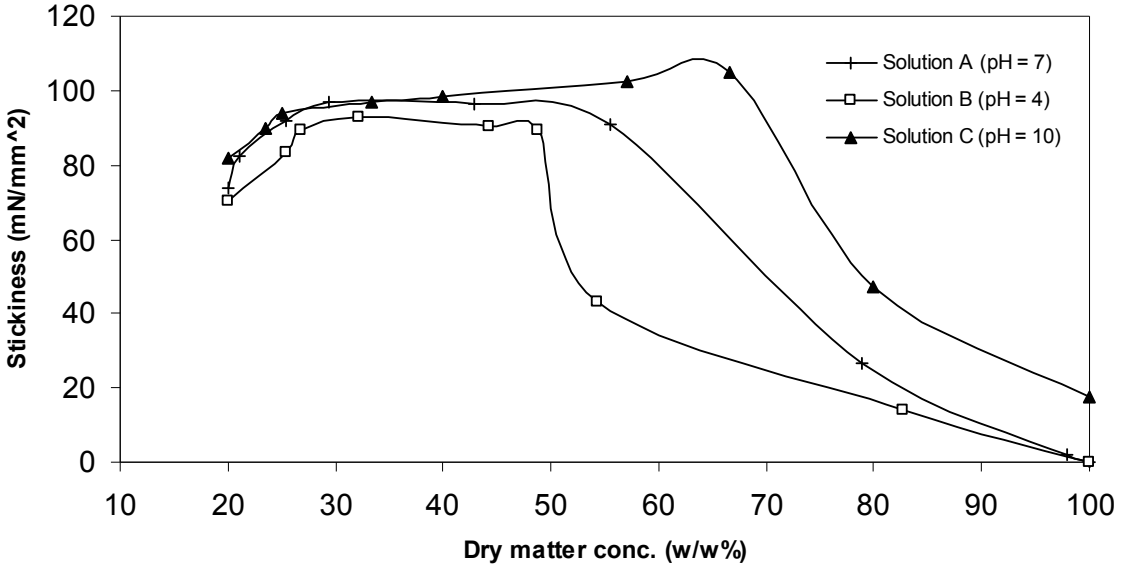

Figure 10.15: Stickiness as a function of dry-matter contents in the coating solution for solution A, B and C.

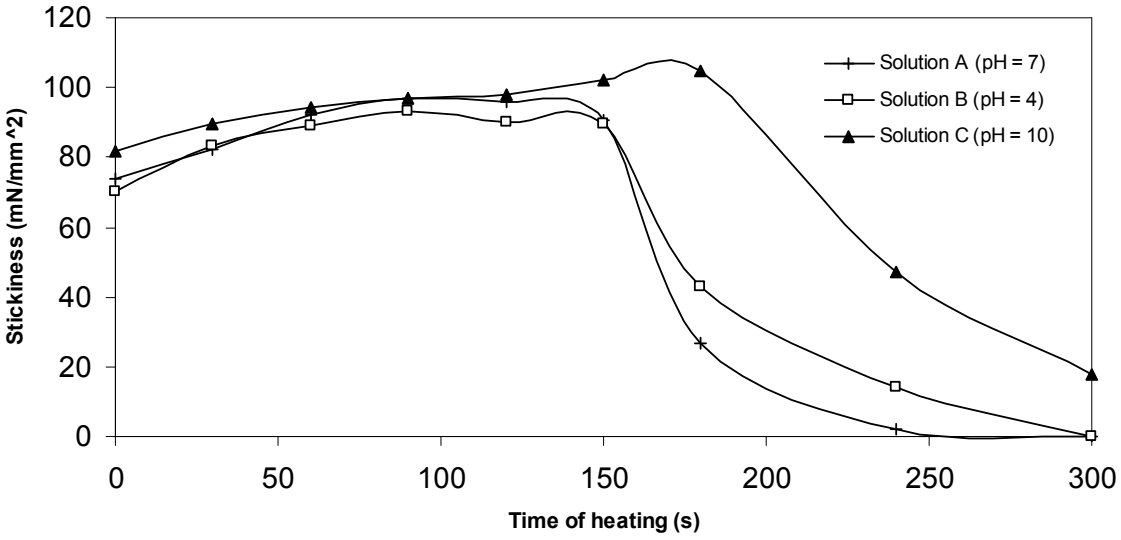

Figure 10.16: Stickiness as a function of the time the heating fan was switched on for solution A, B and C.

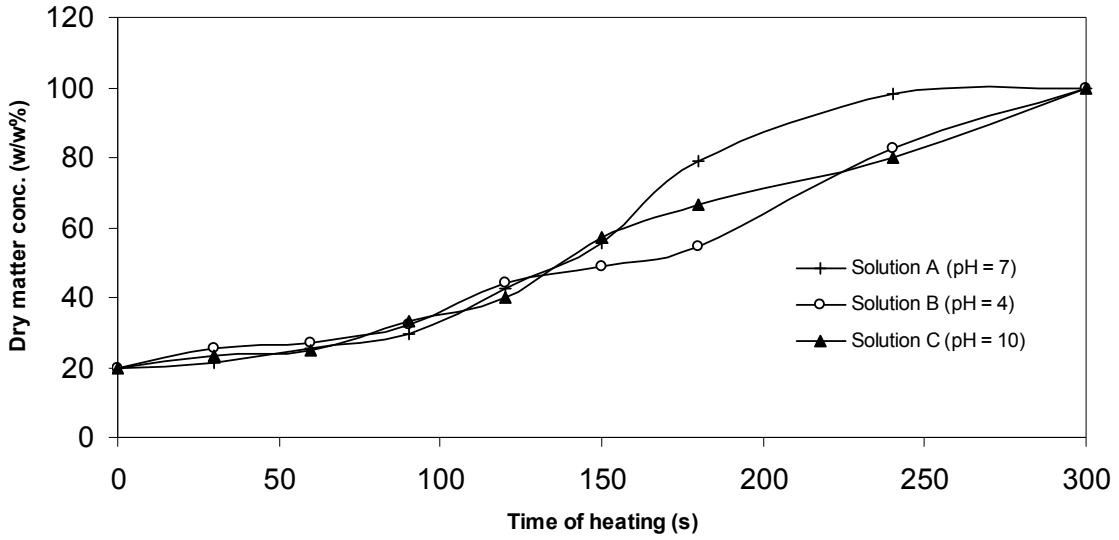

Figure 10.17: Dry-matter contents in the coating solution as a function of the time the heating fan was switched on for solution A, B and C.

One thing is that the bulk viscosity cannot be correlated with stickiness, but as the viscosity (as well as stickiness) changes with dry-matter concentration, it is possible that there is a relation between stickiness and viscosity for similar dry-matter concentrations. In order to test this, the viscosity of the three solutions A, B and C were measured as a function of dry-matter concentration at a constant shear rate of 1000 1/s according to figure 10.18.

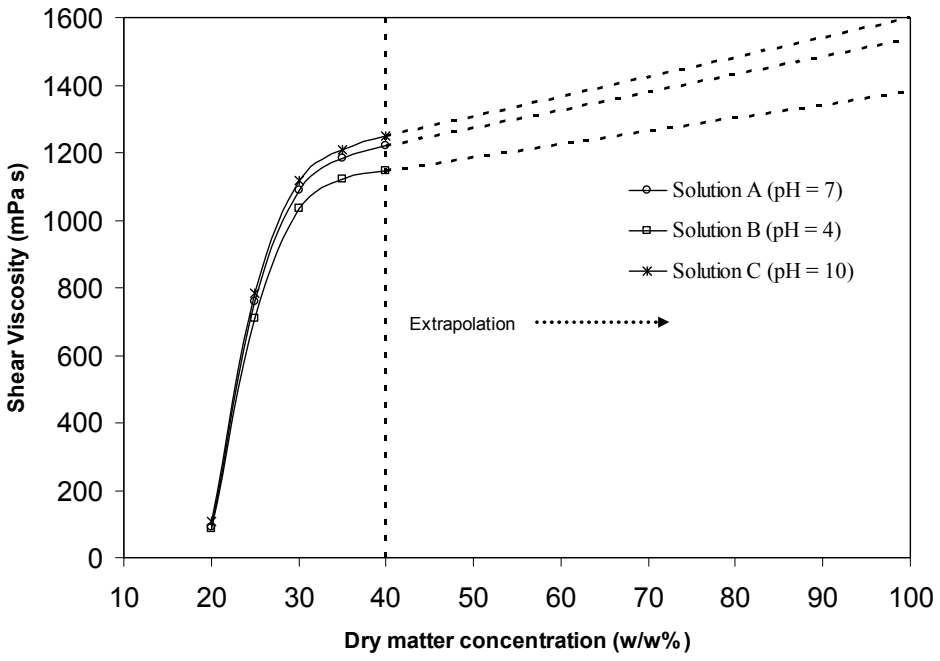

Figure 10.18: Viscosity curves for ramping-up concentrations of PVA/TiO_2 solutions measured at a constant shear rate of 1000 1/s.

It is observed how the viscosity rapidly increases for all three solutions up to roughly 30 w/w% dry-matter concentration where after the curves flatten out, meaning that a further increase in dry-matter concentration does not lead to any significant increase in viscosity.

Based on figure 10.15 and figure 10.18 it was possible in figure 10.19 to plot the viscosity versus the stickiness for data pairs of similar dry-matter concentration. It may be observed that although the stickiness increases with viscosity, there is no direct correlation between the magnitude of viscosity and the measured stickiness. The viscosity value at which the stickiness peaks is different for each coating solution. Not surprisingly, the large stickiness values are observed for large viscosities, but for all three solutions it appears as if there is a maximum viscosity beyond which the stickiness decreases rapidly. In conclusion, there is no obvious relation between viscosity and stickiness.

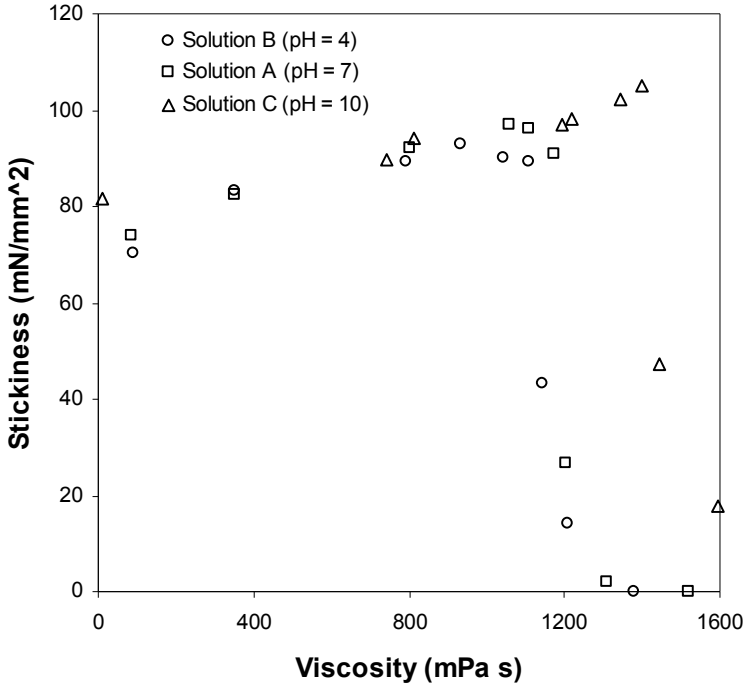

Figure 10.19: Stickiness as a function of viscosity for similar dry-matter concentrations.

Coating experiments for the test of the influence of pH were carried out in accordance with table 10-4. For each batch the weight gain was determined after coating using equation 10.7. For all the experiments the weight gain varied between 19.3 and 19.8 w/w% indicating that the spray drying losses in the experiments were quite small. The corresponding agglomeration tendencies for all six experiments may be observed from table 10-8.

Table 10-8. Results for the coating experiments for the test of the influence of pH in the PVA/TiO_2 solution. The results for solution A were the results obtained in the test of the mean droplet diameter.

	Series 1	**Series 2**
Solution A 10 w/w% PVA 10 w/w% TiO_2 pH = 7.0	Aggl% = 18.7 w/w% Drying Force = 18 kPa Spray rate = 24 g/min	Aggl% = 16.4 w/w% Drying Force = 18 kPa Spray rate = 14 g/min
Solution B 10 w/w% PVA 10 w/w% TiO_2 pH = 4.0	Aggl% = 12.6 w/w% Drying Force = 18 kPa Spray rate = 24 g/min	Aggl% = 11.8 w/w% Drying Force = 18 kPa Spray rate = 14 g/min
Solution C 10 w/w% PVA 10 w/w% TiO_2 pH = 10.0	Aggl% = 27.7 w/w% Drying Force = 18 kPa Spray rate = 24 g/min	Aggl% = 17.1 w/w% Drying Force = 18 kPa Spray rate = 14 g/min

As observed from table 10-8 the agglomeration tendencies decrease with decreasing spray rate irrespectively of the coating solution. Interestingly, the agglomeration tendency decreases with decreasing pH in the coating solution as it was expected from the stickiness curves in figure 10.15, 10.16 and 10.17. Hence, there is a clear relation between the stickiness and the resulting agglomeration tendencies. There is a difference in agglomeration tendency of roughly 10 w/w% points going from solution C (pH = 10) to the solution B (pH = 4). The difference is smallest for the lowest spray rate indicating that, under conditions with very small droplet diameters, the stickiness effect is less pronounced. This could also arise from the fact that with small droplets the drying rate is so fast that the chance of collision between sticky wet granules is significantly reduced.

On the basis of the results, an important conclusion may be drawn: The fact that the PVA/TiO_2 system is a colloidal system may indeed be used to suppress the tendency of agglomeration. Adjusting the pH value in the coating solution to a value far away from the iso-electric point may reduce the agglomeration tendency significantly. Although the effect of adjusting the pH value to pH = 4, instead of leaving it at pH ≈ 7, is rather small, there is indeed a clear effect. Next is to test whether these observed effect can be advantageously combined with additives.

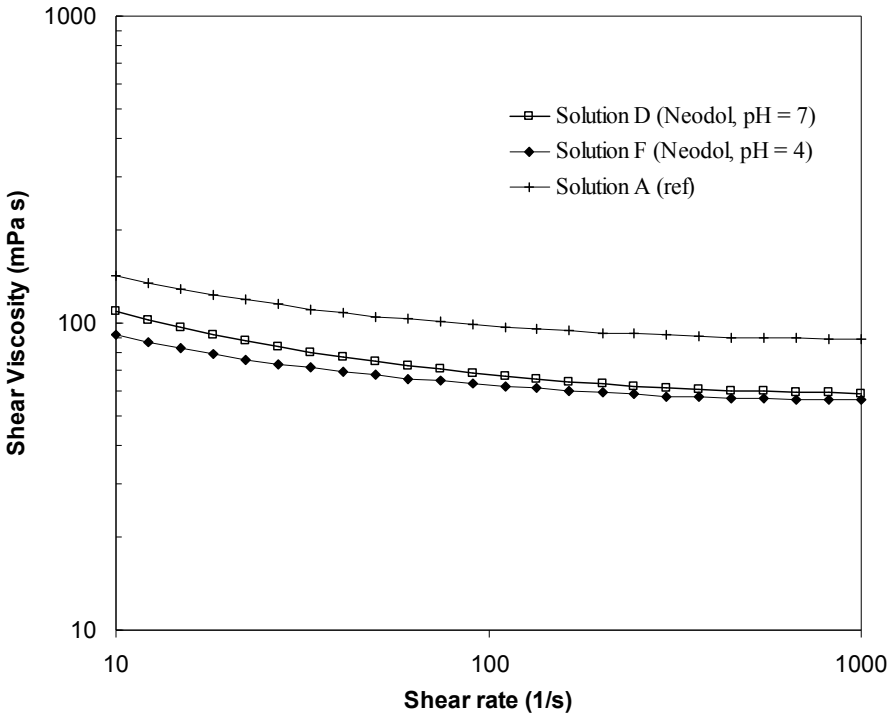

Figure 10.20: Viscosity curves of the solutions A, D and F as a function of shear rate at a constant temperature of 25 ºC.

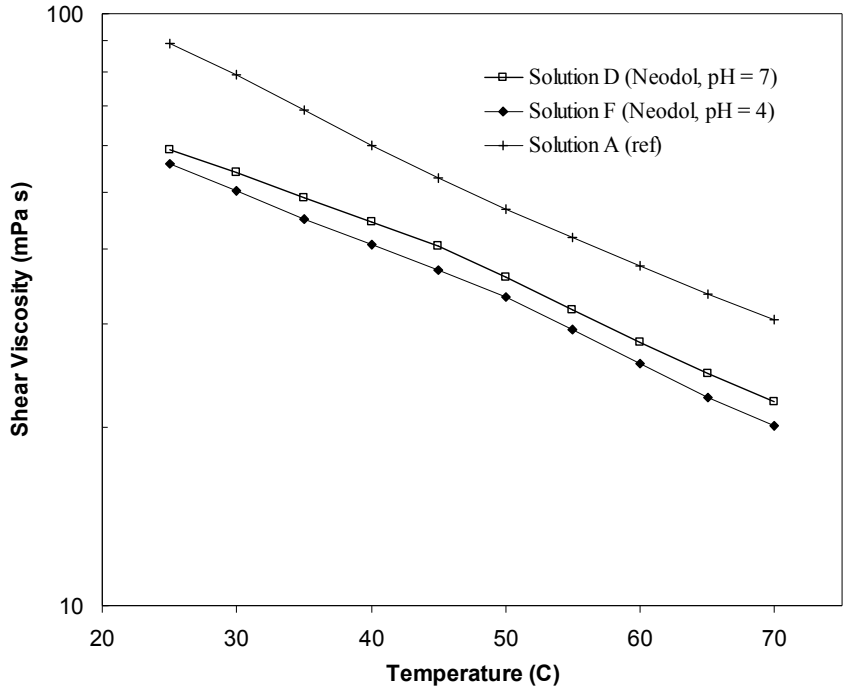

Figure 10.21: Viscosity curves of the solutions A, D and F as a function of temperature at a constant shear rate of 1000 1/s.

Similar to the previous studies, the rheological properties of the coating solutions in the test of adding additives were initially characterised, and detailed viscosity measurements were made for each of the three solutions in terms of both varying the shear rate and the temperature. In figure 10.20 the viscosities of the coating solutions have been determined as a function of shear rate at a constant temperature of 25 ºC. It may be observed first of all that all three solutions exhibit non-Newtonian behaviour as the viscosities all decrease with increasing shear rate. The effect of replacing PVA/TiO_2 with Neodol is clearly observed from figure 10.20 and figure 10.21, where the viscosity as a function of temperature was determined for the three solutions at a constant shear rate of 1000 1/s. Both curves for solution D and solution F are situated significantly below the curves for solution A. Interestingly, there is also an effect of reducing pH in the PVA/TiO_2/Neodol solution, as it was observed in a similar manner with the pure PVA/TiO_2 solutions in the test of the influence of pH.

Texture analyser studies of the stickiness for the three solutions in figure 10.22, 10.23 and figure 10.24 reveal that the stickiness distribute after a similar pattern as the viscosity curves. As observed from figure 10.22, the stickiness for solution A is higher and remains higher for a broader range of dry-matter contents than for the other solutions. The stickiness for solution D and F are in contrary lower than for solution A, and furthermore peak in narrow ranges before rapidly declining. Already at a dry-matter content of roughly 45 w/w% the stickiness are reduced by 50 % for solution D and F.

For the curves in figure 10.23 and figure 10.24 it becomes clear that there is a clear effect of substituting PVA/TiO_2 with Neodol in terms of reduced drying time. Whereas the time for complete drying is roughly 50 seconds longer for solution A, the drying time for solution D and F is roughly the same, meaning that in terms of drying time, pH has no importance. This means in conclusion that solution D and F dry faster than all other solutions tested, and that they, in addition, exhibit significantly lower stickiness for a shorter range of dry-matter contents. What is left to investigate is whether or not these trends correlate with the resulting

agglomeration tendencies when the solutions are being atomised and sprayed onto agitated particles in fluid bed coating processes.

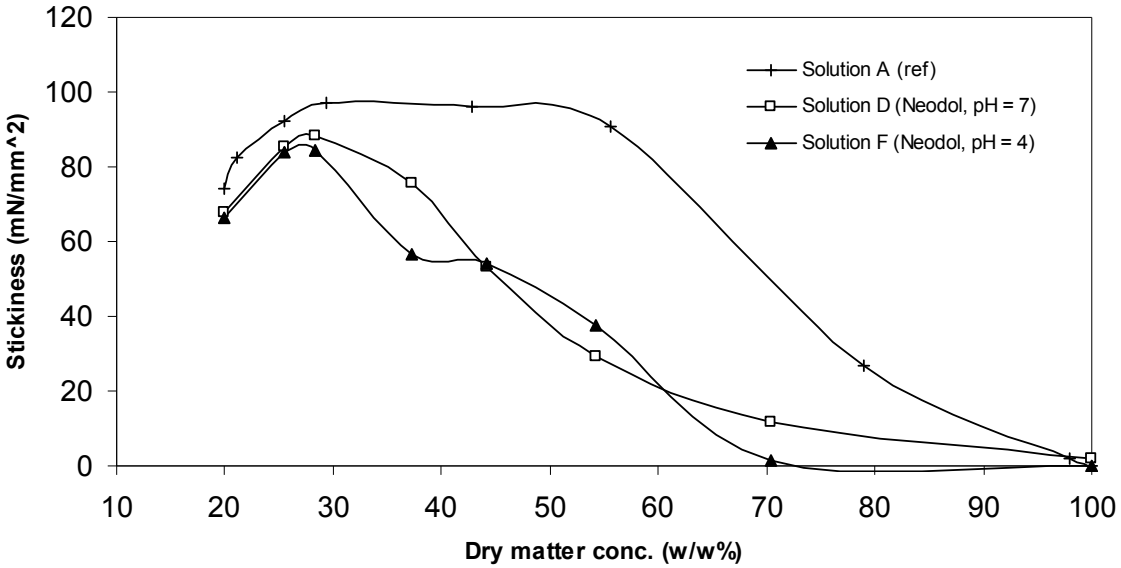

Figure 10.22: Stickiness as a function of dry-matter contents in the coating solution for solution A, D and F.

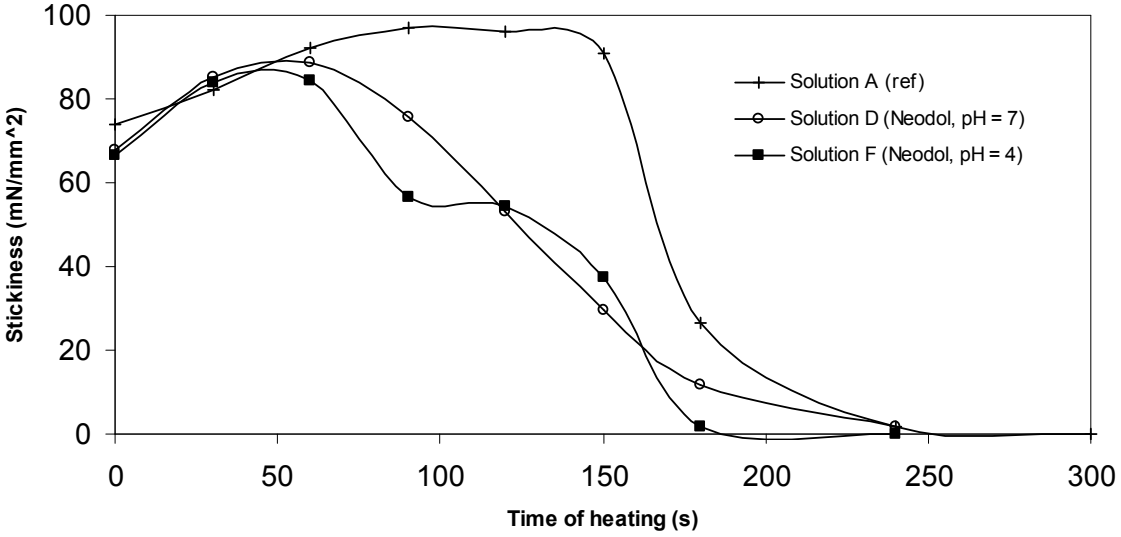

Figure 10.23: Stickiness as a function of the time the heating fan was switched on for solution A, D and F.

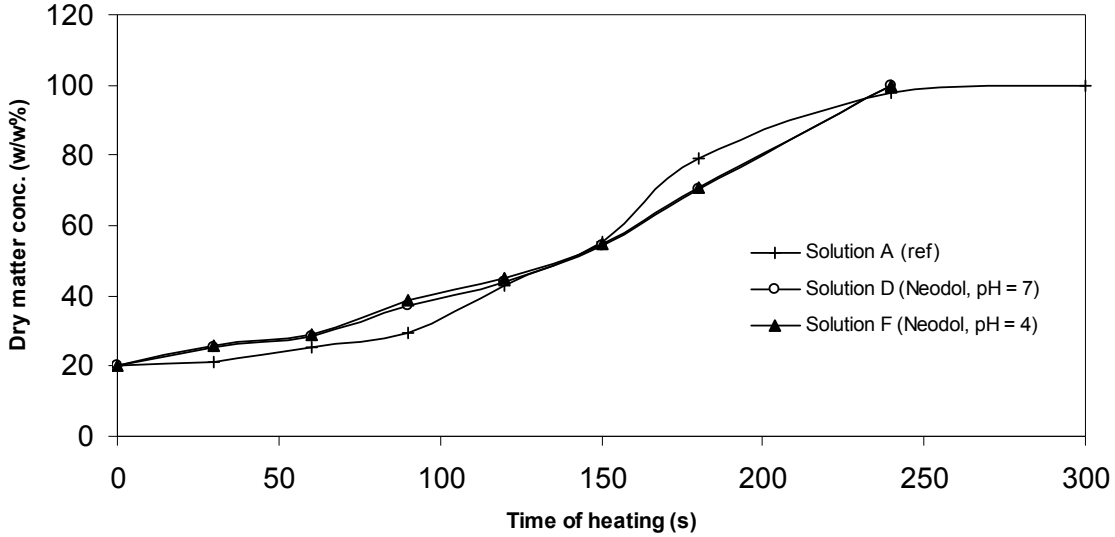

Figure 10.24: Dry-matter contents in the coating solution as a function of the time the heating fan was switched on for solution A, D and F.

Coating experiments for the test of additives were carried out in accordance with table 10-5. For each batch the weight gain was determined after coating. For all the experiments the weight gain varied between 19.2 and 19.5 w/w% meaning that the spray drying losses in the experiments were quite small. The corresponding agglomeration tendencies for all six experiments (determined with the use of equation 10.7) may be observed from table 10-9.

Table 10-9. Results for the coating experiments for the test of additives. The results for solution A were the results obtained in the test of the mean droplet diameter.

	Series 1	**Series 2**
Solution A 10 w/w% PVA 10 w/w% TiO_2 pH = 7.0	Aggl% = 18.7 w/w% Drying Force = 18 kPa Spray rate = 24 g/min	Aggl% = 16.4 w/w% Drying Force = 18 kPa Spray rate = 14 g/min
Solution D 9 w/w% PVA 9 w/w% TiO_2 2 w/w% Neodol 23-6.5 pH = 7.0	Aggl% = 10.8 w/w% Drying Force = 18 kPa Spray rate = 24 g/min	Aggl% = 7.7 w/w% Drying Force = 18 kPa Spray rate = 14 g/min
Solution F 9 w/w% PVA 9 w/w% TiO_2 2 w/w% Neodol 23-6.5 pH = 4.0	Aggl% = 3.9 w/w% Drying Force = 18 kPa Spray rate = 24 g/min	Aggl% = 2.7 w/w% Drying Force = 18 kPa Spray rate = 14 g/min

As observed from the results in table 10-9, the agglomeration tendencies decrease in general with decreasing spray rate as it has been observed for all other solutions. Of primary interest is the clear effect of replacing some of the PVA/TiO_2 with Neodol. Going from solution A to solution D, the agglomeration tendency is remarkably reduced by roughly 10 w/w% points or 60 %. This is a significant reduction and it correlates well with the trends observed from the stickiness and viscosity measurements. The effect of reducing pH in the PVA/TiO_2/Neodol system is clearly observed from table 10-9. In fact the reduction in agglomeration tendency is roughly 5 w/w% points just by reducing pH from 7 to 4. As a support for this observation, the effect of reducing pH is similar to the effect on agglomeration for a simple PVA/TiO_2

solution observed in the test of the influence of pH. Interestingly, by substituting some of the PVA/TiO_2 with Neodol and further reduce pH to 4 it is possible to reduce the tendency of agglomeration significantly. The agglomeration tendency of 3.9 w/w% in table 10-9 is fairly close to the agglomeration percentage of 0.9 w/w% observed for the sodium sulphate solution in the test of the bulk viscosity, processed under identical conditions. Notably, this is achieved even though the bulk viscosity of solution F is roughly six times the bulk viscosity of the sodium sulphate solution. This further supports the previous conclusion that it is the stickiness and the time length to reach complete solvent evaporation and zero stickiness, and not the bulk viscosity of a sprayed coating solution, which is important for the tendency of agglomeration.

On the basis of the test results it may be concluded that there is a significant effect of replacing PVA/TiO_2 in equal amounts by a lubricant as Neodol. The reduced stickiness effect of lowering the pH to a value far from the isoelectric point can also be beneficially exploited in a PVA/TiO_2/Neodol system. In terms of this, the tendency of agglomeration for a PVA/TiO_2/Neodol coating process can be reduced to a level close to the tendency of agglomeration for a sodium sulphate coating process, processed under similar conditions.

10.6. The tack Stokes number

Returning to the viscous Stokes theory, the conclusions from the experiments, especially regarding the viscosity and stickiness, may be used to suggest a modification to the original viscous Stokes number. Instead of defining St_v on the basis of the viscous energy dissipated in the liquid bridge, the suggestion is to define a new tack Stokes number, St_{tack}, on the basis of tack work measured in the probe tack test. Analogously to the original viscous Stokes number, the new tack Stokes number relates the initial kinetic energy of the colliding particles to the energy (work) required to separate the particles upon rebound. However, the separation energy is suggested to be related not to viscous, but to tack-related forces. If the kinetic energy is larger than the work done by the tack force, separation between the particles will occur. Otherwise permanent agglomeration will be the result.

For most materials it would be reasonable to believe that the liquid contact area between the rebounding particles will be reduced significantly with separation distance until the maximum tack force is reached and liquid bridge breakage occurs. Such effects are often related to fibril elongation and are often observed with engineering materials including some polymers (Christensen, 1998). In that case it would be erroneous to relate the maximum tack force simply to initial wetted area. For pressure sensitive adhesives, however, elongation at maximum stress is typically far less than 50 % of the initial sample length (Ukei et al., 2005). This means that upon strain it is reasonable to assume that pressure sensitive adhesives rapidly reach the maximum break force without a significant reduction in contact area in a simple Hooks law manner. This “Velcro effect” observed with PVA/TiO_2 solutions is believed to result from the fact that bonding with pressure sensitive adhesives is a local surface phenomena where only polymer chains present at the surface entangle with the surface of the contact material. Assuming that this behaviour is also the case for the PVA/TiO_2 coating solutions, the suggestion is to define the tack energy as:

$$\text{Work to reach maximum tack} = \int_{s=0}^{s=\kappa\cdot(h_{liq}-h_{asp})} F_{tack}\cdot ds \approx \tfrac{1}{2}\cdot F_{max,tack}\cdot \int_{s=0}^{s=\kappa\cdot(h_{liq}-h_{asp})} ds \approx \tfrac{1}{2}\cdot F_{max,tack}\cdot\kappa\cdot(h_{liq}-h_{asp}) \quad (10.8)$$

Assuming that the tack force increases linearly from zero to the maximum, the first integral in equation 10.8 can be approximated by the second integral using trapezoid integration. The maximum tack force is treated as a constant, and the factor of ½ ensures that an average value is used to calculate the work to reach maximum tack. Defining the maximum tack energy according to equation 10.8 assumes that it requires only a separation distance of $\kappa \cdot (h_{liq}-h_{asp})$ to reach the maximum tack and thereby the distance where breakage of the liquid bridge occurs.

The factor κ accounts for the fact that tack work is not the maximum tack force times the full liquid thickness $h_{liq}-h_a$ but rather the work done over a somewhat smaller length. This is due to the assumption that tack is a surface phenomenon and not a bulk phenomenon. According to the estimations by Ukei et al. (2005) the largest chance of liquid bridge breakage will occur at a distance between 30 – 50% of $h_{liq}-h_{asp}$ depending on the type of adhesive. In this work a factor κ of 0.45 has been chosen. A value of 1 has also been tested giving only little deviation, so this is not a critical parameter. Based on these assumptions the modified Stokes number is suggested to be defined as:

$$St_{tack} = \frac{\text{Initial kinetic energy}}{\text{Tack work}} = \frac{½ \cdot m_{harm} \cdot (2u_0)^2}{2 \cdot ½ \cdot F_{max,tack} \cdot \kappa \cdot (h_{liq} - h_a) \cdot \varphi} = \frac{2 \cdot m_{harm} \cdot u_0^{\,2}}{F_{max,tack} \cdot \kappa \cdot (h_{liq} - h_a) \cdot \varphi} \tag{10.9}$$

where φ is a correction factor suggested to be the ratio between the collision velocity u_0 times the wetted area of the liquid bridge contact point, $A_{liq,wet}$, and the probe test speed used to measure the tack, u_{test}, times the tack probe contact area A_{con} according to:

$$\varphi = \left(\frac{u_0}{u_{test}} \right) \cdot \left(\frac{A_{liq,wet}}{A_{con}} \right) \tag{10.10}$$

By introducing the correction factor φ it is assumed that the tack force relates linearly to the area of contact as well as linearly to the velocity of which two particles collide. Such assumptions are reasonable based on previously observed tendencies with pressure sensitive adhesives, where it is known that the yield stress of polymers often increase linearly with increasing strain rate (Smitthipong et al., 2004 and Christensen, 1998). In order to minimise the influence of φ, the probe test speed should be chosen as close to u_0 as possible.

In order to estimate the liquid layer thickness h_{liq}, contact angles are needed. The contact angles were measured in the present study by dispersing 6.00 µL of coating solution onto a special glass plate and then measure the contact angle using the OCA-20 software interface (see also chapter five). The contact angles were measured at 45 ºC between the coating solutions and a non-porous glass plate. Due to the hygroscopic and porous nature of the sodium sulphate cores it was not possible to measure the contact angles between the coating solutions and the core material. As a reference, the contact angle for pure demineralised water was measured to be 40.81º indicating that the glass plate is quite hydrophilic, hereby resembling well the sodium sulphate core surface.

Measured contact angles for the seven coating solutions may be seen from table 10-10. As observable from table 10-10 and figure 10.25, in comparison with previously presented data tables and figures, the measured contact angles correlate well with the measured

agglomeration tendencies and stickiness etc., as the best wetting is observed for solution D and F. It appears as if Neodol significantly aids the droplet spreading and reduces the contact angle. Interestingly, solution A and G have almost similar contact angles although being otherwise quite different with respect to viscosity, stickiness etc. as previously presented.

Table 10-10. Measured contact angles between the coating solutions and a non-porous glass plate. Data obtained with the use of a DataPhysics OCA-20 video-based contact angle meter (see also chapter five).

	Measured contact angle
Solution A 10 w/w% PVA, 10 w/w% TiO_2 pH = 7.0	57.10 º
Solution B 10 w/w% PVA, 10 w/w% TiO_2 pH = 4.0	51.73 º
Solution C 10 w/w% PVA, 10 w/w% TiO_2 pH = 10.0	73.96 º
Solution D 9 w/w% PVA, 9 w/w% TiO_2, 2 w/w% Neodol 23-6.5 pH = 7.0	34.24 º
Solution E 2 w/w% PVA, 2 w/w% TiO_2 pH = 7.2	41.50 º
Solution F 9 w/w% PVA, 9 w/w% TiO_2, 2 w/w% Neodol 23-6.5 pH = 4.0	31.74 º
Solution G 15 w/w% Na_2SO_4, 1 w/w% Dextrin pH = 7.1	56.59 º

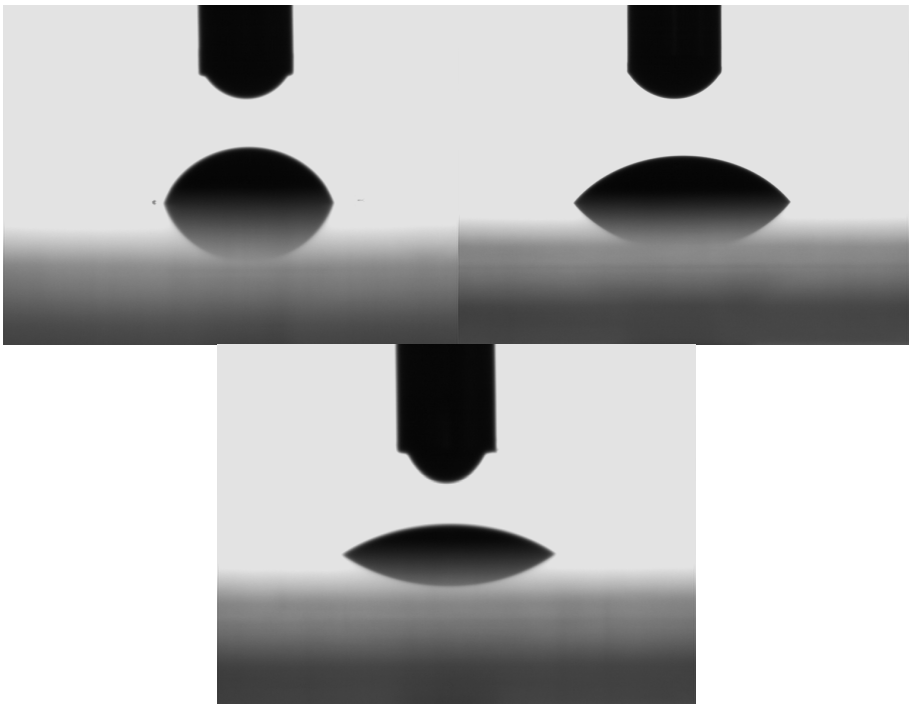

Figure 10.25: Examples of contact angles of: Top left) Solution C; Top right) Solution B; Bottom) Solution F. The diameter of the syringe cylinder is 1.6 mm.

Values for parameters *e* and h_{asp}, needed for the calculation of the critical viscous Stokes number (valid as reference for the original viscous Stokes number only), were adapted for the given core materials from Hede (2005). Values for h_{liq} were estimated from the following equations adapted from Clarke et al. (2005) and Thielmann et al., (2007):

$$h_{liq} = A_{liq,wet} \cdot \left[\frac{1-\cos\theta}{\sin\theta}\right] \quad \text{where} \quad A_{liq,wet} = \left[\frac{3 \cdot V_{dr}}{\pi} \cdot \frac{\sin^3\theta}{2-3\cos\theta+\cos^3\theta}\right]^{1/3} \tag{10.11}$$

where V_{dr} is the volume of a single droplet, θ is the contact angle and $A_{liq,wet}$ is the wetted area. Assuming monodisperse droplets with diameters of d_{32}, equation 2.3 (see chapter two) were used to determine the Sauter mean droplet diameter for the given coating conditions. The collision velocity u_0 should ideally be represented by a distribution of velocities, but similar to the model by Ennis et al. (1991), an average collision velocity for a fluid bed is estimated with the use of equation 3.12 (see chapter three).

Similarly to the original viscous Stokes number a critical viscous Stokes number is needed as a cut-off value between agglomeration and no agglomeration. The original critical viscous Stokes number given by equation 10.6 cannot be used for comparison with the tack Stokes number as it is derived on the basis of viscous dissipation. Instead another expression is needed. Following the definition of the tack Stokes number in equation 10.9, the result of wet particle collision will be agglomeration if the tack work is larger than the initial kinetic energy ($St_{tack} < 1$), and vice versa, no agglomeration will be the result if $St_{tack} > 1$. Hence, the critical tack Stokes number can be represented simply be 1.

In order to compare the viscous Stokes theory with the tack Stokes theory the parameters were made dimensionless with respect to the related critical Stokes number according to equation 10.12 and 10.13. This was done in order to be able to compare the two Stokes approaches in a similar and fair manner. A simple comparison of St_v-St_v^* with St_{tack}-1 gives a worse fit of the original viscous Stokes theory to a straight line, but makes it difficult to compare the performance of the two approaches in a fair manner because the x-axis length scales are different. Hence, a comparison using equation 10.12 and 10.13 is a more fair option.

$$\frac{St_v - St_v^*}{St_v^*} \tag{10.12}$$

and

$$\frac{St_{tack} - 1}{1} \tag{10.13}$$

Using equation 10.2 and equation 10.9 respectively, the original and the tack Stokes number as well as the critical viscous Stokes number (using equation 10.6) were calculated for all coating solutions processed at a Drying Force of 18 kPa and plotted for solutions A – F as functions of the resulting agglomeration tendencies according to figure 10.26 and figure 10.27 using the relations in equation 10.12 and 10.13. For the original viscous Stokes number the values for η_{liq} were chosen not as "time-averaged" viscosities as suggested by Ennis et al. (1991), but as the viscosities at which the tack forces were at maximum. This gives a more

realistic comparison of the viscous versus the tackiness effects. The calculated viscous Stokes numbers for experiments with solution G at a Drying Force of 18 kPa were not included in figure 10.26 and figure 10.27 as the theory is known to be less precise when the agglomeration percentages approaches zero (Ennis et al., 1991 and Tardos, 2005). Calculated values for the difference between St_v and St_v^* for solution G in experiments with agglomeration percentages of 1.5 w/w% and less resulted in values in the range of 15 to 35, indicating that the viscous Stokes theory based on mean overall values for process and formulation variables is less precise for coating conditions near the agglomeration limit.

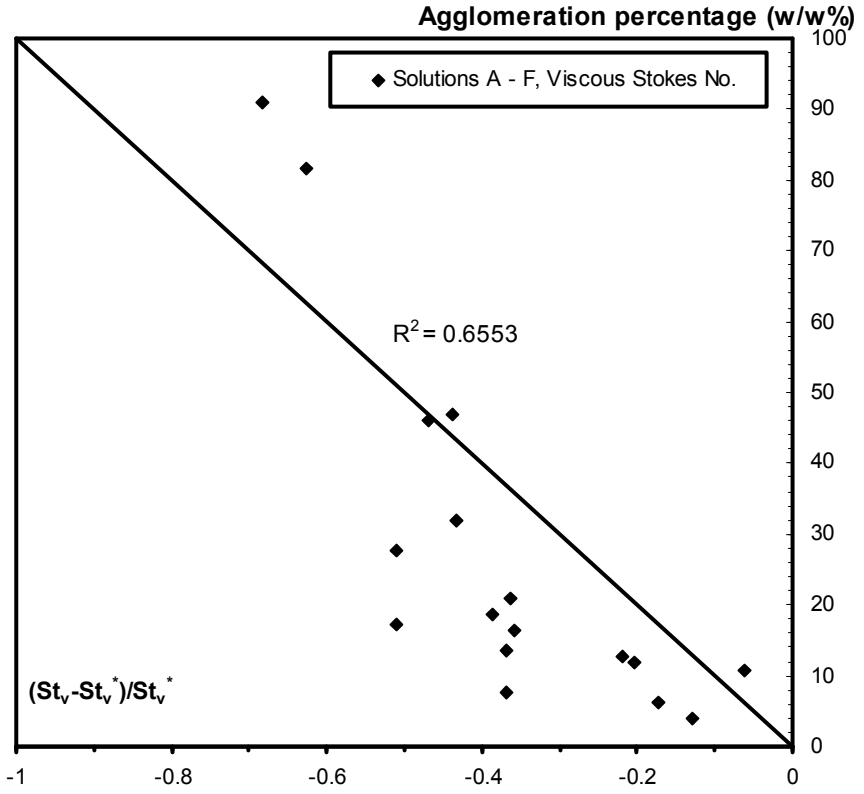

Figure 10.26: The resulting agglomeration percentages obtained in coating experiments for solution A, B, C, D, E and F as a function of the relation $(St_v - St_v^*)/ St_v^*$.

Although some scattering is observed in both figures, especially with the low agglomeration percentages, the overall tendency is clear from figure 10.26 and figure 10.27, namely that the agglomeration tendency increases the larger the difference between the Stokes number and the critical Stokes number, in accordance with the theories proposed by Ennis et al. (1991). A comparison between the data points in figure 10.26 and figure 10.27 reveals several important things. First of all, the tack Stokes number appears to predict the agglomeration tendency almost linearly across the entire range with a trend line having an R^2 value close to 1. This R^2 value refers to the data points adaption to the {(0, 0) ; (-1, 100)} line and thus not to a best linear fit.

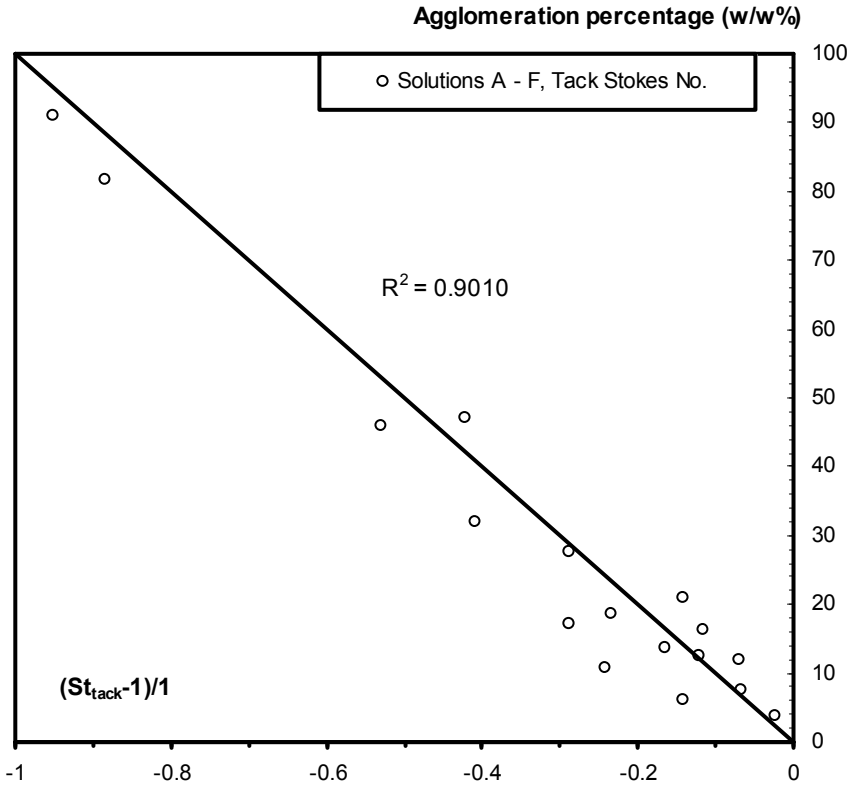

Figure 10.27: The resulting agglomeration percentages obtained in coating experiments for solution A, B, C, D, E and F as a function of the relation (St_{tack} - 1)/ 1.

Similarly, the R^2 value for the viscous Stokes numbers is as low as 0.65 with many of the points below the straight line. For the original viscous Stokes number it appears as if there is no apparent linear relation between the agglomeration tendency and $(St_v - St_v^*) / St_v^*$. Secondly, the tack relation appears to be capable of predicting the agglomeration tendency equally well whether the tendency of agglomeration is high or low. Being a simple theory based on average values for a range of process parameters such as droplet diameter, droplet volume, tack force, collision velocity and more, the tack Stokes number appears to be capable of providing improved first guidelines for the outcome of the fluid bed coating process in terms of agglomeration tendency. The observed good linearity is promising with respect to implementing the tack Stokes number in granulation models. Predicting the agglomeration tendency using either the tack or the original viscous Stokes number will in any case require a-priori measurements of, respectively, the tack force or viscosity. Tack gives better estimates of the agglomeration tendency, but at the cost of more experimental work, as tack measurement is not yet a standard technique as is the measurement of viscosity.

In order to investigate the influence of the choice of viscosity for the calculation of the original viscous Stokes number, the bulk viscosity values adapted from figure 10.7, 10.14 and 10.21 at 60 ºC were inserted in equation 10.3. These values are the lowest viscosity values of what coating droplet experience during their lifetime, but interestingly the resulting tendency from the use of these new F_{vis} values followed closely the one observed in figure 10.26. The viscous Stokes number obviously increased with decreasing viscosity, but the difference between the viscous Stokes number and the critical viscous Stokes number remained more or less unaffected. This is due to the fact that with the tested core material and the tested process conditions, the values of the critical viscous Stokes numbers St_v^* are significantly higher than

the calculated St_v numbers. This indicates that with particles coated with thin liquid layers of polymers, it is not the viscous forces in the droplet bulk phase that are of major importance, but rather the phenomena on the coating layer surface, which are measured well in the probe tack test. If, however, process conditions were chosen differently from the ones in the present study or if e.g. the core materials were non-porous glass ballotini cores without significant surface asperities and/or surface pores, the liquid layer thickness could be larger than in the present study, meaning that the viscous forces could dominate over the tack surface forces with respect to agglomeration. Under such conditions, it is likely that the original viscous Stokes number would be a better way of predicting the agglomeration tendency than the tack Stokes number. The tack Stokes number is thus not likely to always be a better way of predicting the agglomeration tendency. Whether it is the viscous or tack forces that dominate with respect to agglomeration appears to depend especially on the liquid layer thickness and the type of coating material (e.g. polymer or inorganic salt coating).

10.7. Summary and conclusion

In the pursuit of finding the causes why polymer and inorganic salt solutions cannot be processed under similar fluid bed process conditions in order to result in similar tendencies of agglomeration, a number of detailed studies were carried out in order to optimise process and formulation conditions. Experimental studies were based on theories originating from previous experience and theoretical knowledge found in literature.

Although the agglomeration tendencies for salt coating as well as for PVA/TiO_2 coating processes indeed distributed well in categorical bands in agglomeration regime maps, the first test results indicated that the agglomeration tendencies were not similar for the two coating formulations for identical process conditions. Whereas the agglomeration tendency for the sodium sulphate solution was low (< 5 w/w%) for a broad range of coating solution spray rates and Drying Force values, it was not possible to determine a range where the agglomeration tendency is below 10 w/w% for the PVA/TiO_2 solution. Furthermore, the second best 10-20 w/w% agglomeration range for the PVA/TiO_2 solution was very narrow. The studies with different values of the Drying Force and spray rates led to an important conclusion: Namely that the two types of coatings are not equally affected by the spray rate and the Drying Force conditions. The Drying Force combining the bed temperature and bed/outlet humidity is of major importance for the tendency of agglomeration during the salt coating process, and the tendency of agglomeration may well be controlled in terms of these two parameters alone, in accordance with results by Hede et al. (2008b). For the PVA/TiO_2 solution, however, the correct choice of the Drying Force and spray conditions may be seen as a prerequisite, but is not sufficient to control agglomeration. There are in other words no apparent combinations of the two parameters for completely avoiding agglomeration for the PVA/TiO_2 solution. Other parameters must additionally come in to play.

Testing the effect of the bulk viscosity revealed that it is not the bulk viscosity of a coating solution that has the primary importance regarding the tendency of agglomeration, but rather that it is the maximum possible stickiness during coating solution solvent evaporation and the length of the stickiness period that is important. Furthermore, the stickiness may not be correlated directly with bulk viscosity. In the comparison of two different coating formulations it is thereby impossible to predict the tendency of agglomeration based on the bulk viscosities alone. In accordance with previous studies by Hede (2005), it was observed on the other hand, that the bulk viscosity indeed plays an important role regarding the degree of droplet penetration into the core particle and the morphology of the outer coating layer. As

the coating solution bulk viscosity increased, the level of droplet penetration decreased and the final coating layer became increasingly rough and raspberry-like.

Following previous studies by Schæfer & Wørts (1977) and Hede et al. (2008a,b) it was further observed how similar mean droplet diameters for the two coating solutions (salt and PVA/TiO_2) did not result in similar agglomeration tendencies. It was, however, observed how the tendency of agglomeration clearly decreased as the mean droplet diameter decreased, but also that the two types of coating solutions responded differently in the tendency of agglomeration for identical droplet diameters, i.e. the PVA/TiO_2 solution responded clearly with an increased agglomeration percentage upon a small increase in the mean droplet diameter, whereas the agglomeration tendency for the salt solution was hardly affected in the tested range of the mean droplet diameters. This indicates once again, in accordance with qualitative studies by Neidel (2007), that the coating process with salt coatings is far less sensitive towards agglomeration than polymer coating processes.

The colloidal phenomena in the PVA/TiO_2 solution were additionally studied, and it was observed how the viscosity, stickiness, time length of stickiness and agglomeration tendency all could be reduced by reducing the pH to a value far from the isoelectric point. The results were in close agreement with previous studies by Chu et al. (2007) indicating that for coating processes with PVA/TiO_2 solutions, pH should be close to 4. The reduction in pH would most likely also be beneficial regarding the use of a coated enzyme granule for detergent applications as a low pH is known to improve the enzyme stability (van Ee et al., 1997).

The test of additives clearly indicated the advantages of replacing equal amounts of PVA/TiO_2 with Neodol. By replacing 1/10 of the PVA and an equal amount of the TiO_2 with Neodol, the resulting agglomeration tendency could be reduced by roughly 10 w/w% points. The results furthermore revealed that colloidal phenomena in the PVA/TiO_2 solution were not significantly affected by the introduction of Neodol. By reducing pH to 4 in the PVA/TiO_2/Neodol system, it was finally possible to arrive at an agglomeration tendency below 5 w/w%, and thus within range of the agglomeration tendency for a salt solution coating process processed under similar conditions.

In conclusion, the polymer coating process is much more sensitive towars agglomeration than the process of coating with inorganic salt solutions. First of all, the tendency of agglomeration cannot be avoided in terms of proper choices for the process parameters alone. Correct choices of process conditions are even so still important as there is only a narrow regime in which there is a possibility that the agglomeration tendency can be kept low. Most likely, this regime is different for each type of polymer in solution as properties such as glass transition temperature, molecular weight and degree of hydrolysis most likely also play a role. The influence of these properties were, however, not tested in the present study, but have been tested by others (Arnold et al., 1993). The polymer coating formulation is of primary importance for the agglomeration tendency. The fact that a polymer solution with dispersed inorganic particles constitutes a colloidal system requires knowledge of surface and electrostatic phenomena for the correct optimisation of the formulation. This also means that the correct preparation (order of dispersion, temperature range, stirring, correct heating ramping etc.) of the coating solution is of importance. The strict requirements for correct choices of process and formulation properties all together clearly make the polymer coating process a challenging exercise.

The introduction of a tack Stokes number combining particle properties and fluidisation conditions with the maximum tack force was observed to result in a parameter relationship capable of providing improved first guidelines for the indication of agglomeration tendency during the polymer fluid bed coating, in comparison to the original viscous Stokes number. It appears that defining the Stokes number based on viscous forces will lead to erroneous prediction of the agglomeration tendency in cases with fluid bed coating conditions as the ones tested in this paper. A possible reason is the influence of the liquid layer thickness. In the polymer fluid bed coating process the liquid layer is very thin, meaning that any agglomeration tendency is due primarily to liquid surface phenomena and not due to bulk viscous phenomena. These surface phenomena appears to be well predicted by the probe tack test giving reasons to believe that the tack Stokes number is a better way to predict the agglomeration tendency for the polymer coating systems tested in this paper. In any case the Stokes theory does, however, not take into account the clear effect of the Drying Force also observed in the present paper, but for the comparison of coating processes processed under similar Drying Force values, the practical and simple yet intuitive principle of the tack Stokes number appears to be a useful first principle. The observed proportionality between (St_{tack} - 1)/1 and the agglomeration tendency is a promising feature of the modification to the original viscous Stokes number also in a modelling perspective. Even so, more results are needed for a full validation of the tack Stokes number, but the results in the present paper have clearly showed that it is possible to address the polymer coating process quantitatively, and thus be able to reduce the agglomeration tendency to an acceptable level at the same time having a coating process of high intensity.

10.8. Appendix: Derivation of the viscous Stokes numbers

Consider two individual spherical granules with masses and radiuses m_1, r_1 and m_2, r_2 respectively, as indicated in figure 3.6 (please refer to chapter three). Assuming that the two granules are approaching one another at an initial relative velocity of $2u_0$ and that each are covered with a coating layer thickness h_{liq}. As the individual liquid layers come into contact, a dynamic pendular bridge will form between the colliding granules now separated by a gap of distance $2h_{liq}$. For sufficiently large liquid viscosity, the bridge will dissipate the relative kinetic energy of the colliding granules preventing rebound. To determine the minimum velocity required for particle rebound, a force balance on an individual granule can be considered. Ignoring the effect of capillary forces and assuming creep flow between the two granules, the force balance equation of motion (Newton's second law) for the approach stage can be expressed as:

$$m_{harm}\frac{du}{dt} = \frac{3}{2}\pi \cdot \eta_{liq} \cdot r_{harm}^2 \frac{dx}{dt}\frac{1}{x} \tag{A.1}$$

where x is half of the dimensional gap distance at a given time t and m_{harm} and r_{harm} are the harmonic mean mass and radius for the unequal granules given by:

$$m_{harm} = \frac{2 \cdot m_1 \cdot m_2}{m_1 + m_2} \text{ and } r_{harm} = \frac{2 \cdot r_1 \cdot r_2}{r_1 + r_2} \tag{A.2}$$

A solution to equation A.1 can easily be obtained by integrating the left side between u_0 and u, and the right side between h_{liq} and x. The solution can be expressed as:

$$u = u_0\left(1 - \frac{1}{St_v}\ln\left(\frac{h_{liq}}{x}\right)\right) \tag{A.3}$$

where St_v is the viscous Stokes number given by:

$$St_v = \frac{2 \cdot m_{harm} \cdot u_0}{3\pi \cdot \eta_{liq} \cdot r_{harm}^2} \tag{A.4}$$

Assuming that the granules have an equal density of ρ_g and that they are spherical, one may assume:

$$m_{harm} = \frac{4}{3}\pi \cdot r_{harm}^3 \cdot \rho_g \tag{A.5}$$

and by insertion into equation A.4 one finally ends at:

$$St_v = \frac{2\frac{4}{3}\pi \cdot r_{harm}^3 \cdot \rho_g \cdot u_0}{3\pi \cdot \eta_{liq} \cdot r_{harm}^2} \Leftrightarrow St_v = \frac{8 \cdot \rho_g \cdot r_{harm} \cdot u_0}{9 \cdot \eta_{liq}}, \text{ Q.e.d.} \tag{A.6}$$

For rebound of the colliding granules to occur, the Stokes number must exceed a critical value of St_v^*. With the initial velocity of u_0, let the velocity of the colliding granule upon reaching a distance of h_{asp} be u_{asp}, where h_{asp} represents a characteristic length scale of surface asperities. The initial rebound velocity is then $e \cdot u_{asp}$ where *e* is the particle coefficient of restitution with the presence of the coating layer. Realising that the granule velocity u is a scalar velocity and thereby a sign-depend parameter (for the rebound u is decreased as x increases, whereas during approach u decreases as x decreases), the situation of the two granules colliding and afterwards rebounding can be split up into two situations analogously to equation A.1:

$$\text{Approach: } m_{harm}\frac{du}{dt} = \frac{3}{2}\pi \cdot \eta_{liq} \cdot r_{harm}^2 \frac{dx}{dt}\frac{1}{x} \tag{A.7}$$

with the boundary conditions: at $t = 0$: $x = h_{liq}$ and $u = u_0$

and at: $t = t_1$: $x = h_{asp}$ and $u = u_{asp}$

$$\text{Rebound: } -m_{harm}\frac{du}{dt} = \frac{3}{2}\pi \cdot \eta_{liq} \cdot r_{harm}^2 \frac{dx}{dt}\frac{1}{x} \tag{A.8}$$

with the boundary conditions: at $t = t_{1:}$ $x = h_{asp}$ and $u = e \cdot u_{asp}$

and at: $t = t_2$: $x = h_{liq}$ and $u = 0$

By integrating equation A.7 between its boundaries one achieves:

$$m_{harm}(u_{asp} - u_0) = -\frac{3}{2}\pi \cdot \eta_{liq} \cdot r_{harm}^2 \cdot \ln\frac{h_{liq}}{h_{asp}} \tag{A.9}$$

Analogously, one achieves by integration of equation A.8 between its boundaries:

$$m_{harm} \cdot e \cdot u_a = \frac{3}{2}\pi \cdot \eta_{liq} \cdot r_{harm}^2 \cdot \ln\frac{h_{liq}}{h_{asp}} \tag{A.10}$$

and by insertion of equation A.10 into equation A.9 one achieves:

$$\begin{gathered} m_{harm}u_0 - \frac{1}{e}\frac{3}{2}\pi \cdot \eta_{liq} \cdot r_{harm}^2 \cdot \ln\frac{h_{liq}}{h_{asp}} = \frac{3}{2}\pi \cdot \eta_{liq} \cdot r_{harm}^2 \cdot \ln\frac{h_{liq}}{h_{asp}} \Leftrightarrow \\ \frac{2 \cdot m_{harm} \cdot u_0}{3\pi \cdot \eta_{liq} \cdot r_{harm}^2} = \left(1 + \frac{1}{e}\right) \cdot \ln\frac{h_{liq}}{h_{asp}} \end{gathered} \tag{A.11}$$

Dividing by the right-hand side and multiplying and dividing with u_0 in the left-hand side of equation A.11, one finds the critical condition for the fraction between the kinetic energy and the viscous dissipation energy for which agglomeration begins:

$$\frac{2 \cdot m_{harm} \cdot u_0^2}{3\pi \cdot \eta_{liq} \cdot r_{harm}^2 \cdot u_0 \cdot \left(1 + \frac{1}{e}\right) \cdot \ln\frac{h_{liq}}{h_{asp}}} = 1 \tag{A.12}$$

By exploiting the result in equation A.4 one finds that the Stokes number exactly at the beginning of agglomeration is given by:

$$St_v^* = \left(1 + \frac{1}{e}\right) \cdot \ln\left(\frac{h_{liq}}{h_{asp}}\right), \text{ Q.e.d.} \tag{A.13}$$

10.9. Table of symbols

Symbols		Unit
$A_{liq,wet}$	The wetted area	m^2
A_{con}	Area of contact	m^2
d_{32}	The mean Sauter mean droplet diameter	μm
d_p	Particle diameter	μm
e	Particle coefficient of restitution	Dimensionless
F	Force	$kg \cdot m/s^2$
$F_{max(tack)}$	The maximum (peak) tack force measured in a probe tack test	$kg \cdot m/s^2$
F_{vis}	Viscous force	$kg \cdot m/s^2$
h_{asp}	Characteristic height of particle surface asperities	m
h_{liq}	Coating liquid layer thickness covering colliding granules	m

m_1, m_2	Mass of granule 1 and 2, respectively	kg
m_{harm}	Harmonic mean particle mass	kg
r_1, r_2	Radius of granule 1 and 2, respectively	μm
r_{harm}	Harmonic mean particle radius	m
s	Distance	m
St_{tack}	Tack Stokes number	Dimensionless
St_v	Viscous Stokes number	Dimensionless
St_v^*	Critical viscous Stokes number	Dimensionless
t	Time	s
u	Velocity	m/s
u_{asp}	Granule rebound velocity	m/s
u_0	Initial granule collision velocity	m/s
u_{test}	Test speed for the probe tack test	m/s
v_{sep}	Separation rate	m/s
V_{dr}	Droplet volume	m^3
$W_{adhesion}$	Work of adhesion	kg/s^2
x	Length coordinate	m

Greek

η_{bulk}	Bulk viscosity	Centipoises
η_{liq}	Coating solution viscosity	Centipoises
θ	Contact angle	°
κ	Dimensionless factor	Dimensionless
π	Pi	Dimensionless
ρ_g	Granule density	kg/m^3
φ	Correction factor	Dimensionless

10.10. References

Abelthauser, C.B., Schneider, R. and Rupprech, H. (1993) Film coating of pellets with insoluble polymers obtained in situ crosslinking in the fluidized bed, Journal of Controlled Release, No. 27, pp. 149-156.

Adhikari, B., Howes, T., Bhandari, B.R. and Truong, V. (2001) Stickiness in Foods: A Review of Mechanisms and Test Methods, International Journal of Food Properties, No.4, pp. 1-33.

Arnold, R.E., Becker, N.T., Boston, M.G., Mansikkamaki, A., and Wendt, D.J. (1993) Coated Enzyme Containing Granule, International patent WO 93/07263, Genencor International.

Bartenev, G.M., Razumovskaya, I.V., Sanditov, D.S. and Lukyanov, I.A. (1969) A Contribution to the Theory of the Structural Glass Transition, Journal of Polymer Science: Part A-1, Vol. 7, pp. 2147-2157.

Becker, N.T., Flynn, M.J. and Gebert, M.S. (2005) Particle with substituted polyvinyl alcohol coating, Unisted States Patent US 6,872,696.

Beekman, W.J. (2000) Measurement of the Mechanical Strength of Granules, Ph.D. Thesis, Technische Universiteit Delft.

Boisvert, J.-P., Persello, J. and Guyard, A. (2003) Influence of the surface chemistry on the structural and mechanical properties of silica-polymer composites, Journal of Polymer Science Part B. Polymer Physics, No. 41, pp. 3127-3138.

Celanese. (2005) Celvol 205S Polyvinyl Alcohol Sales Specification, Celanese Chemicals, Dallas, Texas, USA.

Chang, S.H., Gupta, R.K. and Ryan, M.E. (1992) Effect of the adsorption of polyvinyl alcohol on the rheology and stability of clay suspensions, Journal of Rheology, No. 36, pp. 273-287.

Chau, K.W. and Swei, G.S. (2004) Contact Time and Interfacial Fracture Energy of Tacky Polymers, Journal of Polymer Science: Part B: Polymer Physics, Vol. 42, pp. 3013-3025.

Chibowski, S. (1986) Adsorption Equilibria in the System TiO_2 – Aqueous Solution containing Polyvinyl Alcohol, Materials chemistry and Physics, No. 14, pp. 471-479.

Chibowski, S and Szcypa, J (1984) Studies of the Adsorption of Polyvinyl Alcohol on TiO2 Surfaces, Journal of Colloid and interface Science, Vol. 100, No. 2, pp. 571-572.

Chopra, S.K. and Tawashi, R. (1982) Tack behaviour of coating solutions I., Journal of Pharmaceutical Sciences, No. 71, pp. 907-911.

Chopra, S.K. and Tawashi, R. (1984) Tack behaviour of coating solutions II., Journal of Pharmaceutical Sciences, No. 73, pp. 477-481.

Chopra, S.K. and Tawashi, R. (1982) Tack behaviour of coating solutions III., Journal of Pharmaceutical Sciences, No. 74, pp. 747-749.

Christensen, S.F. (1998) Rheology of Adhesion, Ph.D. Thesis, Department of Chemical Engineering, Technical University of Denmark.

Chu, W.B., Yang, J.W., Wang, Y.C., Liu, T.J., Tiu, C. and Guo, J. (2006) The effect of inorganic particles on slot die coating of poly(vinyl alcohol) solutions, Journal of Colloid Interface Science, Vol. 297, pp. 215-225.

Chu, W.B., Yang, J.W., Liu, T.J., Tiu, C. and Guo, J. (2007) The effect of pH, molecular weight and degree of hydrolysis of poly(vinyl alcohol) on slot die coating of PVA suspensions of TiO_2 and SiO_2, Colloids and Surfaces A: Physicochem. Eng. Aspects, Vol. 302, pp. 1-10.

Clarke, A., Blake, T.D., Carruthers, K. and Woodward, A. (2002) Spreading and imbibition of liquid droplets on Porous surfaces, Langmuir, No. 18, pp. 2980-2984.

Creton, C. and Leibler, L. (1996) How Does Tack Depend on Time of Contact and Contact Pressure?, Journal of Polymer Science: Part B: Polymer Physics, Vol. 34, pp. 545-554.

Dale, D.A., Gaertner, A.L., Park, G. and Becker, N.T. (1999) Coated enzyme-containing granule, United States Patent US 5,879,920, Genecor International Inc.

Ennis, B.J., Tardos, G.I. and Pfeffer, R. (1991) A micro-level-based characterization of granulation phenomena, Powder Technology, No. 65, pp. 257-272.

Felton, L.A. and McGinity, J.W. (1997) Influence of plasticizers on the adhesive properties of an acrylic resin copolymer to hydrophilic and hydrophobic tablet compcts, International Journal of Pharmaceutics, No. 154, pp. 167-178.

Foley, P.R., Painter, J.D., Leyendecker, M.R., Sadlowski, E.S., Song, B.X. and Thien, J.H. (2003) Enzyme composite particles having an acidic barrier and a physical barrier coating, United States patent US 6,656,898, The Procter & Gamble Company.

Gay, C. (2002) Stickiness – Some Fundamentals of Adhesion, Integr. Comp. Biol., No 42, pp. 1123-1126.

Goodwin, J. (2004) Colloids and Interfaces with Surfactants and Polymers – An Introduction, John Wiley & Sons Ltd., Chichester.

Hede, P.D. (2005) Fluidised bed coating and granulation, M.Sc. Thesis, Department of Chemical Engineering, CHEC Research Center, Technical University of Denmark, pp. 1-227.

Hede, P.D. (2006) Towards Mathesis Universalis: Modern aspects of modelling batch fluidised bed agglomeration and coating systems – a review, CHEC Report R0605, Department of Chemical Engineering, Technical University of Denmark, pp. 1-101.

Hede, P.D., Bach, P. and Jensen, A.D. (2007a) Small-scale top-spray fluidised bed coating: Granule impact strength, agglomeration tendency and coating layer morphology, Powder Technology, No. 176, pp. 156-167.

Hede, P.D., Bach, P. and Jensen, A.D. (2008a) Validation of the Flux Number as scaling parameter for top-spray fluid bed systems, Chemical Engineering Science, Vol. 63, pp. 815-828.

Hede, P.D., Bach, P. and Jensen, A.D. (2008b) Top-spray fluidised bed coating: Scale-up in terms of relative droplet size and Drying Force, Powder Technology, Vol. 184, No. 3, pp. 318-332.

Hede, P.D., Bach, P. and Jensen, A.D. (2008c) Two-fluid spray atomisation and pneumatic nozzles for fluid bed coating/agglomeration purposes: a review, Chemical Engineering Science, Vol. 63, No. 14, pp. 3821-3842.

Hede, P.D., Bach, P. and Jensen, A.D. (2008d) Fluidised bed coating with sodium sulphate and PVA/TiO_2. Part I: Review and agglomeration regime maps, Industrial & Engineering Chemical Research, awaiting publication – proof corrected version.

Hede, P.D., Bach, P. and Jensen, A.D. (2008e) Fluidised bed coating with sodium sulphate and PVA/TiO_2. Part II: Influence of coating solution viscosity, stickiness, pH and droplet diameter on agglomeration, Industrial & Engineering Chemical Research, awaiting publication – proof corrected version.

Hede, P.D., Bach, P. and Jensen, A.D. (2008f) Fluidised bed coating with sodium sulphate and PVA/TiO_2. Part III: The role of tackiness and the tack Stokes number, Industrial & Engineering Chemical Research, awaiting publication – proof corrected version.

Hinds, W.C. (1999) Aerosol Technology. Properties, Behaviour and Measurement of Airborne Particles, John Wiley & Sons Inc., 2nd Edition, New York.

Hsu, E.R., Gebert, M.S., Becker, N.T. and Gaertner, A.L. (2001) The Effects of Plasticizers and Titanium Dioxide on the Properties of Poly (Vinyl Alcohol) Coatings, Pharmaceutical Development and Technology, Vol. 6, No. 2, pp. 277-284.

Hui, C.Y., Lin, Y.Y. and Barney, J.M. (2000) The Mechanics of Tack: Viscoelastic Contact on a Rough Surface, Journal of Polymer Science: Part B: Polymer Physics, Vol. 38, pp. 1485-1495.

Johnson, B.A. and Zograf, G. (1985) Adhesion of Hydroxypropyl Cellulose Films to Low Energy Solid Substrates, Journal of Pharmaceutical Sciences, Vol. 75, No. 6, pp. 529-533.

Jordan. M.P. and Taylor, J (2002) Film coatings and film coating compositions based on polyvinyl alcohol, United States Patent 6,448,323 BPSI Holdings Inc.

Kiilmann, E., Maier, H. and Baker, J.A. (1988) Hydrodynamic Layer Thicknesses of Various Adsorbed Polymers on Precipitated Silica and Polystyrene Latex, Colloids and Surfaces, No. 31, pp. 51-71.

Kiuchi, T., Kohtaro S., Sato, M., Kawamura, J. and Yamada, N. (1998) Enzyme-containing granulated substance and preparation process thereof, United States patent US 5,851,975, Kao Corporation.

Lehtola, V.-M., Heinamaki, J.-T., Nikupaavo, P. and Yliruusi, J.K. (1995) The mechanical and adhesion properties of aqeous-based hydroxypropyl methylcellulose coating systems containing polydextrose and titanium dioxide, Drug Development and Industrial Pharmacy, No. 21, pp. 675-685.

Liang, G.C., Hawkett, B.S. and Tanner. R.I. (2005) The determination of the isoelectric point from measurements of dispersion viscosity as a function of pH, Journal of Dispersion Science Technology, No. 26, pp. 215-225.

Markussen, E.K. (1986) Enzyme containing granulates suitable for use as detergent additives, European Patent EP 0 170 360 B1, Novo Industri A/S.

Markussen, E.K. (2002) Enzyme containing granule, United States Patent US 6,348,442, Novozymes A/S.

McGinity, J.W. (1997) Aqueous polymeric coatings for pharmaceutical dosage forms, Marcel Dekker Inc. NY, 2nd edition.

Michalski, M.C., Desobry, S. and Hardy, J. (1997) Food Materials Adhesion: A Review, Critical Reviews in Food Science and Nutrition, No. 37, pp. 591-619.

Mulhem, B., Fritsching, U. Schulte, G. and Bauckhage, B. (2003) Effect of solid particle characteristics on suspension atomization, Atomization and Sprays, No. 133, pp. 321–343.

Mulhem, B., Schulte, G. and Fritsching, U. (2006) Solid-liquid separation in suspension atomisation, Chemical Engineering Science, No. 61, pp. 2582-2589.

Neidel, B. (2007) Water-soluble polymer fluid bed coatings, M.Sc. Thesis, Department of Chemical Engineering, CHEC Research Center, Technical University of Denmark, pp. 1-123.

Okhamafe, A.O. and York, P. (1985) The adhesion characteristics of some pigmented and unpigmented aqueous-based film coatings applied to aspirin tablet, J. Pharm. Pharmacol., No. 37, pp. 849-853.

Otsubo, Y. (1986) Effect of polymer on the rheological behaviour of silica suspensions, Journal of Colloid Interface Science, No. 112, pp. 380-386.

Paatz, K., Rähse, W., Pichler, W., Upadek, H. and Kühne, N. (1998) Multi-enzyme granules, United States Patent US 5,846,798, Henkel Kommanditgesellscahft auf Aktien.

Parker, M.D., York, P. and Rowe, R.C. (1990) Binder-substrate interactions in wet granulation. 1: The effect of binder characteristics, International Journal of Pharmaceutics, No. 64, pp. 207-216.

Phillips, J.P., Deng, X., Stephen, R.R., Fortenberry, E.L., Todd, M.L., McClusky, D.M., Stevenson, S., Mishra, R., Morgan, S. and Long, T.E. (2007) Nano- and bulk-tack adhesive properties of stimuli-responsive fullerene-polymer blends, containing polystyrene-block-polybutadiene-block-polystyrene and polystyrene-block-polyisporene-block-polystyrene rubber-based adhesives, Polymer, No. 48, pp. 6773-6781.

Rajsharad, C. and Kamble, S. (2006) PVA Based Film Coating and Film Coating Compositions, WO 2006/11980 A2, Majumdar & Co.

Roos, A., Creton, C., Novikov, M.B. and Feldstein, M.M. (2002) Viscoelastic and Tack of Poly(Vinyl Pyrrolidone)-Poly(Ethylene Glycol) Blends, Journal of Polymer Science: Part B: Polymer Physics, Vol. 40, pp. 2395-2409.

Rowe, R.C. (1988) Binder-Substrate Interactions in Tablets: A Theoretical Approach Based on Solubility Parameters, Acta Pharm. Technol., No. 34, pp. 144-146.

Rowe, R.C. (1989) Binder-substrate interactions in granulation: a theoretical approach based on surface free energy and polarity, International Journal of Pharmaceutics, No. 52, pp. 149-154.

Russell, T.P. and Kim, H.C. (1999) Tack – a Sticky Subject, Science, No. 20, pp. 1219-1220.

Sairam, M., M.B. Patil, R.S. Veerapur, S.A. Patil and T.M. Aminabhavi (2006) Novel dense poly(vinyl alcohol) – TiO_2 mixed matrix membranes for pervaporation separation of water-isopropanol mixtures at 30 ºC, Journal of Membrane Science, No. 281, pp. 95-102.

Saxena, S.K. (2004) POLYVINYL ALCOHOL (PVA), Chemical and Technical Assessment (CTA), pp. 1–3.

Schæfer, T. and Wørts, O. (1977) Control of fluidized bed granulation. II. Estimation of droplet size of atomised binder solutions, Archives of Pharmaceutical and Chemical Science, 5th Edition, pp. 178-193.

Shell Chemicals Europe (2005) NEODOL 23-6.5 Product specification sheet, pp. 1-2.

Simonsen, O. (2002) Lubricated Granules, International Patent WO 02/20746 A1, Novozymes A/S.

Smitthipong, W., Nardin, M., Schultz, J., Nipithakul, T. and Suchiva, K. (2004) Study of tack properties of uncrosslinked natural rubber, Journal of Adhesion Science technology, Vol. 18, No., 12, pp. 1449-1463.

Tardos, G., Khan, I.M. and Mort, P.R. (1997) Critical parameters and limiting conditions in binder granulation of fine powders, Powder Technology, No. 94, pp. 245-258.

Tardos, G. (2005) Wet-Granulation Research with Application to Scale-up, China Particuology, Vol. 3, No. 3, pp. 191-195.

Thielmann, F., Naderi, M., Ansari, M.A. and Stepanek, F. (2007) The effect of primary particle surface energy on agglomeration rate in fludised bed wet granulation, Powder Technology, In Press.

Tüske, Z., Regdon, Jr. G., Erös, I., Srcic, S. and Pintye-Hödi, K. (2005) The role of the surface energy in the selection of a suitable excipient in the course of a wet-granulation method, Powder Technology, No. 155, pp. 139-144.

Ukei, H., Yatagai, T., Nagatsu, H., Natsume, M. and Nakagawa, Y. (2005) Pressure-sensitive adhesive tape, NITTO DENKO Corp., European Patent EP1516898.

van Ee, J.H., Misset, O and Baas, E.J. (1997) Enzymes in Detergency, Surfactant Science Series, Volume 69, Marcel Dekker, New York.

Waldie, B. (1991) Growth mechanism and the dependence of granule size on drop size in fluidized-bed granulation, Chemical Engineering Science, No. 46, pp. 2781-2785.

Wan, L.S.C. and Lai, W.F. (1992a) A simple method to asses the tack of coating formulations, S.T.P. Pharma Sciences, No. 2, pp. 174-180.

Wan, L.S.C. and Lai, W.F. (1992b) An application of tack measurement to fluidized bed coating, S.T.P. Pharma Sciences, No. 2, pp. 404-410.

Werner, S.R.L., Jones, J.R. and Paterson, A.H.J. (2007) Stickiness during drying of amorphous skin-forming solutions using a probe tack test, Journal of Food engineering, No. 81, pp. 647-656.

Wesseling, M., Kuppler, F. and Bodmeier, R. (1999) Tackiness of acrylic and cellulosic polymer films used in the coating of solid dosage forms, European Journal of Pharmaceutics and Biopharmaceutics, No. 47, pp. 73-78.

York, P. and Rowe, R.C. (1994) Monitoring granulation size enlargement processes using mixer torque rheometry, 1st International Particle Technology Forum, Denver, USA.

Zosel, A. (1985) Adhesion and tack of polymers: Influence of mechanical properties and surface tensions, Colliod & Polymer Science, No. 263, pp. 541-553.

Chapter 11. Thesis conclusion

Chapter introduction

Chapter eleven contains the general conclusion for the thesis. The chapter discusses the results and conclusions of the previous chapters. The research work results are combined into perspective hereby providing an overview of the thesis and the implications of the obtained results.

11. Thesis conclusion

The top-spray batch fluid bed coating process has been investigated with respect to process and product optimisation as well as scale-up. The focus has been primarily on agglomeration tendency as well as the mechanical strength and morphology of the coating layer, aiming at obtaining a fundamental understanding of the phenomena and variables influencing these topics. In continuation of this, the objective has been to study and apply selected mathematical models and approaches in order to validate their capabilities and limitations. Taking its origin in industrial enzyme fluid bed coating processes, the research work has focussed on two of the most common types of coating processes; coating with aqueous inorganic salt solutions (exemplified in terms of aqueous solutions of sodium sulphate) and coating with aqueous solutions of polymers (exemplified in terms of aqueous solutions of PVA with dispersed TiO_2 particles). Coating experiments have been carried out in three pilot-scale fluid beds ranging from a bed load of 0.5 kg (small-scale) to 4 kg (medium-scale) and 24 kg (large-scale).

The limitations and capabilities of black-box statistical data-driven models were tested in the first part of the experimental research work involving a simple double unreplicated 2^{4-1} fractional factor design. This was applied on small-scale coating experiments in order to test the influence of the fluidisation velocity, atomisation air pressure, coating solution dry-matter concentration and bed temperature on two response parameters being agglomeration tendency and impact strength of salt coated sodium sulphate cores. The derived agglomeration model indicated decreasing agglomeration tendency with increasing coating solution dry-matter concentration and atomisation air pressure. This is explained by the fact that increasing atomisation air pressure produces smaller droplets. Smaller droplets combined with less solvent in each droplet to be evaporated means that the droplets are wet for shorter time hereby reducing the chance of agglomeration. The study further indicated that there is no apparent contradiction between low tendency of agglomeration and high granule impact strength. The derived impact strength model indicated increasing strength with increasing coating solution dry-matter concentration, atomisation air pressure and bed temperature. A reasonable theory is that depleted coating droplets with high dry-matter contents form solid salt bridges inside the pores of the core particles upon drying, and that this will improve the impact stress resistance of the final coated granule. This was partly verified by porosity measurements indicating a decrease in final coated granule porosity with increasing coating solution dry-matter contents. For standard sodium sulphate coating experiments the degree of droplet penetration into the core particles was observed to be significant although droplet penetration was observed to decrease with increasing coating solution bulk viscosity. The

coating layer morphology was further observed to be increasingly rough and raspberry-like with increasing viscosity.

In conclusion, the black-box statistical model approach may be a good approach initially in an optimisation process in order to get a quick and rough screening of the influence of different process and formulation parameters. However, black-box models do not provide any fundamental insight into the particle-level phenomena influencing the coating process, and they cannot be used outside the parameter space on which they were derived. Further, the models are too equipment-specific to be used for scale-up.

Two simple engineering fluid bed coating scale-up principles were tested in salt coating experiments being the Flux Number and the Relative Droplet size/Drying Force approach. Neither of the two principles automatically specifies all the variables involved in the process, and proper choices of e.g. the inlet fluidisation air temperature have to be made. This further means that coating experiments are needed to be carried out in order to find the optimal choice for the inlet fluidisation temperature.

For the selected values of the variables constituting the Flux Number, experiments showed that it is possible to maintain a low tendency of agglomeration and match the particle size distribution across the three pilot-scale fluid beds, but only for a very slow coating process with significant spray drying loss of the coating solution. It was observed how two coating processes with identical Flux Number values could result in completely different agglomeration tendencies based on the choice of the variables constituting the Flux Number. This is due to the fact that a fixed Flux Number states nothing about temperature and humidity conditions inside the bed during processing. Neither does the Flux Number give any indication of how the inlet fluidisation air temperature or nozzle pressure should be chosen, which is an obvious disadvantage. Balancing the particle flux in the spray zone with the liquid spray flux appears in principle to be a sound theoretical approach to control the coating process in terms of agglomeration, and the validation of the Flux Number as scale-up principle did not discard the principle. Rather, the results indicated that the Flux Number alone cannot be used for successful upscaling without selecting the Flux Number variables carefully within narrow boundaries. Apparently, the guidelines provided by the inventors of the Flux Number are too broad for some of the variables, in all leading to too many possible variable combinations for the same Flux Number value. New boundaries have been suggested in the present work that are narrower than the ones presented in the original patent. Even so, the Flux Number scale-up approach is concluded to be a too simple approach to be used as a generic scale-up principle.

With the qualified choices for the variables constituting the Relative Droplet size and Drying Force, results showed that it is possible to keep the agglomeration tendency low and at the same time match the particle size distribution across the three pilot-scale fluid beds. The agglomeration tendency was observed to increase with increasing Relative Droplet size (due to larger mean droplet diameters) and with decreasing Drying Force (due to a lower moisture evaporation force and thereby more moist particles). It was concluded that scale-up in terms of either of the two parameters alone could not be carried out successfully. Only by combining the two parameters could the particle size distribution be matched across scale. Impact and attrition tests showed that it is possible to produce granules with similar attrition and impact strength across fluid bed scale, and that the two types of mechanical properties are inversely related. It was observed that a high bed temperature combined with a high atomisation air pressure lead to strong and homogenous coating layer structures. Coatings on

top of non-porous glass ballotini cores exhibited the best impact strength whereas coatings on top of porous sodium sulphate cores were observed to have the best attrition strength. This was explained by the difference in coating droplet core penetration.

Following the experimental studies of the salt coating process a lumped-region dynamic heat and mass transfer model was set up and implemented into MATLAB allowing simulations of the fluidisation air temperature and humidity as well as particle moisture contents and temperature. The model is based on two-phase theory for bubbling fluid beds and includes detailed heat and mass transfer models as well as heat loss to the surroundings. This simple yet versatile model made it possible to simulate previous salt coating experiments and furthermore be able to obtain detailed scale-up insight. Good agreement between simulations and steady state experimental data was observed for important variables such as the fluidisation air outlet temperature and humidity as well as the bed temperature. Simulations revealed that the three pilot-scale fluid beds are not significantly different with respect to steady state in-bed conditions, and as long as the atomisation air pressure, liquid spray rate and fluidisation air velocity (in m/s) are all above certain values, similar inlet fluidisation air temperatures will lead to similar low tendencies of agglomeration while the process intensity is maintained. This is because such process conditions give similar vertical temperature, humidity and Drying Force profiles again leading to similar particle liquid layer thicknesses, which in turn causes similar tendency of agglomeration as verified using the viscous Stokes theory. Simulations of a 900 kg RICA-TEC production-scale fluid bed revealed that the temperature and humidity gradients increase significantly with respect to the pilot-scale beds, meaning that the error of measuring a representative bed temperature at one location (as typically done industrially) becomes much larger. It hereby becomes erroneous to define and fix an overall Drying Force value. The Relative Droplet size may apparently be fixed across scale during scale-up, but this requires a significant increase in inlet fluidisation air temperature in order to keep out of the agglomeration regime. If the inlet temperature is fixed across scale then the spray intensity must be decreased the larger the fluid bed scale in order to avoid agglomeration. This is a consequence of the poor mixing and longer particle circulation times the higher the fluidised bed is. This illustrates that for similar process intensity the coating process becomes increasingly sensitive towards agglomeration the larger the fluid bed scale.

The choice of the proper modelling approach obviously depends on the interest and the purpose of the model. Both in terms of scale-up and when optimal conditions are to be found for any fluid bed scale, combination of the viscous Stokes theory and particle liquid layer thickness profiles obtained from simulations is concluded to be a strong and versatile tool. Although requiring a heat and mass transfer model, as the one presented in the present work, this optimisation principle is scientifically valid as it is based on thermodynamics, and a generic first-principle particle-level model as the viscous Stokes theory. Contrary to the Flux Number or Drying Force/Relative Droplet approach, this scale-up principle does not have any independent variables and all fluid bed process settings can be determined a-priori at any scale. Alternatively, more detailed particle-level models could serve as guidelines for how different variables and properties affect the coating process in detail, but models at this scale cannot be used to predict the outcome at the macro-level (unit-operation scale). Modelling approaches in terms of advanced hydrodynamic and population balance models are concluded not to be useful approaches in a scale-up or process-control context due to problems related to the mathematical capabilities, limitations and solution techniques as well as potential problems of validating the models with experimental data. In that sense, the lumped-region modelling approach is concluded to be the most versatile and obvious choice. A clear

advantage with this approach is that the model can be continuously expanded to include further details, and elements from other modelling techniques may be implemented in such lumped-region models.

With the obtained results and experience with the salt coating process, focus was next turned toward more complex coatings. The PVA/TiO_2 coating process was studied in the pursuit of finding the causes why polymer and inorganic salt solutions cannot be processed under similar fluid bed process conditions without resulting in significantly different agglomeration tendencies. Fluid bed coating experiments with different values of the Drying Force and the liquid spray rate indicated that the PVA/TiO_2 coating process is much more sensitive towards agglomeration under similar thermodynamic and spray conditions. Detailed studies indicated that such differences do not arise solely from differences in coating solution bulk viscosity or from differences in mean droplet diameters. Rather, the different behaviour results from differences in stickiness (tack) measured in terms of a probe tack tester developed for the purpose. Realising that the PVA/TiO_2 coating solution is a colloidal dispersion of TiO_2 particles this was made use of to suppress the tendency of agglomeration by substituting some of the PVA/TiO_2 with lubricant and plasticizer in the form of Neodol 23-6.5, and further reduce pH to a value far from the isoelectric point. In terms of this it was shown possible to arrive at a low agglomeration tendency within range of the agglomeration tendency for a salt solution coating process processed under similar conditions.

Based on the experimental work with the polymer coating solutions a new tack Stokes number was introduced for the polymer coating process based on the work needed to reach maximum tack (above which breakage occurs) in the probe tack test instead of the viscous dissipation energy used in the traditional viscous Stokes number. The new tack Stokes number correlates well with observed levels of agglomeration, and as a promising feature, proportionality is observed between the agglomeration weight percentages and the new tack Stokes number. The better performance of the tack Stokes number was explained by the influence of the liquid layer thickness. In the polymer fluid bed coating process the liquid layer is very thin and sticky, meaning that agglomeration is primarily due to liquid surface phenomena rather than due to bulk viscous phenomena. Such surface phenomena are well predicted by the probe tack test giving reasons to believe that the tack Stokes number is a better way to predict the agglomeration tendency for the polymer coating systems tested in the research work. An important conclusion from the PVA/TiO_2 studies is that the optimisation of a fluid bed coating process should focus also on the coating solution formulation besides focussing on process-related variables.

Chapter 12. Engineering guidelines

Chapter introduction

Chapter twelve provides simple engineering guidelines and considerations for the scale-up and process optimisation of the top-spray batch fluid bed coating process. The chapter contains short discussions of the implications of the results obtained in the research work in a broad perspective. Such implications necessarily have a character of being general trends and comments rather than unambiguous guidelines. They are nevertheless relevant for future process optimisation and scale-up of the top-spray batch fluid bed coating process. The chapter is finally ended with a section concerning suggestions for future work

12. Engineering guidelines and general optimisation issues

The top-spray configuration is the oldest and simplest fluid bed coating set-up. In an overall perspective, it appears intuitively contradictory to introduce coating solution at the opposite end of where the fluidisation air drying capacity is largest. In this set-up the temperature will decrease vertically up through the bed while the humidity increases. In terms of this it is not surprisingly to find good arguments in the literature why the top-spray fluid bed coater should be replaced with bottom-spray systems such as the Wurster fluid bed. Results from the present research work support such arguments, as the coating layer morphology and mechanical strength is observed to be better if the core particles are coated with many small droplets that dry fast enough to produce amorphous coating layer structures primarily. Such a coating condition is easier to obtain in a bottom-spray fluid bed, where the droplets are introduced where the fluidisation air is hottest. The degree of premature droplet spray drying is also lower in the bottom-spray configuration hereby increasing the coating efficiency. In spite of this, new top-spray fluid beds are still being designed for industrial coating operations, mainly because of simplicity both in design and operation, as well as the fact that the principle works sufficiently well for many coating applications. In terms of this it makes good sense to continue to optimise the top-spray fluid bed configuration for coating purposes.

The core material is an important parameter for the coating process outcome. Especially the porosity of the core particles have been observed to be of primary importance for the morphology and mechanical strength of the final coating layer. Coating droplet penetration into the core particle is typically much faster than the droplet drying time, depending of the coating solution properties and the droplet diameters with respect to the core particle pore diameters. This means that under most of the coating conditions studied in the present work, droplet penetration has been observed to be significant. Whereas this is beneficial in terms of mechanical strength and morphology, it may be a potential problem with certain heat and moisture sensitive active ingredients. Enzyme-containing core particles e.g. are known to lose activity if they are exposed to high levels of moisture during coating. In such situations it may be beneficial to try to reduce the porosity of the core particle prior to coating, or to optimise the coating solution properties in order to suppress droplet penetration.

The coating solution properties are important for the agglomeration tendency and the quality of the coating layer in general, and two different coating solutions cannot be expected to be successfully processed under similar conditions. Both process and coating solution optimisation should be carried out with respect to the coating solution characteristics. Inorganic salt coating processes, where the solute goes from solution to solid state instantaneously, appears to be the easiest to process without much attention to the coating solution formulation. The agglomeration tendency during coating as well as the final granule properties including morphology and mechanical strength are, however, affected by the coating solution dry-matter contents. With the coating solution salt concentrations tested in the present research work, it appears that the mechanical strength will improve if the dry-matter concentration in the coating solution increases. This will at the same time decrease the agglomeration tendency.

Other more advanced polymer coating solutions are more difficult to process as the polymer typically has a long transition time from solution to solid state during which it remains sticky. Optimisations of such sticky coating solutions, in order to reduce the coating solution stickiness and contact angle with the core particles, will often be beneficial. Such modifications could include the addition of e.g. filler particles, lubricants, surfactants and/or plasticizers as well as pH changes etc. An often overseen problem with difficult coating solutions is the way the solutions are being prepared, and many apparent process-related problems result from improper coating solution preparation. Many polymers are sensitive towards the way they are kept and brought into solution, and often careful and extensive measures are needed before the coating process may begin.

Process and operating conditions related to the nozzle appear to be perhaps the most critical part of the coating process. Not just the nozzle design and position with respect to the fluidisation air distribution plate are important, also the implication of the nozzle pressure, i.e. the atomisation airflow, is vital for the outcome of the process. All results point toward the advantage of a high atomisation airflow as this will distribute the coating droplets far into the fluidised bed in vertical direction. This will to some extent suppress any potentially high vertical temperature and humidity gradients. In order to avoid high local particle moisture contents the spray zone should apparently take up more than 50 % of the expanded bed height. This is normally achieved in small pilot-scale fluid beds, but not in larger scales. In order to achieve better coating processes in large scale, it is suggested to decrease the distance between the air distributor plate and the nozzle outlet or perhaps insert nozzles at different vertical positions in the chamber, hereby expanding the vertical extension of the spray zone. Further, a high atomisation airflow has the advantages of ensuring good atomisation of the coating solution with uniform small droplet sizes to the largest possible extent. Small droplets apparently help to reduce the tendency of agglomeration and to improve the mechanical strength of the coating layer (i.e. it gives an amorphous, compact and homogenous coating layer), although small droplets also increase the chance of droplet spray drying loss and sometimes decrease the coating layer homogeneity. In all, the nozzle is a sensitive part of the coating system, and it should be operated carefully and kept fixed during the entire coating process as even minor changes in nozzle operation may have major effects on the process outcome.

The choice of fluidisation velocity should ideally be balanced between two things: The elutriation of the particles due to velocities exceeding the terminal velocity, and the acceptable level of particle/coating layer attrition and breakage. Depending on the type and quality of the granular product, it may most likely be optimal to operate the fluid bed in the

high end of this range close to the terminal velocity of the smallest of the core particle fractions. This will optimise the drying and fluidisation capacity. A high fluidisation velocity has also the advantage that it causes high particle collision velocities hereby helping to reduce the tendency of agglomeration for a given liquid spray rate.

When processing heat-sensitive products the choice of the bed temperature and the inlet fluidisation air temperature should be balanced between the agglomeration limit and the temperature at which the degree of deactivation of the heat-sensitive ingredient becomes unacceptably high. Choosing the bed temperature as low as possible (for a given inlet fluidisation air temperature, i.e. maximising the temperature difference $\Delta T = T_{inlet} - T_{bed}$) will ensure the maximum process intensity and the shortest possible coating time. This will, however, maximize the vertical moisture and temperature gradients through the bed, and thereby increase the chance of agglomeration. Irrespectively of the chosen bed temperature a high inlet fluidisation air temperature will always have the largest drying potential, and as long as the heat-sensitive ingredient is not deactivated to any unacceptable degree, the inlet fluidisation air temperature should be chosen as high as possible in order to optimise the process capacity.

The representation of the bed temperature in terms of a single temperature probe located near the air distribution plate may only be representative for the temperatures at other vertical locations in pilot-scale fluid beds. For larger fluid bed scales such single-point bed temperature measurements become increasingly erroneous with increasing scale, due to increasing vertical temperature and humidity gradients resulting from large increases in expanded particle bed height and poor particle mixing. Even if the temperature probe is inserted closer to the nozzle outlet, the measurement error would still remain higher than for smaller fluid bed scales. It is suggested not to base process control alone on single-point bed temperature measurements in production-scale fluid beds.

The aforementioned guidelines also have implications in terms of future design of fluid bed coating equipment. Currently, production-scale equipment is typically much larger in vertical size compared to pilot-scale, while the horizontal dimensions are only slightly expanded. This results in a significant increase in the expanded particle bed height with scale and leads to problems such as large vertical temperature and humidity gradients and long particle cycle times. From a fluid bed coating process point of view this scale-up design principle is apparently not advantageous as the coating process becomes increasingly sensitive towards agglomeration the larger the scale. Furthermore, the granules with the best mechanical properties are apparently produced in the smallest fluid bed scales. In order to avoid the these problems and to use the advantage of bed homogeneity in the small pilot-scales, it is suggested to built upscaled fluid bed equipment by expanding the horizontal dimensions only, i.e. in principle to put small-scale fluid beds into series side-by-side. This design principle will ensure short particle circulation times, a large relative vertical spray zone as well as small vertical temperature and moisture gradients. It will, furthermore, end most problems with scale-up as the particles will experience the same process conditions at any scale. Although the design of continuous fluid beds in many ways follows this principle, there are, however, a number of potential problems that could explain why it is not used in commercial designs of batch fluid beds. First of all, the design of large production-scale equipment with similar capacities to the present designs would require fluid bed chambers of several meters in diameter at the same time having a height of less than one meter. This would give rise to mechanical engineering problems in terms of the physical design of the chamber as well as the design of the fluidisation inlet air channels and air distributor plate, not to mention most

importantly; practical problems with loading/unloading the particle bed. Furthermore, it would require more steel to build the equipment as well as larger buildings to house the fluid beds than with the present designs.

In all, fluid bed coating process optimisation involves a multi-parameter optimisation problem and cannot readily be solved without a proper model that is capable of simulating the coating process at the macro-level with the inclusion of a certain degree of particle-level models. In terms of scale-up there is probably no simple parameter relationship that simply should be kept constant across scale in order to maintain the particle size distribution, agglomeration tendency and coating layer properties across scale. Instead each scale should be optimised individually with respect to the general guidelines provided above. This could be done in terms of a simple heat and mass transfer model as the one presented in this research work. The implications of this in an industrial perspective is that pilot-scale trials should be carried out in order to optimise and test the granule product properties (e.g. the maximum temperature or humidity level without degradation of the active ingredient etc.) and not to find proper coating process parameter settings that should be kept constant across fluid bed scale. If such product properties can be determined from other techniques than from fluid bed coating process trials, the pilot-scale step in industrial production may eventually be skipped.

12.1. Suggestions for future work

Following the conclusion from the obtained research work it seems obvious to suggest to continue with the lumped-region modelling approach both in the direction of process optimisation and scale-up. The presented model is a one-dimensional discretisation of the fluid bed chamber assuming well-mixed behaviour in each control volume. In reality the coating solution is not distributed evenly in each control volume, but rather sprayed vertically downwards in a cone-shape. An obvious further first step would be to expand the model discretisation into three dimensions (or at least into a two-dimensional axisymmetrical model) hereby being able to account for the cone-shaped spray patterns as well as differences in particle exchange rate with respect to the horizontal position.

Some of the possible further threads that could be taken towards a model optimisation and expansion include:

- Implementation of detailed enzyme deactivation kinetics models in order to obtain a model that could be used for detailed enzyme coating process optimisation. Such models may e.g. be obtained from Differential Scanning Calorimeter (DSC) studies.
- Implementation of a population balance model accounting for agglomeration, breakage and attrition hereby being able to simulate a coating process with a dynamic particle size distribution. This would also make it possible to study the coating layer distribution with respect to the core particle size distribution.
- Implementation of a model capable of predicting the droplet size distribution produced at the nozzle outlet. This could be applied in order to study possible spray drying losses at different process conditions. This could also be expanded with a droplet impingement model in order to account for the fact that not all droplets impact core particles, but instead end up as spray dried debris.
- Implementation of detailed particle-level models treating issues such as droplet spreading on core particles, droplet core penetration and more. Together with the population balance model this would give a more realistic model in terms of agglomeration tendency.

Appendix. Reprint of selected published scientific papers

In order of occurence - Reprinted with permission from the publishers

1) Hede, P.D., Bach, P. and Jensen, A.D.: Small-scale top-spray fluid bed coating: Granule impact strength, agglomeration tendency and coating layer morphology, Powder Technology, Vol. 176, No. 2-3, pp. 156-167.

2) Hede, P.D., Bach, P. and Jensen, A.D.: Validation of the Flux Number as scaling parameter for top-spray fluidised bed systems, Chemical Engineering Science, Vol. 63, No. 3, pp. 815-828.

3) Hede, P.D., Bach, P. and Jensen, A.D.: Top-spray fluid bed coating: Scale-up in terms of Relative Droplet size and Drying Force, Powder Technology, Vol. 184, No. 3, pp. 318-332.

4) Hede, P.D., Bach, P. and Jensen, A.D.: Two-fluid spray atomisation and pneumatic nozzles for fluid bed coating/agglomeration purposes: a review, Chemical Engineering Science, Vol. 63, No. 14, pp. 3821-3842.

5) Hede, P.D., Bach, P. and Jensen, A.D.: Fluidised bed coating with sodium sulphate and PVA/TiO_2. Part I: Review and agglomeration regime maps, Industrial & Engineering Chemical Research, awaiting publication – proof corrected version.

6) Hede, P.D., Bach, P. and Jensen, A.D.: Fluidised bed coating with sodium sulphate and PVA/TiO_2. Part II: Influence of coating solution viscosity, stickiness, pH and droplet diameter on agglomeration, Industrial & Engineering Chemical Research, awaiting publication – proof corrected version.

7) Hede, P.D., Bach, P. and Jensen, A.D.: Fluidised bed coating with sodium sulphate and PVA/TiO_2. Part III: The role of tackiness and the tack Stokes number, Industrial & Engineering Chemical Research, awaiting publication – proof corrected version.

8) Hede, P.D., Bach, P. and Jensen, A.D.: Batch top-spray fluid bed coating: Scale-up insight using dynamic heat and mass transfer modelling, Chemical Engineering Science, Vol. 64, No.6, pp. 1293-1317.

Available online at www.sciencedirect.com
ScienceDirect
Powder Technology 176 (2007) 156–167
POWDER TECHNOLOGY
www.elsevier.com/locate/powtec

Small-scale top-spray fluidised bed coating: Granule impact strength, agglomeration tendency and coating layer morphology

Peter Dybdahl Hede [a,b], Poul Bach [b], Anker D. Jensen [a,*]

[a] CHEC Research Center, Department of Chemical Engineering, Technical University of Denmark, Building 229, DK-2800 Kgs. Lyngby, Denmark
[b] Solid Products Development, Novozymes A/S, Smørmosevej 11, DK-2880 Bagsværd, Denmark

Received 24 March 2006; received in revised form 5 January 2007; accepted 15 February 2007
Available online 28 February 2007

Abstract

The degree of agglomeration and impact strength of Na_2SO_4 cores (all in the size range of 200–300 μm) coated with aqueous solutions of sodium sulphate and dextrin as a function of several process and formulation variables have been investigated. The coating process was performed in a modified small-scale GEA Aeromatic-Fielder Strea-1 top-spray fluidised bed, and the impact strength was tested in bulks using a Pneumatic Impact Gun, in which granule samples of 0.5 g were exposed to ten repeated impacts at 10 m/s. Using an unreplicated double 2^{4-1} fractional factor design, two regression models were derived from experimental data describing quantitatively the degree of agglomeration and impact strength respectively. The agglomeration model suggests in accordance with previous studies that increasing the nozzle pressure as well as coating-solution-dry-matter-concentration decreases the tendency of agglomeration. The consistency between the agglomeration model and new experimental data is concluded to be satisfactory. The impact strength model indicates increasing impact strength with increasing nozzle pressure, coating solution–dry-matter-concentration and bed temperature. These tendencies may be influenced by the large extent of droplet penetration, as observed in additional coating droplet penetration and coating layer morphology studies in the present paper. The validation of the impact strength model shows that the model clearly follows overall experimental tendencies. The derivation of these quantitative models may be seen as a first step towards the development of processes for production of unagglomerated enzyme granules with high mechanical strength and contribute to an improved understanding of fluid bed processes and products.

Keywords: Fluidised bed; Coating; Granulation; Impact strength; Factorial designs; Coating layer morphology

1. Introduction

To improve handling and product properties, enzymes are often incorporated into granules which are commonly produced by fluidised bed processes. As presented by prior work by e.g., Härkonen et al. [1] and Jørgensen et al. [2], inert carrier particles in the fluidised bed are typically coated with a formulated enzyme concentrate sprayed onto the particles through nozzles. The use of conventional top-sprayed fluidised bed systems finds wide use in pharmaceutical and food coating operations in pilot scale as well as in larger production scale, as presented by Rubino [3] and reviewed by Teunou and Poncelet [4]. The desired product is a product consisting of unagglomerated individual carrier particles each coated homogeneously with a layer of the enzyme. If formulation or process conditions such as fluidisation velocity, bed temperature, humidity of the air, spray rate and droplet size etc., are incorrectly chosen, either excessive agglomeration or excessive spray drying of the spray feed will happen. In both cases a poor product quality and loss will be the result. In general the optimum coating conditions with respect to product quality and capacity are close to the agglomeration conditions. Despite the wide use of fluidised bed processing, it is still not possible to predict this limit based on the formulation properties and the basic process conditions. Extensive experiments are needed in order to find the optimum process conditions and at the same time optimise the product properties.

Regarding product properties, the mechanical strength of the final coated granule is of vital importance. Due to handling, transportation, packing and further mixing with e.g. detergents,

* Corresponding author. Tel.: +45 4525 2841; fax: +45 4588 2258.
E-mail address: aj@kt.dtu.dk (A.D. Jensen).

0032-5910/$ - see front matter © 2007 Elsevier B.V. All rights reserved.
doi:10.1016/j.powtec.2007.02.018

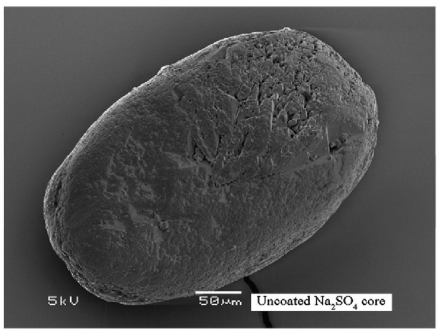

Fig. 1. SEM picture of an uncoated sodium sulphate core.

the enzyme granule is exposed to many types of mechanical stresses, causing degradation and breakdown of the coating layer [2]. This is unwanted not just for health and safety reasons but also because of reduced enzyme activity. Especially impact strength is important regarding mechanical properties of granules made in fluidised beds. Consequently, it is desired to optimise the impact strength by adjustment of the formulation and process conditions. It is the aim of this paper to address the tendency of agglomeration and impact strength quantitatively in terms of models build from statistical valid experimental data based on an unreplicated double 2^{4-1} fractional factor design. In this paper four parameters were screened being the fluidisation velocity, the atomisation pressure, the coating solution salt concentration and the bed temperature.

2. Materials and methods

2.1. Materials used

In all the coating experiments seeded anhydrous sodium sulphate cores sieved into a fraction with diameters between 200 and 300 mm were coated with aqueous solutions of crushed sodium sulphate using Dextrin (bulk density ~ 0.8 g/cm^3) as binder. The moisture contents of the sodium sulphate cores were determined to be less than 0.4 w/w% (inclusive crystal water)

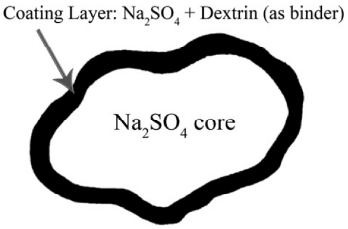

Fig. 2. The principle of a coated sodium sulphate core. Ideally the sodium sulphate core is completely covered with a coating layer of sodium sulphate. The adhesion of the coating layer to the core surface is enhanced by the dextrin functioning as binder. The coating process is done in a top-spray fluid bed.

and the average porosity of the cores was determined to 20.7% using mercury intrusion/extrusion porosimetry. From this analysis it was further seen that the pore size distribution was narrow and unimodal having an average pore diameter of 1.29 mm. SEM analysis of the Na_2SO_4 cores showed rather smooth core surfaces with few but large pores. A typical SEM picture of an uncoated Na_2SO_4 core can be seen in Fig. 1.

Triphenylmethane colour (Sicovit Patent blue) and Colanyl green were used as colouring agent for droplet penetration experiments in amounts of 0.3 w/w% and 0.1 w/w% respectively. Sodium carboxymethylcellulose (purity > 99.5 %) was used as thickener in the droplet penetration and morphology experiments in concentrations up to 5.2 w/w% in order to investigate the influence of increasing the coating solution viscosity. The principle of a coated granule composition can be seen in Fig. 2. Ideally the sodium sulphate core is completely covered with a layer of coated sodium sulphate in the fluid bed coating process. The small amount of the dextrin binder in the coating layer enhances the adhesion of the sodium sulphate coating layer to the core surface. Such granule compositions are typically desired in enzyme granules due to enzyme stabilization issues.

2.2. Equipment

2.2.1. Fluidised bed equipment and process variables

A modified GEA Aeromatic-Fielder Strea-1 top-spray fluidised bed was used with a stainless steel fluidising chamber of 16 L. The air distribution plate consists of a perforated stainless steel plate (Ø 100 mm) with 78 holes (Ø 3 mm) covered with a metal grid with orifice diameters of 100 µm to avoid any particle loss when the bed is not fluidised. The physical dimensions of the fluidisation chamber may further be seen from Fig. 3. Modification to the original vessel design made it possible to insert a digital thermometer into the fluidisation chamber wall thereby making it possible to measure the bed temperature between the air distribution plate and the nozzle outlet. The location of this temperature probe was carefully chosen in order to make sure that no non-uniform temperature profiles due to wall- or spray-effects would interfere with the temperature measurements. In addition, an external humidity measurement apparatus (Testo 645 Thermo-hygrometer) was inserted above the nozzle allowing the relative humidity in the fluidisation chamber to be measured near the exhaust gas outlet.

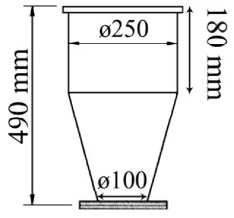

Fig. 3. The Strea-1 fluidising chamber dimensions in mm [20].

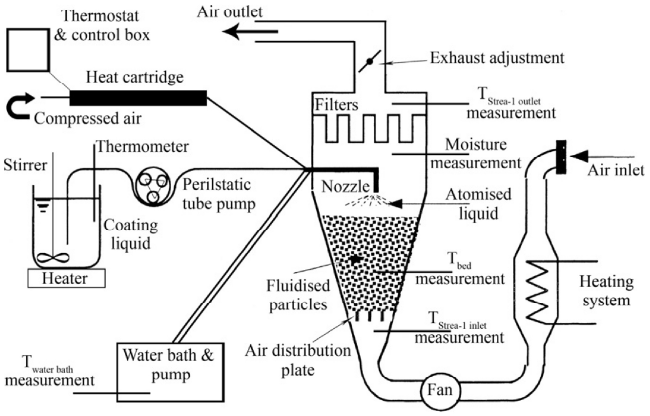

Fig. 4. Sketch of the modified Strea-1 set-up.

Standard Strea-1 reusable nylon filters were inserted at the top of the fluidisation chamber in order to prevent particles and spray-dried coating droplets from being exhausted. The back-flush option in the Strea-1 set-up was switched on allowing the filters to be flushed every fifth second.

The applied spray nozzle was a two-fluid nozzle with an outlet diameter of 0.8 mm. An integrated heating jacket connected to a thermostated external water bath at 80 °C heated the nozzle itself. In the applied set-up, the nozzle was placed 25 cm above the air distribution plate. The compressed atomising air was in addition led through an external heating cartridge at 80 °C before reaching the nozzle. This option was necessary in order to prevent clogging of the nozzle caused by crystallisation of the coating solution due to temperature drop inside the nozzle. The coating liquid feed was led from the external heated reservoir at 80 °C to the nozzle through an adjustable electrical peristaltic tube pump. A sketch of the modified Strea-1 set-up can be seen in Fig. 4 and the general operating process and formulation conditions can be seen in Table 1.

Prior to coating, the sodium sulphate core bed load of 500 g was heated with hot inlet air at 80 °C until the relative humidity inside the fluidisation chamber was constant, typically ranging from 5 RH% to 8 RH% depending on weather conditions. During coating the fluidisation velocity and fluidisation inlet air temperature were kept fixed. In addition, the bed temperature was maintained at the chosen level by adjusting the coating liquid feed rate at the tube pump. In each coating operation the aim was to coat until the bed load had increased 20 wt./wt.%. This was done in order to make sure that a reasonable coating layer (~10 μm) had developed. After coating, the bed load was kept fluidised at identical fluidisation velocity and inlet temperature conditions in order to dry the coated granules. This was done until the relative humidity inside the chamber was identical to the conditions prior to coating. The coated bed load was afterwards weighed and sieved with a combination of four sieves in a stack for 1 min. The stack consisted of a sieve with a diameter of 425 μm on top of sieves with diameters of 355, 300 and 250 μm. From initial visual microscopy analysis it was observed that for a given coated batch the fraction of coated granules above 355 μm consisted primarily of agglomerates whereas the fraction below this limit consisted mainly of single coated granules and fines. Hence this value was set as the cut-off size between agglomerates and single granules according to Eq. (E.1). The obtained fraction of coated granules between 300 μm and 355 μm was the fraction to be strength tested in the Pneumatic Impact Gun.

2.2.2. Impact strength equipment

A P.I.G. (Pneumatic Impact Gun — Genencor Int. Inc.) [21] was applied in order to simulate the impacts that coated enzymes granules experience during handling, further mixing with e.g. detergents etc. The impact gun itself consists of basically two cylindrical parts of which the outer is fixed and the inner is able to move in vertical direction thereby functioning as a piston. Fig. 5 illustrates the principle of the P.I.G. set-up.

Table 1
General operating conditions in all model experiments

Parameter	Operating conditions
Nozzle size	0.8 mm
$T_{\text{Strea-1 inlet}}$	80 °C
$T_{\text{water bath}}$	80 °C
$T_{\text{nozzle air}}$	80 °C
$T_{\text{coating solution}}$	80 °C
$T_{\text{atomisation air}}$ (heating cartridge temperature)	80 °C
Bed load	500 g
Temperature of coating liquid solution	80 °C
Desired weight gain of granules	20 wt./wt.%
Amount of binder (dextrin) in coating solution	1 wt./wt.%
Fluidisation velocity (U) (adjustable parameter)	To be varied (always at $T_{\text{Strea-1 inlet}}$, 1 bar)
Nozzle pressure (Pn) (adjustable parameter)	To be varied
Coating solution salt concentration (Cs) (adjustable parameter)	To be varied
Bed temperature (Tb) (dependent parameter)	To be varied

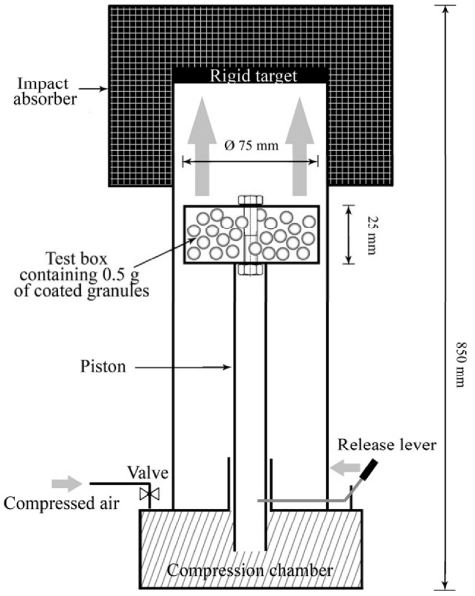

Fig. 5. Schematic illustration of the Pneumatic Impact Gun.

The test box was loaded with the precisely weighed granules sample of 0.5 g (m_{sample}) into a small stainless steel box which again was placed on top of the piston connected to the compression chamber. By building up a pressure in the compression chamber using compressed air it was possible, by pulling a release lever, to let the piston and test box travel in vertical direction and impact a rigid target at a velocity of 10 m/s. For each coated granule sample, the impacts were repeated ten times and the box contents were afterwards sieved on an electrical shaker for 1 min using an especially designed stainless steel sieve having orifices with diameters of 180 μm. The choice of 10 m/s and 10 repetitions was chosen to resemble handling conditions in typical detergent manufacturing processes [2]. Based on microscopy analysis of coated particle size fractions below 180 μm it was observed that such minor fractions consisted of fractured daughter pieces and peeled-off coating layer parts whereas size fractions above this level consisted primarily of coated granules. Hence, the demarcation of dust and coated particles seemed reasonable in terms of the 180 μm sieve and the amount of the created dust fraction with diameters below 180 μm ($m_{dust\ created}$) was thereby considered an indication of the impact strength expressed as a breakage percentage $Y_{Breakage}$ according to Eq. (E.2).

Instead of just choosing a fixed number of P.I.G. tests for each batch and then find the average $Y_{Breakage}$ value, the number of P.I.G. tests to be conducted was determined by the variance. A variance of 0.00040 was set as the maximum allowed variance estimated as a reasonable low variance from initial tests. Hence, if for a given batch the variance among the breakage percentages from the P.I.G. tests was below 0.00040,

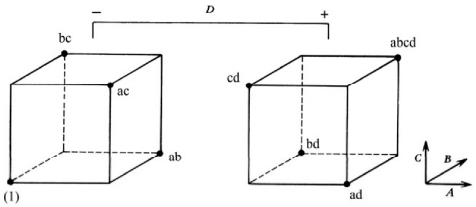

Fig. 6. The formal set-up of the 2^{4-1} fractional factorial design [5].

an average value was found. Otherwise further P.I.G. tests for the given batch were conducted until the variance came below the maximum limit. A minimum of three P.I.G. experiments was performed for each coated batch.

2.2.3. Secondary apparatus

Visual microscopy analysis was performed using an Olympus KL 1500 LCD microscope. Viscosity analysis of the coating solution at different temperatures was determined using a Rheotec Falling Ball KF10 viscometer and SEM pictures were taken using a JEOL Scanning Electron Microscope. A Micromeritics Autopore II 9220 mercury intrusion/extrusion porosimeter was used for the determination of pore sizes and porosity measurements, and Malvern Mastersizer 2000 was used to determine granule size distributions.

2.3. Experimental design and analysis of results

An unreplicated double 2^{4-1} fractional factor design [5] was used to arrange the combinations of the four screened parameters (fluidisation velocity (U), atomisation pressure (Pn), coating solution salt concentration (Cs) and bed temperature (Tb)). The design was double in the sense that for each factor combination, a value of $Y_{Breakage}$ and %Agglomeration was determined using Eqs. (E.2) and (E.1) respectively. The principle set-up of the 2^{4-1} design can be seen in Fig. 6 and Table 2. The coded and actual values of the investigated parameters are illustrated in Table 3.

The software Design-Expert® 6.0.6 (Stat-Ease Corporation, US) was used to fit polynomials to the responses and to draw the normal plots. SAS JMP® 5.0.1 was used for further statistical

Table 2
The formal set-up of the 2^{4-1} fractional factorial design [5]

Run	Basic 2^3 design			D=ABC	Treatment combination
	A	B	C		
1	−	−	−	−	(1)
2	+	−	−	+	ad
3	−	+	−	+	bd
4	+	+	−	−	ab
5	−	−	+	+	cd
6	+	−	+	−	ac
7	−	+	+	−	bc
8	+	+	+	+	abcd

Table 3
The four parameters and their high and low levels to be tested in the double unreplicated 2^{4-1} fractional factor design

	Actual values		Coded values	
Factor	Low	High	Low	High
A (*U*)	1.35 m^3/min	1.77 m^3/min	−1	1
B (Pn)	1.5 bar	3.0 bar	−1	1
C (Cs)	10 wt./wt.%	30 wt./wt.%	−1	1
D (Tb)	45 °C	55 °C	−1	1

A nozzle pressure of 1.5 bar corresponds to an airflow velocity through the nozzle of 42 L/min giving an average liquid droplet size of approximately 31 μm. For a nozzle pressure of 3.0 bar the corresponding value for the nozzle airflow is 65 L/min giving an average liquid droplet size of approximately 8 μm.

treatment of the ANOVA (analysis of variance) data associated with the resulting models.

3. Results and discussion

3.1. Effect of screened process and formulation variables

The experimental parameter combinations and corresponding response values of the impact strength and agglomeration percentage are summarised in Table 4. First order polynomials and first order interaction terms were fitted to the response. From a normal plot of the agglomeration data in Fig. 7 it was seen that for the given fractional factor design only the nozzle pressure (*B*) and the coating-solution–salt-concentration (*C*) and their first order joint term (*B*·*C*) were significant terms. In fact these three terms accounted for more than 99.7% (R^2=0.9976) of the variation of the data set. It seemed thereby reasonable to base a regression model solely on these three terms. Consequently, the agglomeration percentage regression equation was obtained in coded units according to Eq. (E.3)/(E.4) and in real physical units according to Eq. (E.5). According to the ANOVA statistics for the model as such, Prob>*F* was less than 0.0001. Although being very simple this model does in fact describe the experimental data quite well as can be seen from Fig. 8. According to Eq. (E.5) the lowest degree of agglomeration should result from conditions in which the nozzle pressure as well as the coating solution–salt concentration are as high as possible. This seems reasonable since coating droplets produced at the nozzle outlet will decrease in size with increasing nozzle pressure [6,7]. Smaller droplets combined with the fact that there is less solvent in each droplet to be evaporated with increasing coating solution–dry matter contents mean all in all that the coating liquid droplets will remain wet for a shorter time, which again reduces the chance of agglomeration.

Similar to the agglomeration model, an impact strength model was set up based on the data from Table 4. This time however, no interaction terms were found to have significant importance, as only the first order terms of nozzle pressure (*B*), coating solution salt concentration (*C*) and the bed temperature (*D*) were the parameters to have significant importance regarding the impact strength. This can be seen from the normal plot in Fig. 9. These three terms accounted for around 94.6% (R^2=0.9461) of the variation of the data set. Analogously, the impact strength model in coded values was found according to Eq. (E.6)/(E.7) and in real physical units according to Eq. (E.8). For the model as such, ANOVA statistics stated that Prob>*F* was less than 0.0053. Again good fitting to

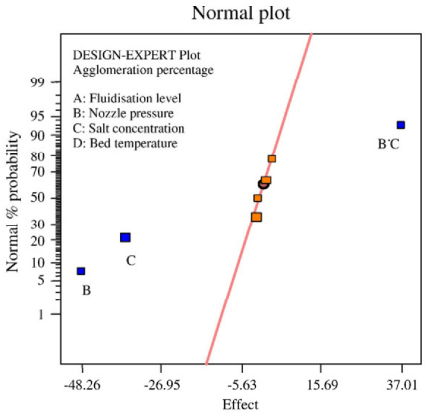

Fig. 7. Normal plot of the agglomeration percentage responses.

Table 4
Agglomeration percentage and breakage percentage responses for the eight model experiments in the double unreplicated 2^{4-1} fractional factor design

Run	*A*	B	C	D	%Agglomeration (response 1)	$Y_{Breakage}$ (response 2)
1	−1	−1	−1	−1	83.1%	14.7%
2	1	−1	−1	1	89.8%	12.7%
3	−1	1	−1	1	0.5%	10.8%
4	1	1	−1	−1	1.9%	13.9%
5	−1	−1	1	1	12.1%	8.4%
6	1	−1	1	−1	13.7%	12.4%
7	−1	1	1	−1	1.4%	8.8%
8	1	1	1	1	1.9%	4.5%

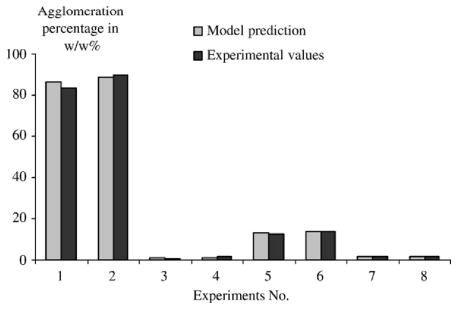

Fig. 8. Model descriptions of agglomeration percentages versus the experimentally determined data.

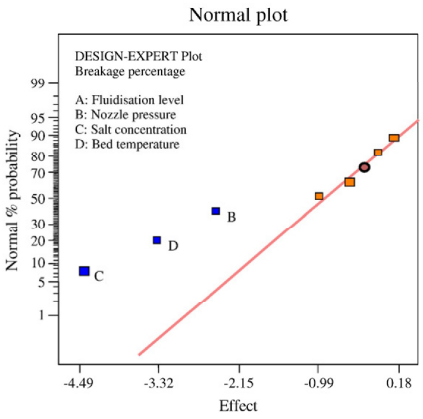

Fig. 9. Normal plot of the impact strength responses.

the experimental data can be observed in Fig. 10 although the model is quite simple.

The impact strength model predictions seem interesting as the highest impact strength according to Eq. (E.8) should be obtained under coating conditions where all three terms are as large as possible. Although not being directly comparable, results by Beekman [8] and Jørgensen et al. [2] indicate that high granule impact strength is often closely related to the morphology of the coating layer, as homogenous and smooth coating layers often tend to have the highest impact strength. According to studies by Link and Schlünder [9] the smoothness of coated alumina spheres improves with dilution of, in their case, a $Ca(OH)_2$ coating solution. The present impact strength results are thereby somewhat in opposition to the previously reported tendencies. The situation in the present studies is, however, different as the sodium sulphate cores have far larger average pore diameters than the alumina spheres used by Link and Schlünder [9]. This was further investigated in morphology and droplet penetration studies.

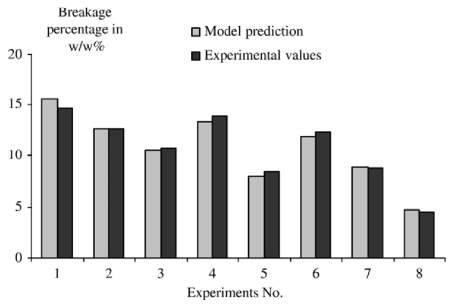

Fig. 10. Model descriptions of $Y_{Breakage}$ values versus the experimentally determined data.

3.2. Morphology and droplet penetration studies

In order to study the coating of a porous core material in detail, a number of additional experiments were conducted where colour agents were added to the coating solution and the coating operation was performed under process conditions according to Table 5. Visual microscopy analysis of the coated sodium sulphate cores was conducted. Fig. 11A and B show cut-through examples of coated granules. It can be observed from these figures that the level of droplet penetration is significant as the coloured coating solution has penetrated far into the core material in both cases. Rough calculations of the droplet drying time using the empirical Eq. (E.9) [10] and the time of droplet penetration using the Eq. (E.10) derived from theoretical droplet considerations [11–13] indicate in accordance with the visual microscopy analysis that the time of penetration is a hundred to a thousand times faster than the coating droplet drying time. The diameter of droplets produced from pneumatic nozzles was calculated with the use of the semi-empirical Eq. (E.11) [14,15]. According to Eq. (E.10), the time of droplet penetration is directly proportional to the coating liquid viscosity. Hence it seems reasonable to expect that the level of droplet penetration decreases with increasing coating liquid viscosity. This was tested in a number of additional coating operations in which Sicovit Patent blue was used in amounts of 0.3 wt./wt.% and CMC was added to the coating solutions in different amounts as thickener in order to increase the viscosity. The data from these coating experiments can be seen in Table 6 and corresponding examples of cut-through coloured coated granules can be seen in Fig. 12. In accordance with calculations, it was seen from visual microscopy analysis that the level of droplet penetration decreased with increasing coating liquid viscosity and that the level of droplet penetration was negligible at conditions in which the coating liquid viscosity was increased to roughly 7000 mPa s (Measured using a Rheotec Falling Ball KF10 viscometer at a temperature identical to the wet bulb temperature inside the fluidised bed during processing — such high viscosity solutions clearly exhibit non-Newtonian behaviour).

Table 5
Operating conditions in additional droplet penetration/morphology experiments

Parameter	Operating conditions
Nozzle size	0.8 mm
$T_{\text{Strea-1 inlet}}$	80 °C
$T_{\text{water bath}}$	80 °C
$T_{\text{nozzle air}}$	80 °C
$T_{\text{coating solution}}$	80 °C
$T_{\text{atomisation air}}$ (heating cartridge temperature)	80 °C
Bed load	500 g
Temperature of coating liquid solution	80 °C
Desired weight gain of granules	20 wt./wt.%
Amount of binder (dextrin) in coating solution	0.3 wt./wt.%
Fluidisation velocity (U) (adjustable parameter)	Level 20 ~ 1.77 m^3/min (at $T_{\text{Strea-1 inlet}}$, 1 bar)
Nozzle pressure (Pn) (adjustable parameter)	2 bar
Coating solution salt concentration (Cs) (adjustable parameter)	From 15 to 30 wt./wt.%
Bed temperature (Tb) (dependent parameter)	50 °C

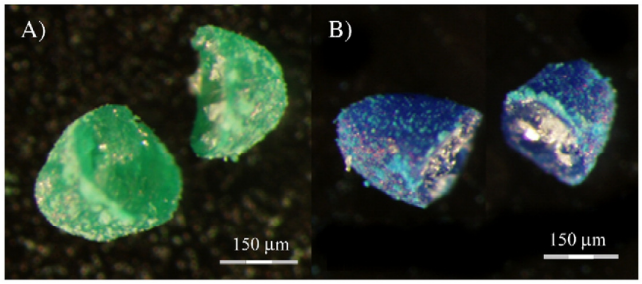

Fig. 11. Microscope pictures of: (A) cut-through profile of a coated granule using Colanyl green colour. (B) Cut-through profile of a coated granule using Patent blue colour.

An interesting thing to note from the results in Table 6 is the significant increase in viscosity of the coating solution of more than ten times from experiment γ5C to γ5F and similar from γ5B to γ5E as only the amount of Na_2SO_4 in the coating solution was changed. It seems that the increased Na_2SO_4 concentration has a salting-out effect on the CMC causing the significant increase in viscosity [16]. Visually there was a difference in solution appearance as well, as the 10 wt./wt.% solutions were slightly dim whereas the 30 wt./wt.% solutions were completely opaque.

From microscopy analysis of the coated granules in Fig. 12 it was seen that the coating surface morphology changes significantly with droplet viscosity. Whereas the coating layer is smooth and homogenous in batch γ5B with a low droplet viscosity, the surface layer becomes increasingly rough and raspberry-like when the droplet viscosity increases from batch γ5B to γ5C and further from batch γ5C to γ5F. These results are in full accordance with experiments by Link and Schlünder [9] indicating that the viscosity-affecting dry matter contents of the coating solution have a primary importance for the resulting roughness of the coating layer, independently of the porosity of the core material. This was investigated further by SEM analysis.

Fig. 13 shows SEM pictures of granules and cut-through edge profiles of coated granules from batch γ5B and γ5F. It can be seen by comparing Fig. 13A with Fig. 13B that although both coating layers are fluffy and covered with small dried droplets, the increase in coating liquid viscosity from Fig. 13A to B makes the coating layer flaky, stratified and inhomogeneous. There is a significant shrinkage in the coating layer in Fig. 13B as the coating liquid layer has dried first on the outer surface leaving the inner layer still wet. As the inner wet layer afterwards dries by the evaporation of remaining coating liquid solvent, the inner coating layer is left as a highly porous cave-like structure, which eventually shrinks and cracks. This is further verified in Fig. 13D where a cut-through edge profile of the coating layer of a granule

Table 6
Summary of important data from additional droplet penetration/morphology experiments

Exp.	Coating solution salt concentration (Cs)	η_{liq} at 30 °C (wet bulb temperature)	d_d	τ_{drying}	τ_d	Qualitative description of the degree of colour penetration	% Agglomeration	$Y_{Breakage}$
γ4B	10.4 wt./wt.%	1.030 mPa s (0 wt./wt.% CMC)	10.8 µm	0.12 s	$6.3 \cdot 10^{-5}$ s	Deep droplet penetration. More than 3/4 of all the studied cut-through granules were all blue	21.9%	6.3%
γ5A	9.2 wt./wt.%	2.178 mPa s (1.3 wt./wt.% CMC)	11.1 µm	0.13 s	$1.4 \cdot 10^{-4}$ s	Deep droplet penetration to the same extent as observed in batch γ4B	86.9%	0.6%
γ5B	9.0 wt./wt.%	22.28 mPa s (2.7 wt./wt.% CMC)	18.8 µm	0.36 s	$4.2 \cdot 10^{-3}$ s	Considerable droplet penetration. The majority of the observed granule cores were blue while minor spots remained unaffected	90.8%	0.3%
γ5C	9.8 wt./wt.%	445.1 mPa s (5.2 wt./wt.% CMC)	65.3 µm	4.3 s	1.0 s	Limited droplet penetration, as only parts of the granule cores were blue while other spots remained white and unaffected	84.1%	1.1%
γ5D	28.1 wt./wt.%	3.183 mPa s (0 wt./wt.% CMC)	9.8 µm	0.10 s	$1.6 \cdot 10^{-4}$ s	Deep droplet penetration. All the observed cut-through granules were all blue although not as dark blue as the granules from batch γ4B and γ5A	12.1%	3.3%
γ5E	29.3 wt./wt.%	4104 mPa s (2.7 wt./wt.% CMC)	98.2 µm	9.6 s	21 s	Limited droplet penetration. Less than 1/4 of the studied cut-through granules had colour penetration into the inner half of the granule core	83.0%	0.7%
γ5F	28.9 wt./wt.%	7241 mPa s (5.2 wt./wt.% CMC)	126.0 µm	16 s	60 s	No droplet penetration in any of the observed cut-through granules. The boundary between the coating layer and the granule core was well defined. The coating layer was roughly 10 µm thick	75.1%	0.8%

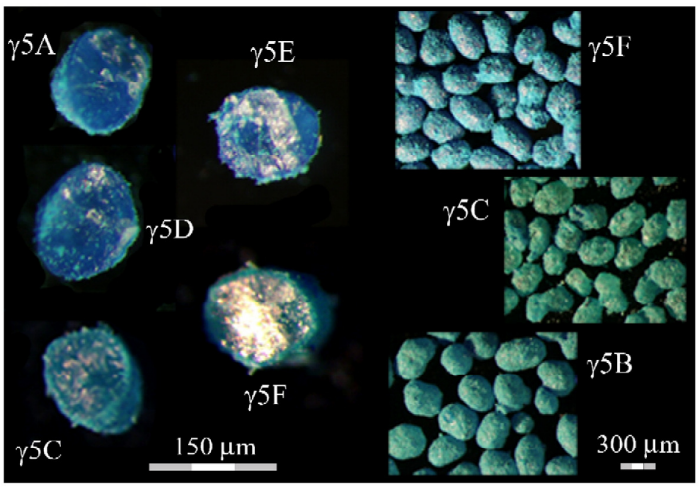

Fig. 12. Examples of microscope pictures of coated granules and coated granule cut-through profiles.

from batch γ5F is seen to be highly porous with a cave-like structure. These observations agree with experiments by Link and Schlünder [9] and results by Keningley et al. [17]. The sharp distinction between core and coating material complies fully with the results in Table 6 stating that for experiment γ5F, the time of droplet penetration is somewhat larger than the droplet drying

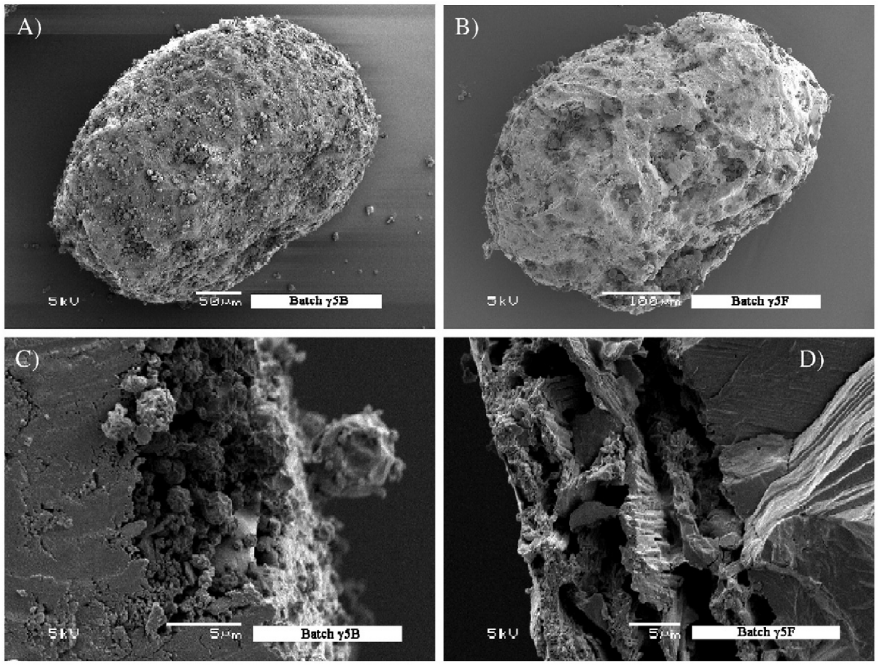

Fig. 13. Examples of SEM pictures of: (A) coated granule from batch γ5B. (B) Coated granule from batch γ5F. (C) Cut-through edge profile of coated granule from batch γ5B. (D) Cut-through edge profile of coated granule from batch γ5F.

time. Hence as expected, the majority of the coating material remains at the core surface in Fig. 13D.

The coating layer is seen to float homogeneously together in Fig. 13C showing a cut-through edge profile of a granule from batch γ5B. In accordance with the results in Table 6, a considerable amount of the coating layer is observed to have penetrated into the core material and the boundary between core and coating layer is not distinguishable. Comparing the core parts in Fig. 13C with D clearly indicates that the granule core spatial structure is highly affected by the degree of droplet penetration. In the case with high droplet penetration in Fig. 13C, the spatial core structure seems to be compressed and homogeneous whereas the original crystal core structure is clearly visible in Fig. 13D. All in all the SEM pictures in Fig. 13 are hereby seen to be in agreement with the viscosity tendencies predicted by the τ_{drying} and τ_d calculations in Table 6.

3.3. Further studies of agglomeration and granule impact strength

Besides making it possible to study the droplet penetration versus droplet drying time, the morphology/droplet penetration experiments also made it possible to study the impact strength and the degree of agglomeration as a function of droplet viscosity. As seen in Table 6, the agglomeration tendency clearly increases with increasing viscosity. Going e.g. from experiment γ4B to γ5A, the viscosity is only roughly doubled whereas the resulting agglomeration percentage increases significantly from 21.9% to 86.9%. This observation is in accordance with previous studies (e.g. by [17–19]) of the effect of viscosity changes on agglomeration, although none of the mentioned authors used as porous particles as in the present studies. As the viscosity increases the liquid coating droplets increase in size, thereby halting the droplet penetration, while at the same time the drying time increases. Besides resulting in wet coated surfaces for a longer time, the surface stickiness increases with viscosity thus providing improved adhesion between wet granules, all in all leading to increased risk of agglomeration, as observed.

Studying the impact strength values for the seven experiments in Table 6 reveals several interesting points: first of all it can be seen by comparing experiment γ4B with γ5D (in which no CMC has been added to the coating solution) that the impact strength increases with increasing salt concentration. In both cases the droplet penetration was significant. A reasonable theory is that the increased impact strength due to increasing salt concentration results from the formation of salt bridges as the droplets with a high salt concentration dry inside the capillary pores partly filling them out and providing additional strength upon evaporation of the solvent. This may happen at a low salt concentration as well, but it is expected that the volume and strength of the salt bridges increase with increasing salt concentration. This theory was partly supported by mercury intrusion/extrusion porosity analysis of granule samples from experiment γ4B and γ5D, as the average porosity of batch γ4B was determined to 19.2%, whereas the average porosity of batch γ5D only was 18.7% compared to the average porosity of 20.7% for the uncoated cores. The measured decrease in porosity may thus originate from salt bridges as suggested, although the decrease in porosity is small. Further detailed studies will have to be conducted before any definitive conclusion regarding the salt bridge theory can be verified.

Furthermore it can be seen from Table 6 that the addition of CMC has an advantageous effect on the impact strength, as the $Y_{Breakage}$ values are all very small in the batches where CMC has been added to the coating solution, compared to the $Y_{Breakage}$ values in experiment γ4B and γ5D as well as the $Y_{Breakage}$ values in Table 4. The $Y_{Breakage}$ values in Table 6 do, however, not decrease with increasing amount of CMC, as the values for experiment γ5A, γ5B, γ5C, γ5E and γ5F are not significantly different. Interestingly, this indicates that even though the coating layer is raspberry-like and rough due to high droplet viscosity, the impact strength may be even higher than for coated granules with smooth surfaces. Apparently the CMC improves the impact strength. Perhaps the long cellulose chains of the CMC act as a reinforcing impact absorber resulting in flexible and strong surfaces. This was nevertheless not tested separately.

The higher impact strengths at high coating liquid viscosity may also be explained by the fact that at high viscosity, the droplet drying times by far exceed the residence time in the fluidised bed drying zone estimated to be roughly 0.2 s on an average using the semi-empirical Eq. (E.12) in which the applied fluidisation velocities in m/s were calculated at the chamber inlet using the chamber cross-section distance of 100 mm [9,13]. Hence, in e.g. experiment γ5F it is reasonable to believe that there was a significant moisture build-up in the Na_2SO_4 cores during coating. This was partly verified by the significantly longer drying time in batch γ5F of 41 min and 38 min in batch γ5C compared to a drying time of only 11 min in experiment γ5D and 12 min in batch γ4B. According to Link and Schlünder [9] this will have a significant effect on the mechanical properties of the final coating layer. For example, the wettability and spreading of coating droplets on the core surface will be improved if the core material is slightly moisturised. Furthermore, the morphology of the final granule is highly influenced by the moisture contents, as well as it seems to improve the homogenisation of the coating layer if each new

Table 7
Parameter combinations for the validation experiments

Parameter to be varied	Exp. δ1	Exp. δ2	Exp. δ3	Exp. δ4	Exp. δ5	Exp. δ6	Exp. δ7	Exp. δ8
Fluidisation velocity	1.55 m^3/min	1.55 m^3/min	1.55 m^3/min	1.55 m^3/min	1.55 m^3/min	1.55 m^3/min	1.55 m^3/min	1.55 m^3/min
Nozzle pressure	1.0 bar	1.5 bar	2.0 bar	2.5 bar	3.0 bar	4.0 bar	1.5 bar	3.0 bar
Salt concentration	5 wt./wt.%	10 wt./wt.%	20 wt./wt.%	25 wt./wt.%	30 wt./wt.%	40 wt./wt.%	10 wt./wt.%	30 wt./wt.%
Bed temperature	55 °C	55 °C	55 °C	55 °C	55 °C	55 °C	45 °C	45 °C

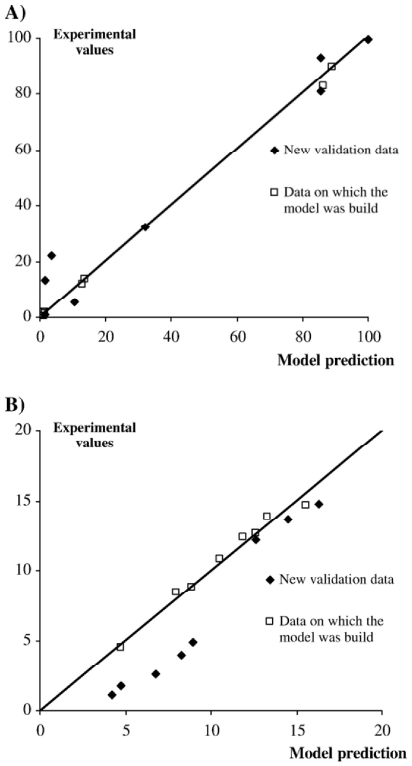

Fig. 14. Model predictions versus the experimentally determined data from the new validation experiments. (A) The agglomeration model. (B) The impact breakage model.

wet droplet impacts a surface still partially wet by older droplets not yet completely dried [9].

3.4. Model validation

The models in Eq. (E.5) and Eq. (E.8) were validated by comparing the model predictions of agglomeration tendency and impact strength with experimental data from eight new experiments with conditions according to Table 7. These parameter combinations were chosen in order to make sure that the validation process would cover a relevant and wide range for each of the three parameters (Pn, Cs and Tb). As the fluidisation velocity was not a significant term in either of the models, a value of 1.55 m^3/min was chosen for all experiments. The conditions in experiments δ1 and δ6 are both beyond the boundaries of the conditions used to derive the models. These conditions were added to the validation test in order to check the general applicability of the model equations. Except for the parameter variation according to Table 7 all other process and formulation combinations were identical to the original conditions in Table 1. Fig. 14A depicts the agglomeration model predictions compared to the experimental values from the validation series. It may be seen from this figure that although there is some slight scattering, the model does predict the degree of agglomeration well, especially inside the original model parameter space. The situation is less successful regarding the impact strength model. It can be seen from Fig. 14B that the model predicts higher impact breakage values than the experimentally determined data in all eight experiments. One reason for this could be that the model lacks certain high order parameter interaction terms. As mentioned previously, the model in Eq. (E.8) accounts for only 94.6% of the non-normality in the original $Y_{Breakage}$ data set in Table 4. The remaining part may be due to high order parameter interaction, which cannot be identified from the 2^{4-1} fractional factor design. An important point to consider is, however, that the model follows the overall $Y_{Breakage}$ tendencies quite closely. The model predicts for instance that increasing the coating solution–salt concentration and the nozzle pressure will decrease the $Y_{Breakage}$ values, and this is in fact what has been observed from the validation experiments. Satisfyingly, the model also follows the tendencies outside the model range as observed for experiments δ1 and δ6. That the lowest experimentally determined impact breakage values are associated with high nozzle pressure, high coating solution–salt concentration and high bed temperature is in full accordance with the model as well as the pore salt bridge theory discussed earlier.

4. Conclusion

Using an unreplicated 2^{4-1} fractional factor design the influence of the fluidisation velocity, nozzle pressure, coating solution–dry matter concentration and bed temperature on fluidised bed coating of Na_2SO_4 core particles was investigated. Based on data, regression models were derived being capable of quantitatively describing the degree of agglomeration and impact strength. In accordance with expectations the agglomeration model indicated decreasing agglomeration tendency with increasing coating solution–dry matter concentration and atomisation pressure. Model validations showed adequate precision inside the parameter space on which the model was derived.

The impact strength model indicated increasing impact strength with increasing coating solution–dry matter concentration, atomisation pressure as well as bed temperature. The observed impact strength tendencies were concluded to be closely associated with the high extent of coating liquid droplet penetration into the Na_2SO_4 cores. Additional experiments indicated that the coating liquid droplet penetration is significant and that this droplet penetration has a significant importance regarding the morphology of the final coated granule. It appears thereby that the porosity of a core being coated has a significant but not yet fully understood influence on the properties of the final, coated granule. A reasonable theory is that depleted coating droplets with high contents of dry matter will form solid salt bridges inside the pores of the carrier particles upon drying, and that this will improve the impact stress resistance of the final, coated granule. This theory was partly verified by porosity measurements indicating a decrease in final coated granule porosity with increasing coating solution–dry matter contents. From viscosity experiments it was observed that addition of CMC to the coating solution has a beneficial influence on the impact strength and that the

agglomeration tendency increases with increasing viscosity of the coating solution.

The validation of the impact strength model was slightly less successful, as the model in all cases predicts higher impact breakage values than the new experimental data, although the model does follow overall impact strength tendencies closely.

According to the derived models, there is no contradiction between high impact strength and low tendency of agglomeration. The models may be seen as a first step towards the design of fluidised bed processes leading to unagglomerated, coated, enzyme granules with high mechanical strength.

Nomenclature		Unit (SI system)
C_{Na_2SO4} (Cs)	Coating solution concentration of dissolved Na_2SO_4	wt./wt.%
d_d	Liquid droplet diameter	m
h_{mf}	Bed height at minimum fluidisation velocity U_{mf}	m
$m_{dust\ created}$	Amount of dust created by impact	kg
m_{sample}	Amount of sample	kg
P_{nozzle} (Pn)	Nozzle/atomising pressure	bar
q_{at}	Atomising air volumetric flow rate	m^3/s
q_{cl}	Coating liquid volumetric flow rate through the nozzle	m^3/s
r_d	Radius of droplet	m
R_{pore}	Radius of parallel capillary pores in porous media	m
T	Temperature	K
T_{bed} (Tb)	Bed (product) temperature	K
U	Fluidisation velocity	m/s
U_{br}	Bubble rise velocity for a fluidised bed	m/s
U_{mf}	Minimum fluidisation velocity	m/s
U_s	Superficial gas velocity	m/s
V_d	Droplet volume	m^3
X	Coded parameter	Dimensionless
$Y_{Breakage}$	Breakage percentage parameter	Dimensionless
Greek		
ε_{pmsp}	Porous media surface porosity (void fraction)	%
γ_{cl}	Coating liquid surface tension	N/m
γ_{lv}	Interfacial tension between liquid and vapour	N/m
Θ	Contact angle	°
η_{cl}	Coating liquid viscosity	mPa s
η_{liq}	Liquid (binder/coating) viscosity	kg/m s
ρ_{cl}	Coating liquid density	kg/m^3
τ_c	Average particle circulation time	s
τ_d	Droplet penetration time	s
τ_{drying}	Droplet drying time	s
$\tau_{res,dry}$	Residence time in the drying zone	s
v_{rel}	Relative velocity between nozzle and fluidisation air	m/s

Acknowledgements

This project was performed in collaboration with Novozymes A/S, who also financially supported the project. The author is a member of the Novozymes Bioprocess Academy as well as the MP_2T Graduate School in Chemical Engineering at the Department of Chemical Engineering, Technical University of Denmark.

Appendix A. Equations

$$\%\ \text{Agglomeration} = \frac{\text{amount of coated bed load with } d_g > 355/\mu\text{m } [g]}{\text{total coated bed load } [g]} \cdot 100\% \tag{E.1}$$

$$Y_{Breakage} = \frac{m_{dust\ created}}{m_{sample}} \cdot 100\% \tag{E.2}$$

$$\%\ \text{Agglomeration} = 25.55 - 24.13 \cdot X_B - 18.27 \cdot X_C + 18.50 \cdot X_B X_C \tag{E.3}$$

$$X_B = \frac{\text{Nozzle pressure in bar} - (1.5\ \text{bar} + 3.0\ \text{bar})/2}{(3.0\ \text{bar} - 1.5\ \text{bar})/2} \text{ and}$$
$$X_C = \frac{Na_2SO_4\ \text{conc. in w/w\%} - (10\ \text{w/w\%} + 30\ \text{w/w\%})/2}{(30\ \text{w/w\%} - 10\ \text{w/w\%})/2} \tag{E.4}$$

$$\begin{aligned}\%\ \text{Agglomeration} = {} & 245.5 - 81.5\ \text{bar}^{-1} \cdot P_{nozzle} \\ & - 7.4\ \text{w/w\%}^{-1} \cdot C_{Na_2SO_4} \\ & + 2.5\ \text{bar}^{-1}\ \text{w/w\%}^{-1} \cdot P_{nozzle} \cdot C_{Na_2SO_4} \\ & \text{where } P_{nozzle} \in \{1.5\ \text{bar}; 3.0\ \text{bar}\} \\ & \text{and } C_{Na_2SO_4} \in \{10\ \text{w/w\%}; 30\ \text{w/w\%}\}.\end{aligned} \tag{E.5}$$

$$Y_{Breakage} = 10.77 - 1.28 \cdot X_B - 2.24 \cdot X_C - 1.66 \cdot X_D \tag{E.6}$$

$$X_B = \frac{\text{Nozzle pressure in bar} - (1.5\ \text{bar} + 3.0\ \text{bar})/2}{(3.0\ \text{bar} - 1.5\ \text{bar})/2} \text{ and}$$
$$X_C = \frac{Na_2SO_4\ \text{conc. in w/w\%} - (10\ \text{w/w\%} + 30\ \text{w/w\%})/2}{(30\ \text{w/w\%} - 10\ \text{w/w\%})/2} \text{ and}$$
$$X_D = \frac{\text{Bed temp. in °C} - (45\ °\text{C} + 55\ °\text{C})/2}{(55\ °\text{C} - 45\ °\text{C})/2} \tag{E.7}$$

$$Y_{\text{Breakage}} = 35.7 - 1.7\ \text{bar}^{-1} \cdot P_{\text{nozzle}} - 0.2\ \text{w/w\%}^{-1} \cdot C_{Na_2SO_4} - 0.3°\text{C}^{-1} \cdot T_{\text{bed}}$$
$$\text{where } P_{\text{nozzle}} \in \{1.5\ \text{bar};\ 3.0\ \text{bar}\},$$
$$C_{Na_2SO_4} \in \{10\ \text{w/w\%}; 30\ \text{w/w\%}\}$$
$$\text{and } T_{\text{bed}} \in \{45°\text{C}; 55°\text{C}\}. \quad \text{(E.8)}$$

$$\tau_{\text{drying}} = 0.001s \cdot \left(\frac{d_{\text{d}}}{1\mu m}\right)^2 \quad \text{(E.9)}$$

$$\tau_{\text{d}} = \frac{2V_{\text{d}}^2}{\pi^2 \varepsilon_{\text{pmsp}}{}^2 r_d^4 R_{\text{porc}}} \frac{\eta_{\text{liq}}}{\gamma_{\text{lv}} \cdot \cos\Theta} \quad \text{(E.10)}$$

$$d_{\text{d}} = \frac{585 \cdot 10^3 \cdot \sqrt[3]{\gamma_{\text{cl}}}}{v_{\text{rel}} \sqrt{\rho_{\text{cl}}}} + 597 \cdot \left(\frac{\eta_{\text{cl}}}{\sqrt{\gamma_{\text{cl}} \cdot \rho_{\text{cl}}}}\right)^{0.45} \left(\frac{1000 \cdot q_{\text{cl}}}{q_{\text{at}}}\right)^{1.5} \quad \text{(E.11)}$$

$$\tau_{\text{res,dry}} \approx \tau_c = \frac{h_{\text{mf}}}{0.6 \cdot (U_{\text{s}} - U_{\text{mf}}) \cdot [1 - (U_{\text{s}} - U_{\text{mf}})/U_{\text{br}}]}, \quad \text{(E.12)}$$

at high fluidisation velocities.

References

[1] H. Härkönen, M. Koskinen, P. Linko, M. Siika-aho, K. Poutanen, Granulation of enzyme powders in a fluidized bed spray granulator, Lebensmittel-Wissenschaft und -Technologie 26 (1993) 235–241.

[2] K. Jørgensen, P. Bach, A.D. Jensen, Impact and attrition shear breakage of enzyme granules and placebo particles—application to particle design and formulation, Powder Technology 149 (2004) 157–167.

[3] O.P. Rubino, Fluid-bed technology. Overview and criteria for process selection, Pharmaceutical Technology (23) (1999) 104–117.

[4] E. Teunou, D. Poncelet, Batch and continuous fluid bed coating—review and state of the art, Journal of Food Engineering 53 (2002) 325–340.

[5] D.C. Montgomery, Design and Analysis of Experiments, 4th Edition, John Wiley & Sons Inc., NY, 1997.

[6] B. Guignon, A. Duquenoy, E.D. Dumoulin, Fluid bed encapsulation of particles: principles and practice, Drying Technology 20 (2002) 419–447.

[7] K. Dewettinck, W. Messens, L. Derro, A. Huyghebaert, Agglomeration tendency during top-spray fluidized bed coating with gelatin and starch hydrolysate, Lebensmittel-Wissenschaft and Technologie 32 (1999) 102–106.

[8] Beekman, W.J.: Measurement of the mechanical strength of granules, PhD Thesis, Technische Universiteit Delft, 2000.

[9] K.C. Link, E.U. Schlünder, Fluidized bed spray granulation. Investigation of the coating process on a single sphere, Chemical Engineering and Processing 36 (1997) 443–457.

[10] W.C. Hinds, Aerosol Technology. Properties, Behaviour and Measurement of Airborne Particles, 2nd Edition, John Wiley & Sons Inc., New York, 1999.

[11] M. Denesuk, G.L. Smith, B.J.J. Zelinski, N.J. Kreidl, D.R. Uhlmann, Capillary penetration of liquid droplets into porous materials, Journal of Colloid Interface Science 158 (1993) 114–120.

[12] M. Denesuk, B.J.J. Zelinski, N.J. Kreidl, D.R. Uhlmann, Dynamics of incomplete wetting on porous materials, Journal of Colloid Interface Science 168 (1994) 141–151.

[13] Hede, P.D.: Fluid bed coating and granulation, Master Thesis, Department of Chemical Engineering, CHEC Research Center, Technical University of Denmark, 2005.

[14] K. Masters, Spray Drying Handbook, 4th Edition, Halsted Press, London, 1985.

[15] Dewettinck, K.: Fluidized bed coating in food technology: process and product quality, PhD Thesis, University of Gent, 1997.

[16] T. Nakano, H. Yuasa, Y. Kanaya, Suppression of agglomeration in fluidized bed coating. III. Hofmeister series in suppression of particle agglomeration, Pharmaceutical Research 10 (1999) 1616–1620.

[17] S.T. Keningley, P.C. Knight, A.D. Marson, An investigation into the effects of binder viscosity on agglomeration behaviour, Powder Technology 91 (1997) 95–103.

[18] Abbott, A.: Boundary between coating and granulation, Master Thesis, Department of Chemical Engineering, The University of Queensland, 2002.

[19] S.H. Schaafsma, P. Vonk, P. Segers, N.W.F. Kossen, Description of agglomerate growth, Powder Technology 97 (1998) 183–190.

[20] GEA, Aeromatic-Fielder Strea-1 brochure, Niro Pharma Systems, GEA Powder Technology Division, 2005.

[21] Genencor International Inc., Pneumatic impact gun equipment manual, 2003.

ELSEVIER

Chemical Engineering Science 63 (2008) 815–828

Chemical Engineering Science

www.elsevier.com/locate/ces

Validation of the flux number as scaling parameter for top-spray fluidised bed systems

Peter Dybdahl Hede[a,b], Poul Bach[b], Anker D. Jensen[a,*]

[a]*Department of Chemical Engineering, CHEC Research Center, Technical University of Denmark, Building 229, DK-2800 Kgs. Lyngby, Denmark*
[b]*Solid Products Development, Novozymes A/S, Smørmosevej 11, DK-2880 Bagsværd, Denmark*

Received 1 June 2007; received in revised form 15 October 2007; accepted 15 October 2007
Available online 22 October 2007

Abstract

Top-spray fluidised bed coating scale-up experiments have been performed in three scales in order to test and validate the Akkermans flux number as possible scale-up parameter. Coating operations were performed on low porosity sodium sulphate cores (180–350 μm) coated with aqueous solutions of Na_2SO_4 using Dextrin as binder in three top-spray fluidised bed scales, i.e. a small-scale (type: GEA Aeromatic-Fielder Strea-1), medium-scale (type: Niro MP-1) and large-scale (type: GEA MP-2/3). Following the parameter guidelines adapted from the original patent description, the flux number was tested in the preferred range of 3.5–4.5 as well as with a value of 4.7 in a total of 24 experiments. The agglomeration tendency was observed to decrease with increasing flux number on an overall basis, but coating conditions with flux number values below 4.5 resulted in a complete collapse of the bed. Coating conditions with flux number values of 4.5 and 4.7 were however successful in terms of agglomeration tendency and match of particle size fractions, but indicated in addition a strong influence of nozzle pressure. The present paper suggests even narrower boundaries for the flux number compared to the patent descriptions, and adds further new guidelines for the successful scale-up of top-spray fluidised bed coating systems in terms of the flux number.

Keywords: Fluidised bed; Scale-up; Flux number; Coating; Granulation

1. Introduction

Many types of biological ingredients are formulated into solid products by spraying the concentrate onto inactive filler cores in a fluidised bed. The desired product consists thereby of unagglomerated individual carrier particles each coated homogeneously with a layer of the active ingredient. If formulation or process conditions are incorrectly chosen, either excessive agglomeration or excessive spray drying of the feed may happen (van Ee et al., 1997). In both cases a poor product quality is achieved, and in any case, control of agglomeration is essential during scale-up.

Often product and process properties are optimised in small- and medium-scale fluidised beds and then transferred to production-scale. The scale-up of a fluidised bed granulation process requires decisions to be made at many levels, including: fixed parameters (e.g. nozzle and fluidisation chamber dimensions), parameters related to the core material (such as porosity, sphericity and more), coating solution (e.g. viscosity, surface tension, contact angle and more) and the type of fluidised bed, input parameters, operating conditions including spraying and fluidisation conditions as well as processing time, etc. With such a variety of interlinked parameters and properties, combined with a general lack of fundamental understanding of the granulation process, it is obvious that scale-up of a fluidised bed granulation process is a challenging task (Hede et al., 2007a).

Fluidised bed scaling principles at the macro-scale level have been studied intensively for fluidised catalytic cracking regenerators and bubbling fluidised beds for more than 30 years (Glicksman et al., 1993; Schouten et al., 1996). A typical macro-scale approach determines desired conditions over a range of dimensionally similar unit operations typically using well-known dimensionless groups as Froude number, Stokes number, Reynolds numbers and Power numbers (Mort, 2005; Knowlton et al., 2005). In addition, several other dimensioned

* Corresponding author. Tel.: +45 4525 2841; fax: +45 4588 2258.
E-mail address: aj@kt.dtu.dk (A.D. Jensen).

0009-2509/$ - see front matter © 2007 Elsevier Ltd. All rights reserved.
doi:10.1016/j.ces.2007.10.017

parameters or parameter groups are used, including specific energy input and excess gas fluidisation velocity, etc. These operation parameters typically affect multiple product transformations, and the challenge is to scale-up the equipment in a way that maintains key product attributes while at the same time achieves an industrially efficient operation (Mort, 2005).

Scale-up attempts based on the dimensionless parameters rely typically on analogies in the hydrodynamic behaviour of the flow regimes in the fluidised beds, and especially on proper description of the bubble hydrodynamics. A number of the classical hydrodynamic scaling expressions and so-called *scaling laws*, based on the superficial gas velocity and minimum fluidisation velocity, may be found for bubbling fluidised beds in Ellenberger and Krishna (1994) and Werther (1980). Horio et al. (1986) developed a rule of hydrodynamic similarity for a scale change of fluidised beds based on the governing equations of bubble and interstitial gas dynamics. Similar scaling laws by Glicksman (1984, 1988) proposed a full set of scaling relationships by non-dimensionalising the equations of motion for the particles and the fluid phase in a fluidised bed along with their boundary conditions, using the length from the air distributor plate to the fluidisation chamber exhaust exit, L_{bed}, as a typical length dimension.

Macro-level scaling laws, as the above presented, do not normally take interparticle forces in fluidised beds into account. They also typically omit any influence of the particle coefficient of restitution as well as the influence of frictional forces (Glicksman et al., 1993). What is even more critical is that the scaling principles completely neglect any influence from the sprayed liquid phase. This means that scaling principles developed for pure gas–solid systems, such as e.g. fluidised bed combustors, cannot be applied alone for fluidised bed coating or agglomeration processes, as the liquid phase is known to be of utmost importance for the control of the process. A fluidised bed system involving all three phases of solid, liquid and gas is more complicated than a fluidised bed having only a solid and a gas phase, and thus new principles for scale-up of agglomerating and coating fluidised beds must be used.

Scaling up of coating fluidised bed processes is a common industrial exercise and traditionally the field has not had much academic interest. As reviewed by Hede (2006) advances in scaling principles are often done in industry and typically only reach the public in the form of patents. Recent scientific articles by e.g. Rambali et al. (2003), Mehta (1988), Boerefijn and Hounslow (2005) and Hede et al. (2007a) indicate some progress in the field although the scale-up procedures are somewhat different. Mort (2005) suggests that scale-up of the wet-granulation process should focus on combined particle-level and unit-operation level properties and parameters. Results by Hede et al. (2007a) follow these trends by suggesting scale-up in terms of a drying force and a relative droplet parameter. These principles focus especially on temperature and humidity conditions as well as on nozzle conditions. Although promising there are also limitations to the application of these scale-up principles. The flux number by Akkermans et al. (1998) is a different approach as the primary focus here is on particle density, gas velocities, spray area and liquid binder distribution on an overall scale. The flux number combines these parameters into a single dimensionless parameter claimed to govern the overall possible outcome during wet-granulation in fluidised beds. Based on the flux number, Boerefijn and Hounslow (2005) provide a domain-map for coating, agglomeration and wet-quenching regimes which may be seen from Fig. 1.

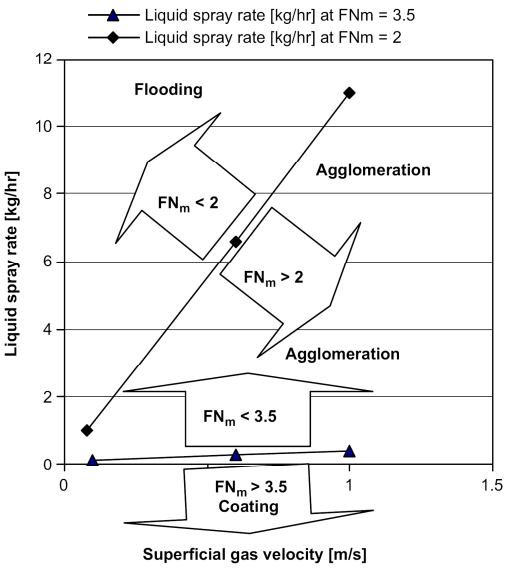

Fig. 1. Domain-map for wet-quenching (flooding), agglomeration and coating regimes based on values of the flux number (Boerefijn and Hounslow, 2005).

Although the flux number is claimed by Boerefijn and Hounslow (2005) to be a commonly accepted suitable descriptor of the balance between the flux of solids in the spray zone and the spray flux that wets the solids, no experimental evidence has been presented in detail so far in the open literature. It is the aim of this paper to provide a systematic experimental validation of the flux number as scaling parameter for top-spray fluidised bed coating systems.

1.1. The dimensionless flux number FN_m

A series of International Patent Classifications by Unilever Research concerns the use of a flux number in the process of top-spray fluidised bed production of detergent granules. The flux number and the expressions for the associated parameters are adapted from Akkermans et al. (1998). The flux number is expressed according to the following equation:

$$\mathrm{FN}_m = \log\left[\frac{\rho_p \cdot U_e}{\dot{q}_{m\mathrm{liq}}}\right], \tag{1}$$

where ρ_p is the particle density determined according to the following equation:

$$\rho_p = \frac{BD}{1-\varepsilon_{\text{bed}}}, \tag{2}$$

in which BD is the bulk density of the powder and ε_{bed} is the bed porosity determined by e.g. mercury porosimetry. The parameter $\dot{q}_{m\text{liq}}$ is the spray mass flux in kg/(s m^2) at a normalised distance D_0 from the nozzle outlet, and U_e is the excess gas velocity in m/s determined in the usual way as the difference between the superficial gas velocity U_s and the minimum fluidisation velocity U_{mf} shown in the following equation:

$$U_e = U_s - U_{mf}. \tag{3}$$

Preferably U_s is determined at the position in the fluidisation chamber corresponding to the bed height H_{bed}. Similarly, the gas velocity at minimum fluidisation U_{mf} is measured at the height of the bed at minimum fluidisation H_{mf}.

If a discernible bed is apparent then H_{bed} can be measured directly but often the bed height H_{bed} cannot easily be determined as the degree of turbulence in the cloud of fluidised particles will be so high that no discernible bed will be formed. This is often the case with bubbling fluidisation as is the case with the materials and particle sizes processed in the experiments in this paper. As an estimate when no discernible bed is formed, H_{bed} may be calculated from the following equation (Akkermans et al., 1998):

$$H_{\text{bed}} = 1.67 \cdot H_{mf}. \tag{4}$$

Having determined the H_{bed} and the H_{mf} it is possible to determine the so-called normalised length D_0 from the expression in Eq. (5). D_0 thereby has the units of metres although being referred to in the original Akkermans et al. (1998) patent description as a normalised length.

$$D_0 = H_{\text{nozzle}} - H_{\text{bed}}. \tag{5}$$

H_{nozzle} is the height of the spray nozzle above the bottom of the fluidisation chamber. If D_0 is 15 cm or less then D_0 is taken as 15 cm for purposes of determining the contact area A. This is because for practical purposes it has been found that the mean penetration of the spray for a nozzle situated below or within the cloud of solids is about 15 cm. The contact area A is the contact area wetted by the spray in a horizontal plane situated at D_0 below the nozzle. The value of A must be determined in terms of experiments or by simple calculations based on known spray angles. In the present paper, the contact area A was found by first determining the nozzle outlet spray angle by photo analysis at the given nozzle pressure, and then simply calculate the wetted area at the distance of D_0 assuming full-cone spray characteristics. The area A is used to determine the liquid mass flux $\dot{q}_{m\text{liq}}$ according to the following equation:

$$\dot{q}_{m\text{liq}} = \frac{Q_{m\text{liq}}}{A}, \tag{6}$$

where $Q_{m\text{liq}}$ represents the mass flow of liquid applied.

According to the invention by Akkermans et al. (1998), the value of FN_m must be such that FN_m is at a value above 2 and preferably at least 3 for a major proportion of the process time (at least 30% but preferably around 95%). FN_m should never exceed a value of 6 and preferably not exceed 4.5. According to the patent description, U_s should be preferably in the range of 0.8–1.2 m/s and $\dot{q}_{m\text{liq}}$ at least 0.15 kg/(s m)^2, preferably in the range of 0.20–1.5 kg/(s m)^2.

A Proctor & Gamble patent by Wasserman et al. (2000) states, in accordance with Akkermans et al. (1998), that the fluidised bed operation conditions should be such that FN_m preferably is from 3.5 to 5. In addition to the flux number specification, the patent by Wasserman et al. (2000) states that coating conditions should be met in order for the Stokes number St to be greater than 10, more preferably in the range of 100–1000. The Stokes number is a measure of particle coalescence for describing the degree of mixing occurring in an equipment such as the fluidised bed, and the number is defined analogously to the original viscous Stokes number by Ennis et al. (1991) according to the following equation (Wasserman et al., 2000; Achanta and Beimesch, 1999):

$$St = \frac{4 \cdot \rho_g \cdot d_{\text{particle}} \cdot U_e}{9 \cdot \eta_{\text{liq}}}, \tag{7}$$

where η_{liq} is the liquid binder viscosity, ρ_g is the apparent granule density, d_{particle} is the mean particle diameter and U_e is the excess gas velocity. More fundamental information about the Stokes number may be found in Ennis et al. (1991) and Iveson et al. (2001) whereas a full derivation of Eq. (7) may be found in Hede (2005). A Proctor & Gamble patent by Achanta and Beimesch (1999) further explains the usefulness of the Stokes number in the context of producing detergent granules stating that the Stokes number should be less than 1 in order for the fluidised bed system to start to agglomerate.

2. Experimental

2.1. Fluidised bed equipment

In the effort to test the flux number as a possible scaling parameter three different fluidised bed set-ups were used. All three were top-sprayed fluidised beds each having a single external-mixing two-fluid nozzle similar to the simple two-substance 970-series nozzles manufactured by Düsen–Schlick GmbH (Germany), thereby following the nozzle design guidelines insinuated by the patent by Akkermans et al. (1998). In all three cases, a liquid orifice diameter of 1.2 mm was used. Likewise, the coating liquid feed was in each case led from an external heated reservoir at a constant temperature of 60 °C to the nozzle through an adjustable peristaltic tube pump. A sketch of the general set-up in each of the three fluidised bed systems may be seen from Fig. 2.

The small-scale fluidised bed was a modified GEA Aeromatic-Fielder Strea-1 top-spray fluidised bed with a stainless steel fluidisation chamber of 12 L allowing a particle bed load of 500 g to be fluidised. A detailed picture of the

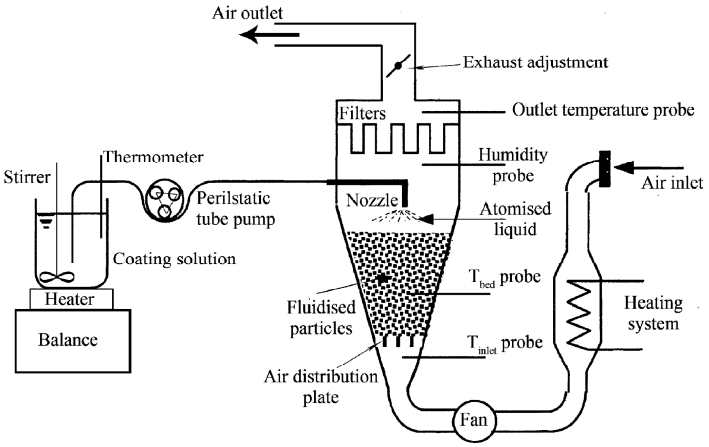

Fig. 2. Sketch of the general top-spray set-up used in all three fluidised bed scales (Hede, 2005).

modified Strea-1 set-up can be found in Hede et al. (2007a). Modification to the original vessel design made it possible to insert a digital thermometer into the fluidisation chamber wall thereby being able to measure the bed temperature between the bottom air distribution plate and the nozzle spray outlet. In addition, a humidity measurement apparatus (Testo 645 Thermohygrometer) was inserted above the nozzle allowing the relative humidity in the fluidisation chamber to be measured. The vertical position of 15 cm above the nozzle outlet and a horizontal probe depth of 12 cm were carefully chosen in order not to let the humidity measurements be directly affected by the nozzle spray outlet. Custom-made reusable stainless steel filters were inserted in the top of the fluidisation chamber in order to prevent particles and spray-dried coating droplets from being exhausted. The back-flush option in the Strea-1 set-up was switched on allowing the filters to be flushed every 60 s.

The medium-scale top-spray fluidised bed was a standard Niro-Aeromatic Multiprocessor type MP-1. It had a stainless steel fluidising chamber of 16 L allowing a particle bed load of 4000 g, thereby being eight times larger in capacity than the Strea-1. A detailed picture of the MP-1 set-up can be found in Hede et al. (2007a). As for the Strea-1 set-up, it was possible to measure the bed temperature between the bottom air distribution plate and the nozzle outlet. The same humidity measurement apparatus (Testo 645 Thermohygrometer) was inserted 28 cm above the nozzle outlet at a horizontal depth of 14 cm allowing the relative humidity in the fluidisation chamber to be measured. The back-flush option in the MP-1 set-up was switched on allowing the filters to be flushed every 60 s in the same way as for the small-scale set-up.

The large-scale fluidised bed was a GEA Aeromatic-Fielder MP-2/3 with a vessel volume of 60 L allowing a particle bed load of 24 kg to be processed, thereby being six times larger in capacity with respect to the MP-1 and 48 times with respect to the Strea-1 set-up. A detailed picture of the MP-2/3 set-up can be found in Hede et al. (2007a). As for the other fluidised bed scales, it was possible to measure the bed temperature between the bottom air distribution plate and the nozzle outlet. The same humidity measurement apparatus (Testo 645 Thermohygrometer) was inserted 82 cm above the nozzle outlet at a horizontal depth of 21 cm allowing the relative humidity in the fluidisation chamber to be measured. The back-flush option in the MP-2/3 was set to be identical to the other scales.

2.2. Sieve equipment

For the sieving analysis, a Retsch Sieve Shaker AS 200 control was used with a sieve stack consisting of sieves with orifice diameters of 180, 212, 250, 300, 355, 425, 500 and 600 μm. A sample of 200 g from each batch was sieved for 3 min with amplitude of 1.1 mm and the weight of each fraction was determined with the AS 200 control interface using a connected Mettler balance.

It was verified by microscope analysis of the different fractions that coated granules with diameters above 425 μm consisted of agglomerates whereas particles below this limit were primarily single coated granules. Thus, this sieve orifice diameter was set as the agglomeration limit and based on the weight of each of the fractions, an agglomeration percentage was determined for each batch according to the following equation:

$$\text{agglomeration\%} = \frac{\text{coated batch weight fraction with } d_p > 425\,\mu\text{m}}{\text{total coated batch weight}} \times 100\%. \quad (8)$$

2.3. Materials

Low porosity sodium sulphate cores (porosity fraction around 20.7% determined with Micromeritics Autopore II

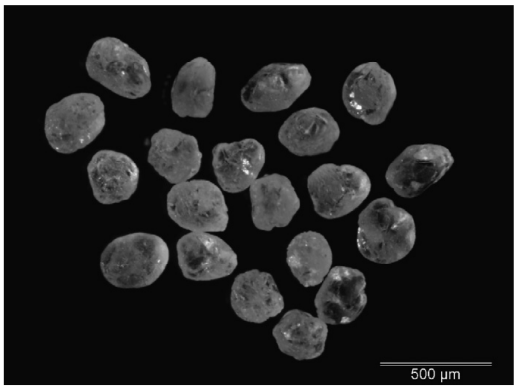

Fig. 3. Microscope picture of uncoated sodium sulphate cores used in the coating experiments (obtained with an Olympus KL 1500 LCD microscope).

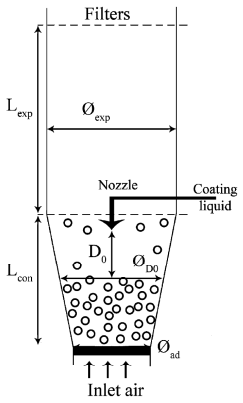

Fig. 4. Sketch of the fluidised bed dimensions for the three fluidised bed scales. The dimensions are: small-scale Strea-1: $L_{exp} = 18.0$ cm, $L_{con} = 31.0$ cm, $Ø_{exp} = 25.0$ cm, $Ø_{D0} = 17.3$ cm and $Ø_{ad} = 10.0$ cm, medium-scale MP-1: $L_{exp} = 93.0$ cm, $L_{con} = 48.5$ cm, $Ø_{exp} = 28.8$ cm, $Ø_{D0} = 21.7$ cm and $Ø_{ad} = 17.0$ cm, large-scale MP-2/3: $L_{exp} = 270.0$ cm, $L_{con} = 63.0$ cm, $Ø_{exp} = 64.0$ cm, $Ø_{D0} = 48.1$ cm and $Ø_{ad} = 27.0$ cm.

intrusion/extrusion mercury porosimetry) pre-sieved in the size range of 180–350 µm was used as core material. The sodium sulphate cores have sphericities in the range of 0.86 and microscope pictures of the sodium sulphate cores may be seen from Fig. 3.

The sodium sulphate cores were coated with aqueous solutions of sodium sulphate in the amount of 15 w/w% using 1 w/w% (of the amount of sodium sulphate) dextrin as binder. Demineralised water was used as solvent and the viscosity of the coating solution was determined to be 2.903 mPa s at 60 °C using a KF10 Rheotec Falling Ball viscometer.

2.4. Scaling procedure

In order to test the applicability of the flux number, a number of choices had to be made prior to the coating experiments. Being a dimensionless logarithmic relationship, small changes in the flux number correspond to large changes in values for vital process parameters. Furthermore, a given flux number value allow in principle (although obviously not in practice) an infinity of different values for U_e and $\dot{q}_{mliq}$ to be chosen, indicating that a given flux number value does not give the exact fluidised bed operation conditions unambiguously. Results by Hede et al. (2007b), obtained with the small-scale fluidised bed with the same type of core materials and coating solution, indicate that the actual fluidisation velocity has a minor influence on agglomeration above a certain value compared to the nozzle conditions which are of importance for the overall agglomeration tendency, irrespective of the exact values. Thus, the choice of the excess gas velocity is most likely not as important as the choice of the liquid mass flux for the given flux number. The guidelines for the parameters in the flux number provided by the Akkermans et al. (1998) patent are unfortunately quite vague allowing e.g. the value for $\dot{q}_{mliq}$ to range preferably between 0.20 and 1.5 kg/(s m)^2. This vagueness could be intentional, intended to widen the coverage and applicability of the flux number. This is unfortunate in terms of testing the scale-up parameter but may be an advantage regarding the patent coverage. The guidelines for U_s were however the narrowest and this was the starting point for the scale-up tests in the present paper. According to Section 1.1 the value for U_s in m/s should preferably be chosen in the range of 0.8–1.2 m/s, which is well within the range where the exact value is of minor importance regarding agglomeration (Hede et al., 2007b). Hence as a starting point, the value for U_s was chosen to be 1.0 m/s at the bed height H_{bed} in all three fluidised bed set-ups. Having fixed the value for U_s this also fixed the value for U_e as the value for U_{mf} for a mean particle diameter of 300 µm was determined to be 0.07 m/s with the use of a modified Ergun expression for particles above 100 µm (Kunii and Levenspiel, 1991; Teunou and Poncelet, 2002). The choice of this excess gas velocity, together with the coating formulation properties, resulted in a Stokes number being close to 900 and thereby safely within the preferred range of 10–1000, hereby following additionally the guidelines from the Achanta and Beimesch (1999) and Wasserman et al. (2000) patents for successful coating operations.

It should be noted that even though the fluidisation conditions are chosen such that the superficial gas velocity U_s at the bed height is 1.0 m/s in all three fluidised beds, this does not mean that the superficial gas velocity is identical at the air distribution plate in the bottom of the three beds. This is due to the fact that the three fluidised beds are not dimensionally consistent. As is indicated from the sketch of the dimensions of the three beds in Fig. 4, the three fluidisation chambers are quite different in shape and dimensions. The fluidised beds are thereby not dimensionally consistent according to the rules by Leuenberger (1983, 2003) stating that systems are similar when the ratio of the linear dimensions of the small-scale and the scaled-up system are constant. This is a typical issue with

different commercial fluidised bed scales as there is no general agreement on how to design the fluidisation vessels. Dimensionally consistency is however not a requirement for the use or validation of the flux number as the parameter seeks to overcome these issues by focusing on process-related parameters. Having U_s at the bed height at 1.0 m/s corresponds to gas velocities just above the air distribution plate of 2.9 m/s in the small-scale, 2.2 m/s in the medium-scale and 3.2 m/s in the large-scale. The volumetric fluidisation flow rate necessary to maintain U_s at the bed height at 1.0 m/s requires 82 N m^3/h in the small-scale, 137 N m^3/h in the medium-scale and 651 N m^3/h in the large-scale.

Having determined the value for U_e the next step was to find a value for the particle density ρ_p. Following the guidelines presented in Section 1.1 the bulk density was determined to be 1428 kg/m^3 by pouring the uncoated granules into a container with a well-defined known volume. The surface of the solids in the container was levelled by carefully scraping-away the excess with a metal slid at right angles to the surface of the solids and to the rim of the container. The solids in the container were then weighted, and the weighted mass was divided by the internal volume of the container to give the bulk density of the particles according to the patent description (Akkermans et al., 1998). The resulting bed porosity ε_{bed} has been determined previously by Hede (2005) to be close to 0.37 with Micromeritics Autopore II intrusion/extrusion mercury porosimetry thereby giving an apparent density of 2266 kg/m^3 according to Eq. (2).

Having determined the apparent particle density and fixed a level for the superficial gas velocity, the only parameter that would have to be changed according to the different flux number values is the liquid mass flux $\dot{q}_{m\text{liq}}$. As mentioned earlier, the liquid mass flux is the mass flow of liquid applied per unit contact area where the contact area A is measured at the so-called normalised nozzle-to-bed distance D_0. However, the contact area at D_0 is not a constant property even though the fluidisation velocity and thereby D_0 is. This is due to the fact that with nozzle pressure, the spray angle from the two-fluid nozzle changes. For the medium-scale fluidised bed, e.g., the spray angle is roughly 14° at a nozzle pressure of 3 bar whereas the spray angle is roughly 21° at a nozzle pressure of 1 bar. This means that the value for A (and thereby obviously the required liquid mass flux $\dot{q}_{m\text{liq}}$ for a given flux number) is strongly dependent on the nozzle pressure. Unfortunately, the Akkermans et al. (1998) patent does not give any specific information about the operating conditions for the nozzles. The patent only emphasises that the value of the Sauter average droplet diameter d_{32} of the liquid binder should preferably not be greater than the value of the d_{32} of that fraction of the total solid starting material which has a particle diameter ranging from 20 to 200 μm. The patent further loosely states that the d_{32} average droplet diameter should preferably be between 20 and 200 μm. The first condition was easily met with the given fluidised bed equipment and the particle size distribution of the sodium sulphate core processed, but the second condition with the droplet size interval was only achievable in the medium- and large-scale as droplets much above 10 μm tend to overwet the bed in the small-scale, resulting in complete collapse of the bed. Average droplet sizes were estimated with the use of the standard two-fluid nozzle correlation in Eq. (9) adapted from Masters (1972).

$$d_{\text{mmd}} = \left[\frac{249 \cdot \gamma_{\text{liq}}^{0.41} \cdot \eta_{\text{liq}}^{0.32}}{(v_{\text{rel}}^2 \cdot \rho_{\text{air}})^{0.57} \cdot A_{\text{annulus}}^{0.36} \cdot \rho_{\text{liq}}^{0.16}}\right] + 1260 \times \left[\left(\frac{\eta_{\text{liq}}}{\gamma_{\text{liq}} \cdot \rho_{\text{liq}}}\right)^{0.17} \cdot \left(\frac{1}{v_{\text{rel}}^{0.54}}\right) \cdot \left(\frac{\dot{m}_{\text{nozzle air}}}{\dot{m}_{\text{spray}}}\right)^{m}\right], \quad (9)$$

where

$$m = -1 \text{ at } \left(\frac{\dot{m}_{\text{nozzle air}}}{\dot{m}_{\text{spray}}}\right) < 3 \quad \text{and}$$

$$m = -0.5 \text{ at } \left(\frac{\dot{m}_{\text{nozzle air}}}{\dot{m}_{\text{spray}}}\right) > 3,$$

and $\dot{m}_{\text{nozzle air}}$ is the mass rate of atomisation air, $\dot{m}_{\text{spray}}$ is the mass rate of liquid, d_{mmd} is the mass median droplet diameter in μm, γ_{liq} is the coating liquid surface tension (in dynes/cm), A_{annulus} is the area of the air annulus in in^2, η_{liq} is the coating liquid viscosity (in cP), v_{rel} is the difference between the nozzle atomising air velocity and the liquid velocity at the nozzle outlet (in ft/s) and the densities are in lb/ft^3. The mass median droplet diameter in μm correlates with the Sauter mean diameter d_{32} in μm according to the empirical correlation in the following equation (Masters, 1972):

$$d_{32} = 0.83 \cdot d_{\text{mmd}}. \quad (10)$$

With the use of Eqs. (9) and (10) Sauter mean diameters were estimated to be between 4 and 10 μm for the small-scale, between 9 and 43 μm for the medium-scale and between 15 and 99 μm for the large-scale depending on the nozzle pressure and the liquid feed rates. As mentioned earlier, the spray angle changes with nozzle pressure, but what is more important regarding the droplet size is that the gas flow rate through the nozzle changes as well with nozzle pressure. For the three nozzles used in the present study an almost linear dependency between the nozzle pressure in bar and the nozzle air flow in m^3/h was observed. All other conditions being the same, if the nozzle pressure increases so does the gas flow rate through the nozzle, meaning that the average droplet size decreases.

In order to test the sensitivity of the flux parameter with respect to values of $\dot{q}_{m\text{liq}}$ two nozzle pressures were chosen for each fluidised bed scale being 1 and 3 bar. For each nozzle pressure and for each type of fluidised bed equipment, a contact area A was determined in terms of experiments for the given nozzle pressure at the distance of D_0 as explained earlier. As it may be seen from Table 1, the contact area is quite dependent on the nozzle pressure.

Having determined the values for A for all three fluidised bed scales the only parameter that will change with the choice of flux number and nozzle pressure is the mass flow of liquid applied $Q_{m\text{liq}}$ which is the value that the tube pump feeding the nozzle will be set at.

Although temperature is not a property directly associated with the flux or the Stokes number a long history of published

Table 1
Overview of the determined values of the contact area A at D_0 for the two tested nozzle pressures

Fluidised bed scale	Normalised nozzle-to-bed distance D_0 (cm)	Nozzle pressure (bar)	Contact area A (cm^2)
Strea-1 (small-scale)	14.5 (set to 15 cm according to patent guidelines)	1	28.3
		3	19.6
MP-1 (medium-scale)	32.3	1	130.8
		3	51.3
MP-2/3 (large-scale)	32.6	1	283.4
		3	153.9

The values for D_0 was determined with the use of experimental observations of H_{bed} and measurement of H_{nozzle} in combination with the correlations in Section 1.1.

fluidised bed coating results clearly show that the bed temperature during coating has a primary importance regarding the tendency of agglomeration (e.g. Schæfer and Wørts, 1978). Even a minor change in bed temperature of a few degrees may have a significant effect on the agglomeration tendency (Hede, 2005). Akkermans et al. (1998) nevertheless, state only in very general terms that the bed temperature should be between ambient temperature and 60 °C. However, the experience with the given fluidised bed equipment, core particles and coating solution is that at temperatures below 50 °C the bed tend to agglomerate easily and hence, the choice in the present studies was to aim at a bed temperature of 55 °C in all coating experiments regardless of the choice of flux number, nozzle pressure and mass flow of liquid. The choice of this bed temperature ought to limit the bed temperature effect towards agglomeration. Having fixed the bed temperature and gas velocity through the bed throughout the experiments, the only independent parameter for each single experiment was the inlet air temperature which is the only parameter that cannot be determined prior to the experiments. The advantages of running the fluidised bed process in terms of an adjustable inlet air temperature and choosing all other process parameters a priori were presented in detail in Hede et al. (2007a).

In order to test the flux number, a number of 24 coating experiments were planned. Throughout the experiments the coating formulation was kept constant thereby giving a constant Stokes number in the range of 900. Furthermore the superficial gas velocity U_s at H_{bed} was kept constant at 1 m/s and the bed temperature was maintained at 55 °C throughout each coating operation. The flux number was tested for each fluidised bed scale in four levels at values of 3.5, 4.0, 4.5 and 4.7 and each flux number condition was carried out two times—once with a nozzle pressure of 1 bar and once with a nozzle pressure of 3 bar.

In accordance with coating guidelines presented by Hede et al. (2007a, b) the core bed load was heated prior to coating until the relative humidity inside the fluidisation chamber was constant, typically ranging from 5 to 7 RH% depending on weather conditions. In each coating operation the aim was to coat until the bed load had increased 20 w/w%. This was done in order to make sure that a reasonable coating layer ($\sim$ 5–10 μm) had developed on the core particles. After coating, the bed load was kept fluidised at identical fluidisation velocity and inlet temperature conditions in order to dry the coated granules. This was done until the relative humidity inside the chamber was identical to the conditions prior to coating. The coated bed load was afterwards weighed in order to make sure that the bed load had gained in weight about 20 w/w%. For all the experiments in this paper, the actual batch weight gain may be seen from Table 2. As observed, most experiments have had minor losses of core material as well as minor losses of coating solution due to spray drying.

3. Results and discussion

Issues concerning reproducibility of data with the same type of fluidised bed equipment and core materials were treated in detail by Hede et al. (2007a). It was observed how the standard deviation from the Retsch Sieve Shaker AS 200 equipment was 0.82% in terms of the agglomeration percentage thereby indicating as a common rule of thumb that different batches having agglomeration percentages in the range of ±1.64% are not statistically different. From detailed analysis of the three fluidised bed scales it was further observed in this paper how statistic sound reproducible data could be produced and how a χ^2 tests could be used to determine how well the nine different particle size classes were reproduced across scale (Hede et al., 2007a).

3.1. Scale-up results in terms of the flux number: matching the agglomeration percentages and particle size fractions across scale

Following the overall plan for the scaling experiments the coating experiments were planned and carried out according to Table 2. As large-scale experiments are time-consuming and require large amounts of core materials, experiments were carried out first in the small- and medium-scale. If the given conditions resulted in wet-quenching and a complete collapse of the bed in the small- and medium-scale these process conditions were not tested in the large-scale. The experiments were conducted in a 4 week period under similar weather conditions with room temperatures around 23 °C and room humidity's in the range of 35–42 RH%. Table 2 presents the results from the scaling trials.

There are several important things to note from the results in Table 2. First of all it was observed that flux number conditions at 3.5 and 4.0 were in all cases unsuccessful as the bed collapsed within the first few minutes of the coating process. For the flux number value of 3.5 the bed collapsed irrespectively of the nozzle pressure clearly indicating that the required spray rate at this flux number is far too high for the coating process. This is even though the values for $\dot{q}_{mliq}$ were in the lower end of the preferred range. At a flux number of 4.0 the bed collapsed in the medium-scale for nozzle pressures of 1 and

Table 2
Results from the flux number scaling attempts

Fluidised bed equipment	Scaling attempt	Experiment code	Flux number	Nozzle pressure (bar)	Required Q_{mliq} (g/min)	Agglomeration percentage (w/w%)	Coating time (h:min)	Coating time per kg core load (min/kg)	Comment
Strea-1 (small-scale)	A	X1	3.5	1	113.1	100	N/A	N/A	The bed collapsed due to overwetting within the first few minutes of the coating process. At the time of collapse the humidity inside the fluidisation chamber exceeded 50 RH%. Actual batch weight gain: N/A
	B	X2	3.5	3	78.5	100	N/A	N/A	The bed collapsed due to overwetting within the first few minutes of the coating process. Actual batch weight gain: N/A
	C	X3	4.0	1	35.8	100	N/A	N/A	The bed collapsed within the first 10 min of the coating process. Actual batch weight gain: N/A
	D	X4	4.0	3	24.8	93.8	0:31	62	Large bubble fluidisation was observed. A steady coating state was never reached. Actual batch weight gain: N/A
	E	X5	4.5	1	11.3	24.5	1:02	124	There was observed some build-up of particles adhered to the nozzle during coating. Actual batch weight gain: 17.1 w/w%
	F	X6	4.5	3	7.9	0.2	1:20	160	Good fluidisation conditions. No particle-adhesion to the nozzle. Less than 10 w/w% loss of coating solution due to spray drying. Actual batch weight gain: 19.3 w/w%
	G	X7	4.7	1	7.1	35.9	1:37	194	Adequate fluidisation conditions but ~35 w/w% loss of coating feed due to spray drying loss. Actual batch weight gain: 17.4 w/w%

	H	X8	4.7	3	5.0	0.1	2:19	278		Good fluidisation conditions but ~15 w/w% loss of coating feed due to spray drying loss. Actual batch weight gain: 19.1 w/w%
MP-1 (medium-scale)	A	Y1	3.5	1	523.2	100	N/A	N/A		The bed collapsed due to overwetting within the first few minutes of the coating process. Actual batch weigh gain: N/A
	B	Y2	3.5	3	205.4	100	N/A	N/A		The bed collapsed due to overwetting within the first few minutes of the coating process. Actual batch weigh gain: N/A
	C	Y3	4.0	1	165.5	100	N/A	N/A		The bed collapsed within the first few minutes of the coating process. Actual batch weight gain: N/A
	D	Y4	4.0	3	64.9	100	N/A	N/A		The bed collapsed within the first 10 min of the coating process. Actual batch weigh gain: N/A
	E	Y5	4.5	1	52.3	62.3	1:31	23		The iriside of the fludisation chamber and the nozzle wes gradually covered with wet particles during the coating process
	F	Y6	4.5	3	20.5	0.1	4:26	67		Good fluidisation conditions. No particle-adhesion to the nozzle. Less than 10 w/w% loss of coating solution due to spray drying. Actual batch weight gain: 19.4 w/w%
	G	Y7	4.7	1	33.0	37.0	2:39	40		Adequate fluidisation conditions but ~50 w/w% loss of coating feed due to spray drying loss. Actual batch weight gain: 16.4 w/w%
	H	Y8	4.7	3	13.0	0.1	6:31	98		Good fluidisation conditions but 25 w/w% loss of coating feed due to spray drying loss. Actual batch weigh gain: 18.9 w/w%

Table 2 *(Continued)*

Fluidised bed equipment	Scaling attempt	Experiment code	Flux number	Nozzle pressure (bar)	Required $Q_{m\,liq}$ (g/min)	Agglomeration percentage (w/w%)	Coating time (h:min)	Coating time per kg core load (min/kg)	Comment
MP-2/3 (large-scale)	A	Z1	3.5	1	1133.5	N/A	N/A	N/A	The coating experiment was not conducted as the small- and medium-scale experiments were unsuccessful.
	B	Z2	3.5	3	615.4	N/A	N/A	N/A	The coating experiment was not conducted as the small- and medium-scale experiments were unsuccessful.
	C	Z3	4.0	1	358.5	N/A	N/A	N/A	The coating experiment was not conducted as the small- and medium-scale experiments were unsuccessful.
	D	Z4	4.0	3	194.6	97.8	2:43	7	Large bubble fluidisation was observed. Actual batch weight gain: 19.3 w/w%
	E	Z5	4.5	1	113.4	4.4	4:25	11	Minor tendency of particle adhesion to the nozzle but no coverage of the chamber walls. Adequate fluidisation conditions. Actual batch weight gain: 19.5 w/w%
	F	Z6	4.5	3	61.5	0.7	8:41	22	Good fluidisation conditions. No particle-adhesion to the nozzle. Less than 15 w/w% loss of coating solution due to spray drying. Actual batch weight gain: 19.2 w/w%
	G	Z7	4.7	1	71.5	37.9	6:52	17	Adequate fluidisation conditions but ~30 w/w% loss of coating feed due to spray drying loss. Some build-up of particles on the nozzle and at the chamber walls. Actual batch weight gain: 18.9 w/w%
	H	Z8	4.7	3	38.8	0.1	12:57	32	Good fluidisation conditions but 35 w/w% loss of coating feed due to spray drying loss. Actual batch weight gain: 18.7 w/w%

3 bar in scaling attempts C and D whereas collapse was the case for the large- and small-scale with nozzle pressures of 1 bar. Only in two experiments X4 and Z4 the bed did not collapse although the agglomeration tendencies in both cases were close to 100%. Even though the patents by Wasserman et al. (2000) and Akkermans et al. (1998) state that the preferred range for the flux number includes values as low as 3.5 this cannot be verified by the results in this work.

The effect of nozzle pressure within experiments having identical flux number was clearly observed for the experiments with flux numbers of 4.5. Whereas for e.g. experiments X5 and X6 the only difference is the nozzle pressure and thereby the liquid spray rate, the effect on agglomeration tendency is unambiguously detected; the agglomeration tendency increases with decreasing nozzle pressure irrespectively of the fluidised bed scale and the fact that the flux number is fixed. This tendency is also observed with the experiments having a flux number of 4.7.

Qualitatively the observed agglomeration tendencies in Table 2 do indeed follow the domain map in Fig. 1 indicating that the agglomeration tendency decreases with increasing flux number. In the scaling attempts A, B, C and D having the smallest flux numbers the agglomeration tendencies are the largest. There is however a deviation from this overall tendency. Although some scattering in the agglomeration tendencies within the scaling attempt E, the trends are the opposite of the domain map. Whereas the tendency of agglomeration ought to decrease with increasing flux number this tendency is not observed when scaling attempts E and G are compared. There is statistic significant difference between the agglomeration tendencies in the following experiments: X5 and X7 as well as between Z5 and Z7. These observations clearly indicate that there are more important factors involved in agglomeration tendency than is predicted by the domain map, and further that nozzle pressure is a factor of primary importance when it comes to the prediction of agglomeration tendency in terms of the flux number.

In the pursuit of reproducing the agglomeration tendency across scale it is observed from Table 2 that only three scaling attempts are successful. The agglomeration tendencies for the three different batches within scaling attempts F, G and H are all within the ±1.64% range indicating that the agglomeration tendencies are not statistically different. This means in other words that the fixed coating conditions in these three times three experiments have resulted in similar agglomeration tendency across the scales.

As discussed in the paper by Hede et al. (2007a) the reproducibility of the agglomeration percentage within the ±1.64% interval does not necessarily indicate that the particle size distribution also is reproduced, as the different size classes do not necessarily have to be identical in order to achieve a similar agglomeration percentage. If the flux number should have any practical usefulness as a scaling parameter, the particle size fractions should also be reproduced across scale in addition to the agglomeration percentage. In order to check for the reproducibility of the particle size fractions within each flux number coating condition a χ^2 test was performed for all nine particle size classes (in case any of the size fractions were in the range of 0.01 w/w%, the size class was pooled into the next size class as χ^2 tests on very small intervals may lead to false conclusions). This was obviously only done for the flux number conditions that did not cause a complete collapse of the bed. The results may be seen from Table 3.

Table 3
P-values from a χ^2 test resulting from a comparative test of the three times nine particle fractions within each scaling attempt

Scaling attempt	*P*-value from χ^2 test
E (experiments $x4$, $y4$, $z4$)	<0.01
F (experiments $x5$, $y5$, $z5$)	0.26
G (experiments $x6$, $y6$, $z6$)	0.09
H (experiments $x7$, $y7$, $z7$)	0.59

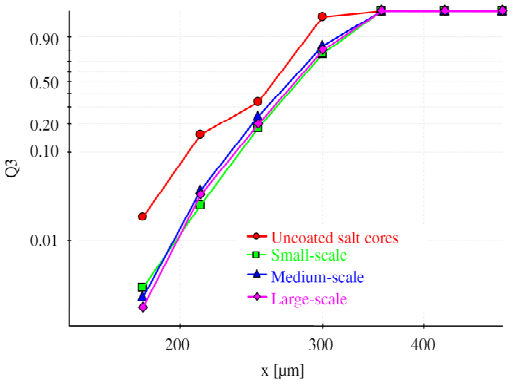

Fig. 5. RRSB-plot (Rosin–Rammler–Bennet–Sperling) of particle size fractions from scaling attempt H. On the x-axis are the particle diameters and on the y-axis is the particle sum distribution $Q3(x)$ in relation to particle volume.

From Table 3 it is observed how the *P*-values from the χ^2 tests are above the 0.05 limit for scaling attempts F, G and H indicating that, on a 95% confidence level, the nine particle size fractions were matched across scale for all three scaling attempts. The particle size fractions were not matched in scaling attempt E but this was also expected from the large deviations in agglomeration tendency as observed in Table 2. By far the best match of particle size fractions was achieved in the scaling attempts F and H where there is almost no agglomeration tendency at all. This may also be visualised in a Rosin–Rammler–Bennet–Sperling-plot (RRSB-plot), as may be seen from Fig. 5, showing the particle size fractions from scaling attempt H. The RRSB-plot is a common way to describe the sum distribution $Q3(x)$ as a function of different particle sizes in a mixture.

Adequate matching is also observed in scaling attempt G and visualised in Fig. 6 where the particle size fractions are matched in spite of the agglomeration tendencies being around 37%. One thing is to be able to match agglomeration tendencies and particle size fractions under coating conditions where no agglomeration occurs. This should seem somewhat

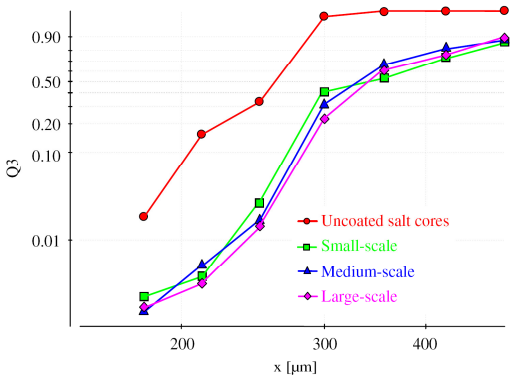

Fig. 6. RRSB-plot (Rosin–Rammler–Bennet–Sperling) of particle size fractions from scaling attempt G. On the x-axis are the particle diameters and on the y-axis is the particle sum distribution $Q3(x)$ in relation to particle volume.

straightforward compared to the match of significant agglomeration tendencies which is another and far more complicated exercise. Hence, it seems reasonable that the P-values are the largest for the scaling attempts F and H. The most significant achievement is however, that the P-value for scaling attempt G lies above the 0.05 level. For the process parameter conditions in the three scaling attempts F, G and H it is thereby reasonable to conclude that it is indeed possible to scale-up successfully in terms of the flux number irrespective of the tested nozzle pressures.

3.2. Discussion of the flux number and scaling results

The flux number is an interesting parameter for scale-up purposes as it focuses on parameters known to have primary importance for the agglomeration tendency during the fluidised bed coating process. As reviewed by Hede (2005) and Iveson et al. (2001) control of the liquid distribution is essential for the tendency of agglomeration, and it makes sense to let the spray rate be a primary parameter in a scale-up relation. Likewise, it is common knowledge that the fluidisation velocity has a primary importance with respect to agglomeration. In that sense it seems reasonable to let the fluidisation velocity be a part of a scaling relationship. Whether or not the apparent density of the particle bed is important enough to be included in a scaling parameter may be discussed, but it does make the flux number a dimensionless parameter.

The flux number is nevertheless not an easily applicable parameter as it requires some detailed a priori knowledge of the fluidisation chamber dimensions, bed height at different fluidisation conditions and more. Many of these parameters will also vary with the given types of core materials and coating liquid formulation and may eventually have to be determined each time these conditions change. Even if these parameters and properties have been determined, other choices will have to be made as well regarding the values for the parameters constituting the flux number. Although the original patent description by Akkermans et al. (1998) indicates some wide ranges for the parameters, the results in this work show that these ranges may not be useful in general. The values for the mass spray flux $\dot{q}_{m\mathrm{liq}}$ tested in this paper have all been either below or in the lowest part of the value range suggested in the patent description. Even so, the agglomeration tendency was observed to be heavy for some cases although all other parameters were in the midst of the suggested range.

Other additions to the flux number in form of the Stokes number suggested by Wasserman et al. (2000) and Achanta and Beimesch (1999) have proven not to be sufficient to control the tendency of agglomeration. The present results have indicated that maintaining the Stokes number even far above the value of 1 does not ensure successful coating conditions with limited agglomeration. There are several possible reasons why the Stokes number cannot be used even as a rough simple parameter for determining the boundaries for agglomeration. The viscosity of the liquid droplets changes first of all with temperature and the degree of drying. Secondly, the apparent density changes with time due to coating or possible agglomeration. Thirdly, the Stokes number only uses one excess gas velocity whereas there is a whole range of excess gas velocities in the conical fluidisation chambers used in the present studies. Furthermore, the Stokes number requires only one particle diameter even though there is a whole particle size distribution. All of these issues are not accounted for in Eq. (7) and in all constitute plausible reasons why the Stokes number does not bring any further control of the coating system in combination with the flux number.

The results in the present study show interestingly that the nozzle pressure has a strong influence on the tendency of agglomeration irrespective of the flux number value. The largest agglomeration tendencies were observed with the lowest nozzle pressures in accordance with other studies by Hede et al. (2007b). As may be estimated from Eq. (9) a high nozzle pressure combined with a low liquid solution mass feed rate means smaller droplets. As was seen from the determination of spray area A a nozzle pressure of 1 bar has a significantly larger spray area than a nozzle pressure of 3 bar. Furthermore, a low nozzle pressure means less extent of droplet penetration vertically into the bed which has importance regarding the degree of possible droplet spray drying. It was observed from the results in Table 2 how the loss of coating solution due to spray drying increased with decreasing nozzle pressure. Irrespective of this, as a consequence of Eq. (6), maintaining a similar flux number and thereby a similar value for the mass spray flux $\dot{q}_{m\mathrm{liq}}$ means that at a low nozzle pressure, more liquid will have to be introduced through the nozzle per time due to larger spray area. These conditions means all in all that larger droplets are produced faster at the nozzle, and even though a relative large amount of these droplets are spray dried, those who actually reach the core surfaces are large in volume meaning that the coated particles are wet for a longer time in all increasing the chance of agglomeration. These tendencies have been proven by several authors elsewhere (e.g. Schæfer and Wørts, 1977). The nozzle pressure tendencies observed in the present studies clearly illustrate an important weakness associated with

the flux number: Even though two coating conditions have identical flux numbers the tendency of agglomeration is strongly influenced by the choice of nozzle pressure. The results in this paper strongly call for a further specification of the nozzle pressure in association with the flux number. So far it seems as if 3 bar for the tested nozzle types is the reasonable nozzle pressure in order to limit agglomeration, but further studies have to be conducted in order to determine a generic suitable range.

The fact that the experimental validation shows even narrower flux number boundaries around 4.5–4.7 for a successful coating regime compared to the patent descriptions indicates first of all that there is more to the principles of scaling the coating process than accounted for in the flux number. Secondly, it highlights the need for unambiguous validation and specification of value ranges for the parameters constituting the flux number. Testing the flux number in high-end levels of 4.5 and 4.7 also indicates that it is relatively easy to perform a coating operation without the tendency of agglomeration: If agglomeration is a problem the solution is simply to increase the flux number. This will decrease the liquid feed rate to the nozzle and if this is not sufficient, the nozzle pressure may additionally be increased to produce smaller droplets. There are however two major problems with this procedure. Firstly, as observed with the present experiments, the coating time is prolonged by this procedure. As observed from the comparison of scaling attempts E–H, the coating time increases significantly with increasing flux number. Coating operations lasting e.g. almost 9 and 13 h in experiments Z6 and Z8, respectively, is not desirable in practice. A second problem with high flux numbers is the high degree of spray drying loss of the liquid feed. At conservative coating conditions a large fraction of the liquid droplets dry up before reaching the core particle surfaces. This means that larger quantities of the coating solution is required but also give rise to problems concerning the properties of the coated core particles. It is well known from previous studies (Beekman, 2000; Hede, 2005) that partly dried-up droplets result in porous and flaky coating layers that exhibit poor mechanical properties when exposed to impact and attrition. Hence, there are indeed many reasons for not simply increasing the flux number in order to avoid agglomeration.

There is a long history in the field of dimensionless parameters from e.g. chemical reactor engineering, and it is indeed understandable to aim at finding dimensionless parameters that may describe the process in simple terms. The present results have shown that for granulation processes it is difficult to establish a simple dimensionless parameter that involves all relevant properties and parameters.

4. Conclusions

The paper has experimentally tested the dimensionless flux number on a standard top-spray fluidised bed sodium sulphate coating process as a possible scaling parameter suggested to be kept constant across scale. The flux number was tested in four discrete levels of 3.5, 4.0, 4.5 and 4.7 testing the influence of nozzle pressures of 1 and 3 bar for each flux number value. Systematic studies of scaling fluidised bed coating processes have been carried out in three fluidised bed scales testing the tendency of agglomeration and the match of particle size fraction across scale.

On an overall level only, successful scaling up of top-spray fluidised bed coated particles by 48 times in weight from the small-scale over medium-scale to the large-scale fluidised bed has been achieved for flux number conditions of 4.5 and 4.7. For the flux number values of 4.7 the scaling up was successful irrespective of the nozzle pressure whereas only the high-nozzle pressure condition was successful for a flux number of 4.5. For these flux number values in general the agglomeration tendency decreased with increasing flux number and increasing nozzle pressure. For all other flux number conditions the bed collapsed due to overwetting within the first minutes of the coating process.

The present study clearly indicates the limitations of the flux number as scaling parameter and further discard the Stokes number as indicator for a successful coating regime. It is possible to successfully scale-up in terms of the flux number but only within a narrow range and only with detailed knowledge of the value range for the parameters constituting the flux number. On the basis of the present study the following guidelines are suggested when using the flux number for fluidised bed coating scale-up purposes:

- Coating conditions with limited or no agglomeration require flux numbers in the range of 4.5–4.7. Higher flux numbers prolong the coating time unnecessarily and add severe problems with high spray drying losses of the coating solution. The lower end of the narrow flux number range is within a practical range regarding the time of coating, the liquid spray rate and more.
- Two values of the nozzle pressure were tested (1 and 3 bar) indicating that a high nozzle pressure is preferable in the tested sodium sulphate coating process.
- Stokes numbers values in the range of 100–1000 may be a prerequisite for successful coating operations but still excessive agglomeration may occur.
- Values for the mass spray flux $\dot{q}_{m\mathrm{liq}}$ may well be chosen below a value of $0.15\,\mathrm{kg/(s\,m)^2}$—preferably in the range of $0.05–0.08\,\mathrm{kg/(s\,m)^2}$ for the tested sodium sulphate coating process.
- Product temperatures in the range of 55 °C are preferable for the tested sodium sulphate coating process whereas product temperatures below 50 °C lead to agglomeration with the flux number values tested in this study. Maintaining the product temperature should be done by adjustment of the inlet fluidisation air temperature. All other process conditions should be fixed and chosen a priori.

Notation

A	contact area, m^2
A_{annulus}	area of the air annulus, m^2
BD	bulk density of the powder, $\mathrm{kg/m}^3$
d_{32}	sauter mean diameter, m

d	mean particle diameter, m
d_{mmd}	mass median diameter, m
D_0	normalised distance, m
FN_m	flux number, dimensionless
H_{bed}	bed height, m
H_{mf}	bed height at minimum fluidisation velocity, m
H_{nozzle}	the height of the spray nozzle above the bottom of the fluidisation chamber, m
L_{bed}	length from the air distributor plate to the fluidisation chamber exhaust exit, m
$\dot{m}_{\mathrm{nozzle\ air}}$	mass rate of atomisation air, kg/s
$\dot{m}_{\mathrm{spray}}$	mass rate of liquid, kg/s
$\dot{q}_{m\mathrm{liq}}$	spray mass flux, $\mathrm{kg/(s\,m^2)}$
$Q_{m\mathrm{liq}}$	the mass flow of liquid applied, kg/s
St	viscous Stokes number, dimensionless
U_e	excess gas velocity, m/s
U_{mf}	minimum fluidisation velocity, m/s
U_s	superficial gas velocity, m/s
v_{rel}	the difference between the nozzle atomising air velocity and the liquid velocity at the nozzle outlet, m/s

Greek letters

γ_{liq}	liquid surface tension, N/m
$\varepsilon_{\mathrm{bed}}$	bed porosity, dimensionless
η_{liq}	liquid viscosity, kg/(m s)
ρ_{air}	atomisation air density, $\mathrm{kg/m^3}$
ρ_g	apparent granule density, $\mathrm{kg/m^3}$
ρ_{liq}	liquid density, $\mathrm{kg/m^3}$
ρ_p	particle density, $\mathrm{kg/m^3}$

Acknowledgements

This project was performed in collaboration with Novozymes A/S, who also financially supported the project. Peter Dybdahl Hede is a member of the Novozymes Bioprocess Academy as well as the $\mathrm{MP_2T}$ Graduate School in Chemical Engineering at the Department of Chemical Engineering, Technical University of Denmark, funded by the Danish Technical Research Council, the European Union, the Nordic Energy Research, Dong Energy A/S, Vattenfall A.B., F.L. Smidth A/S and Public Service Obligation funds from Energinet.dk and the Danish Energy Research programme.

References

Achanta, S., Beimesch, W.E., 1999. Process for making a low density detergent composition by controlled agglomeration in a fluidised bed dryer. Patent WO99/03964.

Akkermans, J.H.M., Edwards, M.F., Groot, A.T.J., Montanus, C.P.M., Van Pomeren, R.W.J., Yuregir, K.R., 1998. Production of detergent granulates. Patent WO98/58046.

Beekman, W.J., 2000. Measurement of the mechanical strength of granules. Ph.D. Thesis, Technische Universiteit Delft.

Boerefijn, R., Hounslow, M.J., 2005. Studies of fluidised bed granulation in an industrial R&D context. Chemical Engineering Science 60, 3879–3890.

Ellenberger, J., Krishna, R., 1994. A unified approach to the scale-up of gas–solid fluidized bed and gas–liquid bubble column reactors. Chemical Engineering Science 49 (24B), 5391–5411.

Ennis, B.J., Tardos, G., Pfeffer, R., 1991. A microlevel-based characterization of granulation phenomena. Powder Technology 65, 257–272.

Glicksman, L.R., 1984. Scaling relationships for fluidized beds. Chemical Engineering Science 39 (9), 1373–1379.

Glicksman, L.R., 1988. Scaling relationships for fluidized beds. Chemical Engineering Science 43 (6), 1419–1421.

Glicksman, L.R., Hyre, M., Woloshun, K., 1993. Simplified scaling relationships for fluidized beds. Powder Technology (77), 177–199.

Hede, P.D., 2005. Fluidised bed coating and granulation. Master Thesis, Department of Chemical Engineering, CHEC Research Center, Technical University of Denmark, pp. 1–227.

Hede, P.D., 2006. Towards Mathesis Universalis: modern aspects of modelling batch fluidised bed agglomeration and coating systems—a review. CHEC Report R0605, Department of Chemical Engineering, Technical University of Denmark, pp. 1–101.

Hede, P.D., Jensen, A.D., Bach, P., 2007a. Top-spray fluidised bed coating: scale-up in terms of relative droplet size and drying force. Powder Technology, in press, doi: 10.1016/j.powtec.2007.09.009.

Hede, P.D., Jensen, A.D., Bach, P., 2007b. Small-scale top-spray fluidised bed coating: granule impact strength, agglomeration tendency and coating layer morphology. Powder Technology (176), 156–167.

Horio, M., Nonaka, A., Sawa, Y., Muchi, I., 1986. A new similarity rule for fluidized bed scale-up. A.I.Ch.E. Journal 32 (9), 1466–1482.

Iveson, S.M., Litster, D.L., Hapgood, K., Ennis, B.J., 2001. Nucleation, growth and breakage phenomena in agitated wet granulation processes: a review. Powder Technology 117, 3–39.

Knowlton, T.M., Karri, S.B.R., Issangya, A., 2005. Scale-up of fluidized-bed hydrodynamics. Powder Technology (158), 72–77.

Kunii, D., Levenspiel, O., 1991. Fluidization Engineering. second ed. Butterworth-Heinemann, Stoneham.

Leuenberger, H., 1983. Scale-up of granulation processes with reference to process monitoring. Acta Pharmaceutical Technology (29), 274–280.

Leuenberger, H., 2003. Scale-up in the 4th dimension in the field of granulation and drying or how to avoid classical scale-up. Powder Technology (130), 225–230.

Masters, K., 1972. Spray Drying—An Introduction to Principles Operational Practice and Applications. Leonard Hill Books, London.

Mehta, A.M., 1988. Scale-up considerations in the fluid-bed process for controlled-release products. Pharmaceutical Technology 12, 46–52.

Mort, P.R., 2005. Scale-up of binder agglomeration processes. Powder Technology 150, 86–103.

Rambali, B., Baert, L., Massart, D.L., 2003. Scaling up of the fluidized bed granulation process. International Journal of Pharmaceutics 252, 197–206.

Schæfer, T., Wørts, O., 1977. Control of fluidized bed granulation. II. Estimation of droplet size of atomised binder solutions. In: Archives of Pharmaceutical and Chemical Science, fifth ed., pp. 178–193.

Schæfer, T., Wørts, O., 1978. Control of fluidized bed granulation. III. Effects of inlet air temperature and liquid flow rate on granule size and size distribution. Control of moisture content of granules in the drying phase. In: Archives of Pharmaceutical and Chemical Science, sixth ed., pp. 1–13.

Schouten, J.C., Van der Stappen, M.L.M., van den Bleek, C.M., 1996. Scale-up of chaotic fluidized bed hydrodynamics. Chemical Engineering Science 51 (10), 1991–2000.

Teunou, E., Poncelet, D., 2002. Batch and continuous fluidised bed coating—review and state of the art. Journal of Food Engineering (53), 325–340.

van Ee, J.H., Misset, O., Baas, E.J., 1997. Enzymes in Detergency, Surfactant Science Series, vol. 69, Marcel Dekker, New York.

Wasserman, M.I., Ridyard, M.W., Capeci, S.W., Beimesch, W.E., Mort, P.R., 2000. Process for coating detergent granules in a fluidized bed. Patent WO00/78912A1.

Werther, J., 1980. Modelling and scale-up of industrial fluidized bed reactors. Chemical Engineering Science (35), 372–379.

Available online at www.sciencedirect.com
ScienceDirect
Powder Technology 184 (2008) 318–332
POWDER TECHNOLOGY
www.elsevier.com/locate/powtec

Top-spray fluid bed coating: Scale-up in terms of relative droplet size and drying force

Peter Dybdahl Hede [a,b], Poul Bach [b], Anker D. Jensen [a,*]

[a] CHEC Research Center, Department of Chemical Engineering, Technical University of Denmark, Building 229, DK-2800 Kgs. Lyngby, Denmark
[b] Solid Products Development, Novozymes A/S, Smørmosevej 11, DK-2880 Bagsværd, Denmark

Received 23 April 2007; received in revised form 3 September 2007; accepted 7 September 2007
Available online 20 September 2007

Abstract

Top-spray fluid bed coating scale-up experiments have been performed in three scales in order to test the validity of two parameters as possible scaling parameters: The drying force and the relative droplet size. The aim was to be able to reproduce the degree of agglomeration as well as the mechanical properties of the coated granules across scale. Two types of placebo enzyme granule cores were tested being non-porous glass ballotini cores (180–350 μm) and low porosity sodium sulphate cores (180–350 μm). Both types of core materials were coated with aqueous solutions of Na_2SO_4 using Dextrin as binder. Coating experiments were repeated for various drying force and relative droplet size values in three top-spray fluid bed scales being a small-scale (Type: GEA Aeromatic-Fielder Strea-1), medium-scale (Type: Niro MP-1) and large-scale (Type: GEA MP-2/3). The tendency of agglomeration was assessed in terms of particle size fractions larger than 425 μm determined by sieve analysis. Results indicated that the particle size distribution may be reproduced across scale with statistical valid precision by keeping the drying force and the relative droplet size constant across scale. It is also shown that none of the two parameters alone may be used for successful scaling. Morphology and microscope studies indicated that the coating layer is homogenous and has similar structures across scale only when both the drying force and the relative droplet size were fixed. Impact and attrition tests indicated that it is possible to produce granules with similar attrition and impact strength across scale and that the two types of mechanical properties are inversely related.

Keywords: Fluidised bed; Coating; Impact strength; Attrition; Granulation; Scale-up

1. Introduction

In the production of solid enzyme products, coating of the enzyme formulation onto inactive filler cores in fluid beds is a common process. The desired product consists of unagglomerated individual carrier particles each coated homogeneously with a layer of enzyme containing matrix. If formulation or process conditions are incorrectly chosen, either excessive agglomeration or excessive spray drying of the feed may happen. In both cases a poor product quality is achieved and in any case, control of agglomeration is essential during scale-up. Often product and process properties are optimised in small- and medium-scale fluid beds and then transferred to production-scale. The scale-up of a fluid bed granulation process requires decisions to be made at many levels. Scaling decisions must be closely related to a large number of parameters including: apparatus related (e.g. nozzle and fluidisation chamber dimensions), parameters related to the core material (such as porosity, mechanical properties and more), coating solution (e.g. viscosity, surface tension, contact angle and more) and the type of fluid bed, input parameters, operating conditions including spraying and fluidisation conditions as well as processing time etc. With such a variety of interlinked parameters and properties, combined with a general lack of fundamental understanding of the coating process, it is obvious that scale-up of a fluid bed granulation process is a challenging task.

A number of different scaling laws and principles have previously been suggested; in principle on either the unit-operation (macro) scale or on the particle-level (micro) scale. Recent work on scale-up of top-spray fluid bed granulation processes (e.g. by [1,2]) indicate successful scale-up of agglomeration processes from small-scale fluid bed to large-scale fluid bed in terms of the

* Corresponding author. Tel.: +45 4525 2841; fax: +45 4588 2258.
E-mail address: aj@kt.dtu.dk (A.D. Jensen).

0032-5910/$ - see front matter © 2007 Elsevier B.V. All rights reserved.
doi:10.1016/j.powtec.2007.09.009

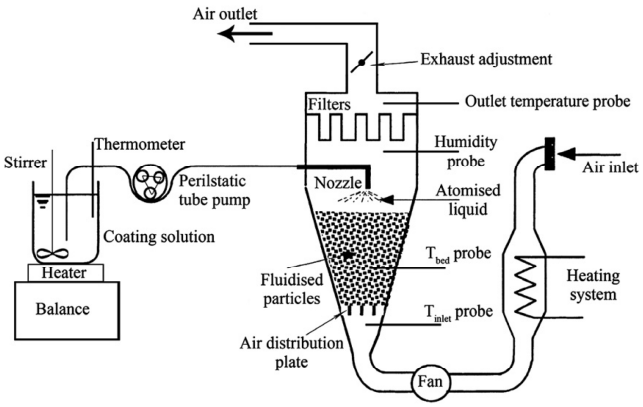

Fig. 1. Formal sketch of the general top-spray set-up used in all three fluid bed scales [3].

so-called relative droplet size, defined as the liquid spray rate in g/min divided by the airflow through the nozzle in g/min squared according to Eq. (5). In the granulation experiments by Rambali et al. [2] with corn starch and lactose monohydrate cores (mesh 200 μm) using an aqueous HPMC binder solution it was seen that the effect on mean granule size of the change in relative droplet size was different for each fluid bed scale, but that the granulation process was successful by scaling up to the large-scale bed from small-scale, considering only the relative droplet size. In their studies, the scale-up was restricted only to granule size having a target mean granule size of 400 μm, and other important granule properties such as porosity and flowability was not taken into account. Studies by Hede [3] indicate that besides nozzle conditions the relative humidity as well as the temperature inside the fluidisation chamber during coating are important properties with respect to agglomeration. Both properties may be combined into a single parameter, the drying force, suggested to be kept constant during scale-up. In terms of fixed values of the drying force and the relative droplet size a range of vital process parameters are implicitly given. Hence, there is reason to believe that these two parameters are capable of controlling the tendency of agglomeration during fluid bed processing. The present paper aims at testing those two parameters as possible scaling parameters — alone as well as in combination. The scale-up targets are to be able to reproduce the tendency of agglomeration, the entire particle size distribution as well as the mechanical properties of the coated granules across scale in a fluid bed coating context in terms of fixed values of the drying force and the relative droplet size. Match of these three properties across scale are vital for industrial fluid bed processes and products and are often subject to numerous trial-and-error attempts in industry.

2. Experimental

2.1. Fluid bed equipment

In the effort to fix as many parameters as possible across scale, the three different fluid bed set-ups were carefully chosen to be as similar as possible. All three were top-sprayed fluid beds each having a single two-fluid nozzle. In all three cases an outlet nozzle liquid orifice diameter of 1.2 mm was used. Likewise, the coating liquid feed was in each case led from an external heated reservoir at a constant temperature of 60 °C to the nozzle through an adjustable peristaltic tube pump. A sketch of the general set-up in each of the three fluid bed systems may be seen from Fig. 1 and the physical dimensions of the three fluid bed scales may be seen from Fig. 2. For all three fluid beds the fluidisation air inlet temperature and fluidisation velocity as well as the nozzle pressure was controlled independently via the fluid bed control interface. All other parameters had to be adjusted accordingly.

The small-scale fluid bed was a modified GEA Aeromatic-Fielder Strea-1 top-spray fluidised bed with a stainless steel

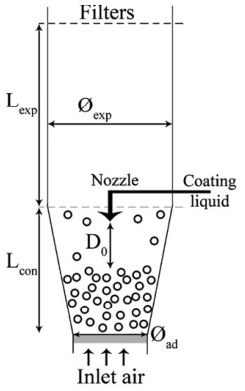

Fig. 2. Sketch of the fluid bed dimensions for the three fluid bed scales. The dimensions are: Small-scale Strea-1: L_{exp}=18.0 cm, L_{con}=31.0 cm, $Ø_{exp}$=25.0 cm, $D_0 \approx 15$ cm and $Ø_{ad}$=10.0 cm. Medium-scale MP-1: L_{exp}=93.0 cm, L_{con}=48.5 cm, $Ø_{exp}$=28.8 cm, $D_0 \approx 32$ cm and $Ø_{ad}$=17.0 cm. Large-scale MP-2/3: L_{exp}=270.0 cm, L_{con}=63.0 cm, $Ø_{exp}$=64.0 cm, $D_0 \approx 33$ cm and $Ø_{ad}$=27.0 cm.

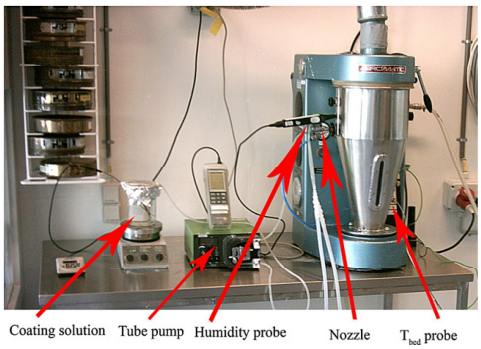

Fig. 3. Picture of the small-scale Strea-1 set-up [3].

fluidising chamber with a bottom plate diameter of 10.0 cm allowing a particle bed load of 500 g to be fluidised. A picture of the modified Strea-1 set-up can be seen in Fig. 3. Modification to the original vessel design made it possible to insert a digital thermometer into the fluidisation chamber wall thereby enabling measurement of the bed temperature between the bottom air distributor plate and the nozzle outlet. In addition, a humidity measurement apparatus (Testo 645 Thermohygrometer with TopSafe probe measuring humidity highly accurately with a sensitivity of ± 1 rH% in the range of 0.1–99.9 rH%) was inserted above the nozzle allowing the relative humidity in the fluidisation chamber to be measured. The vertical position of 15 cm from the nozzle outlet and a horizontal probe depth of 12 cm were carefully chosen in order not to let the humidity measurements be directly affected by the nozzle outlet. Custom-made reusable stainless steel filters were inserted in the top of the fluidisation chamber in order to prevent particles and spray-dried coating droplets from being exhausted. The back-flush option in the Strea-1 set-up was switched on allowing the filters to be flushed every 60 s.

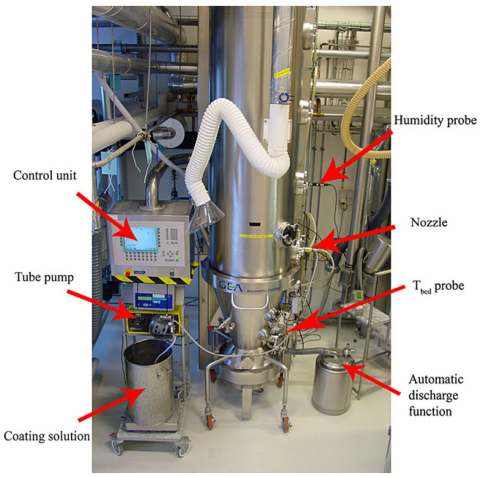

Fig. 5. Picture of the large-scale MP-2/3 set-up.

The medium-scale top-spray fluid bed was a standard Niro-Aeromatic Multiprocessor type MP-1. It had a stainless steel fluidising chamber with a bottom plate diameter of 17.0 cm allowing a particle bed load of 4000 g, thereby being eight times larger in bed load capacity than the Strea-1. A picture of the MP-1 set-up can be seen in Fig. 4. As for the Strea-1 set-up, it was possible to measure the bed temperature between the bottom air distributor plate and the nozzle outlet. The Testo 645 Thermohygrometer was inserted 28 cm above the nozzle outlet at a horizontal depth of 14 cm allowing the relative humidity in the fluidisation chamber to be measured at a location similar to the Strea-1 set-up. The back-flush option in the MP-1 set-up was switched on allowing the filters to be flushed every 60 s in the same way as for the small-scale set-up.

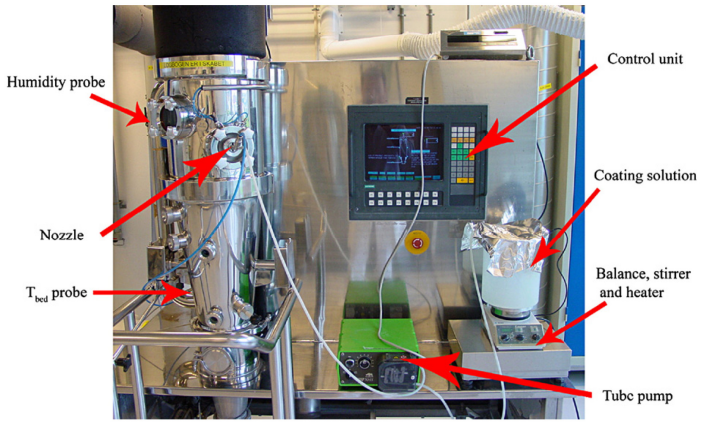

Fig. 4. Picture of the medium-scale MP-1 set-up.

The large-scale fluid bed was a GEA Aeromatic-Fielder MP-2/3 with a bottom plate diameter of 27.0 cm allowing a particle bed load of 24 kg to be processed, thereby being six times larger in bed load capacity with respect to the MP-1 and 48 times with respect to the Strea-1 set-up. A picture of the MP-2/3 set-up can be seen in Fig. 5. As for the other fluid bed scales, it was possible to measure the bed temperature between the bottom air distributor plate and the nozzle outlet. The Testo 645 Thermohygrometer was inserted 82 cm above the nozzle outlet at a horizontal depth of 21 cm allowing the relative humidity in the fluidisation chamber to be measured at a location identical to the other fluidised bed scales. The back-flush option in the MP-2/3 was set to be identical to the other set-ups.

2.2. Sieve equipment

For the sieving analysis, a Retsch Sieve Shaker AS 200 control was used with a sieve stack consisting of sieves with orifice diameters of 180 μm, 212 μm, 250 μm, 300 μm, 355 μm, 425 μm, 500 μm and 600 μm. Sieving also at the initial particle size limit was done in order to check for the level of debris and peeled-off coating layer flakes caused by attrition and particle impacts during processing. A sample of 200 g from each coated batch was sieved for 3 min with amplitude of 1.1 mm and the weight of each fraction was determined with the AS 200 control interface using a connected Mettler balance.

It was verified by microscope analysis of the different fractions that coated granules with diameters above 425 μm consisted of agglomerates whereas particles below this limit were primarily single coated granules. Thus, this sieve orifice diameter was set as the agglomeration limit and based on the weight of each of the fractions, the degree of agglomeration was determined for each batch according to Eq. (1).

$$\text{Agglomeration\%} = \frac{\text{coated batch weight fraction with } d_p > 425\ \mu\text{m}}{\text{total coated batch weight}} \cdot 100\% \quad (1)$$

The obtained fraction of coated granules between 355 μm and 425 μm was the fraction to be tested in the mechanical strength test equipment.

2.3. Mechanical strength test equipment

Two types of mechanical strength test equipment were used in order to quantitatively be able to determine important mechanical properties of the coated granules from the scaling attempts: The pneumatic impact gun and the spouted bed attrition tester.

2.3.1. Impact strength equipment

A P.I.G. (Pneumatic Impact Gun — Genencor Int. Inc.) was applied in order to simulate the impacts that coated enzyme granules experience during handling, further mixing with e.g. detergents etc. The impact gun itself consists basically of two cylindrical parts of which the outer is fixed and the inner is able to move in vertical direction thereby functioning as a piston. Fig. 6 illustrates the principle of the P.I.G. set-up.

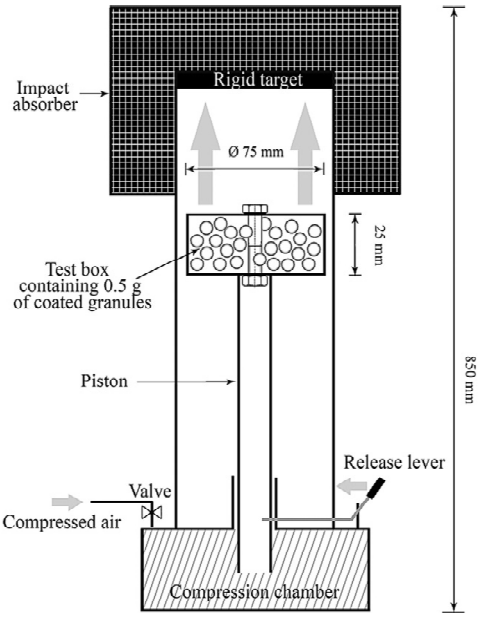

Fig. 6. Schematic illustration of the Pneumatic Impact Gun [13].

The test box was loaded with the precisely weighed bulk granules sample of 0.5 g (m_{sample}) into a small stainless steel box which again was placed on top of the piston connected to the compression chamber. By building up a pressure in the compression chamber using compressed air it was possible, by pulling a release lever, to let the piston and test box travel in vertical direction and impact a rigid target at a velocity of 10 m/s. For each coated granule sample, the impacts were repeated ten times and the box contents were afterwards sieved on an electrical shaker for 1 min using a specially designed stainless steel sieve having orifices with diameters of 180 μm. Based on microscopy analysis of coated particle size fractions below 180 μm it was observed that such minor fractions consisted of fractured daughter pieces and peeled-off coating layer parts, whereas size fractions above this level consisted primarily of coated granules. Hence, the demarcation of dust and coated particles seemed reasonable in terms of the 180 μm sieve and the amount of the created dust fraction with diameters below 180 μm ($m_{dust\ created}$) was thereby considered an indication of the impact strength expressed as a breakage percentage $Y_{Breakage}$ according to Eq. (2).

$$Y_{Breakage} = \frac{m_{dust\ created}[g]}{m_{sample}[g]} \cdot 100\% \quad (2)$$

Instead of just choosing a fixed number of P.I.G. tests for each batch and then find the average $Y_{Breakage}$ value, the number of P.I.G. tests to be conducted was determined by the coefficient of variance. A coefficient of variance of 10% was set as the

maximum allowed value estimated as a reasonable low variance from prior tests. Hence, if for a given batch the coefficient of variance among the breakage percentages was below 10%, an average value was found. Otherwise further P.I.G. tests for the given batch were conducted until the coefficient of variance came below the maximum limit. A minimum of three P.I.G. experiments were performed for each coated batch.

2.3.2. Spouted bed attrition test equipment

Attrition tests were performed using a fluidised bed jet known as the Unilever elutriation dust or simply spouted bed attrition test (see e.g. [4,5] or [6]). The principle is simply to fluidise a sample of coated granules with a specific gas velocity for a specific amount of time in a vertical cylindrical glass column. This column has an air distributor plate in the bottom with only a single orifice in the middle having a diameter of 1000 μm. The attrition in such a simplified fluid bed involves the entrainment of particles from the dense phase region near the tube walls into the dilute jet core. Once in this region, particles are accelerated by the gas jet and collide with each other as well as with the tube walls. The dust formed by attrition will then be elutriated and collected in an attached filter in the top of the glass column. The filters used in the present spout test are glass fibre filters designed to hold back dust debris having diameters above 1 μm. Fig. 7 illustrates the schematic set-up of the attrition tester.

In each attrition run a sample of coated granules corresponding to the column of 50 mL was weighted off and placed in the glass column. The precise mass of the clean filters was determined and placed in the set-up. The airflow was turned on corresponding to a gas velocity through the single orifice of 245 m/s. This gives a fluidisation velocity in the upper column of 0.2 m/s thereby exceeding the terminal velocity for particles with diameters less than 50 μm [7,8]. Hence, at these conditions particles and debris with diameters less than 50 μm were caught in the filters and accounted as dust.

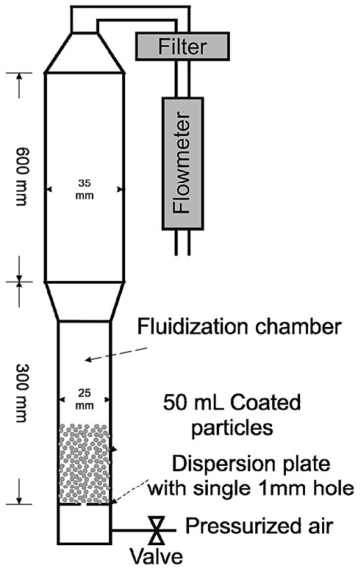

Fig. 7. Schematic illustration of the spouted bed attrition tester.

After 5 min of fluidisation the flow was stopped and the filter was weighted. The system was reassembled and the fluidisation continued for another 35 min. The filter was weighted again and a quantitative attrition parameter $Y_{\text{attrition}}$ was determined for the granule sample according to Eq. (3).

$$Y_{\text{Attrition}} = \frac{m_{\text{dust created}}[\text{g}]}{m_{\text{sample}}[\text{g}]} \cdot 100\% \tag{3}$$

in which $m_{\text{dust created}}$ is determined according to Eq. (4).

$$m_{\text{dust created}} = m_{\text{dust filter 40 min}} - m_{\text{dust filter 5 min}} \tag{4}$$

Prior experience with the spouted bed equipment has shown that the dust caught in the filters during the first few minutes of fluidisation primarily results from spray dried coating droplets and not from attrition of the coating layer. In order not to let this interfere with the attrition test results the amount of the created attrition dust was found from Eq. (4) thereby neglecting the first 5 min of dust caught in the filter.

Analogously to the P.I.G procedure the number of attrition tests was determined by the coefficient of variance. A minimum number of three attrition tests were conducted for each batch and a coefficient of variance of 20% was set as the maximum allowed value estimated as a reasonable low variance from prior tests. Hence, if for a given batch the coefficient of variance among the attrition percentages from the attrition tests was below 20%, an average value was calculated. Otherwise, further attrition tests were conducted until the value came below 20%. A minimum of three attrition tests were performed for each coated batch.

According to standard attrition dust guidelines good granule mechanical properties correspond to values for $Y_{\text{attrition}}$ of less than 0.1% (~1000 ng/g) [9]. With respect to Eq. (3), this means that values below 0.1% indicate acceptable attrition strength in an industrial context.

2.4. Materials

Two types of core materials were used for the coating experiments — low porosity sodium sulphate cores (Porosity fraction around 20.7% determined with Micromeritics Autopore II intrusion/extrusion mercury porosimetry) pre-sieved in the size range of 180–350 μm and non-porous glass ballotini (Potters Industries) pre-sieved in the size range of 180–350 μm. The sodium sulphate cores have sphericities in the range of 0.86 whereas the glass ballotini cores are almost perfect spheres. Microscope pictures of both core materials may be seen in Fig. 8.

Both types of core materials were coated with aqueous solutions of sodium sulphate in the amount of 15 w/w% using 1 w/w% Dextrin (CAS no. 9004-53-9 — Bulk density ~0.8 g/cm^{-3}) as binder. Demineralised water was used as solvent.

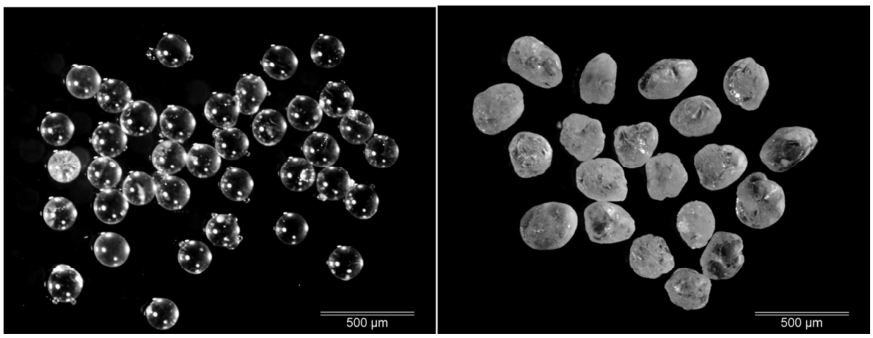

Fig. 8. Materials used in the coating experiments. Left) Uncoated glass ballotini cores. Right) Uncoated sodium sulphate cores.

Triphenylmethane colour (Sicovit Patent blue- CAS no. 3536-49-0) was used as colouring agent for all experiments in amounts of 0.1 w/w% in order to study the level of droplet penetration and the coating layer structure of the final coated granules.

2.5. Scaling parameters and scaling procedure

The relative droplet size and the drying force were tested as possible scaling parameters.

Based on the results by Mehta [1], Rambali et al. [2] scaled up a fluidised agglomeration process from small-scale (bed load 5 kg) to medium- (bed load 30 kg) and large-scale (bed load 120 kg) by looking at the effect of the particle bed moisture contents during and at the end of the spraying process and the effect of coating solution droplet size on the granule size. The fluidisation flow rate in m/s at the air distributor plate was kept constant in all their experiments in order to have approximately similar breaking forces on the granules. For the small- and medium-scale the same nozzle (liquid orifice diameter of 1.8 mm) was used whereas a three-head nozzle (liquid orifice diameters of 3×3.0 mm) was used for the large-scale fluid bed. The droplet size was controlled in terms of a relative droplet size Rd defined as the ratio of the coating solution mass spray rate $\dot{m}_{\text{spray}}$ divided by the mass airflow rate through the nozzle $\dot{m}_{\text{nozzle air}}$ squared according to Eq. (5).

$$\text{Rd} = \frac{\dot{m}_{\text{spray}}}{\left(\dot{m}_{\text{nozzle air}}\right)^2} \tag{5}$$

There is no scientific explanation for the definition of Rd in Eq. (5). Rambali et al. [2] claim that the Düsen-Schlick manufacturer of two-fluid nozzles have found that the droplet size is proportional to the ratio in Eq. (5). This is in agreement with Masters [10] suggesting that the mean spray droplet size d_{d} produced by pneumatic two-fluid nozzles follows the general relation in Eq. (6).

$$d_{\text{d}} = \frac{A}{\left(v_{\text{rel}}^2 \cdot \rho_{\text{air}}\right)^{\alpha}} + B \cdot \left(\frac{\dot{m}_{\text{nozzle air}}}{\dot{m}_{\text{spray}}}\right)^{\beta} \tag{6}$$

where v_{rel} is the relative velocity between air and liquid at the nozzle head and ρ_{air} is the atomisation air density. The exponents α and β are functions of nozzle design and A and B are constants involving both nozzle design and liquid properties. The general relationship in Eq. (6) indicates that the relation in Eq. (5) has some influence towards the mean droplet size although the exponent of 2 in the denominator in Eq. (5) is yet to be explained. It is however not an aim in the process of scale-up to keep the mean droplet size constant across scale. Instead it is the relative relationship in Eq. (5) that is kept fixed across scale in the present study as will be explained later.

Results by Hede [3] indicate that the drying force may be closely related to the tendency of agglomeration during fluid bed coating. The drying force indicates the rate of moisture evaporation from the particles. It combines the bed temperature and the bed moisture contents during steady state coating conditions in one parameter according to Eq. (7).

$$\text{Drying Force} = P_{\text{sat}}|_{T_{\text{bed}},100\%\text{rH}} - P_{\text{actual}} \tag{7}$$

where $P_{\text{sat}}|_{T_{\text{bed}},100\%\text{rH}}$ is the saturated pressure at the dry bulb temperature and P_{actual} is the actual vapour pressure of the fluidisation air at the bed temperature and the bed relative humidity conditions (measured above the nozzle thereby being an outlet relative humidity). P_{sat} is calculated from the Antoine equation and P_{actual} is given by Eq. (8).

$$P_{\text{actual}} = \frac{\text{Bed rH\%}}{100\ \text{rH\%}} \cdot P_{\text{sat}}|_{T_{\text{bed}}} \approx \frac{\text{Outlet rH\%}}{100\ \text{rH\%}} \cdot P_{\text{sat}}|_{T_{\text{bed}}} \tag{8}$$

In order to test the scalability in terms of the drying force, different levels of the bed temperature were chosen and fixed. The humidity of the inlet air could not be controlled in any of the three fluid bed set-ups but they were all recorded and no significant variation was observed. Eqs. (7) and (8) indicate furthermore, that the drying force is less sensitive to the relative humidity than to the bed temperature. Thus, it was possible to maintain the drying force at almost distinct levels without being able to precisely control the humidity of the inlet air.

The fluidisation velocity in m/s was kept constant at 3.3 m/s at a height in the fluidisation chamber just above the bottom plate through all experiments and across scale in order to try to maintain a similar granule collision velocity as well as a similar level of attrition across scale. All three types of fluid beds have a conical fluidisation chamber shape but the wall angles, bottom plate and other length dimensions are not dimensionally consistent going from small- to medium- and large-scale. A fluidisation velocity just above the bottom plate at 3.3 m/s corresponds in Nm^3/h to 93 Nm^3/h in the Strea-1 set-up, 270 Nm^3/h in the MP-1 and 680 Nm^3/h in the MP-2/3 set-up.

In the present studies, the relative droplet size was kept constant during scale-up as the nozzle pressure was kept constant at two distinct levels (1 bar or 3 bar) in each scale and the liquid feed rate to the nozzle controlled and fixed at the tube pump in order to maintain a constant relative droplet size across scale. Even though the nozzle liquid orifice diameter of 1.2 mm was identical and the nozzle pressure identical in all three scales, the nozzle airflows in g/min were not identical as the nozzle air annulus orifices were different for each type of nozzle. This means in other words that for fixed values of the relative droplet size the nozzle liquid feed flow in g/min and the nozzle airflow in g/min were different for each fluid bed. Initial experiments had to be conducted in order to determine the airflow through the nozzle for different nozzle pressures without connecting the liquid feed. This was done by connecting a simple household gas-meter to the nozzle outlet and then measure the airflow rate versus the nozzle pressure. The relative droplet parameter was kept constant across scale as follows: Knowing the airflow rate through the given nozzle at a given nozzle pressure, the value of the relative droplet size from the small-scale fluid bed was kept constant during up-scaling by calculating the liquid feed rate in g/min necessary to achieve an identical relative droplet size in the medium- and large-scale. The tube pump was thereby adjusted and fixed at this value throughout the coating experiment. With the given choice of drying force value and the choice of bed temperature, only the inlet air temperature was changed in each experiment in order to match the drying force and the relative droplet size across scale. As the heat loss per kg bed load to the surroundings is larger the smaller the fluid bed this operation principle means in practice that a smaller inlet temperature is necessary to maintain identical bed temperature the larger the bed.

Prior to coating, the core bed load was heated until the relative humidity inside the fluidisation chamber was constant, typically ranging from 5 rH% to 7 rH% depending on weather conditions. In each coating operation the aim was to coat until the bed load had increased 20 w/w%. This was done in order to make sure that a reasonable coating layer (~5–10 μm) had developed. After coating, the bed load was kept fluidised at identical fluidisation velocity and temperature conditions in order to dry the coated granules. This was done until the relative humidity inside the chamber was identical to the conditions prior to coating. This drying phase typically lasted less than 10% of the total coating time meaning that the amount of debris caused by attrition in the drying phase was of negligible importance for the final particle size distribution. The coated bed load was afterwards weighted in order to make sure that the bed load had gained in weight about 20 w/w%. For all the experiments in this paper, the batch weight gain was in the range of 18.7 w/w%–19.5 w/w% indicating little loss of core material as well as little loss of coating solution due to spray drying.

Table 1
Verification of the reproducibility of data from the three different fluid bed scales

Fluid bed scale	Experiment 1	Experiment 2	p-value from the χ^2 test
Strea-1 (small-scale)	Aggl%=49.0%	Aggl%=49.8%	0.21
MP-1 (medium-scale)	Aggl%=41.3%	Aggl%=40.7%	0.92
MP-2/3 (large-scale)	Aggl%=35.9%	Aggl%=37.1	0.16

The bed temperature was maintained at 55 °C and the nozzle pressure was kept at 1 bar in all experiments. Sodium sulphate cores (180–350 μm) were used in all experiments and the coating liquid was the standard 15 w/w% dry matter solution with 1 w/w% Dextrin as binder.

3. Results and discussion

3.1. Reproducibility of data

Quantitative analysis of data requires certainty of reproducibility of data as well as knowledge of equipment variances. Several reproducibility issues have been treated in the present paper: First of all the reproducibility of size fraction data from the sieve analysis. Ten samples from a representative coated batch were sieved independently in order to determine a standard deviation for the Retsch Sieve Shaker AS 200 control equipment. In terms of the agglomeration percentage, it was seen that the standard deviation was 0.82% thereby indicating that different batches having agglomeration percentages in the range of ±1.64% are not statistically different.

The reproducibility of data from the three different fluid bed scales was tested by performing two experiments with identical process and formulation conditions for each of the three fluid bed scales. As it may be seen from Table 1, the agglomeration percentage is well repeated within all three fluid bed types.

Formally, the reproducibility of the agglomeration percentage within the ±1.64% interval does not necessarily indicate that the particle size distribution also is reproduced, as the different size classes not necessarily have to be identical in order to achieve a similar agglomeration percentage. In order to check this, a χ^2 test was performed for all nine size classes in the two identical experiments for each scale (in case any of the size fractions were in the range of 0.01 w/w%, the size class was pooled into the next size class, as χ^2 tests on very small intervals may lead to false conclusions). The χ^2 test is used throughout the paper as it is a simple and widely used test for statistical significant analysis of categorical data as the sieve fractions.

As observed from Table 1, all the p-values are far above 0.05 (corresponding to a 95% confidence interval) indicating that the six different particle size fractions are well reproduced in pairs. The conclusion from these first experiments is that, with identical process and formulation conditions, it is possible to

reproduce results with sufficient accuracy to perform statistical quantitative analysis and comparison of the data.

3.2. Matching the degree of agglomeration and particle size distributions across scale

In order to test the application of the drying force and relative droplet size as scaling parameters, a campaign of different fluid bed coating experiments was set up. An overview of the different experiments may be seen from Table 2.

The conditions for the eighteen coating experiments (six in each fluid bed scale) in Table 2 were carefully chosen in order to test the influence of the various parameters involved in the fluid bed coating process including the influence of the drying force, the relative droplet size and the type of core material. The experiments were conducted in a six week period under similar weather conditions with room temperatures around 23 °C and room humidities in the range of 35–52 rH%.

Important to note is that the coating time naturally increased with scale. Whereas the coating time in the small-scale took about 30 min (drying phase ~4–5 min) and about 1 h and 30 min in the medium-scale (drying phase ~5–8 min), the coating time in the large scale took about 3 h and 30 min (drying phase ~9–15 min). Seen in respect to the difference in core material bed load with scale this means that the coating time is roughly 60 min per kg core material in the small-scale, 23 min/kg in the medium-scale and 9 min/kg in the large scale. These coating conditions are in the intense end of the usual range for all three scales.

Table 2
Overview of the scaling experiments

Fluid bed equipment	Experiment code	Core material	Bed temperature (°C)	Nozzle pressure (bar)
Strea-1 (small-scale)	S1	Na_2SO_4	55	3
	S2	Glass ballotini	55	3
	S3	Na_2SO_4	55	1
	S4	Na_2SO_4	50	3
	S5	Na_2SO_4	45	3
	S7	Glass ballotini	55	1
MP-1 (medium-scale)	M1	Na_2SO_4	55	3
	M2	Glass ballotini	55	3
	M3	Na_2SO_4	55	1
	M4	Na_2SO_4	50	3
	M5	Na_2SO_4	45	3
	M7	Glass ballotini	55	1
MP-2/3 (large-scale)	L1	Na_2SO_4	55	3
	L2	Glass ballotini	55	3
	L3	Na_2SO_4	55	1
	L4	Na_2SO_4	50	3
	L5	Na_2SO_4	45	3
	L7	Glass ballotini	55	1

As the coating times are so different according to the fluid bed scale, a phenomenon such as attrition is an important phenomenon to consider regarding the match of particle size distribution across fluid bed scale. Formally, it seems to be important whether the particles are coated in 30 min or in 3 h. However, the level of attrition is not in any way linearly dependent on time. Results by Hede [3] have shown that rather than a linear relationship between the amount of attrition and processing time there is a power law relationship (the so-called Gwyn relationship presented first by Gwyn [11]). This means that the majority of the debris caused by attrition is produced in the first phase of fluidisation and thus, that the total amount of debris is not significantly affected by a prolonged processing time. At the fluidisation velocities used in the present studies the majority of debris is produced within the first 15 min of fluidisation. Hence, concerning the level of attrition it is of minor practical importance whether the coating time lasts 30 min of 3 h and 30 min.

A schematic overview of the resulting agglomeration percentages and levels of corresponding drying forces and relative droplet sizes may be seen from Table 3. Note that the rightmost column shows p-values from χ^2 tests performed on the three sets of sieve fractions within the same scaling attempt.

There are many interesting things to extract from the results in Table 3. Going horizontally in Table 3, the drying force as well as the relative droplet size are maintained whereas either one or both of these parameters are changed going in the vertical direction. Comparing scaling attempts A, D and E, in which only the relative droplet size has been kept constant, it becomes evident that there is a relation between the drying force and the agglomeration tendency but that the relation is not in any way linear. For example, the drying force has been reduced from around 12 kPa in attempt A to around 8.5 kPa in attempt D whereas the agglomeration percentages are not statistically significant different. When further reducing the drying force to around 6 kPa, the agglomeration tendency increases significantly. These tendencies are qualitatively reasonable since a higher agglomeration tendency is expected with decreasing drying force due to slower drying rate. With decreasing drying force the coating droplets will dry slower leaving the coating layer wet for a longer time on the core surfaces, increasing the chance of liquid bridge building between particles resulting in solid bridge bonding formation upon drying and thereby permanent agglomeration.

The influence of the relative droplet size on the agglomeration tendency may be observed from the comparison of scaling attempts A and C. Going from attempt A to C, the relative droplet size is roughly increased seven times whereas the agglomeration tendency is increased more than thirty-five times. This tendency seems qualitatively reasonable. With the increased relative droplet size, the actual droplet size is increased as well, although not as much as seven times as it will be discussed in a coming section. With increased droplet diameter under similar drying force conditions, the larger droplets will remain wet for a longer time thereby increasing that chance of liquid bridge building between particles and thereby increased chance of agglomeration.

Table 3
Overview of results from the six scaling attempts in terms of relative droplet size (Rd) in min/gram and drying force (Df) in kPa

Scaling attempt	T_{bed} in °C	P_{nozzle} in bar	Strea-1 (small-scale)		MP-1 (medium-scale)		MP-2/3 (large-scale)		p-value from χ^2 test
A	55	3	Exp. S1 Rd=3.5×10^{-3}	Aggl%=0.07 Df=12.2	Exp. M1 Rd=3.5×10^{-3}	Aggl%=1.27 Df=12.0	Exp. L1 Rd=3.5×10^{-3}	Aggl%=1.45 Df=12.5	0.07
B	55	3	Exp. S2 Rd=3.5×10^{-3}	Aggl%=0.15 Df=11.6	Exp. M2 Rd=3.5×10^{-3}	Aggl%=0.24 Df=12.1	Exp. L2 Rd=3.5×10^{-3}	Aggl%=0.18 Df=11.8	0.59
C	55	1	Exp. S3 Rd=24.5×10^{-3}	Aggl%=49.77 Df=10.9	Exp. M3 Rd=24.5×10^{-3}	Aggl%=41.23 Df=12.0	Exp. L3 Rd=24.5×10^{-3}	Aggl%=35.93 Df=12.0	0.02
D	50	3	Exp. S4 Rd=3.5×10^{-3}	Aggl%=0.23 Df=8.4	Exp. M4 Rd=3.5×10^{-3}	Aggl%=1.51 Df=8.9	Exp. L4 Rd=3.5×10^{-3}	Aggl%=0.89 Df=8.6	0.14
E	45	3	Exp. S5 Rd=3.5×10^{-3}	Aggl%=33.64 Df=5.5	Exp. M5 Rd=3.5×10^{-3}	Aggl%=7.18 Df=6.4	Exp. L5 Rd=3.5×10^{-3}	Aggl%=13.10 Df=6.8	<0.01
F	55	1	Exp. S7 Rd=24.5×10^{-3}	Aggl%=49.54 Df=11.7	Exp. M7 Rd=24.5×10^{-3}	Aggl%=48.39 Df=11.9	Exp. L7 Rd=24.5×10^{-3}	Aggl%=48.26 Df=11.8	0.48

The p-values in the rightmost column arise from a χ^2 test of the three sets of sieved fractions within the same scaling attempt. Scaling attempts B and F were carried out with glass ballotini cores whereas the other scaling attempts were done with sodium sulphate cores.

Comparing the agglomeration tendencies within each scale in attempts A, D and E as well as in attempts A and C indicates that granulation process control in terms of either drying force alone or relative droplet size alone is not a successful choice as the agglomeration tendency within each scale cannot be maintained in terms of fixing either of these parameters alone. Next is to determine whether or not a combination of the relative droplet size and the drying force may be applied for successful up-scaling.

Comparing the agglomeration tendencies from the six scaling attempts, and the corresponding p-values from the χ^2 tests, indicate that successful scaling is achieved in scaling attempts A, B, D and F all having agglomeration percentages far inside the ±1.64% range within each scaling attempt and furthermore, all have p-values above 0.05. This means that not only are the cut-off values corresponding to the agglomeration percentages matched across three scales, but in addition the different particle size fractions are identical on a 95% confidence level. An example of how well the particle size classes are matched across scale may be seen from Fig. 9 showing a Rosin–Rammler–Sperling–Bennet plot of the particle size fractions from scaling attempt D. Interestingly, the best results are found with the glass ballotini core experiments in scaling attempts B and F. Here the tendency of agglomeration is closely reproduced across scale and the p-values are far above 0.05 indicating high reproducibility of the particle size fractions. The glass ballotini cores may in many ways be seen as the ideal core material. Besides being almost perfectly spherical, glass ballotini cores are furthermore non-porous and so an issue such as droplet penetration is not likely to interfere with the tendency of agglomeration in the same complex manner as it may be the case with sodium sulphate cores. The comparison of scaling attempt A with B and attempt C with F indicate however that the agglomeration tendency is fairly similar on an overall level whether the core material is sodium sulphate cores or glass ballotini cores. The somewhat smaller agglomeration tendencies in the medium- and large-scale experiments in attempt C compared to attempt F may indicate that possible droplet penetration into the sodium sulphate cores could result in decreased tendency of agglomeration in accordance with other experiments by Hede [3].

Two scaling attempts C and E are statistically unsuccessful as the agglomeration percentages are beyond the ±1.64% range. Likewise are the p-values from the χ^2 tests below the 0.05 limit although scaling attempt C is not far away with a p-value of 0.02. In both cases the agglomeration tendency is largest in the small-scale indicating that, with identical process and formulation conditions, the small-scale fluid bed is less resistant to agglomeration. The reasons for this could be the fact that the temperature is less uniform within the bed the smaller the scale whereas the heat loss from the particle bed load is much higher the smaller the scale. The scaling attempts C and E are characterised by having a combination of a high relative droplet size and high drying force and a combination of a low drying force and low relative droplet size respectively, which means that the experiments could be in the extreme ends of the plausible range of the drying force and relative droplet size parameters. This could explain why these two scaling attempts are not successful while the others are.

Even though the coating conditions in scaling attempts A, B, D in overall have caused a low tendency of agglomeration the processes were not run under particular conservative coating

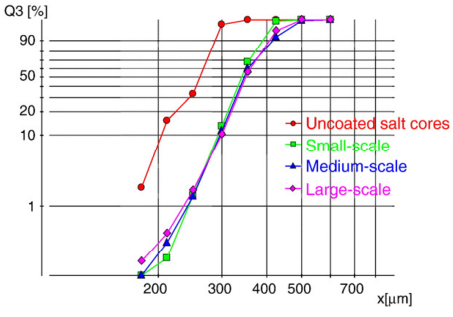

Fig. 9. RRSB-plot (Rosin–Rammler–Sperling–Bennet) of particle size fractions from scaling attempt D.

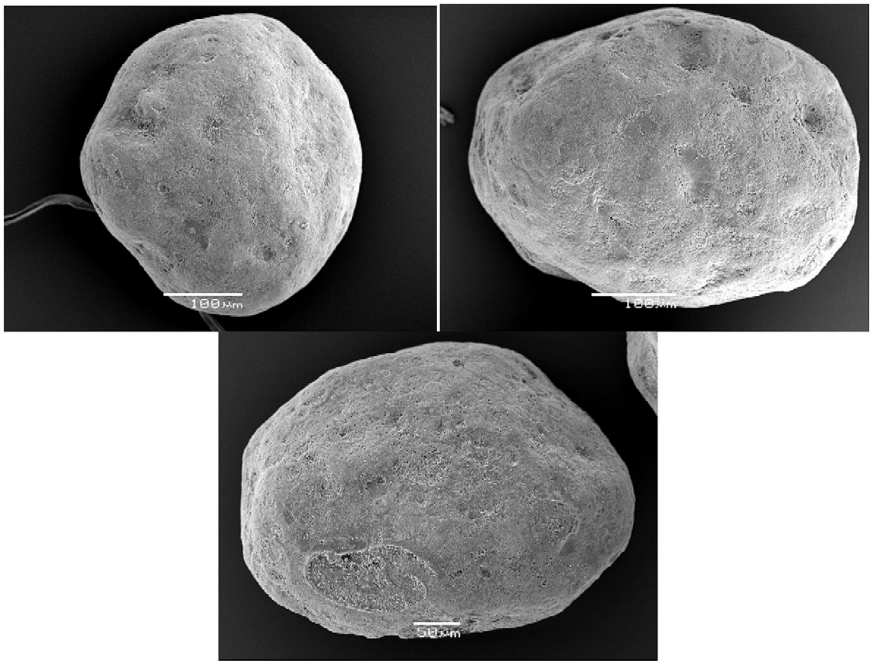

Fig. 10. SEM pictures from scaling attempt A. Above left) Sodium sulphate core coated in the small-scale. Above right) Sodium sulphate core coated in the medium-scale. Below) Sodium sulphate core coated in the large-scale.

conditions as mentioned previously. The coating conditions in scaling attempts C, E and F, all causing a high degree of agglomeration, were on the other hand not significantly more intense than for the other scaling attempts although these three scaling attempts were performed with either a low nozzle pressure or a low bed temperature. This illustrates that agglomeration is a phenomenon that indeed is sensitive and often occurs due to small changes in the process conditions.

3.3. Morphology and droplet penetration studies

Although maintaining the particle size distribution across scale is essential for most practical applications of fluid bed coating processes, issues such as the coating layer morphology and appearance may also have a significant importance regarding the final product properties. Morphology of the coating layer may not necessarily be identical just because the agglomeration tendency and particle size fractions are, and this may again strongly affect the mechanical properties of the granules as observed previously by Beekman [12] and Hede et al. [13] among others. In order to test this, selected coated granule batches from all three scales were examined in optical microscope (Olympus KL 1500 LCD) and further by SEM (JEOL Scanning Electron Microscope).

An example of SEM pictures of sodium sulphate cores coated in three different fluid bed scales from the same scaling attempt A may be seen in Fig. 10. As observed, the morphology of the coating layer is relatively homogenous in all three cases and there is no significant difference in smoothness among the three batches. The coating layer structure of granules from the medium-scale batch M1 from the same scaling attempt A was furthermore examined in a number of cut-through profiles in SEM. As seen from a typical profile in Fig. 11, there are primarily amorphous regions in the coating layer with some crystalline regions. The coating layer is well attached to the core

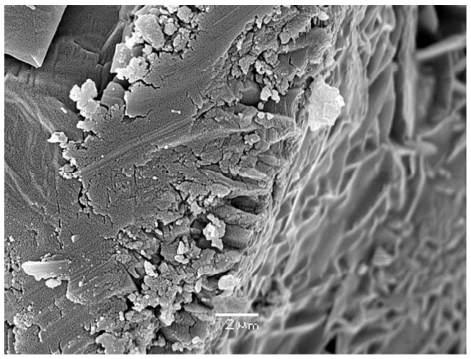

Fig. 11. A typical cut-through profile of a coated sodium sulphate core.

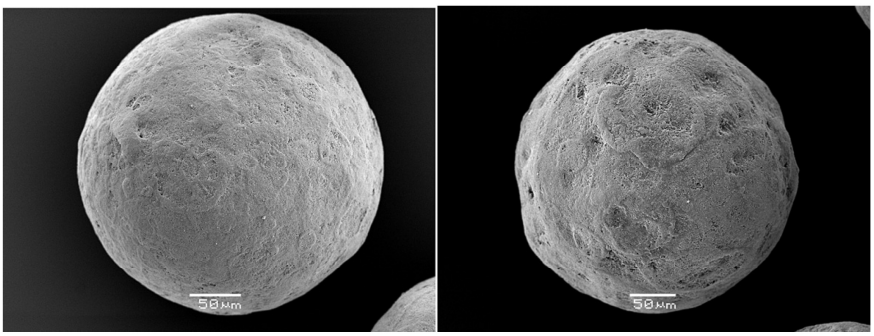

Fig. 12. Effect of relative and actual average droplet size on coating layer morphology. Left) Coated glass ballotini core from experiment M2. Right) Coated glass ballotini core from experiment M7.

structure and it is difficult to distinguish between the coating and core. Good adhesion of the coating layer often implies good coating layer mechanical properties which are almost always desired for practical applications of coated granules [12].

The process conditions used to coat the three granules in Fig. 10 and the granule in Fig. 11 have a high drying force and low relative droplet size. This indicates that the bed temperature was high and the average coating liquid droplet diameter was small during coating. That high nozzle pressure and high bed temperature lead to a strong and homogenous coating layer structure is in full accordance with previous fluid bed coating experiments performed by Hede et al. [13]. Although one might have expected that large droplets and low bed temperature would be optimal conditions for the coating droplets to merge homogenously together on the core surface, there is now sufficient evidence to state that this is not likely to always be the case. Instead, it seems more optimal in terms of morphology to coat each particle with many small droplets that dry fast enough to produce an amorphous coating layer structure. These tendencies however have only been observed so far for relative dilute coating solutions with dry matter contents not exceeding 15 w/w%. Probably, with such low dry matter contents, a certain re-dissolution of the outer coating layer takes place upon impact with new droplets and this seems to have a beneficial effect of the compactness and homogeneity of the final coating morphology.

The effect of the relative droplet size and thereby the actual average droplet size on morphology was further studied by comparison of SEM pictures from experiments M2 and M7 in which only the relative droplet size was changed in the medium-scale glass ballotini core experiments. As observed from Fig. 12, the effect of increasing the relative droplet size seven times, which corresponds to an increase in the Sauter mean droplet diameter around five times from roughly 8 µm to 41 µm estimated with the use of Eq. (9), is quite clear. Although both granules have relatively smooth coating surfaces, the droplet footprints are significantly larger on the right photo. Apparently, the large droplets have not had sufficient time to merge homogenously together before complete drying. This more uneven coating may very well result in poor mechanical properties with possible chance of chipping off flakes of the coating layer upon granule impact. This is further investigated in Section 3.4.

The influence of droplet penetration for the mechanical strength and morphology of a coating layer were observed by Hede et al. [13]. In the present studies, cut-through samples of coated granules from scaling attempts A, C and E was examined in optical microscope. Although the conditions, under which the

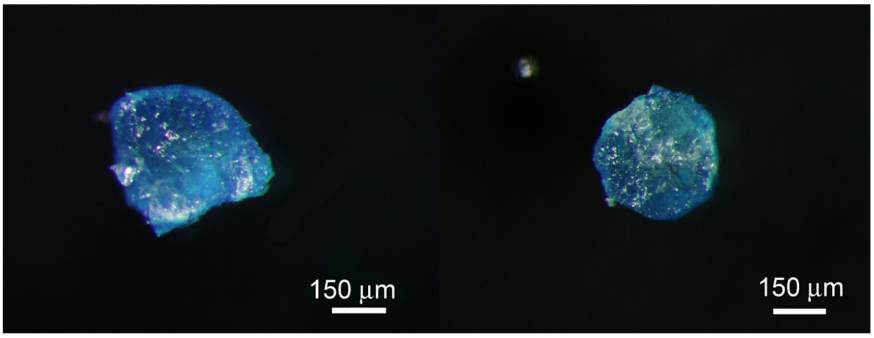

Fig. 13. Cut-through samples of: Left) Coated sodium sulphate cores from experiment S4. Right) Coated sodium sulphate cores from experiment M5.

granules from these three scaling attempts were processed, are quite different, the level of droplet penetration was significant and similar in all cases. Typical cut-through pictures from batches S4 and M5 may be seen in Fig. 13. As observed, the blue colour from the coating solution has penetrated almost equally all through the otherwise white sodium sulphate core. As the composition of the coating liquid solution is similar throughout the experiments, the similar level of droplet penetration is in accordance with expectations [18]. Results by Hede et al. [13] indicate that it is the viscosity of the coating solution that has the primary influence on droplet penetration, whereas parameters such as droplet size and bed temperature only play a secondary role in that respect.

3.4. Impact and attrition strength test results

Mechanical strength tests in the form of impact and attrition tests were carried out for all the 18 batches according to the principles in Section 2.3. A schematic overview of the resulting impact strength and attrition results from the 18 batches may be seen from Table 4. Note that the two rightmost columns show *p*-values from χ^2 tests performed on the three sets of attrition and P.I.G data respectively within the same scaling attempt. The choice to use χ^2 tests to determine whether or not the attrition and/or impact strength were repeated across scale was necessary due to the large spread in the values in Table 4. As the strength values are widespread it is not possible to simply find a statistic sound standard deviation and to use this to determine how well the strength results are matched across scale as it was done with the agglomeration data.

Analysing the impact strength and attrition strength results separately in Table 4 reveals several interesting things. Starting with the attrition results, it is observed from Table 4 first of all, that most attrition values are below the 0.1% limit provided by the Novozymes guideline. This means that most of the granules in the present study exhibit attrition dust levels below the required level for industrial coated granules. It may be further observed from Table 4 that in only two scaling attempts A and D the attrition values are well matched across scale on a 95% confidence level as the *p*-values both exceed 0.05. These two scaling attempts have both used sodium sulphate cores as core material and these two batches were the only ones with this core material that were successful in terms of matching the agglomeration tendency and particle size fraction in Table 3. It is interesting that the successful match of attrition strength in scaling attempts A and D are associated with some of the lowest attrition values in Table 4. This is most likely no coincidence. It is reasonable to expect that if two batches have granules highly resistant to attrition it will be much easier to match the amount of dust created compared to two batches that contains a higher proportion of weak granules. This is due to the fact that just a small portion of weak granules may unpredictably create relative large amounts of dust decreasing the chance of repeatable results.

Interestingly, the two scaling attempts B and F are unsuccessful regarding attrition. By far the worst attrition strength in Table 4 is observed for the glass ballotini cores. Being non-porous the coating droplets have no possibility to penetrate into the core structure and to build a cohesive structure to the same extent as with the sodium sulphate cores. Furthermore, it is reasonable to believe that that the sodium sulphate coating attach worse to glass ballotini cores than to sodium sulphate cores. This is likely to cause the poor attrition strength for these batches as is observed from Table 4. As with scaling attempts B and F the other scaling attempts C and E are unsuccessful towards the match of attrition strength. There is, however, one important overall tendency to extract from the scaling attempts B, C, E and F: It seems as if the attrition strength decreases with increasing scale meaning that the strongest granules are produced in the smallest scale. In a scale-up perspective this is an important discovery. Whereas it was seen from the agglomeration results in Table 4 that the agglomeration tendency often is larger the smaller scale, the attrition results show that the coated particles have a better resistance towards attrition when being produced in the small scale.

Regarding the match of impact strength across scale the tendencies in Table 4 are somewhat the opposite of the attrition tendencies. As it may be seen from the *p*-values in the rightmost column in Table 4 the impact strength tendencies were matched well in scaling attempts B, C and F whereas all the other scaling attempts were unsuccessful in that respect. As discussed earlier those three scaling attempts B, C and F all failed in the attempt to reproduce attrition strength across scale. Two of these scaling attempts have used glass ballotini cores and so it seems as if the impact breakage mechanisms are more well-defined and thereby easier to reproduce if the core materials are glass ballotini cores instead of sodium sulphate cores. Although being in the high end of the observed impact strength tendencies, the breakage percentages for the scaling

Table 4
Overview of the mechanical strength test results from the six scaling attempts

Scaling attempt	T_{bed} in °C	P_{nozzle} in bar	Strea-1 (small-scale)		MP-1 (medium-scale)		MP-2/3 (large-scale)		*p*-value from χ^2 test of attrition tests	*p*-value from χ^2 test of PIG tests
			$Y_{attrition}$ (%)	$Y_{breakage}$ (%)	$Y_{attrition}$ (%)	$Y_{breakage}$ (%)	$Y_{attrition}$ (%)	$Y_{breakage}$ (%)		
A	55	3	0.06	4.6	0.04	14.2	0.09	11.1	0.12	<0.01
B	55	3	0.20	7.6	1.26	8.1	2.13	7.9	<0.01	0.19
C	55	1	0.16	6.1	0.08	9.4	0.14	7.8	0.03	0.06
D	50	3	0.03	4.3	0.08	10.5	0.05	8.3	0.09	0.01
E	45	3	0.05	6.5	0.07	10.1	0.15	11.0	<0.01	0.02
F	55	1	0.40	5.9	3.38	7.1	5.85	6.3	<0.01	0.14

Scaling attempts B and F were carried out with glass ballotini cores whereas the other scaling attempts were done with sodium sulphate cores.

attempts B and F are not significantly larger than the breakage percentages observed for the sodium sulphate cores. In fact the impact strengths of the granules in scaling attempt F are among the best. Another interesting thing to note from Table 4 is that in general the particles with the poorest impact strength are produced in the medium-scale whereas the coated granules with the best impact strength are produced in the small-scale. This means in general that granules coated in the small-scale fluid bed have the best attrition as well as the best impact strength.

Overall, the results in Table 4 reveal an interesting general point, namely that good impact strength properties often mean poor attrition properties. The table also reveals that within a given fluid bed scale a low agglomeration tendency gives granules with poor impact strength but with good attrition properties although the tendency is not unambiguous. This may also be observed from Fig. 14 showing the measured $Y_{attrition}$ values in % versus the measured $Y_{breakage}$ values in %. Especially if the values for the small-scale fluid bed are left out a reciprocal tendency appears. Attrition mechanisms and failure due to impacts are in nature different, and from a theoretical point of view it seems reasonable that the two types of properties are inversely related. Whereas attrition often occurs as a result of gradual small-force wear (e.g. erosion, peeling or simply fatigue), fragmentation or chipping of the coating layer due to impacts on the other hand often occur at once and as a widespread damage phenomena [12,14]. This means that if a granule should be resistant to attrition, surface cracks in the coating layer should not be able to propagate. This requires a dense homogenous coating layer as has been observed in the SEM pictures for the coated sodium sulphate cores. Correlating the observations from the SEM pictures with the attrition results in Table 4, it seems reasonable to state that the attrition strength resistance increases with increasing homogeneity of the coating layer surface.

High impact strength resistance is somewhat different from attrition strength resistance as it requires a hindrance of crack propagation not just in the coating layer but also in the granule bulk phase. As the glass ballotini cores are denser and mechanically strong compared to sodium sulphate cores it is reasonable to expect a higher resistance towards crack propagation in the glass core structure than with the sodium sulphate cores. In accordance with this, the best impact strength tendencies are observed with the coated glass ballotini cores. Most likely more of the coating layer itself is removed upon impact compared to the coated sodium sulphate cores, due to a lower force of cohesion between the glass cores and coating layer as discussed earlier, but as the core structure remains relatively unaffected by the impacts, smaller amounts of fines is created on a weight basis. Thus a better impact strength value is observed for the coated glass ballotini cores although this in reality do not necessarily mean that less of the coating layer is removed upon impact.

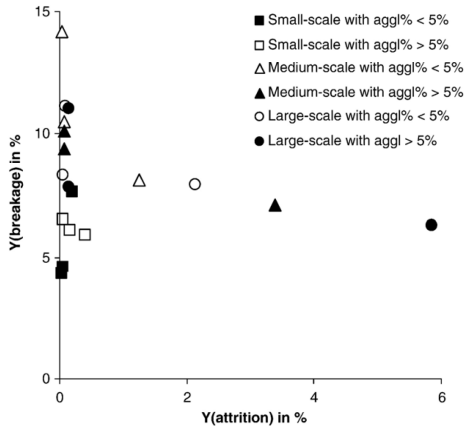

Fig. 14. Graph showing the measured $Y_{attrition}$ values in % versus the measured $Y_{breakage}$ values in %.

3.5. Scaling experience

The relative droplet size may at first seem as an odd scaling parameter as it has the unit of time per mass and just simply relates the nozzle air and liquid flow rate. Previous scaling attempts have alternatively used the average droplet size of the spray in a dimensionless scaling parameter [15,16,17]. However, since the distance from the nozzle outlet to the bed surface is often increasing when going up in scale, a constant average droplet size may not be the best choice during scale-up as the degree of droplet spray drying increases with distance. Instead the relative droplet size suggested by Rambali et al. [2] used in the present work seems as a more successful yet simple alternative. According to Eq. (5) the relative droplet size suggests that the ratio between the spray rate $\dot{m}_{spray}$ divided by the airflow through the nozzle $\dot{m}_{nozzle}$ squared should be kept constant across scale. Fixing the relative droplet size across scale automatically increases the average droplet size with scale as the nozzle airflow increases with scale at a given nozzle pressure thereby requiring a significant increase in the coating liquid flow rate. Although the increase in the average droplet size with scale not necessarily corresponds to the increase in the distance from bed surface to nozzle outlet it seems to be an adequate increase for practical purposes.

Estimations of the average droplet size from two-fluid nozzles used in this paper may be done in terms of the empirical correlation in Eq. (9) suggested by Masters [10].

$$d_{mmd} = \left[\frac{249 \cdot \gamma_{liq}^{0.41} \cdot \eta_{liq}^{0.32}}{\left(v_{rel}^2 \cdot \rho_{air}\right)^{0.57} \cdot A_{annulus}^{0.36} \cdot \rho_{liq}^{0.16}}\right] + 1260 \times \left[\left(\frac{\eta_{liq}}{\gamma_{liq} \cdot \rho_{liq}}\right)^{0.17} \cdot \left(\frac{1}{v_{rel}^{0.54}}\right) \cdot \left(\frac{\dot{m}_{nozzle\ air}}{\dot{m}_{spray}}\right)^{m}\right] \quad (9)$$

where

$$\dot{m} = -1 \text{ at } \left(\frac{\dot{m}_{nozzle\ air}}{\dot{m}_{spray}}\right) < 3 \text{ and } \dot{m} = -0.5 \text{ at } \left(\frac{\dot{m}_{nozzle\ air}}{\dot{m}_{spray}}\right) > 3$$

and d_{mmd} is the mass mean droplet diameter in μm, γ_{air} is the coating liquid surface tension (in dynes/cm), A is the area of the

air annulus in in.^{2}, η_{liq} is the coating liquid viscosity (in cP), v_{rel} is the difference between the nozzle atomising air velocity and the liquid velocity at the nozzle outlet (in ft/s) and the densities are in (in lb/ft^3). The mass mean droplet diameter in μm correlates with the Sauter mean diameter d_{32} in μm according to the empirical correlation in Eq. (10) [10].

$$d_{32} = 0.83 \cdot d_{mmd} \quad (10)$$

Maintaining the relative droplet size e.g. at $3.5 \cdot 10^{-3}$ min/g from the small-scale to the medium- and large-scale (as it was done in the successful scaling attempts A, B and D) corresponds to an increase in the d_{32} droplet size from 4.9 μm to 8.6 μm and 16.7 μm respectively. This means that even though the relative droplet size is maintained, the average droplet size does increase with scale as suggested by Rambali et al. [2].

Many prior studies of the fluid bed coating process tend to fix the nozzle pressure and inlet fluidisation temperature and then seek to maintain a chosen bed temperature by adjusting the nozzle spray rate. This operation principle has the advantage of being easy to apply in practice for the operator, but unfortunately has the disadvantage that the average droplet size will be varied with changes in the liquid feed rate to the nozzle until the desired bed temperature level is reached. Experience indicate that only minor changes in droplet size distributions will have significant influence on the chance of agglomeration [18], and earlier results by Hede [3] indicate that the agglomeration tendency is far more sensitive to minor changes in the droplet size distributions than to minor changes in the bed temperature. Furthermore, as the presented SEM pictures indicate, the morphology of the final coating layer is closely related to the droplet size distribution. To overcome some of these issues the present paper suggests to run nozzle conditions during coating strictly conservative by maintaining fixed values of the nozzle pressure as well as the liquid flow rate to the nozzle throughout the entire coating experiment. The bed temperature should be adjusted only in terms of adjusting the inlet air temperature either manually or by automatic adjustment available in most modern large-scale fluid bed equipment.

4. Conclusion

On an overall level, successful up-scaling of top-spray fluid bed coated particles by 48 times in weight from the small-scale over medium-scale to the large-scale fluid bed has been achieved. The tendency of agglomeration and particle size distribution were repeated across scale. Although two of the six scaling attempts were statistically unsuccessful with respect to agglomeration tendency, and clearly illustrates the limitations of the drying force and relative droplet size as universal scaling parameters, the scaling results presented in this paper are promising in terms of maintaining particle size fractions across scale. The best results were achieved with non-porous highly spherical glass ballotini cores but also statistically sound scale-up results were achieved with commercial sodium sulphate cores.

Studies of coated granules in SEM and by visual microscopy showed similar coating morphology across scale when the drying force and the relative droplet size were kept constant. Impact and attrition strength tests showed some scattering in the tendencies although most of the attrition values were below the required 1000 ng/g level. The best impact strength tendencies were observed with the coated glass ballotini cores whereas the best attrition strength values were observed with sodium sulphate cores coated under conditions with high bed temperature and high nozzle pressure. It was observed how high impact strength is often inversely related to high attrition strength.

The results presented in this paper suggest that two parameters should be kept constant during scale-up: A drying force parameter combining bed temperature with humidity conditions inside the fluidisation chamber during steady state coating conditions, and a relative droplet size parameter relating the liquid nozzle feed rate to the nozzle airflow. The present scale-up attempts thereby focus on nozzle conditions and temperature and humidity conditions during coating — all properties known to be of major importance regarding agglomeration tendency and coating layer properties. The paper further propose that nozzle conditions are fixed throughout the coating process and that conditions inside the fluidisation chamber are adjusted only in terms of the inlet air temperature.

Scale-up in terms of combined drying force and relative droplet size is a new proposal involving both the particle-level and the unit-operation scale. The principles presented in this paper provide simple engineering principles for scale-up of fluid bed coating processes.

Acknowledgements

This project was performed in collaboration with Novozymes A/S, who also financially supported the project. Peter Dybdahl Hede is a member of the Novozymes Bioprocess Academy as well as the MP$_2$ T Graduate School in Chemical Engineering at the Department of Chemical Engineering, Technical University of Denmark, funded by the Danish Technical Research Council, the European Union, the Nordic Energy Research, Dong Energy A/S, Vattenfall A.B., F L Smidth A/S, and Public Service Obligation funds from Energinet.dk and the Danish Energy Research program.

References

[1] A.M. Mehta, Scale-up considerations in the fluid-bed process for controlled-release products, Pharmaceutical Technology (12) (1988) 46–52.
[2] B. Rambali, L. Baert, D.L. Massart, Scaling up of the fluidized bed granulation process, International Journal of Pharmaceutics (252) (2003) 197–206.
[3] P.D. Hede, Fluid bed coating and granulation, Master Thesis, Department of Chemical Engineering, CHEC Research Center, Technical University of Denmark, 2005.
[4] A.C. Bentham, C.C. Kwan, R. Borefijn, M. Ghadiri, Fluidised-bed jet milling of pharmaceutical powders, Powder Technology 141 (2004) 233–238.
[5] R. Boerefijn, N.J. Gudde, M. Ghadiri, A review of attrition of fluid cracking catalyst particles, Advanced Powder Technology: The International Journal of the Society of Powder Technology, Japan 11 (2) (2000) 145–174.

[6] W.L. Forsythe, W.R. Hertwig, Attrition characteristics of fluid cracking catalysts — laboratory studies, Industrial Engineering Chemistry (41) (1949) 1200–1206.
[7] R. Boerefijn, S.H. Zhang, M. Ghadiri, Analysis of ISO fluidized bed jet test for attrition of fluid cracking catalyst particles, in: L.-S. Fan, M. Knowlton (Eds.), Fluidization IX, ECI Engineering Foundation, New York, 1998, pp. 325–332.
[8] S.-H. Zhang, R. Boerefijn, M. Ghadiri, The effect of orifice size on the breakage of fluid cracking catalyst particles in fluidised bed jets, Proceedings from Third World Congress on Particles Technology, Brighton, UK, 1998.
[9] Novozymes, Internal Attrition Guidelines by Novozymes A/S, Bagsværd, Denmark, 2006.
[10] K. Masters, Spray drying — an Introduction to Principles Operational Practice and Applications, Leonard Hill Books, London, 1972.
[11] J.E. Gwyn, On the particle size distribution function and the attrition of cracking catalysts, AIChE Journal 15 (1) (1969).
[12] W.J. Beekman, Measurement of the Mechanical Strength of Granules, Ph.D. Thesis, Technische Universiteit Delft, 2000.
[13] P.D. Hede, A.D. Jensen, P. Bach, Small-scale top-spray fluid bed coating: Granule impact strength, agglomeration tendency and coating layer morphology, Powder Technology 176 (2007) 156–167.
[14] R. Pitchumani, G.M.H. Meesters, B. Scarlett, Breakage behaviour of enzyme granules in repeated impact test, Powder Technology (130) (2003) 421–427.
[15] K. Hapgood, Nucleation and binder dispersion in wet granulation, Ph.d. Thesis, University of Queensland, 2000.
[16] J.D. Litster, K.P. Hapgood, J.N. Michaels, A. Sims, M. Roberts, S.K. Kameneni, Scale-up of mixer granulators for effective liquid distribution, Powder Technology 124 (2002) 272–280.
[17] J.D. Litster, Scaleup of wet granulation processes: science not art, Powder Technology 130 (2003) 35–40.
[18] P.D. Hede, Towards Mathesis Universalis: modern aspects of modelling batch fluid bed agglomeration and coating systems —a review, Department of Chemical Engineering, Technical University of Denmark, 2006, pp. 1–101.

Chemical Engineering Science 63 (2008) 3821 – 3842

Contents lists available at ScienceDirect

Chemical Engineering Science

journal homepage: www.elsevier.com/locate/ces

Review

Two-fluid spray atomisation and pneumatic nozzles for fluid bed coating/agglomeration purposes: A review

Peter Dybdahl Hede[a,b], Poul Bach[b], Anker D. Jensen[a,*]

[a]CHEC Research Center, Department of Chemical Engineering, Technical University of Denmark, Building 229, DK-2800 Kgs. Lyngby, Denmark
[b]Solid Products Development, Novozymes A/S, Smørmosevej 11, DK-2880 Bagsvaerd, Denmark

ARTICLE INFO

Article history:
Received 1 February 2008
Received in revised form 1 April 2008
Accepted 1 April 2008
Available online 10 April 2008

Keywords:
Atomisation
Two-fluid nozzle
Pneumatic nozzle
Airblast atomizers
Droplet size
Coating
Fluid bed

ABSTRACT

In fluid bed processing in the chemical, food or pharmaceutical industries, pneumatic nozzles are typically used to convert binder or coating liquids into droplets. Producing fine droplets from liquids in a gas phase is termed atomisation, and it involves complex phenomena which are not yet fully understood. This paper provides a systematic and up-to-date review of two-fluid nozzle designs and principles together with a presentation of nozzle fundamentals introducing basic nozzle theory and thermodynamics. Correlations for the prediction of mean droplet diameters are reviewed, compared and accompanied by a discussion of their use.

Contents

* Corresponding author. Tel.: +45 4525 2841; fax: +45 4588 2258.
E-mail address: aj@kt.dtu.dk (A.D. Jensen).

0009-2509/$ - see front matter © 2008 Elsevier Ltd. All rights reserved.
doi:10.1016/j.ces.2008.04.014

1. Introduction

Pneumatic atomisation is the process of producing sprays by the disruptive action of a high velocity gas upon a liquid stream. As two fluid streams are involved this is usually referred to as *two-fluid atomisation*, and nozzles that work by these principles are known as *two-fluid nozzles* (Kim and Marshall, 1971). The atomisation of a liquid into multiple droplets has many important industrial applications including e.g. in atomisation of fuels in combustion processes, in mass-transfer operations, in making granular products in fluid beds and coating of surfaces and particles, etc. (Rizkalla and Lefebvre, 1975; Walzel, 1993). Usually the main reason for atomising a liquid is to obtain a large and rapid increase in its surface area and thereby a corresponding increase in its rate of evaporation. Although the phenomena behind atomisation are difficult to model and fully understand, the atomisation of a liquid in practice is fortunately fairly easy to accomplish. Basically, it is simply a matter of creating a high relative velocity between the liquid and the surrounding air. In general, the higher the relative velocity the smaller is the resulting mean droplet size (Lefebvre, 1989a; Rizkalla and Lefebvre, 1975).

One example of industrial application of two-fluid nozzles is the fluid bed coating process. To improve handling and product properties, active ingredients such as enzymes and pharmaceuticals are often incorporated into granules. Typically, inert carrier particles are coated with an aqueous solution of the ingredient being sprayed onto the agitated particle bed through two-fluid nozzles in the fluidised bed set-up. As an indication of the importance of nozzle conditions for such processes, fluid beds used for agglomeration or coating purposes are typically classified according to the nozzle position (Guignon et al., 2002). In general, there exist four basic types of batch granulation systems being the top-spray, bottom spray, Wurster and rotor with side spray. A sketch of the four types can be seen in Fig. 1. In such batch fluid beds the fluidisation chamber typically has a cylindrical or conical shape where the fluidisation air is distributed from the bottom through a grid with an adequate partition and size of holes. Small-scale fluid beds typically have only a single nozzle. but larger production—scale fluid beds can have more than a few dozen nozzles (Guignon et al., 2002).

The desired product in a fluid bed coating process is typically a product consisting of unagglomerated individual carrier particles each coated homogenously with a layer of the active ingredient. If formulation or process conditions such as fluidisation velocity, bed temperature, humidity of the air, spray rate and droplet size, etc., are incorrectly chosen, either excessive agglomeration or excessive spray drying of the spray feed will happen. In both cases a poor product quality and loss is achieved. Previous studies of fluid bed granulation, especially by Schæfer et al. (1977a,b,1978a–c), Hede et al. (2007a–c), Waldie (1991) and Schaafsma (1998,2000a,b) have identified spray conditions, and thereby the operation of the two-fluid nozzle, as one of the most critical factors for the whole process. Experience has indicated that a priori knowledge and control of the droplet size distribution and the mean droplet diameter is vital for the successful fluid bed coating process (Salman et al., 2007). It is thereby essential for theoretical fluid bed considerations and of practical importance to study two-fluid atomisation in detail. Even so, droplet size data from scientific two-fluid atomisation studies are scarce and partly inconsistent (Lefebvre, 1989a, 1996).

The present paper is a review of two-fluid nozzle theory presenting first two-fluid nozzle designs covering both internal and external mixing nozzles. The principles of atomisation is presented including topics such as dripping, break-up of the laminar jet, flow regimes in a circular-shaped nozzle, liquid-sheet formation and break-up as well as break-up of liquid in gases. The paper further introduces nozzle thermodynamics with focus on flow velocities. Next, variables affecting the mean droplet size are discussed, and various droplet size correlations are reviewed, dividing the correlations into categories of internal and external mixing correlations. The following section addresses the issue of droplet size distributions, and the review is concluded with a practical summary comparing the reviewed droplet size correlations in the context of a standard commercial two-fluid nozzle.

2. Two-fluid nozzle designs

There are various nozzle designs and nozzle sizes available to produce optimum conditions of liquid–air contact for atomisation. The types of nozzles of interest to fluid bed operations fall into a category commonly known as *airblast atomisers* (Lefebvre, 1989a). For the most commonly used designs, the contact between the liquid and gas phase takes place at the nozzle exit. This principle is known as *external mixing*. In other airblast designs, the liquid is injected into the high-velocity airstream in the form of one or more discrete jets. This principle is commonly known as *plain jet* or *internal mixing* atomisation (Ayres et al., 2001; Lefebvre, 1989a, 1996). The design principles of internal and external two-fluid nozzles may be seen from Fig. 2.

Both internal and external mixing nozzles can be prefilming nozzles. The principle behind prefilming nozzles (see e.g. Fig. 3a) is that the liquid is first spread out into a thin continuous sheet and then subjected to the atomising air, which is known to give a better control of the droplet size distribution. In general, the atomisation performance of such prefilming nozzles (being internal or external mixing), is superior to that of simple designs, but they are only really effective when both sides of the liquid sheet are exposed to the gas stream. This requirement gives complications in the physical design which is one of the reasons why there are numerous prefilming nozzle designs available but only few being used industrially (Niro, 2007). Overall, it is reasonable to divide the two-fluid nozzles into the following categories (Masters, 1972; Ayres et al., 2001; Walzel and Broll, 2000):

- Contacting of air and liquid within the nozzle head (internal mixing).
- Contacting of air and liquid outside the nozzle head (external mixing).
- Contacting air and liquid at the rim of a rotating nozzle head (pneumatic cup atomiser).

A fourth type of nozzle combines internal and external mixing by using two air flows within the nozzle head. Such types of nozzle are commonly known as three-fluid nozzles. Such advanced nozzles and other types of rotary atomisers are seldom used in fluid bed equipment and are not discussed here (Guignon et al., 2002; Teunou and Poncelet, 2002).

2.1. Internal or external mixing nozzle

There is some overlap with respect to performance for the internal and the external mixing two-fluid nozzles, and the choice between the two types is often based on several things. All two-fluid nozzles have either limited gas flow rates, high specific gas consumption, modest liquid capacities, a wide droplet size distribution or a combination of these limitations (Lefebvre, 1989a). The external mixing nozzle has the liquid supply in the centre and the atomising gas supplied concentrically. Scaling this principle to larger liquid and gas flows shows typically an increasing gas-to-liquid rate for a given mean droplet diameter (Gretzinger and Marshall, 1961; Lefebvre,

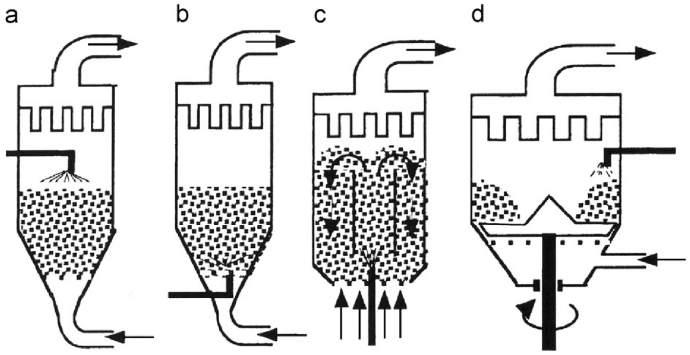

Fig. 1. Different types of batch fluid beds: (a) top spray, (b) bottom spray, (c) Wurster type, (d) rotor with side spray (Teunou and Poncelet, 2002).

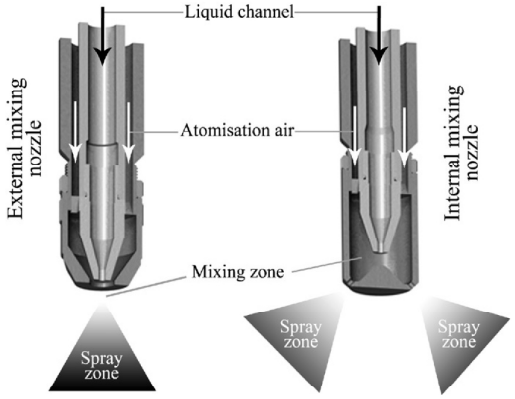

Fig. 2. Examples of two-fluid nozzle designs. Left: simple external mixing nozzle. Right: simple internal mixing nozzle (Salman et al., 2007).

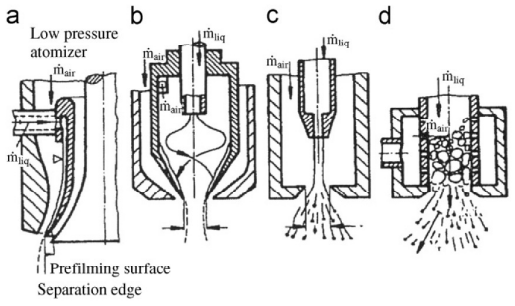

Fig. 3. Principles of two-fluid nozzles with internal mixing: (a) prefilming type, (b) type with central inlet and gas-swirl chamber, (c) simple type, (d) type with a central liquid channel with gas inlet sideways (Walzel, 1993).

1989a). For liquid rates higher than 30 kg/h and the demand for a mean droplet size below 10 μm, gas flows are no longer found within a realistic range. Internal mixing nozzles in general require less air than external mixing nozzles in order to produce droplets with the same mean droplet diameter. This is due to a higher energy transfer between the air and the liquid, as the atomisation takes place under pressure difference inside the mixing chamber because the air and liquid pressures become equal first at the mixing chamber outlet (Hund, 1994). This is especially an advantage during nozzle scale-up where the increase in gas-to-liquid flow rate with scale is much less than for external mixing nozzles (Lefebvre, 1989a, b). The downside is however, that over time, the impact surface becomes eroded and affects the spray droplet size pattern. The lifetime of an internal mixing nozzle can be very short if the liquid has solid impurities in it. External mixing nozzles require more air, but the advantage is that it is possible to atomise a liquid that otherwise would have evaporated inside the mixing chamber of an internal mix nozzle (Spray Drying Systems Co., 2000).

For fluid bed processes the nozzle type and nozzle location in the bed is known to have significant importance. In that respect, preferably, two-fluid nozzles with external mixing, often of the simplest designs, are used to atomise the coating liquid into droplets, because the droplet size can be varied independently from the liquid flow. Furthermore, the chance of clogging is reduced with external mixing nozzles by the extended liquid insert. The nozzle can be placed above, or in the bed, spraying sideways, upwards or downwards (Salman et al., 2007). Some authors (Smith and Nienow, 1982, 1983) have used two-fluid nozzles with internal mixing in a fluid bed context. In their studies the nozzle was placed in the bottom of the bed and in this way Smith and Nienow (1982, 1983) were able to avoid caking of the nozzle by spraying upwards, although collapse of the wet particle bed occurred at lower liquid feed rates compared to top-spraying. A disadvantage of spraying upwards in the bed is the greater attrition of granules due to the high air velocities near the nozzle (Salman et al., 2007). Other detailed fluid bed nozzle studies have been reviewed by Schaafsma (2000).

2.2. Internal mixing nozzles

Internal mixing designs offer the advantage of achieving higher energy transfer than with external mixing (Masters, 1972). With these nozzles, the required input pressure of the liquid depends on where the liquid is introduced into the nozzle. The degree of mixing inside the nozzle increases from the left to the right in the internal mixing nozzles of different designs as shown in Fig. 3 (Walzel, 1993).

In Fig. 3a is shown a prefilming type of internal mixing nozzle in which the liquid is supplied to the prefilming part through a distributor slit and is accelerated by the gas flow in axial direction

all the way to the separating edge. This edge is usually exposed to the gas impact not only from the front but also from the backside. More on these special and rare internal nozzle designs may be found in Lefebvre (1980) and Wittig et al. (1985).

The type in Fig. 3b is a nozzle with a central liquid inlet and a gas-swirl chamber. The liquid here precipitates on the walls of the swirl chamber and is transported by the gas in film form to the separation edge where it is subsequently broken up. Such types of nozzle constructions are particularly suited for atomising suspensions (Walzel, 1993; Mulhem et al., 2006).

The nozzle design in Fig. 3c is the oldest and simplest internal mixing design. With this configuration a cylindrical liquid jet is produced in an accelerating chamber, which is transported by the gas to the nozzle orifice where the jet is atomised. Nukiyama and Tanasawa (1939, 1940) conducted the first studies for this type of nozzle in the thirties of which some will be presented in Section 6.1.

The nozzle type in Fig. 3d has a central liquid channel with constant cross-sectional area into which the gas is introduced from the outside toward the center through small perforations. A particular intensive mixing of liquid and gas results by predispersion followed by subsequent atomisation by expanding the gas past the point of least cross-sectional area. Nozzles of this construction have been found particularly useful for high liquid loadings with $\dot{m}_{\mathrm{liq}}/\dot{m}_{\mathrm{air}} > 5$, where $\dot{m}_{\mathrm{air}}$ is the mass rate of atomisation air and $\dot{m}_{\mathrm{liq}}$ is the mass rate of liquid (Walzel, 1993). The ratio between $\dot{m}_{\mathrm{air}}$ and $\dot{m}_{\mathrm{liq}}$ is some times referred to as the air-to-liquid ratio (ALR) being $\mathrm{ALR} = \dot{m}_{\mathrm{air}}/\dot{m}_{\mathrm{liq}}$.

2.3. External mixing nozzles

Although internal mixing nozzles still find use for fluid bed purposes, external mixing nozzles enable greater control of atomisation by independent control of both liquid and air streams, and for that reason external mixing nozzles are typically preferred for fluid bed processes. For nozzles with external mixing, the liquid may be introduced either under or without excess pressure (Walzel, 1993). Usually the liquid is supplied at a low velocity and therefore the momentum of the liquid is negligible. At $\dot{m}_{\mathrm{liq}}/\dot{m}_{\mathrm{air}} \ll 1$ the liquid can be accelerated at the nozzle exit up to the gas velocity v_{air}. For higher values of the liquid to air mass ratio however, the liquid can be accelerated at best to the average or mixing rate velocity v_{mr} which can be approximated by Eq. (1), if the momentum exchange with the surroundings is neglected (Walzel, 1993).

$$v_{\mathrm{air}} \cdot \dot{m}_{\mathrm{air}} = v_{mr} \cdot \dot{m}_{\mathrm{air}} + v_{mr} \cdot \dot{m}_{\mathrm{liq}} \Leftrightarrow \quad v_{mr} = \frac{v_{\mathrm{air}}}{1 + \dot{m}_{\mathrm{liq}}/\dot{m}_{\mathrm{air}}} \tag{1}$$

The spray jet cross-sectional area A_{ss} after a mixing length of L_{mix} (which is the distance from the nozzle outlet where the liquid and air have the same velocity) is larger than the cross-sectional area A_G of the annulus gas jet as it may be seen from Fig. 4.

Letting $\dot{m}_{\mathrm{liq}} \cdot v_{\mathrm{liq}} \ll \dot{m}_{\mathrm{air}} \cdot v_{\mathrm{air}}$ for conditions where $\rho_{\mathrm{liq}} \gg \rho_{\mathrm{air}}$ the expression in Eq. (2) is obtained for A_{ss} (Walzel, 1993).

$$A_{ss} \cdot v_{mr} = A_G \cdot v_{\mathrm{air}} \Leftrightarrow \quad A_{ss} = A_G(\dot{m}_{\mathrm{liq}}/\dot{m}_{\mathrm{air}} + 1) \tag{2}$$

The power in Watts transferred to the liquid by the gas in order to accelerate the liquid up to v_{mr} is given by Eq. (3).

$$\Psi_{\mathrm{air/liq}} = \frac{v_{mr}^2}{2} \cdot \dot{m}_{\mathrm{liq}} \Rightarrow \quad \Psi_{\mathrm{air/liq}} = \frac{v_{\mathrm{air}}^2 \cdot \dot{m}_{\mathrm{liq}}}{2(\dot{m}_{\mathrm{liq}}/\dot{m}_{\mathrm{air}} + 1)^2} \tag{3}$$

Hereby the work in Joules carried out by the gas on unit mass of the liquid is given by Eq. (4).

$$W_{\mathrm{air/liq}} = \frac{v_{\mathrm{air}}^2}{2(\dot{m}_{\mathrm{liq}}/\dot{m}_{\mathrm{air}} + 1)^2} \tag{4}$$

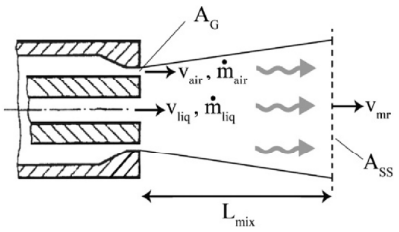

Fig. 4. External mixing two-fluid nozzle. The liquid velocity v_{liq} at the nozzle orifice is significantly lower than the air velocity v_{air}. Past the mixing length L_{mix}, which is normally equal to only a few liquid orifice diameters, the gas and liquid have the same average velocity v_{mr} (Based on Walzel, 1993.).

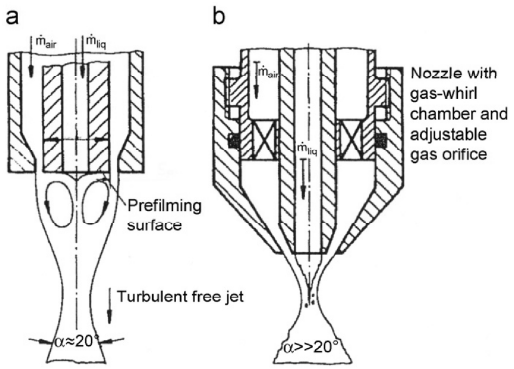

Fig. 5. External mixing two-fluid nozzle design: (a) simple design, (b) type with swirl insert (Walzel, 1993).

The ratio of the power transferred by the gas to the liquid to the power used to operate the nozzle (defined analogously to Eq. (3) as: $\Psi_{\mathrm{air}} = \frac{1}{2} \cdot v_{\mathrm{air}}^2 \cdot \dot{m}_{\mathrm{air}}$) is given by Eq. (5).

$$\frac{\Psi_{\mathrm{air/liq}}}{\Psi_{\mathrm{air}}} = \frac{\dot{m}_{\mathrm{liq}}/\dot{m}_{\mathrm{air}}}{(\dot{m}_{\mathrm{liq}}/\dot{m}_{\mathrm{air}} + 1)^2)} \tag{5}$$

It is obvious that Eq. (5) has an optimum for $\dot{m}_{\mathrm{liq}}/\dot{m}_{\mathrm{air}} = 1$ meaning that the atomisation efficiency at the same point has a maximum. On the other hand, the smallest droplet size is obtained for external mixing nozzles for $\dot{m}_{\mathrm{liq}}/\dot{m}_{\mathrm{air}} \to 0$ (Walzel, 1993).

In the simplest external mixing nozzle design both the gas and the liquid are discharged in the axial direction. The principle is showed in Fig. 5a. Here the channel is arranged concentrically relative to the annular gas-channel. The secondary flow resulting in the vicinity of the nozzle causes the liquid to spread out as a film on the outflow surface and to be carried to the separating edge where the actual atomisation takes place. The original annular jet contracts to a cylindrical jet where the cross-sectional area of the jet may be estimated with the help of Eq. (2). Next, jet expansion takes place under the angle of 15–20° which is common to all free jets (Walzel, 1993).

With respect to liquid flow rates, it is possible to optimise the version in Fig. 5a to have a more versatile nozzle. With the nozzle type in Fig. 5b it is possible to adjust the gas orifice dimensions. Furthermore, a swirl insert in the gas channel in the design in Fig. 5b

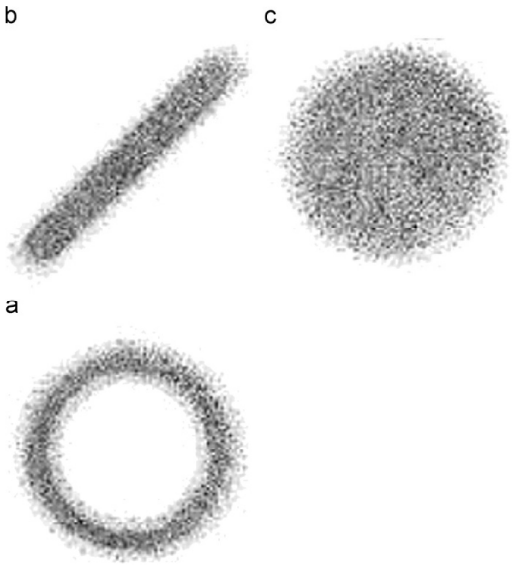

Fig. 6. Examples of different spray characteristics for external mixing two-fluid nozzles. Target spray patterns from: (a) hollow-cone nozzles, (b) flat-spray nozzles, (c) full-cone nozzles (Schick, 2006).

makes it possible to obtain spray angles in excess of 20° which is sometimes an advantage (Walzel, 1993).

In addition to the different types of external mixing designs, nozzles may have differently shaped orifices and thereby produce various spray patterns such as hollow cone, full cone and flat spray. Examples of this may be seen from Fig. 6.

3. The principles of atomisation in two-fluid nozzles

Pneumatic nozzle atomisation involves impacting a bulk liquid with high velocity gas. The mechanism of atomisation is one of high velocity gas creating high frictional forces over liquid surfaces causing liquid disintegration into spray droplets. Liquid disintegration in the presence of gaseous flow involves complex situations of liquid instability, but the overall process can be considered to occur in two phases: The first phase involves the tearing of the liquid into filaments and large droplets. The second phase completes the atomisation by further breaking these liquid forms into smaller and smaller droplets. The entire process is influenced by the magnitude of the liquid properties such as: surface tension, density and viscosity, and the gaseous flow properties such as velocity and density (Spray Drying Systems Co., 2000). Gaseous media used in pneumatic nozzle atomisation in the context of fluid beds is most often air but steam may also be used (Masters, 1972).

During atomisation a high relative velocity between liquid and air must be generated so that liquid is subjected to optimum frictional conditions. These conditions are generated by either expanding the air to sonic or super-sonic velocities prior to contacting the liquid, or directing the air flow on unstable thin liquid sheets formed within the nozzle (Lefebvre, 1989a). According to common nomenclature, the term "liquid sheet" is used both for a flat and for a cylindrical jet. High velocity air can typically readily penetrate a low velocity liquid jet thereby causing the necessary turbulence

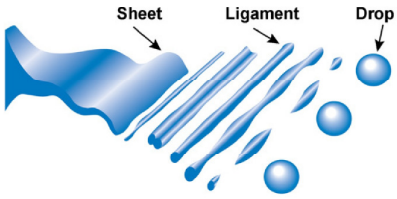

Fig. 7. The process of atomisation begins by forcing liquid through a nozzle. In this process, the liquid typically forms a liquid sheet that breaks up into ligaments. These ligaments then break up further into very small "entities", which are usually called drops, droplets or liquid particles (Spray Drying Systems Co., 2006).

and energy transfer to form a spray of narrow spray angle. At larger liquid feed rates however, even high velocity air cannot penetrate the thick liquid jets involved. Atomisation is thus incomplete, and a wide droplet size distribution results. A high percentage of liquid remains in the center of the spray as a connected jet, and, in fluid bed processes, penetrates far into the particle bed, significantly increasing the chances of particle bed collapse due to excessive agglomeration. At higher commercial feed rates the liquid bulk must first be formed into thin sheets to assist liquid instability, for effective air–liquid contact and break down of liquid into ligament forms or individual droplets. Unless the sheet formation or feed prefilming takes place, ineffective atomisation results, even at high air velocities. In such case the solid jet of liquid is simply accelerated by the air so rapidly that the liquid acquires the air velocity, minimising the shear forces between liquid and air (Masters, 1972; Schick, 2006). The whole atomisation mechanism depends upon these shear forces and the principle of the atomisation process may be seen from Fig. 7.

The fundamentals of droplet formation linking the different droplet formation processes with mathematical models are limited. Often detailed studies concern only one of the processes in detail and thus the theories cannot be used to describe the entire atomisation process (Schick, 2006; Spray Drying Systems Co., 2000; Lefebvre, 1989a). There are nevertheless many important discoveries and fundamentals to be learned from the isolated studies and some of the most important results and models will be shortly reviewed in the following sections. This is done in order to introduce important parameters as well as to present how advanced droplet size correlations for two-fluid nozzles often are closely related in form to the equations derived from more simple droplet generation studies.

3.1. Dripping

The simplest method of making droplets is by letting the liquid drop from a solid surface under the influence of gravity. Pendant droplets are formed for limited liquid supply. Equilibrium is established at some point between the forces of capillarity and gravity, and this determines the diameter of the liquid droplet detached slowly from the solid surface. Due to the slow rate of deformation, viscosity usually does not play a significant role in dripping, but a number of other parameters such as the liquid density and liquid surface tension do. When a liquid flows downward on a vertical surface with a sharp edge at its, i.e. the vertical surface's, bottom end, pendant droplet formation at low flow rates gives droplet diameters in the range given by Eq. (6) (Walzel, 1993).

$$d_{\text{droplet}} = 2.7\sqrt{\frac{\gamma_{\text{liq}}}{\rho_{\text{liq}} \cdot g}} \tag{6}$$

where $d_{droplet}$ is the mean droplet diameter in μm, ρ_{liq} is the coating liquid density, g is gravity and γ_{liq} is the coating liquid surface tension.

Dripping from capillaries is more important with respect to droplets formed by nozzles, and for this situation the droplet diameter depends on the liquid orifice diameter $d_{orifice}$ according to Eq. (7) (Walzel, 1993).

$$d_{droplet} = \left(\frac{6 \cdot d_{orifice} \cdot \gamma_{liq}}{\rho_{liq} \cdot g} \right)^{1/3} \tag{7}$$

Experiments by Hozawa et al. (1981) have resulted in another approximation for the droplet size produced from dripping from small orifices given by Eq. (8) predicting smaller droplets than predicted by Eq. (7).

$$\frac{d_{droplet}}{d_{orifice}} = 1.6 \cdot Bo^{-1/3} \tag{8}$$

where Bo is the Bond number defined according to Eq. (9) (Walzel, 1993).

$$Bo = \frac{d^2_{orifice} \cdot \rho_{liq} \cdot g}{\gamma_{liq}} \tag{9}$$

The Bond number is a measure of the importance of surface tension forces compared to body forces as gravity or centrifugal forces. A high Bond number indicates that the system is relatively unaffected by surface tension whereas a low Bond number (typically less than 1) indicates that surface tension dominates (Walzel, 1993). For large capillaries ($Bo > 25$) it has been found that the liquid orifice diameter does not play a role regarding the droplet diameter. Under these conditions the droplet sizes are in the range of $2.9 > d_{droplet}\sqrt{(\rho_{liq} \cdot g)/\gamma_{liq}} > 3.3$ and Eq. (8) is no longer valid (Walzel and Klaumünzer, 1981). For Bo number above 28 it has been found that the liquid surface becomes unstable and that the liquid starts to run out of the capillaries (Walzel and Klaumünzer, 1981).

3.2. Break-up of the laminar liquid jet

At higher rates of flow from the bottom edge of a vertical surface, a percolating horizontal porous plate or from a capillary tube, laminar liquid jets or threads are formed that break-up into droplets beyond a certain distance from the solid surface. Such liquid threads are intrinsically unstable. On their surface centrally symmetrical surface-waves are formed which grow fast for wave lengths $\lambda > \pi \cdot d_{jet}$ where d_{jet} is the diameter of the jet stream, in the case with flow from a capillary tube. The fastest growing wave disturbance corresponds to the optimum wave length λ_{opt} given by Eq. (10) (Walzel, 1993; Rayleigh, 1878).

$$\lambda_{opt} = \pi \cdot d_{jet}\sqrt{2 + 6 \cdot Oh} \tag{10}$$

where Oh is the so-called Ohnesorge number that relates surface tension and viscosity according to Eq. (11) (Lefebvre, 1989a).

$$Oh = \frac{\eta_{liq}}{\sqrt{\gamma_{liq}\rho_{liq}d_{jet}}} \tag{11}$$

where η_{liq} is the liquid viscosity.

For liquids with low viscosity, such as water having $Oh \approx 0$, $\lambda_{opt} = 4.4 \cdot d_{jet}$. Following the theories by Rayleigh (1878) being presented in Section 3.4, Hartman et al. (2000) argued that it is reasonable to assume that the droplet diameter relates directly to the jet diameter at the jet break up position. Under this assumption it was shown by Hartman et al. (2000) that the droplet diameter may be determined according to Eq. (12).

$$d_{droplet} = d_{jet} \cdot (44 + 133 \cdot Oh)^{1/6} \tag{12}$$

3.3. Flow regimes in a circular-shaped nozzle

With increasing liquid velocity v_{liq} at the orifice of a circular tube shaped nozzle (still without any gas flow), the events of dripping, laminar jet break-up, wave break-up and finally atomisation follow one after the other consecutively. For large liquid orifice dimensions the liquid can run out, meaning that the liquid is discharged while the nozzle is only partially filled (Lefebvre, 1989a). Neglecting the effect of gravity, transition from dripping to liquid column break-up into droplets is reached when the longitudinal contraction rate of the liquid jet is exactly equal to its rate of discharge. The conditions here are given by Eq. (13) (Walzel, 1993).

$$We_{liq} = \frac{v^2_{liq}\rho_{liq}d_{orifice}}{\gamma_{liq}} = 4 \tag{13}$$

where We_{liq} is the so-called liquid Weber number. It can be thought of as a measure of the relative importance of the fluid's inertia compared to its surface tension. In practice, higher exit velocities in the range of $8 < We_{liq} < 10$ are required in order to ensure jet formation. At lower exit velocities gravity also plays a role (Lindblad and Schneider, 1965).

3.4. Liquid-sheet formation and break-up

As it has been discussed earlier, the process of forming a continuous liquid stream into droplets involves first a process of break-up of the liquid sheets. Walzel (1993) distinguish between the following three mechanisms of liquid sheet break-up without the presence of a gas stream: rim contraction, aerodynamic laminar wave formation and turbulent break-up. Often the different mechanisms are present simultaneously (Walzel, 1993; Carvalho and Heitor, 1998). Usually liquid sheets extend transversely to the flow direction and therefore they become thinner with increasing distance from the nozzle outlet. The product of the liquid sheet thickness δ_{sheet} and the distance x measured from the liquid orifice is constant over a certain range of distances and is called the *sheet-thickness parameter* K_{sheet} given by Eq. (14) (Fraser et al., 1962; Dombrowski et al., 1960).

$$K_{sheet} = \delta_{sheet} \cdot x \tag{14}$$

In studies with nozzles having round liquid orifices, Walzel (1993) has chosen to normalise K_{sheet} with respect to the round cross sectional area of the nozzle outlet. Hereby, the liquid sheet coefficient χ_{sheet} is obtained according to Eq. (15) (Walzel, 1993):

$$\chi_{sheet} = \frac{4 \cdot \delta_{sheet} \cdot x}{\pi \cdot d^2_{orifice}} \tag{15}$$

Approximately in the range of $\sqrt{\chi_{sheet}}We_{liq} > 370$ liquid sheets characterised by low turbulence are brought into oscillation by the gas drag force (Walzel, 1993). The amplitudes of oscillations grow rapidly with increasing distance from the nozzle and lead to break up of the sheet. This phenomenon is termed *aerodynamic wave break-up* (Lefebvre, 1989a). Ligaments are thereby formed from the sheet fragments and these break-up into droplets by so-called Rayleigh

mechanisms of laminar jet break-up. In 1873 Plateau determined experimentally that the length at which a cylindrical column of liquid becomes unstable is between 3.13 and 3.18 times the diameter of the column (McCuan, 1997). Later, Rayleigh (1879), and more recently Barbosa and do Carmo (1984), showed theoretically that a vertically falling column of inviscid liquid with a circular cross-section should break up into droplets if its length exceeds its circumference, or π times its diameter. Liquids are typically viscous and the Rayleigh theory has only theoretical importance. Considering a more realistic case where the liquid has finite viscosity and where the thickness of the liquid sheet diminishes as it moves away from the orifice, a semi-empirical equation for the approximation of the mean droplet size has been suggested by Dombrowski and Johns (1963) according to Eq. (16).

$$d_{32} = C_1(\delta_{\text{sheet}} \cdot x)^{1/3}\left(\frac{\gamma_{\text{liq}}}{\rho_{\text{air}} \cdot v_{\text{rel\_sheet}}^2}\right)^{1/3}\left(\frac{\rho_{\text{liq}}}{\rho_{\text{air}}}\right)^{1/6} \Leftrightarrow$$

$$d_{32} = C_1 \cdot d_{\text{orifice}} \cdot \left(\frac{\gamma_{\text{sheet}} \cdot \pi}{4 \cdot We_{\text{air}}}\right)^{1/3}\left(\frac{\rho_{\text{liq}}}{\rho_{\text{air}}}\right)^{1/6} \quad (16)$$

where $v_{\text{rel\_sheet}}$ is the difference between the velocity of the nozzle atomising air and the liquid sheet (in practice close to v_{air}), C_1 is a constant between 1.2 and 1.7, and d_{32} is the Sauter mean droplet diameter in μm. The Sauter mean droplet size is a means of expressing the fineness of a spray in terms of the surface area produced by the spray. The d_{32} is the diameter of a droplet having the same volume-to-surface area ratio as the total volume of all the droplets to the total surface area of all the droplets (Spray Drying Systems Co., 2000). The form of Eq. (16) has many similarities to the empirical droplet size correlations presented in Section 6.

3.5. Break-up of liquid in gases

If a gas impinges on a liquid surface with sufficiently high relative rate, the liquid accelerates and is broken up. Break-up takes place when the dynamic pressure of the gas exceeds the pressure inside the droplet to a considerable extent. The ratio of gas dynamic pressure ($v_{\text{air}}^2 \cdot \rho_{\text{air}}$) to liquid capillary pressure ($\gamma_{\text{liq}}/d_{\text{orifice}}$) at the outset of the process is the gas-Weber number given by Eq. (17) (Walzel, 1993).

$$We_{\text{air}} = \frac{v_{\text{air}}^2 \rho_{\text{air}} d_{\text{orifice}}}{\gamma_{\text{liq}}} \quad (17)$$

When a gas stream is directed onto the liquid surface, the surface oscillates which facilitates disintegration. With increasing viscosity of the liquid these oscillations are damped so that for $Oh_{\text{droplet}} = \eta_{\text{liq}}/\sqrt{\gamma_{\text{liq}}\rho_{\text{liq}}d_{\text{droplet}}} > 4$ no more disintegration can occur. This limit may, in terms of the We_{air} number, be expressed approximately by Eq. (18) (Walzel, 1993).

$$We_{\text{air}} \geqslant 12 + 14 \cdot Oh_{\text{droplet}}^{1.6} \quad (18)$$

An estimate by Walzel (1993) shows that for two-fluid nozzles at $v_{\text{air}} \geqslant 300$ m/s, for liquid droplets with diameters above 50 μm, the gas-Reynolds number at the outset of the atomisation process is given by Eq. (19).

$$\text{Re}_{\text{air}} = \frac{v_{\text{air}} \rho_{\text{air}} d_{\text{droplet}}}{\eta_{\text{air}}} > 1000 \quad (19)$$

This means that the drag coefficient of the droplets is independent of the air viscosity at the beginning of the acceleration and disintegration phase. Therefore the gas-Reynolds number plays only a minor role for two-fluid nozzles (Walzel, 1993).

4. Nozzle thermodynamics

Droplet formation in terms of gas break-up of liquids, as presented in the last part of the previous section, adds further complexity to the system which is mainly due to the characteristics of the gas phase. Whereas liquids in general are incompressible at normal pressures this is not the case for gases being indeed compressible which influences a number of other important properties such as temperature and density (Smith et al., 2001). The principles of nozzle design and two-fluid atomisation are closely related to thermodynamics. This section treats the basic thermodynamics of nozzles considering only a single compressible fluid such as e.g. air.

From a thermodynamic point of view a nozzle is a device that causes the interchange of kinetic and internal energy of a fluid as a result of changing the cross-sectional area available for flow. The relationship between nozzle length and flow cross-sectional area is not susceptible to thermodynamics but is a problem in fluid mechanics as it was introduced in the previous section.

Isentropic flows occur when the change in flow variables is small and gradual, and largely as a result of experience, it is possible to taper nozzles so that near-isentropic flow is achieved (Smith and Van Ness, 1975; Smith et al., 2001). In addition, flow in nozzles are nearly adiabatic because the velocity is high (short residence time of the fluid) and the area for heat transfer small. As the shaft work (work done by or on the fluid flowing through a piece of equipment and transmitted by a mechanical device) associated with the flow process is zero, and the heat transfer and potential-energy changes are negligible, the enthalpy change of the gas is given by Eq. (20). This equation may be found in standard thermodynamic text books for maximum velocity conditions in pipe flow (Smith and Van Ness, 1975).

$$-\mathrm{d}H = u \cdot \mathrm{d}u \quad (20)$$

where H is the enthalpy (per unit mass) and u the velocity of the stream. The mechanical energy equation takes the form of Eq. (21) if the flow is considered isentropic.

$$-V \cdot \mathrm{d}P = u \cdot \mathrm{d}u \quad (21)$$

where V is the specific volume (in m^3/kg) and P the pressure. The other relation available is the continuity equation. For steady flow, the differential mass flow rate may be expressed according to Eq. (22).

$$d(\dot{m}) = 0 = d\left(\frac{u \cdot A}{V}\right) \quad (22)$$

where A is the cross-sectional area of the channel. Combined with the relations between the thermodynamic properties (e.g. P vs. V) at constant entropy, the Eqs. (20)–(22) determine how the velocity varies with the cross-sectional area of the nozzle. There are forms of the relation for compressible fluids, such as gases, depending on whether the velocity is below or above the velocity of sound in the fluid (Smith and Van Ness, 1975).

As a flow in a channel crosses the velocity of sound and becomes supersonic, one significant change takes place. Common sense would lead one to expect that contracting the flow channel would increase the flow speed (i.e. making the channel narrower results in faster air flow) and at subsonic speeds this holds true. However, once the flow becomes supersonic, the relationship of flow area and speed is reversed: expanding the channel actually increases the speed. The obvious result is that in order to accelerate a flow to supersonic, one needs a convergent–divergent nozzle of the type in Fig. 8, where the converging section accelerates the flow to sonic speeds, and the diverging section continues the acceleration. Such nozzles are called *Laval* nozzles and in extreme cases, as e.g. in a modern rocket engine,

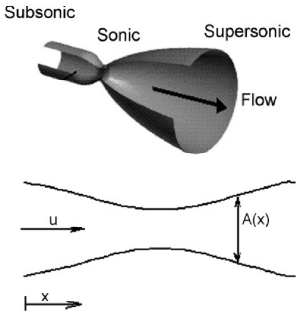

Fig. 8. Example and principles of a converging–diverging (Laval-type) nozzle (Florida College, 2007).

flows are able to reach hypersonic velocities, typically in the range of 2.5–4.5 times the sonic velocity (Masters, 1972; Smith and Van Ness, 1975; Park et al., 1996).

The velocity of sound is important in the treatment of nozzles because this is typically the velocity at the throat (minimum cross-sectional area) of a converging–diverging nozzle (see Fig. 8). This condition is often referred to as *choked flow* and it follows from the fact that at the throat, A is constant and Eq. (22) becomes (Smith et al., 2001):

$$0 = A \cdot d\left(\frac{u}{V}\right) \tag{23}$$

or expressed as

$$\mathrm{d}u = u \cdot \frac{\mathrm{d}V}{V} \tag{24}$$

Substituting Eq. (24) into Eq. (21) gives for the throat velocity in an isentropic nozzle:

$$u_{\text{throat}}^2 = -V^2 \cdot \left(\frac{\partial P}{\partial V}\right)_S \tag{25}$$

The result in Eq. (25) is identical to the equation derived in physics for the velocity of sound in a compressible fluid, indicating that u_{throat} is equal to the sonic velocity (Smith and Van Ness, 1975). It is also true that in the converging section of a converging–diverging nozzle the maximum velocity obtainable is the sonic velocity existing in the throat. This is because a further decrease in pressure (i.e. increase in specific volume) requires an increase in cross-sectional area, i.e. a diverging section. The explanation for this has been provided by Smith and Van Ness (1975). At the relatively high pressures in the converging section, a given pressure drop causes a small increase in specific volume. However, at low pressures the increase in V is large. Meanwhile, the change in enthalpy with respect to pressure is simply $\mathrm{d}H/\mathrm{d}P = V$. These conclusions follow directly from the thermodynamic properties of fluids which may be visualised e.g. through a pressure–enthalpy diagram. From these facts and from Eq. (21) it may be concluded that the velocity will increase more or less proportionally with a pressure decrease. Eq. (22) furthermore shows that (provided the change in specific volume is small, as is the case at high pressure) the increase in velocity will be offset by the decrease in A. However, at low pressures a large increase in V cannot be balanced by the increase in A and thus the velocity must also increase.

As the gas enters a converging–diverging nozzle, it travels at subsonic velocities. As the throat contracts the gas it is forced to accelerate until at the nozzle throat, where the cross-sectional area is the smallest and the linear velocity becomes sonic. From the throat the cross-sectional area then increases in a converging–diverging nozzle and the gas expands and the linear velocity becomes progressively more supersonic. The linear velocity of the exiting exhaust gas u_{exhaust} can be calculated under the assumption of ideal gas behaviour using Eq. (26) (Lefebvre, 1989a).

$$u_{\text{exhaust}} = \sqrt{\frac{T_{\text{inlet}} \cdot R}{M_{\text{air}}} \cdot \frac{2 \cdot \gamma}{\gamma - 1} \cdot [1 - (P_{\text{exit}}/P_{\text{inlet}})^{(\gamma-1)/\gamma}]} \tag{26}$$

where γ is the ratio of heat capacities according to Eq. (27).

$$\gamma = \frac{C_P}{C_V} \tag{27}$$

and M_{air} is the molecular weight of the gas, T_{inlet} is the inlet gas temperature, R is the universal gas constant, P_{exit} is the absolute pressure at the nozzle exit, being most often atmospheric pressure, and P_{inlet} is the absolute pressure at the nozzle inlet. Next the case with a converging nozzle is treated.

Suppose a converging nozzle is supplied with a compressible fluid at a pressure P_1 and suppose the pressure P_2 in the chamber into which the nozzle discharges is variable. If this discharge pressure is P_1 the flow will be zero. As P_2 is decreased below P_1, the flow rate and the velocity increase. Finally, a pressure ratio P_2/P_1 is reached such that the velocity in the throat is sonic. Further reduction in P_2 has no effect on the conditions in the nozzle. The flow rate remains constant and the velocity in the throat is that given by Eq. (25) regardless of the value of P_2/P_1 (Smith and Van Ness, 1975).

The variation in velocity with pressure in a nozzle can be displayed in analytical form if the fluid behaves as an ideal gas. For such a fluid undergoing an isentropic expansion, Eq. (28) provides a relation between P and V:

$$P_1 \cdot V_1^{\gamma} = P_2 \cdot V_2^{\gamma} = P \cdot V^{\gamma} = \text{Constant} \tag{28}$$

With the relation in Eq. (28), the integration of Eq. (21) gives:

$$u_2^2 - u_1^2 = -2 \cdot \int_{P_1}^{P_2} V \cdot \mathrm{d}P = \frac{2 \cdot \gamma \cdot P_1 \cdot V_1}{\gamma - 1}\left[1 - \left(\frac{P_2}{P_1}\right)^{(\gamma-1)/\gamma}\right] \tag{29}$$

where the conditions at the nozzle entrance are designated by subscript 1 (Smith and Van Ness, 1975).

The value of the pressure ratio P_2/P_1 (for the limiting case where $u_1 = 0$), such that sonic velocity is obtained in the throat of a converging nozzle, can be evaluated directly from Eqs. (25) and (28) if ideal gas behaviour is assumed. If the derivative $(\partial P/\partial V)_S$ is evaluated for the reversible adiabatic expansion of an ideal gas, in accordance with Eq. (28), then Eq. (25) becomes

$$u_{\text{throat}}^2 = \gamma \cdot P_2 \cdot V_2 \tag{30}$$

Substituting this value of the throat velocity for u_2 into Eq. (29) and solving for the pressure ratio (with the limiting case where $u_1 = 0$) one achieves:

$$\frac{P_2}{P_1} = \left(\frac{2}{\gamma + 1}\right)^{\gamma/(\gamma-1)} \tag{31}$$

For air under normal conditions this ratio is roughly 0.53 meaning that at moderate temperature and pressures:

$$1.9 \cdot P_2 \approx P_1 \quad \text{for air at normal conditions} \tag{32}$$

Assuming that the flow is frictionless, this means that if the pressure which the nozzle gas expands into is 1 bar, the sonic velocity will be reached already for a nozzle pressure of roughly 1.9 bar. The speed of sound is thereby attained at the throat of a converging–diverging nozzle only when the pressure at the throat is low enough so that the critical value of P_2/P_1 is reached. For real nozzles however, friction

does play a role for the flow meaning that a smaller value of P_2/P_1 is required in order to reach sonic velocity.

A general relationship between the velocity and cross-sectional area expressed in terms of the properties (P, V) of the fluid in terms of the velocity of sound can be derived from Eqs. (21), (22) and (25). As in the previous derivation of the throat velocities, one may start with the continuity equation in Eq. (22) although one may this time express the derivative according to Eq. (33) (Smith and Van Ness, 1975):

$$\frac{1}{V}(u \cdot \mathrm{d}A + A \cdot \mathrm{d}u) - u \cdot A \cdot \frac{\mathrm{d}V}{V^2} = 0 \tag{33}$$

Or in another way as

$$\frac{u \cdot \mathrm{d}A + A \cdot \mathrm{d}u}{u \cdot A} = V \cdot \frac{\mathrm{d}V}{V^2} \tag{34}$$

The next step is to replace V in the numerator on the right-hand side with its value from Eq. (21) noting that the process is isentropic. One thereby arrives at Eq. (35).

$$\frac{\mathrm{d}A}{A} + \frac{\mathrm{d}u}{u} = -\frac{u \cdot \mathrm{d}u}{V^2(\partial P/\partial V)_S} \tag{35}$$

From Eq. (25) the denominator of the right-hand side is the square of the sonic velocity. Hence

$$\frac{\mathrm{d}A}{A} = \frac{u \cdot \mathrm{d}u}{u^2_{\mathrm{sonic}}} - \frac{\mathrm{d}u}{u} = \left(\frac{u^2}{u^2_{\mathrm{sonic}} - 1}\right)\frac{\mathrm{d}u}{u} = (M^2 - 1)\frac{\mathrm{d}u}{u} \tag{36}$$

The ratio of the actual velocity to the sonic velocity is called the *Mach number M*. Hence, Eq. (36) expresses a relation between the cross-sectional area, velocity and local Mach number at any axial position in the nozzle. Depending upon whether M is greater than (supersonic) or less than (subsonic) unity, the velocity will increase or decrease with increase in cross-sectional area. Note that Eq. (36) is applicable to any type of nozzle as long as the flow is isentropic. However, the requirement that sonic velocity is reached at the nozzle throat is based on the premise that the pressure at the throat is low enough for the critical ratio P_2/P_1 to be reached. If insufficient pressure drop is available in the nozzle to reach this critical value, the diverging section of the nozzle will act like a venturi-meter (i.e. a diffuser). That is, after the throat is reached the pressure rises and the velocity decreases. This is the conventional behaviour for subsonic flow in diverging sections (Smith et al., 2001). The relationships between velocity, area and pressure in the nozzle are illustrated further in a number of calculation examples in Smith and Van Ness (1975).

5. Variables affecting the mean droplet size

Given the variety of nozzle designs and types, it may seem difficult to extract universal trends that can be used as a rule-of-thumb for any given nozzle. There are however a number of general and rough rules of thumb that are useful in understanding the factors that influence the droplet size. Droplet size and the uniformity of the droplet size distribution will in general vary based on several factors such as: characteristics of the liquid, the liquid viscosity, the spray nozzle design, the flow through the spray nozzle, the air pressure and more (Schick, 2006; Masters, 1972). A brief overview of some of the most important qualitative trends is presented below.

5.1. Design and operation

The nozzle type is one factor affecting droplet size, and typically, full cone nozzles produce the largest droplet size followed by flat spray and hollow cone nozzles. The liquid flow rate has a direct influence on droplet size. An increase in flow rate will typically increase the droplet size and similarly, a decrease in flow rate will decrease the droplet size (Schick, 2006; Spray Drying Systems Co., 2000).

The air pressure has in general an inverse relationship effect on droplet size. An increase in pressure will typically reduce the droplet size while a reduction in pressure will increase the droplet size. Similarly, the spray angle has an inverse relationship effect on droplet size (a zero spray angle is parallel to the jet). An increase in spray angle will typically reduce the droplet size and a reduction in spray angle will increase the droplet size (Schick, 2006; Lefebvre, 1989a).

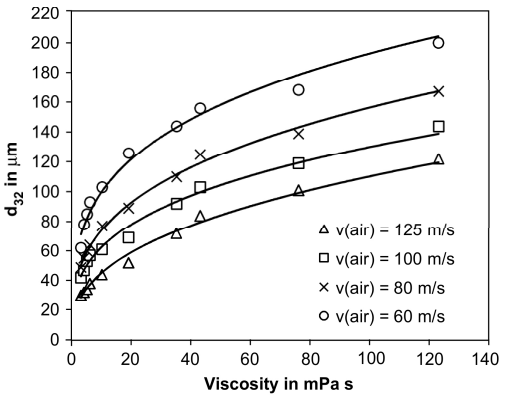

Fig. 9. Variation in d_{32} with liquid viscosity for an external mixing prefilming airblast atomiser. $T = 296$ K, $P = 1$ bar, $\dot{m}_{\mathrm{liq}} = 15$ g/s, $\rho_{\mathrm{liq}} = 995$ kg/m^3, $\gamma_{\mathrm{liq}} = 0.072$ kg/s^2. (Data adapted from Rizkalla and Lefebvre, 1975; Lefebvre, 1989a.)

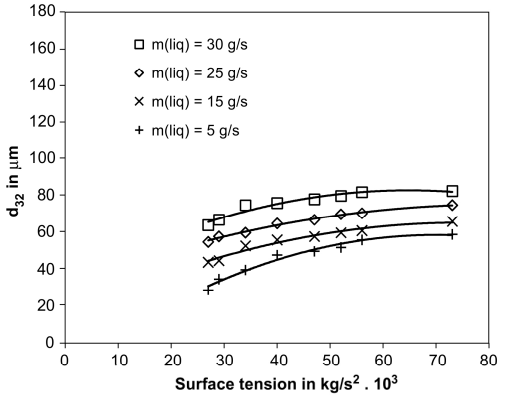

Fig. 10. Variation in d_{32} with surface tension for an external mixing prefilming airblast atomiser. $T = 296$ K, $P = 1$ bar, $v_{\mathrm{air}} = 100$ m/s, $\rho_{\mathrm{liq}} = 995$ kg/m^3, $\eta_{\mathrm{liq}} = 1.2$ mPa s. (Data adapted from Rizkalla and Lefebvre, 1975; Lefebvre, 1989a)

5.2. Liquid properties

The liquid properties of importance with respect to two-fluid atomisation are: viscosity, liquid density and surface tension. An increase in viscosity will typically increase the Sauter mean diameter (d_{32}) which is demonstrated in Fig. 9 where d_{32} is plotted against

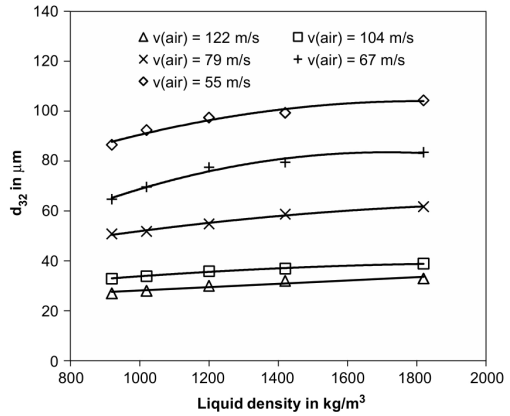

Fig. 11. Variation in d_{32} with liquid density for an external mixing prefilming airblast atomiser. $T=296$ K, $\dot{m}_{liq}=15$ g/s, $P=1$ bar, $\gamma_{liq}=0.072$ kg/s^2, $\eta_{liq}=1.2$ mPa s. (Data adapted from Rizkalla and Lefebvre, 1975.)

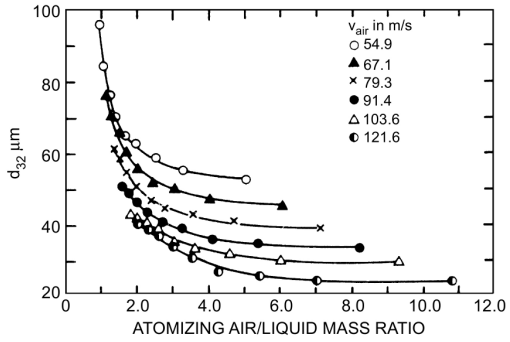

Fig. 12. Variation in d_{32} with air/liquid mass ratio for a prefilming external mixing airblast atomiser $T=296$ K, $P=1$ bar, $\gamma_{liq}=0.072$ kg/s^2, $\rho_{liq}=995$ kg/m^3, $\eta_{liq}=1.2$ mPa s. (Lefebvre, 1980).

viscosity for various levels of air velocity at a constant liquid flow rate in a prefilming external mixing airblast atomiser (Rizkalla and Lefebvre, 1975).

Further effects upon an increase in liquid viscosity are (Schick, 2006; Lefebvre, 1989a):

- Decreased liquid flow rate.
- Requirement of a higher minimum pressure to maintain adequate spray angle/coverage.
- Increasing capacity (more volume of liquid at a given d_{32} and distribution being produced per unit time).

Likewise, an increase in surface tension typically means an increase in d_{32} which is illustrated in Fig. 10.

Other effects of an increase in surface tension are (Schick, 2006; Lefebvre, 1989a):

- Increased minimum operating pressure.
- Decreasing spray angle.

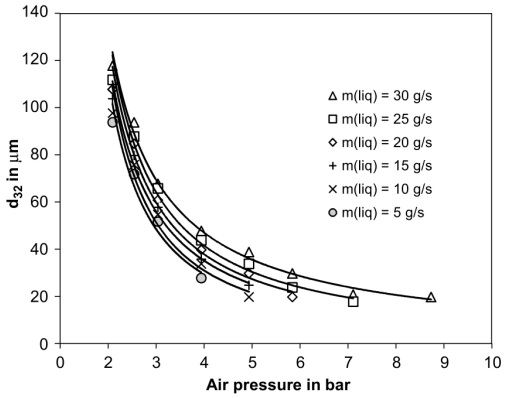

Fig. 13. Variation in d_{32} with air pressure for an external mixing prefilming airblast atomiser. $T=296$ K, $\rho_{liq}=995$ kg/m^3, $\gamma_{liq}=0.072$ kg/s^2, $\eta_{liq}=1.2$ mPa s. (Data adapted from Rizkalla and Lefebvre, 1975.)

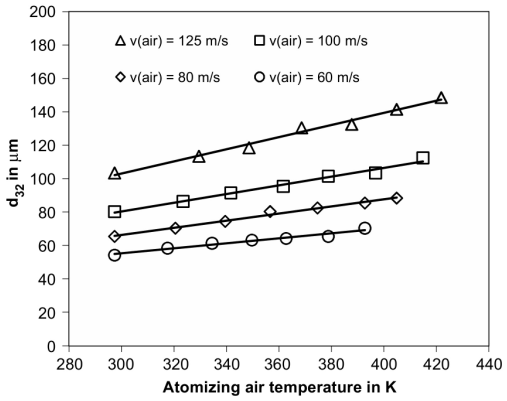

Fig. 14. Variation in d_{32} with air temperature for an external mixing prefilming airblast atomiser. $P=1$ bar, $\rho_{liq}=995$ kg/m^3, $\gamma_{liq}=0.072$ kg/s^2, $\eta_{liq}=1.2$ mPa s. (Data adapted from Rizkalla and Lefebvre, 1975.)

The effect on d_{32} upon an increase in either the surface tension or the viscosity is due to an increase in the amount of energy required to atomise the spray. The result is fewer but larger droplets (Lefebvre, 1989a).

Liquid density affects droplet size in a complex manner. E.g. with prefilming atomisers, the distance to which the coherent liquid sheet extends downstream of the atomising lip increases with density, so that ligament formation occurs later and under conditions of lower relative velocity between the air and the liquid (at this increased distance, the velocity of the atomisation air has decreased). Furthermore, for any given mass flow rate, an increase in liquid density produces a more compact spray that is less exposed to the atomising action of the high-velocity air. These two effects combine to increase the mean droplet size. However, an increase in liquid density can also improve atomisation by reducing the thickness of the sheet produced at the atomising lip of prefilming systems and by increasing the relative velocity for plain jet nozzles. The net effect of these

conflicting factors is that the influence of liquid density on d_{32} is fairly small as illustrated for a prefilming airblast atomiser in Fig. 11 (Lefebvre, 1989a; Rizkalla and Lefebvre, 1975). If however, the nozzle pressure increases, the increase in d_{32} with increasing viscosity is somewhat larger than what is illustrated in Fig. 11 (Lefebvre, 1996).

5.3. Air properties

Of all the factors influencing the mean droplet size, air velocity is undoubtedly the most important. This trend becomes clear from inspection of Figs. 9–12. For low-viscosity liquids d_{32} is roughly inversely proportional to the air velocity which underlines the importance of arranging for the liquid to be exposed to the highest possible air velocity consistent with the available pressure drop (Lefebvre, 1989a).

The effects of air pressure (used to accelerate the air flow thus being the gauge pressure) and temperature on d_{32} are illustrated in Figs. 13 and 14, respectively. These results taken together suggest that for prefilming nozzles, d_{32} is proportional to the air density to the −0.6 power (Lefebvre, 1989a).

6. Droplet size correlations

Literature on droplet size correlations are sparse. Pneumatic two-fluid nozzles have received attention from many authors through the last 60 years, but often authors have developed their own type of nozzle and developed an empirical correlation for the mean droplet size for this particular nozzle. Droplet size correlations are often limited to a narrow parameter range, but nonetheless often cited without stating the associated parameter intervals or droplet size distributions. Being able to predict the mean droplet size is nevertheless an important topic for the practical application of two-fluid nozzles. This section reviews some of the most cited and used correlations for fluid bed processes. The review is divided into correlations for internal and external mixing nozzles.

6.1. Internal mixing droplet size correlations

Probably the best known and most widely quoted work on pneumatic atomisation is that of Nukiyama and Tanasawa (1939, 1940). Their work on a simple internal mixing nozzle of the type in Fig. 3c was done as early as in the 1930s with the technique of measuring droplet sizes by collecting samples of the spray on oil-coated glass slides. Their work with water, alcohol, heavy fuel oil and gasoline resulted in the empirical correlation (converted to SI-units) according to Eq. (37).

$$d_{32} = \frac{0.585 \cdot \sqrt{\gamma_{\mathrm{liq}}}}{v_{\mathrm{rel}}\sqrt{\rho_{\mathrm{liq}}}} + 53 \cdot \left(\frac{\eta_{\mathrm{liq}}^2}{\gamma_{\mathrm{liq}} \cdot \rho_{\mathrm{liq}}}\right)^{0.225} \left(\frac{1000 \cdot \dot{q}_{\mathrm{liq}}}{\dot{q}_{\mathrm{air}}}\right)^{1.5} \quad (37)$$

where η_{liq} is the liquid viscosity, ρ_{liq} is the liquid density, γ_{liq} is the coating liquid surface tension, $\dot{q}_{\mathrm{liq}}$ is the coating liquid volumetric flow rate through the nozzle (in m^3/s), $\dot{q}_{\mathrm{air}}$ is the volumetric flow rate of atomising air through the nozzle (in m^3/s) and v_{rel} is the difference between the nozzle atomising air velocity and the liquid velocity at the nozzle outlet. The validity range for Eq. (37) and for all other correlations presented in the review can be seen from Table 1.

It is interesting to note from Eq. (37) that the right-hand side is expressed as the sum of two separate terms one of which is dominated by the relative velocity and surface tension and the other by viscosity. Eq. (37) is not dimensionally consistent and various other forms of the Nukiyama and Tanasawa equation exist depending on the unit of the parameters (Lefebvre, 1989a; Gretzinger and Marshall, 1961). Although not being dimensionally correct the correlation allows some useful conclusions to be drawn. E.g. for liquid of low viscosity the correlation predicts that the mean droplet size is inversely proportional to the relative velocity between the air and the liquid. Analysis of the Nukiyama and Tanasawa equation shows that for $\dot{q}_{\mathrm{air}}/\dot{q}_{\mathrm{liq}}$ greater than 5000, the second term in the right-hand side contributes very little to the predicted droplet size for most low viscosity liquids. As the relative velocity of gas to liquid approaches sonic velocity, at a $\dot{q}_{\mathrm{air}}/\dot{q}_{\mathrm{liq}}$ value of 5000 for most nozzles, the value of the predicted droplet size approaches a constant which depends primarily on liquid density and surface tension (Lefebvre, 1989a; Nukiyama and Tanasawa, 1939, 1940).

Interestingly, neither the diameter of the liquid orifice nor the dimensions of the air channel are part of the Nukiyama and Tanasawa equation. Based on tests carried out with different sizes and shapes of the particular plain jet nozzle, Nukiyama and Tanasawa (1939) concluded that these factors have virtually no effect on the mean droplet size. Thus, the absence of atomiser dimensions is a notable feature of Eq. (37) (Lefebvre, 1989b). A serious limitation with the Nukiyama and Tanasawa equation is that air density was kept constant in all of their experiments which is why this parameter is absent in the correlation. This limitation prohibits the application of Eq. (37) to many types of atomisers that are required to operate over a wide range of air pressures and temperatures (Lefebvre, 1989a). Gretzinger and Marshall (1961) conclude on the basis of these observations that the application of the Nukiyama and Tanasawa equation to atomisation for a size range of 5–30 μm is of doubtful value. It is nevertheless often this size range that the equation is used for practical droplet size predictions. Eq. (37) is frequently cited for general purposes although the equation was established for liquid feed rates only up to ca. 500 g/min with small diameter nozzles. The correlation was originally derived for internal nozzle designs, but has been shown to produce adequate droplet diameter predictions for small external nozzles as well under moderate pressure and low liquid feed rates (Dewettinck, 1997). There is doubt in the validity of the equation if air velocities approach sonic values. Experience has shown that air velocities in the order of sonic with mass air–liquid ratios in the order of 10 are required to produce mean droplet sizes under 25 μm (Masters, 1972).

Other droplet size correlations have been developed for specially designed internal mixing nozzles by e.g. Lorenzetto and Lefebvre (1977), Rizkalla and Lefebvre (1975). These designs have little practical importance although the trends derived from the detailed nozzle studies are interesting. In the studies by Lorenzetto and Lefebvre (1977) results indicated that atomisation quality deteriorates with increase in liquid viscosity and surface tension, and that for liquids with low viscosity the mean droplet size is inversely proportional to the relative velocity between the air and the liquid at the nozzle outlet. It was also observed, in agreement with the Nukiyama and Tanasawa studies, that nozzle dimensions appear to have little influence on the mean droplet size for liquids of low viscosity. For high viscosity liquids however, d_{32} appears to vary roughly in proportion to the orifice diameter to the power of 0.5 (Lefebvre, 1989a).

Rizk and Lefebvre (1984) studied spray characteristics for simple plain-jet nozzles and suggested a correlation according to Eq. (38) based on experimental data determined by light-scattering technique.

$$d_{32} = L_c \cdot \left[0.48\left(\frac{\gamma_{\mathrm{liq}}}{\rho_{\mathrm{air}} \cdot v_{\mathrm{rel}}^2 \cdot d_{\mathrm{orifice}}}\right)^{0.4} \left(1 + \frac{\dot{m}_{\mathrm{liq}}}{\dot{m}_{\mathrm{air}}}\right)^{0.4} + 0.15\left(\frac{\eta_{\mathrm{liq}}^2}{\gamma_{\mathrm{liq}} \cdot \rho_{\mathrm{liq}} \cdot d_{\mathrm{orifice}}}\right)^{0.5} \left(1 + \frac{\dot{m}_{\mathrm{liq}}}{\dot{m}_{\mathrm{air}}}\right)\right] \Leftrightarrow$$

Table 1
Summary of reviewed droplet size correlations

Nozzle type	Investigators	Eq. no.	Liquid properties				Air properties			Mass ratio $\dot{m}_{air}/\dot{m}_{liq}$ = ALR	Droplet diameter prediction range (μm)	Method of droplet size measurement
			Type of liquid tested	Surface tension $\times 10^3$ (kg/s^2)	Liquid density (kg/m^3)	Liquid viscosity $\times 10^3$ (kg/m s)	Pressure 10^{-2} (kPa)	Temp. (K)	Flow velocity			
Internal mixing, simpleplain jet	Nukiyama and Tanasawa (1939, 1940)	37	Water, methyl alcohol, glycerine, gasoline, heavy fuel oils	19–73	700–1200	1.0–5.0	1.0	295	60–340 m/s	1–14	(d_{32}) 15–19	oil coated glass slide collection
Internal mixing, simple plain jet	Rizk and Lefebvre (1984)	38	Aviation kerosene, gas oil, blended fuel	27.5–28.5	780–840	1.3–3.0	1.0–7.7	298	10–120 m/s	2–8	(d_{32}) 15–75	light-scattering technique
Internal mixing, simple plain jet	Nguyen and Rhodes (1998)	39	Water	75	1000	1.0	1.0–25	291–293	2.4×10^{-3}–2.12×10^{-2} g/s	0.2–2.0	($d_{v0.5}$) 5–25	Fraunhofer laser diffraction
Simple external mixing	Gretzinger and Marshall (1961)	40	Aqueous solutions of black dye	50	N/A	1.0	1.6–4	295	< Sonic	1–16	(d_{32}) 5–30	high speed photographs, counting under microscope
Simple external mixing	Kim and Marshall (1971)	43	Wax melts	30–50	800–960	1.0–5.0	0.76–2.0	298	75–393 m/s	0.06-40	(d_{32}) 10–160	counting under microscope and sieve analysis
Simple external mixing	Walzel(1993)	49	Water and aqueous solutions of glycerol	64–72	950–1100	1.0–100	0.5–3	N/A	N/A	N/A	(d_{32}) 5–25	laser diffraction
Simple external mixing	Mulhem et al. (2003, 2006)	51	Water, glycerol, various kaolin suspensions and CMC-water mixtures	56–72	1000–1130	1.0–80	1.1–1.6	293	< 250 m/s	2–100	(d_{32}) 15–100	laser diffraction/CCD camera
Prefiliming external mixing	Rizkalla and Lefebvre (1975)	46	Water, kerosine	26–74	780–1500	1.0–44	1–8.5	296–424	70–125 m/s	2–6	(d_{32}) 30–120	light-scattering technique
Prefiliming external mixing	El-Shanaway and Lefebvre (1980)	48	Water, kerosene, miscellaneous aqueous solutions	26–74	784–1000	1.0–44	1.0–8.5	295	60–190 m/s	0.5–5.0	(d_{32}) 25–125	light-scattering technique
Prefiliming external mixing	Nguyen and Rhodes (1998)	50	Water	75	1000	1.0	1.0–25	291–293	2.4×10^{-3}–2.12×10^{-2} g/s	0.2–2.0	($d_{v0.5}$) 5–25	Fraunhofer laser diffraction

$$d_{32}=L_c\cdot\left[0.48(We_{\text{air}})^{-0.4}\left(1+\frac{\dot{m}_{\text{liq}}}{\dot{m}_{\text{air}}}\right)^{0.4}+0.15\cdot Oh\cdot\left(1+\frac{\dot{m}_{\text{liq}}}{\dot{m}_{\text{air}}}\right)\right] \quad (38)$$

where L_c is the characteristic dimension of the nozzle often set as the diameter of the liquid orifice for plain-jet nozzles. The studies by Rizk and Lefebvre (1984) on plain-jet atomisers confirm previous findings for prefilming atomisers with respect to the effects of air and liquid properties on the droplet size distribution. Their measurements showed that any change in atomiser geometry, liquid properties, or operating conditions that reduces the mean droplet size diameter will also increase the uniformity of the droplet size distribution.

Nguyen and Rhodes (1998) recently carried out new experiments on a simple internal mixing nozzle of the type in Fig. 3c in order to derive an empirical equation for the droplet volume median diameter. Their results indicated in general that the median droplet size decreases to the power of −0.28 with increasing $\dot{m}_{\text{air}}/\dot{m}_{\text{liq}}$ ratio in the range of 0.02–0.1. This is in accordance with Fig. 12, but in contrast to studies by Sakai et al. (1978) using a similar atomiser, indicating that the volume median diameter $d_{v0.5}$ is independent of the liquid flow rate for values of $\dot{m}_{\text{air}}/\dot{m}_{\text{liq}}$ in a similar range. Nguyen and Rhodes (1998) suggest that differences among the studies in air/liquid flow regimes present in the atomisers may account for this difference. The authors further observed that as the nozzle length increases, the quality of spray remains unchanged (high quality implies small uniform droplets). This is claimed to be expected, as even for the shorter nozzle, the air/liquid flow is already fully developed. A rule of thumb stated by Smith et al. (2001) claims that flow will be fully developed when the ratio of nozzle length to nozzle orifice diameter is greater than 50 which is most often the case with commercial nozzles (Spray Drying Systems Co., 2000). This leads to the important conclusion that at a given mass flow rate, the air velocity at the nozzle exit is the same for various nozzle lengths (Nguyen and Rhodes, 1998).

It was found in general by Nguyen and Rhodes (1998) that the size of the mixing chamber did not influence the volume median droplet diameter and that for some test conditions, the volume median droplet size was only a weak function of the air/liquid mass ratio. The last result is in contradiction to previous work suggesting that the droplet size always strongly depends on the air/liquid mass ratio. The claimed reason for this is that, in this study for higher liquid flow rates, the required air pressure was higher than for lower liquid flow rates at the same air mass flow rate. This means that the air pressure at the exit is higher for a high liquid flow rate thus damping out the effect on the resulting $d_{v0,5}$. In order to fully account for the influence of the increased air pressure at high liquid flows on the droplet size, Nguyen and Rhodes (1998) suggested a modified Lefebvre (1980) equation with the inclusion of a $\rho_{\text{liq}}/\rho_{\text{air}}$ term according to Eq. (39).

$$d_{v0.5}=d_{\text{orifice}}\left(\frac{\rho_{\text{liq}}}{\rho_{\text{air}}}\right)^{0.39}\left[0.010\left(\frac{\gamma_{\text{liq}}}{\rho_{\text{air}}\cdot v_{\text{air}}^2\cdot d_{\text{orifice}}}\right)^{0.5}+1.22\left(\frac{\eta_{\text{liq}}^2}{\gamma_{\text{liq}}\cdot\rho_{\text{liq}}\cdot d_{\text{orifice}}}\right)^{0.5}\right]\left(1+\frac{\dot{m}_{\text{liq}}}{\dot{m}_{\text{air}}}\right)^{0.28} \quad (39)$$

where $d_{v0.5}$ is the volume median diameter being found by dividing the total spray volume in half (50% of the total volume will have larger diameter droplets and 50% will have smaller diameter droplets). Calculations using this method give more consideration to the larger droplet sizes and as a common rule of thumb $d_{v0.5}$ is 1.3–1.5 times d_{32} (Rhodes, 1998).

A deficiency of all the published droplet size equations for internal mixing nozzles is that they take no account of the time required for atomisation. The importance of time to obtain the mean droplet size is due to the fact that if for some reason atomisation is delayed, it will take place further downstream from the nozzle in a region of lower relative velocity, so that the resulting droplets are larger in size. It is postulated by Lefebvre (1989b) that the effects of various fluid properties such as liquid viscosity and air density on mean droplet size are manifested, at least in part, through their influence on break-up time. An increase in air pressure improves atomisation quality by reducing the break-up time, whereas an increase in liquid viscosity, by increasing the break-up time, has an adverse effect on atomisation quality. These considerations suggest that the time element should be included as a basic ingredient in the further development of analytical models for mean droplet sizes (Lefebvre, 1989b).

6.2. External mixing droplet size correlations

The wide use of external mixing two-fluid nozzles in fluid bed coaters makes droplet size correlations for this nozzles type highly relevant. Gretzinger and Marshall (1961) studied the characteristics of mean droplet size and droplet size distribution for a simple convergent external mixing nozzle of the type in Fig. 5a. Sprays of aqueous solutions of black dye were first dried and then collected in mineral oil and counted using a light microscope. Liquid orifice diameters of 2.4, 2.8 and 3.2 mm were tested and the experiments covered liquid flow rates from 2 to 17 L/h making the tested conditions close to a large pilot-scale fluid bed coating processes. The resulting droplet diameters were mainly between 5 and 30 μm resulting in the correlation in Eq. (40) derived from experimental data.

$$d_{\text{mmd}}=2600\cdot\left[\left(\frac{\dot{m}_{\text{liq}}}{\dot{m}_{\text{air}}}\right)\cdot\left(\frac{\eta_{\text{air}}}{G_a\cdot L_c}\right)\right]^{0.4} \quad (40)$$

where η_{air} is the atomisation air viscosity in Poise, G_a is the mass flux (mass flow of air per area gas jet orifice at the nozzle outlet) in lb/(min ft^2) (for most nozzle designs equal to $\dot{m}_{\text{air}}/A_G$), L_c is a characteristic length (in cm) of the nozzle equal to L_{peri}, being the wetted periphery between the air and liquid streams, often approximated by the liquid orifice diameter d_{orifice}, and d_{mmd} is the mass median droplet diameter in μm. The mass mean droplet diameter is a means of expressing droplet size in terms of the mass of liquid sprayed. The d_{mmd} is a value where 50% of the total mass of liquid sprayed is made up of droplets with diameters larger than the median value and 50% with smaller diameters (Spray Drying Systems Co., 2000).

The results from the work by Gretzinger and Marshall (1961) generally confirm previous findings with respect to the beneficial effects of increases in air/liquid mass ratio, air velocity and air density on atomisation quality. It was observed that the droplet size varied inversely with the mass ratio of gas-to-liquid and with the length of the air to liquid contact periphery, as long as the liquid was in the form of a thin stable film. If the liquid film was of non-uniform thickness or if the flow rate was non-uniform, sprays having larger-than-expected droplet sizes were produced. Pulsating flow evidently produced relatively thick films for atomisation which gave droplet sizes larger than expected. Interestingly, it was observed that the uniformity of sprays increased as the mean droplet size decreased. Gretzinger and Marshall (1961) suggested that this is a result of the nearness of approach to direct droplet formation from the liquid film in contrast to the usual sequence of film-to-ligament to droplet formation as presented in Fig. 7.

An interesting feature of Eq. (40) is that it contains an air viscosity term although the effect of air viscosity on mean droplet size was not studied directly. More surprising is the result that an increase

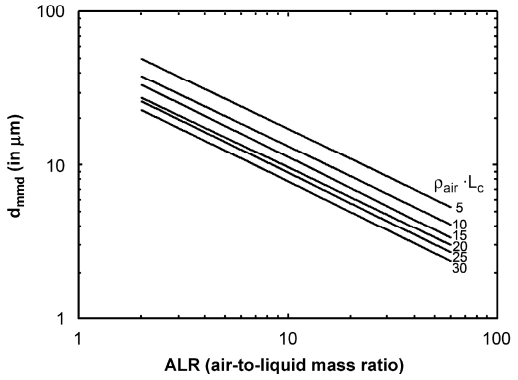

Fig. 15. Plot of Eq. (40) for converging two-fluid nozzles for different values of $\rho_{air} \cdot L_c$ (here the product is expressed in cm g/cm^3).

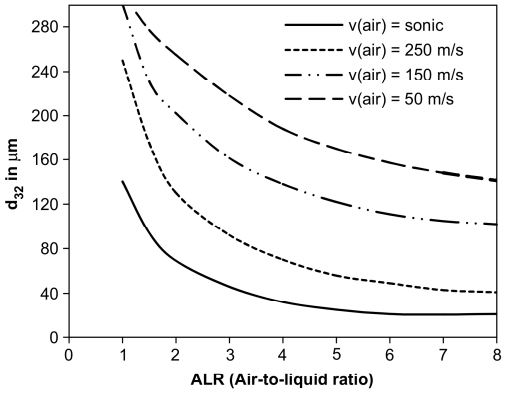

Fig. 16. Typical performance curves for external mixing two-fluid nozzles at intermediate feed rates: Effect of air liquid mass ratio and air velocity on spray mean droplet diameter for $T = 298$ K, $\rho_{liq} = 1000$ kg/m^3, $\gamma_{liq} = 0.072$ kg/s^2, $\eta_{liq} = 1$ mPa s. Data depicted on the basis of Eq. (45). Note the similarity with Fig. 12.

in nozzle size reduces the mean droplet size. This was interpreted as an indication of the fact that a longer wetted perimeter creates a thinner film and hence a finer spray (Gretzinger and Marshall, 1961; Lefebvre, 1989a). Eq. (40) is shown plotted in Fig. 15 in terms of $\dot{m}_{liq}/\dot{m}_{air}$ also known as 1/ALR. Units of cm g/cm^3 are applied to the parameter $(\rho_{air} \cdot L_c)$ in this figure.

The mass median diameter correlation in Eq. (40) was developed from data using a convergent external nozzle design at low liquid feed rates. The correlation is restricted to co-current contact between air and liquid and is not applicable if air contacts the liquid at right angles. The mass median diameter determined by Eq. (40) may be correlated with the Sauter mean diameter according to (Gretzinger and Marshall, 1961)

$$\log d_{mmd} = \log d_{32} + 1.1513 \cdot \log^2 (S_g) \tag{41}$$

where S_g is the standard deviation for the droplet size distribution for the tested nozzle expressed as (Gretzinger and Marshall, 1961):

$$S_g = 1.77 \cdot d_{mmd}^{0.14} \tag{42}$$

In the work by Kim and Marshall (1971) studies were made on a convergent external mixing type of nozzle similar to the one used by Gretzinger and Marshall (1961). Droplet size measurements were carried out on melts of wax mixtures over a range of liquid viscosity from 0.001 to 0.050 kg/m s, relative velocities from 75 to 393 m/s, air/liquid flow mass ratios of 0.06 to 40, liquid density of 800–960 kg/m^3 and air densities of 0.93–2.4 kg/m^3 (all evaluated at the nozzle entrance prior to expansion). Based on experimental data, the empirical equation (43) was derived.

$$d_{mmd} = \left[\frac{249 \cdot \gamma_{liq}^{0.41} \cdot \eta_{liq}^{0.32}}{(v_{rel}^2 \cdot \rho_{air})^{0.57} \cdot A_{annulus}^{0.36} \cdot \rho_{liq}^{0.16}} \right] + 1260 \cdot \left[\left(\frac{\eta_{liq}}{\gamma_{liq} \cdot \rho_{liq}} \right)^{0.17} \cdot \left(\frac{1}{v_{rel}^{0.54}} \right) \cdot \left(\frac{\dot{m}_{air}}{\dot{m}_{liq}} \right)^m \right] \tag{43}$$

where

$$m = -1 \text{ at } \left(\frac{\dot{m}_{air}}{\dot{m}_{liq}} \right) < 3 \quad \text{and} \quad m = -0.5 \text{ at } \left(\frac{\dot{m}_{air}}{\dot{m}_{liq}} \right) > 3$$

and d_{mmd} is the mass median droplet diameter in µm and $A_{annulus}$ is the area of the air annulus in^2. The units of η_{liq}, γ_{liq}, v_{rel} and ρ_{liq} are centipoise, dynes/cm, ft/sec, lb/ft^3, respectively. Eq. (43) expresses the mass median droplet diameter in terms of nozzle dimensions and operating conditions. The discontinuity for the parameter m is an unfortunate feature of Eq. (43) as the influence of the exact value of m for the prediction of d_{mmd} is significant. The correlation is applicable to convergent external mixing designs operating with Newtonian liquids. For comparison of data obtained with Eq. (43) with alternative correlations involving the Sauter mean diameter d_{32}, the following relation is suggested in accordance with Simmons (1976) (Kim and Marshall, 1971):

$$d_{32} = 0.83 \cdot d_{mmd} \tag{44}$$

Although determined empirically. Eq. (44) has proven to fit excellent with theoretical considerations concerning the Rosin–Rammler droplet size distribution, as will be presented in Section 7.

Kim and Marshall (1971) concluded from their studies that the operating variables of primary importance are the air/liquid mass ratio and the dynamic forces being expressed as $\rho_{air} \cdot v_{rel}^2$. Increasing either of the two was observed to reduce the mass median droplet size. The droplet size in the coarse sprays depends largely upon the mass ratio while the effect of the dynamic force predominates in the finer range. Sprays become coarser as the Newtonian viscosity increases. Based on these observations, Kim and Marshall (1971) suggested that the mean spray droplet size d_d (being d_{32} or d_{mmd}) produced by external mixing two-fluid nozzles has the general form of Eq. (45).

$$d_d = \frac{A''}{(v_{rel}^2 \cdot \rho_{air})^{\alpha}} + B'' \cdot \left(\frac{\dot{m}_{air}}{\dot{m}_{liq}} \right)^{\beta} \tag{45}$$

where v_{rel} is the relative velocity between air and liquid at the nozzle outlet and ρ_{air} is the atomisation air density. The exponents α and β are functions of nozzle design and A'' and B'' are constants involving both nozzle design and liquid properties (Kim and Marshall, 1971). Based on experimental data, Kim and Marshall (1971) suggest values for α and β of, respectively, 0.57 and 0.36 (these are the values used to generate the curves in Figs. 16 and 17). In Eq. (45), important properties such as the liquid orifice diameter, liquid density, liquid viscosity and liquid surface tension, etc. are absent in a direct form and only implicitly given by the constants A'' and B'', which,

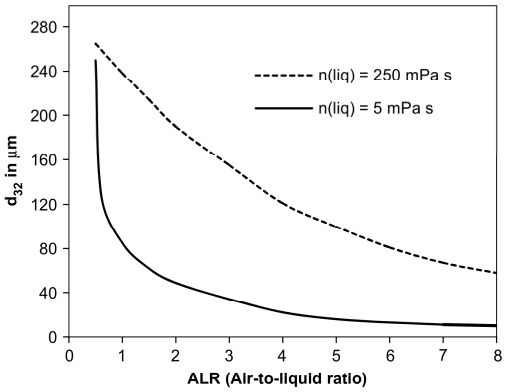

Fig. 17. Typical performance curves for external mixing two-fluid nozzles at intermediate feed rates: Effect of air liquid mass ratio and liquid viscosity on spray mean droplet diameter for $T = 298\,\mathrm{K}$, $\rho_{liq} = 1000\,\mathrm{kg/m^3}$, $\gamma_{liq} = 0.072\,\mathrm{kg/s^2}$, $\eta_{liq} = 1\,\mathrm{m\,Pa\,s}$. Data depicted on the basis of Eq. (45).

in comparison with Eq. (43) clearly are influenced by these parameters. Eq. (45) has nevertheless led to some general tendencies that may help to explain the qualitative tendencies outlined in Section 5. Some of the most important results will be briefly introduced in the following subsections.

The mass ratio $\dot{m}_{air}/\dot{m}_{liq}$ was found by Kim and Marshall (1971) to be one of the most important variables to affect the mean droplet size. An increase in this ratio decreases the droplet size. When the nozzle is used to produce coarse sprays the mass ratio becomes the most significant variable depicted in Eq. (45). Values of $\dot{m}_{air}/\dot{m}_{liq}$ should preferably range from 0.1 to 10 (Kim and Marshall, 1971). At values below 0.1 atomisation deteriorates rapidly even with liquids that are readily atomised. The upper value of 10 is the limit for which it is possible to decrease the droplet size just by increasing the mass ratio $\dot{m}_{air}/\dot{m}_{liq}$. Above ratio values of 10, atomisation proceeds with excess energy expenditure without marked decrease in mean droplet size. Other investigators have indicated that droplets of 5 μm do not disintegrate into smaller sizes in the presence of high velocity air, but experimental sampling of sprays from nozzles show that sizes down to 1 μm are apparent (Masters, 1972). The mean droplet size approaches a limiting value asymptotically for increased values of the mass ratio. This is shown in Fig. 16, where the effect of air–liquid mass ratio on spray mean droplet diameter is depicted at various values of the atomising air velocity.

The effect of air–liquid mass ratio on spray mean droplet diameter for various values of the feed viscosity is shown in Fig. 17. The limiting value decreases with the approximately 0.36 power of the total nozzle air flow rate (Masters, 1972).

Mean droplet size decreases with increase in relative velocity (Kim and Marshall, 1971; Masters, 1972). This can be seen from Fig. 16. Increase of the relative velocity between air and liquid at the point of contact increases the air dynamic force $v_{rel}^2 \cdot \rho_{air}$ in Eq. (45) and more energy is thereby available for atomisation. Hence, the limiting mean droplet size is directly related to the air velocity as observed from Fig. 16. In fact, mean droplet size varies inversely with the air velocity to the power of 1.14 (Masters, 1972).

Kim and Marshall (1971) found that an increase in the liquid viscosity increases the mean droplet size. This is in agreement with the basic atomisation theory presented in Section 3. The complexity of the atomisation mechanism prevents a precise variation to be established over the range of values tested by the different authors. The exponent of viscosity lies in the range of 0.30–0.37 (Masters, 1972). Kim and Marshall (1971) propose an approximate exponent of 0.32.

Rizkalla and Lefebvre (1975) conducted detailed studies on a specially designed prefilming airblast atomizer in which the liquid is first spread into a thin sheet and then exposed on both sides to high-velocity air streams. They used dimensional analysis to derive a droplet size correlation according to Eq. (46) (expressed as function of the tested prefilmer lip diameter $d_{prefilm}$) for various constants and indices being deduced from experimental data.

$$d_{32} = \left[3.33 \times 10^{-3} \left(\frac{\sqrt{\gamma_{liq} \cdot \rho_{liq} \cdot d_{prefilm}}}{v_{air} \cdot \rho_{air}} \right) + 13.10 \times 10^{-3} \left(\frac{\eta_{liq}^2}{\gamma_{liq} \cdot \rho_{liq}} \right)^{0.425} d_{prefilm}^{0.575} \left(1 + \frac{\dot{m}_{liq}}{\dot{m}_{air}} \right) \right] \times \left(1 + \frac{\dot{m}_{liq}}{\dot{m}_{air}} \right) \quad (46)$$

Based on the results by Rizkalla and Lefebvre (1975), Lefebvre (1983) suggested a basic but slightly different equation for Sauter mean droplet sizes produced by prefilming nozzles according to Eq. (47).

$$d_{32} = L_c \cdot \left[A' \left(\frac{\gamma_{liq}}{\rho_{air} \cdot v_{air}^2 \cdot d_{prefilm}} \right)^{0.5} + B' \left(\frac{\eta_{liq}^2}{\gamma_{liq} \cdot \rho_{liq} \cdot d_{prefilm}} \right)^{0.5} \right] \times \left(1 + \frac{\dot{m}_{liq}}{\dot{m}_{air}} \right) \quad (47)$$

where L_c is the characteristic dimension of the nozzle set as the prefilmer lip diameter $d_{prefilm}$ for practical applications of Eq. (47). A' and B' are constants whose values depend on the atomiser design. When L_c is set to $d_{prefilm}$, Eq. (47) shows that d_{32} is proportional to the square root of the prefilmer lip diameter $d_{prefilm}$. This is reasonable, as if other parameters are kept constant, a decrease in $d_{prefilm}$ will slightly reduce the liquid film thickness at the atomising lip and hence reduce d_{32}.

A number of different correlations have been based on the general relationship in Eq. (47). If L_c is set to $d_{prefilm}$, El-Shanawany and Lefebvre (1980) have derived a correlation of the same form leading to Eq. (48).

$$d_{32} = d_{prefilm} \cdot \left[0.33 \left(\frac{\gamma_{liq}}{\rho_{air} \cdot v_{air} \cdot d_{prefilm}} \right)^{0.6} \left(\frac{\rho_{liq}}{\rho_{air}} \right)^{0.1} + 0.068 \left(\frac{\eta_{liq}^2}{\gamma_{liq} \cdot \rho_{liq} \cdot d_{prefilm}} \right)^{0.5} \right] \left(1 + \frac{\dot{m}_{liq}}{\dot{m}_{air}} \right) \quad (48)$$

Following the improvements in droplet sizes measuring techniques, modern droplet size studies have focussed especially on droplet size correlations for commercial nozzles and droplet size correlations for complex fluid atomisation such as suspensions, slurries and special polymer solutions (Mulhem et al., 2003, 2006; Juslin et al., 1995a,b; Yliruusi et al., 1992).

Considering the ratio of the energy present in the atomising gas to the surface energy as the main factor determining the droplet sizes, and considering also the liquid loading and the liquid viscosity, Walzel (1993) and Groom et al. (2004) derived a semi-empirical

droplet size correlation according to Eq. (49).

$$d_{32} = d_{\text{orifice}} \cdot 0.35 \cdot \left[\frac{\Delta p_{\text{air}} \cdot d_{\text{orifice}}}{\gamma_{\text{liq}} \cdot \left(1 + \frac{\dot{m}_{\text{liq}}}{\dot{m}_{\text{air}}}\right)^2} \right]^{-0.40} \cdot (1 + 2.5 \cdot Oh) \quad (49)$$

where d_{orifice} is the liquid orifice diameter and Δp_{air} is the pressure drop in the gas through the nozzle (often simplified as the difference between the nozzle pressure and the ambient pressure into which the nozzle stream expands). The ratio between Δp_{air}, d_{orifice} and γ_{liq} is known as the gas-Laplace number and may for simplicity be approximated by the We_{air} number (Groom et al., 2004). The three tested nozzles were geometrically similar with $d_{\text{orifice}}/d_{\text{gasslit}} = 3.5$ and $s_{\text{gasslit}}/d_{\text{gasslit}} = 0.3$, where d_{gasslit} is the inside diameter of atomisation air gas slit and s_{gasslit} is the atomisation air gas-channel slit thickness (see e.g. Fig. 5a). The experiments on which the correlation was derived were performed with water and aqueous glycerol solutions in the viscosity range of 1–100 m Pa s and with a Δp_{air} value in the range of 0.5–3 bar. The tested liquid orifice diameter was 1 mm. The correlations by Walzel (1993) are particularly interesting as they were derived from commercial nozzles under conditions not far from industrial conditions.

Juslin et al. (1995a,b) have studied the effect of atomising air pressure, liquid flow rate and polymer solution concentration on the droplet size and the droplet size distribution using a 3^3 factorial design in a top-sprayed fluid bed coater. Juslin et al. (1995a,b) used a commercial two-fluid external mixing nozzle from the Schlick 940 series which are simple circular full-cone nozzles with orifice diameters in the range of 0.5–2.3 mm having spray angles in the range of 10–40°. Such nozzles are the standard type in many types of commercial fluid bed coaters such as the ones provided by e.g. Niro-Aeromatic-Fielder and Glatt (Schick, 2006). Although the resulting regression models from factorial design studies are very specific and cannot be used in general, the conditions that were studied by Juslin et al. (1995a,b) are very close to standard operations in commercial fluid coating processes, making the results highly interesting.

Juslin et al. (1995a) found that the atomising air pressure was the most significant factor affecting the spray angle and the cross sectional area of the spray cone. Increasing the air pressure led to a decline in the spray angle and to a decreased spray area. The effect of the liquid flow rate was observed to affect the spray angle and the spray area inversely. A similar tendency was observed for a change in the polymer solution concentration, whereas the mean droplet size increased with increasing liquid flow rate and concentration (Juslin et al., 1995a,b). The regression analysis revealed some interactions between independent variables. E.g., the atomising air pressure had a stronger effect on the median of droplet size when the polymer concentration was low. This tendency was suggested to be due to changes in viscosity thereby supporting previously reported tendencies (Juslin et al., 1995b).

For a prefilming external mixing nozzle of novel design capable of producing very fine droplets at low ALR ratios, Nguyen and Rhodes (1998) suggested a modified version of Eq. (47) according to Eq. (50).

$$d_{v0.5} = d_{\text{prefilm}} \left[7.99 \left(\frac{\gamma_{\text{liq}}}{\rho_{\text{air}} \cdot v_{\text{air}}^2 \cdot d_{\text{prefilm}}} \right)^{0.87} + 144.6 \left(\frac{\eta_{\text{liq}}^2}{\gamma_{\text{liq}} \cdot \rho_{\text{liq}} \cdot d_{\text{prefilm}}} \right)^{0.87} \right] \left(1 + \frac{\dot{m}_{\text{liq}}}{\dot{m}_{\text{air}}}\right)^{0.45} \quad (50)$$

In certain types of fluid bed granulation processes the coating/binder liquid is a suspension or a slurry rather than a solution. This is e.g. the case in polymer fluid bed coating processes where often dry matter in the form of e.g. TiO_2 particles is added to the aqueous polymer solution in order to reduce the stickiness of the coating layer. In contrast to atomisation of pure liquid or homogenous solutions, studies on suspension atomisation is a rather new field with only a few articles published. Schütz et al. (2004) recently, published some numerical investigations with suspensions providing a mathematical–physical model capable of calculating the aerodynamically induced atomisation. The boundary conditions for this model at the nozzle orifice were determined by CFD codes calculating the state variables inside the nozzle. The resulting d_{32} was determined by considering the nozzle geometry, operating conditions and fluid properties. Comparison of the experimental data from a simple hollow-cone nozzle with measured droplet sizes via laser diffraction showed good agreement although model predictions are clearly limited by the necessary model assumptions. Following previous authors, some correlations for suspension droplet sizes produced from internal mixing two-fluid nozzles are published in Shirley and Truc (1987), Glaser (1989). Only recently, Mulhem et al. (2003, 2006) have published a correlation for suspension droplet sizes generated by an external mixing two-fluid nozzle according to Eq. (51).

$$d_{32} = 0.21 \cdot d_{\text{orifice}} \cdot (Oh)^{0.0622} \cdot \left(We_{\text{air}} \cdot \frac{\dot{m}_{\text{air}}}{\dot{m}_{\text{liq}}} \right)^{-0.4} \quad (51)$$

Eq. (51) has shown good agreement with suspensions containing small particles with diameters in the range of 6–10 μm and for d_{32} values from 15 to 100 μm. Apparently, the atomization process is not significantly affected by the presence of the tested particles in suspension and Eq. (51) has shown adequate precision with pure water droplets (Mulhem et al., 2003). However, Mulhem et al. (2006) also showed that as the particles in the suspension increase in size up to the diameter of the liquid droplets, the solid particles and liquid will be more and more separated. This is indicated by a bimodal size distribution.

7. Droplet size distributions

Due to the heterogeneous nature of the atomisation process, the liquid threads and ligaments formed by the various mechanisms of jet and liquid sheet disintegration vary widely in diameter, and the resulting main droplets vary in size. Practical nozzles do therefore not produce sprays of uniform droplet size at any given operating condition. Instead the spray can be regarded as a spectrum of droplet sizes distributed about some arbitrarily defined mean value (Lefebvre, 1989b). Thus, in addition to mean droplet size, another parameter of importance in the definition of a spray is the distribution of droplet sizes it contains. As no complete theory has yet been developed to describe the hydrodynamic and aerodynamic processes involved when jet and sheet disintegration occurs under normal atomising conditions, a number of functions have been proposed, based on either probability or purely empirical considerations that allow the mathematical representation of measured droplet size distributions. Those generally used include normal, lognormal, Nukiyama-Tanasawa, Rosin–Rammler and upper-limit distributions (Lefebvre, 1989b; Nukiyama and Tanasawa, 1939, 1940). Comparison of these distributions parameters reveals that all of them have deficiencies of one kind or another. So far, no single distribution has emerged that has a clear advantage over the others. For any given application the best distribution function is one that provides the best fit to the experimental data. The most widely used expression for droplet size distribution is one that was originally developed for particles being the Rosin–Rammler distribution accordingto Eq. (52).

$$1 - Q = \exp\left(-\frac{d_d}{X}\right)^q \quad (52)$$

where Q is the fraction of the total volume (or total mass) contained in droplets of diameters less than d_d, and X and q are constants. The Rosin–Rammler relationship thus describes the droplet size distribution in terms of two parameters X and q. The exponent q provides a measure of the spread of droplet sizes. The higher the value of q the more uniform is the spray (Rosin and Rammler, 1933). Modern nozzles typically operate with q values in the range of 1.5–2.9 (Niro, 2007).

Although the Rosin–Rammler distribution assumes an infinite range of droplet sizes the distribution has a virtue of simplicity. Furthermore, it permits data to be extrapolated into the range of very fine droplets where measurements are often difficult and least accurate. Another useful advantage of the Rosin–Rammler distribution is that all the droplet distribution representative diameters are uniquely related to each other via the distribution parameter q. This makes it possible to express certain spray properties in terms of the parameters q and thereby deduce one characteristic diameter from another if one of them is known. Lefebvre (1989b) and Chin and Lefebvre (1987) presented some of the most important expressions according to Eqs. (53)–(57).

$$\frac{d_{v0.1}}{d_{\mathrm{mmd}}} = (0.152)^{1/q} \tag{53}$$

where $d_{v0.1}$ is the droplet diameter such that 10% of the total liquid volume is in droplets of smaller diameter.

$$\frac{d_{v0.5}}{d_{\mathrm{mmd}}} = 1 \tag{54}$$

where $d_{v0.5}$ is the droplet diameter such that 50% of the total liquid volume is in droplets of smaller diameter. Eq. (54) is obvious as $d_{v0.5}$ is related to d_{mmd} via the liquid density,

$$\frac{d_{v0.9}}{d_{\mathrm{mmd}}} = (3.322)^{1/q} \tag{55}$$

where $d_{v0.9}$ is the droplet diameter such that 90% of the total liquid volume is in droplets of smaller diameter.

$$\frac{d_{v0.999}}{d_{\mathrm{mmd}}} = (9.968)^{1/q} \tag{56}$$

where $d_{v0.999}$ is the droplet diameter such that 99.9% of the total liquid volume is in droplets of smaller diameter.

$$\frac{d_{\mathrm{mmd}}}{d_{32}} = (0.693)^{1/q}\Gamma\left(1 - \frac{1}{q}\right) \tag{57}$$

where Γ is the gamma function known from mathematics as the extension of the factorial function to real and complex numbers. Interestingly, for sprays with a narrow size distribution where q approaches a value of at least 2.5, Eq. (57) predicts a value of the d_{mmd}/d_{32} fraction close to 1.2 which is close to the result found by Kim and Marshall (1971) and Simmons (1976) in Eq. (44). The relationships in Eqs. (53) and (55)–(57) are plotted as function of the parameter q in Fig. 18.

From analysis of a considerable amount of droplet size data obtained with various different nozzle types, Rizk and Lefebvre (1985) found that a better fit to the experimental data, especially for the larger droplet sizes, could be obtained by a modified Rosin–Rammler correlation according to Eq. (58).

$$1 - Q = \exp\left(-\frac{\ln d_d}{\ln X}\right)^q \tag{58}$$

These findings have however not been followed by other authors and a wide range of other statistical relationships have been suggested as reviewed by Lefebvre (1989a,b). Generally, little attention has been given in literature to the droplet size distribution in comparison with the attention given to the mean droplet diameter. Although modern two-fluid nozzles have been designed to produce narrow droplet size distributions with values of the q parameter in the range of 2.5 and higher, it must be stressed that droplet size distributions are just as important for any practical application, as are the mean droplet diameters (Schlick, 2007; Spray Drying Systems Co., 2000).

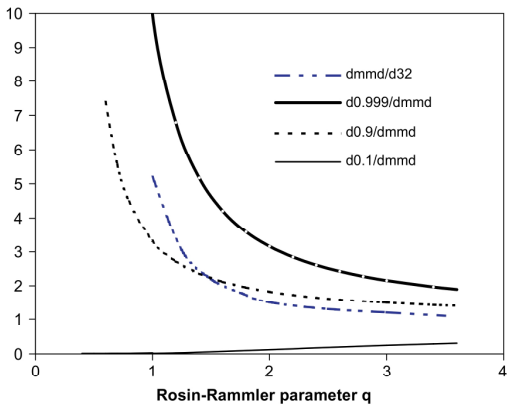

Fig. 18. Relationship between the Rosin–Rammler distribution parameter q and various spray characteristics. Data obtained from Eqs. (53) and (55)–(57).

Table 2
Nozzle dimensions and operating conditions to be used in the comparison of the correlations for predicting the mean droplet size

Parameter	Value
Liquid orifice diameter ($d_{\mathrm{orifice}} = d_{\mathrm{prefilmer}}$)	1.2 mm
Air annulus area (A_G)	1.77 mm^2
Liquid temperature	25 °C
Liquid surface tension (γ_{liq})	0.072 kg/s^2
Liquid viscosity (η_{liq})	0.001 kg/m s
Liquid density (ρ_{liq})	1000 kg/m^3
Nozzle pressure	3 bar
Air temperature	25 °C
Air viscosity	1.9×10^{-5} kg/m s
Air density(ρ_{air})	1.18 kg/m^3
Rosin–Rammler parameter q	2.5
Basic assumption	$d_{32} \sim 0.8 \cdot d_{v0.5}$

8. Practical summary—which correlations should be used

The conditions associated with each of the presented droplet size correlations are presented in Table 1. Following the presentation of the correlations in Section 6 it becomes clear that it is not in any way obvious which correlation that predicts the mean droplet size best in a given situation. The situation is complicated by the fact that some of the correlations have been derived for specially designed nozzle types and that only a few authors have determined a droplet size distribution associated with their correlation. However, if the correlations should have any practical importance it is necessary to make a choice between the correlations and hence, to know how well the correlations predict the mean droplet size for a given set of nozzle conditions. This section aims at testing the presented correlations for realistic nozzle conditions in order to illustrate the use and limitations of the presented correlations.

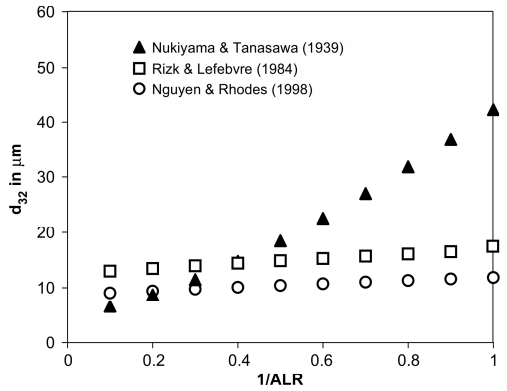

Fig. 19. Comparison of predicted Sauter mean droplet diameters for different values of the mass rate of liquid flow divided by the mass rate of atomisation air flow for the simple plain jet internal mixing nozzle correlations. Data obtained for $Oh = 0.003$ and $We_{air} = 40$.

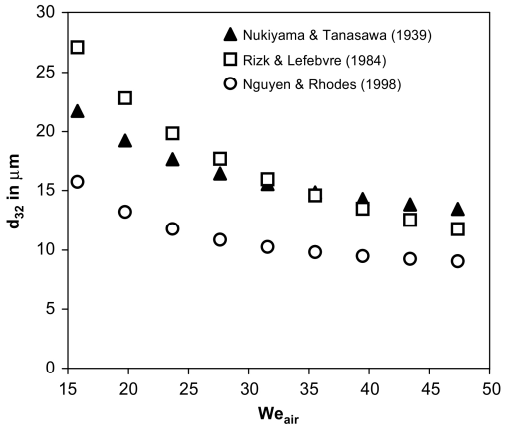

Fig. 20. Comparison of predicted Sauter mean droplet diameters for different values of the gas-Weber number for the simple plain jet internal mixing nozzle correlations. Data obtained for $Oh = 0.003$ and $1/\mathrm{ALR} = 0.4$.

For comparison, the different nozzle correlations have been tested for atomisation of pure water with air. All the parameters used for the study are summed up in Table 2. Nozzle dimensions are taken from a versatile commercial circular full-cone Schlick 970 which is a common type for fluid bed coating purposes. This nozzle type is a small external mixing nozzle, but the dimensions are not far off the dimensions in a simple internal mixing nozzle, and for comparison the conditions in Table 2 are also used for such types of nozzles. Following the division in Section 6 the tests of the correlations have been divided into simple internal and simple external mixing correlations as well as in a third category treating the prefilming nozzle correlations.

8.1. Comparison of simple internal mixing nozzle droplet size correlations

According to Table 1, three correlations have been presented for simple plain jet internal mixing nozzles being Eq. (37) by Nukiyama and Tanasawa (1939, 1940), Eq. (38) by Rizk and Lefebvre (1984) and Eq. (39) by Nguyen and Rhodes (1998). For the conditions in Table 2 a comparison has been made for the three correlations. Fig. 19 shows data obtained for fixed values of the Ohnesorge and gas-Weber number varying only the $\dot{m}_{liq}/\dot{m}_{air} = 1/\mathrm{ALR}$ fraction.

From Fig. 19 it can be seen that there is fair agreement between the three correlation predictions in a 1/ALR range of 0.1–0.5. Especially the two recent correlations by Rizk and Lefebvre (1984) and Nguyen and Rhodes (1998) show good agreement across the entire range of tested 1/ALR values although the difference in droplet size prediction remains constant across the entire range. A quick look at these two correlations shows that they have been derived on essentially the same basic form although the exponents of the different terms are quite different. As the 1/ALR fraction increases in Fig. 19, large deviations are observed for the Nukiyama and Tanasawa (1939, 1940) correlation. The droplet sizes predicted by this equation for large 1/ALR values by far exceeds the values found by other authors for identical nozzle conditions (Lefebvre, 1989a,b). However, the normal operating range for smaller internal mixing nozzles typically lies well below 1/ALR values of 1. Particularly at the 1/ALR values below 0.5, the three correlations predict d_{32} values reasonably close to each other irrespectively of the nozzle pressure which may be observed from Fig. 20. Here d_{32} is depicted as function of the gas Weber number for a fixed value of the Ohnesorge number at $1/\mathrm{ALR}=0.4$. The results in Fig. 20 are interesting as the Nukiyama and Tanasawa (1939, 1940) equation is based on volumetric flow velocities whereas the equation by Rizk and Lefebvre (1984) is based on mass flow rates. Furthermore, the Nukiyama and Tanasawa (1939, 1940) equation does not even account for nozzle geometry which may be part of the reason for the deviation in Fig. 19. Even so the three correlations seem to predict mean droplet sizes reasonably close to each other in a broad range of nozzle pressures for 1/ALR values close to 0.5 as observed from Fig. 20.

In conclusion, the brief analysis of the three internal mixing droplet size correlations has shown that at normal nozzle operating conditions the three correlations predict mean droplet sizes close to each other. In that sense it is less important which correlation is chosen although the results in Fig. 19 indicate that the Rizk and Lefebvre (1984) and Nguyen and Rhodes (1998) equations are the most versatile and follow best the trends found by other authors for small values of the 1/ALR fraction (Lefebvre, 1989a).

8.2. Comparison of simple external mixing nozzle droplet size correlations

Four correlations for simple external mixing nozzles have been presented in previous sections being the Gretzinger and Marshall (1961) (Eq. (40)), Kim and Marshall (1971) (Eq. (43)), Walzel (1993) (Eq. (49)) and Mulhem et al. (2003, 2006) (Eq. (51)) correlations. Similar to the test of the internal mixing correlations, a comparison has been made of the four equations. Fig. 21 shows data obtained for fixed values of the Ohnesorge and gas-Weber number varying only the 1/ALR fraction.

First of all it may be observed from Fig. 21 that all four curves overall follow the same trends; namely that the Sauter mean diameter increases with increasing 1/ALR fraction which is in accordance with presented qualitative trends. Furthermore, it may be seen that the correlations by Gretzinger and Marshall (1961) predicts significantly lower mean droplet diameters than the other three correlations across the testes 1/ALR range. This trend is a common observation with the Gretzinger and Marshall (1961) equation and in

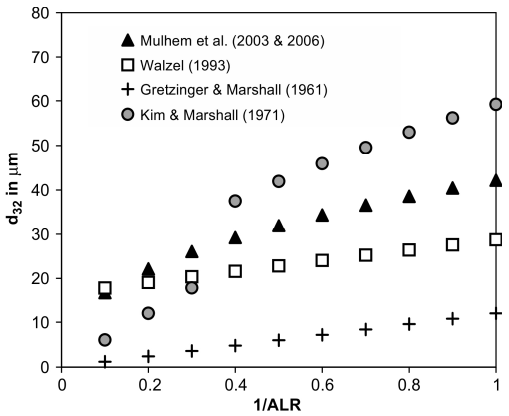

Fig. 21. Comparison of predicted Sauter mean droplet diameters for different values of the mass rate of liquid flow divided by the mass rate of atomisation air flow for the simple external mixing nozzle correlations. Data obtained for $Oh = 0.003$ and $We_{air} = 40$.

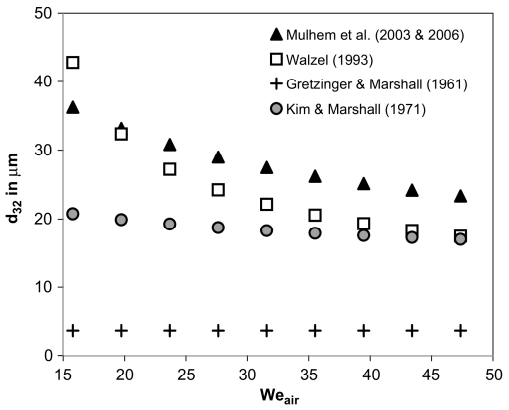

Fig. 22. Comparison of predicted Sauter mean droplet diameters for different values of the gas-Weber number for the four presented external mixing nozzle correlations. Data obtained for $Oh = 0.003$ and $1/ALR = 0.3$.

fact it has been commonly known that this correlation often predicts lower droplet sizes than what is actually obtained from experimental data (Lefebvre, 1989a; Masters, 1972). As mentioned in Section 6.2 the Gretzinger and Marshall (1961) correlation is the oldest and by far the simplest of the four equations as it does not account for liquid density, viscosity of surface tension, etc. Hence, it is not surprising that this equation predicts mean droplet diameters far away from the other three correlations. Even so the correlation follows closely the overall trends of the other equations. This argues strongly in favour of the observations determined by Gretzinger and Marshall (1961): Namely that the 1/ALR ratio perhaps is the most important property regarding the mean droplet size.

The correlation by Kim and Marshall (1971) predicts lower mean droplet diameters for $1/ALR < 0.33$, but larger mean droplet diameters for $1/ALR > 0.33$. The discontinuity observed in Fig. 21 arises from the discontinuity associated with the value of the parameter m in Eq. (43), and it clearly shows that including a discontinuity in the mean droplet size correlation does not necessarily add further precision to the estimations.

Interestingly, there is a significant difference between the recent equations especially at 1/ALR values above 0.5. The nozzle designs that were used to derive the Walzel (1993) and Mulhem et al. (2003, 2006) correlations have many similarities, but even so the correlations predicts different d_{32} values for most 1/ALR values. One of the reasons for this could be that the Mulhem et al. (2003, 2006) correlation was derived for suspensions whereas the Walzel (1993) was derived for solutions. It is reasonable to believe that the difference in liquid properties, as observed, is more pronounced at either high liquid or high air flow rates, where the particles in suspension may affect the atomisation process, and thereby d_{32}, the most. As was the case for the internal mixing correlations the best predictions are made in a 1/ALR range around the value of 0.3, this time in a narrow interval of 0.2–0.3. In Fig. 22, d_{32} is depicted as function of the gas-Weber number for a fixed value of the Ohnesorge number at $1/ALR = 0.3$. Again the Gretzinger and Marshall (1961) correlation predicts mean droplet diameters below those of the other equations, whereas two recent correlations predict d_{32} values close to each other, but deviate increasingly at increasing gas-Weber numbers. Interestingly, the Kim and Marshall (1971) equation approaches the

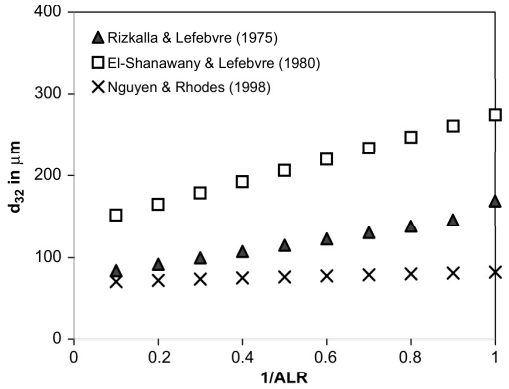

Fig. 23. Comparison of predicted Sauter mean droplet diameters for different values of the mass rate of liquid flow divided by the mass rate of atomisation air flow for the prefilming external mixing nozzle correlations. Data obtained for $Oh = 0.003$ and $We_{air} = 40$.

prediction of the recent correlations at high We_{air}. In conclusion, based on the results in Figs. 21 and 22 as well as previous experience with the Gretzinger and Marshall (1961) and Kim and Marshall (1971) correlations, it appears that the Walzel (1993) equation is the best choice for atomising solutions whereas the Mulhem et al. (2003, 2006) correlation should be consulted when atomising suspensions.

8.3. Comparison of specially designed prefilming external mixing nozzle droplet size correlations

Three correlations have been derived for specially designed prefilming nozzles that do not fit well into a comparison with simple internal or external mixing nozzles. The three correlations are the Rizkalla and Lefebvre (1975) (Eq. (46)), El-Shanawany and Lefebvre (1980) (Eq. (48)) and Nguyen and Rhodes (1998) (Eq. (50)). Similar to the test of the other correlations a comparison has been made of the three equations with varying 1/ALR ratio. Fig. 23 shows data

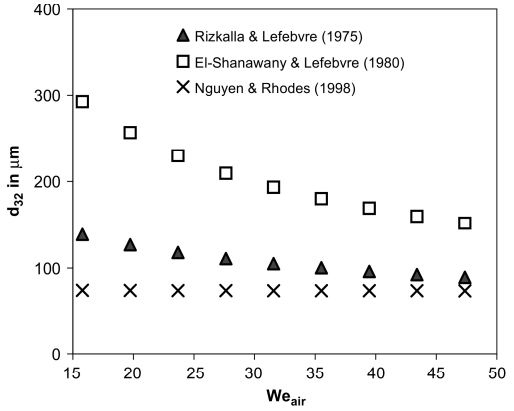

Fig. 24. Comparison of predicted Sauter mean droplet diameters for different values of the gas-Weber number for the prefilming external mixing nozzle correlations. Data obtained for $Oh = 0.003$ and $1/\mathrm{ALR} = 0.3$.

obtained for fixed values of the Ohnesorge and gas-Weber number varying only the 1/ALR fraction.

As observed from Fig. 23 there are significant differences among the three correlations. As mentioned, the correlations have all been derived for a specific nozzle and it is thus not surprising that the correlations do not predict identical values of d_{32}. The three prefilming correlations predict far larger mean droplet diameters than the simple internal and external mixing nozzle correlations. This is a consequence of the choice of $d_{\mathrm{orifice}} = d_{\mathrm{prefilmer}}$ in Table 2. This was chosen in order to make a direct comparison between the correlations, although in normal prefilming nozzle designs, the choice for $d_{\mathrm{prefilmer}}$ would often be somewhat smaller than the choice of d_{orifice} for a nozzle of similar capacity. Similar to the simple correlations, which scale with d_{orifice}, the prefilming correlations have proportionality between the characteristic length, $d_{\mathrm{prefilmer}}$, and d_{32}. Hence, normal prefilming nozzle gives values for d_{32} in the range of the other simple designs. Despite the deviations between the correlations, the same trend, as was observed in Figs. 19 and 21, is also observed from Fig. 23: Namely that the correlations are closest to each other at 1/ALR values around 0.3. At this value a comparison of the predicted d_{32} values as function of the gas-Weber number is made in Fig. 24. It may be observed in this figure how the predictions tend to converge with increasing gas velocity thereby following the tendencies observed in Figs. 20 and 22.

With the results in Figs. 23 and 24 it is difficult to argue which one of the three correlations for the prefilming external mixing nozzles would be the best choice in a given practical situation. With such a large spread in the predictions it is necessary to carefully study the original published papers in order to see to which extent the nozzle designs match the one in question. Even so the correlations for the prefilming external mixing nozzles do follow the same overall trends as the correlations derived from nozzles of a more simple design.

9. Conclusion

Fundamentals and applications of two-fluid spray atomisation have been reviewed. The paper has presented a systematic and up-to-date review of two-fluid nozzle designs and principles together with a presentation of nozzle fundamentals introducing basic nozzle theory and thermodynamics. Droplet size correlations for the prediction of the mean droplet diameter have been reviewed and accompanied by a discussion of their use.

The review showed that although many parameters and properties are suggested to be of importance regarding the resulting d_{32} the correlations and qualitative tendencies show some agreement with respect to which parameters that are the most important. From an engineering standpoint, the most important parameters in controlling the mean droplet size may be summed up as:

- The ratio of the air-to-liquid mass flow rate (the ALR ratio).
- The nozzle pressure and thereby the gas velocity in m/s at the nozzle outlet.
- The type of nozzle (external, internal—simple jet or prefilming) and orifice dimensions such as e.g. the diameter of the liquid orifice or the diameter of the prefilming section.
- The liquid properties such as surface tension, density and viscosity of which the liquid viscosity play the most important role.

The paper has further addressed the most relevant droplet size correlations observed from a fluid bed coating process perspective including qualitative tendencies that in practice often are more useful than a detailed droplet size correlation. These tendencies show in general that the Sauter mean droplet diameter increases most significantly with increasing liquid viscosity, but also with increasing surface tension, liquid density and temperature of the atomisation air. Further, the Sauter mean diameter decreases with increasing air-to-liquid mass ratio and with increasing atomisation pressure.

It becomes clear from the present review that no single droplet size correlation can be used to predict the mean droplet size from any given two-fluid nozzle. The correlations presented are all closely related to the nozzle design and to the conditions under which they where derived. The comparison of the mean droplet size correlations has however shown that despite some diversion in the predicted d_{32} diameter, it is possible to provide qualified suggestions for which correlations that should be used under given conditions.

Notation

A'	constant, dimensionless
A''	constant, dimensionless
A	cross-sectional area of the pipe, m^2
A_{annulus}	area of the air annulus, m^2
A_G	the cross-sectional area of the annulus gas jet, m^2
A_{ss}	the spray jet cross-sectional area, m^2
ALR	ratio of mass flow rate of air to liquid ($\mathrm{ALR} = \dot{m}_{\mathrm{air}}/\dot{m}_{\mathrm{liq}}$), dimensionless
B'	constant. dimensionless
B''	constant, dimensionless
Bo	Bond number, dimensionless
C_1	constant, dimensionless
C_p	heat capacity of constant pressure, J/(g K)
C_v	heat capacity of constant volume, J/(g K)
$d_{v0.1}$	the droplet diameter such that 10% of the total liquid volume is in droplets of smaller diameter, μm
$d_{v0.5}$	volume median diameter, μm
$d_{v0.9}$	the droplet diameter such that 90% of the total liquid volume is in droplets of smaller diameter, μm
$d_{v0.999}$	the droplet diameter such that 99.9% of the total liquid volume is in droplets of smaller diameter, μm
d_{32}	the Sauter mean droplet diameter, μm
d_d	mean droplet size, μm

d_{jet}	the diameter of the liquid jet stream, mm
d_{mmd}	mass median droplet diameter, μm
$d_{orifice}$	diameter of liquid orifice at liquid exit, m
$d_{gasslit}$	inside diameter of atomisation air gas slit, m
$d_{prefilm}$	diameter of the prefilmer section, m
G_a	mass flux of air at the nozzle outlet, kg/(m^2 s)
H	enthalpy, J/kg
K_{sheet}	the sheet-thickness parameter, m^2
L_c	the characteristic dimension of the nozzle, m or cm
L_{peri}	the wetted periphery between the air and liquid streams, m
L_{mix}	mixing length of liquid and gas after nozzle exit, m
$\dot{m}$	mass flow rate, g/s
$\dot{m}_{air}$	mass rate of atomisation air, g/s
$\dot{m}_{liq}$	mass rate of liquid, g/s
M	Mach number, dimensionless
M_{air}	the molecular weight of the gas, g/mol
Oh	Ohnesorge number, dimensionless
$Oh_{droplet}$	droplet Ohnesorge number, dimensionless
P	pressure, Pa
P_{inlet}	the absolute pressure at the nozzle inlet, Pa
P_{exit}	the absolute pressure at the nozzle exit, Pa
q	Rosin–Rammler parameter, dimensionless
$\dot{q}_{air}$	the volumetric flow rate of atomising air through the nozzle, m^3/s
$\dot{q}_{liq}$	the coating liquid volumetric flow rate through the nozzle, m^3/s
Q	fraction of the total volume contained in droplets of diameters less than d_d, dimensionless
R	the universal gas constant, J/(mol K)
$s_{gasslit}$	atomisation air gas-channel slit thickness,m
S	entropy, J/K
S_g	standard deviation, dimensionless
$t_{break\text{-}up}$	time for complete break-up into droplets, s
T	temperature, K
T_{inlet}	the inlet gas temperature, K
u	velocity, m/s
$u_{exhaust}$	exhaust gas velocity at the orifice, m/s
$u_{max\ pipe\ flow}$	maximum pipe flow velocity, m/s
u_{throat}	exhaust throat velocity, m/s
v_{air}	air velocity, m/s
v_{liq}	liquid velocity, m/s
v_{rel}	the difference between the nozzle atomising air velocity and the liquid velocity at the nozzle exit, m/s
v_{rel_sheet}	the relative velocity of the liquid sheet to the nozzle atomising air, m/s
v_{mr}	average or mixing rate velocity, m/s
V	specific volume, m^3/kg
$W_{air/liq}$	work carried out by the gas on unit mass of the liquid, J
We_{air}	air Weber number, dimensionless
We_{liq}	liquid Weber number, dimensionless
x	distance, m
X	Rosin–Rammler parameter, dimensionless

Greek letters

α	constant (a function of nozzle design), dimensionless
β	constant (a function of nozzle design), dimensionless
γ	ratio of heat capacities, dimensionless
γ_{liq}	liquid surface tension, kg/s^2
δ_{sheet}	liquid sheet thickness, μm
Δp_{air}	pressure drop in the gas through the nozzle, Pa
η_{air}	air viscosity, centipoises
η_{liq}	liquid viscosity.centipoises
λ_{opt}	optimum wave length, μm
λ	Wave length, μm
π	Pi, dimensionless
ρ_{air}	atomising air density, kg/m^3 or g/cm^3
ρ_{liq}	liquid density, kg/m^3 or g/cm^3
χ_{sheet}	liquid sheet coefficient, dimensionless
$\Psi_{air/liq}$	the power transferred by the gas to the liquid, W
Ψ_{air}	the power used to operate the nozzle, W

Acknowledgements

This project was performed in collaboration between CHEC Research Centre, Department of Chemical Engineering, Technical University of Denmark, and Novozymes A/S who also financially supported the project. Peter Dybdahl Hede is a member of the Novozymes Bioprocess Academy as well as the MP$_2$T Graduate School in Chemical Engineering at the Department of Chemical Engineering, Technical University of Denmark, funded by the Danish Research Council for Technology and Production Sciences, the European Union, the Nordic Energy Research, Dong Energy A/S, Vattenfall A.B., F.L. Smidth A/S, and Public Service Obligation funds from Energinet.dk and the Danish Energy Research programme.

The authors are grateful to the reviewers for an excellent review with many relevant suggestions and comments, significantly improving the quality of the manuscript.

References

Ayres, D., Caldas, M., Semião, V., da Graca Carvalho, M., 2001. Prediction of the droplet size and velocity joint distribution for sprays. Fuel 80, 383–394.
Barbosa, J.L., do Carmo, M.P., 1984. Stability of hypersurfaces with constant mean curvature. Mathematische Zeitschrift 185, 339–353.
Carvalho, I.S., Heitor, M.V., 1998. Liquid film break-up in a model of a prefilming airblast nozzle. Experiments in Fluids 24, 408–415.
Chin, J.S., Lefebvre, A.H., 1987. Some comments on the characterization of drop-size distributions in sprays. In: ICLASS-85.
Dewettinck, K., 1997. Fluidized bed coating in food technology: process and product quality. Ph.D. Thesis, University of Gent.
Dombrowski, N., Johns, W.R., 1963. The aerodynamic instability and disintegration of viscous liquid sheets. Chemical Engineering Science 18, 203–242.
Dombrowski, N., Hasson, D., Ward, D.E., 1960. Some aspects of liquid flow through fan spray nozzles. Chemical Engineering Science 12, 35–50.
El-Shanawany, M.S.M.R., Lefebvre, A.H., 1980. Airblast atomization: the effect of linear scale on mean drop size. Journal of Energy 4 (4), 184–189.
Florida College, 2007. College of Engineering, Florida A&M University and the Florida State University, March. Visit to the homepage ⟨http://www.eng.fsu.edu/⟩.
Fraser, R.P., Eisenklam, P., Dombrowski, N., Hasson, D., 1962. Drop formation from rapidly moving liquid sheets. A.I.Ch.E. Journal 8, 672–680.
Glaser, H.W., 1989. Das Zerstäuben von Suspensionen mit Ein- und Zweistoffdüsen. VDI Verlag, Düsseldorf.
Gretzinger, J., Marshall Jr., W.R., 1961. Characteristics of pneumatic atomisation. A.I.Ch.E. Journal 7 (2), 312–318.
Groom, S., Schaldach, G., Ulmer, M., Walzel, P., Berndt, H., 2004. Adaptation of a new pneumatic nebulizer for sample introduction in ICP spectrometry. Journal of Analytical Atomic Spectrometry 20, 169–175.
Guignon, B., Duquenoy, A., Dumoulin, E.D., 2002. Fluid bed encapsulation of particles: principles and practice. Drying Technology 20, 419–447.
Hartman, R.P.A., Brunner, D.J., Camelot, D.M.A., Marijnissen, J.C.M., Scarlett, B., 2000. Jet break-up in electrohydrodynamic atomization in the cone-jet mode. Journal of Aerosol Science 31 (1), 65–95.
Hede, P.D., Jensen, A.D., Bach, P., 2007a. Small-scale top-spray fluidised bed coating: granule impact strength, agglomeration tendency and coating layer morphology. Powder Technology 176, 156–167.
Hede, P.D., Jensen, A.D., Bach, P., 2007b. Top-spray fluidised bed coating: scale-up in terms of relative droplet size and drying force. Powder Technology 184 (3), 318–332.

Hede, P.D., Jensen, A.D., Bach, P., 2007c. Validation of the flux number as scaling parameter for top-spray fluid bed systems. Chemical Engineering Science 63 (3), 815–828.
Hozawa, M., Tsukada, T., Imaishi, N., Fujinawa, K., 1981. Journal of Chemical Engineering Japan 14 (5), 358–364.
Hund, J., 1994. Ssshh! Internal mix atomization—the finishing industry's best kept secret. Wood and Wood Products 1.
Juslin, L., Antikainen, O., Merkku, P., Yliruusi, J., 1995a. Droplet size measurement: I. Effect of three independent variables on droplet size distribution and spray angle from a pneumatic nozzle. International Journal of Pharmaceutics 123, 247–256.
Juslin, L., Antikainen, O., Merkku, P., Yliruusi, J., 1995b. Droplet size measurement: II. Effect of three independent variables on droplet size distribution from a pneumatic nozzle studied by multilinear stepwise regression analysis. International Journal of Pharmaceutics 123, 257–264.
Kim, K.Y., Marshall, W.R., 1971. Drop-size distributions from pneumatic atomisers. A.I.Ch.E. Journal 17 (3), 575–584.
Lefebvre, A.H., 1980. Airblast atomization. Progress in Energy and Combustion Science 6, 233–261.
Lefebvre, A.H., 1983. Gas Turbine Combustion. Hemisphere Publishing Corporation, Washington, DC.
Lefebvre, A.H., 1989a. Atomisation and Sprays. Hemisphere Publishing Corporation, Washington, DC.
Lefebvre, A.H., 1989b. Properties of sprays. Particle & Particle Systems Characterization 6, 176–186.
Lefebvre, A.H., 1996. Some recent developments in twin-fluid atomisation. Particle & Particle Systems Characterization 13, 205–216.
Lindblad, M.R., Schneider, J.M., 1965. Scientific Instrumentation 42, 635–658.
Lorenzetto, G.E., Lefebvre, A.H., 1977. Measurements of drop size on a plain jet airblast atomizer. AIAA Journal 14 (7), 1006–1010.
Masters, K., 1972. Spray Drying. Leonard Hill Books, International Textbook Company Limited, London.
McCuan, J., 1997. Retardation of PLATEAU-RAYLEIGH instability. A distinguishing characteristics among perfectly wetting fluids, arXiv:math.AP/9701214 v1.
Mulhem, B., Fritsching, U., Schulte, G., Bauckhage, B., 2003. Effect of solid particle characteristics on suspension atomization. Atomization and Sprays 133, 321–343.
Mulhem, B., Schulte, G., Fritsching, U., 2006. Solid-liquid separation in suspension atomisation. Chemical Engineering Science 61, 2582–2589.
Nguyen, D.A., Rhodes, M.J., 1998. Producing fine drops of water by twin-fluid atomisation. Powder Technology 99. 285–292.
Niro. Narrowspan ™ Atomization—Powder Production with Narrow PSD. GEA Niro Powder Technology, 2007.
Nukiyama, S., Tanasawa, Y., 1939. An experiment on atomisation of liquid—the effect of the properties of liquid on the size of drops. Transactions of the Society of Mechanical Engineers, Japan (JSME Journal) 18 (5), 68–75.
Nukiyama, S., Tanasawa, Y., 1940. An experiment on atomisation of liquid—the atomisation pattern of liquid by means of air stream. Transactions of the Society of Mechanical Engineers, Japan (JSME Journal) 22 (6), 7–15.
Park, B.K., Lee, J.S., Kilun, K.D., 1996. Comparative study of twin-fluid atomisation using sonic or supersonic gas jets. Atomization and Sprays 6, 285–304.
Rayleigh, L., 1879. On the instability of jets. In: Proceedings of London Mathematical Society, third ed., vol. 10(4), pp. 4–13.
Rhodes, M., 1998. Introduction to Particle Technology. Wiley, Chicester, England.
Rizk, N.K., Lefebvre, A.H., 1984. Spray characteristics of plain-jet airblast atomizers. Transactions of the ASME 106, 634–638.
Rizk, N.K., Lefebvre, A.H., 1985. Drop-size distribution characteristics of spill-return atomizers. AIAA Journal of Propulsion and Power 1, 16–22.
Rizkalla, A.A., Lefebvre, A.H., 1975. The influence of air and liquid properties on airblast atomisation. ASME Journal of Fluids Engineering 97 (3), 316–320.
Rosin, P., Rammler, E., 1933. The laws governing the fineness of powdered coal. Journal of the Institute of Fuel 31, 29–36.
Sakai, T., Kito, M., Saito, M., Kambe, T., 1978. In: Proceedings from International Conference on Liquid Atomization Spray Systems, p. 235.
Salman, A.D., Hounslow, M.J., Seville, J.P.K., 2007. Handbook of Powder Technology, Granulation. Elsevier Publishing, Amsterdam.
Schaafsma, S.H., 2000. Down-scaling of a fluidised bed agglomeration process. Ph.D. Thesis, University of Groningen.
Schaafsma, S.H., Vonk, P., Segers, P., Kossen, N.W.F., 1998. Description of agglomerate growth. Powder Technology 97, 183–190.
Schaafsma, S.H., Vonk, P., Kossen, N.W.F., 2000. Fluid bed agglomeration with a narrow droplet size distribution. International Journal of Pharmaceutics 193, 175–187.
Schæfer, T., Wørts, O., 1977a. Control of fluidized bed granulation. I. Effects of spray angle, nozzle height and starting materials on granule size and size distribution. Archives of Pharmaceutical and Chemical Science 51–60 (5th edition).
Schæfer, T., Wørts, O., 1977b. Control of fluidized bed granulation. II. Estimation of droplet size of atomised binder solutions. Archives of Pharmaceutical and Chemical Science 178–193 (5th edition).
Schæfer, T., Wørts, O., 1978a. Control of fluidized bed granulation. III. Effects of inlet air temperature and liquid flow rate on granule size and size distribution. Control of moisture content of granules in the drying phase. Archives of Pharmaceutical and Chemical Science 1–13 (6th edition).
Schæfer, T., Wørts, O., 1978b. Control of fluidized bed granulation. IV. Effects of binder solution and atomisation on granule size and size distribution. Archives of Pharmaceutical and Chemical Science 14–25 (6th edition).
Schæfer, T., Wørts, O., 1978c. Control of fluidized bed granulation. V. Factors affecting granule growth. Archives of Pharmaceutical and Chemical Science 69–82 (6th edition).
Schick, R.J., 2006. Spray Technology Reference Guide: Understanding Drop Size, Spray Analysis and Research Services. Spray Drying Systems Co.
Schlick, 2007. Series 940-943 two-substance nozzles. Technical Information 16/01.
Schütz, S., Breitling, M., Piesche, M., 2004. Atomization of suspensions with shear-thinning behavior by aerodynamic wave breakup. Chemical Engineering Technology 27 (6), 619–624.
Shirley, C.T., Truc, V., 1987. Atomization of coal-water slurry using twin-fluid jet atomizer. Fuel 66, 1596–1602.
Simmons, H.C., 1976. The correlation of drop-size distributions in fuel nozzle sprays, Part 1: the drop-size/volume-fraction distribution. ASME Paper 75.
Smith, J.M., Van Ness, H.C., 1975. Introduction to Chemical Engineering Thermodynamics. McGraw-Hill Book Co., New York.
Smith, P.G., Nienow, A.W., 1982. On atomising a liquid into a gas fluidised bed. Chemical Engineering Science 37 (6), 950–954.
Smith, P.G., Nienow, A.W., 1983. Particle growth mechanisms in fluidised bed granulation—I. The effect of process variables. Chemical Engineering Science 38 (8), 1223–1231.
Smith, J.M., Van Ness, H.C., Abbott, M.M., 2001. Introduction to Chemical Engineering Thermodynamics. McGraw-Hill Book Co., Singapore.
Spray Drying Systems Co., 2000. Engineer's guide to spray drying technology.
Teunou, E., Poncelet, D., 2002. Batch and continuous fluid bed coating—review and state of the art. Journal of Food Engineering 53, 325–340.
Waldie, B., 1991. Growth mechanism and the dependence of granule size on drop size in fluidized-bed granulation. Chemical Engineering Science 46, 2781–2785.
Walzel, P., 1993. Liquid atomisation. International Chemical Engineering 33 (1), 46–60.
Walzel, P., Broll, P., 2000. Pneumatic nozzle for small size scales. In: Eighth International Conference on Liquid Atomization and Spray Systems, Pasadena, July 2000.
Walzel, P., Klaumünzer, U., 1981. Flow regimes on horizontal porous plates. German Chemical Engineering 4, 154–160.
Wittig, S., Sattelmayer, T., Aigner, M., Sakbani, K., 1985. Strömungsvorgänge und Tropfenbildungsmechanismen in Luftgestützten Zerstäubungsdüsen. Brennstoff-Wärme-Kraft 37 (10), 380–387.
Yliruusi, J., Merkku, P., Antikainen, O., Kristoffersson, E., 1992. Effect of atomizing air pressure and surfactant concentration on the droplet size in a fluid bed granulator. Pharmaceutical Research 9, S-124.

Ind. Eng. Chem. Res. **XXXX,** *xxx,* 000 A

Fluidized-Bed Coating with Sodium Sulfate and PVA−TiO_2, 1. Review and Agglomeration Regime Maps

Peter Dybdahl Hede,[†,‡] Poul Bach,[‡] and Anker D. Jensen*[,†]

CHEC Research Center, Department of Chemical and Biochemical Engineering, Technical University of Denmark, Building 229, DK-2800 Kgs. Lyngby, Denmark, and Solid Products Development, Novozymes A/S, Smørmosevej 11, DK-2880 Bagsværd, Denmark

This paper, and two associated papers [Hede, P. D.; Jensen, A. D.; Bach, P. *Ind. Eng. Chem. Res.* **2009**, *48*, XXXX and XXXX], address the fluid-bed coating of placebo enzyme granules (i.e., sodium sulfate cores, with a size range of 400−500 μm) using two types of coatings: sodium sulfate and PVA−TiO_2. The coating experiments were conducted in a medium-scale top-spray MP-1 fluid bed, and many rheological experiments were performed on the coating formulations to support the interpretation of the fluid-bed coating results. In this first part of the study, a thorough introduction to the inorganic salt and polymer film coating is provided, along with a presentation of the equipment and materials being used in this and the following papers. Results from agglomeration studies over a broad range of process conditions are presented, showing that the tendency toward agglomeration is always less for the salt coating process than for the polymer coating process, under similar process conditions. Based on the experimental results, an agglomeration regime map is suggested for each of the two types of coating solutions, based on values of the drying force and the coating solution spray rate.

1. Introduction

In the industrial production of granules in the enzyme, food, agricultural, and pharmaceutical industry, particles are commonly coated with one or several different layers in a fluidized bed. This paper, as well as others in this series of studies,[1,2] examines such particles.

A spray-coated granule is thereby typically structured in a series of concentric layers in an onion-like fashion.[3] Coating layers typically serve many functions, depending on the end-use of the granules. For enzyme-containing granules, the coating may contain the enzyme itself or may be used to protect the enzyme-containing core by improving the enzyme resistance to degradation or inactivation by components, such as oxygen or bleach components, from the surrounding detergent matrix, which are capable of oxidizing or otherwise inactivating the enzyme.[4] Furthermore, the coating layer may have controlled release properties upon introduction of the granule into an aqueous medium, or it may provide a barrier against ambient moisture, to enhance the storage stability of the enzyme and reduce the possibility of microbial growth within the granule.[5] The ability of a coating to serve as a barrier to protect the enzyme is thereby related to the permeability of the protective coating, primarily by water and H_2O_2. In addition, the coatings also keep the enzyme granules from generating dust when they are handled. This is important because enzymes are proteins that have the potential of inducing allergenic response when humans are exposed to aerosols of enzymatic active dust. The ability of a coating to prevent an enzyme granule from releasing dust is closely related to its mechanical properties of which attrition and impact strength are of primary importance.[6,7]

This paper presents a review of commercial fluid-bed coatings, focusing on coating materials and their function. Two categories are presented: inorganic salt coatings and polymer coatings. Furthermore, in the pursuit of explaining differences and similarities in processing and operations, fluid-bed experiments over a broad range of process conditions with two representative coating solutions (one from each category) are presented.

2. Review of Inorganic Salt and Polymer Fluid-Bed Coatings

The most common types of fluid-bed coating processes, with respect to enzyme granules, may be divided into two general categories: coatings with aqueous solutions of inorganic salts (with or without active ingredients) and coatings with aqueous suspensions (or solutions) of film-forming water-soluble polymers (with or without additional compounds). These types of coating processes have been treated in several industrial patents that have been filed by some of the large enzyme companies, such as Genencor International/Danisco,[5,8,9] Kao Corporation,[10] Novozymes,[4,11,12] Procter & Gamble,[13] and Henkel.[14] [A broad review of the types of fluid-bed equipment used industrially may be found in ref 70.] Schematic representations of typical commercial enzyme granules with both types of layers can be observed in Figures 1 and 2. Figure 1 shows the structure of a commercial Genencor Enzoguard granule. The core consists of a rounded sugar/starch particle with partially hydrolyzed

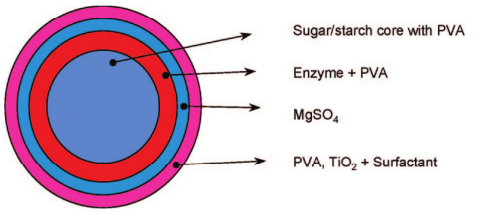

Figure 1. Schematic showing the structure of a commercial Genencor Enzoguard granule.[8]

* Author to whom correspondence should be addressed. Tel.: +45 4525 2841. Fax: +45 4588 2258. E-mail address: aj@kt.dtu.dk.
† CHEC Research Center, Department of Chemical and Biochemical Engineering, Technical University of Denmark.
‡ Solid Products Development, Novozymes A/S.

10.1021/ie800940e CCC: $40.75

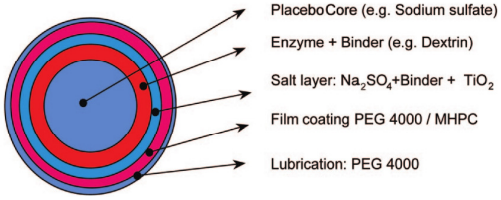

Figure 2. Schematic showing the structure of a commercial Novozymes granule.[4,12]

poly(vinyl alcohol) (PVA) as a thin outer layer. Atop that layer are three additional layers, where the inner layer consists of an enzyme mixed with fully hydrolyzed PVA, the middle layer is magnesium (or sodium) sulfate, and the outer layer consists of a mixture of partially hydrolyzed PVA, titanium dioxide, and a surfactant/lubricant/plasticizer. All layers are sprayed successively onto the core in a fluid bed.[8] Figure 2 shows the structure of a commercial Novozymes granule. The granulation process is based on a combination of mixer and fluid-bed technology, where the active granulate is build around an inert carrier/core, which is produced in a high-shear mixer. Enzyme and functional layers are added onto the core in successive steps. First, the enzyme is added by absorption of concentrate into the carrier/core in a high-shear mixer. Additional concentrate then is added by spraying in a fluid bed to attain the specified product activity. Next, the granule is coated in a fluid bed with a layer of sodium sulfate (optionally, binders and titanium dioxide are added to the salt layer). The granule is finally equipped with an outer film coating that consists of a mixture of methyl hydroxypropyl cellulose (MHPC) and poly(ethylene glycol) (PEG), for perfecting the dust control. An additional layer of PEG4000 may be added as a lubricant.[4,12]

Although the principles behind the coating process of inorganic salts and polymer solutions are the same, screening studies by Neidel[15] clearly show that the coating process of polymer solutions is far more difficult, in terms of process control. This was the general observation within a broad range of coating solution formulations that have been tested. It is not obvious what causes these differences in processing, and it is thereby not obvious which process or formulation conditions could be kept similar or what conditions should be chosen differently and to what extent. Phenomena such as agglomeration during coating and the loss of coating liquid due to spray drying loss are notoriously far more prominent with polymer coating than with the inorganic salt coating process.[15] In addition, results reported by Chu and co-workers[16,17] indicate that different colloidal phenomena in the polymer solutions also play a role in the coating process. Therefore, finding optimum coating conditions where the coating process can be conducted in a reasonable time without agglomeration or spray drying loss of the coating feed, for any of the two coating processes, is not an easy task. Thus far, only limited fundamental research in the open literature has been reported in this field, because previous work was done mostly in industry and often is protected in patents. It is the objective of this paper to highlight and suggest explanations for the similarities and differences in coating with inorganic salt solutions and polymer solutions in top-spray fluid beds. First, the different coating ingredients are discussed, together with prior coating experiences.

2.1. Salt Coatings. Salt coatings are typically added together with the enzyme or preferably between the enzyme core/layer and an outer polymer coating layer. The salt layer provides a protective layer toward bleach components when the enzyme granule is stored in a bleach-containing detergent under elevated temperatures and humidity. In one of the first Genencor patents by Arnold et al.,[5] a chlorine scavenger layer such as ammonium sulfate was preferred, because the ammonium (NH_4^+) ion is able to react with washwater chlorine, thereby protecting the enzyme by actively neutralizing oxidants. However, because of the possible smell of ammonia, recent enzyme granules typically use low-cost compounds as magnesium sulfate or sodium sulfate, although they do not function as chlorine scavengers. However, these compounds do resemble similar water and H_2O_2 barrier properties and, furthermore, help to reduce enzymatic dust problems when the granules are used.[4]

In recent publications by Hede and co-workers,[18−21] fluid-bed coating processes with sodium salt solutions were treated in detail in the context of fundamentals and scale-up issues. Results are promising regarding control of the process, at the same time, being able to produce salt-coated granules with high mechanical strength and a low tendency for agglomeration during processing. Results indicate that nozzle conditions especially play an important role in the outcome of the process, and that the temperature and humidity conditions inside the bed during coating have primary importance regarding agglomeration. Hede et al.[19] suggested that the bed temperature and bed humidity during steady-state coating conditions were combined into a so-called drying force parameter, according to eq 1, indicating the moisture evaporation rate from the coated particles:

$$\text{drying force} = P_{\text{sat}}\left(1 - \frac{\text{Bed rH\%}}{\text{100\% relative humidity}}\right) \quad (1)$$

where P_{sat} is the saturated pressure at the dry bulb temperature and Bed rH% denotes the relative humidity of the fluid bed. The advantages of the drying force parameter in a scale-up context was emphasized in the work by Hede et al.[19] This paper further argues in favor of fluid-bed process operation, in terms of fixed nozzle conditions and fixed fluidization velocity throughout the coating process, with the conditions inside the fluidization chamber being adjusted only in terms of the inlet fluidization air temperature.

2.2. Polymer Film Coatings. A polymer layer is typically added as the final outer layer to provide simultaneous benefits of low dust, as well as good color appearance and moisture barrier properties and controlled release of the enzyme into washing machines. The film coating of granules with water-insoluble substances is usually based on organic solutions of the film-forming material or on aqueous colloidal dispersions of polymer particles.[22] Typically, however, water-soluble polymers are used and numerous polymers are used commercially for enzyme granule coatings, including, most often, PVA, PEG, methyl cellulose (MC), and methyl hydroxypropyl cellulose (MHPC or HMPC). With only a few exceptions, a range of other components are typically added to the aqueous polymer solution, including plasticizers, pigments (as antiagglomerating agents), and lubricants.[3,23]

2.2.1. Poly(vinyl alcohol) (PVA). PVA is used in a variety of pharmaceutical and drug delivery applications, such as active-component jellies, protein-based pharmaceuticals, and sustained-release oral dosage forms.[23] Recently, PVA has been used for many pharmaceutical formulations, because of its low cost and good barrier and tensile properties. As a component of tablet coating formulations intended for products such as, for example, food supplement tablets, PVA protects the active ingredients from moisture, oxygen, and other environmental components, while simultaneously masking their taste and odor. It allows for easy handling of finished products and facilitates ingestion

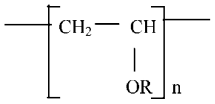

Figure 3. Chemical repeat unit structure of partially hydrolyzed poly(vinyl alcohol) (PVA).[24] (Here, R = H or $COCH_3$.)

and swallowing. The viscosity of PVA allows for the application of the polymer in tablets, capsules, and other forms to which film coatings are typically applied at relatively high solids contents.[6,23] A repeat unit structure of PVA can be observed in Figure 3.

In the context of commercial enzyme granules, PVA is used for outer as well as inner coatings of the enzyme granules, where PVA serves as a barrier to protect the enzyme from exposure to harsh chemicals that may be present in the final product, in which the enzyme is used. PVA has been proven to be a very effective coating for detergent enzyme granules. PVA is particularly useful because it simultaneously provides a coating with reduced permeability to moisture and oxidants, a strong and attrition-resistant coating, and a coating that is readily soluble in water and detergent solutions in both cold and hot water. It is also sufficiently water-soluble to be prepared in aqueous coating solutions and sprayed onto enzyme-containing granules at a reasonable rate.[6,8] It is soluble in water and typically a 5 w/w% PVA solution exhibits a pH in the range of 5.0−6.5. PVA has a melting point of 180−190 °C, and, furthermore, the polymer has the advantage of being nontoxic, hydrophilic, and relatively easy to handle.[24] It is an odorless and tasteless, translucent, white or cream-colored compound that typically is manufactured in granular form.[25]

PVA is commercially available in a wide range of molecular weights and varying degree of hydrolysis from the polymer acetate precursor, making it possible to control the relative solubility and physical properties of the polymer coating, which again can be optimized to balance factors such as the ease of coating, dissolution rate of the granule, attrition resistance, and permeability of the granule to moisture and oxidants.[6,24] Suitable PVA types for an outer enzyme granule coating layers include typically partially to fully hydrolyzed PVA having a low viscosity in the range of 5−15 cP in a 4 w/w% aqueous solution.[5]

Additional advantages of PVA include the facts that (i) it can readily be plasticized with water, glycerol, PEG, and other polyhydric compounds, and (ii) it is compatible with pigments and fillers such as titanium dioxide, talc, and carbonates, among others.[24] For coating purposes, PVA is often dissolved in aqueous solutions, together with inert filler particles such as TiO_2, to help reduce the tendency of agglomeration, as well as to make the granules appear white. PVA solutions also may be colored with different types of color dyes.[26]

2.2.2. Tackiness and the Work of Adhesion of Polymer Solutions. Coating formulations that consist of water-soluble polymeric film-formers such as PVA are known to be inherently tacky (sticky) in nature and spontaneously adhere to many materials on contact, readily forming adhesive joints with no need for primary chemical bonding.[27] The tack problem is especially troublesome in the coating of small particles such as granules, whereby the tendency to agglomerate is known to increase significantly with stickiness.[28] Most film-forming polymers become tacky during their drying phase, which is believed to be the major cause of undesired particle agglomeration during the fluid-bed coating process.[29] Although the liquid spray rate, bed temperature, and moisture have been identified as critical parameters in the prevention of agglomeration,[18,30] sometimes it is not possible to use these operating parameters alone in controlling the extent of agglomeration. For coating application, a low tackiness is generally desirable. A polymer formulation with a low tackiness generally shows a lesser tendency for film-coating defects and results in an easier coating process and reduced processing time.[31]

The mechanisms behind the stickiness of polymers in solution are not yet fully understood. It is believed that mainly viscoelastic effects and fibrillation of the adhesive are responsible for a large energy dissipation and strong adhesion and tackiness.[32−34] Chemically, the stickiness of PVA is believed to be closely related to the conformation of the polymer chains. While being in solution, the polymer chains normally do not touch each other very often and slide over each other quite easily. Thus, PVA solutions are quite flexible and able to get into the microscopic cracks and crevices in the core particle surface. Upon solvent evaporation, the polymer chains will get closer, and, depending on the length of the chains, they will hook in the surface cracks and adhere well to the surface in mechanical interlocking mechanisms.[35] The result is a sticky surface ready for agglomeration. This theory is supported by various experiments, indicating that there is a strong connection between tack and the contact with rough surfaces. In the presence of asperities on the solid surface, the actual area of contact is always less than the nominal area. This is because the polymer solution sinks into the surface valleys, making contact possible mainly between the asperity heights. The results reported by Hui et al.[36] support previous findings by Creton and Leibler[32] that this true area is dependent on both the applied load and the time of contact between the adhesive and the adherent. With regard to other pressure-sensitive adhesives (an adhesive that retains tack after release of the solvent, so that it can be bonded by simple hand pressure), PVA needs a certain pressure to cohere, meaning that a certain force is necessary for two objects covered with PVA to stick together. Clamping is believed to be necessary for the PVA chains to become intertwined with each other. After the PVA chains have been forced to coil into each other, they will leave a strong network upon solvent evaporation. This network is believed to cause the good cohesion properties of PVA and may be part of the explanation for the agglomeration tendency of wet PVA-coated particles.[37]

In the literature, a distinction is often made between adhesion studies and tackiness studies, although these properties, indeed, are related. Adhesion is the work required to separate a unit-cross-sectional area of two materials and it is governed by mechanical interlocking, wetting, and electrostatic and chemical forces.[35] From a mechanical point of view, the strength of an adhesive joint can be characterized by the work of detachment per unit area of interface A_{con}, which is given by the following equation:[38]

$$W_{adhesion} = \frac{1}{A_{con}} \int F v_{sep} \, dt \qquad (2)$$

where v_{sep} is the rate of separation and F is the tensile force during the unbonding process. This fracture energy per unit area of interface or intrinsic adhesive failure energy is a measure for the adhesive bond energy.[38] From a theoretical point of view, the work of adhesion is interesting, because it can be related to well-known physical and chemical parameters such as contact angle, surface tensions, and the spreading coefficient, with the latter being the difference between the work of adhesion and the work of cohesion.[39] Furthermore, the work of adhesion may

be combined with solubility theory such as the Hansen or Hildebrand solubility parameters, giving a theoretical possibility for a priori prediction of the work of adhesion.[40] Considerable research has been conducted in an attempt to correlate the physical properties of polymer binder and coating solutions with subsequent granule and tablet properties, but often with limited success.[40−46] Experimental work has been somewhat inconclusive in demonstrating any quantitative relationship between the surface energetics of the coating solution and the solid substrate and the resulting adhesive strength. One reason for this, which is a general problem faced in studying film adhesion, is the difficulty in accounting for the effect of bulk film properties on the adhesion measurement. Further problems often occur when static surface energetics are compared to the dynamic interactions that are occurring during granulation. Correlation between measured values for the work of adhesion with those predicted from theory requires optimum or fully developed interfacial contact between the adhesive and the adherent, which almost never occurs during granulation. Measured adhesion energies are often observed to be several orders of magnitude larger than the predicted thermodynamic work of adhesion.[32] In that respect, the work of adhesion theory must be regarded as less interesting for dynamic particle processes such as the fluid-bed coating process, as the interface interactions here are so fast that dynamics and possible imperfect interfacial contact also must be taken into account. More on polymer adhesion and measurement techniques for adhesion may be found in the thorough review by Michalski and co-workers.[47,48]

Tack or tackiness is the main property of pressure-sensitive adhesives and is defined as the ability of an adhesive to develop interactions under short contact time with a substrate under light pressure and during short contact time. Contrary to the work of adhesion, tack is not a material parameter that can be theoretically related to fundamental physical/chemical parameters. Because tack is evaluated by the maximum energy (stress) required to propagate an interfacial fracture, it is strongly dependent on the interfacial adhesion strength between the adhesive and adherent, but also on the energy dissipated in the polymer during separation, through viscoelastic losses, fibrillation phenomena, etc.[34,49] Both viscoelasticity and the wetting of the adherent by the adhesive are particularly important during the bond formation,[35] and tack is generally observed to be dependent on surface roughness and increase with contact time, contact force, and separation rate, as it has been demonstrated in the results by Zosel[38] and Hui et al.[36] Tack is associated with the glass transition of the adhesive and is related to the corresponding compliance just above the glass-transition temperature (T_g) range, which itself is determined by the entanglement network of the polymer.[50,51] The T_g parameter is the temperature below which the physical properties of amorphous materials, such as polymers, vary in a manner similar to those of a solid phase (glassy state), and above which amorphous materials behave like liquids (rubbery state). Above T_g, the secondary, noncovalent bonds between the polymer chains become weak in comparison to thermal motion and the polymer becomes rubbery and capable of elastic or plastic deformation without fracture.[52]

The fact that tackiness cannot be unambiguously related to well-known physical parameters means that many other types of equipment for the measurement of tackiness has been developed, as reviewed by Christensen[53] and Gay.[54] These methods of expressing tack are useful in many practical cases, but the physical meaning of these values is not necessarily clear. The values determined by any tack tester are relative values under fixed conditions and do not necessarily compare with values determined under different conditions with other measurement techniques. The most popular method is generally the "probe test", as the current texture analyzer setup, in which the butt end of a cylindrical probe is brought into contact with the liquid sample at a specified load and time and then is removed at a specific rate. Several detailed stickiness studies have used this method previously.[38,55] Probe tack tests for coating solutions have been reported by Chopra and Tawashi[56−58] and Wan and Lai.[28,29] The probe tack test provides two measures of tack: the work spent in debonding the probe from the adhesive and the maximum tensile force achieved during the debonding step. Usually, only the last maximum tensile force is considered as a measure of tack, although this $F_{max(tack)}$ parameter is qualitatively different in nature from other measures of tack, because it cannot be expressed as an integral of force or tension over time, distance, or strain. It is unclear how $F_{max(tack)}$ is dependent on the rheological response of the adhesive during debonding, but it certainly is not as strongly influenced by the ability of the adhesive to dissipate energy during the debonding step as the various other measures of tack. Thus, $F_{max(tack)}$ may be a better measure of the quality of the bond between the adhesive and the substrate in a fluid bed with fast interface interactions than any other commonly employed measures of tack.[53] Therefore, the "probe test" with the measurement of $F_{max(tack)}$ is the test principle, which is selected to simulate the stickiness of the coating solutions in the present paper. A thorough review of mechanisms and test methods for stickiness determination may be found in Adhikari et al.[35]

2.2.3. Plasticizers. Plasticizers are usually high-boiling organic solvents that are used to improve the flexibility of otherwise hard or brittle polymers. They are typically added to aqueous colloidal polymer dispersions, to reduce the minimum film formation temperature.[31] The effects of plasticizers on mechanical properties and permeability of polymers are well-known. Plasticizers generally cause a reduction in the cohesive intermolecular forces along the polymer chains, resulting in various changes in the polymer properties, such as a reduction in tensile strength, while the elongation and flexibility are increased. Furthermore, T_g typically is reduced significantly by the addition of plasticizer.[23] Small molecules of plasticizer embed themselves between the polymer chains, increasing the spacing and free volume and allowing them to move past each other, even at lower temperatures. The decrease in the T_g value of a polymeric film, as the plasticizer concentration increases, is a common measure of the plasticizer effectiveness. The degree of plasticization of the polymer is dependent, to a large extent, on the amount of plasticizer, with respect to the polymer, and the interaction between the plasticizer and the polymer. For a plasticizer to be effective, it must be able to diffuse into and interact with the polymer and have minimal or no tendency for migration or exudation from the polymer.[23]

On the negative side of adding plasticizers to a polymer solution, the water permeability typically is increased. These effects are due to the interaction of the plasticizer with the polymer molecules. The interactions decrease the intermolecular forces along the polymer chains, reducing internal hydrogen bonding while increasing intermolecular spacing. Furthermore, the addition of plasticizers to reduce the minimum film formation temperature is known to increase the stickiness of the coating solution, because of softening of the polymer.[31]

Plasticizers do not necessarily need to be soluble in the solvent used for dissolving the polymer. For plasticizers that are soluble in the solvent phase, these can be added directly to the mixture

or may be dissolved first in the solvent, prior to the addition of the polymer. Otherwise, a proper suspension is required.[23] Examples of commonly used plasticizers are polyols such as glycerol, propylene glycol, PEG, urea, triethyl citrate, or dibutyl or dimethyl phthalate.[23]

2.2.4. Lubricants. The term "lubricants" is usually understood to identify any nonaqueous compound, or mixture of compounds, that forms a liquid at 25 °C and 1 bar, reduces the particle surface friction, lubricates the surface of the granule, decreases static electricity, and/or reduces the friability of the granules.[8] Lubricants are thereby added to the coating solution to reduce the relative friction coefficient between the coated granules, thereby functioning at the outer granule surface at the particle level, contrary to the plasticizers, which work at the intermolecular level. Such thin layers of liquid on each individual granule reduce the frictional forces that might otherwise cause the granules to break. Lubricants can also play a related role in improving the coating process by reducing the stickiness of the coating layer, thus serving as an antiagglomerating agent, although the fundamental understanding of the mechanisms behind this effect is not yet fully understood.[36] Some plasticizers, such as some liquid alcohols of alkenes or alkenes with a carbon atom chain length in the range of 9−15, also have particle-level lubricating effects other than being a plasticizer and surfactant; however, generally, the preferred lubricants are different from the preferred plasticizers and surfactants. Suggested lubricating agents for commercial use include preferably fatty acids, plant oils, animal oils, and minerals oils, as well as silicone oils. However, other compounds or mixtures forming low-viscosity nonaqueous liquids at 25 °C also may be used, in principle.[12] Preferably, the lubricant is also a surfactant, reducing the surface tension of the coating solution and hereby improving the coating solution wetting of the core particles.

One advantage of using lubricants that have a low viscosity is that they are considerably easier to apply as a thin layer in small amounts on a granule surface, and that a homogeneous distribution of the small amounts of lubricant on the entire granule surface is facilitated by a low viscosity. When using lubricants that have a relative high viscosity, the lubricant has a tendency to adhere inhomogenously to the granule surface in the form of sticky lumps. Hence, such types are not typically used for coating purposes, because of the increased risk of particle agglomeration. Commercial lubricants such as Neodol 23-6.5 and Softanol 50 have viscosities in the range of 20−40 mPa s at 25 °C.[8,12]

2.2.5. Pigments. Insoluble ingredients may be included in the coating formulation for a variety of reasons. Sometimes, pigments are simply used as a filler, to reduce the percentage of the amount of other more costly components in the film composition.[26] Another important application is to use pigments that help reduce the agglomeration or stickiness of coated particles during processing. Following the principles described in section 2.2.2, the filler particles act as surface asperities and therefore help to reduce that actual contact area, reducing the chance of permanent bonding. Suitable antiagglomeration agents include fine insoluble materials such as talc, TiO_2, clays, amorphous silica, magnesium stearate, and kaolin. Generally, the antiagglomerating agent should be inert with respect to the enzyme and preferably not affect the granule properties in a negative manner. Surface and morphology properties, including the hydrophilicity of insoluble filler particles, are known to be important factors that contribute to the properties of the final polymer film. Similarly, the concentration of pigment material has a strong influence on the final mechanical and barrier properties of the film.[23] Application of insoluble materials in the film coating composition may not be used uncritically, because adding pigments to a polymer film coating composition typically decreases the tensile strength, meaning that a weaker film is obtained as the amount of pigments in the film coating increases.[26]

Pigments also act as coloring agents. In the sense of appearance for the granule end-users, it is often desired to produce granules with homogeneous color. Often, white is the preferred color and such pigments are typically finely divided whiteners such as titanium dioxide (TiO_2) or calcium carbonate. Preferably, such pigments are low-residue pigments upon dissolution.[5,59] TiO_2 is preferred in commercial enzyme granules, because of its brightness and very high refractive index. Furthermore, TiO_2 particles added in a PVA solution have the advantage of producing a film with high gloss, good light diffusion, and uniform dimensions.[17] TiO_2 is an inexpensive, nontoxic, all-use white pigment that is well-known from food and cosmetic products.

2.2.6. Rheology and Colloidal Phenomena in the PVA/TiO_2 System. Contrary to an inorganic salt solution, a system consisting of polymer and dispersed particles, such as the PVA/TiO_2 solution, constitutes a colloidal system in which the TiO_2 particles are dispersed among the PVA chains in the aqueous solvent. The interactions between these species could possibly have an influence on the observed agglomeration tendencies. However, such interactions are complex, and the behavior of suspensions in the presence of polymers has been studied for many years, because of the numerous applications of the processes occurring in such systems. Adding a polymer to a suspension to control colloidal dispersion has been the subject of extensive research, because of its importance in industrial applications.[17] From these studies, valuable information about the PVA/TiO_2 systems may be obtained.

Several authors have studied the rheological behavior of suspensions of inorganic particles in polymer solutions. Suspensions such as the PVA/TiO_2 generally behave as Newtonian liquids at low particle volume fractions, but become non-Newtonian at high particle concentrations, exhibiting shear thinning/shear thickening, time dependency, yield stress, etc.[60,61] Changing the suspension pH affects the particle surface charges and, hence, the rheological behavior. Particles in suspension experience various interparticle forces, and the stability of a uniformly dispersed suspension is determined by the relative magnitude of various interparticle forces such as Brownian, van der Waals, electrostatic, and hydrodynamic forces.[62] Particles have a tendency to aggregate when the van der Waal force of attraction is larger than the electrostatic and/or repulsive force, and the suspension is thus not stable. On the other hand, a well-dispersed suspension can be obtained when the repulsive force is greater than the attractive force. Suspensions generally exhibit shear-thinning characteristics and sometimes yield stress, depending on the particle concentration near the isoelectric point. Newtonian behavior prevails when pH is remote from the isoelectric point.[17]

The surface of uncoated TiO_2 particles has hydroxyl groups that, at high pH, can ionize to give O^- groups and at low pH protonate to give OH_2^+ groups. The reactions of the amphoteric surface are given by the following reaction scheme:[17,52]

$$\text{Surface TiOH}_2^+ \xleftarrow{H_3O^+} \text{Surface TiOH} \xrightarrow{OH^-} \text{Surface TiO}^- + H_2O$$

Hence, the TiO_2 surface not only shows a variation in the magnitude of the surface charge with pH but also a variation in

the sign. At a certain pH value, the charge can be reduced to zero, and the pH at which this occurs is termed the isoelectric point.[52] For suspensions that contain polymer, the phenomenon of polymer adsorption on particle surfaces in suspension has been theoretically verified and widely used for the creation of stable suspensions. When PVA is adsorbed on the surfaces of TiO_2, it generates a steric stabilization repulsive force, which aids the stabilization of the suspension system. The active sites on the particle surface, at which the polymer chains are attached, are known as attachment points. According to the aforementioned reaction scheme, increasing the pH results in a decrease of $TiOH_2^+$ and an increase of TiO^-, whereas TiOH has a tendency to increase initially and then decrease. The adsorption of PVA on TiO_2 is primarily due to hydrogen bonding, and the amount of PVA adsorbed on the TiO_2 surfaces increases significantly as the pH increases. For 15 w/w% TiO_2 in 2.5 w/w% PVA suspensions, Chu et al.[17] determined that the adsorption increased from 0.024 g PVA/g TiO_2 to 0.080 g PVA/g TiO_2 as the suspension pH increased from pH 4 to pH 10. The increased adsorption was suggested by Chu et al.[17] to be due to the differences in polymer chain conformations under different solvent environments causing the adsorbed macromolecules to form network structures on the particles surface.

To understand the mechanism of polymer adsorption on solid particle surfaces, it is important to consider the role of the functional groups present in the polymer. The main functional group in PVA is the hydroxyl group; however, because of the presence of a small residual of nonhydrolyzed acetate groups after polymerization, the adsorption of PVA on the TiO_2 surface is greatly influenced by the acetate groups. Because the affinity of the acetate group with TiO_2 is greater than that of the hydroxyl group, more segments of PVA chains will be attached to the particle surfaces as the degree of hydrolyzation in the PVA decreases, resulting in a flatter conformation. In contrast, PVA with a higher degree of hydrolysis contains less acetate groups, and the adsorbed segments form loops and tails arranged perpendicularly on the particle surface. This allows more TiO_2 surface area available for polymer adsorption, meaning that, in all, more PVA is adsorbed on TiO_2 surfaces as the degree of hydrolysis increases.[17,63]

The change in the coating solution characteristics with a change in pH goes beyond the effect in viscosity; the surface tension also is affected. As the pH changes from acidic to basic, an increasing number of PVA macromolecules are adsorbed on the TiO_2 surfaces, resulting in a higher surface tension. This has been experimentally verified by Chu et al.[17] Because of the stronger steric repulsive forces, the dispersion is more uniform and able to withstand higher stress fields encountered during, e.g., atomization. However, with time, sedimentation occurred at high pH in the PVA/TiO_2 solutions tested by Chu et al.[17] Chu et al.[17] measured an isoelectric point of pH 9.2 for a 15 w/w% TiO_2−2.5 w/w% PVA suspension (compared to an isoelectric point of 3.5 for pure TiO_2, which was reported by Goodwin[52]) and observed how the suspended particles started to agglomerate when the pH approached the neighborhood of the isoelectric point. Although the amount of PVA adsorbed on the TiO_2 surfaces is relatively large at pH ~10, the concentration of TiO_2 in the continuous phase is actually less than that at lower pH, because of the sedimentation of flocs. Generally, Chu et al.[17] found that dilute PVA/TiO_2 suspensions at pH close to the isoelectric point were not ideal for coating purposes. Chu et al.[17] found that the surface tension increased as the degree of hydrolysis decreased but decreased as the molecular weight of PVA increased. At the same time, the amount of PVA adsorbed on the TiO_2 surface increases as the degree of hydrolysis and molecular weight each increase.

Chibowski[64] has studied the kinetics of the PVA adsorption on TiO_2 particles at different pH values for 0.05 w/w% PVA solutions. He observed that the adsorption of PVA on the TiO_2 particles is fast, irrespective of the pH value of the solution. At pH 10, the time necessary for the establishment of the equilibrium state is longer than that at pH 4, because of the difference in adsorption density. The adsorption density of PVA (expressed in units of g/m^2 TiO_2 surface area) increases slightly when the pH value of the suspension increases, because of the change of surface properties of TiO_2 and the change of hydration of the surface groups, as presented earlier. However, Chibowski and Szcypa[65] and Chibowski[64] observed that, generally, the rate of PVA adsorption on TiO_2 is not affected considerably by the surface charge of TiO_2. The electrostatic interactions are thereby concluded to be unimportant in the mechanism of polymer adsorption on TiO_2 particles.

The mechanism of adsorption of PVA on inorganic particles has been further investigated by Killmann et al.[66] Their results clearly indicated that the amount of adsorbed PVA is strongly dependent on the molecular weight and the number of acetate groups of PVA, resulting in different adsorption layer thickness. The adsorption force was observed to increase as the degree of hydrolysis of PVA increases, in accordance with Chu et al.[17] and Chibowski.[64] The presence of the hydrophilic acetate groups also affect the conformation of polymer chains adsorbed on the particle surface.[66] The adsorption mechanisms of PVA on different types of particles are also different. For example, the amount of PVA adsorbed on TiO_2 particles increases with the suspension pH, because the thickness of the double layer surrounding the TiO_2 particle is determined mainly by the molecular weight and the number of acetate groups of PVA. In contrast, the affinity of PVA and SiO_2 particles is strong at low pH but weak at high pH. That is, the quantity of PVA adsorbed on the silica surface decreases as the pH increases.[67] Because the adsorption of nonionic polymers such as PVA occurs because of hydrogen bonding with the silanol group on the silica surface, the adsorption is favorable at low pH. Several other papers also have reported the importance of pH on the adsorption of nonionic polymers on metallic oxide particles as reviewed by Chu et al.[17] Most of the studies reported have focused on the adsorption mechanisms, but very little research has been done on the effect of the surface tension of the suspension.

Although there is a general agreement that much of the behavior of PVA/TiO_2 suspensions is due to the adsorption of PVA on the surface of the TiO_2 particles, there is no general theory describing the adsorption of macromolecular compounds from the electrolyte solutions. The studies of the effect of polymers on colloid stability show that the flocculation and stabilization processes are dependent on the amount of polymer adsorbed.[17] The other factors affecting the colloid system behavior are the pH value of the solution, the surface properties of the TiO_2 solid particles, the type of PVA, and the ionic composition of the liquid phase—that is, the presence of foreign ionic species. All of the aforementioned factors affect the magnitude of polymer adsorption and the polymer configuration on the solid TiO_2 particle surface. The effect of pH is particularly great in the case of polyelectrolytes. Because the ionization of surface groups is dependent on pH, the shape of the polymer particles in the solution and on the surface may change considerably with pH.[64]

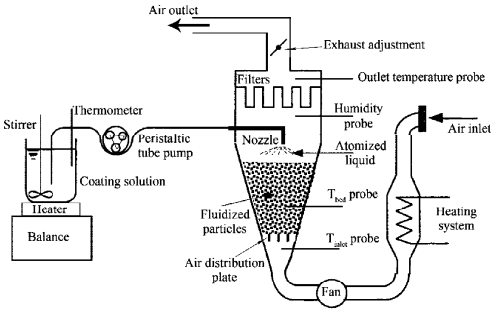

Figure 4. Formal sketch of the general top-spray setup used in the present study.[30]

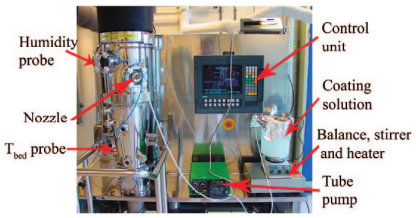

Figure 5. Picture of the MP-1 setup.

Despite the numerous studies on the adsorption and rheological behavior of adding PVA in inorganic suspensions, very little information is available on the coating behavior of these polymer suspensions. Studies by Chu et al.[17] indicated that the coating window is enlarged by the addition of inorganic particles such as TiO_2 and SiO_2 in PVA solutions, which is consistent with the patent by Arnold et al.[5]

3. Equipment, Methods, and Materials

3.1. Fluid-Bed Equipment. All fluid-bed coating experiments were performed on a standard Niro-Aeromatic Multiprocessor (type MP-1), which is a single-nozzle pilot-scale batch top-spray fluidized bed. It had a stainless steel fluidizing chamber with a capcity of 16 L, which allowed a particle bed load of 3000 g to be processed. In all experiments, a fluidization velocity of 400 Nm^3/h was used and fixed throughout each experiment. A sketch of the fluidized-bed system setup is shown in Figure 4, and a picture of the MP-1 setup is given in Figure 5. In this setup, the coating liquid feed was, in each case, led from an external heated reservoir, which could be maintained at a constant temperature, to the nozzle through an adjustable peristaltic tube pump. Furthermore, it was possible to measure the bed temperature between the bottom air distribution plate and the nozzle outlet. A humidity measurement apparatus (Testo 645 Thermohygrometer) was inserted 28 cm above the nozzle outlet and 14 cm from the wall, which allowed the relative humidity in the fluidization chamber to be measured at a location where the humidity measurements were not affected directly by the nozzle outlet. The back-flush option in the MP-1 setup was always switched on, which allowed the filters to be cleaned every 60 s. The MP-1 multiprocessor has a single external-mixing nozzle with a liquid orifice diameter of 1.2 mm. A nozzle pressure of 3 bar was chosen for all experiments.

In accordance with coating guidelines presented by Hede et al.,[19,21] the core-bed load was heated prior to coating until the relative humidity inside the fluidization chamber was constant, typically in the range of 3−5 RH%, depending on the weather conditions. [The unit "RH%" denotes the percentage relative humidity.] In each coating operation, the objective was to coat until the bed load had increased 20 w/w%. This was done to ensure that a reasonable coating layer (~5−10 μm) had developed on the core particles. After coating, the bed load was kept fluidized under identical fluidization velocity and inlet temperature conditions, to dry the coated granules. This was done until the relative humidity inside the chamber was identical to the conditions prior to coating. Afterward, the coated-bed load was weighed to ensure that the bed load had gained in weight (by ~20 w/w%).

For the sieving analysis, a Retsch Sieve Shaker AS 200 control was used with a sieve stack that consisted of sieves with mesh orifice diameters of 500, 600, 710, and 1000 μm. A 200-g sample from each batch was sieved for 3 min with amplitude of 1.1 mm, and the weight of each fraction was determined with the AS 200 control interface, using a connected Mettler balance.

Microscopic analysis of the different fractions verified that coated granules with diameters of >710 μm consisted of agglomerates, whereas particles below this limit were primarily single coated granules. Thus, this mesh orifice diameter was set as the agglomeration limit, and based on the weight of each of the fractions, an agglomeration percentage was determined for each batch, according to eq 3:

$$\text{Agglomeration (\%)} = \frac{\text{coated batch weight fraction with } d_p > 710\ \mu\text{m}}{\text{total coated batch weight}} \times 100 \quad (3)$$

Issues concerning reproducibility of data with the same type of fluidized-bed equipment and core materials were treated in detail by Hede et al.[19] Analogous to the works by Hede et al.,[21] it was observed, in the present study, how the standard deviation from the Retsch Sieve Shaker AS 200 equipment for the given core materials was 0.44 w/w%, in terms of the agglomeration percentage, thereby indicating, as a common rule of thumb, that different batches that have agglomeration percentages within a range of ±0.88 w/w% are not statistically different.

3.2. Measurement of Coating Properties. Viscosity measurements were performed with a Physica MCR 301 Rheometer (Anton Paar GmbH, Austria), which allowed the shear viscosity to be measured at different temperatures and shear rates. Viscosity measurements were performed using the concentric coaxial cylinder principle in rotational tests with a controlled shear rate. The stainless steel cup in which the stainless steel cylinder rotated was inserted into a Peltier C-PTD 200 thermocup that was connected to a circulating cooling/heating liquid.

Stickiness measurements were performed in a TA.XT2i Texture Analyzer (Stable Micro Systems, England). The probe was a standard Perspex 20 mm probe that had an acrylic cylinder with sharp edges and a well-defined surface area. A specially designed stainless steel plate was applied for the coating liquid samples. For the liquid sample, a cylinder-shaped hole with a diameter of 30 mm and a depth of exactly 200 μm was cut with a milling cutter into the stainless steel plate.

To simulate the stickiness during evaporation of the aqueous solvent, a Steinel type 3482 2000 W electronically controlled heating fan was pointed toward the contact point between the texture analyzer probe and the liquid sample, as shown in Figure 6. With the use of a thermometer, it was possible to precisely adjust the heating fan, to maintain a constant temperature of 35 °C at the contact point.

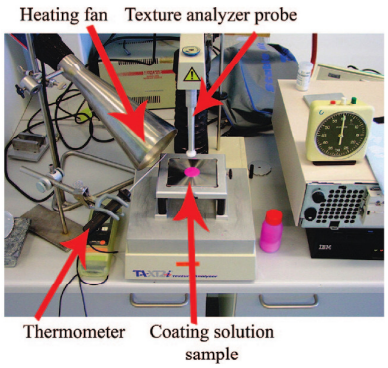

Figure 6. Picture of the TA.XT2i Texture Analyzer setup. The texture analyzer probe is a Perspex 20 mm probe, and the coating solution sample has a diameter of 30 mm and a thickness of 200 μm.

The texture analyzer settings made the probe advance toward the liquid sample at a velocity of 10.0 mm/s (pre-test speed) until a 5-g trigger force is detected. The probe then quickly begins to compress the liquid sample until it reaches a force of 50 g. This force is maintained for 0.05 s, to allow only brief contact between the probe and the sample, to assemble the short particle−particle contact time in a fluid bed. After this time, the probe then withdraws to a distance of 4 mm away from the sample at a constant speed of 10.0 mm/s (post-test speed), during which time the force to separate the probe from the sample surface is recorded. The maximum force normalized with the probe area is taken as the measurement of stickiness.

The procedure for the texture analyzer was as follows. The liquid, which was maintained at 25 °C, was injected into the reservoir at the stainless steel plate, and then the surface was carefully scraped off with a small glass plate, to ensure uniform sample thickness. After the measurement, the probe and sample plate were cleaned and a new sample was prepared. In the next test run, the heating fan was switched on for 30 s before a new probe tack measurement was made. This procedure—with cleaning, preparation, and measurements—was repeated, each time adding 30 s to the heating time before sampling the tack with the probe, until the liquid sample was completely dried. Correlations between the time the heating fan was switched on and the dry matter contents of the liquid sample were obtained for each coating solution, in terms of combined weight difference measurements and Karl Fisher titration using a 701 KF Titrino and a 703 Titrino stand (Metrohm AG, Switzerland). Initial measurements of 20 repititions with a standard PVA/TiO_2 solution showed that the standard deviation for the stickiness was 0.396 mN/mm^2. This indicates that differences in stickiness in the range of ±0.792 mN/mm^2 are not statistically different.

The texture analyzer setup has been developed for the measurement of the adhesive failure energy and simulates the bonding and unbonding process. With the previously described apparatus, the strength of adhesive bonds can be determined under variation of the most important parameters, such as contact pressure, contact time, rate of separation, and temperature. This is essential if relationships between tackiness and viscoelastic properties are to be studied.

Contact angles for all coating solutions were obtained using an OCA-20 video-based contact angle meter (DataPhysics Instruments GmbH, Germany), and all measurements of pH were conducted using a MeterLab PHM210 digital pH meter (Radiometer Analytical, Denmark).

3.3. Materials. Low-porosity sodium sulfate cores (a porosity of ∼20.7%, as determined using Micromeritics Autopore II intrusion/extrusion mercury porosimetry), presieved twice in the size range of 400−500 μm, were used as core material for all coating experiments. The sodium sulfate cores have sphericities in the range of 0.86.

In the salt coating experiments, the sodium sulfate cores were coated with aqueous solutions of sodium sulfate in the amount of 15 w/w%, using 1 w/w% (of the amount of the sodium sulfate) Dextrin W80 from AVEBE as binder. Demineralized water was used as the solvent in all experiments.

The PVA type used in the polymer coating experiments was Celanese Celvol E5/88 (similar to Elvanol 51-05 or Celvol 205S used in studies by, e.g., Hsu et al.[6] and Becker et al.[9]) that had a degree of hydrolysis of 88.5 ± 1.00, thereby being a partially hydrolyzed PVA type. In a 4 w/w% solution, the pH is 5.5 ± 1.00. The T_g value for this type of PVA is reported to be ∼58 °C.[25]

The primary alcohol ethoxylate, under the Shell trademark Neodol 23-6.5, was used as a combined plasticizer, surfactant, and lubricant in two coating solutions as a substitute for a small amount of PVA/TiO_2. Neodol 23-6.5 is based on high-purity C12−C13 primary alcohol ethoxylate with an average of ∼6.5 mol of ethylene oxide per mole of alcohol. The density of Neodol 23-6.5 is 0.97 g/cm^3 at 40 °C, and the viscosity at 40 °C is 26.1 mPa s.[68]

The type of titanium dioxide used as pigment in the PVA solutions was a Kronos type 2044 pigment with a volume median particle size ($d_{v0,5}$) of 0.28 μm. This type of TiO_2 is a rutile pigment that has been given a surface treatment with aluminum and silicon compounds that ensures opacity and tint-reducing properties in dispersions.[69]

3.4. Preparation of the Coating Solutions. The sodium sulfate coating solutions were prepared by pouring the Dextrin and the crushed sodium sulfate into the vortex of cold water. Afterward, the solution was heated to 60 °C, to avoid any precipitation of Glaubers salt (sodium sulfate decahydrate), which melts at 32 °C and forms anhydrous sodium sulfate. Stirring was maintained at all times during the coating process, and the temperature of the coating solutions was always kept at 50 °C.

Preparation of the PVA suspension was a more complex exercise. The most critical step in effectively dissolving PVA is to completely disperse the PVA granules in water. Because the surface of the PVA granules will swell very quickly and clump together, it is very important to control the agitation as well as the temperature of the dispersion. Initially, the pigment material TiO_2 was added into the vortex of cold water at temperatures of <25 °C. While stirring was maintained, the PVA granules were added slowly into the vortex. The use of cold water at <25 °C is important, to allow good dispersion before PVA swelling; if PVA is added into hot water, the particles swell rapidly and clump together before complete dissolution can be achieved. After the PVA granules were well-dispersed in cool water, stirring was continued for 0.5 h before any other ingredients were added. Next, the dispersion was carefully heated, ramping up to 85 °C, and then was maintained at this temperature for 2 h. Afterward, the coating suspension was cooled and kept at a constant temperature of 50 °C during the coating process.

3.5. Coating Solutions. According to the preparation guidelines presented in section 3.4, seven different aqueous coating

Table 1. Formations of Seven Different Coating Solutions Tested in the Three Parts of This Study[a]

solution	composition	pH in the coating solution	measured contact angle[b] (deg)
A	10 w/w% PVA, 10 w/w% TiO_2	measured to pH 7.0	57.10
B	10 w/w% PVA, 10 w/w% TiO_2	adjusted to pH 4.0, using 1 M HNO_3	51.73
C	10 w/w% PVA, 10 w/w% TiO_2	adjusted to pH 10.0, using 1 M NaOH	73.96
D	9 w/w% PVA, 9 w/w% TiO_2, 2 w/w% Neodol 23-6.5	measured to pH 7.0	34.24
E	2 w/w% PVA, 2 w/w% TiO_2	measured to pH 7.2	41.50
F	9 w/w% PVA, 9 w/w% TiO_2, 2 w/w% Neodol 23-6.5	adjusted to pH 4.0, using 1 M HNO_3	31.74
G	15 w/w% Na_2SO_4, 1 w/w% W80 Dextrin	measured to pH 7.1	56.59

[a] The solvent was pure demineralized water in all coating solutions. [b] i.e. between the coating solutions and a non-porous glass plate.

solutions were prepared, to allow the proper testing of the theories presented in this paper and the two companion articles.[1,2] The compositions of these coating solutions and suspensions can be observed in Table 1. The use of PVA and TiO_2 in equal amounts in experiments A−F (experiment E involves the solution from experiment A being diluted by a factor of 5) follows suggestions by Arnold et al.[5] and Becker et al.[9] In experiments D and F, some of the PVA and TiO_2 are replaced by Neodol 23-6.5. The advantages of using plasticizers and lubricants in polymer coating suspensions have been presented previously. Neodol 23-6.5 is used commercially and included in several Genencor patents (e.g., see refs 5 and 8). The advantage of Neodol 23-6.5 is that it functions both as a lubricant and as a plasticizer, as well as a surfactant.[5] Arnold et al.[5] suggested that the lubricant should replace up to 30% of the polymer or pigment, but recent studies by Hsu et al.[6] have indicated that the best coatings are obtained with Neodol 23-6.5 concentrations in the range of 10−20 w/w%, to have the best plasticizing effects. In the solutions from experiments D and F, Neodol 23-6.5 constitutes 20 w/w% of the coating solution, replacing both PVA and TiO_2 in equal amounts, hereby following the newest guidelines.

The contact angles in Table 1 were measured by dispersing 6.00 μL of coating solution onto the glass plate and then measuring the contact angle using the SCA 20 software interface. The contact angles were measured at 45 °C between the coating solutions and a nonporous glass plate. Because of the hygroscopic and porous nature of the sodium sulfate cores, it was not possible to measure the contact angles between the coating solutions and the core material. As a reference, the contact angle for pure demineralized water was measured to be 40.81°, which indicates that the glass plate is quite hydrophilic, hence well-resembling the sodium sulfate core surface. As observed in Table 1, the best wetting is observed for solutions D and F. Neodol 23-6.5 seems to aid the droplet spreading significantly.

4. Coating Experiments

4.1. The Drying Force and Spray Rate. Previous experience with sodium sulfate coatings,[19−21,30] and initial trials with PVA coatings by Neidel,[15] provided the basis for detailed studies of several possible reasons why the two types of coating solutions behave differently, with respect to agglomeration. As presented in Hede et al.,[19] fixing the drying force, as well as a spray-related parameter (called the relative droplet size), made it possible to match the agglomeration tendency, as well as the particle size distribution of the final coated granules, across three fluid-bed scales in the salt coating process, where sodium sulfate cores were coated with coating solution G. Fixing the nozzle conditions and the drying force gives adequate control over the salt coating process, because a clear relation exists between the nozzle conditions and the drying force on one hand, and the agglomeration tendency on the other. Being a successful tool for the control of the salt coating process, it seems possible

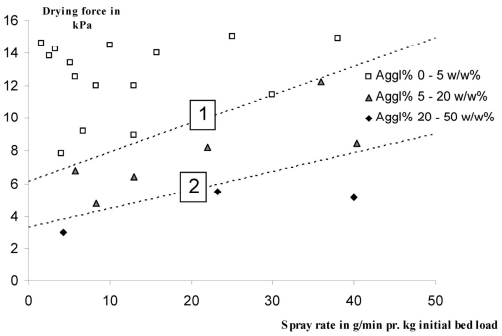

Figure 7. Agglomeration regime map for the salt coating process (with solution G) in the MP-1 fluid bed. The dashed lines indicate the demarcation between the different agglomeration regimes.

that fixing the same properties also will lead to regimes of successful coating with no or little tendency of agglomeration for PVA/TiO_2 solutions. However, it is difficult to estimate in advance if the PVA/TiO_2 coating process will respond to the changes in the drying force and spray rate in a similar manner as the salt coating solution. Therefore, as a start, 24 coating experiments were conducted for each of the coating solutions A and G for drying force values in a broad range (3−19 kPa) and for spray rates in a broad range (2−120 g/min). This initial screening study is aimed at providing a first basis regarding how the two types of coating solutions respond to relevant ranges of temperature/humidity and spray rate conditions.

5. Results and Discussion

5.1. Influence of the Drying Force and Spray Rate. In accordance with the guidelines for the first study, 24 coating experiments with solution A and 24 coating experiments with solution G were conducted for different values of the drying force and spray rate (expressed in units of g/min, always at a nozzle pressure of 3 bar). For each batch, the weight gain was determined after coating. For all the experiments in the test of the drying force versus agglomeration tendency, the weight gain varied between 18.6 w/w% and 19.7 w/w%, meaning that the spray-drying losses in the experiments were quite small. All the resulting agglomeration tendencies for the sodium sulfate coating experiments were plotted in terms of their spray rate and drying force coordinates and may be observed in Figure 7.

As observed from Figure 7, the agglomeration tendencies are distributed in quite distinct bands. In accordance with results by Hede et al.,[19] the agglomeration tendency is observed to increase as the drying force decreases. With decreasing drying force, the coated particles are wet for a longer time and with more liquid, thus increasing the likelihood of agglomeration. Similarly, the agglomeration tendency is observed to increase with increasing spray rate at an identical drying force, which is

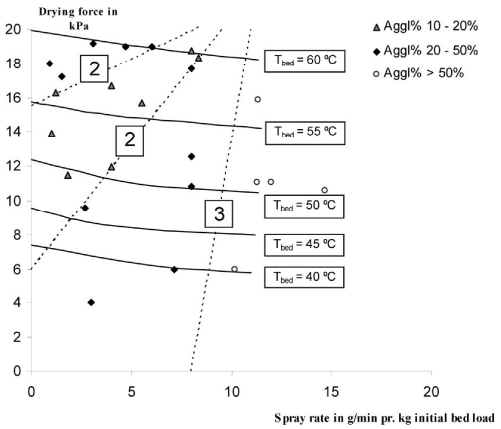

Figure 8. Agglomeration regime map for the PVA/TiO_2 coating process (with solution A) in the MP-1 fluid bed. The dashed lines indicate the demarcation between the different agglomeration regimes. Iso-bed-temperature lines are added to indicate at which bed temperatures the experiments were processed.

reasonable because, at increasing spray rate, more particles will be wet locally in the bed, thus increasing the chance of agglomeration, as observed. Of interest in Figure 7 is the fact that there is a wide range of drying force and spray rate values at which the agglomeration tendency is small.

A similar plot for the PVA/TiO_2 coating process in Figure 8 indicates several interesting points. A first look reveals that the demarcations between the agglomeration categories are somewhat different from Figure 7. Furthermore, it can be observed that it was not possible to get below an agglomeration level of 10 w/w% in any of the 24 experiments. The agglomeration tendency in Figure 7 was observed to decrease when the drying force increases, irrespective of the spray rate; however, in Figure 8, the agglomeration tendency seems to be low only in a narrow regime surrounded by agglomeration tendencies in the range of 20−50 w/w%. A plausible reason for this could be that, at drying force values close to and above 16 kPa, the bed temperature during steady-state coating was approaching the T_g value for PVA, which is ∼58 °C for the type of PVA used. At a temperature above T_g, the PVA is soft and can be easily deformed, which most likely increases its stickiness. Therefore, it is not surprising to observe an increasing agglomeration tendency for the PVA/TiO_2 solution as the drying force increases beyond a certain boundary.

A comparison of Figures 7 and 8 clearly shows that the tendency of agglomeration for the two types of coating solutions is not the same for identical value of the drying force and the spray rate. The two coating processes do not respond in a similar manner toward change in the drying force and the spray conditions, and, within the tested range for the PVA/TiO_2 solution, it has not been possible to find coating conditions that lead to agglomeration percentages of 10 w/w% or less. Hence, it may be concluded that similar spray and drying force conditions do not lead to similar agglomeration tendencies for the two types of coating processes. However, the results from the test have indicated that the agglomeration tendency for both types of processes distribute into regimes based on the spray rate and drying force.

6. Summary and Conclusion

In the pursuit of determining the causes why polymer and inorganic salt solutions cannot be processed under similar fluid-bed process conditions to result in similar tendency of agglomeration, several coating experiments with either sodium salt solutions or PVA/TiO_2 solutions were performed, to optimize process and formulation conditions. Although the agglomeration tendencies for salt coatings as well as for PVA/TiO_2 coatings indeed distributed well in distinct bands, the results indicated that the agglomeration tendency was not similar for the two coating formulations for identical process conditions. Although the agglomeration tendency for the sodium sulfate solution was low (<5 w/w%) for a broad range of spray rates and drying force values, it was not possible to determine a range where the agglomeration tendency is <10 w/w% for the PVA/TiO_2 solution. Furthermore, the second-best 10−20 w/w% agglomeration regime for the PVA/TiO_2 solution was very narrow. The studies with different values of the drying force and spray rates led to an important conclusion, namely that the two types of coatings are not equally affected by the spray rate and drying force conditions. The drying force, in combination with the bed temperature and bed humidity, is of major importance for the tendency of agglomeration during the salt coating process, and the tendency of agglomeration may be well-controlled in terms of these two parameters alone, in accordance with results by Hede et al.[19] For the PVA/TiO_2 solution, the correct choice of the drying force and spray conditions may be seen as a requisite, but it is not sufficient to control agglomeration. In other words, there are no observed combinations of the two parameters for the complete reduction of the agglomeration tendency for the PVA/TiO_2 solution: other parameters must additionally come into play. In Parts 2^1 and 3^2 of this study, the PVA/TiO_2 solution especially is studied in detail, with respect to rheological and colloidal phenomena, to obtain a deeper understanding of the agglomeration mechanisms of such coatings.

Acknowledgment

This project was performed in collaboration with Novozymes A/S, which also financially supported the project. Peter Dybdahl Hede is a member of the Novozymes Bioprocess Academy, as well as the MP_2T Graduate School in Chemical Engineering at the Department of Chemical and Biochemical Engineering, Technical University of Denmark, and his research is funded by the Danish Technical Research Council, the European Union, the Nordic Energy Research, Dong Energy A/S, Vattenfall A.B., F L Smidth A/S, and Public Service Obligation funds from Energinet.dk and the Danish Energy Research programme.

7. Table of symbols

Nomenclature

A_{con} = area of contact (m^2)
$d_{v0,5}$ = volume mean particle size (μm)
F = force (kg m/s^2)
$F_{max(tack)}$ = maximum (peak) tack force measured in a probe tack test (kg m/s^2)
P_{sat} = saturated vapor pressure (Pa)
t = time (s)
v_{sep} = separation rate (m/s)
$W_{adhesion}$ = work of adhesion (kg/s^2)

Literature Cited

(1) Hede, P. D.; Jensen, A. D.; Bach, P. Fluidized-Bed Coating with Sodium Sulfate and PVA−TiO_2, 2. Influence of Coating Solution Viscosity,

Stickiness, pH and Droplet Diameter on Agglomeration. *Ind. Eng. Chem. Res.* **2009**, *48*, XXXX.

(2) Hede, P. D.; Jensen, A. D.; Bach, P. Fluidized-Bed Coating with Sodium Sulfate and PVA−TiO_2, 3. The Role of Tackiness and the Tack Stokes Number. *Ind. Eng. Chem. Res.* **2009**, *48*, XXXX.

(3) van Ee, J. H.; Misset, O; Baas, E. J. *Enzymes in Detergency*; Surfactant Science Series, Vol. 69; Marcel Dekker: New York, 1997.

(4) Markussen, E. K. Novozymes A/S. *Enzyme containing granule*, U.S. Patent 6,348,442, 2002.

(5) Arnold, R. E.; Becker, N. T.; Boston, M. G.; Mansikkamaki, A.; Wendt, D. J. Genencor International. *Coated Enzyme Containing Granule*, International Patent WO 93/07263, 1993.

(6) Hsu, E. R.; Gebert, M. S.; Becker, N. T.; Gaertner, A. L. The Effects of Plasticizers and Titanium Dioxide on the Properties of Poly (Vinyl Alcohol) Coatings. *Pharm. Dev. Technol.* **2001**, *6* (2), 277–284.

(7) Beekman, W. J. Measurement of the Mechanical Strength of Granules, Ph.D. Thesis, Technische Universiteit Delft, Delft, The Netherlands, 2000.

(8) Dale, D. A.; Gaertner, A. L., Park, G.; Becker, N. T. Genencor International, Inc. Coated enzyme-containing granule, U.S. Patent 5,879,920, 1999.

(9) Becker, N. T.; Flynn, M. J.; Gebert, M. S. Particle with substituted polyvinyl alcohol coating, U.S. Patent 6,872,696, 2005.

(10) Kiuchi, T.; Kohtaro S.; Sato, M.; Kawamura, J.; Yamada, N. Kao Corporation. Enzyme-containing granulated substance and preparation process thereof, U.S. Patent 5,851,975, 1998.

(11) Markussen, E. K. Novo Industri A/S. Enzyme containing granulates suitable for use as detergent additives, Eur. Patent EP 0170360 B1, 1986.

(12) Simonsen, O. Novozymes A/S. Lubricated Granules, International Patent WO 02/20746 A1, 2002.

(13) Foley, P. R.; Painter, J. D.; Leyendecker, M. R.; Sadlowski, E. S.; Song, B. X.; Thien, J. H. Procter & Gamble Company. Enzyme composite particles having an acidic barrier and a physical barrier coating, U.S. Patent 6,656,898, 2003.

(14) Paatz, K.; Rähse, W.; Pichler, W.; Upadek, H.; Kühne, N. Henkel Kommanditgesellscahft auf Aktien. Multi-enzyme granules, U.S. Patent 5,846,798, 2003.

(15) Neidel, B. Water-soluble polymer fluid bed coatings, M.Sc. Thesis, Department of Chemical Engineering, CHEC Research Center, Technical University of Denmark, Lyngby, Denmark, 2007, pp 1−123.

(16) Chu, W. B.; Yang, J. W.; Wang, Y. C.; Liu, T. J.; Tiu, C.; Guo, J. The effect of inorganic particles on slot die coating of poly(vinyl alcohol) solutions. *J. Colloid Interface Sci.* **2006**, *297*, 215–225.

(17) Chu, W. B.; Yang, J. W.; Liu, T. J.; Tiu, C.; Guo, J. The effect of pH, molecular weight and degree of hydrolysis of poly(vinyl alcohol) on slot die coating of PVA suspensions of TiO_2 and SiO_2. *Colloids Surf. A* **2007**, *302*, 1–10.

(18) Hede, P. D. *Towards Mathesis Universalis: Modern aspects of modelling batch fluidised bed agglomeration and coating systems—A review*, CHEC Report R0605, Department of Chemical Engineering, Technical University of Denmark, Lyngby, Denmark, 2006, pp 1−101.

(19) Hede, P. D.; Jensen, A. D.; Bach, P. Top-spray fluidised bed coating: Scale-up in terms of relative droplet size and drying force. *Powder Technol.* In press. (DOI:, 10.1016/j.powtec.2007.09.009.)

(20) Hede, P. D.; Jensen, A. D.; Bach, P. Small-scale top-spray fluidised bed coating: Granule impact strength, agglomeration tendency and coating layer morphology. *Powder Technol.* **2007**, *176*, 156–167.

(21) Hede, P. D.; Jensen, A. D.; Bach, P. Validation of the flux number as scaling parameter for top-spray fluid bed systems. *Chem. Eng. Sci.* **2008**, *63*, 815–828.

(22) Abelthauser, C. B.; Schneider, R.; Rupprech, H. Film coating of pellets with insoluble polymers obtained in situ crosslinking in the fluidized bed. *J. Controlled Release* **1993**, *27*, 149–156.

(23) McGinity, J. W. *Aqueous Polymeric Coatings for Pharmaceutical Dosage Forms*, 2nd Edition; Marcel Dekker: New York, 1997.

(24) Saxena, S. K. Polyvinyl Alcohol (PVA). In *Chemical and Technical Assessment (CTA)*, 2004; pp 1−3.

(25) *Celvol 205S Polyvinyl Alcohol Sales Specifications*, Celanese Chemicals, Dallas, TX, 2005.

(26) Jordan, M. P.; Taylor, J. BPSI Holdings, Inc. Film coatings and film coating compositions based on polyvinyl alcohol, U.S. Patent 6,448,323, 2002.

(27) Chau, K. W.; Swei, G. S. Contact Time and Interfacial Fracture Energy of Tacky Polymers. *J. Polym. Sci., Part B: Polym. Phys.* **2004**, *42*, 3013 3025.

(28) Wan, L. S. C.; Lai, W. F. A simple method to assess the tack of coating formulations. *STP Pharma Sci.* **1992**, *2*, 174–180.

(29) Wan, L. S. C.; Lai, W. F. An application of tack measurement to fluidized bed coating. *STP Pharma Sci.* **1992**, *2*, 404–410.

(30) Hede, P. D. Fluidised bed coating and granulation, M.Sc. Thesis, Department of Chemical Engineering, CHEC Research Center, Technical University of Denmark, Lyngby, Denmark, 2005, pp 1−227.

(31) Wesseling, M.; Kuppler, F.; Bodmeier, R. Tackiness of acrylic and cellulosic polymer films used in the coating of solid dosage forms. *Eur. J. Pharm. Biopharm.* **1999**, *47*, 73–78.

(32) Creton, C.; Leibler, L. How Does Tack Depend on Time of Contact and Contact Pressure. *J. Polym. Sci., Part B: Polym. Phys.* **1996**, *34*, 545–554.

(33) Russell, T. P.; Kim, H. C. Tack—A Sticky Subject. *Science* **1999**, *20*, 1219–1220.

(34) Roos, A.; Creton, C.; Novikov, M. B.; Feldstein, M. M. Viscoelastic and Tack of Poly(Vinyl Pyrrolidone)−Poly(Ethylene Glycol) Blends. *J. Polym. Sci.: Part B: Polym. Phys.* **2002**, *40*, 2395–2409.

(35) Adhikari, B.; Howes, T.; Bhandari, B. R.; Truong, V. Stickiness in Foods: A Review of Mechanisms and Test Methods. *Int. J. Food Prop.* **2001**, *4*, 1–33.

(36) Hui, C. Y.; Lin, Y. Y.; Barney, J. M. The Mechanics of Tack: Viscoelastic Contact on a Rough Surface. *J. Polym. Sci., Part B: Polym. Phys.* **2000**, *38*, 1485–1495.

(37) Rajsharad, C.; Kamble, S. Majumdar & Co. PVA Based Film Coating and Film Coating Compositions, International Patent WO 2006/11980 A2, 2006.

(38) Zosel, A. Adhesion and tack of polymers: Influence of mechanical properties and surface tensions. *Colloid Polym. Sci.* **1985**, *263*, 541–553.

(39) York, P.; Rowe, R. C. *Monitoring granulation size enlargement processes using mixer torque rheometry*. Presented at the 1st International Particle Technology Forum, Denver, CO, 1994.

(40) Rowe, R. C. Binder−Substrate Interactions in Tablets: A Theoretical Approach Based on Solubility Parameters. *Acta Pharm. Technol.* **1988**, *34*, 144–146.

(41) Okhamafe, A. O.; York, P. The adhesion characteristics of some pigmented and unpigmented aqueous-based film coatings applied to aspirin tablet. *J. Pharm. Pharmacol.* **1985**, *37*, 849–853.

(42) Johnson, B. A.; Zograf, G. Adhesion of Hydroxypropyl Cellulose Films to Low Energy Solid Substrates. *J. Pharm. Sci.* **1985**, *75* (6), 529–533.

(43) Rowe, R. C. Binder-substrate interactions in granulation: a theoretical approach based on surface free energy and polarity. *Int. J. Pharm.* **1989**, *52*, 149–154.

(44) Parker, M. D.; York, P.; Rowe, R. C. Binder−substrate interactions in wet granulation. 1: The effect of binder characteristics. *Int. J. Pharm.* **1990**, *64*, 207–216.

(45) Felton, L. A.; McGinity, J. W. Influence of plasticizers on the adhesive properties of an acrylic resin copolymer to hydrophilic and hydrophobic tablet compacts. *Int. J. Pharm.* **1997**, *154*, 167–178.

(46) Tüske, Z.; Regdon, G., Jr.; Erös, I.; Srcic, S.; Pintye-Hódi, K. The role of the surface energy in the selection of a suitable excipient in the course of a wet-granulation method. *Powder Technol.* **2005**, *155*, 139–144.

(47) Michalski, M. C.; Desobry, S.; Hardy, J. Food Materials Adhesion: A Review. *Crit. Rev. Food Sci. Nutr.* **1997**, *37*, 591–619.

(48) Michalski, M. C.; Desobry, S.; Babk, V.; Hardy, J. Adhesion of food emulsions to packaging and equipment surfaces. *Colloids Surf. A* **1999**, *149*, 107–121.

(49) Smitthipong, W.; Nardin, M.; Schultz, J.; Nipithakul, T.; Suchiva, K. Study of tack properties of uncrosslinked natural rubber. *J. Adhesion Sci. Technol.* **2004**, *18* (12), 1449–1463.

(50) Bartenev, G. M.; Razumovskaya, I. V.; Sanditov, D. S.; Lukyanov, I. A. A Contribution to the Theory of the Structural Glass Transition. *J. Polym. Sci., Part A-1* **1969**, *7*, 2147–2157.

(51) Phillips, J. P.; Deng, X.; Stephen, R. R.; Fortenberry, E. L.; Todd, M. L.; McClusky, D. M.; Stevenson, S.; Mishra, R.; Morgan, S.; Long, T. E. Nano- and bulk-tack adhesive properties of stimuli-responsive fullerene-polymer blends, containing polystyrene-block-polybutadiene-block-polystyrene and polystyrene-block-polyisoporene-block-polystyrene rubber-based adhesives. *Polymer* **2007**, *48*, 6773–6781.

(52) Goodwin, J. *Colloids and Interfaces with Surfactants and Polymers—An Introduction*; John Wiley & Sons, Ltd.: Chichester, U.K., 2004.

(53) Christensen, S. F. *Rheology of Adhesion*, Ph.D. Thesis, Department of Chemical Engineering, Technical University of Denmark, Lyngby, Denmark, 1998.

(54) Gay, C. Stickiness—Some Fundamentals of Adhesion. *Integr. Comp. Biol.* **2002**, *42*, 1123–1126.

(55) Werner, S. R. L.; Jones, J. R.; Paterson, A. H. J. Stickiness during drying of amorphous skin-forming solutions using a probe tack test. *J. Food Eng.* **2007**, *81*, 647–656.

(56) Chopra, S. K.; Tawashi, R. Tack behaviour of coating solutions, I. *J. Pharm. Sci.* **1982**, *71*, 907–911.

(57) Chopra, S. K.; Tawashi, R. Tack behaviour of coating solutions, II. *J. Pharm. Sci.* **1984**, *73*, 477–481.

(58) Chopra, S. K.; Tawashi, R. Tack behaviour of coating solutions, III. *J. Pharm. Sci.* **1982**, *74*, 747–749.

(59) Lehtola, V.-M.; Heinamaki, J.-T.; Nikupaavo, P.; Yliruusi, J. K. The mechanical and adhesion properties of aqeous-based hydroxypropyl methylcellulose coating systems containing Polydextrose and titanium dioxide. *Drug Dev. Ind. Pharm.* **1995**, *21*, 675–685.

(60) Chang, S. H.; Gupta, R. K.; Ryan, M. E. Effect of the adsorption of polyvinyl alcohol on the rheology and stability of clay suspensions. *J. Rheol.* **1992**, *36*, 273–287.

(61) Otsubo, Y. Effect of polymer on the rheological behaviour of silica suspensions. *J. Colloid Interface Sci.* **1986**, *112*, 380–386.

(62) Liang, G. C.; Hawkett, B. S.; Tanner, R. I. The determination of the isoelectric point from measurements of dispersion viscosity as a function of pH. *J. Dispers. Sci. Technol.* **2005**, *26*, 215–225.

(63) Sairam, M.; Patil, M. B.; Veerapur, R. S.; Patil, S. A.; Aminabhavi, T. M. Novel dense poly(vinyl alcohol)−TiO_2 mixed matrix membranes for pervaporation separation of water−isopropanol mixtures at 30 °C. *J. Membr. Sci.* **2006**, *281*, 95–102.

(64) Chibowski, S. Adsorption Equilibria in the System TiO_2−Aqueous Solution Containing Polyvinyl Alcohol. *Mater. Chem. Phys.* **1986**, *14*, 471–479.

(65) Chibowski, S.; Szcypa, J. Studies of the Adsorption of Polyvinyl Alcohol on TiO_2 Surfaces. *J. Colloid Interface Sci.* **1984**, *100* (2), 571–572.

(66) Kiilmann, E.; Maier, H.; Baker, J. A. Hydrodynamic Layer Thicknesses of Various Adsorbed Polymers on Precipitated Silica and Polystyrene Latex. *Colloids Surf.* **1988**, *31*, 51–71.

(67) Boisvert, J.-P.; Persello, J.; Guyard, A. Influence of the surface chemistry on the structural and mechanical properties of silica−polymer composites. *J. Polym. Sci., Part B: Polym. Phys.* **2003**, *41*, 3127–3138.

(68) *NEODOL 23-6.5 Product Specification Sheet*, Shell Chemicals Europe B.V., Rotterdam, The Netherlands, 2005, pp 1−2.

(69) *Kronos 2044 Titanium Dioxide Information Sheet*, Kronos, Ltd., Cheshire, U.K., 1999.

(70) Teunou, E.; Poncelet, D. Batch and continuous fluid bed coating−Review and state of the art. *J. Food Eng.* **2002**, *53*, 325–340.

Received for review June 16, 2008
Revised manuscript received October 3, 2008
Accepted November 20, 2008

IE800940E

Ind. Eng. Chem. Res. **XXXX,** *xxx,* 000 **A**

Fluidized-Bed Coating with Sodium Sulfate and PVA−TiO_2, 2. Influence of Coating Solution Viscosity, Stickiness, pH, and Droplet Diameter on Agglomeration

Peter Dybdahl Hede,[†,‡] Poul Bach,[‡] and Anker D. Jensen*[,†]

CHEC Research Center, Department of Chemical and Biochemical Engineering, Technical University of Denmark, Building 229, DK-2800 Kgs. Lyngby, Denmark, and Solid Products Development, Novozymes A/S, Smørmosevej 11, DK-2880 Bagsværd, Denmark

In the first part of this study [Hede, P. D.; Bach, P.; Jensen, A. D. *Ind. Eng. Chem. Res.* **2009**, *49*, XXXX], agglomeration regime maps were developed for two types of coatings: sodium sulfate and PVA−TiO_2. It was observed here how the agglomeration tendency is always lower for the salt coating process than for the polymer coating process, under similar process conditions. This is investigated further in this second part and concluded to be due to differences in coating solution stickiness, rather than differences in bulk viscosities. Furthermore, results show that it is possible to optimize the PVA−TiO_2 coating formulation and process to achieve a low tendency of agglomeration, similar to that of the salt coating process. The best results for the PVA−TiO_2 solution are obtained by substituting the PVA−TiO_2 in equal amounts with Neodol 23-6.5 and further reducing the pH value in the coating solution to pH 4.

1. Introduction

Fluid-bed coating is, in principle, a technique that is used to apply a shell layer onto individual core particles during fluidization. In terms of this process, it is possible to encapsulate active ingredients such as pharmaceuticals and enzymes, and the desired product consists thereby of unagglomerated individual carrier particles, each coated homogeneously. Different types of coating materials may be used, depending on their abilities, in terms of, e.g., controlled release properties and mechanical and dust-reducing properties, as well as moist barrier properties.[1] Agglomeration of core particles during the coating process is a severe industrial problem, and, unfortunately, different coating materials behave differently, in terms of agglomeration tendency, even when processed under similar conditions. It is still not clear what causes these differences.

In the first part of this study,[2] a thorough literature review provided as the background for the detailed study of two types of industry-relevant coatings: sodium sulfate and PVA−TiO_2. The sodium sulfate coating solution is a fairly simple chemical system, whereas the PVA solution that contains dispersed TiO_2 particles is a complex system, where colloidal phenomena and rheology must be taken into account in the coating process. It was observed how the agglomeration tendency is always less for the salt coating process than for the polymer coating process, under similar process conditions, but also that rough agglomeration regime maps may be built based on the coating solution spray rate and the drying force, which is a thermodynamic property that links the bed temperature with the humidity of the outlet air. However, for the PVA−TiO_2 coating solution, it was not possible to obtain agglomeration percentages of <10 w/w%. The objective of this second part of the series of papers is to study the PVA−TiO_2 coating solution in greater detail, and to obtain principles under which the agglomeration tendency of a PVA−TiO_2 coating process may be reduced to a level similar to that of the sodium salt coating process. The equipment and coating solutions used in the present paper may be found in the first part of this study.[2]

* To whom correspondence should be addressed. Tel.: +45 4525 2841. Fax: +45 4588 2258. E-mail address: aj@kt.dtu.dk.
† CHEC Research Center, Department of Chemical and Biochemical Engineering, Technical University of Denmark.
‡ Solid Products Development, Novozymes A/S.

2. Coating Experiments: Testing Possible Causes for Differences in Coating Solution Processing

2.1. Bulk Viscosity of the Coating Solutions, Stickiness, and the Influence of the Mean Droplet Diameter. An apparent difference between the sodium sulfate and the PVA−TiO_2 solution is the significant difference in bulk viscosity observable already during the preparation of the coating solution. Although the sodium sulfate solution has a viscosity close to pure water, the PVA−TiO_2 solution is far more viscous. The viscosity of the coating solution is believed to play an important role, regarding the tendency of agglomeration.[3,4] In addition, viscosity is known to affect the mean droplet diameter produced at the nozzle and, thereby, also phenomena such as droplet penetration into the cores and droplet drying time.[3] It is thereby likely that these apparent differences in bulk viscosities could be part of the reason for the observed differences in agglomeration tendency.

An important consequence of the difference in coating liquid bulk viscosities is the differences in stickiness as the droplets dry on the core particle surface. As the coating solution droplets dry upon evaporation of the aqueous solvent, the viscosity and stickiness increase. Upon solvent evaporation, PVA solutions are known to be sticky and, for that reason, PVA is used in many commercial glues often simply with water as the solvent. It is known to have good adhesion properties to objects upon complete drying and leaves a nonsticky film layer, although PVA glue is known to become sticky again on contact with moist surfaces or under humid conditions. Although there is no uniform agreement on how the PVA glue works, its stickiness is believed to be closely related to the polymer chains, as discussed in the first part of this study.[5]

It is reasonable to believe that the viscosity and stickiness are closely related phenomena. It is hereby possible that the viscosity of the PVA−TiO_2 solutions will increase to a higher

10.1021/ie800941x CCC: $40.75

Table 1. Coating Experiments Used To Test the Influence of Bulk Viscosity

parameter	Solution A, 10 w/w% PVA−10 w/w% TiO_2, pH 7.0	Solution E, 2 w/w% PVA−2 w/w% TiO_2, pH 7.2	Solution G, 15 w/w% Na_2SO_4−1 w/w% W80 Dextrin, pH 7.1
Series 1			
drying force (kPa)	18	18	18
spray rate (g/min)	24	24	24
Series 2			
drying force (kPa)	18	18	18
spray rate (g/min)	90	90	90
Series 3			
drying force (kPa)	18	18	18
spray rate (g/min)	120	120	120

Table 2. Coating Experiments Used To Test the Influence of Mean Droplet Size[a]

parameter	Solution A, 10 w/w% PVA−10 w/w% TiO_2, pH 7.0	Solution G, 15 w/w% Na_2SO_4−1 w/w% W80 Dextrin, pH 7.1
Series 1		
drying force (kPa)	18	18
spray rate (g/min)	24	62
mean droplet diameter (μm)	11.3	11.2
Series 2		
drying force (kPa)	18	18
spray rate (g/min)	19	50
mean droplet diameter (μm)	8.0	8.0
Series 3		
drying force (kPa)	18	18
spray rate (g/min)	14	37
mean droplet diameter (μm)	5.2	5.2

[a] Values for d_{32} were calculated using eqs 1−3.

level than the viscosity of the sodium sulfate solution upon evaporation of the solvent, and that this increase in viscosity increases the coating stickiness and, therefore, the tendency of agglomeration. It seems thereby obvious to test the influence of the coating solution bulk viscosity and the development in stickiness upon solvent evaporation. For this purpose, three coating solutions were selected for rheological characterization, as well as for fluid-bed coating experiments. The three coating solutions were solutions A, E, and G, which were described in the first part of this series of reports.[2] Three coating experiments were performed for each coating solution, for three sets of drying force/spray rate conditions, according to Table 1.

It is well-known from detailed two-fluid nozzle studies that the liquid viscosity plays an important role, with regard to the resulting mean droplet diameter.[6] The mean droplet diameter is important for the coating process for several reasons.[4] First of all, the droplet diameter influences the droplet drying time. There is roughly a log−log linear dependency between the droplet diameter and the droplet drying time.[7] With increasing droplet diameter, and thereby increasing droplet drying time, the coated particles will be wet and sticky for a longer time, thereby increasing the chance of agglomeration. Furthermore, the droplet diameter influences other important phenomena such as the time of droplet penetration into the core particle and the morphology of the final coating layer.[3] Hence, there are indeed many reasons to believe that a careful control of the droplet diameter may be crucial, with respect to the control of agglomeration. Knowing that the bulk viscosity of coating solutions A and G are significantly different, this means that, for identical spray rates at identical nozzle pressures, the resulting mean droplet diameters also are different in a similar way. This could be part of the reason for the observed differences in agglomeration tendency between the coating formulations. Following the studies of bulk viscosities and stickiness, it seems reasonable to perform detailed studies of the influence of the mean droplet diameter.

From the review of two-fluid nozzles for coating purposes in fluid beds by Hede et al.,[6] it becomes clear that the determination and a priori prediction of the mean droplet diameter produced in external mixing nozzles, such as that used in the present fluid bed setup, is not an easy task. Direct measurement techniques often give different results. Nevertheless, there are a variety of correlations that may be used to estimate the mean droplet diameter from the coating liquid properties and the nozzle dimensions as well as process conditions. Not all correlations can be used for the conditions in the present study, but the expression in eq 1 proposed by Mulhem and co-workers[8,9] was shown to give precise estimations of the mean droplet size for coating solutions similar to those used in the present study.

$$d_{32} = 0.21 d_{\text{orifice}} Oh^{0.0622} \left(We_{\text{air}} \frac{\dot{m}_{\text{liq}}}{\dot{m}_{\text{air}}} \right)^{-0.4} \quad (1)$$

where d_{32} is the Sauter mean droplet diameter (expressed in micrometers). The d_{32} parameter represents the diameter of a droplet that has the same volume-to-surface area ratio as the total volume of all the droplets to the total surface area of all the droplets.[10] The parameter d_{orifice} is the liquid orifice diameter at the nozzle outlet. Furthermore, $\dot{m}_{\text{air}}$ is the mass rate of atomization air, and $\dot{m}_{\text{liq}}$ is the mass rate of liquid.[11] Oh is the so-called Ohnesorge number, which relates surface tension and viscosity according to eq 2:[20]

$$Oh = \frac{\eta_{\text{liq}}}{\sqrt{\gamma_{\text{liq}} \rho_{\text{liq}} d_{\text{orifice}}}} \quad (2)$$

where η_{liq} is the coating liquid viscosity, ρ_{liq} the coating liquid density, and γ_{liq} the coating liquid surface tension. We_{air} is the gas Weber number, which expresses the ratio of dynamic pressure to capillary pressure at the outset of the process according to eq 3:[11]

$$We_{\text{air}} = \frac{v_{\text{rel}}^2 \rho_{\text{air}} d_{\text{orifice}}}{\gamma_{\text{liq}}} \quad (3)$$

where v_{rel} is the difference between the nozzle atomizing air velocity and the liquid velocity at the nozzle outlet, which, in practice, is very close to the atomizing air velocity.

Equation 1 was developed for aqueous polymer/glass particle suspensions, but it also shows adequate precision for pure water droplets. Hence, eq 1 is used in the present study to estimate the droplets produced by the PVA−TiO_2 suspensions and the sodium sulfate solutions. Knowing the dimensions of the applied two-fluid nozzle and the corresponding atomizing air mass flow rate, as well as the coating liquid properties, made it possible to adjust the liquid flow rate to produce similar mean droplet sizes for solutions A and G. To test the influence of the mean droplet diameter, six experiments were performed, following Table 2.

2.2. The Influence of pH, Colloidal Phenomena, and Additives in the PVA−TiO_2 System. In terms of the previous experience with the colloidal phenomena in the PVA−TiO_2 system presented in the first part of this study,[2] it seems reasonable to test the influence of pH in the PVA−TiO_2 system on the tendency of agglomeration. To test this phenomenon, three coating solutions were selected for rheological characterization and for fluid-bed coating experiments. The three coating solutions were solutions A, B, and C, which were described in

Table 3. Coating Experiments Used To Test the Influence of pH in the PVA−TiO_2 Solution

parameter	Solution A, 10 w/w% PVA−10 w/w% TiO_2, pH 7.0	Solution B, 10 w/w% PVA−10 w/w% TiO_2, pH 4.0	Solution C, 10 w/w% PVA−10 w/w% TiO_2, pH 10.0
Series 1			
drying force (kPa)	18	18	18
spray rate (g/min)	24	24	24
Series 2			
drying force (kPa)	18	18	18
spray rate (g/min)	14	14	14

Table 4. Coating Experiments Used To Test the Influence of Additives and pH in the PVA−TiO_2 System

parameter	Solution A, 10 w/w% PVA−10 w/w% TiO_2, pH 7.0	Solution D, 9 w/w% PVA−9 w/w% TiO_2−2 w/w% Neodol 23-6.5, pH 7.0	Solution F, 9 w/w% PVA 9 w/w% TiO_2−2 w/w% Neodol 23-6.5, pH 4.0
Series 1			
drying force (kPa)	18	18	18
spray rate (g/min)	24	24	24
Series 2			
drying force (kPa)	18	18	18
spray rate (g/min)	14	14	14

the first part of this series of reports.[2] Two coating experiments were performed for each coating solution for two sets of drying force/spray rate conditions, according to Table 3.

Lastly, the influence of additives in the PVA−TiO_2 system will be tested. Based on the advantages of using plasticizers and lubricant emphasized in the first part of this study,[2] there are reasons to believe that the introduction of Neodol 23-6.5 will reduce the tendency of agglomeration, in comparison to the original PVA−TiO_2 solution under similar process conditions. According to the manufacturer (Shell Chemicals Europe),[12] Neodol 23-6.5 is not charged and it will thereby most likely be less sensitive to changes in pH. This also indicates that Neodol 23-6.5 should be chemically stable at acidic pH values, although this has not yet been tested properly. Nor have the lubricating and plasticizing effects for Neodol 23-6.5 at acidic pH been tested, but there is no reason to believe that Neodol 23-6.5 should function differently at pH 4 than under conditions with pH 7. Hence, it is believed that, if a low pH value is beneficial, in terms of reduced agglomeration tendency for the pure PVA−TiO_2 system, this will also be the case for a PVA−TiO_2−Neodol 23-6.5 system. In that sense, it seems reasonable to study the influence of substituting PVA−TiO_2 with an additive and study how this substitution will work under acidic conditions. For this purpose, three coating solutions were selected for rheological characterization, as well as for fluid-bed-coating experiments. The three coating solutions were solutions A, D, and F, which have been described in the first part of this series of reports.[2] Two coating experiments were performed for each coating solution for two sets of drying force/spray rate conditions, according to Table 4.

3. Results and Discussion

3.1. Testing the Influence of Bulk Viscosity of the Coating Solutions, Stickiness, and the Influence of the Mean Droplet Diameter. Prior to the test of the influence of the bulk viscosity, the coating solutions were initially characterized with respect to rheological properties, and detailed viscosity measurements were made for each of the three coating solutions from Table 1, in terms of varying both the shear rate and the temperature. In Figure 1, the viscosities of the coating solutions have been determined as a function of shear rate at a constant temperature of 25 °C. It becomes obvious from the curves in Figure 1 that there are major differences between solutions A and G, with respect to rheological behavior. Solution A, being the PVA−TiO_2 solution, exhibits non-Newtonian behavior, because the viscosity clearly decreases as the shear rate increases. Furthermore, solution A has a viscosity that is ~20−30 times higher than that of the two other solutions. In contrast, Newtonian behavior is observed for solutions E and G, up to a shear rate of 300 s^{-1}, at which point possible eddy flow regimes occur in the rheometer. Solution E is solution A, diluted by a factor of 5, and, therefore, the graph in Figure 1 shows that it is possible to have a PVA−TiO_2 and a sodium sulfate solution with similar bulk viscosities, when the PVA−TiO_2 solution is sufficiently diluted.

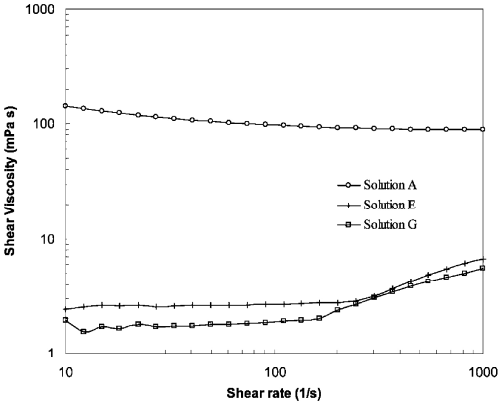

Figure 1. Viscosity of solutions A, E, and G, as a function of shear rate at a constant temperature of 25 °C.

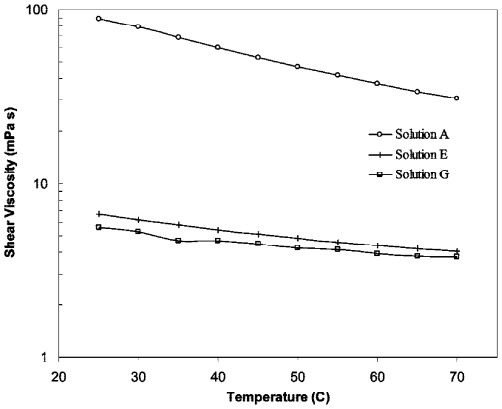

Figure 2. Viscosity of solutions A, E, and G, as a function of temperature at a constant shear rate of 1000 s^{-1}.

Similar differences in viscosities can be observed from Figure 2, where the viscosity, as a function of temperature, was determined for the three solutions for a constant shear rate of 1000 s^{-1}. For solution A, a dramatic decrease is observed, with the viscosity being more than halved when going from a solution

Table 5. Results for the Coating Experiments for the Test of the Bulk Viscosity[a]

parameter	Solution A, 10 w/w% PVA−10 w/w% TiO_2, pH 7.0	Solution E, 2 w/w% PVA−2 w/w% TiO_2, pH 7.2	Solution G, 15 w/w% Na_2SO_4−1 w/w% W80 Dextrin, pH 7.1
Series 1			
rate of agglomeration, Aggl% (w/w%)	19.1	17.8	0.9
bulk viscosity, η_{bulk} (mPa s)	46.7	4.8	4.3
spray rate (g/min)	24	24	24
Series 2			
rate of agglomeration, Aggl% (w/w%)	81.7	74.4	1.3
bulk viscosity, η_{bulk} (mPa s)	46.7	4.8	4.3
spray rate (g/min)	90	90	90
Series 3			
rate of agglomeration, Aggl% (w/w%)	91.1	88.1	1.5
bulk viscosity, η_{bulk} (mPa s)	46.7	4.8	4.3
spray rate (g/min)	120	120	120

[a] The viscosities were adapted from Figure 2 at a temperature of 50 °C. The drying force in all experiments was 18 kPa.

temperature of 25 °C up to 70 °C. The dependences of viscosity on temperature for the diluted solution (solution E) and for the sodium sulfate solution (solution G) are fairly small in comparison.

To test the influence of bulk viscosity, coating experiments were conducted in accordance with Table 1. For each batch, the weight gain was determined; for all the experiments, the weight gain varied between 19.1 and 19.7 w/w%, meaning that the spray drying losses in the experiment were quite small. The corresponding agglomeration tendencies for all nine experiments may be observed from Table 5.

First of all, it may be observed from Table 5 that, for solutions G and A, the resulting agglomeration tendencies are nicely within the regimes predicted by the suggested agglomeration regime maps in the first part of this study,[2] adding further validity to the regimes maps. Of further interest from the results in Table 5 are the differences between the resulting agglomeration tendencies for solutions A and E, and solutions E and G. Although solutions E and G have similar coating solution bulk viscosities, the resulting agglomeration tendencies are far from being similar, even though the coating process conditions were indeed similar. In fact, the agglomeration tendencies observed for the three experiments with solution E are similar to the agglomeration tendencies observed for solution A, although the similarities are not statistically significant. The observed agglomeration tendencies are only slightly smaller for coating solution A than for coating solution E. Hence, with regard to agglomeration tendency, there is no obvious advantageous effect by diluting the PVA−TiO_2 solutions. The disadvantage is more outspoken for the processing point of view, because the coating time required for solution E to apply the same dry matter content on the particle core bed is five times longer than the time required for solution A. One plausible explanation for the similar agglomeration tendencies with solutions E and A could be that, although the diluted droplets from coating solution E have a lower initial bulk viscosity, they will eventually reach the properties of the droplets of solution A as the solvent evaporates. This was studied in texture analyzer tests that studied the

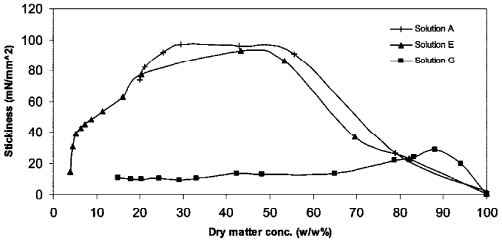

Figure 3. Stickiness, as a function of dry matter contents in the solution for solutions A, E, and G.

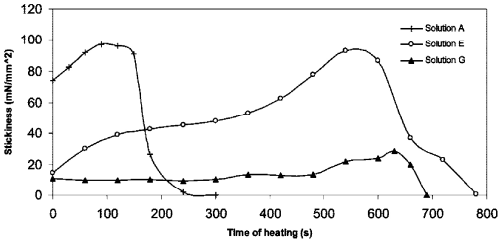

Figure 4. Stickiness as a function of the time that the heating fan was switched on for solutions A, E, and G.

stickiness for the three solutions. Figure 3 shows the stickiness as a function of the dry matter contents for the three solutions.

As observed in Figure 3, the stickiness curves for solutions A and E peak at almost the same value (∼95 mN/mm^2) and, furthermore, closely follow each other. This means that even though solution E has a solute concentration 5 times lower than that of solution A, the stickiness upon evaporation of the aqueous solvent will eventually reach an almost identical value for the two solutions. Therefore, there are no advantages of diluting the PVA−TiO_2 solution, from a stickiness point of view. Figure 3 reveals that, although the stickiness of solutions E and G are similar initially, the developments in stickiness upon solvent evaporation are quite different. For comparison with the PVA−TiO_2 solutions, the stickiness of the sodium sulfate solution (solution G) peaks several magnitudes lower, at a maximum stickiness of ∼30 mN/mm^2. Interestingly, the peak in stickiness for solution G is observed at dry matter contents of ∼90 w/w% in a narrow peak, whereas it peaks for a broader range of dry matter contents—ranging from ∼30 w/w% to 55 w/w%—for the PVA−TiO_2 solutions. This shows that, generally, the stickiness of a sodium sulfate coating solution is significantly lower than that for the PVA−TiO_2 solution, which is a plausible reason for the observed differences in agglomeration tendencies among the three solutions.

One parameter that influences agglomeration is the stickiness of a coating solution, with respect to the dry matter content. Another parameter is the time required to evaporate all moisture and thereby reach 100 w/w% dry matter content. Figure 4 shows the stickiness as a function of time that the heating fan was switched on, and Figure 5 shows the dry matter contents in the coating solution as a function of the time that the heating fan was switched on. As observed from these two figures, solution A, with the highest dry matter contents, requires the shortest time to reach complete drying. The sample with solution A has no measurable stickiness after 250 s of drying, whereas ∼700 s are required before solution G is completely dried, even though the dry matter concentration between solution A and solution

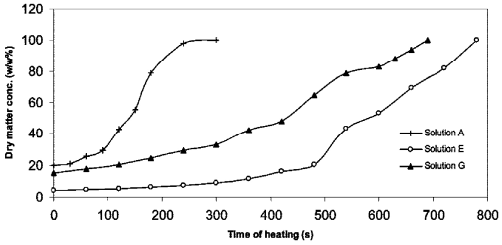

Figure 5. Dry matter contents in the solution as a function of the time that the heating fan was switched on for solution A, E, and G.

G differs by only 5 w/w%. It is obviously questionable whether or not this drying time can be compared to the actual drying time in a fluid bed, but there is reason to believe that the drying times in Figures 4 and 5 indeed are representative of what is occurring during fluid-bed processing. As expected, Figures 4 and 5 show that complete drying of solution E requires the longest time, because that solution initially has a dry matter content that is five times lower than that of solution A.

The data obtained in the test of the influence of the bulk viscosity have revealed several important things. First of all, the hypothesis suggesting similar tendencies of agglomeration when the bulk coating liquid viscosities are similar cannot be confirmed. Although the bulk viscosities of the PVA−TiO_2 solution and the sodium sulfate solution are identical, the resulting agglomeration tendencies are far from being similar. It may furthermore be concluded from the data that there is no beneficial effect regarding the dilution of the PVA−TIO_2 coating solution. In contrast, by diluting the PVA−TiO_2 solution, the stickiness eventually goes through the same magnitudes of stickiness of a more concentrated PVA−TiO_2 solution upon evaporation of the solvent, resulting in a similar agglomeration tendency.

Coating experiments to test the influence of the mean droplet diameter were performed in accordance with Table 2. For each batch, the weight gain was determined after coating. For all the experiments, the weight gain varied between 18.8 w/w% and 19.5 w/w%, indicating that the spray drying losses in the experiment were quite small. For both coating solutions, the spray drying losses were highest in the third series, where the mean droplet diameters were the smallest. The corresponding agglomeration tendencies for all six experiments may be observed in Table 6.

First of all, it may be observed from the results in Table 6 that, even though the droplet diameters are identical, the resulting agglomeration tendencies are significantly different for coating solutions A and G, irrespective of the mean droplet size levels. The agglomeration tendencies are statistical similar in the three experiments with coating solution G; the three agglomeration percentages are within the a range of ±0.88%, as determined for the sieve equipment in the first part of this study.[2] The situation is different for the experiments with coating solution A, because there are significant differences between the agglomeration percentages. In accordance with expectations, the agglomeration tendency decreases as the mean droplet size decreases.

Studies of cut-through profiles of particles coated with the same coating solution but with a different mean droplet diameter did not reveal any significant differences, with respect to droplet penetration for both of the two solutions. However, the outer coating layer morphology was affected by the mean droplet diameter. It was observed how the appearance of the coating layer became increasingly rough and raspberry-like as the mean droplet diameter increased. This tendency was most pronounced for coating solution A, because no significant differences in coating layer morphology were observed for granules coated with solution G. These findings clearly support previous results by Hede,[3] Neidel,[14] and Waldie,[15] stating that the mean droplet diameter is an important parameter regarding the final coating layer morphology. Apparently, under identical process conditions, this effect is most pronounced for polymer coatings.

Table 6. Results for the Coating Experiments Used To Test the Influence of the Mean Droplet Diameter

parameter	Solution A, 10 w/w% PVA 10 w/w% TiO_2, pH 7.0	Solution G, 15 w/w% Na_2SO_4 1 w/w% W80 Dextrin, pH 7.1
Series 1		
rate of agglomeration, Aggl% (w/w%)	18.7	0.7
mean droplet diameter, d_{32} (μm)	11.3	11.2
spray rate (g/min)	24	62
Series 2		
rate of agglomeration, Aggl% (w/w%)	16.4	0.8
mean droplet diameter, d_{32} (μm)	8.0	8.0
spray rate (g/min)	19	50
Series 3		
rate of agglomeration, Aggl% (w/w%)	13.7	0.2
mean droplet diameter, d_{32} (μm)	5.2	5.2
spray rate (g/min)	14	37

[a] Values for d_{32} were calculated using eqs 1−3. The drying force in all experiments was 18 kPa.

In conclusion, the results have shown that similar mean droplet sizes for solutions A and G clearly do not result in similar agglomeration tendencies. However, it was observed how the tendency of agglomeration in fact could be reduced by reducing the mean droplet diameter, although the reduction was only limited for solution A and not even statistically significant for solution G, having agglomeration percentages close to zero. For solution A, further reductions of the mean droplet size did lead to coated particles with a smoother coating layer, which, in addition, most likely gives granules with improved mechanical properties. Nevertheless, one problem with the reduction of the mean droplet diameter is that losses from spray drying may increase (depending on the nozzle position and drying conditions), and if the droplet diameter is reduced simply by reducing the liquid feed rate, the coating time will increase as the mean droplet diameter decreases.

3.2. Testing the Influence of pH, Colloidal Phenomena, and Additives in the PVA−TiO_2 System. To test the influence of pH in the PVA−TiO_2 system, the coating solutions were initially characterized with respect to rheological properties, and viscosity measurements were made for each of the three solutions, in terms of varying both the shear rate and the temperature, similar to the previous study. In Figure 6, the viscosities of the coating solutions have been determined as a function of shear rate at a constant temperature of 25 °C. It may be observed that all three solutions exhibit non-Newtonian behavior, because the viscosities all decrease as the shear rate increases. The largest decrease with shear rate is observed for solution C, which has the highest pH value. A general trend in Figure 6 is that the viscosity decreases as the pH decreases. Going from solution C (pH 10) to solution B (pH 4), the viscosity is more than halved. The tendencies of the curves in Figure 6 fully comply with the tendencies of the PVA−TiO_2 viscosity curves that have been determined by Chu et al.,[16] although Chu et al.[16] studied a more dilute 15 w/w% TiO_2−2.5 w/w% PVA suspension.

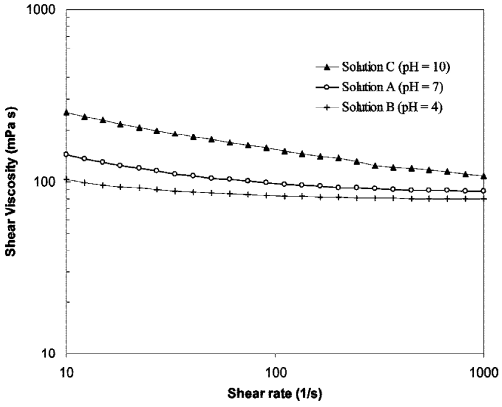

Figure 6. Viscosity of solutions A, B, and C, as a function of shear rate at a constant temperature of 25 °C.

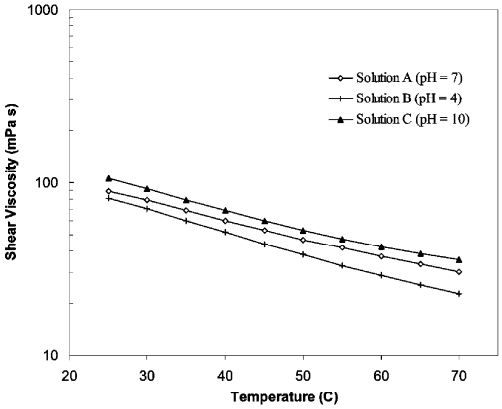

Figure 7. Viscosity of solutions A, B, and C, as a function of temperature at a constant shear rate of 1000 s^{-1}.

Similar differences in viscosities can be observed in Figure 7, where the viscosity, as a function of temperature, was determined for the three solutions at a constant shear rate of 1000 s^{-1}. For all these solutions, a dramatic decrease is observed, with the viscosity being more than four times lower when going from a solution temperature of 25 °C to 70 °C.

The results from the previous study indicated that the bulk viscosity properties cannot directly be correlated with the tendency of agglomeration. Texture analyzer studies of the stickiness for the three solutions A, B, and C reveal, in addition, that the magnitude of difference in bulk viscosity cannot be directly correlated with the difference in stickiness. Comparison of Figures 8, 9, and 10 indicates that solution C exhibits both the greatest stickiness and that it, in addition, requires the longest time to reach complete evaporation. Figure 8 reveals that the lowest stickiness is found for solution B, which has the lowest pH value, followed by solution A, which has a higher peak stickiness for a broader range of dry matter contents. The decline in stickiness for solution B is the most pronounced and the effect in stickiness upon reducing the pH is clearly observed in Figure 8. A possible reason for the reduced stickiness at pH 4 is that, at this pH level, far away from the isoelectric point, the TiO_2 particles are well-distributed among the PVA chains and therefore function more effectively as

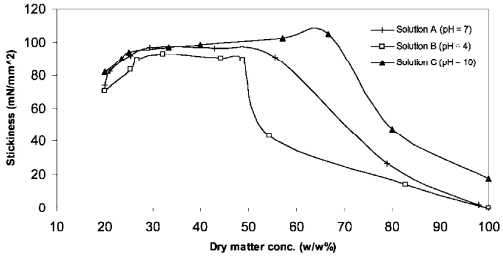

Figure 8. Stickiness, as a function of dry matter contents in the solution, for solutions A, B, and C.

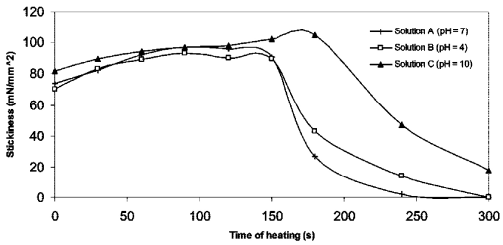

Figure 9. Stickiness, as a function of the time that the heating fan was switched on, for solutions A, B, and C.

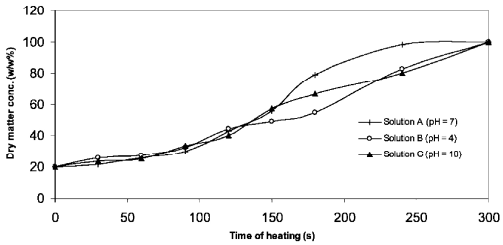

Figure 10. Dry matter contents in the solution, as a function of the time that the heating fan was switched on, for solutions A, B, and C.

antistickiness agents. Although there is only a minor difference between solutions A and B in Figure 9, in terms of stickiness, it can be observed from Figure 10 that it takes ~50 s longer to reach complete drying of solutions B and C, compared to solution A. However, the actual stickiness in these 50 s is fairly low for solution B but relatively large for solution C, as observed from Figure 9. It may thereby be concluded that there is a statistically significant effect of reducing the pH in the PVA−TiO_2 system, in terms of stickiness. What is left to investigate is whether or not this effect can be correlated with any differences in agglomeration tendency.

Coating experiments to test the influence of pH were conducted in accordance with Table 3. For each batch, the weight gain was determined after coating, and for all the experiments, the weight gain varied between 19.3 w/w% and 19.8 w/w%, indicating that the losses from spray drying in the experiments were quite small. The corresponding agglomeration tendencies for all six experiments may be observed in Table 7.

As observed from Table 7, the agglomeration tendencies decrease as the spray rate decreases, irrespective of the coating solution. Interestingly, the agglomeration tendency decreases the pH in the coating solution decreases, as was expected from the stickiness curves in Figures 8−10. Therefore, a clear relation

Table 7. Results for the Coating Experiments Used To Test the Influence of pH

parameter	Solution A, 10 w/w% PVA−0 w/w% TiO_2, pH 7.0	Solution B, 10 w/w% PVA−10 w/w% TiO_2, pH 4.0	Solution C, 10 w/w% PVA−10 w/w% TiO_2, pH 10.0
Series 1			
rate of agglomeration, Aggl% (w/w%)	18.7	12.6	27.7
spray rate (g/min)	24	24	24
Series 2			
rate of agglomeration, Aggl% (w/w%)	16.4	11.8	17.1
spray rate (g/min)	14	14	14

[a] The results for solution A were the results obtained in the test of the mean droplet diameter. The drying force in all experiments was 18 kPa.

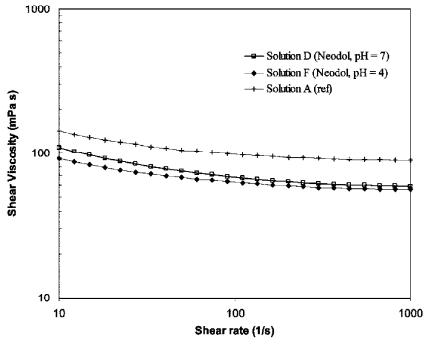

Figure 11. Viscosity of solutions A, D, and F, as a function of shear rate at a constant temperature of 25 °C.

exists between the stickiness and the resulting agglomeration tendencies. There is a difference in agglomeration tendency of ∼10 w/w% when going from solution C (pH 10) to solution B (pH 4). The difference is smallest for the lowest spray rate, indicating that, under conditions with very small droplet diameters, the stickiness effect is less pronounced. This could also arise from the fact that, with small droplets, the drying rate is so fast that the collision between sticky wet granules is significantly reduced.

Based on the results, an important conclusion may be drawn: The fact that the PVA−TiO_2 system is a colloidal system may indeed be used to suppress the tendency of agglomeration. Adjusting the pH value in the coating solution to a value far away from the isoelectric point may reduce the agglomeration tendency significantly. Although the effect of adjusting the pH value to pH 4, instead of leaving it at pH ∼7, is rather small, there is indeed a clear effect. The next step is to test whether these observed effects can be combined beneficially with additives.

Similar to previous studies, the rheological properties of the coating solutions in the test of adding additives were initially characterized, and detailed viscosity measurements were made for each of the three solutions, in terms of varying both the shear rate and the temperature. In Figure 11, the viscosities of the coating solutions have been determined as a function of shear rate at a constant temperature of 25 °C. First of all, it may be observed that all three solutions exhibit non-Newtonian behavior, because the viscosities all decrease as the shear rate increases. The effect of replacing PVA−TiO_2 with Neodol is clearly

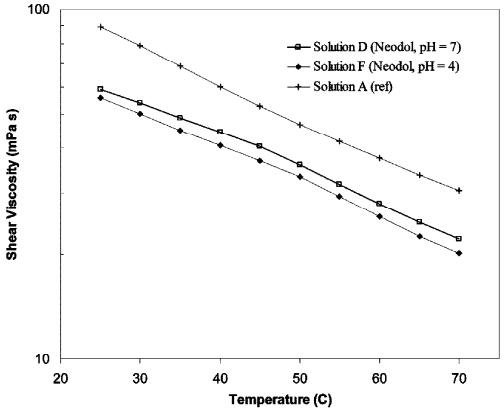

Figure 12. Viscosity of solutions A, D, and F as a function of temperature at a constant shear rate of 1000 s^{-1}.

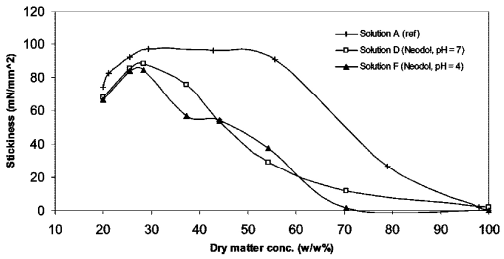

Figure 13. Stickiness as a function of dry matter contents in the solution for solutions A, D, and F.

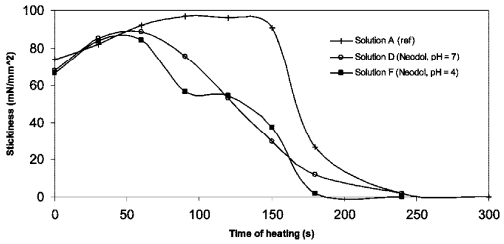

Figure 14. Stickiness as a function of the time that the heating fan was switched on for solutions A, D, and F.

observed in Figures 11 and 12, where the viscosity, as a function of temperature, was determined for the three solutions at a constant shear rate of 1000 s^{-1}. Both curves for solutions D and F are situated significantly below the curves for solution A. Interestingly, there is also an effect of reducing the pH in the PVA−TiO_2−Neodol solution, as was observed in a similar manner with the pure PVA−TiO_2 solutions in the test of the influence of pH. Texture analyzer studies of the stickiness for the three solutions in Figures 13, 14, and 15 reveal that the distribution of the stickiness follows a pattern similar to that of the viscosity curves. As observed from Figure 13, the stickiness for solution A is greater and remains greater for a broader range of dry matter contents than for the other solutions. In contrast, the stickiness for solutions D and F is less than that for solution A and, furthermore, peaks in narrow ranges before rapidly

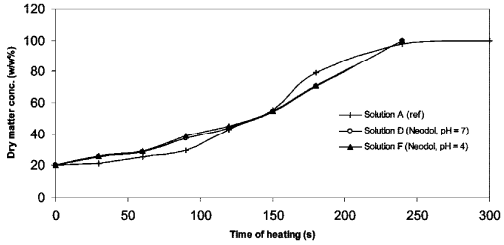

Figure 15. Dry matter contents in the solution as a function of the time that the heating fan was switched on for solutions A, D, and F.

Table 8. Results for the Coating Experiments for the Test of Lubricants

parameter	Solution A, 10 w/w% PVA−10 w/w% TiO_2, pH 7.0	Solution D, 9 w/w% PVA−9 w/w% TiO_2−2 w/w% Neodol 23-6.5, pH 7.0	Solution F, 9 w/w% PVA−9 w/w% TiO_2−2 w/w% Neodol 23-6.5, pH 4.0
Series 1			
rate of agglomeration, Aggl% (w/w%)	18.7	10.8	6.1
spray rate (g/min)	24	24	24
Series 2			
rate of agglomeration, Aggl% (w/w%)	16.4	7.7	3.9
spray rate (g/min)	14	14	14

[a] The results for solution A were the results obtained in the test of the mean droplet diameter. The drying force in all experiments was 18 kPa.

declining. Already at a dry matter content of ~45 w/w%, the stickiness is reduced by 50% for solutions D and F.

For the curves in Figures 14 and 15, there is a clear effect of substituting PVA−TiO_2 with Neodol, in terms of reduced drying time. Whereas the time for complete drying is ~50 s longer for solution A, the drying times for solutions D and F are approximately the same, meaning that, in terms of drying time, pH has no importance. This means, in conclusion, that solutions D and F dry faster than all other solutions tested, and that they, in addition, exhibit significantly lower stickiness for a shorter range of dry matter contents. What is left to investigate is whether or not these trends correlate with the resulting agglomeration tendencies when the solutions are being coated in fluid-bed processes.

Coating experiments for the test of lubricants were conducted in accordance with Table 4. For each batch, the weight gain was determined after coating, and for all the experiments, the weight gain varied between 19.2 w/w% and 19.5 w/w%, meaning that the losses from spray drying in the experiments were quite small. The corresponding agglomeration tendencies for all six experiments may be observed in Table 8.

As observed from the results in Table 8, the agglomeration tendencies generally decrease as the spray rate decreases, as has been observed for all other solutions. Of primary interest is the clear effect of replacing some of the PVA−TiO_2 with Neodol. Going from solution A to solution D, the agglomeration tendency is remarkably reduced by ~10 w/w% points (or 60%). This is a significant reduction and it correlates well with the trends observed from the stickiness and viscosity measurements. The effect of reducing the pH in the PVA−TiO_2−Neodol system is clearly observed from Table 8. In fact, the reduction in agglomeration tendency is roughly 5 w/w% points just by reducing pH from 7 to 4. As a support for this observation, the effect of reducing the pH is similar to the effect on agglomeration for a simple PVA−TiO_2 solution observed in the test of the influence of pH. Interestingly, by substituting some of the PVA−TiO_2 with Neodol and further reducing the pH value to 4, it is possible to reduce the tendency of agglomeration significantly. The agglomeration tendency of 3.9 w/w% in Table 8 is fairly close to the agglomeration percentage of 0.9 w/w% observed for the sodium sulfate solution in the test of the bulk viscosity, processed under identical conditions. Notably, this is achieved even though the bulk viscosity of solution F is ~6 times greater than that of the sodium sulfate solution. This further supports the previous conclusion that it is the stickiness and the time length to reach complete solvent evaporation and zero stickiness, and not the bulk viscosity of a sprayed liquid, that is important for the tendency of agglomeration.

Based on the test results, it may be concluded that there is a significant effect of replacing PVA−TiO_2 in equal amounts by a lubricant as Neodol. The reduced stickiness effect of reducing the pH to a value far from the isoelectric point can also be beneficially exploited in a PVA−TiO_2−Neodol system. In terms of this observation, the tendency of agglomeration for a PVA−TiO_2−Neodol coating process can be reduced to a level close to the tendency of agglomeration for a sodium sulfate coating process, processed under similar conditions.

4. Summary and Conclusion

This paper, which is the second part of this series, has continued the investigation from the first part of this study,[2] with regard to why polymer and inorganic salt solutions cannot be processed under similar fluid-bed process conditions to result in similar tendency of agglomeration. To dig deeper into possible causes, several detailed studies (both fluid-bed coating experiments and characterization of the coating solutions) were performed, treating many different process and coating formulation phenomena.

The results show that it is not the bulk viscosity of a coating solution that has the primary importance regarding the tendency of agglomeration, but rather that it is the maximum stickiness obtained during solvent evaporation and the length of the stickiness period that is important. The stickiness may thus not be correlated directly with bulk viscosity. In the comparison of two different coating formulations, it is thereby impossible to predict the tendency of agglomeration based on the bulk viscosities alone. In accordance with previous studies by Hede,[3] on the other hand, it was observed that the bulk viscosity indeed plays an important role with regard to the degree of droplet penetration into the coated core and the morphology of the outer coating layer. As the coating solution bulk viscosity increased, the level of droplet penetration decreased and the final coating layer became increasingly rough and raspberry-like in appearance.

Following previous studies by Schæfer and Wørts[4] and Hede et al.,[13,17] it was further observed how similar mean droplet sizes for the two solutions did not result in similar agglomeration tendencies. However, it was observed how the tendency of agglomeration clearly decreased as the mean droplet size decreased, but also that the two types of coating solutions responded differently in the tendency of agglomeration for identical droplet sizes. For example, the PVA−TiO_2 solution clearly responded with increased agglomeration percentage upon a small increase in the mean droplet size, whereas the agglomeration tendency for the salt solution was hardly affected in the tested range of the mean droplet sizes. This indicates, once again, in accordance with qualitative studies by Neidel,[14] that the coating process of salt coatings is far less sensitive towards agglomeration than polymer coating processes.

The colloidal phenomena in the PVA−TiO_2 suspension were additionally studied, and it was observed how the viscosity, stickiness, time of stickiness, and agglomeration tendency all could be reduced by reducing the pH to a value far from the isoelectric point. The results were in close agreement with previous studies by Chu et al.,[16] indicating that, for coating processes with PVA−TiO_2 suspensions, the pH value should be close to 4. The reduction in pH, most likely, would also be beneficial, with regard to using a coated enzyme granule for detergent applications, because a low pH is known to improve the enzyme stability.[2]

The test of lubricants clearly indicated the advantages of replacing equal amounts of PVA TiO_2 with Neodol. By replacing 10% of the PVA, and an equal amount of the TiO_2, with Neodol, the resulting agglomeration tendency could be reduced by ~10 w/w%. The results furthermore revealed that colloidal phenomena in the PVA−TiO_2 suspension were not significantly affected by the introduction of Neodol. By reducing the pH value to 4 in the PVA−TiO_2−Neodol system, it was finally possible to arrive at an agglomeration tendency of <5 w/w%, which is within range of the agglomeration tendency for a salt solution coating process processed under similar conditions.

In conclusion, the polymer coating process is much more sensitive than the process of coating with inorganic salts. First of all, the coating process cannot be controlled, in terms of process parameters alone. Correct choices of process conditions are even more important, because there is only a narrow regime in which there is a possibility that the agglomeration tendency can be kept low. Most likely, this regime is different for each type of polymer in solution, because properties such as the glass-transition temperature, molecular weight, and degree of hydrolysis most likely also play a role. The influence of these properties were not tested in the present study but have been tested by other researchers.[18] The polymer coating formulation is also of primary importance for the agglomeration tendency. The fact that a polymer solution with dispersed inorganic particles constitutes a colloidal system requires knowledge of surface and electrostatic phenomena for the correct optimization of the formulation. This also means that the correct preparation (order of dispersion, temperature range, stirring, correct heating ramping, etc.) of the coating liquid is important. The strict requirements for correct choices of process and formulation properties altogether clearly make the polymer coating process a challenging exercise. In the third part of this study,[19] an attempt is made to correlate the measurement of stickiness with the observed agglomeration tendencies to obtain a parameter that could predict the tendency of agglomeration a priori, without having to perform the fluid-bed coating experiments.

Acknowledgment

This project was performed in collaboration with Novozymes A/S, who also financially supported the project. Peter Dybdahl Hede is a member of the Novozymes Bioprocess Academy as well as the MP_2T Graduate School in Chemical Engineering at the Department of Chemical and Biochemical Engineering, Technical University of Denmark, funded by the Danish Technical Research Council, the European Union, the Nordic Energy Research, Dong Energy A/S, Vattenfall A.B., F L Smidth A/S, and Public Service Obligation funds from Energinet.dk and the Danish Energy Research program.

Nomenclature

d_{32} = mean Sauter droplet diameter (μm)
$d_{orifice}$ = diameter of the liquid orifice at the liquid exit (m)
$\dot{m}_{liq}$ = mass rate of liquid (g/s)
$\dot{m}_{air}$ = mass rate of atomization air (g/s)
Oh = Ohnesorge number
v_{rel} = difference between the nozzle atomizing air velocity and the liquid velocity at the nozzle exit (m/s)
We_{air} = air Weber number

Greek Symbols

ρ_{air} = atomizing air density (kg/m^3)
ρ_{liq} = liquid density (kg/m^3)
η_{bulk} = bulk viscosity (cP)
η_{liq} = liquid viscosity (cP)
γ_{liq} = liquid surface tension (kg/s^2 or dyne/cm)

Literature Cited

(1) van Ee, J. H.; Misset, O.; Baas, E. J. *Enzymes in Detergency*; Surfactant Science Series, Vol. 69; Marcel Dekker: New York, 1997.
(2) Hede, P. D.; Jensen, A. D.; Bach, P. Fluidized-Bed Coating with Sodium Sulfate and PVA−TiO_2, 1. Review and Agglomeration Regime Maps. *Ind. Eng. Chem. Res.*, **2009**, *48*, XXXX.
(3) Hede, P. D. Fluidised Bed Coating and Granulation, M.Sc. Thesis, Department of Chemical Engineering, CHEC Research Center, Technical University of Denmark, Lyngby, Denmark, 2005, pp 1−227.
(4) Schæfer, T.; Wørts, O. Control of fluidized bed granulation. II. Estimation of droplet size of atomized binder solutions. In *Archives of Pharmaceutical and Chemical Science*, 5th Edition; Sonderdruck, 1977; pp 178−193.
(5) Rajsharad, C.; Kamble, S. Majumdar & Co. PVA Based Film Coating and Film Coating Compositions, WO Patent 2006/11980 A2, 2006.
(6) Hede, P. D.; Jensen, A. D.; Bach, P. Two-fluid spray atomisation and pneumatic nozzles for fluid bed coating/agglomeration purposes: A review. *Chem. Eng. Sci.* **2008**, *63* (14), 3821–3842.
(7) Hinds, W. C. Aerosol Technology: Properties. In *Behaviour and Measurement of Airborne Particles*, 2nd Edition; John Wiley & Sons: New York, 1999.
(8) Mulhem, B. Effect of solid particle characteristics on suspension atomization. *Atomization Sprays* **2003**, *133*, 321–343.
(9) Mulhem, B.; Schulte, G.; Fritsching, U. Solid−liquid separation in suspension atomisation. *Chem. Eng. Sci.* **2006**, *61*, 2582–2589.
(10) *Engineer's Guide to Spray Technology*; Spraying Systems Co.: Wheaton, IL, 2000.
(11) Walzel, P. Liquid atomisation. *Int. Chem. Eng.* **1993**, *33* (1), 46–60.
(12) NEODOL 23-6.5 Product Specification Sheet, Shell Chemicals Europe, Rotterdam, The Netherlands, 2005; pp 1−2.
(13) Hede, P. D.; Jensen, A. D.; Bach, P. Top-spray fluid bed coating: Scale-up in terms of relative droplet size and drying force. Powder Technol., **2008**, *184*, 3, 312−332.
(14) Neidel, B. Water-soluble polymer fluid bed coatings, M.Sc. Thesis, Department of Chemical Engineering, CHEC Research Center, Technical University of Denmark, Lyngby, Denmark, 2007, pp 1−123.
(15) Waldie, B. Growth mechanism and the dependence of granule size on drop size in fluidized-bed granulation. *Chem. Eng. Sci.* **1991**, *46*, 2781–2785.
(16) Chu, W. B.; Yang, J. W.; Liu, T. J.; Tiu, C.; Guo, J. The effect of pH, molecular weight and degree of hydrolysis of poly(vinyl alcohol) on slot die coating of PVA suspensions of TiO_2 and SiO_2. *Colloids Surf., A* **2007**, *302*, 1–10.
(17) Hede, P. D.; Jensen, A. D.; Bach, P. Validation of the Flux number as scaling parameter for top-spray fluid bed systems. *Chem. Eng. Sci.* **2008**, *63*, 815–828.
(18) Arnold, R. E.; Becker, N. T.; Boston, M. G.; Mansikkamaki, A.; Wendt, D. J. (Genencor International). Coated Enzyme Containing Granule, International Patent WO 93/07263, 1993.
(19) Hede, P. D.; Jensen, A. D.; Bach, P. Fluidized-Bed Coating with Sodium Sulfate and PVA−TiO_2, 3. The Role of Tackiness and the Tack Stokes Number. *Ind. Eng. Chem. Res.*, **2008**, *48*, XXXX.
(20) Lefebvre, A. H. *Atomization and Sprays*; Hemisphere Publishing Corporation: New York, 1989.

Received for review June 16, 2008
Revised manuscript received October 3, 2008
Accepted November 20, 2008

IE800941X

Ind. Eng. Chem. Res. **XXXX,** *xxx,* 000 **A**

Fluidized-Bed Coating with Sodium Sulfate and PVA−TiO_2, 3. The Role of Tackiness and the Tack Stokes Number

Peter Dybdahl Hede,[†,‡] Poul Bach,[‡] and Anker D. Jensen*[,†]

CHEC Research Center, Department of Chemical and Biochemical Engineering, Technical University of Denmark, Building 229, DK-2800 Kgs. Lyngby, Denmark, and Solid Products Development, Novozymes A/S, Smørmosevej 11, DK-2880 Bagsværd, Denmark

In the first and second parts of this study [Hede, P. D.; Bach, P.; Jensen, A. D. *Ind. Eng. Chem. Res.* **2009**, *48*, XXXX and XXXX], agglomeration tendencies were studied for two types of coatings: sodium sulfate and PVA−TiO_2. Results showed that the agglomeration tendency is always lower for the salt coating process than for the polymer coating process, under similar process conditions, because of differences in stickiness, not because of differences in bulk viscosities. It was further shown that it is possible to optimize the PVA−TiO_2 coating formulation and process to achieve a low tendency of agglomeration, similar to the salt coating process. With the PVA−TiO_2 coating liquid layer thicknesses encountered during these fluid-bed coating processes, agglomeration seems to be governed primarily by liquid surface phenomena. A modification to the original viscous Stokes number is suggested in the present paper, which defines the Stokes number in terms of the work needed to reach maximum tack instead of the viscous dissipation energy. The new tack Stokes number correlates well with the observed levels of agglomeration and, as a promising feature, proportionality is observed between the agglomeration weight percentage and the difference between the new tack Stokes number and the critical tack Stokes number.

1. Introduction

The fluid-bed coating process involves the spraying of an atomized coating liquid onto a fluidized core particle bed, hereby encapsulating the core particles in shell−layer structures. In such a process, the desired product consists of unagglomerated individual carrier particles, each coated homogeneously, with the coating material being typically either a polymer or inorganic salt solution. As the coating droplets travel from the two-fluid nozzle outlet and impact the core particles, small patches of wetted spots are being formed at the core particle surfaces. It is well-known that if two particles collide with a contact point at wetted spots, there is a chance that the two particles will stick together permanently. This phenomenon is known as agglomeration and is unwanted in fluid-bed coating processes, but it is desired in certain other types of fluid-bed processes.[1] In any case, control of the agglomeration tendency is essential in industrial fluid bed processing. If possible, an a priori determination of the agglomeration tendency is desired, in which it becomes possible to predict the agglomeration tendency of a fluid-bed process without having to perform the fluid-bed experiments.

The results from the first part of this study[2] and the second part of this study[3] have revealed that the polymer coating process is much more sensitive than the coating with inorganic salts, with respect to agglomeration tendency. From these studies, the agglomeration tendency seems to correlate closely with the stickiness of the polymer coating solution. Nevertheless, stickiness is not an easy property to quantify and measure, and, so far, no suggestion has been proposed to incorporate stickiness into a parameter that is capable of describing the tendency of agglomeration. In this third part of the study, the objective is to try to correlate the measurement of stickiness with the observed agglomeration tendencies from the second part of this study, to obtain a parameter that could predict the tendency of agglomeration a priori. The equipment and coating solutions used in the present paper may be found in the first part of this study.[2]

* To whom correspondence should be addressed. Tel.: +45 4525 2841. Fax: +45 4588 2258. E-mail address: aj@kt.dtu.dk.
† CHEC Research Center, Department of Chemical and Biochemical Engineering, Technical University of Denmark.
‡ Solid Products Development, Novozymes A/S.

2. Viscous Stokes Theory: Agglomeration of Nondeformable Granules

Only a limited number of theoretical models are available in the literature for predicting whether or not the collision of two wetted particles will either result in permanent agglomeration or in rebound, as reviewed by Hede.[4] However, none of them include stickiness but, instead, focus on viscous phenomena. The models typically address the situation in which nondeformable particles collide and agglomerate. Under low-agitative conditions, such as those in the fluid bed, particles are assumed to agglomerate via viscous dissipation in the surface liquid before the core surfaces contact.[5] As the two particles approach each other, first contact is made by the outer liquid layer. The liquid will subsequently be squeezed out from the space between the particles to the point where the two solid surfaces will touch. A solid rebound will occur based on the elasticity of the surface, characterized by a coefficient of restitution e. The particles will start to move apart and coating liquid will be sucked into the interparticle gap, up to the point where a liquid bridge will form. This bridge will either break due to further movement in the bed or solidify, leading to permanent agglomeration.[6] In the principle described, the chance of permanent particle agglomeration will occur only if there is a liquid layer present at the surface of the colliding particles. This growth principle continues until insufficient liquid is available at the surface to bind new particles.[7]

Realizing the importance of liquid layer properties for the tendency of agglomeration in fluid-bed processes, the viscous Stokes theory has been suggested by Ennis et al.[8] as a way to express the likelihood of permanent coalescence between two

10.1021/ie800942c CCC: $40.75

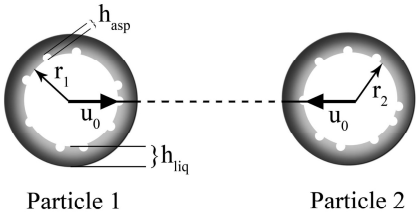

Figure 1. Schematic of two colliding particles, each of which is covered by a viscous liquid layer of thickness h_{liq}. (Based on Ennis et al.[8])

nondeformable spherical particles, each covered equally with a liquid layer of height h_{liq}. The simplified situation can be observed in Figure 1. The outcome of the collision of the two particles is determined by the ratio of the initial kinetic energy of the system (relative to the center of mass) and the energy dissipated from the viscous force in the liquid bridge and in the particles. This can be expressed analytically by the definition of the viscous Stokes number (St_v), according to[8]

$$St_v = \frac{\text{initial kinetic energy}}{\text{dissipated viscous energy in the liquid bridge}} = \frac{0.5 m_{harm}(2u_0)^2}{2F_{vis}h_{liq}} \quad (1)$$

where F_{vis} is the viscous force due to the liquid bridge, defined according to

$$F_{vis} = \frac{3\pi\eta_{liq} r_{harm}^2 u_0}{2h_{liq}} \quad (2)$$

and the harmonic mean mass and diameters between two different particles is given by

$$r_{harm} = \frac{2r_1 r_2}{r_1 + r_2} \quad (3)$$

and

$$m_{harm} = \frac{2m_1 m_2}{m_1 + m_2} \quad (4)$$

The parameter η_{liq} is some time-average liquid viscosity of the granulation process, and u_0 is the initial collision velocity. The initial collision velocity is not easily obtainable, because of the chaotic pattern of motion for the particles in fluid beds. A rough estimate based on the bubble rise velocity, v_{bu}, has been presented by Ennis et al.:[8]

$$u_0 \approx \frac{12 v_{bu} r_{harm}}{d_{bu}\delta^2} \quad (5)$$

where d_{bu} is the gas bubble diameter and δ the dimensionless bubble space, which is defined as the axial fluid-bed bubble spacing divided by the fluidization gas bubble radius. The gas bubble diameter and spacing can be estimated by the dimensions of the air distributor plate, or determined using experiments, whereas the bubble rise velocity can be determined according to the formula devised by Davidson and Harrison:[9]

$$v_{bu} = v_a - v_{mf} + 0.711(g d_{bu})^{0.5} \quad (6)$$

Based on simple energy considerations, the viscous Stokes theory shows that, if the viscous Stokes number is smaller than a critical value St_v^*, collisions between particles result in permanent agglomeration. If $St_v \gg St_v^*$, particles will rebound, because the total incoming energy is greater than that dissipated during collision.[10] The critical viscous Stokes number St_v^* is given by[8]

$$St_v^* = \left(1 + \frac{1}{e}\right) \ln\left(\frac{h_{liq}}{h_a}\right) \quad (7)$$

where h_a is the height of surface asperities and e is the coefficient of restitution.[8] The viscous Stokes number (St_v) and the critical viscous Stokes number (St_v^*) are both derived in the Appendix, because this was not done in the paper that was written by Ennis et al.[8]

If agglomeration occurs during fluid-bed coating, St_v increases as the granules grow in size. This leads to three possible situations. The first so-called *noninertial regime* occurs when $St_v \ll St_v^*$. All collisions result in successful agglomeration, regardless of the size of the colliding granules, granule kinetic energy, or binder viscosity. As the granules grow larger, the *inertial regime* occurs when $St_v \approx St_v^*$. The likelihood of agglomeration now is dependent on the size of the colliding granules and the kinetic energy of the granules, and liquid viscosity begins to play a role.[11,12] Equations 1 and 3 show that the collision between two small granules or one small granule and one large granule is more likely to result in permanent agglomeration than the collision between two large granules, because of their size (r_{harm}) and, thereby, the magnitude of St_v versus St_v^*. This is a convenient way to understand why small particles agglomerate into larger particles.[6] Eventually, the system enters the *coating regime* when $St_v \gg St_v^*$. Here, all collisions between granules are unsuccessful, in terms of agglomeration, and any further increase in St_v will maintain the size of the granules.[6,11] The existence of the three regimes has been proven experimentally in different types of granulators.[8,13]

Agglomeration is promoted by low St_v values and high value St_v^* values. For instance, increasing the granule liquid content will increase the liquid layer thickness (h_{liq}), which will increase St_v^* and, hence, increase the likelihood of successful agglomeration. The effect of the liquid viscosity is not easily predictable in that, e.g., increasing the value of η_{liq} (reducing St_v) alters the coefficient of restitution e, which also decreases St_v^*.[11]

Although St_v and St_v^* are important parameters in the prediction of agglomeration, they are only valid for predicting the maximum size of granules that can coalesce. The parameters state nothing about the rate of agglomeration. However, different authors have shown that fast growth rates are attributed to the noninertial regime whereas slower growth is attributed to St_v values close to or above St_v^*. With fast growth rates, systems have a tendency to be collision-limited.[8,14]

Although focusing on liquid viscosity rather than tack or work of adhesion, the viscous Stokes theory does account for the influence of surface asperities, i.e., if the parameter h_a increases (because of increased roughness of the core particle surface), the critical viscous Stokes number St_v^* will decrease, allowing a smaller range of St_v values for permanent agglomeration. Analogously, an increased liquid layer (increasing h_{liq} values) result in larger St_v^* values meaning that more particles will agglomerate. More information on the viscous Stokes theory may be found in the work of Ennis et al.,[8] Tardos and co-workers,[5,10] and Salman et al.[3]

3. Testing Possible Causes for Differences in Processing

3.1. The Tack Stokes Number. The conclusions from the experiments in the first part of this study[2] and the second part

of this study,[3] especially regarding the viscosity and stickiness, may be used to suggest a modification to the original viscous Stokes number. Instead of defining St_v based on the viscous energy dissipated in the liquid bridge, the suggestion is to define a tack Stokes number (St_{tack}) based on the tack work measured in the probe tack test. Analogous to the original viscous Stokes number, the modified Stokes number relates the initial kinetic energy of the colliding particles to the energy (work) required to separate the particles upon rebound. However, the separation energy is suggested to be related to tack-related forces, rather than viscous forces. If the kinetic energy is larger than the work done by the tack force, separation between the particles will occur. Otherwise, permanent agglomeration will be the result.

For most materials, it would be reasonable to believe that the liquid contact area between the rebounding particles will be reduced significantly with separation distance until the maximum tack force is reached and breakage occurs. Such effects are often related to fibril elongation and are often observed with engineering materials, including some polymers.[15] In that case, it would be erroneous to relate the maximum tack force simply to the initial wetted area. For pressure-sensitive adhesives, however, elongation at maximum stress is typically far less than 50% of the initial sample length.[16] This means that, when subjected to strain, it is reasonable to assume that pressure-sensitive adhesives rapidly reach the maximum break force without a significant reduction in contact area in a simple Hook's law manner. This "Velcro effect" that is observed with PVA−TiO_2 solutions is believed to result from the fact that bonding with pressure-sensitive adhesives is a local surface phenomena where only polymer chains present at the surface become entangled with the surface of the contact material. Assuming that this behavior is also the case for the PVA−TiO_2 coating solutions, the suggestion is to define the tack energy as

$$\text{Work to reach maximum tack} = \int_{s=0}^{s=\kappa(h_{liq}-h_a)} F_{tack}\,ds \approx 0.5F_{max,tack}\int_{s=0}^{s=\kappa(h_{liq}-h_a)} ds \approx 0.5F_{max,tack}\kappa(h_{liq}-h_a) \quad (8)$$

Assuming that the tack force increases linearly from zero to the maximum, the first integral in eq 8 can be approximated by the second integral, using trapezoid integration. The maximum tack force is treated as a constant, and the factor of 0.5 ensures that an average value is used to calculate the work to reach maximum tack. Defining the maximum tack energy according to eq 8 assumes that it requires only a separation distance of $\kappa(h_{liq} - h_a)$ to reach the maximum tack and, thereby, the distance at which breakage of the liquid bridge occurs.

The factor κ accounts for the fact that tack work is not the multiplication product of the maximum tack force and the full liquid thickness ($h_{liq} - h_a$) but rather the work done over a somewhat smaller length. This is due to the assumption that tack is a surface phenomenon and not a bulk phenomenon. According to the estimations by Ukei et al.,[16] the largest chance of liquid bridge breakage will occur at a distance of 30%−50% of the term ($h_{liq} - h_a$), depending on the type of adhesive. In this work, a factor of $\kappa = 0.45$ has been chosen. A value of 1 has also been tested, giving little deviation, so this is not a critical parameter. Based on these assumptions, the modified Stokes number is suggested to be defined as

$$St_{tack} = \frac{\text{initial kinetic energy}}{\text{tack work}} = \frac{0.5m_{harm}(2u_0)^2}{2\times 0.5F_{max,tack}\kappa(h_{liq}-h_a)\phi} = \frac{2m_{harm}{u_0}^2}{F_{max,tack}\kappa(h_{liq}-h_a)\phi} \quad (9)$$

where φ is a correction factor that is suggested to be the ratio between the multiplication product of the collision velocity (u_0) and the wetted area of the liquid bridge contact point ($A_{liq,wet}$), and the multiplication product of the probe test speed used to measure the tack (u_{test}) and the tack probe contact area (A_{con}), according to

$$\phi = \left(\frac{u_0}{u_{test}}\right)\left(\frac{A_{liq,wet}}{A_{con}}\right) \quad (10)$$

By introducing the correction factor φ, it is assumed that the tack force relates linearly to the area of contact, as well as linearly to the velocity at which two particles collide. Such assumptions are reasonable, based on previously observed tendencies with pressure-sensitive adhesives, where the yield stress of polymers is known to increase as the strain rate increases.[15,17] To minimize the influence of φ, the probe test speed should be chosen to be as similar to u_0 as possible.

Values for parameters e and h_a, which are needed for the calculation of the critical viscous Stokes number St_v* (valid as reference for the original viscous Stokes number only), were adapted for the given core materials from Hede.[18] Estimates of the liquid layer thickness h_{liq} were based on contact angles, according to the following equations, which have been adapted from the published works of Clarke et al.[19] and Thielmann et al.[20]

$$h_{liq} = A_{liq,wet}\left(\frac{1-\cos\theta}{\sin\theta}\right) \quad (11)$$

where

$$A_{liq,wet} = \left[\left(\frac{3V_{dr}}{\pi}\right)\left(\frac{\sin^3\theta}{2-3\cos\theta+\cos^3\theta}\right)\right]^{1/3}$$

Here, V_{dr} is the volume of a single droplet and $A_{liq,wet}$ is the wetted area. Assuming monodisperse droplets with diameters of d_{32}, Sauter mean droplet diameters for the given coating conditions were estimated using the formula suggested by Mulhem and co-workers[21,22] (please refer to the second part of this series[3]). The collision velocity u_0 should ideally be represented by a distribution of velocities; however, similar to the model by Ennis et al.,[8] the average collision velocity for a fluid bed is estimated using eq 5.

Similar to the original viscous Stokes number, it is relevant to obtain a critical Stokes number as the cutoff value between agglomeration and no agglomeration. The original critical Stokes number given by eq 7 cannot be used for comparison with the tack Stokes number, because it is derived based on viscous dissipation (please refer to the Appendix). Analogous to eq A.12 in the Appendix, it follows from the definition of the tack Stokes number in eq 9 that the result of wet-particle collision will be agglomeration if the tack work is greater than the initial kinetic energy ($St_{tack} < 1$); conversely, no agglomeration will result if $St_{tack} > 1$. Hence, the critical tack Stokes number can be represented to simply be 1.

To compare the viscous Stokes theory with the tack Stokes theory, the parameters were made dimensionless, with respect to the related critical Stokes number, according to eqs 12 and 13. This is done to allow the two Stokes approaches to be compared in a similar and fair manner. A simple comparison of ($St_v - St_v$*) with ($St_{tack} - 1$) gives a worse fit of the original viscous Stokes theory to a straight line, but it does make comparing the performance of the two approaches in a fair manner difficult, because the x-axis length scales are different. Hence, a comparison using eqs 12 and 13 is a fairer option:

$$\frac{St_v - St_v^*}{St_v^*} \tag{12}$$

and

$$\frac{St_{tack} - 1}{1} \tag{13}$$

Using eqs 1 and 9, respectively, the original and tack Stokes number, as well as the critical viscous Stokes number (using eq 7), were calculated for all coating solutions processed at a drying force of 18 kPa and are plotted for solutions A−F as functions of the resulting agglomeration tendencies, according to Figures 2 and 3, using the relations described in eqs 12 and 13. For the original viscous Stokes number, the values for η_{liq} were chosen as a "time-averaged" viscosity, as suggested by Ennis et al.[8] The calculated viscous Stokes numbers for experiments with solution G at a drying force of 18 kPa were not included in Figures 2 and 3 as the theory is known to be less precise when the agglomeration percentages approaches zero.[8,10] Calculated values for the difference between St_v and St_v^* for solution G (using the tack Stokes number) in experiments with agglomeration percentages of ≤1.5 w/w% resulted in values in the range of 15−35, indicating that viscous Stokes numbers that have been estimated based on the mean values of process variables is not sufficient to determine exactly when the particles will start to agglomerate.

Although some scattering is observed in both figures, especially with the low agglomeration percentages, the overall tendency is clear from Figures 2 and 3, namely, the larger the difference between the Stokes number and the critical Stokes number, the greater the agglomeration tendency, in accordance with the theories proposed by Ennis et al.[8] A comparison between the data points in Figures 2 and 3 reveals several important things. First of all, the tack number seems to predict the agglomeration tendency linearly across the entire range with a trend line that has an R^2 value of ∼1. This R^2 value refers to the data point adaption to the ((0,0);(−1,100)) line and, thus, not to a best linear fit.

Similarly, the R^2 value for the viscous Stokes numbers is as low as 0.65, with many of the points below the straight line. For the original viscous Stokes number, there seems to be no apparent linear relationship between the agglomeration tendency and $(St_v - St_v^*)/St_v^*$. In addition, the tack relation seems to be capable of predicting the agglomeration tendency equally well, regardless of whether the agglomeration tendency is high or low. Being a simple theory based on average values for a range of process parameters such as droplet diameter, droplet volume, tack force, collision velocity, and more, the tack Stokes number seems to be capable of providing improved first guidelines for the outcome of the fluid-bed coating process, in terms of agglomeration tendency. The observed good linearity seems promising, with respect to implementing the tack Stokes number in granulation models. Predicting the agglomeration tendency using either the tack or the original viscous Stokes number will, in any case, require a priori measurements of the tack force or viscosity, respectively. Tack gives better estimates of the agglomeration tendency, but at the cost of more experimental work, because tack measurement is not yet a standard technique, as is the measurement of viscosity.

To investigate the influence of the choice of viscosity for the calculation of the original Stokes number, the bulk viscosity values adapted from the second part of this study[3] at 45 °C were inserted into eq 1. These values are the lowest viscosity values that the coating droplets experience during

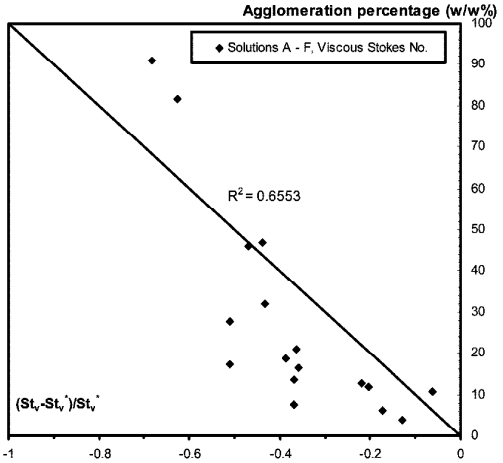

Figure 2. Resulting agglomeration tendencies obtained in coating experiments for solutions A, B, C, D, E, and F, as a function of the relation $(St_v - St_v^*)/St_v^*$.

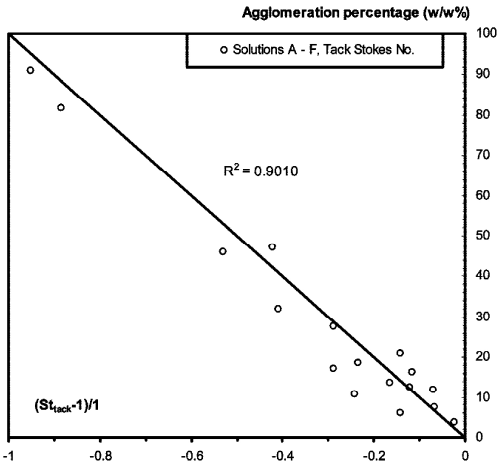

Figure 3. Resulting agglomeration tendencies obtained in coating experiments for solutions A, B, C, D, E, and F, as a function of the relation $(St_{tack} - 1)/1$.

their lifetime; however, interestingly, the tendency closely followed that observed in Figure 2. The Stokes number obviously increased as the viscosity decreased, but the difference between the Stokes number and the critical Stokes number remained more or less unaffected. This is due to the fact that, with the tested core material and the tested process conditions, the values of the critical Stokes numbers St_v^* are significantly higher than the calculated St_v numbers. This indicates that, with particles coated with thin liquid layers of polymers, it is not the viscous forces in the droplet bulk phase that are of major importance, but rather the phenomena in the boundary between the thin liquid and the solid particle surfaces, which are measured well in the probe tack test. If, however, process conditions were chosen differently from those in the present study or if, for example, the core materials were nonporous glass ballotini cores without

significant surface asperities and/or surface pores, the liquid layer thickness could be larger than in the present study, meaning that the viscous forces would be likely to dominate over the tack surface forces, with respect to agglomeration. Under such conditions, it is likely that the original viscous Stokes number would be a better way of predicting the agglomeration tendency than the tack Stokes number. Therefore, the tack Stokes number is not likely to always be a better way of predicting the agglomeration tendency. Whether the viscous or tack forces dominate with respect to agglomeration seems to be dependent especially on the liquid layer thickness and the type of coating material (e.g., polymer or inorganic salt coating).

4. Summary and Conclusion

The introduction of a tack Stokes number (St_{tack}), which combines the particle properties and fluidization conditions with the maximum tack force, was observed to result in a parameter relationship that is capable of providing improved first guidelines for the agglomeration tendency during fluid-bed coating, compared to the original version of the Stokes viscosity number (St_v). A possible reason is the influence of the liquid layer thickness. In the fluid-bed coating process, the liquid layer is very thin, meaning that any agglomeration tendency is due to liquid surface phenomena and not due to bulk viscous phenomena. These surface phenomena seem to be well-predicted by the probe tack test, which gives reason to believe that the tack Stokes number is a better way to predict the agglomeration tendency for the coating systems tested in this paper. In any case, however, the Stokes theory does not take into account the clear effect of the drying force, which also has been observed in the first part of this study,[2] but for the comparison of coating processes processed under similar drying force values, the practical and simple, yet intuitive, principle of the tack Stokes number could be a useful first principle. The observed proportionality between (St_{tack} − 1)/1 and the agglomeration tendency is a promising feature of the modification to the original Stokes number also in a modeling perspective. Even so, more results are needed for a full validation of the tack Stokes number, but, however, the results in the present study have shown that it is possible to address the polymer coating process semiquantitatively and, thus, be able to reduce the agglomeration tendency to an acceptable level and, at the same time, have a high-intensity coating process.

Acknowledgment

This project was performed in collaboration with Novozymes A/S, who also financially supported the project. Peter Dybdahl Hede is a member of the Novozymes Bioprocess Academy as well as the MP_2T Graduate School in Chemical Engineering at the Department of Chemical and Biochemical Engineering, Technical University of Denmark, funded by the Danish Technical Research Council, the European Union, the Nordic Energy Research, Dong Energy A/S, Vattenfall A.B., F L Smidth A/S, and Public Service Obligation funds from Energinet.dk and the Danish Energy Research program.

Appendix: Derivation of the Stokes Viscous Number and the Stokes Critical Viscous Number

Consider two individual spherical granules with masses and radiuses m_1, r_1 and m_2, r_2, respectively, as indicated in Figure 1. Assume that the two granules are approaching each other at an initial relative velocity of $2u_0$ and that each are covered with a binder layer thickness h_{liq}. As the individual liquid layers come into contact, a dynamic pendular bridge will form between the colliding granules which are now separated by a gap of distance $2h_{liq}$. For sufficiently large liquid viscosities, the bridge will dissipate the relative kinetic energy of the colliding granules, preventing rebound. To determine the minimum velocity required for particle rebound, a force balance on an individual granule can be considered. Ignoring the effect of capillary forces and assuming creep flow between the two granules, the force balance equation of motion (Newton's second law) for the approach stage can be expressed as

$$m_{harm}\frac{du}{dt} = \frac{3}{2}\pi\eta_{liq}r_{harm}^2\frac{dx}{dt}\frac{1}{x} \tag{A.1}$$

where x is one-half of the dimensional gap distance at a given time t and m_{harm} and r_{harm} are, respectively, the mean harmonic mass and radius for the unequal granules, given by

$$m_{harm} = \frac{2m_1m_2}{m_1 + m_2} \tag{A.2a}$$

and

$$r_{harm} = \frac{2r_1r_2}{r_1 + r_2} \tag{A.2b}$$

A solution to eq A.1 can easily be obtained by integrating the left side between $u' = u_0$ and u and the right side between $x' = h_{liq}$ and x. The solution can be expressed as

$$u = u_0\left[1 - \frac{1}{St_v}\ln\left(\frac{h_{liq}}{x}\right)\right] \tag{A.3}$$

where St_v is the viscous Stokes number, which is given by

$$St_v = \frac{2m_{harm}u_0}{3\pi\eta_{liq}r_{harm}^2} \tag{A.4}$$

Assuming that the granules have an equal density of ρ_g and that they are spherical, one may assume

$$m_{harm} = \frac{4}{3}\pi r_{harm}^3\rho_g \tag{A.5}$$

and, by insertion into eq A.4, one finally obtains the relation

$$St_v = \frac{2\times\frac{4}{3}\pi r_{harm}^3\rho_g u_0}{3\pi\eta_{liq}r_{harm}^2} \quad\Leftrightarrow\quad St_v = \frac{8\rho_g r_{harm}u_0}{9\eta_{liq}}, \quad \text{Qed} \tag{A.6}$$

For rebound of the colliding granules to occur, the Stokes number must exceed a critical value of St_v*. With the initial velocity of u_0, let the velocity of the colliding granule upon reaching a distance of h_a be u_a, where h_a represents a characteristic length scale of surface asperities. The initial rebound velocity is then equal to eu_a, where e is the particle coefficient of restitution with the presence of binder layer. Realizing that the granule velocity u is a scalar velocity and thereby a sign-dependent parameter (for the rebound, u decreases as x increases, whereas during approach, u decreases as x decreases), the situation of the two granules colliding and afterwards rebounding can be split into two situations, analogous to eq A.1:

$$\text{Approach:}\quad m_{harm}\frac{du}{dt}=\frac{3}{2}\pi\eta_{liq}r_{harm}{}^{2}\frac{dx}{dt}\frac{1}{x} \tag{A.7}$$

with boundary conditions

at $t=0$: $x=h_{liq}$ and $u=u_0$ at $t=t_1$: $x=h_a$ and $u=u_a$

$$\text{Rebound:}\quad -m_{harm}\frac{du}{dt}=\frac{3}{2}\pi\eta_{liq}r_{harm}{}^{2}\frac{dx}{dt}\frac{1}{x} \tag{A.8}$$

with boundary conditions

at $t=t_1$: $x=h_a$ and $u=eu_a$ at $t=t_2$: $x=h_{liq}$ and $u=0$

By integrating eq A.7 between its boundaries, one achieves

$$m_{harm}(u_a-u_0)=-\frac{3}{2}\pi\eta_{liq}r_{harm}^{2}\ln\left(\frac{h_{liq}}{h_a}\right) \tag{A.9}$$

Analogously, via integration of eq A.8 between its boundaries, one achieves

$$m_{harm}eu_a=\frac{3}{2}\pi\eta_{liq}r_{harm}{}^{2}\ln\left(\frac{h_{liq}}{h_a}\right) \tag{A.10}$$

and via insertion of eq A.10 into eq A.9, one achieves

$$m_{harm}u_0-\frac{1}{e}\left(\frac{3}{2}\right)\pi\eta_{liq}r_{harm}{}^{2}\ln\left(\frac{h_{liq}}{h_a}\right)=\frac{3}{2}\pi\eta_{liq}r_{harm}{}^{2}$$

$$\ln\left(\frac{h_{liq}}{h_a}\right)\leftrightarrow\frac{2m_{harm}u_0}{3\pi\eta_{liq}r_{harm}{}^{2}}=\left(1+\frac{1}{e}\right)\ln\left(\frac{h_{liq}}{h_a}\right) \tag{A.11}$$

Dividing by the right-hand side and multiplying and dividing with u_0 on the left-hand side of eq A.11, one finds the critical condition for the fraction between the kinetic energy and the viscous dissipation energy for which agglomeration begins:

$$\frac{2m_{harm}u_0{}^{2}}{3\pi\eta_{liq}r_{harm}{}^{2}u_0\left(1+\frac{1}{e}\right)\ln\left(\frac{h_{liq}}{h_a}\right)}=1 \tag{A.12}$$

By exploiting the result in eq A.4, one finds that the Stokes number exactly at the beginning of agglomeration is given by

$$St_v{}^{*}=\left(1+\frac{1}{e}\right)\ln\left(\frac{h_{liq}}{h_a}\right),\quad \text{Qed} \tag{A.13}$$

Table of Symbols

$A_{liq,wet}$ = wetted area (m^2)
A_{con} = area of contact (m^2)
c = extrapolated constant
d_{bu} = gas bubble diameter (m)
e = particle coefficient of restitution
F_{vis} = viscous force (kg m/s^2)
$F_{max(tack)}$ = maximum (peak) tack force measured in a probe tack test (kg m/s^2)
g = gravity (m/s^2)
h_a = height of asperities (m)
h_{liq} = thickness of the coating liquid layer covering colliding granules (m)
m_1 = mass of granule 1 (kg)
m_2 = mass of granule 2 (kg)
m_{harm} = harmonic mean particle mass(kg)
$\dot{m}_{liq}$ = mass rate of liquid (g/s)
r_1 = radius of granule 1 (μm)
r_2 = radius of granule 2 (μm)
r_{harm} = harmonic mean particle radius (m)
St_{tack} = tack Stokes number
St_v = viscous Stokes number
$St_v{}^{*}$ = critical viscous Stokes number
S_w = wetting saturation
u_0 = initial granule collision velocity (m/s)
u_{test} = test speed for the probe tack test (m/s)
v_a = fluidization air velocity (m/s)
v_{bu} = bubble rise velocity in a fluid bed(m/s)
v_{mf} = minimum fluidization velocity (m/s)
V_{dr} = droplet volume (m^3)
x = distance (m)

Greek Symbols

π = mathematical pi; π = 3.1415927...
δ = dimensionless bubble spacing
κ = dimensionless factor
ρ_g = granule density (kg/m^3)
η_{liq} = liquid viscosity (centipoise)
φ = correction factor
θ = contact angle (°)

Literature Cited

(1) Salman, A. D.; Hounslow, M. J.; Seville, J. P. K. Granulation. In *Handbook of Powder Technology*; Elsevier: Amsterdam, 2007.

(2) Hede, P. D.; Bach, P.; Jensen, A. D. Fluidized-Bed Coating with Sodium Sulfate and PVA−TiO_2, 1. Review and Agglomeration Regime Maps. *Ind. Eng. Chem. Res.* **2009**, *48*, XXXX.

(3) Hede, P. D.; Bach, P.; Jensen, A. D. Fluidized-Bed Coating with Sodium Sulfate and PVA−TiO_2, 2. Influence of Coating Solution Viscosity, Stickiness, pH and Droplet Diameter on Agglomeration. *Ind. Eng. Chem. Res.* **2009**, *48*, XXXX.

(4) Hede, P. D. Towards Mathesis Universalis: Modern aspects of modelling batch fluidised bed agglomeration and coating systems—A review, CHEC Report R0605, Department of Chemical Engineering, Technical University of Denmark, Lyngby, Denmark, 2006, pp 1−101.

(5) Liu, L. X.; Litster, J. D.; Iveson, S. M.; Ennis, B. J. Coalescence of Deformable Granules in Wet Granulation Processes. *AIChE J.* **2000**, *46* (3), 529–539.

(6) Tardos, G.; Khan, I. M.; Mort, P. R. Critical parameters and limiting conditions in binder granulation of fine powders. *Powder Technol.* **1997**, *94*, 245–258.

(7) Schaafsma, S. H.; Vonk, P.; Segers, P.; Kossen, N. W. F. Description of agglomerate growth. *Powder Technol.* **1998**, *97*, 183–190.

(8) Ennis, B. J.; Tardos, G. I.; Pfeffer, R. A micro-level-based characterization of granulation phenomena. *Powder Technol.* **1991**, *65*, 257–272.

(9) Davidson, J. F.; Harrison, D. *Fluidized Particles*; Cambridge University Press: New York, 1963.

(10) Tardos, G. Wet-Granulation Research with Application to Scale-up. *China Particul.* **2005**, *3* (3), 191–195.

(11) Iveson, S. M.; Litster, D. L.; Hapgood, K.; Ennis, B. J. Nucleation, growth and breakage phenomena in agitated wet granulation processes: a review. *Powder Technol.* **2001**, *117*, 3–39.

(12) Abbott, A. Boundary Between Coating and Granulation, M.S. Thesis, Department of Chemical Engineering, The University of Queensland, Brisbane, Australia, 2002.

(13) Achanta, S.; Beimesch, W. E. Process for making a low density detergent composition by controlled agglomeration in a fluidised bed dryer, International Patent WO99/03964, 1999.

(14) Cryer, S. A. Modelling Agglomeration Processes in Fluid-Bed Granulation. *AIChE J.* **1999**, *45* (10), 2069–2078.

(15) Christensen, S. F. Rheology of AdhesionPh.D. Thesis, Department of Chemical Engineering, Technical University of Denmark, Lyngby, Denmark, 1998.

(16) Ukei, H.; Yatagai, T.; Nagatsu, H.; Natsume, M.; Nakagawa, Y. (NITTO DENKO Corp.). Pressure-sensitive adhesive tape, European Patent EP1516898, 2005.

(17) Smitthipong, W.; Nardin, M.; Schultz, J.; Nipithakul, T.; Suchiva, K. Study of tack properties of uncrosslinked natural rubber. *J. Adhes. Sci. Technol.* **2004**, *18* (12), 1449–1463.

(18) Hede, P. D. Fluidised bed coating and granulation, M.Sc. Thesis, Department of Chemical Engineering, CHEC Research Center, Technical University of Denmark, Lyngby, Denmark, 2005, pp 1−227.

(19) Clarke, A.; Blake, T. D.; Carruthers, K.; Woodward, A. Spreading and imbibition of liquid droplets on Porous surfaces. *Langmuir* **2002**, *18*, 2980–2984.

(20) Thielmann, F.; Naderi, M.; Ansari, M. A.; Stepanek, F. The effect of primary particle surface energy on agglomeration rate in fluidised bed wet granulation. *Powder Technol.* **2008**, *181*, 160–168.

(21) Mulhem, B. Effect of solid particle characteristics on suspension atomization. *Atomization Sprays* **2003**, *133*, 321–343.

(22) Mulhem, B.; Schulte, G.; Fritsching, U. Solid−liquid separation in suspension atomisation. *Chem. Eng. Sci.* **2006**, *61*, 2582–2589.

Received for review June 16, 2008
Revised manuscript received October 3, 2008
Accepted November 20, 2008

IE800942C

Chemical Engineering Science 64 (2009) 1293 – 1317

Contents lists available at ScienceDirect

Chemical Engineering Science

journal homepage: www.elsevier.com/locate/ces

Batch top-spray fluid bed coating: Scale-up insight using dynamic heat- and mass-transfer modelling

Peter Dybdahl Hede[a,b], Poul Bach[b], Anker D. Jensen[a,*]

[a]Department of Chemical and Biochemical Engineering, CHEC Research Center, Technical University of Denmark, Building 229, DK-2800 Kgs. Lyngby, Denmark
[b]Solid Products Development, Novozymes A/S, Smørmosevej 11, DK-2880 Bagsværd, Denmark

ARTICLE INFO

Article history:
Received 2 July 2008
Received in revised form 30 October 2008
Accepted 31 October 2008
Available online 12 November 2008

Keywords:
Fluid bed
Coating
Granulation
Drying
Fluidisation
Mass transfer
Heat transfer
Simulation
Thermodynamics

ABSTRACT

A mathematical model was developed for batch top-spray fluid bed coating processes based on Ronsse et al. [2007a, b. Combined population balance and thermodynamic modelling of the batch top-spray fluidised bed coating process. Part I—model development and validation. Journal of Food Engineering 78, 296–307; Combined population balance and thermodynamic modelling of the batch top-spray fluidised bed coating process. Part II—model and process analysis. Journal of Food Engineering 78, 308–322]. The model is based on one-dimensional discretisation of the fluid bed into a number of well-mixed control volumes. In each control volume, dynamic heat and mass balances were set up allowing the simulation of the contents of water vapour, water on core particles and deposited coating mass as well as fluidisation gas, particle and chamber wall temperature. The model was used to test different scale-up principles by comparing simulation results with experimental temperature and humidity data obtained from inorganic salt coating of placebo cores in three pilot fluid bed scales being a 0.5 kg small-scale (GEA Aeromatic-Fielder Strea-1), 4 kg medium-scale (GEA Niro MP-1) and 24 kg large-scale (GEA MP-2/3). Results show good agreement between simulated and experimental outlet fluidisation air temperature and humidity as well as bed temperature. Simulations reveal that vertical temperature and humidity gradients increase significantly with increasing scale and that in fluid beds as the simulated 900 kg (RICA-TEC Anhydro) production-scale, the gradients become too large to use the simple combined drying force/relative droplet size scale-up approach without also increasing the inlet fluidisation air temperature significantly. Instead, scale-up in terms of combinations of the viscous Stokes theory with simulated particle liquid layer profiles (obtained with the model) is suggested. In this way, the given fluid bed scale may be optimised in terms of low agglomeration tendency for a given process intensity across scale.

1. Introduction

In the chemical and pharmaceutical industry sensitive active solid products, such as enzyme containing granules, are often produced by coating the active ingredient onto inactive filler cores in fluid beds. The desired product thereby consists of unagglomerated individual carrier particles each coated homogeneously with a layer of the active ingredient. Besides being able to maintain and protect the activity of the active ingredient, process optimisation often goes in the direction of finding correct formulation and process conditions in order to balance between excessive agglomeration and excessive spray drying of the feed (van Ee et al., 1997). If either of the phenomena is dominant, a poor product quality is achieved. In any case, control of agglomeration is essential during scale-up and this is known to be closely connected to the humidity and temperature inside the fluidisation chamber during the process (Hede et al., 2008b). For the sake of activity of the active ingredient, control of the humidity and temperature throughout the coating process is likewise of utmost importance (van Ee et al., 1997).

In industry, product and process properties are typically optimised in small- and medium-scale pilot fluid beds and then transferred to production-scale. The scale-up of a fluid bed granulation process requires decisions to be made at many levels, including: fixed parameters (e.g. nozzle and fluidisation chamber dimensions), parameters related to the core material (such as price, composition, porosity, sphericity and more), coating solution (e.g. viscosity, work of adhesion and more) and the type of fluid bed, input parameters, operating conditions including spraying and fluidisation conditions as well as processing time, etc. With such a variety of interlinked parameters and properties, combined with a general lack of quantitative understanding of the granulation process, it is obvious that

* Corresponding author. Tel.: +45 4525 2841; fax: +45 4588 2258.
E-mail address: aj@kt.dtu.dk (A.D. Jensen).

0009-2509/$ - see front matter © 2008 Elsevier Ltd. All rights reserved.
doi:10.1016/j.ces.2008.10.058

scale-up of a fluid bed granulation process is a challenging task (Hede et al., 2007a).

Up-scaling of fluid bed processes is a common industrial engineering exercise and up to now the field has not had much academic interest. Typically, the task goes in the direction of matching first of all the particle size distribution across scale and, secondly, if possible at the same time, to maintain a high-intensity process during scale-up. Other scale-up targets include morphology and appearance as well as mechanical properties of the final coating layer (van Ee et al., 1997). As reviewed by Hede (2006) advances in scaling principles are often done in industry and typically only reach the public in the form of patents. Recent articles by e.g. Rambali et al. (2003), Boerefijn and Hounslow (2005) and Hede et al. (2007a,c) indicate some progress in the field although the scale-up procedures are somewhat different. Mort (2005) suggests that scale-up of wet-granulation processes should focus on combined particle-level and unit-operation level properties and variables. Hede et al. (2007a) followed these trends by suggesting scale-up in terms of a combined drying force (DF) and a relative droplet (RD) parameter explained in detail later (see Eqs. (1) and (2)). These principles focus especially on temperature and humidity conditions as well as on nozzle conditions. However, there are also limitations to the application of these scale-up principles in terms of keeping the agglomeration tendency as low as possible at maximum process intensity. The flux number (FN) (see Eq. (3)) suggested by Akkermans et al. (1998) is a different approach as the primary focus here is the balance between the particle flux in the spray zone and the liquid spray flux that wets the solids. The validation of the FN by Hede et al. (2007c) indicates that it does not perform as good, with respect to agglomeration tendency, as the principles by Hede et al. (2007a) in the context of coating placebo cores with inorganic salt solutions. Nevertheless, neither of these simple scale-up principles provide detailed insight of the processes and conditions inside the bed. It is believed that temperature and humidity profiles play an important role, but it is difficult to obtain detailed experimental insight into how these variables distribute vertically through the bed. Typically, the bed temperature is measured at one location only and the adjustment of the inlet fluidisation air temperature is based on this single measurement. It is hereby assumed that the measured temperature is representative for the entire bed which is not necessarily the case.

It is the aim of this paper to investigate the scale-up of top-spray fluid bed coating processes. Selected experimental data from previous (scale-up) studies by Hede et al. (2007a,c) are chosen, and simulations are performed in order to be able to explain the agglomeration outcome for these experiments. Simulations are done in terms of a thermodynamic heat- and mass-transfer model by which it becomes possible to obtain steady state temperature and humidity profiles as well as particle moisture profiles vertically through the bed. Viscous Stokes theory is applied in order to link the simulation and experimental data with a mechanistic particle-level agglomeration model.

2. Model

Results by Maronga and Wnukowski (1998) indicate that the temperature and humidity during the coating process in a top-spray fluid bed vary significantly with radial and especially vertical position. During the coating process, pockets of low temperature and high humidity are formed deep inside the bed, causing temperature fluctuations. Based on these systematic fluctuations, the top-spray fluid bed is suggested to be formally divided into four zones, which can be seen in Fig. 1 (Maronga and Wnukowski, 1998).

The experimental results obtained by Maronga and Wnukowski (1997b) among others have formed the basis for a recent dynamic heat- and mass-transfer model suggested by Ronsse (2006) and Ronsse et al. (2007a,b). The model is capable of describing the temperature, humidity and coating mass concentration fields along the vertical axis of the coating process in a top-spray fluidised bed. This simple model approach fulfils the industrial needs for an intuitive model that captures only the most important phenomena during the coating process at the same time allowing short calculation times and results that can be straightforwardly interpreted and used for direct comparison with experimental data.

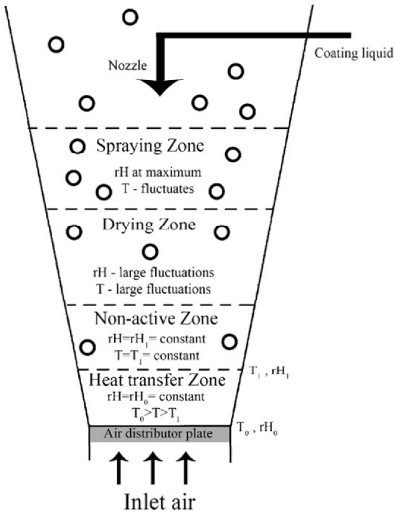

Fig. 1. Zones in a top-spray fluid bed during steady state coating (based on Maronga and Wnukowski, 1998). The sizes of the zones are not to scale.

The model being set up and tested in the present paper is essentially the same model as presented by Ronsse et al. (2007a). The model is based on one-dimensional vertical discretisation of the fluid bed into a number of well-mixed control volumes. In each control volume, dynamic heat- and mass-balances are set up allowing the simulation of the contents of water vapour, water on core particles and deposited coating mass as well as gas, particle and chamber wall temperature. The model furthermore accounts for heat losses to the external environment. However, the original Ronsse model was not developed in a scale-up context and we have carefully reviewed, modified and slightly expanded the model in order to be better able to predict process changes at different fluid bed scales. The model tested in the present paper is presented in its full form in Appendix A and the associated assumptions may be seen in Appendix B.

3. Model validation

3.1. Experimental validation set-up

Model validation data were obtained with commercial top-spray fluid beds in three pilot scales being a small-scale GEA Aeromatic-Fielder Strea-1, a medium-scale Niro-Aeromatic Multiprocessor type MP-1 and a large-scale GEA Aeromatic-Fielder MP-2/3. Set-up details and the principles of operation for these three fluid beds have been treated in detail elsewhere (Hede et al., 2007a–c). Fig. 2 shows a sketch of the physical dimensions of the fluid beds and Table 1 summarises the important process conditions under which the validation experiments were carried out. Other process and physical parameters kept constant during all simulations may be seen in Appendix C.

In all three experimental fluid bed set-ups a Testo 645 Thermo-hygrometer (combined humidity and temperature probe) was located just above the nozzle measuring the outlet fluidisation gas relative humidity and temperature. The uncertainty of the Thermo-hygrometer was ±1%rH, ±1 °C, while the uncertainties of the other temperature probes were ±2 °C.

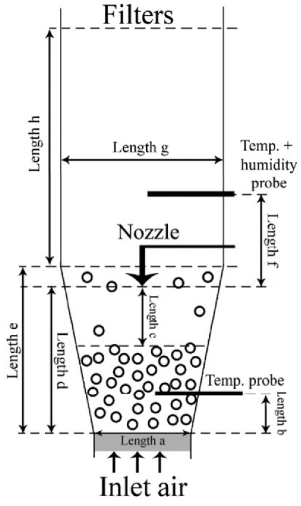

Fig. 2. Sketch of the fluid bed dimensions for the three fluid bed scales. Length dimensions corresponding to the symbols in the figure according to Table 1.

Choosing a control volume height of $h_{S,i}$=1.5 cm for all three fluid beds ensured a sufficient high number of control volumes without extending the computational time unnecessarily. Initially, simulations for the small-scale fluid bed showed that the results depended on the number of control volumes up to roughly $n=14$. A number of 18 control volumes for the small-scale fluid bed thus ensured simulation results being independent of the number of control volumes. As a consequence of the choice of $h_{S,i}$, the other fluid bed scales were assigned a larger number of control volumes than the small-scale, and problems with the result-dependency of n were not observed for these scales.

Assigning the right number of control volumes to be coating control volumes is likely to be important with respect to the comparison of the simulated bed temperatures with the experimentally determined values. The outlet conditions should obviously be less affected by the assignment. In simulations by Ronsse (2006) a fixed value of $c/n = 0.125$ was chosen based on considerations for that particular fluid bed scale made by Dewettinck (1997). Based on detailed temperature and humidity studies, Maronga and Wnukowski (1997a,b, 1998), however, concluded that the spray zone in practice often is significantly larger, especially for small fluid beds. In the present paper, estimations of the c/n ratio were made based on experimental observations from empty vessel nozzle operations combined with spray fan depth estimations during coating experiments. Although empirical, these estimations do not conflict with experimental results by Maronga and Wnukowski (1997a,b, 1998) and it would be in contradiction with observations to assign a single c/n value for all three scales. The estimated c/n values range from 0.66 for the small-scale to 0.46 for the large-scale at a nozzle pressure of 3 bar, and correspondingly, from 0.50 to 0.33 at a nozzle pressure of 1 bar.

Table 1
Process- and model-related parameters for the present study.

Process parameter	Small-scale Strea-1	Medium-scale MP-1	Large-scale MP-2/3
Type of nozzle	External mixing two-fluid	External mixing two-fluid	External mixing two-fluid
Liquid orifice diameter	1.2 mm	1.2 mm	1.2 mm
Fluidisation velocity (simulation of the flux number exp.)	82 N m^3/h ~ 1.0 m/s at the top of the expanded bed height ~ $r = 2.26\,s^{-1}$	137 N m^3/h ~ 1.0 m/s at the top of the expanded bed height ~ $r = 1.47\,s^{-1}$	651 N m^3/h ~ 1.0 m/s at the top of the expanded bed height ~ $r = 1.01\,s^{-1}$
Fluidisation velocity (simulation of the DF/RD exp.)	93 N m^3/h ~ 3.3 m/s 4 cm above the air distributor plate ~ $r = 2.58\,s^{-1}$	270 N m^3/h ~ 3.3 m/s 4 cm above the air distributor plate ~ $r = 1.98\,s^{-1}$	680 N m^3/h ~ 3.3 m/s 4 cm above the air distributor plate ~ $r = 1.09\,s^{-1}$
Bed height at minimum fluidisation (h_{mf})	6 cm	13 cm	26 cm
Initial core bed load	0.5 kg	4 kg	24 kg
Diameter of the orifices in the air distributor plate	3 mm	3 mm	Stainless steel wire frame with mesh orifices of 90 μm ~ porous air distributor plate
Number of orifices in the air distributor plate	92	260	
Coating solution dry matter contents	10–30 w/w%	15 w/w%	15 w/w%
FB dimensions			
Length *a*	10 cm	17 cm	27 cm
Length *b*	10.5 cm	6 cm	11 cm
Length *c*	18 cm (at 3 bar)	32 cm (at 3 bar)	37 cm (at 3 bar)
Length *d*	27 cm	57.5 cm	81 cm
Length *e*	31 cm	48.5 cm	63 cm
Length *f*	15 cm	28 cm	82 cm
Length *g*	25 cm	29 cm	64 cm
Length *h*	18 cm	93 cm	270 cm
Model-related parameters			
Total number of control volumes	18 ~ $h_{S,i} = 1.5$ cm	38 ~ $h_{S,i} = 1.5$ cm	54 ~ $h_{S,i} = 1.5$ cm
Number of coating control volumes	12 ($P_{nozzle} = 3$ bar) 9 ($P_{nozzle} = 1$ bar)	21 ($P_{nozzle} = 3$ bar) 15 ($P_{nozzle} = 1$ bar)	25 ($P_{nozzle} = 3$ bar) 18 ($P_{nozzle} = 1$ bar)
Bed temperature measurement corresponds to control volume number	7	4	7

Notably, the decreasing ratio of c/n with increasing scale illustrate a general latent problem with fluid bed coating scale-up being that the spray zone characteristics are not kept constant during scale-up. This is discussed further in Section 4.2.

Hede et al. (2007a,c) concluded that the best practical principle to run a fluid bed coating process in general is by fixing nozzle conditions a priori (i.e. fixing both the liquid and nozzle air mass flow rates), choosing a level for the bed temperature and maintain these conditions throughout the coating process by adjusting initially in the process only the inlet fluidisation air temperature in order to reach the target bed temperature. All other process conditions, including the fluidisation velocity, should be fixed and chosen a priori. These principles of operation were chosen for all validation experiments in the present paper. In all cases, the experimental conditions obtained under steady state were the ones to be compared with the simulation results.

3.1.1. Materials

Low porosity sodium sulphate cores (porosity fraction around 20.7% determined with Micromeritics Autopore II intrusion/extrusion mercury porosimetry) pre-sieved in the size range of 180–350 μm were used as core material. The sodium sulphate cores have sphericities of about 0.86.

The sodium sulphate cores were coated with aqueous solutions of sodium sulphate in the amount of 10–30 w/w% using 1 w/w% (of the amount of sodium sulphate) dextrin as binder. Demineralised water was used as solvent. More information about the salt coating process may be found in Hede et al. (2008b).

3.2. Calculation procedure

The model consists of six times n coupled ordinary differential equations (ODEs): one equation for each of the six main variables to be calculated for each control volume S_i as a function of time. The six main variables are the deposited coating mass, $Y_{p,i}$, the particle surface temperature, $T_{p,i}$, the particle water contents, $W_{p,i}$, the gas phase temperature, $T_{a,i}$, the gas phase water contents (absolute humidity), $X_{a,i}$, and the control volume wall temperature, $T_{w,i}$. A number of the parameters and properties in these ODEs are functions of one of more of the six parameters and they are calculated in a number of functions. The connections between the independent and the dependent variables are thus complex, and it not possible to obtain an analytical solution to the system of ODEs. Thus a numerical solution procedure is required.

The numerical solution is aided by implementing the ODE system in Matlab version 2007a (The MathWorks Inc., US) using the standard ode15s standard Matlab solver (Shampine and Reichelt, 1997). When allowing Matlab to choose its own value for the step size, Δt, and setting the error value to 10^{-6}, a typical simulation example from $t_0 = 0$ to $t_{end} = 800$ s in the medium-scale fluid bed with 38 control volumes, whereof 21 are coating control volumes, takes roughly 15 min to complete on a 1.86 GHz, 512 MB of RAM, Pentium M (two single-core 32-bit ×86 microprocessors).

3.3. First validation of steady state data — matching the outlet and product temperature as well as the outlet humidity in three pilot-scale fluid beds

For the validation of the model, steady state simulation results were compared with the measured values of the outlet fluidisation air temperature and outlet relative humidity. This was done for 35 fluid bed experiments in total in three fluid bed scales. The data were adapted from Hede et al. (2007a–c, 2008b). Assuming that the outlet conditions are equal to the conditions in the last upper control volume, it was possible to compare the simulated temperature and humidity with the experimentally determined values for a broad range of different process conditions, ranging from high- to low-process intensity. Depending on the process intensity, the difference between the bed temperature and the outlet temperature typically ranged between 2 and 8 °C. The experimentally measured outlet temperatures and humidities are compared to the values obtained from the simulations as shown in Figs. 4 and 5, respectively.

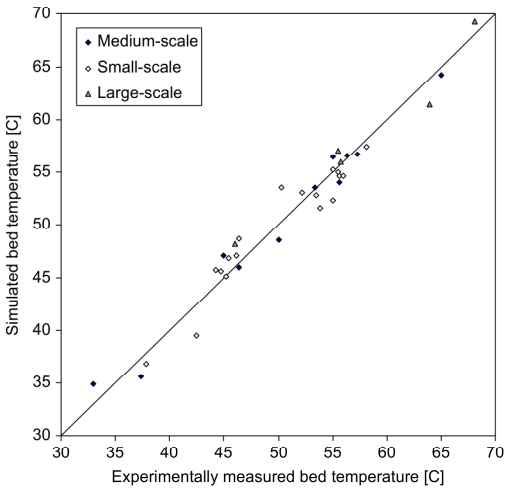

Fig. 3. Simulated versus experimentally measured steady state bed temperatures.

In addition, the model predictions of the bed temperature were compared to experimental data at the location where the temperature probe was located as shown in Fig. 3. As observed from Table 1, these locations are different from fluid bed scale to fluid bed scale thus giving valuable indication of the performance of the model.

Figs. 3–5 show in general a good agreement between model and experimental values for all three variables. Although some scattering is observed in all three plots, the data points distribute equally well on both sides along the straight line for the entire intervals indicating that no systematic errors are apparent. This illustrates that the basic thermodynamics, including heat loss, is well accounted for by the model.

The best fit between model and experimental results is observed for the bed temperatures in Fig. 3. The bed temperature probes are for all three scales located deep within the bed at a safe distance from the spray zone. Being close to the bottom inlet and away from the assigned coating control volumes, the chance of cumulated calculation error, e.g. due to the simplicity of the heat loss terms in the model versus the actual heat loss, is thus small in the calculation of the fluidisation air temperature in the control volumes, which are used in the comparison with measured bed temperatures. In light of the chance of cumulated errors in vertical direction, the relations in Figs. 4 and 5 between model and experimentally measured outlet conditions are satisfactory.

It is furthermore observed from Figs. 3–5 that the model is capable of predicting conditions equally well ranging from high- to low-process-intensity coating operations giving credit to the model. In addition, the model performs observably just as well with the small- and medium-scale as with the large-scale, making it reasonable to use the model in a scale-up context.

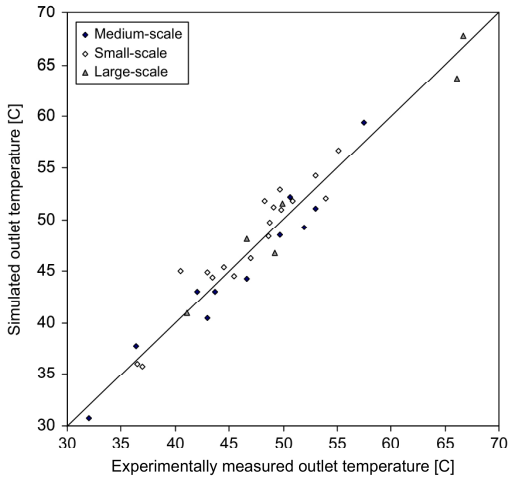

Fig. 4. Simulated versus experimentally measured steady state outlet temperatures.

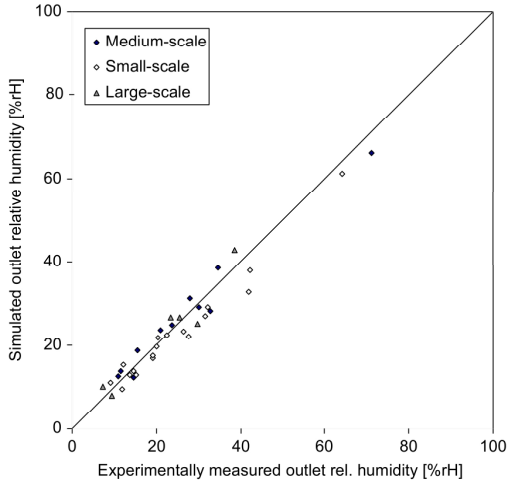

Fig. 5. Simulated versus experimentally measured outlet steady state relative humidity values.

3.3.1. *Dynamic behaviour*

A typical start-up situation in the medium-scale was selected with conditions according to Table 2. Before the nozzle is switched on, the particles are normally heated by the fluidisation air at an inlet temperature close to what is believed to be the correct inlet temperature for the spray phase. The heating process is typically maintained until the system reaches steady state where the outlet relative humidity is usually only a few %rH and the bed and outlet temperatures are close to that of the inlet temperature.

For the medium-scale fluid bed set-up, the inlet air is supplied from an external steam-based heating source, which also supplies other equipment. The temperature control is maintained by a thermostat which has some delay in response. This means that, in reality,

Table 2
Conditions for comparison of experimental data with simulation results in terms of the time needed to reach steady state in the medium-scale fluid bed.

Process conditions	Values
Initial particle moisture contents	4×10^{-3} kg water/kg core (experimentally measured)
External air temperature	23.6 °C
External air humidity	35.7%rH (at 23.6 °C) ~ 6.5×10^{-3} kg H_2O/kg dry air
Initial fluidisation chamber temperature ($T_{w,i}$)	23.6 °C
Inlet fluidisation air temperature ($T_{a,in}$)	80 °C
Fluidisation air velocity	270 N m³/h ~ $r - 1.98\,s^{-1}$
Inlet fluidisation air humidity	2.2%rH (at 80 °C) ~ 6.5×10^{-3} kg H_2O/kg dry air
Bed load	4.0 kg

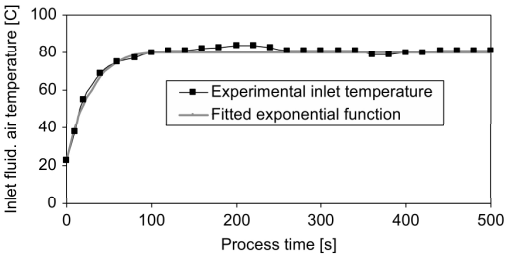

Fig. 6. The inlet fluidisation air temperature as a function of process/simulation time.

it will take some time for the inlet air to adjust to the set point. Such phenomena are observed for all three fluid bed scales. For the present coating experiment, the inlet temperature was recorded and observed to develop according to Fig. 6. As observed from Fig. 6, it takes roughly 100 s before the inlet temperature reaches the set point at 80 °C and another 350 s before the oscillation damps out. If the model is to be used for dynamic studies such non-ideal phenomena must be accounted for. An exponential function was thus fitted to the measured inlet fluidisation air temperature data and implemented into the model for simulations up to 500 s of process time.

By measuring the outlet and bed temperature as well as the outlet relative humidity each 20 s during start-up, it was possible to compare the measured values with those obtained from simulations under identical process conditions. The simulated data were obtained as follows: initially the particles and fluidisation vessel were set to room conditions according to Table 2. Setting all control volumes to non-coating control volumes, the model was set to run until steady state which corresponds to the initial heating up of the particles prior to the spray phase. Comparison with experimentally measured points can be seen from Figs. 7A–C.

Starting with Fig. 7A, it is observed that the curve for the simulated bed temperature follows the experimental data closely all the way up to steady state. For both the simulation and the experiment, it takes roughly 200 s to reach steady state. The tendency of reaching steady state at roughly 200 s is also observed for the outlet conditions in Figs. 7B and C. However, in these two figures the experimental data are observed to lack slightly behind the simulation results in the first 200 s although the deviations are close to the temperature and humidity probe uncertainty. Especially the humidity probe is known to have some seconds of response delay which could account for some of the deviation at the steepest gradients in Fig. 7B. In all, the test has showed that the model is indeed capable of predicting the dynamic thermodynamic behaviour during fluid bed processing, as the model predicts the three important variables well at any given time of operation.

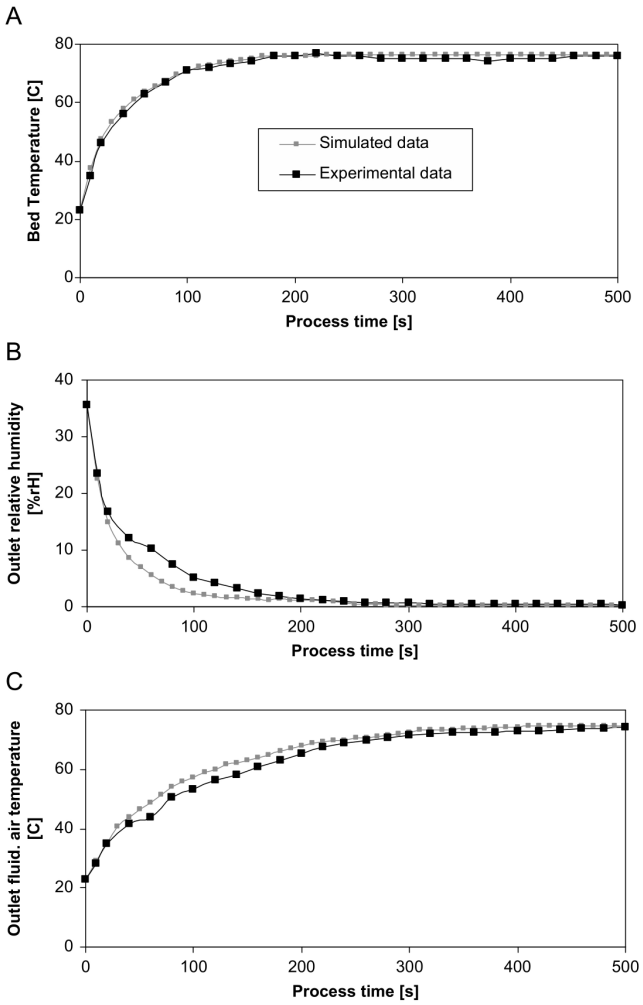

Fig. 7. Comparison of experimental and simulated data as a function of process/simulation time: (A) bed temperature, (B) outlet relative humidity, (C) outlet temperature.

4. Scale-up simulations

The principles, advantages and disadvantages of scaling up the top-spray fluid bed inorganic salt coating process in terms of the combined RD size and DF have been thoroughly presented in a number of articles (Hede et al., 2007a, 2008b–d; Rambali et al., 2003; Mehta, 1988). Likewise, a number of articles have treated the scale-up using the FN (Hede et al., 2007c; Boerefijn and Hounslow, 2005). The conclusions obtained from these experimental scale-up studies indicate that product temperature and humidity are vital parameters for the result of the coating process.

Both scale-up principles have shown to be capable of producing coated granules with statistically similar low degree of agglomeration across the three fluid bed scales used in the present paper. It is important to note that none of the two scale-up principles automatically fix all process conditions for the coating process. The scale-up principles rather give certain possibilities for some process parameters once others are chosen. This means in principle that other levels of agglomeration could have been observed by Hede et al. (2007a,b) for identical FN and RD/DF values. Furthermore, both scale-up principles need experiments to be carried out in order to determine the correct setting for the inlet fluidisation air temperature. That is, both the DF/RD and the FN approach have an independent parameter being the inlet fluidisation air temperature which cannot be determined a priori from the DF/RD or the FN expressions, but needs to be found by adjustment in the coating process start-up phase in order to reach the required target bed temperature. Similarly, both scale-up principles are focused primarily on being able to reproduce the

Table 3
Scale-up data adapted from Hede et al. (2007a,c).

Scaling conditions	Strea-1 (small-scale)	MP-1 (medium-scale)	MP-2/3 (large-scale)
Scale-up in terms of combined relative droplet (RD) size and drying force (DF)	RD = 3.5×10^{-3} min/g, $P_{nozzle} = 3$ bar, DF = 12.2 kPa ($T_{bed} = 55\,^{\circ}$C), $T_{inlet} = 74\,^{\circ}$C, 93 N m^3/h Results: Aggl. = 0.07 w/w%, process time: 0:37, outlet abs. hum. = 15.9 g H_2O/kg dry air	RD = 3.5×10^{-3} min/g, $P_{nozzle} = 3$ bar, DF = 12.0 kPa ($T_{bed} = 54\,^{\circ}$C), $T_{inlet} = 78\,^{\circ}$C, 270 N m^3/h Results: Aggl. = 1.27 w/w%, process time: 1:28, outlet abs. hum. = 18.3 g H_2O/kg dry air	RD = 3.5×10^{-3} min/g, $P_{nozzle} = 3$ bar, DF = 12.5 kPa ($T_{bed} = 56\,^{\circ}$C), $T_{inlet} = 79\,^{\circ}$C, 680 N m^3/h Results: Aggl. = 1.45 w/w%, process time: 3:46, outlet abs. hum. = 19.1 g H_2O/kg dry air
Scale-up in terms of the flux number (FN)	FN = 4.5, $P_{nozzle} = 1$ bar, $T_{bed} = 55\,^{\circ}$C, $T_{inlet} = 75\,^{\circ}$C, 82 N m^3/h Results: Aggl. = 24.5 w/w%, process time: 1: 02, outlet abs. hum. = 16.1 g H_2O/kg dry air	FN = 4.5, $P_{nozzle} = 1$ bar, $T_{bed} = 55\,^{\circ}$C, $T_{inlet} = 97\,^{\circ}$C, 137 N m^3/h Results: Aggl. = 62.3 w/w%, process time: 1:31, outlet abs. hum. = 25.9 g H_2O/kg dry air	FN = 4.5, $P_{nozzle} = 1$ bar, $T_{bed} = 55\,^{\circ}$C, $T_{inlet} = 74\,^{\circ}$C, 651 N m^3/h Results: Aggl. = 4.4 w/w%, process time: 4:25, outlet abs. hum. = 17.6 g H_2O/kg dry air

particle size distribution across scale and thereby avoid agglomeration. Although also important in a commercial framework, the two scale-up principles focus, however, to a lesser extent on process intensity. The two scale-up principles will be briefly introduced below, hereby illustrating how process conditions for the coating experiments were obtained with the scale-up parameters.

Based on the results by Mehta (1988), Rambali et al. (2003) scaled up a fluidised agglomeration process from small-scale (bed load 5 kg) to medium- (bed load 30 kg) and large-scale (bed load 120 kg) by looking at the effect of the particle bed moisture contents during and at the end of the spraying process and the effect of coating solution droplet size on the granule size. The fluidisation flow rate in m/s at the air distributor plate was kept constant in all their experiments in order to have approximately similar breaking forces on the granules. For the small- and medium-scale the same nozzle (liquid orifice diameter of 1.8 mm) was used whereas a three-head nozzle (liquid orifice diameters of 3×3.0 mm) was used for the large-scale fluid bed. The droplet size was controlled in terms of a RD parameter defined as the ratio of the coating solution mass spray rate $\dot{m}_{spray}$ divided by the mass airflow rate through the nozzle $\dot{m}_{nozzle\ air}$ squared according to

$$RD = \frac{\dot{m}_{spray}}{(\dot{m}_{nozzle\ air})^2} \tag{1}$$

The idea of RD is to maintain a similar droplet size across scale and the value of RD is only unambiguous if both the nozzle pressure and the liquid feed rate are chosen (Hede et al., 2008a). A further discussion of the RD parameter may be found in Hede et al. (2007a).

Hede et al. (2007a) further suggested that the bed temperature and outlet relative humidity (assumed equal to the average bed relative humidity) during steady state coating conditions were combined into a so-called DF parameter, according to Eq. (2), indicating the fluidisation air moisture evaporation force:

$$DF = P_{sat} \cdot \left(1 - \frac{\text{Outlet rH\%}}{100\ \text{rH\%}}\right) \tag{2}$$

where P_{sat} is the saturated pressure at the dry bulb bed temperature. Results by Hede et al. (2007a) showed that scale-up in terms of fixed values of both the DF and the RD parameter could lead to similar agglomeration tendencies as well as similar granule mechanical properties across the three pilot fluid bed scales used in the present paper.

Likewise, a number of articles have treated the scale-up using the FN (Hede et al., 2007c; Boerefijn and Hounslow, 2005). The FN and the expressions for the associated parameters were suggested in a Unilever patent by Akkermans et al. (1998). In principle being based on similar principles as the dimensionless spray flux suggested by Litster et al. (2002), the FN is expressed according to

$$FN = \log\left[\frac{\rho_p \cdot v_e}{\dot{q}_{mliq}}\right] \tag{3}$$

where ρ_p is the particle density determined according to

$$\rho_p = \frac{BD}{1 - \varepsilon_{bed}} \tag{4}$$

in which BD is the bulk density of the powder bed and ε_{bed} is the bed porosity determined by e.g. mercury porosimetry according to guidelines provided by Akkermans et al. (1998). The parameter $\dot{q}_{mliq}$ is the spray mass flux in kg/(s m^2) at a normalised distance D_0 from the nozzle outlet, and v_e is the excess gas velocity in m/s. D_0 is determined according to

$$D_0 = h_{nozzle} - h_{bed} \tag{5}$$

where h_{nozzle} is the height of the spray nozzle above the bottom of the fluidisation chamber and height h_{bed} is the expanded bed height.

One example of a scale-up attempt across the three fluid bed scales with low and statistical similar agglomeration tendencies obtained under high-intensity coating conditions may be seen from the first row in Table 3, adapted from Hede et al. (2007a). Using this successful scaling attempt as benchmark, an unsuccessful scaling attempt of similar coating time using the FN scale-up principle was adapted from Hede et al. (2007c). The data from the FN scaling attempt may be seen from the last row in Table 3.

Comparing the data in Table 3 from experiments at the same scale, the resulting agglomeration tendencies are far from being similar, and a similar low tendency of agglomeration across the scales was not achieved in the FN scale-up attempt. This results from the selection of the parameters for the two scaling principles and does not necessarily indicate that one of the scale-up principles is superior to the other. Hede et al. (2007c) argue that a low nozzle pressure of 1 bar causes a larger two-dimensional spray area at the distance of D_0 than at higher pressures and that this, as a consequence of the choice of the definition of the FN and hereby the parameter choices made by Hede et al. (2007c), forces a high spray rate and a poor atomisation, which in all causes critically high *local* particle moisture contents combined with a low temperature of the fluidisation air in the spray zone. Furthermore, at a nozzle pressure of 1 bar the vertical extension of the spray zone is likely to be smaller than at 3 bar. So far it has not been possible to validate these suggested explanations. Simulations using the present model, however, make it possible to study local temperatures and humidity conditions in detail.

Initially, the conditions from the successful scaling attempt in terms of the combined RD and the DF parameter have been simulated. Steady state fluidisation air temperature and relative humidity profiles as well as DF profiles for the three fluid bed scales may be seen from Figs. 8 to 10.

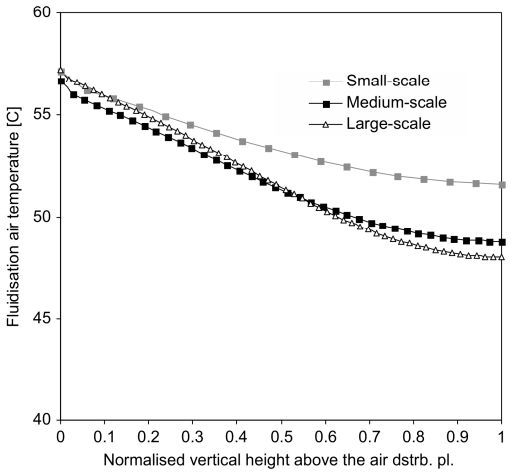

Fig. 8. Steady state fluidisation air temperature profiles for the three fluid bed scales. RD = 3.5 × 10^{-3} min/g, DF = 12.0–12.5 kPa, P_{nozzle} = 3 bar. Other model parameters according to Tables 1 and 3.

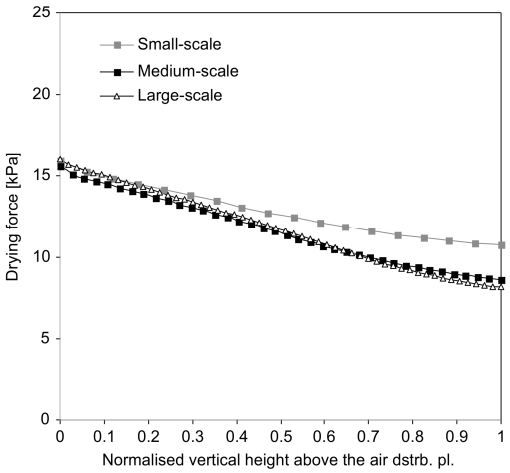

Fig. 10. Steady state drying force profiles for the three fluid bed scales. RD = 3.5 × 10^{-3} min/g, DF = 12.0–12.5 kPa, P_{nozzle} = 3 bar. Other model parameters according to Tables 1 and 3.

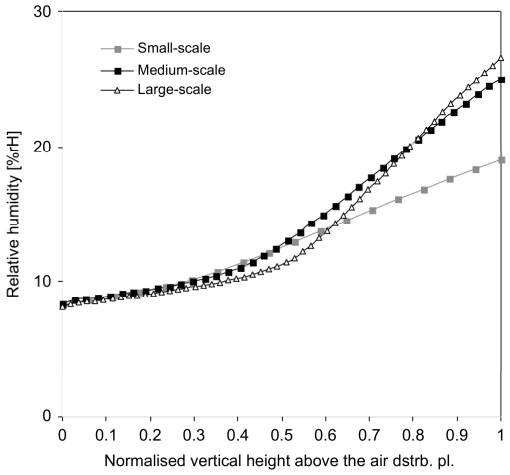

Fig. 9. Steady state fluidisation air relative humidity profiles for the three fluid bed scales. RD = 3.5 × 10^{-3} min/g, DF = 12.0–12.5 kPa, P_{nozzle} = 3 bar. Other model parameters according to Tables 1 and 3.

From the comparison of the temperature and the relative humidity profiles in Figs. 8 and 9 several points are revealed: in accordance with the principle of which the coating operations were carried out, it is observed for all three scales that the fluidisation air temperatures are close to 55 °C in the control volume where the bed temperature probe physically is located (see Table 1). Taking the outlet relative humidity as the relative humidity value at normalised length of 1 in Fig. 9 this indicates that the overall DF values were close to 12 kPa during scale-up, which is in accordance with the data in Table 3. It appears that the temperature in the spray zone is slightly higher in the small-scale fluid bed than for the medium- and large-scale which are quite similar. Regarding the humidity profiles, it appears that the largest relative humidity gradients are observed for the large-scale followed by the medium- and small-scale. Based on the temperature and relative humidity profiles it becomes clear that there is a greater homogeneity the smaller the fluid bed scale indicating that the particle mixing is significantly better the smaller the scale and more importantly, that the spray zone constitutes a larger percentage of the total expanded bed height (the *c*/*n* fraction is greater the smaller the fluid bed size).

The keypoint of the scale-up approach in Figs. 8–10 was to maintain a constant DF across scale. As presented by Hede et al. (2007a) this was done in terms of the measured outlet humidity and the measured bed temperature at one location. Hence, the scale-up principle was based on a single (overall) DF value, and it was therefore not on beforehand certain that the DF profiles would be similar across scale on a detailed level. Even so, it appears from Fig. 10 that there is a great similarity in the DF profiles for all three scales in particular for the first half of the chamber height. Similar tendencies have been observed for simulations with other RD/DF values across the three fluid bed scales. It is likely that this homogeneity and similarity in the DF profiles across scale is part of the reason why the scale-up approach was successful regarding the production of particles with similar low tendency of agglomeration and similar mechanical properties of the coating layer. This becomes evident in the comparison with the FN scale-up approach. Similar to the profiles in Figs. 8–10, profiles for the FN scaling attempt can be seen in Figs. 11–13.

In comparison to the profiles in Figs. 8–10, it is clearly observed from Figs. 11 to 13 how the temperature and humidity profiles vary from scale to scale, but also how different the DF profiles are with identical FN. Whereas the DF ranges between 12 and 18 kPa in the small-scale, the range is 5–16 kPa in the medium-scale and 8–15 kPa in the large-scale. This means that particles in all scales and especially in the medium-scale are exposed to a dramatic temperature and moisture change during their drying–wetting cycle. With these simulation results in mind, it is not surprising to observe from Table 3 that the far largest agglomeration tendency was observed in the medium-scale.

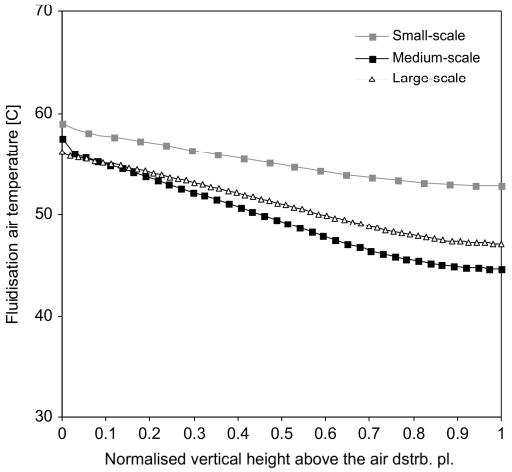

Fig. 11. Steady state fluidisation air temperature profiles for the three fluid bed scales. FN = 4.5, $P_{nozzle} = 1$ bar. Other model parameters according to Tables 1 and 3.

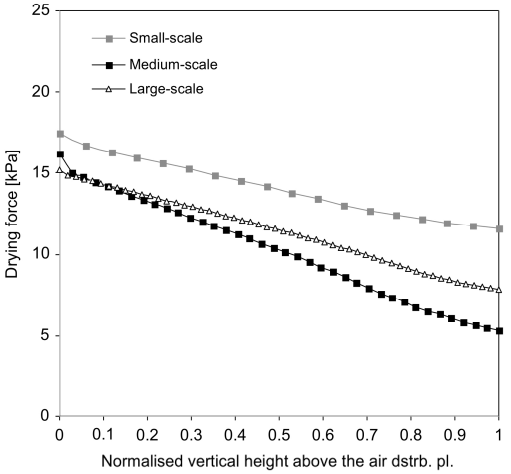

Fig. 13. Steady state drying force profiles for the three fluid bed scales. FN = 4.5, $P_{nozzle} = 1$ bar. Other model parameters according to Tables 1 and 3.

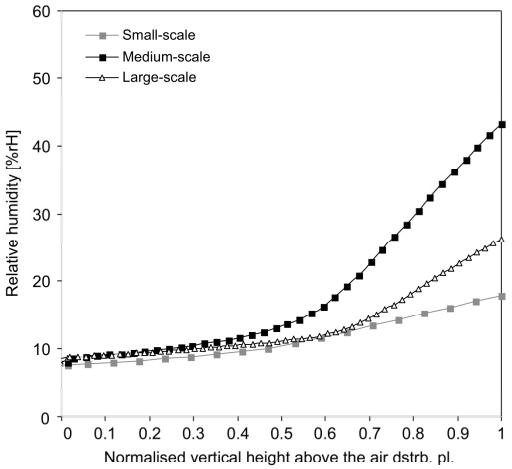

Fig. 12. Steady state fluidisation air relative humidity profiles for the three fluid bed scales. FN = 4.5, $P_{nozzle} = 1$ bar. Other model parameters according to Tables 1 and 3.

The comparison of the RD/DF and FN scale-up experiments should be evaluated in terms of the conditions under which the experiments were carried out. The fluidisation air inlet temperatures were close to identical in the RD/DF experiments and the fluidisation velocities were also higher than for the FN experiments. It is thus not surprising to observe lower agglomeration tendencies for these experiments. Compared to the RD/DF experiments, the fluidisation velocities were lower in the FN experiments (as a consequence of the FN patent guidelines proposed by Akkermans et al., 1998) although the liquid spray rates were similar and the spray zones shorter in vertical extension due to lower nozzle pressures. Especially for the medium-scale the fluidisation velocity was almost halved increasing the particle circulation time which meant that the inlet air temperature had to be as high as 97 °C in order to maintain the product temperature at 55 °C. This leads to high humidity and temperature gradients and local zones with low temperature and high fluidisation air humidity which are known to cause severe agglomeration. Low temperature and high humidity leads to a low DF causing slower drying, more moist particles and enhanced chance of agglomeration (Hede, 2005, 2006). The comparison of the scale-up experiments clearly shows that it is difficult to compare the scale-up principles in terms of temperature and humidity profiles without also including a comparison of the selection of vital parameters such as fluidisation air inlet temperature, nozzle pressure and fluidisation air velocity. What is needed is a combination of the model with a fundamental agglomeration model. The advantages of this will become evident when combining the model simulations of the particle moisture contents with the viscous Stokes theory in the next section.

4.1. Application of the viscous Stokes theory

The comparisons of the DF profiles in Figs. 10 and 13 with the measured agglomeration percentages in Table 3 indicate that zones of low temperature and high humidity increase the tendency of agglomeration. It is well-known that a low DF results in a low drying capacity and thereby moist particles. The correlation between the particle moisture contents and the resulting agglomeration percentages in Table 3 may be checked in terms of the present model, as one of the six calculated variables in each control volume is the particle moisture contents in kg H_2O/kg core. Fig. 14 shows the steady state particle water content profiles from the two scale-up experiments.

Comparison of the FN approach profiles in Fig. 14 with the agglomeration tendencies in Table 3 clearly reveals that there is a close relation between the observed agglomeration percentage and the particle water contents in the spray zone. The agglomeration percentages in Table 3 distribute according to the spray zone level of particle moisture contents observed in Fig. 14. Similarly for the RD/DF approach curves in Fig. 14, the curves reach close to similar levels of particle moisture contents in the spray zone, corresponding to the agglomeration tendencies in Table 3, which again are at levels

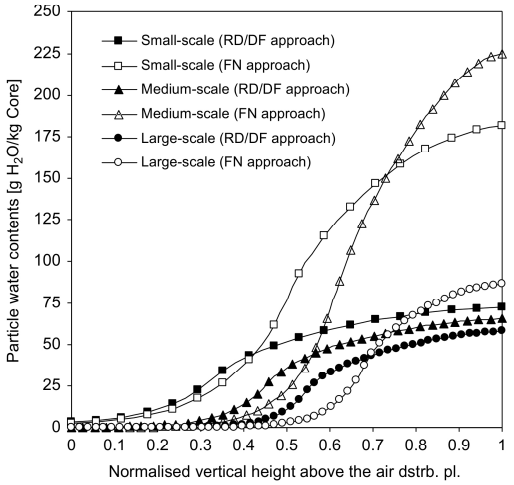

Fig. 14. Steady state particle water content profiles for the three fluid bed scales. RD/DF approach: RD = 3.5×10^{-3} min/g, DF = 12.5 kPa, P_{nozzle} = 3 bar. FN approach: FN = 4.5, P_{nozzle} = 1 bar. Other model parameters according to Tables 1 and 3.

much smaller than what is observed for the FN approach. The results obtained in Fig. 14 follow closely the trends observed from the DF profiles meaning that similar DF profiles (obtained under conditions with similar RD value) will ensure similar particle moisture content profiles, and possibly similar tendencies of agglomeration. This will become evident from the inclusion of the viscous Stokes theory presented below.

It is well known from numerous studies that the tendency of agglomeration increases with increasing particle moisture contents (Iveson et al., 2001). These observations have lead to an agglomeration model suggested originally by Ennis et al. (1991). The model assumes permanent agglomeration to occur if the kinetic energy of impact is entirely dissipated by viscous dissipation in the liquid layer and only elastic losses in the solid phase. The model predicts that collisions will result in permanent agglomeration when the viscous Stokes number (St_v) is less than a critical viscous Stokes number (St_v^*). The two numbers are given as (Ennis et al., 1991):

$$St_v = \frac{8 \cdot \rho_g \cdot r_{harm} \cdot u_0}{9 \cdot \eta_{liq}} \tag{6}$$

and

$$St_v^* = \left(1 + \frac{1}{e}\right) \ln\left(\frac{h_{liq}}{h_{asp}}\right) \tag{7}$$

where η_{liq} is the liquid coating viscosity, e is the coefficient of restitution, ρ_g is the granule density, h_{liq} is the thickness of the liquid surface, h_{asp} is the characteristic height of the surface asperities and r_{harm} is the harmonic mean granule radius of the two particles given as (Iveson et al., 2001):

$$r_{harm} = \frac{2 \cdot r_1 \cdot r_2}{r_1 + r_2} \tag{8}$$

u_0 is the initial collision velocity which is not easily obtainable due to the chaotic pattern of motion for the particles in fluid beds. A rough estimate based on the bubble rise velocity, v_{bu}, has been presented by Ennis et al. (1991):

$$u_0 \approx \frac{12 \cdot v_{bu} \cdot r_{harm}}{d_{bu} \cdot \delta^2} \tag{9}$$

where d_{bu} is the gas bubble diameter and δ the dimensionless bubble space defined as the axial fluid bed bubble spacing divided by the fluidisation gas bubble radius. Whereas the gas bubble diameter and spacing can be estimated by the dimensions of the air distributor plate, or found by experiments, the bubble rise velocity can be found according to the Davidson and Harrison (1963) formula:

$$v_{bu} = v_a - v_{mf} + 0.711 \cdot (g \cdot d_{bu})^{0.5} \tag{10}$$

The fact that the present model assumes an equal number of particles (each having the same diameter) in each control volume at a given time makes it possible to calculate the liquid layer thickness on the core particle surfaces. Although the uncoated sodium sulphate cores are porous, it is reasonable to assume that the pores have been fully filled early in the process, and thereby that all the particle moisture contents is present at the core particle surfaces only. Such an assumption is reasonable based on previous droplet penetration studies made by Hede et al. (2007b) and Hede (2005).

With the use of the parameters in Table 4 the liquid coating layer thicknesses are calculated for each control volume according to

Table 4
Parameters for the viscous Stokes analyses.

Parameter	Values
Gravity (g)	9.82 m/s^2
Coefficient of restitution (e)	0.8
Characteristic length scales of surface asperities (h_{asp})	1 μm
Granule density (ρ_g)	2600 kg/m^3
Coating solution viscosity (η_{liq})	3.5 mPa s
Coating solution density (ρ_{liq})	1.1 kg/m^3

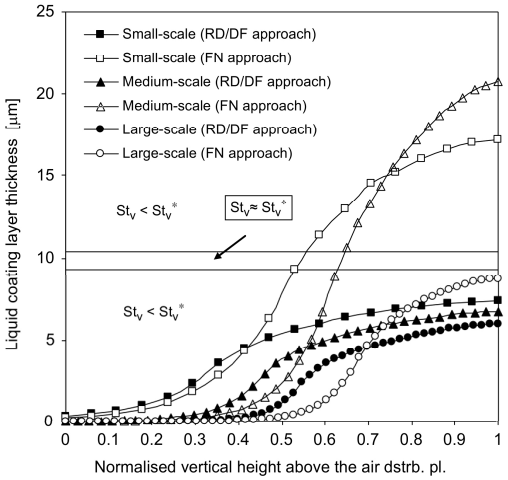

Fig. 15. Steady state coating liquid thickness profiles for the three fluid bed scales. RD/DF approach: RD = 3.5×10^{-3} min/g, DF = 12.5 kPa, P_{nozzle} = 3 bar. FN approach: FN = 4.5, P_{nozzle} = 1 bar. Other model parameters according to Tables 1 and 4.

the moisture contents in Fig. 14. These liquid thickness profiles are depicted in Fig. 15. Likewise are the viscous Stokes number, St_v, and the critical viscous Stokes number, St_v^*, calculated for each control volume. The value of the difference between St_v and St_v^* indicates the chance of agglomeration and the different regimes have been added to Fig. 15. The boundaries of these regimes are obviously dependent on the value of St_v. As parameters such as the gas bubble diameter, d_{bu}, and the dimensionless bubble space, δ, change with vertical distance from the air distribution plate, the estimate of the initial collision velocity, u_0 (and thereby the value of St_v) is different from control volume to control volume and, in addition, different from each of the six experiments in Fig. 15. This means that no uniform single line may be drawn in Fig. 15 for the $St_v = St_v^*$ condition, but rather that this condition is indicated by a regime. As observed from Fig. 15 the regime is nevertheless quite narrow as the differences between the St_v values have limited practical influence on the $St_v - St_v^*$ values.

The addition of the regimes based on the viscous Stokes theory in Fig. 15 provides a quantitative basis for the previous conclusions regarding the effect of the particle water contents on agglomeration. A clear relation is observed in Fig. 15 between the agglomeration tendencies in Table 3 and the curve shapes. Whereas the three experiments in the RD/DF scale-up attempt, with agglomeration percentages close to zero, are located solely in the coating regime ($St_v > St_v^*$), the curves for the experiments in the small- and medium-scale from the FN scale-up attempt cross the $St_v = St_v^*$ boundary into the agglomeration regime ($St_v < St_v^*$), just as was expected from the results in Table 3.

4.2. Sensitivity analysis

In a series of detailed sensitivity analyses Ronsse et al. (2007b) and Ronsse (2006) concluded that the most important properties with respect to the position of the steady state conditions of the fluid bed coating process are the fluidisation air inlet temperature and the volumetric fluidisation velocity. Ronsse et al. (2007b) also concluded that an increase in the relative size of the spray zone or an increase of the particle exchange rate had a narrowing effect of the overall coating mass distribution. Results further indicated that the outlet conditions were not affected by a change in the c/n ratio or a change in the value for r. Similar observations were observed in this study. More interesting is the effect on particle moisture content profiles as a function of the choice of r and c/n, which is investigated in the present sensitivity analysis. For the sensitivity analysis, the medium-scale fluid bed was selected and the model parameters for the sensitivity analysis can be seen from Table 5. In all the experiments for the sensitivity analysis, the volumetric fluidisation air velocity was fixed at 270 N m^3/h and the r value was varied without the use of the correlation in Eq. (B.1) (see Appendix B).

Initially a value of $r = 2\,s^{-1}$ was selected and fixed while the c/n ratio was varied. Fig. 16 shows how the particle moisture content profiles vary as a function of the c/n fraction.

It can be observed from Fig. 16 that there is a significant effect of the c/n value on the resulting particle moisture content profile. As the number of coating control volumes decreases, the particle moisture gradients increase significantly. The disadvantages of operating the fluid bed coating process with a small spray zone are clearly observed from Fig. 16 as the liquid is concentrated close to the nozzle leading to high particle moisture values and possible agglomeration. It appears, however, that beyond a c/n value of about 42% there is only minor effects of increasing the number of coating control volumes any further. This value is slightly scale-dependent as the same effect is observed for increasing c/n fractions the larger the fluid bed scale. In terms of the viscous Stokes theory, the $St_v = St_v^*$ boundary is reached for the medium-scale at a particle water content of 64 g H_2O/kg core for the given conditions meaning that, in order to avoid agglomeration, the spray zone should take up roughly 50% or more of the total expanded bed volume. This requirement is easily met in the small and medium pilot-scale fluid beds, but not in the larger fluid bed scales.

Table 5
Model parameters for the sensitivity analyses.

Process conditions	Values
Initial particle moisture content	4×10^{-3} kg water/kg core
External air temperature	20.0 °C
External air humidity	35%rH (at 20.0 °C) ~ 5.1×10^{-3} kg H_2O/kg dry air
Inlet fluidisation air temperature ($T_{a,in}$)	80 °C
Fluidisation air velocity	270 N m^3/h
Inlet fluidisation air humidity	1.7%rH (at 80 °C) ~ 5.1×10^{-3} kg H_2O/kg dry air
Bed load	4.0 kg
P_{nozzle}	3 bar
Coating solution spray rate	3 kg/h
Coating volume fraction (c/n ratio in % of total bed volume)	10.5–100%
Particle exchange rate (r parameter)	0.5–3.0 s^{-1}

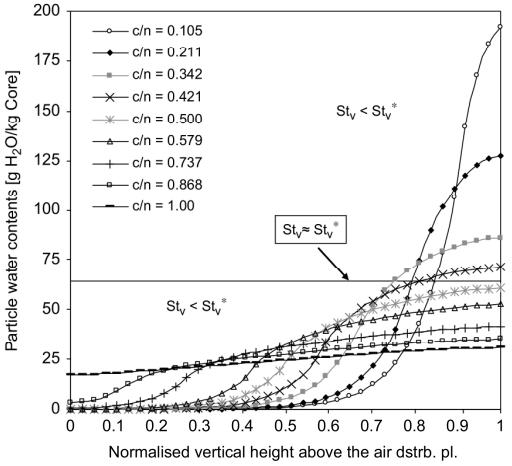

Fig. 16. Steady state particle moisture content force profiles as functions of the coating volume fraction, c/n, for the medium-scale pilot fluid bed.

In order to test the influence of the particle exchange rate r for a given fixed fluidisation velocity, the c/n value was fixed at 55.3% (~ 21 out of 38 control volumes were assigned to coating control volumes which corresponds to a nozzle pressure of 3 bar—see Table 1) while the r value was varied between 0.5 and 3.0. All other conditions were chosen from Table 4. Fig. 17 shows the variation in the particle moisture profiles as functions of the r value.

Contrary to Fig. 16, the effect of the particle exchange rate value on the particle moisture content profiles is observed from Fig. 17 to be rather small. Apparently, the moisture content in and near the spray zone is less affected by the value of r while the moisture content near the air distributor plate is slightly affected. If, however, a c/n value of 0.42 or less is chosen, the effect of r has been observed to be increasingly significant with decreasing c/n value. In

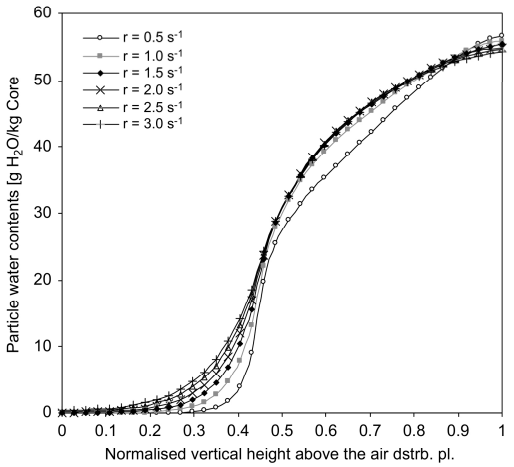

Fig. 17. Steady state particle moisture content force profiles as functions of the particle exchange rate, *r*, for the medium-scale pilot fluid bed.

conclusion, this indicates that as long as the spray zone is of considerable size (i.e. probably larger than 50% of the total expanded bed volume), the exact value of *r* is less important for the particle moisture content, but as the spray zone decreases in size, the particle circulation time becomes increasingly important. It is reasonable to relate the *r* parameter to the fluidisation velocity as the vertical particle transport in a fluid bed is known to be closely related to the bubble rise velocity for Geldart B particles as the ones being simulated in the present study. In that perspective, the use of Eq. (B.1) seems to be a reasonable choice.

4.3. Scale-up into a production-scale fluid bed

The present scale-up study did not allow experiments with production-scale fluid beds, but the model was used to simulate the conditions in a RICA-TEC (Anhydro A/S, Denmark) multi-nozzle production-scale top-spray fluid bed. Initial simulations of the production-scale revealed much larger temperature and humidity gradient vertically through the bed than was observed with the pilot-scale fluid beds. This means that the measured bed temperature at a single location is representative for the gas phase temperature at other positions in the chamber to a much lesser extent. Irrespectively of the vertical position, the bed temperature probe is positioned, the measurement will be far away from being representative. These observations reveal that scale-up into production-scale in terms of single fixed DF value is associated with greater uncertainty than scale-up between pilot-scale fluid beds where vertical temperature homogeneity is larger.

Following the combination of the viscous Stokes theory with the particle moisture content profiles obtained with the model, the task was to obtain conditions for the production-scale in which the coating liquid layer thickness profile stays just below the $St_V = St_V^*$ boundary. According to the RD/DF scale-up attempt by Hede et al. (2007a) in Table 3 the fluidisation velocity was chosen to be 3.3 m/s 4 cm above the air distributor plate for all three pilot-scale fluid beds. This ensured a reasonable high fluidisation air velocity of roughly 0.5 m/s at the top of the freeboard. The production-scale fluid bed is, however, designed physically different meaning that the chamber cross-section expansion is not as large as in the pilot-scale fluid beds. A choice of 3.3 m/s close to the air distributor plate requires 18 280 N m^3/h of fluidisation air (and leads to a gas velocity as high as 0.8 m/s at the top of the freeboard) which is beyond the actual capacity of the equipment. Instead a velocity of 11 080 N m^3/h was chosen, giving 0.5 m/s at the top of the freeboard. The average particle circulation time in the production-scale was calculated to 3.5 s with the use of Eq. (B.1). Although the particle circulation time distribution especially in large fluid bed scales is often observed to be quite broad with values ranging from a few seconds and up to about 20 s, estimated on the basis of positron emission particle tracking (PEPT) experiments performed by Stein et al. (2002) among others, an average value of 3.5 s is in accordance with estimations made by Ronsse (2006) and Mostoufi and Chaouki (2001). For the simulation of the production-scale an average particle circulation time was hereby chosen to be 3.5 s thereby giving a particle exchange rate of 0.28 s^{-1}.

Table 6
Process- and model-related parameters for the production-scale scale-up study. Fluid bed dimensions correspond to Fig. 2.

Process parameter	Production-scale RICA-TEC (Anhydro A/S)
Type of nozzle	External mixing two-fluid, 3 lances with 3 nozzle each (a total of 9 nozzles)
Nozzle pressure	3 bar
Liquid orifice diameters	1.2 mm
Inlet fluidisation air temperature	79 °C
Fluidisation velocity	11 080 N m^3/h ~ 0.5 m/s at the top of the freeboard
Particle exchange rate	$r = 0.28\ s^{-1}$
Coating feed reservoir temperature	60 °C
Initial core bed load	900 kg
Coating solution dry matter contents	15 w/w%
External air temperature	20.0 °C
External air humidity	35%rH (at 20.0 °C) ~ 5.1 × 10^{-3} kg H_2O/kg dry air
FB dimensions	
Length *a*	140 cm
Length *b*	30 cm
Length *c*	69 cm (at 3 bar)
Length *d*	174 cm
Length *e*	279 cm
Length *f*	–
Length *g*	280 cm
Length *h*	339 cm
Model-related parameters	
Total number of control volumes	116 ~ $h_{S,i} = 1.5$ cm
Number of coating control volumes	46 ($P_{nozzle} = 3$ bar)
Bed temperature measurement corresponds to control volume number	20

Fluid bed dimensions correspond to Fig. 3.

Following the RD/DF scale-up principle in Table 3 by Hede et al. (2007a), the RD size was initially kept fixed at RD = 3.5 × 10^{-3} min/g (~ liquid spray rate=221 kg/h) and other conditions selected according to Table 6. Under these conditions it was necessary to increase the inlet fluidisation air temperature to 95 °C in order to keep out of the agglomeration regime. This is more than 15 °C higher than what was needed in the pilot-scale RD/DF experiments, in order to obtain liquid layer profiles below the $St_V = St_V^*$ boundary. This resulted in an outlet absolute humidity of 25.8 g H_2O/kg dry air hereby indicating that scale-up in terms of combined RD/DF dictates increasing process intensity in order to stay out of the agglomeration regime when going into production-scale.

In industrial fluid bed coating processes such a high increase in inlet fluidisation air temperature from pilot-scale to production-scale would often not be feasible in practice due to a possible damage of the active ingredient in the granule core or coating layer. Granule properties such as appearances and morphology will probably also

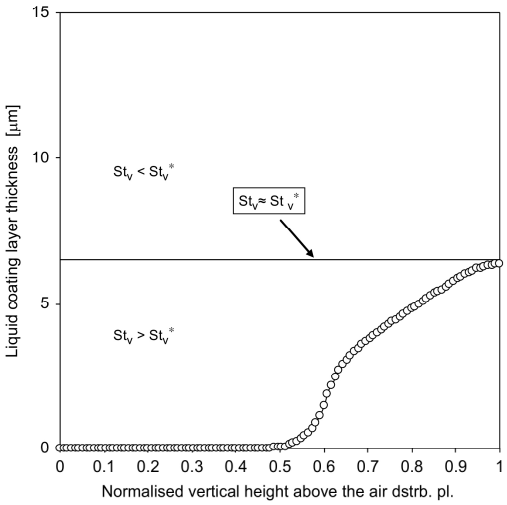

Fig. 18. Steady state coating liquid thickness profiles for the production-scale fluid bed. RD = 5.2 × 10^{-5} min/g, P_{nozzle} = 3 bar. Other model parameters according to Table 6.

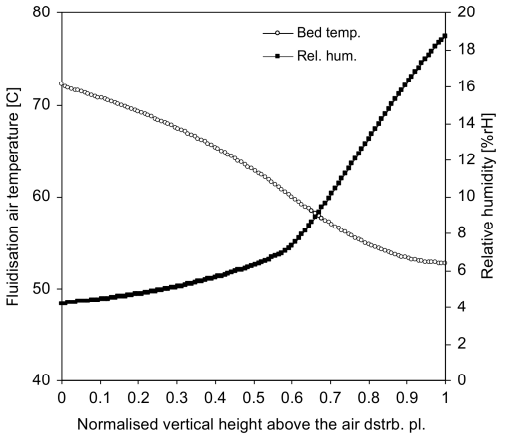

Fig. 19. Steady state fluidisation air temperature and humidity profiles for the production-scale fluid bed. RD = 5.2 × 10^{-5} min/g, P_{nozzle} = 3 bar. Other model parameters according to Table 6.

be affected by an increase in the inlet fluidisation air temperature. In order to maximise the process intensity, the inlet temperature in pilot-scale would probably be chosen to be as high as possible, meaning that the inlet temperature in production-scale could not be increased beyond that of the pilot-scale. From the pilot-scale RD/DF experiments in Table 3 it was observed how the inlet temperatures were close to each other ranging from 74 to 79 °C while the bed temperatures were close to 55 °C. Assuming that 79 °C is the maximum inlet temperature that could be allowed before the granule or coating components would be destroyed, simulations are performed in order to find the maximum spray intensity these conditions could allow while still being just below of the $St_V = St_V^*$ boundary. Dimensions and process conditions for the simulation in the production-scale may be seen from Table 6.

With the conditions in Table 6 a number of simulations were performed in order to adjust the liquid spray rate so that the particle liquid coating layer thickness profiles remained solely in the coating regime. An example where the profile touches the coating/agglomeration regime boundary in the upper part of the spray zone can be seen in Fig. 18. The curve indicates that the coating process would have had a low level of agglomeration. This is nevertheless achieved for a liquid spray rate of 108 kg/h giving a RD value as low as 5.2 × 10^{-5} min/g. Such a low spray rate would mean that it would take more than 11 h to coat the 900 kg with a 20 w/w% salt layer which is unacceptably long in practice.

The simulation with the conditions in Table 6 and a spray rate of 108 kg/h gives an outlet absolute humidity of 15.4 g H_2O/kg dry air. Compared to the outlet absolute humidity values in Table 3 ranging between 16 and 19 g H_2O/kg dry air, this indicates that the process intensity needs to be slightly smaller for the production-scale at similar inlet fluidisation air temperature in order to avoid agglomeration. Furthermore, as indicated from the RD/DF curves in Fig. 15, none of these three pilot-scale experiments came as close to the $St_V = St_V^*$ boundary as the production-scale in Fig. 18. This means that the RD/DF experiments in Table 3 could have been optimised further to run at slightly higher spray intensity before starting to agglomerate. If the liquid spray rate is optimised in terms of the model with fixed inlet fluidisation air temperatures of 79 °C, similar to the principle applied in Fig. 18, the outlet absolute humidity values for the pilot-scale fluid beds would range between 19 and 21 g H_2O/kg dry air with the larger outlet humidity values the smaller the fluid bed scale. Hence, the difference between the optimal pilot-scale and the production-scale process intensity without agglomeration is in reality somewhat larger for fixed inlet temperature. The fact that the differences in process intensity are not significantly larger between the pilot- and production-scale is due to the counter-acting fact that the heat loss from the fluidisation vessel to the surroundings relative to the bed load is smaller the larger the fluid bed scale.

In comparison to the three pilot-scale fluid beds having bed temperatures ranging from 54 to 57 °C at similar conditions, a bed temperature of 69 °C was simulated for the production-scale at the location of the temperature probe. This is partly a consequence of the design of the large fluid bed where the distance from the nozzle outlet to the air distributor plate increases significantly with scale, while the bed temperature measurement is measured at a similar vertical height across scale. Furthermore, the increased expanded bed height in the production-scale significantly increases the average particle circulation time and broadens the circulation time distribution hereby reducing the overall mixing leading to large temperature and fluidisation air humidity gradients. Figs. 19 and 20 presents the steady state fluidisation air temperature/relative humidity and DF profiles, respectively.

As observed from Fig. 19 there is a much larger temperature gradient than what was observed for the pilot-scale fluid beds in Fig. 8. From the fluidisation air inlet the temperature drops more than 20 °C while the relative humidity at the same time increases up to a level similar to Fig. 9 even though the RD value is far below the values for the experiments in Fig. 9. The overall DF (calculated with the use of Eq. (2)) is about 24 kPa which is far from the values of 12 kPa for the three pilot-scales in Table 3. This is due to the large temperature gradients in the production-scale fluid bed. In terms of DF, this also has an effect as it can be observed from Fig. 20 showing the steady state DF profile for the production-scale.

The simulations of the production-scale fluid bed have revealed a classical problem with fluid bed coating process up-scaling, which

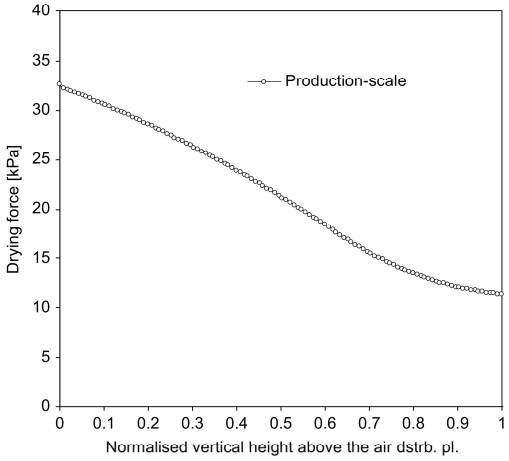

Fig. 20. Steady state drying force profile for the production-scale fluid bed. RD = 5.2×10^{-5} min/g, $P_{nozzle} = 3$ bar. Other model parameters according to Table 6.

is related to the typical design of fluid bed equipment. Compared to pilot-scale equipment, production-scale equipment is typically much larger in vertical size, while the horizontal dimension is only slightly expanded. This means, among many things, that the expanded particle bed height increases significantly with scale. Typically, similar types of external mixing nozzles are used for any fluid bed scale, and the need for increasing spray capacity in the large-scale is solved by adding more identical nozzles. As a consequence of this, even with increasing nozzle air flow rate in production-scale fluid bed equipment, the droplet penetration depth is not increased accordingly to the increased expanded particle bed height. In all, this means that while the spray zone remains close to similar in extension, the expanded bed height increases significantly with scale, causing large temperature and humidity gradients vertically across the bed as well as longer drying–wetting cycles for each particle. This is expected to result in accelerated agglomeration tendencies and different coating layer properties, as reported elsewhere (Werner et al., 2007a,b).

It was observed for the RD/DF pilot-scale experiments that similar high fluidisation velocities (in m/s) combined with close to similar fluidisation air inlet temperatures result in similar tendency of agglomeration indicating that these fluid bed scales do not behave significantly different with respect to coating behaviour as long as the nozzle pressure is not too low. These simple principles, however, cannot be followed into production-scale as the average particle circulation time significantly increases when going from pilot fluid bed scales to production-scale. This is another consequence of the design of large fluid beds, and comparison of the average particle exchange rates from the different scales reveals that the particle circulation time is roughly seven times larger in the production-scale compared to the small pilot-scale. This means that a much higher inlet and product fluidisation air temperature for a given spray rate is needed for the production-scale in order keep conditions in the spray zone outside the agglomeration regime.

As observed from Table 6 the c/n ratio is less than 40% which is where the value of r begins to play a role. as it was presented in the sensitivity analysis. As an indication of this, simulations revealed that the production-scale fluid bed required a simulation time of roughly 400 s to reach steady state for all properties, contrary to the pilot-scale fluid beds that required only a few hundred seconds to reach steady state. Besides affecting agglomeration tendency, a low average particle circulation time is likely to affect important properties not considered in the present study such as the quality of coating in terms of morphology and mechanical properties among other things. To overcome such fluid bed design problems the use of models as the one presented in this paper are useful tools in the optimisation of each fluid bed scale to produce unagglomerated coated granules at the same time having a high-intensity process.

5. Conclusion

A dynamic heat- and mass-transfer model for the top-spray batch fluid bed coating process was presented, enabling the calculation of the fluidisation air temperature and humidity as well as particle moisture contents. The model proved good agreement with steady state experimental data for important variables such as outlet temperature and humidity as well as the product temperature.

The model was applied to study how changing scale influences the in-bed process conditions from an up-scaling point of view. To illustrate successful as well as unsuccessful fluid bed coating process scale-up, experimental data across three pilot fluid beds were selected for model comparison from two papers by Hede et al. (2007a.c). Detailed simulations revealed that the three pilot-scales are not significantly different with respect to steady state in-bed conditions, and as long as the nozzle pressure, liquid spray rate and fluidisation air velocity (in m/s) are all above certain values, similar inlet fluidisation air temperatures will lead to similar low tendencies of agglomeration while the process intensity is maintained. This is because such process conditions give similar temperature, humidity and DF profiles again leading to similar particle liquid layer thicknesses which in turn causes similar tendency of agglomeration as verified using the viscous Stokes theory.

When scaling up to production-scale the temperature and humidity gradients increase significantly, meaning that the error of measuring the bed temperature at one location becomes much larger. It hereby becomes erroneous to define and fix an overall DF value. The RD parameter may apparently be fixed across scale during scale-up, just as it was observed by Rambali et al. (2003), but this requires a significant increase in the inlet fluidisation air temperature in order to keep out of the agglomeration regime. If the inlet temperature is fixed across scale, due to product-activity considerations, etc., then the spray intensity must be decreased the larger the fluid bed scale in order to avoid agglomeration. This results in a decreasing outlet absolute humidity and is a consequence of the poor mixing and longer particle circulation times the higher the fluidised bed is. This illustrates that for similar process intensity the coating process becomes increasingly sensitive towards the tendency of agglomeration the larger the fluid bed scale.

In general, when optimal conditions are to be found for any fluid bed scale, combination of the viscous Stokes theory and particle liquid layer thickness profiles obtained from simulations appears to be a strong tool. Although requiring a mass- and heat-transfer model, as the one presented in this paper, this optimisation principle is scientifically valid as it is based on thermodynamics and a generic first-principle model as the viscous Stokes theory. Contrary to the FN or DF/RD approach, this scale-up principle does not have any independent variables (such as the inlet fluidisation air temperature) and all fluid bed process settings can be determined a priori at any scale.

In all, the dynamic thermodynamic modelling and simulations have provided valuable insight into the top-spray fluid bed coating process. The simplicity, accuracy and versatility of the developed fluid bed coating model makes it a promising simulation tool in future scale-up studies, as well as for the study of response of the sys-

tem to a change in the process conditions. The scale-up conclusions may be summed up as:

- For each fluid bed scale the nozzle pressure has a great influence in terms of the vertical extension of the spray zone (besides an influence on the mean droplet size and the droplet size distribution). The larger the nozzle pressure, the further into the fluidised particle bed the droplets reach. In order to avoid high local particle moisture contents the spray zone should ideally take up more than 50% of the expanded bed height. This is normally achieved in small pilot-scale fluid beds, but not in larger scales. In order to achieve better coating processes in large-scale, it is suggested to decrease the distance between the air distributor plate and the nozzle outlet or perhaps insert nozzles at difference vertical positions in the chamber, hereby expanding the vertical extension of the spray zone. Adjusting the fluidisation velocity accordingly should ideally ensure similar particle circulation time across scale.
- The representation of the bed temperature in terms of a single temperature probe located near the air distribution plate may be representative for the temperatures at other locations only in pilot-scale fluid beds. Due to the large increase in expanded particle bed height with increasing scale and the resulting large temperature gradients, such single point temperature measurements are not representative for the temperature at other locations in production-scale fluid beds. It is suggested not to base process control alone on single point bed temperature measurements in production-scale fluid beds.
- Agglomeration tendency during coating with salt solutions is closely related to the particle liquid layer profile. The spray rate per kg bed mass and the inlet temperature may be chosen differently from scale to scale, still resulting in a similar low tendency of agglomeration, as long as the vertical particle liquid layer profile through the bed stays below a certain limit determined by the viscous Stokes theory. In scale-up of the fluid bed salt coating process into production-scale it is suggested to use lumped-region models (as the one presented in this paper) in order to combine particle liquid layer simulation results with generic particle-level agglomeration models as the viscous Stokes theory.

Notation

a_{Langmuir}	Langmuir coefficient, dimensionless
A	constant, dimensionless
A_{p}	surface area of a single particle, m^2
$A_{\text{w},i}$	total wall area in S_i, m^2
Ar	Archimedes number, dimensionless
B	constant, dimensionless
BD	bulk density of the powder bed, kg/m^3
Bi_{dr}	droplet Biot number, dimensionless
Bi_{p}	particle Biot number, dimensionless
c	number of coating control volumes, dimensionless
$C_{p,\text{a},i}$	moist air specific heat capacity in S_i, J/(kg K)
$C_{p,\text{c}}$	coating solution specific heat capacity, J/(kg K)
$C_{p,\text{Core}}$	specific heat capacity of cores, J/(kg K)
$C_{p,\text{dry air}}$	specific heat capacity of dry air, J/(kg K)
$C_{p,\text{H}_2\text{O}}$	specific heat capacity of water, J/(kg K)
$C_{p,\text{p}}$	particle specific heat capacity, J/(kg K)
$C_{p,\text{vapour}}$	specific heat capacity of vapour, J/(kg K)
$C_{p,\text{w}}$	reactor wall specific heat capacity, J/(kg K)
d_{bottom}	reactor bottom diameter, m
d_{bu}	gas bubble diameter, m
d_{dr}	droplet diameter, m
d_{p}	particle diameter, m
d_{plate}	diameter of gas distributor plate, m
d_{top}	reactor top diameter, m
d_{w}	reactor wall thickness, m
D_0	normalised distance, m
$D_{\text{v},i}$	molecular diffusion coefficient for vapour, m^2/s
DF	drying force, kPa
DM_{c}	coating solution dry matter content, kg drymatter/kg solution
e	particle coefficient of restitution, dimensionless
f_{bu}	bubble frequency, 1/s
$f_{\text{bu,w}}$	bubble frequency at the vertical surface, 1/s
FN	flux number, dimensionless
g	gravity, m/s^2
G_{a}	fluidisation dry air mass flow rate, kg/s
G_{at}	atomisation dry air mass flow rate, kg/s
Gr	Grasshof number, dimensionless
h_{asp}	characteristic length scales of surface asperities, m
h_{bed}	bed height, m
h_{bu}	vertical bubble position above the distributor plate, m
h_{FB}	Fluid bed height, m
h_{liq}	liquid layer height, m
h_{nozzle}	the height of the spray nozzle above the bottom of the fluidisation chamber, m
$h_{S,i}$	height of control volume S_i, m
i	index, dimensionless
$\dot{m}_{\text{nozzle air}}$	mass rate of atomisation air, kg/s
$\dot{m}_{\text{spray}}$	mass rate of liquid, kg/s
$M_{\text{a},i}$	mass of air in S_i, kg
M_{bed}	overall bed mass, kg
$\dot{M}_{\text{c}}$	mass flow rate of coating solution, kg/s
$M_{\text{dr},i}$	mass of droplets in control volume i, kg
M_{p}	mass of a single particle, kg
MW_{a}	molecular weight of fluidisation air, kg/mol
MW_{w}	molecular weight of water, kg/mol
n	number of control volumes, dimensionless
N_i	number of particles in control volume i, dimensionless
N_{bed}	total number of particles in the system, dimensionless
N_{or}	total number of perforations in the gas distributor plate,dimensionless
N_{sim}	number of simulated particles, dimensionless
Nu	Nusselt number, dimensionless
P_{ambient}	ambient pressure, Pa
P_{at}	atomisation air pressure, Pa
P_{atm}	atmospheric pressure, Pa
P_{e}	external atmospheric pressure, Pa
P_i	pressure in S_i, Pa
P_{nozzle}	nozzle pressure, Pa or bar
$P_{\text{v,a},i}$	vapour pressure in gas phase in S_i, Pa
$P_{\text{v,p},i}$	vapour pressure at particle surface in S_i, Pa
$P_{\text{v,sat}}$	saturated vapour pressure, Pa
$P_{\text{v\_dp}}$	vapour pressure at dew point, Pa
Pr_i	Prandtl number in S_i, dimensionless
$\dot{q}_{\text{mliq}}$	spray mass flux, $kg/(s\,m^2)$
$Q_{\text{lat},i}$	latent heat in S_i, J/kg
$Q_{\text{rad},i}$	radiative heat loss, J
r	particle exchange rate, 1/s
r_{harm}	harmonic mean granule radius, m
r_1, r_2	radius of granule 1 and 2, respectively, μm
$R_{\text{cond},i}$	thermal heat transfer resistance from vertical heat conduction coming from an adjacent wall element S_{i-1}, m^2 K/W
$R_{\text{conv},i}$	thermal heat transfer resistance from convection from fluidisation gas to chamber wall in S_i, m^2 K/W
$R_{\text{D},i}$	drying rate in S_i, kg water/(kg core s)

R_g	gasconstant, m^3 Pa/(K mol)
R_i	thermal heat transfer resistance from the bed to a vertical submerged surface in the bed in S_i, m^2 K/W
$R_{p,i}$	thermal heat transfer resistance from the particles to chamber wall in S_i, m^2 K/*W*
$R_{packet,i}$	thermal heat transfer resistance due to the presence of emulsion packets in S_i, m^2 K/W
$R_{pcd,i}$	thermal heat transfer resistance through the particle–vertical surface contact point and the surrounding thin gas layer in S_i, m^2 K/W
$R_{rad,i}$	thermal radiative heat transfer resistance in S_i, m^2 K/W
$R_{rad\_ext,i}$	thermal radiative heat transfer resistance in the surroundings, m^2 K/W
R_w	thermal heat transfer resistance from the wall to surroundings, m^2 K/W
Re	Reynolds number of gas phase in S_i, dimensionless
$Re_{p,i}$	particle Reynolds number in S_i, dimensionless
RD	relative droplet size, min/g
S_i	the *i*th control volume, dimensionless
$Sh_{p,i}$	particle Sherwood number, dimensionless
St_v	viscous Stokes number, dimensionless
St_v^*	critical viscous Stokes number, dimensionless
t	time, s
t_{heat}	time of heating stage, s
t_{sim}	simulated time, s
t_{spray}	spraying time, s
$T_{a,i}$	fluidisation air temperature in S_i,K
$T_{a,in}$	inlet fluidisation temperature, K
T_{at}	atomisation air temperature, K
T_{bed}	bed temperature, K
T_c	coating solution temperature, K
T_{db}	dry bulb temperature, K
T_e	external air temperature, K
$T_{p,i}$	particle temperature in S_i, K
T_{ref}	reference temperature (arbitrarily chosen), K
T_{wb}, i	wetbulb temperature in S_i, K
u_0	initial granule collision velocity, m/s
$v_{a,i}$	fluidisation air velocity in S_i, m/s
v_{bu}	bubble rise velocity, m/s
v_e	excess gas velocity, m/s
v_{mf}	minimum fluidisation velocity, m/s
v_{rel}	the difference between the nozzle atomising air velocity and the liquid velocity at the nozzle outlet, m/s
V_{bed}	bed volume, m^3
V_i	volume of S_i, m^3
$W_{p,i}$	particle water content in S_i, kg water/(kg core)
$X_{a,i}$	absolute air humidity in S_i, kg water/kg dry air
$X_{a,in}$	inlet fluidisation air absolute humidity, kg water/kg dry air
X_{at}	absolute humidity of nozzle air, kg water/kg dry air
X_{a_sat}	fluidisation air absolute humidity at saturation, kg water/kg dry air
Y_i	collected coating mass, kg dry matter/kg core
$Y_{p,i}$	coating mass deposited in S_i, kg dry matter/kg core

Greek letters

α_{dr}	droplet convective heat transfer coefficient, W/(m^2 K)
$\alpha_{p,i}$	particle convective heat transfer coefficient in S_i, W/(m^2 K)
$\alpha'_{p,i}$	mass transfer coefficient in S_i, m/s
β_a	thermal expansion coefficient of the fluidisation air, K^{-1}
δ	dimensionless bubble spacing, dimensionless
δ_w	bubble voidage at the submerged surface, dimensionless
Δ_{sim}	simulation time step, s
ε_{bed}	bed porosity, dimensionless
ε_i	bed voidage in S_i (volume not occupied by particles), dimensionless
ε_{mf}	bed voidage at minimum fluidisation, dimensionless
$\varepsilon_{mf,w}$	bed voidage at the submerged vertical surface at minimum fluidisation, dimensionless
ε_{wall}	reactor wall emittance for far-infrared radiation, dimensionless
$\eta_{a,i}$	fluidisation air viscosity in S_i, Pa s
η_{liq}	Coating solution viscosity, kg/m s
θ_w	reactor wall emittance, dimensionless
κ_w	wall mixing constant, dimensionless
$\lambda_{a,i}$	fluidisation air thermal conductivity in S_i, W/(m K)
$\lambda_{amark,i}$	thermal conductivity for stagnant gas in the bed in S_i, W/(m K)
$\lambda_{aw,i}$	thermal conductivity for stagnant gas in the vicinity of the submerged vertical surface in S_i,W/(m K)
λ_p	particle thermal conductivity, W/(m K)
$\lambda_{w,i}$	reactor wall thermal conductivity, W/(m K)
$\rho_{a,i}$	fluidisation air density in S_i, kg/m^3
ρ_g	granule density, kg/m^3
ρ_{liq}	Coating solution viscosity, kg/m^3
ρ_p	particle density, kg/m^3
ρ_w	reactor wall density, kg/m^3
σ	Stefan–Boltzmann constant, W/(m^2 K^4)
τ_{mark}	equivalent gas film thickness of the gas film around the adjacent particle–particle contact point (compared to the particle diameter), dimensionless
τ_w	equivalent gas film thickness of the gas film around the surface–particle contact point (compared to the particle diameter), dimensionless
ϕ_e	external air relative humidity, dimensionless
ϕ_p	atomisation relative humidity, dimensionless
$\Phi_{loss,a,i}$	fluidisation air heat loss (air-to-wall heat transfer), J/s
$\Phi_{loss,p,i}$	particle loss (particle-to-wall heat transfer), J/s
ψ_p	particle sphericity, dimensionless

Acknowledgements

This project was performed in collaboration with Novozymes A/S, who also financially supported the project. Peter Dybdahl Hede is a member of the Novozymes Bioprocess Academy as well as the MP_2T Graduate School in Chemical Engineering at the Department of Chemical and Biochemical Engineering, Technical University of Denmark, funded by the Danish Technical Research Council, the European Union, the Nordic Energy Research, Dong Energy A/S, Vattenfall A.B., F L Smidth A/S, and Public Service Obligation funds from Energinet.dk and the Danish Energy Research programme.

Appendices

The following appendices provide a detailed description of the model used in this paper. The current model is very similar to that of Ronsse et al. (2007a) and Ronsse (2006). but with several corrections and critical updates, including the calculation of the local exchange rate as a function of the fluidisation velocity and other local parameters. For clarity, the entire model is presented here.

Appendix A. Model equations

A.1. Particle balance on a single control volume

As a result of the model assumptions, the population balance for the particles in control volume S_i may be written according to Eq. (A.1). The unit on both side of Eq. (A.1) is number of particles per second:

$$\underbrace{\frac{dN_i}{dt}}_{\substack{\text{Rate of change in}\\ \text{number of particles}\\ \text{in control volume } S_i}} = \underbrace{r \cdot N_{bed}}_{\substack{\text{Particles entering from}\\ \text{control volume } S_{i-1}}} + \underbrace{r \cdot N_{bed}}_{\substack{\text{Particles entering from}\\ \text{control volume } S_{i+1}}} - \underbrace{r \cdot N_{bed}}_{\substack{\text{Particles leaving to}\\ \text{control volume } S_{i+1}}} - \underbrace{r \cdot N_{bed}}_{\substack{\text{Particles leaving to}\\ \text{control volume } S_{i-1}}} = 0 \quad (A.1)$$

A.2. Moisture (water) balance of the particles

A.2.1. In a non-coating control volume

In each non-coating control volume, the balance of moisture on the surface of the core particles is governed by the amount of water introduced by the particles entering S_i from S_{i-1} and S_{i+1}, the amount of water removed by the particles leaving S_i to S_{i-1} and S_{i+1} as well as the water evaporated from or condensed on the particle surfaces according to Eq. (A.2). The unit on both side of Eq. (A.2) is kg H_2O per second:

$$\underbrace{M_p N_i \frac{dW_{p,i}}{dt}}_{\substack{\text{Rate of change in water}\\ \text{contents on particle surfaces}\\ \text{in control volume } S_i}} = \underbrace{M_p \cdot N_{bed} \cdot W_{p,i-1} \cdot r}_{\substack{\text{Mass of water from wet particles}\\ \text{entering from control volume } S_{i-1}}} + \underbrace{M_p \cdot N_{bed} \cdot W_{p,i+1} \cdot r}_{\substack{\text{Mass of water from wet particles}\\ \text{entering from control volume } S_{i+1}}} - \underbrace{M_p \cdot N_{bed} \cdot W_{p,i} \cdot r}_{\substack{\text{Mass of water from wet particles}\\ \text{leaving to control volume } S_{i+1}}} - \underbrace{M_p \cdot N_{bed} \cdot W_{p,i} \cdot r}_{\substack{\text{Mass of water from wet particles}\\ \text{leaving to control volume } S_{i-1}}} - \underbrace{R_{D,i} \cdot M_p \cdot N_i}_{\substack{\text{Mass of water from wetted particles}\\ \text{disappearing due to evaporation}}} \quad (A.2)$$

for $1 \leqslant i \leqslant n-c$.

A.2.2. In a coating control volume

In a coating control volume, the introduction of coating solution needs to be taken into account, resulting in

$$\underbrace{M_p N_i \frac{dW_{p,i}}{dt}}_{\substack{\text{Rate of change in water}\\ \text{contents on particle surfaces}\\ \text{in control volume } S_i}} = \underbrace{M_p \cdot N_{bed} \cdot W_{p,i-1} \cdot r}_{\substack{\text{Mass of water from wet particles}\\ \text{entering from control volume } S_{i-1}}} + \underbrace{M_p \cdot N_{bed} \cdot W_{p,i+1} \cdot r}_{\substack{\text{Mass of water from wet particles}\\ \text{entering from control volume } S_{i+1}}} - \underbrace{R_{D,i} \cdot M_p \cdot N_i}_{\substack{\text{Mass of water from wetted particles}\\ \text{disappearing due to evaporation}}} - \underbrace{M_p \cdot N_{bed} \cdot W_{p,i} \cdot r}_{\substack{\text{Mass of water from wet particles}\\ \text{leaving to control volume } S_{i+1}}} - \underbrace{M_p \cdot N_{bed} \cdot W_{p,i} \cdot r}_{\substack{\text{Mass of water from wet particles}\\ \text{leaving to control volume } S_{i-1}}} + \underbrace{\frac{1}{c}(1 - DM_c) \cdot \dot{M}_c}_{\substack{\text{Mass of water coming from the}\\ \text{coating solution droplets}}} \quad (A.3)$$

for $n-c < i \leqslant n$.

In the model, it is assumed that the coating solution is uniformly divided over all coating control volumes c. Hence the term $1/c$ in Eq. (A.3).

A.3. Moisture (water) balance in the gas phase

A.3.1. In a non-coating control volume

The change in air moisture in a non-coating control volume S_i is determined by the incoming moisture in the process air from S_{i-1}, the moisture in the process air leaving towards S_{i+1} and the amount of water coming from evaporated water on the particle surfaces. Because the volume fraction of the bed, in which the atomisation air is homogeneously mixed, is unknown, it is further assumed that the sprayed coating solution and the atomisation air are divided over the same fraction of the fluidised bed being the upper c control volumes. Hence, the air moisture balance may be written according to Eq. (A.4). The unit on both side of Eq. (A.4) is kg H_2O per second:

$$\underbrace{M_{a,i} \frac{dX_{a,i}}{dt}}_{\substack{\text{Rate of change in water}\\ \text{contents in the gas phase}\\ \text{in control volume } S_i}} = \underbrace{G_a \cdot X_{a,i-1}}_{\substack{\text{Mass of water from the}\\ \text{fluidisation air entering}\\ \text{from control volume } S_{i-1}}} - \underbrace{G_a \cdot X_{a,i}}_{\substack{\text{Mass of water from the}\\ \text{fluidisation air leavingto}\\ \text{control volume } S_{i+1}}} + \underbrace{R_{D,i} \cdot M_p \cdot N_i}_{\substack{\text{Mass of water entering}\\ \text{the gas phase from}\\ \text{particle surface drying}}} \quad (A.4)$$

for $1 \leqslant i \leqslant n-c$.

where $M_{a,i} = V_i \cdot \rho_{a,i} \cdot \varepsilon_i$ and ε_i is the fraction of the control volume S_i that is not occupied by particles.

A.3.2. In a coating control volume

Similar to Eq. (A.4), Eq. (A.5) expresses the water balance for the coating control volumes:

$$\underbrace{M_{a,i} \frac{dX_{a,i}}{dt}}_{\substack{\text{Rate of change in water}\\ \text{contents in the gas phase in}\\ \text{control volume } S_i}} = \underbrace{\left(G_a + \frac{i-(n-c)-1}{c} \cdot G_{at}\right) \cdot X_{a,i-1}}_{\substack{\text{Mass of water from the cummulated fluidisation}\\ \text{atomisation air entering from control volume } S_{i-1}}} - \underbrace{\left(G_a + \frac{i-(n-c)}{c} \cdot G_{at}\right) \cdot X_{a,i}}_{\substack{\text{Mass of water from the cummulated fluidisation}\\ \text{atomisation air leaving to control volume } S_{i+1}}} + \underbrace{\frac{1}{c} G_{at} \cdot X_{at}}_{\substack{\text{Mass of water from the}\\ \text{atomisation air entering}\\ \text{control volume } S_i}} + \underbrace{R_{D,i} \cdot M_p \cdot N_i}_{\substack{\text{Mass of water entering the gas phase}\\ \text{from particle surface drying}}} \quad (A.5)$$

for $n-c < i \leqslant n$.

A.4. Coating mass balance of the particles

A.4.1. In a non-coating control volume

Particles are assumed only to receive coating if they are in coating control volumes. Hence, for the non-coating control volume, the coating mass balance is simply:

$$\underbrace{M_{\mathrm{p}} N_i \frac{\mathrm{d}Y_{\mathrm{p},i}}{\mathrm{d}t}}_{\substack{\text{Rate of change in coating}\\ \text{mass in control volume } S_i}} = 0 \tag{A.6}$$

for $1 \leqslant i \leqslant n - c$.

A.4.2. In a coating control volume

According to the assumptions, all particles located inside a single coating control volume receive an equal amount of coating mass. Hence, the equation for the coating mass balance is given by:

$$\underbrace{M_{\mathrm{p}} N_i \frac{\mathrm{d}Y_{\mathrm{p},i}}{\mathrm{d}t}}_{\substack{\text{Rate of change in coating}\\ \text{mass in control volume } S_i}} = \underbrace{\frac{1}{c} \cdot \mathrm{DM_c} \cdot \dot{M}_{\mathrm{c}}}_{\substack{\text{Mass of water coming from}\\ \text{the coating solution droplets}}} \tag{A.7}$$

for $n - c < i \leqslant n$.

A.5. Energy balance of the particles

A.5.1. In a non-coating control volume

The enthalpy balance of the particles within any control volume S_i depends on the enthalpy of the particles entering and leaving S_i, the convective heat transfer between the air and the particles, the latent heat of evaporation of water on the particle surface and the heat losses through the shell of the reactor. The unit in Eq. (A.8) is in J/s:

$$\begin{aligned}
\underbrace{N_i \cdot M_{\mathrm{p}} \cdot C_{p,\mathrm{p}} \frac{\mathrm{d}T_{\mathrm{p},i}}{\mathrm{d}t}}_{\substack{\text{Enthalpy exhange rate}\\ \text{in control volume } S_i}} &= \underbrace{M_{\mathrm{p}} \cdot N_{\mathrm{bed}} \cdot C_{p,\mathrm{p}} \cdot r \cdot (T_{\mathrm{p},i+1} - T_{\mathrm{ref}})}_{\substack{\text{Enthalpy from particles entering}\\ \text{from control volume } S_{i+1}}} \\
&+ \underbrace{M_{\mathrm{p}} \cdot N_{\mathrm{bed}} \cdot C_{p,\mathrm{p}} \cdot r \cdot (T_{\mathrm{p},i-1} - T_{\mathrm{ref}})}_{\substack{\text{Enthalpy from particles entering}\\ \text{from control volume } S_{i-1}}} \\
&- \underbrace{M_{\mathrm{p}} \cdot N_{\mathrm{bed}} \cdot C_{p,\mathrm{p}} \cdot r \cdot (T_{\mathrm{p},i} - T_{\mathrm{ref}})}_{\substack{\text{Enthalpy from particles leaving}\\ \text{to control volume } S_{i+1}}} \\
&- \underbrace{M_{\mathrm{p}} \cdot N_{\mathrm{bed}} \cdot C_{p,\mathrm{p}} \cdot r \cdot (T_{\mathrm{p},i} - T_{\mathrm{ref}})}_{\substack{\text{Enthalpy from particles leaving}\\ \text{to control volume } S_{i-1}}} \\
&+ \underbrace{\alpha_{\mathrm{p},i} \cdot N_i \cdot A_{\mathrm{p}} \cdot (T_{\mathrm{a},i} - T_{\mathrm{p},i})}_{\substack{\text{Heat from convective heat}\\ \text{transfer from fluidisation air to particles}}} \\
&- \underbrace{R_{\mathrm{D},i} \cdot N_i \cdot M_{\mathrm{p}} \cdot Q_{\mathrm{lat},i}}_{\substack{\text{Latent heat needed for}\\ \text{the drying of particles}}} \\
&- \underbrace{\Phi_{\mathrm{loss,p},i}}_{\substack{\text{Heat loss to surroundings}\\ \text{(particle-to-wall heat transfer)}}}
\end{aligned}$$

$$\Rightarrow$$

$$\underbrace{N_i \cdot M_{\mathrm{p}} \cdot C_{p,\mathrm{p}} \frac{\mathrm{d}T_{\mathrm{p},i}}{\mathrm{d}t}}_{\substack{\text{Enthalpy exhange rate}\\ \text{in control volume } S_i}} = \underbrace{M_{\mathrm{p}} \cdot N_{\mathrm{bed}} \cdot C_{p,\mathrm{p}} \cdot r \cdot (T_{\mathrm{p},i+1} - T_{\mathrm{p},i})}_{\substack{\text{Netto enthalpy from particles entering}\\ \text{from control volume } S_{i+1}}}$$

$$\begin{aligned}
&+ \underbrace{M_{\mathrm{p}} \cdot N_{\mathrm{bed}} \cdot C_{p,\mathrm{p}} \cdot r \cdot (T_{\mathrm{p},i-1} - T_{\mathrm{p},i})}_{\substack{\text{Netto enthalpy from particles entering}\\ \text{from control volume } S_{i-1}}} \\
&+ \underbrace{\alpha_{\mathrm{p},i} \cdot N_i \cdot A_{\mathrm{p}} \cdot (T_{\mathrm{a},i} - T_{\mathrm{p},i})}_{\substack{\text{Heat from convective heat}\\ \text{transfer from fluidisation air to particles}}} \\
&- \underbrace{R_{\mathrm{D},i} \cdot N_i \cdot M_{\mathrm{p}} \cdot Q_{\mathrm{lat},i}}_{\substack{\text{Latent heat needed for}\\ \text{the drying of particles}}} \\
&- \underbrace{\Phi_{\mathrm{loss,p},i}}_{\substack{\text{Heat loss to surroundings}\\ \text{(particle-to-wall heat transfer)}}}
\end{aligned} \tag{A.8}$$

for $1 \leqslant i \leqslant n - c$.

In Eq. (A.8), A_{p} is the total surface of one particle in control volume S_i and $Q_{\mathrm{lat},i}$ is the latent heat of vaporisation for pure water approximated by:

$$Q_{\mathrm{lat},i} = 10^3 (2500.6 - 2.364356 \cdot (T_{\mathrm{p},i} - 273.15)) \tag{A.9}$$

A.5.2. In a coating control volume

Analogously to Eq. (A.8) with the addition of a coating-related term, the enthalpy balance for the particle phase in a coating control volume can be expressed in terms of Eq. (A.10). Since the diameter of the sprayed droplets is generally between 10 and 40 μm (Lefebvre, 1989), it is assumed that the droplets, travelling from the nozzle towards the particle surface, reach the wet bulb temperature (T_{wb}) before colliding with the particle surface:

$$\begin{aligned}
\underbrace{N_i \cdot M_{\mathrm{p}} \cdot C_{p,\mathrm{p}} \frac{\mathrm{d}T_{\mathrm{p},i}}{\mathrm{d}t}}_{\substack{\text{Particle enthalpy exhange rate}\\ \text{in control volume } S_i}} &= \underbrace{M_{\mathrm{p}} \cdot N_{\mathrm{bed}} \cdot C_{p,\mathrm{p}} \cdot r \cdot (T_{\mathrm{p},i+1} - T_{\mathrm{ref}})}_{\substack{\text{Enthalpy from particles entering}\\ \text{from control volume } S_{i+1}}} \\
&+ \underbrace{M_{\mathrm{p}} \cdot N_{\mathrm{bed}} \cdot C_{p,\mathrm{p}} \cdot r \cdot (T_{\mathrm{p},i-1} - T_{\mathrm{ref}})}_{\substack{\text{Enthalpy from particles entering}\\ \text{from control volume } S_{i-1}}} \\
&- \underbrace{M_{\mathrm{p}} \cdot N_{\mathrm{bed}} \cdot C_{p,\mathrm{p}} \cdot r \cdot (T_{\mathrm{p},i} - T_{\mathrm{ref}})}_{\substack{\text{Enthalpy from particles leaving}\\ \text{to control volume } S_{i+1}}} \\
&- \underbrace{M_{\mathrm{p}} \cdot N_{\mathrm{bed}} \cdot C_{p,\mathrm{p}} \cdot r \cdot (T_{\mathrm{p},i} - T_{\mathrm{ref}})}_{\substack{\text{Enthalpy from particles leaving}\\ \text{to control volume } S_{i-1}}} \\
&+ \underbrace{\alpha_{\mathrm{p},i} \cdot N_i \cdot A_{\mathrm{p}} \cdot (T_{\mathrm{a},i} - T_{\mathrm{p},i})}_{\substack{\text{Heat from convective heat}\\ \text{transfer from fluidisation air to particles}}} \\
&- \underbrace{R_{\mathrm{D},i} \cdot N_i \cdot M_{\mathrm{p}} \cdot Q_{\mathrm{lat},i}}_{\substack{\text{Latent heat from}\\ \text{the drying of particles}}} \\
&+ \underbrace{\frac{1}{c} \dot{M}_{\mathrm{c}} \cdot C_{p,\mathrm{c}} \cdot (T_{\mathrm{wb},i} - T_{\mathrm{ref}})}_{\substack{\text{Enthalpy comming from droplets entering } S_i\\ \text{with the wet bulb temperature}}} \\
&- \underbrace{\frac{1}{c} \dot{M}_{\mathrm{c}} \cdot C_{p,\mathrm{c}} \cdot (T_{\mathrm{p},i} - T_{\mathrm{ref}})}_{\substack{\text{Enthalpy needed to heat the droplets up to}\\ \text{particle temperature}}} \\
&- \underbrace{\Phi_{\mathrm{loss,p},i}}_{\substack{\text{Heat loss to surroundings}\\ \text{(particle-to-wall heat transfer)}}}
\end{aligned}$$

$$\Rightarrow$$

$$\underbrace{N_i \cdot M_{\mathrm{p}} \cdot C_{p,\mathrm{p}} \frac{\mathrm{d}T_{\mathrm{p},i}}{\mathrm{d}t}}_{\substack{\text{Particle enthalpy exhange rate}\\ \text{in control volume } S_i}} = \underbrace{M_{\mathrm{p}} \cdot N_{\mathrm{bed}} \cdot C_{p,\mathrm{p}} \cdot r \cdot (T_{\mathrm{p},i+1} - T_{\mathrm{p},i})}_{\substack{\text{Netto enthalpy from particles entering}\\ \text{from control volume } S_{i+1}}}$$

$$
\begin{aligned}
&+ \underbrace{M_{\mathrm{p}} \cdot N_{\mathrm{bed}} \cdot C_{p,\mathrm{p}} \cdot r \cdot (T_{\mathrm{p},i-1} - T_{\mathrm{p},i})}_{\substack{\text{Netto enthalpy from particles entering}\\ \text{from control volume } S_{i-1}}} \\
&+ \underbrace{\alpha_{\mathrm{p},i} \cdot N_i \cdot A_{\mathrm{p}} \cdot (T_{\mathrm{a},i} - T_{\mathrm{p},i})}_{\substack{\text{Heat from convective heat}\\ \text{transfer from fluidisation air to particles}}} \\
&- \underbrace{R_{\mathrm{D},i} \cdot N_i \cdot M_{\mathrm{p}} \cdot Q_{\mathrm{lat},i}}_{\substack{\text{Latent heat from}\\ \text{the drying of particles}}} \\
&- \underbrace{\frac{1}{c}\dot{M}_{\mathrm{c}} \cdot C_{p,\mathrm{c}} \cdot (T_{\mathrm{p},i} - T_{\mathrm{wb},i})}_{\substack{\text{Enthalpy needed to heat the droplets}\\ \text{up to the particle temperature}}} \\
&- \underbrace{\Phi_{\mathrm{loss,p},i}}_{\substack{\text{Heat loss to surroundings}\\ \text{(particle-to-wall heat transfer)}}} \qquad \text{(A.10)}
\end{aligned}
$$

for $n - c < i \leqslant n$.

A.6. Energy balance of the gas phase

A.6.1. In a non-coating control volume

The equation for the enthalpy balance of the gas phase within each control volume S_i is given by the enthalpy of the air entering from S_{i-1} and the enthalpy leaving to S_{i+1}, the enthalpy of the atomisation air, the heat transferred between the gas phase and the droplet phase, the heat transferred between the gas phase and the particles in S_i. The unit in Eq. (A.11) is in J/s:

$$
\begin{aligned}
\underbrace{M_{\mathrm{a},i} \cdot C_{p,\mathrm{a},i} \frac{\mathrm{d}T_{\mathrm{a},i}}{\mathrm{d}t}}_{\substack{\text{Enthalpy exhange rate}\\ \text{in control volume } S_i}} &= \underbrace{G_{\mathrm{a}} \cdot C_{p,\mathrm{a},i} \cdot (T_{\mathrm{a},i-1} - T_{\mathrm{ref}})}_{\substack{\text{Enthalpy from fluidisation air entering}\\ \text{from control volume } S_{i-1}}} \\
&- \underbrace{G_{\mathrm{a}} \cdot C_{p,\mathrm{a},i} \cdot (T_{\mathrm{a},i} - T_{\mathrm{ref}})}_{\substack{\text{Enthalpy from droplets leaving}\\ \text{to control volume } S_{i+1}}} \\
&- \underbrace{\alpha_{\mathrm{p},i} \cdot N_i \cdot A_{\mathrm{p}} \cdot (T_{\mathrm{a},i} - T_{\mathrm{p},i})}_{\substack{\text{Heat from convective heat}\\ \text{transfer from fluidisation air to particles}}} \\
&- \underbrace{R_{\mathrm{D},i} \cdot N_i \cdot M_{\mathrm{p}} \cdot C_{p,\mathrm{v},i} \cdot (T_{\mathrm{a},i} - T_{\mathrm{ref}})}_{\substack{\text{Enthalpy required to heat the vapour up to gas temp.}}} \\
&+ \underbrace{R_{\mathrm{D},i} \cdot N_i \cdot M_{\mathrm{p}} \cdot C_{p,\mathrm{v},i} \cdot (T_{\mathrm{p},i} - T_{\mathrm{ref}})}_{\substack{\text{Enthalpy from the generated steam}}} \\
&- \underbrace{\Phi_{\mathrm{loss,a},i}}_{\substack{\text{Heat loss to surroundings}\\ \text{(gas-to-wall heat transfer)}}} \\
&\Rightarrow \\
\underbrace{M_{\mathrm{a},i} \cdot C_{p,\mathrm{a},i} \frac{\mathrm{d}T_{\mathrm{a},i}}{\mathrm{d}t}}_{\substack{\text{Enthalpy exhange rate}\\ \text{in control volume } S_i}} &= \underbrace{G_{\mathrm{a}} \cdot C_{p,\mathrm{a},i} \cdot (T_{\mathrm{a},i-1} - T_{\mathrm{a},i})}_{\substack{\text{Netto enthalpy contribution}\\ \text{from fluidisation air}}} \\
&- \underbrace{\alpha_{\mathrm{p},i} \cdot N_i \cdot A_{\mathrm{p}} \cdot (T_{\mathrm{a},i} - T_{\mathrm{p},i})}_{\substack{\text{Heat from convective heat transfer}\\ \text{from fluidisation air to particles}}} \\
&- \underbrace{R_{\mathrm{D},i} \cdot N_i \cdot M_{\mathrm{p}} \cdot C_{p,\mathrm{v},i} \cdot (T_{\mathrm{a},i} - T_{\mathrm{p},i})}_{\substack{\text{Enthalpy required to evaporate water}\\ \text{and heat the vapour up to gas temp.}}} \\
&- \underbrace{\Phi_{\mathrm{loss,a},i}}_{\substack{\text{Heat loss to surroundings}\\ \text{(gas-to-wall heat transfer)}}} \qquad \text{(A.11)}
\end{aligned}
$$

for $1 \leqslant i \leqslant n - c$.

A.6.2. In a coating control volume

$$
\begin{aligned}
\underbrace{M_{\mathrm{a},i} \cdot C_{p,\mathrm{a},i} \frac{\mathrm{d}T_{\mathrm{a},i}}{\mathrm{d}t}}_{\substack{\text{Enthalpy exhange rate}\\ \text{in control volume } S_i}} &= \underbrace{\left(G_{\mathrm{a}} + \frac{i-(n-c)-1}{c} \cdot G_{\mathrm{at}}\right) \cdot C_{p,\mathrm{a},i} \cdot (T_{\mathrm{a},i-1} - T_{\mathrm{ref}})}_{\substack{\text{Enthalpy from cummulated fluidisation/atomisation air}\\ \text{entering from control volume } S_{i-1}}} \\
&- \underbrace{\left(G_{\mathrm{a}} + \frac{i-(n-c)}{c} \cdot G_{\mathrm{at}}\right) \cdot C_{p,\mathrm{a},i} \cdot (T_{\mathrm{a},i} - T_{\mathrm{ref}})}_{\substack{\text{Enthalpy from cummulated fluidisation/atomisation air}\\ \text{leaving to control volume } S_{i+1}}} \\
&+ \underbrace{\frac{1}{c} \cdot G_{\mathrm{at}} \cdot C_{p,\mathrm{a},i} \cdot (T_{\mathrm{at},i} - T_{\mathrm{ref}})}_{\substack{\text{Enthalpy from atomisation air entering } S_i}} \\
&- \underbrace{\alpha_{\mathrm{p},i} \cdot N_i \cdot A_{\mathrm{p}} \cdot (T_{\mathrm{a},i} - T_{\mathrm{p},i})}_{\substack{\text{Heat from convective heat}\\ \text{transfer from fluidisation air to particles}}} \\
&- \underbrace{R_{\mathrm{D},i} \cdot N_i \cdot M_{\mathrm{p}} \cdot C_{p,\mathrm{v},i} \cdot (T_{\mathrm{a},i} - T_{\mathrm{ref}})}_{\substack{\text{Enthalpy required to heat the vapour up to gas temp.}}} \\
&+ \underbrace{R_{\mathrm{D},i} \cdot N_i \cdot M_{\mathrm{p}} \cdot C_{p,\mathrm{v},i} \cdot (T_{\mathrm{p},i} - T_{\mathrm{ref}})}_{\substack{\text{Enthalpy from the generated steam}}} \\
&- \underbrace{\Phi_{\mathrm{loss,a},i}}_{\substack{\text{Heat loss to surroundings}\\ \text{(gas-to-wall heat transfer)}}} \\
&\Rightarrow \\
\underbrace{M_{\mathrm{a},i} \cdot C_{p,\mathrm{a},i} \frac{\mathrm{d}T_{\mathrm{a},i}}{\mathrm{d}t}}_{\substack{\text{Enthalpy exhange rate}\\ \text{in control volume } S_i}} &= \underbrace{G_{\mathrm{a}} \cdot C_{p,\mathrm{a},i} \cdot (T_{\mathrm{a},i-1} - T_{\mathrm{a},i})}_{\substack{\text{Enthalpy from fluidisation air}}} \\
&+ \underbrace{\frac{i-(n-c)}{c} \cdot G_{\mathrm{at}} \cdot C_{p,\mathrm{a},i} \cdot (T_{\mathrm{a},i-1} - T_{\mathrm{a},i})}_{\substack{\text{Enthalpy from cummulated atomisation air}}} \\
&+ \underbrace{\frac{1}{c} \cdot G_{\mathrm{at}} \cdot C_{p,\mathrm{a},i} \cdot (T_{\mathrm{at},i} - T_{\mathrm{a},i-1})}_{\substack{\text{Enthalpy from atomisation air entering } S_i}} \\
&- \underbrace{\alpha_{\mathrm{p},i} \cdot N_i \cdot A_{\mathrm{p}} \cdot (T_{\mathrm{a},i} - T_{\mathrm{p},i})}_{\substack{\text{Heat from convective heat}\\ \text{transfer from fluidisation air to particles}}} \\
&- \underbrace{R_{\mathrm{D},i} \cdot N_i \cdot M_{\mathrm{p}} \cdot C_{p,\mathrm{v},i} \cdot (T_{\mathrm{a},i} - T_{\mathrm{p},i})}_{\substack{\text{Enthalpy required to evaporate water}\\ \text{and heat the vapour up to gas temp.}}} \\
&- \underbrace{\Phi_{\mathrm{loss,a},i}}_{\substack{\text{Heat loss to surroundings}\\ \text{(gas-to-wall heat transfer)}}} \qquad \text{(A.12)}
\end{aligned}
$$

for $n - c < i \leqslant n$.

The parameter $C_{p,\mathrm{a},i}$ is the specific heat of moist air in S_i. It is calculated using the following equation:

$$C_{p,\mathrm{a},i} = C_{p,\mathrm{dry\ air}} + X_{\mathrm{a},i} \cdot C_{p,\mathrm{v}} \qquad \text{(A.13)}$$

where $C_{p,\mathrm{dry\ air}}$ is the specific heat of dry air being 1000 J/(kg K) and $C_{p,\mathrm{v}}$ is the specific heat capacity of vapour being 1850 J/(kg K).

A.7. Determining the model parameters

For the application of the model equations is it necessary to find expressions for the model parameters. The applied equations are presented in the following section.

A.7.1. Gas/solid heat and mass transfer

The convective heat transfer coefficient between the particles and the gas phase $\alpha_{\mathrm{p},i}$ can be approximated using the Whitaker equation

according to:

$$Nu_{p,i} = 2 + Pr_i^{2/5}(0.43 \cdot Re_{p,i}^{1/2} + 0.06 \cdot Re_{p,i}^{2/3})$$
$$\text{for} \begin{cases} 3.5 < Re_{p,i} < 76\,000, & Re_{p,i} = \dfrac{\rho_{a,i} \cdot v_{a,i} \cdot d_p}{\eta_{a,i}} \\ 0.71 < Pr_i < 380, & Pr_i = \dfrac{C_{p,a,i} \cdot \eta_{a,i}}{\lambda_{a,i}} \end{cases} \quad (A.14)$$

The Nusselt number provides a basis for comparing the rates of convective heat loss from geometrically similar bodies immersed in a moving fluid. The thermal conductivity of the fluidisation air λ_a is required to calculate the Nusselt number, and the following equation was obtained by regression analysis by Ronsse (2006) based on data adapted from Janna (2000):

$$\lambda_{a,i} = 1.5207 \times 10^{-11} \cdot T_{a,i}^3 - 4.8574 \times 10^{-8} \cdot T_{a,i}^2 + 1.0184 \times 10^{-4} T_{a,i} - 3.9333 \times 10^{-4} \quad \text{where } T_{a,i} \text{ is in K} \quad (A.15)$$

Further, the viscosity of air in kg/(m s) is calculated using the following equation:

$$\eta_{a,i}(T_{a,i}) = 10^{-6} \frac{1.458 \cdot T_{a,i}^{3/2}}{T_{a,i} + 110.4} \quad \text{where } T_{a,i} \text{ is in K} \quad (A.16)$$

For the calculation of the *Sc* and *Re* numbers, the density of moist air $\rho_{a,i}$ is calculated using the ideal gas law simply as:

$$\rho_{a,i} = \frac{P_i(1 + X_{a,i})}{T_{a,i} \cdot R_g \cdot \left(\dfrac{1}{MW_a} + \dfrac{X_{a,i}}{MW_w}\right)}$$

where $T_{a,i}$ is in K, $MW_a = 0.028966$ kg/mol,

$$MW_w = 0.018015 \text{ kg/mol and } R_g = 8.314472 \frac{\text{m}^3 \text{ Pa}}{\text{K mol}} \quad (A.17)$$

The Nusselt number is given as:

$$Nu_{p,i} = \frac{\alpha_{p,i} \cdot d_p}{\lambda_{a,i}} \quad (A.18)$$

In the model equations, the drying rate $R_{D,i}$ is expressed as mass unit of water evaporated per mass unit of core particles per time. The drying rate is related to the vapour concentration gradient across the boundary layer according to:

$$R_{D,i} = \frac{\alpha'_{p,i} \cdot A_p \cdot \left(\dfrac{W_{p,i}}{|W_{p,i}| + a_{Langmuir}}\right) \cdot (P_{v,p,i} - P_{v,a,i})}{M_p \cdot (R_g/MW_v) \cdot (T_{a,i} + T_{p,i})/2} \quad (A.19)$$

In Eq. (A.19) the parenthesis containing $a_{Langmuir}$ is added to the drying rate term in order to avoid steep gradients in situations where the particle water contents approaches zero. The Langmuir expression has thus been added in order to make the simulations more stable by avoiding zero-order drying, which the Matlab ode solvers have difficulties to overcome. The parameter has nothing to do with the thermodynamic end result, but influences the $W_{p,i}(t)$ curve shape only. A value of 0.05 has been selected for the simulation in the present paper. Other values have been tested, but a value of 0.05 gives the best curve shape. The term $P_{v,p,i}$ is the vapour pressure at the particle surface and $P_{v,a,i}$ is the vapour pressure in the gas phase. $P_{v,p,i}$ is a function of the particle surface temperature and can be approximated through the following equation assuming that the boundary gas layer at the surface of a wetted particle is saturated (Campbell, 1977; Ronsse et al., 2007b):

$$P_{v,p,i}(T_p) \approx P_{v,sat}(T_p) = 10^3 \exp\left(52.57633 - 6790.4985 \times \frac{1}{T_p} - 5.02808 \ln(T_p)\right) \quad (A.20)$$

where the temperature is in K and $P_{v,p,i}$ is in Pa. The term $(T_{a,i}+T_{p,i})/2$ corresponds to the film temperature and the parameter R_g/MW_v is the specific gas constant for water vapour being 461.9 J/(kg K).

The vapour pressure in the fluidisation air is calculated as:

$$P_{v,a,i} = \left(\frac{rH\%}{100\%}\right) \cdot P_{v,a,i}(T_{a,i}) = \frac{P_i \cdot X_{a,i}}{\left(\dfrac{MW_w}{MW_a} + X_{a,i}\right)} \quad (A.21)$$

The mass transfer coefficient $\alpha'_{p,i}$ is calculated through an approximation in terms of the dimensionless Sherwood number for which the calculation is analogous to the calculation of the Nusselt number in Eq. (A.14).

$$Sh_{p,i} = 2 + Sc_i^{2/5}(0.43 \cdot Re_{p,i}^{1/2} + 0.06 \cdot Re_{p,i}^{2/3}) \quad (A.22)$$

where the dimensionless Schmidt number, *Sc*, is the ratio of the momentum diffusivity (or viscosity) to mass diffusivity given by:

$$Sc_i = \frac{\eta_{a,i}}{\rho_{a,i} \cdot D_{v,i}} \quad (A.23)$$

where $D_{v,i}$ is the molecular diffusion coefficient for water vapour in air being approximated by:

$$D_{v,i} = 24.2 \times 10^{-6}\left(\frac{T_{a,i}}{293.15}\right)^{1.75}\left(\frac{10^5}{P_i}\right)$$

where the temperature is in K and *P* is in Pa (A.24)

where the control volume pressure P_i is approximated by atmospheric pressure. Thus, P_i in Eq. (A.24) is 101 325 Pa.

The Sherwood number is given as:

$$Sh_{p,i} = \frac{\alpha'_{p,i} \cdot d_p}{D_{v,i}} \quad (A.25)$$

where $D_{v,i}$ is the molecular diffusion coefficient for water vapour in air being approximated in the same manner as for the *Sc* number according to Eq. (A.24).

The wet bulb temperature is estimated on the basis of the given fluidisation air temperature and humidity using Eqs. (A.26) and (A.27). Initially the vapour pressure at dew point P_{v_dp} is calculated according to:

$$P_{v\_dp} = \frac{\%\text{ relative humidity}}{100\text{ rH\%}} \cdot P_{sat}(T_a) \quad (A.26)$$

The vapour pressure at dewpoint is also equal to (Cheresources.com., 2008)

$$P_{v\_dp} = P_{v,sat}(T_{wb}) - \frac{(P_{atm} - P_{sat}(T_{wb})) \cdot (T_{db} - T_{wb})}{1555.56 - 0.722 \cdot T_{wb}} \quad (A.27)$$

where P_{sat} in found analogously to Eq. (A.20) as:

$$P_{v,sat}(T_{wb}) = 10^3 \exp\left(52.57633 - 6790.4985 \times \frac{1}{T_{wb}} - 5.02808 \ln(T_{wb})\right) \quad (A.28)$$

where the temperature is in K and *P* is in Pa. Conversion between absolute and relative humidity is done in terms of the following formulas realising that (Clement et al., 2004):

$$\frac{P_{actual}}{P_{ambient}} = \frac{X_a}{X_a + \dfrac{18.02\text{ g/mol}}{28.85\text{ g/mol}}} \quad (A.29)$$

where $P_{ambient}$ is assumed 101 325 Pa. The relative humidity is found according to:

$$rH\% = \frac{P_{actual} \cdot 100\%}{P_{v,sat}} \quad (A.30)$$

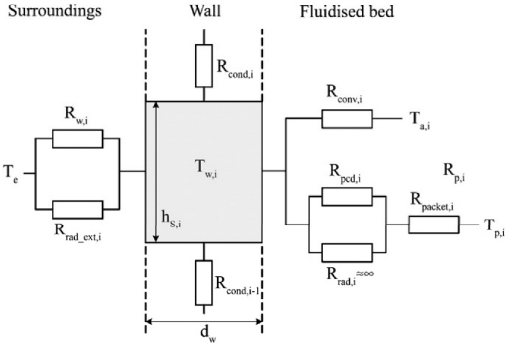

Fig. A1. Schematic representation of the heat losses in a single control volume S_i (Based on Ronsse et al., 2007a).

A.8. Wall element heat balance and heat losses

To quantify the overall heat losses in each control volume S_i, the reactor shell is modelled into different elements or control volumes according to Fig. A1 .

The number of wall elements equals the number of fluidised bed control volumes. In modelling the temperature of the wall element, a number of in- and output heat terms were considered. The different terms are presented below.

A.8.1. Bed to inner wall heat transfer

In a bubbling fluidised bed some of the rising bubbles sweep past the inner reactor wall thereby washing away the particles located there and bringing fresh particles into direct contact with the surface. These groups of particles, which are continuously being swept away along the inner reactor wall, are denoted as emulsion packets. To take into account the coexistence of bubbles and particle emulsion packets in bubbling fluidised beds, the thermal resistance from the bed to the vertical and submerged surface in the bed (i.e. the inner wall), is denoted R_i (having units of m^2 K/W), and for control volume S_i given by:

$$\frac{1}{R_i} = \frac{\delta_w}{R_{conv,i}} + \frac{(1-\delta_w)}{R_{p,i}} \tag{A.31}$$

where δ_w is the bubble voidage at the submerged surface given as (using the Davidson and Harrison, 1963 approach—see also Section 4.1)

$$\delta_w = \frac{\dot{V}_{bu}}{A_{bed}\cdot v_{bu}} = \frac{v_a - v_{mf}}{v_{bu}} \cong \frac{v_a - v_{mf}}{v_a - v_{mf} + 0.711\cdot(g\cdot d_{bu})^{0.5}} \tag{A.32}$$

where A_{bed} is the bed surface area, v_{bu} is the bubble velocity in m/s, v_{mf} the minimum fluidisation velocity and d_{bu} is the gas bubble diameter for Geldart group B particles given by (Rhodes, 1998):

$$d_{bu} = \frac{0.54}{g^{0.2}}(v_{a,i} - v_{mf})^{0.4}\left(h_{bu} + 4\cdot\left(\frac{\pi\cdot(d_{plate}/2)^2}{N_{or}}\right)^{0.5}\right)^{0.8} \tag{A.33}$$

where g is gravity and h_{bu} is the bubble position above the air distributor plate, having a diameter of d_{plate}. N_{or} is the total number of perforations (plate orifices) in the gas distributor plate. In case the air distributor plate is not a perforated plate, but rather a porous plate, such as a stainless steel wire frame, the term $4\cdot(\pi\cdot(d_{plate}/2)^2/N_{or})^{0.5} \approx 0.03$. The gas velocity at minimum fluidisation is found by an approximation of the Ergun equation for particles with diameters above 100 μm (Teunou and Poncelet, 2002) as:

$$v_{mf} = \frac{\eta_{a,i}}{\rho_{a,i} d_p}\{(33.7^2 + 0.04084\cdot Ar)^{1/2} - 33.7\},\quad d_p > 100\,\mu m \tag{A.34}$$

where Ar is the Archimedes number defined as (Kunii and Levenspiel, 1991):

$$Ar = \frac{d_p^3 \rho_{a,i}(\rho_p - \rho_{a,i})g}{\eta_{a,i}^2} \tag{A.35}$$

and $v_{a,i}$ is found simply as:

$$v_{a,i} = \frac{G_{a,i}}{\rho_a \cdot \frac{\pi}{4}\cdot \bar{d}_{S,i}^2} \tag{A.36}$$

A.8.2. Particles to inner wall heat transfer

The heat transfer from the particles to the inner reactor wall $R_{p,i}$ can be further divided into two serially connected heat transfers being the heat transfer by the emulsion packets and heat transfer through the combination of the wall–particle contact point and the thin gas layer surrounding the wall–particle contact point. The latter is composed of conductive and radiative heat transfer as given by:

$$R_{p,i} = \left(\frac{1}{R_{pcd,i}} + \frac{1}{R_{rad,i}}\right)^{-1} + R_{packet,i} \tag{A.37}$$

where R_{pcd} is the heat transfer resistance through the particle–vertical surface contact point and the surrounding thin gas layer, R_{rad} is the radiative heat transfer and R_{packet} is the heat transfer resistance due to the presence of emulsion packets. According to Kunii and Levenspiel (1991) the radiative heat transfer can be neglected when the temperature is lower than 400 °C, which is the case for commercial fluid bed coaters. As a result, Eq. (A.37) is approximated as:

$$R_{p,i} = R_{pcd,i} + R_{packet,i} \tag{A.38}$$

The heat transfer through the contact point between the particle and the vertical surface R_{pcd} can be calculated as:

$$\frac{1}{R_{pcd,i}} = \frac{2\cdot\lambda_{aw,i}}{d_p} + \kappa_w \cdot C_{p,a,i}\cdot\rho_{a,i}\cdot v_{a,i} \tag{A.39}$$

where κ_w is the wall mixing constant assumed to be 0.05 according to Kunii and Levenspiel (1991). The thermal conductivity for stagnant gas in the vicinity of the submerged vertical surface $\lambda_{aw,i}$ can be estimated according to:

$$\lambda_{aw,i} = \varepsilon_{mf,w}\cdot\lambda_{a,i} + (1-\varepsilon_{mf,w})\cdot\lambda_p\cdot\left[\frac{1}{\tau_w\cdot(\lambda_p/\lambda_{a,i}) + 1/3}\right] \tag{A.40}$$

where τ_w is the ratio of effective thickness of gas film around a contact point to particle diameter for contact between particle and surface. According to data adapted from Kunii and Levenspiel (1991), τ_w may be approximated as:

$$\tau_w = 0.3361\cdot(\lambda_p/\lambda_{a,i})^{-0.1862} \quad \text{for } 1 \leqslant (\lambda_p/\lambda_{a,i}) \leqslant 10^4 \tag{A.41}$$

In Eq. (A.40) the variable $\varepsilon_{mf,w}$ is the bed voidage at the submerged vertical surface and at minimum fluidisation gas velocity. This parameter is assumed to be equal to the overall bed voidage at minimum fluidisation, and thus:

$$\varepsilon_{mf,w} \cong \varepsilon_{mf} \tag{A.42}$$

Considering thermal diffusion through an emulsion packet and assuming that the properties of the emulsion are equal to those at minimum fluidisation, R_{packet} can be calculated as:

$$\frac{1}{R_{packet,i}} = \frac{2}{\sqrt{\pi}} \cdot \left(\frac{\lambda_{amark,i} \cdot \rho_p \cdot (1-\varepsilon_{mf}) \cdot C_{p,p} \cdot f_{bu,w}}{1-\delta_w} \right)^{0.5} \quad (A.43)$$

where $f_{bu,w}$ is the bubble frequency at the vertical surface. Generally, it is assumed to be equal to the overall bubble frequency in the bed f_{bu}. The bubble frequency can be estimated on the basis of the volumetric flow rate of the fluidisation gas and the bubble size as:

$$f_{bu} = \frac{G_a}{\frac{\pi}{6} \cdot d_{bu}^3} \quad (A.44)$$

For the use in Eq. (A.40), ε_{mf} is calculated as (using the Broadhurst and Becker equation):

$$\varepsilon_{mf} = 0.586 \cdot \psi_p^{-0.72} \left(\frac{\eta_{a,i}^2}{\rho_{a,i} \cdot g \cdot (\rho_p - \rho_{a,i}) \cdot d_p^3} \right)^{0.029} \cdot \left(\frac{\rho_{a,i}}{\rho_p} \right)^{0.021} \quad (A.45)$$

where ψ_p is the particle sphericity.

$\lambda_{amark,i}$ is the thermal conductivity for stagnant gas in the bed and is approximated as:

$$\lambda_{amark,i} = \varepsilon_{mf} \cdot \lambda_{a,i} + (1-\varepsilon_{mf}) \cdot \lambda_p \cdot \left[\frac{1}{\tau_{mark} \cdot (\lambda_p/\lambda_{a,i}) + 2/3} \right] \quad (A.46)$$

where τ_{mark} is the ratio of effective thickness of gas film around a contact point to particle diameter for contact between adjacent particles. According to data adapted from Kunii and Levenspiel (1991), τ_{mark} may be approximated as:

$$\tau_{mark} = 0.3116 \cdot (\lambda_p/\lambda_{a,i})^{-0.2174} \quad \text{for } 1 \leqslant (\lambda_p/\lambda_{a,i}) \leqslant 10^4 \quad (A.47)$$

A.8.3. Bubbles to inner wall heat transfer

In Eq. (A.31), the term $\delta_w/R_{conv,i}$ describes the heat transfer resistance between the gas bubbles and the inner reactor wall. The heat transfer through convection at a submerged surface in the fluidised bed depends on the geometry of the heat transfer surface. However, as an approximation, $R_{conv,i}$ was calculated through the Nusselts number for forced convection in a vertical tube according to the Dittus–Boelter equation for fluids in turbulent flow (Ronsse. 2006):

$$Nu_{w,i} = 0.023 \cdot Re_{w,i}^{0.8} \cdot Pr_i^{0.4} \quad (A.48)$$

where

$$Nu_{w,i} = \frac{\alpha_{w,i} \cdot d_{S,i}}{\lambda_{a,i}} \quad (A.49)$$

and

$$Re_{w,i} = \frac{\rho_{a,i} \cdot v_{a,i} \cdot d_{S,i}}{\eta_{a,i}}$$
$$Pr_i = \frac{C_{p,a,i} \cdot \eta_{a,i}}{\lambda_{a,i}} \quad (A.50)$$

Thus:

$$R_{conv,i} = \frac{1}{\alpha_{w,i}} = \frac{d_{S,i}}{Nu_{w,i} \cdot \lambda_{a,i}} \quad (A.51)$$

A.8.4. Heat transfer along the reactor wall

Because of the relatively small heat transfer resistance of the reactor wall (it is stainless steel) compared to the heat transfer resistance from the bed towards the wall and from the wall towards the environment, the wall element is considered to have a single temperature $T_{w,i}$. Due to the geometric nature of the wall element ($h_{S,i} \gg d_w$), vertical heat conduction to or from adjacent wall element is also taken into account, meaning that:

$$R_{cond,i} = \frac{h_{S,i} + h_{S,i+1}}{2 \cdot \lambda_w} \quad (A.52)$$

A.8.5. Heat transfer from the wall towards the environment

This heat transfer towards the environment is composed of convective and radiative heat transfer. The convective heat transfer is approximated by calculating the Nusselt number of a vertical cylinder with height h_{bed} (corresponding to natural or free convection):

$$Nu_e = 0.59 \cdot (Gr_e \cdot Pr_e)^{0.25} \text{ when } 10^4 < Gr_e \cdot Pr_e < 10^9$$

where

$$Gr_e = \frac{\beta_a \cdot g \cdot (d_{S,i})^3 \cdot \rho_{film,i}^2 \cdot (T_{w,i} - T_e)}{\eta_{film,i}^2}$$

and

$$Pr_e = \frac{C_{p,film,i} \cdot \eta_{film,i}}{\lambda_{film,i}} \quad (A.53)$$

and

$$Nu_e = \frac{\alpha_{film} \cdot d_{S,i}}{\lambda_{film,i}}$$

where β_a is the thermal expansion coefficient of the fluidisation air being approximated as $3.0 \times 10^{-3}\ K^{-1}$. All other physical properties in Eq. (A.53) should be evaluated at the film temperature being $T_{film} = (T_e + T_w)/2$, where T_e is the external air temperature. Hence the subscript "film" in the parameters in Eq. (A.53).

Thus:

$$R_{w,i} = \frac{1}{\alpha_{film}} = \frac{d_{S,i}}{Nu_e \cdot \lambda_{film,i}} \quad (A.54)$$

The radiative heat loss is calculated by:

$$Q_{rad,i} = \upsilon \cdot \theta_w \cdot A_{w,i} \cdot (T_{w,i}^4 - T_e^4) \quad (A.55)$$

where $A_{w,i}$ is the wall area in control volume S_i (it is assumed throughout the model that the outer and inner area of the control volume is the same), σ is the Stefan–Boltzmann constant being equal to $5.669 \times 10^{-8}\ W\,m^{-2}\,K^{-4}$, and θ_w is the emissivity which is used to describe the extent to which a surface behaves similar to a blackbody ($\theta_w = 1$). A black body is an ideal surface which emits the maximum possible energy at a given wavelength and temperature. For the present fluid bed model, a value of $\theta_w = 0.28$ is chosen, corresponding to emittance for far-infra-red radiation for stainless steel (Omega.com, 2008).

A.8.6. Total heat transfer balance towards environment

By combining all described heat transfer terms, the total energy balance for the reactor wall may be written as:

$$C_{p,w} \cdot M_{w,i} \cdot \frac{dT_{w,i}}{dt} - \left[\begin{matrix} \text{heat inputs from bed} \\ \text{and adjacent wall elements} \end{matrix} \right] - \left[\begin{matrix} \text{heat output to environment} \\ \text{and adjacent wall elements} \end{matrix} \right] \quad (A.56)$$

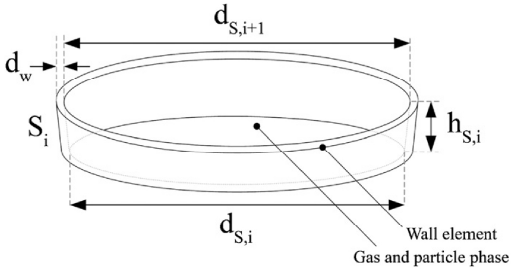

Fig. A2. Schematic representation of the reactor wall control volume (Based on Ronsse et al., 2007a).

where the mass of the reactor element $M_{w,i}$ is calculated as:

$$M_{w,i} = \pi \cdot d_{S,i} \cdot d_w \cdot h_{S,i} \cdot \rho_w \tag{A.57}$$

where $d_{S,i}$ is the inner (bottom) diameter of the control volume S_i, d_w is the reactor wall thickness, $h_{S,i}$ is the height of the wall element and ρ_w is the specific density of the reactor wall material. The reactor wall control volume can be observed in Fig. A2.

In terms of symbols, Eq. (A.56) becomes:

$$\underbrace{C_{p,w} \cdot \rho_w \cdot A_{w,i} \cdot d_w \cdot \frac{dT_{w,i}}{dt}}_{\text{Enthalpy exchange rate at the wall in control volume } S_i} = \underbrace{\frac{A_{w,i} \cdot \delta_w \cdot (T_{a,i} - T_{w,i})}{R_{conv,i}}}_{\text{Convective heat from gas bubbles}} + \underbrace{\frac{A_{w,i} \cdot (1-\delta_w) \cdot (T_{p,i} - T_{w,i})}{R_{p,i}}}_{\text{Convective heat from particles}} - \underbrace{\sigma \cdot \theta_w \cdot A_{w,i}(T_{w,i}^4 - T_e^4)}_{\text{Radiative heat transfer from wall to surroundings}} - \underbrace{\frac{A_{w,i}}{R_{w,i}}(T_{w,i} - T_e)}_{\text{Convective heat transfer from wall to surroundings}} + \underbrace{\frac{\pi \cdot d_{S,i} \cdot d_w}{R_{cond,i-1}}(T_{w,i-1} - T_{w,i})}_{\text{Conductive heat from } S_{i-1}} - \underbrace{\frac{\pi \cdot d_{S,i} \cdot d_w}{R_{cond,i}}(T_{w,i} - T_{w,i+1})}_{\text{Conductive heat leaving to } S_{i+1}} \tag{A.58}$$

In the heat and mass balance equations, the heat transfer from the fluidised bed towards the inner reactor wall is divided into two parts being the particles-to-wall heat transfer $\Phi_{loss,p,i}$ and gas-to-wall heat transfer $\Phi_{loss,a,i}$. These two heat transfer contributions correspond to the first two terms on the right-hand side in Eq. (A.58) according to:

$$\Phi_{loss,a,i} = \frac{A_{w,i} \cdot \delta_w \cdot (T_{a,i} - T_{w,i})}{R_{conv,i}}$$

$$\Phi_{loss,p,i} = \frac{A_{w,i} \cdot (1-\delta_w) \cdot (T_{p,i} - T_{w,i})}{R_{p,i}} \tag{A.59}$$

Appendix B. Model assumptions

Being a one-dimensional model, the basic principle is to divide the fluidised bed vertically into n control volumes from the bottom air distributor plate and up to the nozzle outlet, each having the same height being $h_{S,i} = h_{FB}/n$. Most fluid beds have frustum shapes where the diameter is smallest at the bottom plate and largest at the spray zone, which obviously affects the fluidisation air velocity in m/s in vertical direction. In a model perspective, this means that the upper and lower diameters are different for each control volume which is accounted for in the present model. The control volumes are numbered from 1 to n where the first control volume is nearest the fluidisation air distributor plate.

It is assumed that the droplets containing the coating solution have only a limited penetration depth into the bed, and consequently, that particle–droplet contact takes place only in a certain upper part of the volume of the fluidised bed (Maronga and Wnukowski, 1997a). Therefore, two types of control volumes are assumed to exist being non-coating and coating control volumes. Numbering the coating control volumes with the integer c means that out of n control volumes in total, c are coating control volumes and $n-c$ are non-coating control volumes. It is assumed that each coating control volume receives a fraction M_c/c of the coating liquid. It is furthermore assumed that all sprayed coating solution is collected on the particles without premature droplet evaporation, and that the liquid is uniformly deposited on all particles in each coating control volume. A schematic representation of the model principle can be seen from Fig. B1.

A number of other assumptions are made being:

- Particles and air in each control volume (being coating or non-coating) are perfectly mixed. This means that the temperature and moisture content is the same for all particles in a control volume. It further implies that moisture and temperature is instantaneously exchanged when particles and air enter a new control volume.
- All particles have the same diameter d_p.
- Both the size of each control volume and the number of particles contained in each control volume are constant at all times.

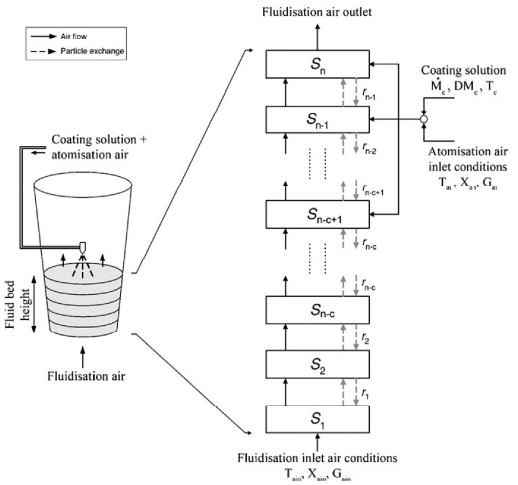

Fig. B1. Schematic representation of the overall model principle (Based on Ronsse et al., 2007a).

- The weight of the coating mass added to each particle is small compared to the weight of the particle itself. Consequently, the weight of each individual particle is assumed constant throughout the process. Similarly, the thickness of the deposited coating film is small compared to the particle diameter, therefore the particle diameter is assumed to be constant. The coating deposition is assumed not to affect fluidisation properties.
- Particles are mechanically strong; there is neither attrition nor agglomeration. This means that neither coating material nor core material can be exhausted during the process.
- The air exhaust is at atmospheric pressure. The pressure drop across the fluidised bed is small compared to the overall atmospheric pressure. Consequently, the drying process is assumed to take place at constant atmospheric pressure.
- The atomisation air specific heat capacity, $C_{p,at}$, and the moist air specific heat capacities from two adjacent control volumes, $C_{p,a,i}$ and $C_{p,a,i-1}$, are assumed to be independent of temperature and assumed for a given control volume to be represented by $C_{p,a,i}$.
- Considering the diameter range of both droplets ($0 \leqslant d_{dr} \leqslant 50\,\mu m$) and particles ($100\,\mu m \leqslant d_p \leqslant 500\,\mu m$) the following conditions may be assumed according to Ronsse (2006):

$$Bi_p = \frac{\alpha_p \cdot d_p}{\lambda_p} \ll 0.1 \quad \text{and} \quad Bi_{dr} = \frac{\alpha_{dr} \cdot d_{dr}}{\lambda_{dr}} \ll 0.1$$

As a consequence of the small Biot numbers, the internal heat transfer in both the particles and the droplets are negligible compared to the convective heat transfer resistance at the particle surface. Hence, it is assumed that each droplet and each particle are isothermal and can be represented as having a single uniform temperature.

Another basic assumption is that the rate at which particles are transferred from control volume S_i towards its neighbouring control volume S_{i+1} (or S_{i-1}) equals the particle transfer rate from S_{i+1} (or S_{i-1}) towards S_i. The rate at which particles are exchanged is expressed by r, as the fraction of the particle population exchanged between neighbouring control volumes S_i and S_{i+1} per time unit. Estimating a reasonable value for r over the entire control volume boundaries is not an easy task. Ronsse et al. (2007a) estimated for a Glatt GPCG-1 fluid bed values between 0.81 and $1.82\,s^{-1}$ based on experiments performed by Mostoufi and Chaouki (2001). For simplicity, Ronsse et al. (2007a) chose a fixed value of $1.4\,s^{-1}$ irrespectively of fluidisation conditions. Alternatively, the exchange rate r may be calculated from theoretical considerations based on the average particle circulation time τ_c for which an estimation has been proposed by Rowe (1972) for bubbling fluid beds according to:

$$r = \frac{1}{\tau_c} = \frac{0.6 \cdot (v_a - v_{mf}) \cdot (1 - (v_a - v_{mf})/v_{bu})}{h_{mf}} \tag{B.1}$$

In the present study, the choice was to let r vary as a function of the fluidisation conditions according to Eq. (B.1), instead of fixing a single value for r for all simulations. The value for v_a was always chosen to be the value in the middle of the fluidisation chamber. It was assumed that the exchange rate was constant across all control volumes, and h_{mf} values were estimated from guidelines presented by Hede et al. (2007c). These values can be seen in Table 1. For the tested fluidisation conditions in the three fluid bed scales tested, r values ranged between 2.26 and $2.70\,s^{-1}$ for the small-scale, between 1.47 and $2.83\,s^{-1}$ for the medium-scale and between 1.01 and $1.09\,s^{-1}$ for the large-scale. It seems reasonable that the r values are largest the smaller the fluid bed scale, as the average time of circulation τ_c is known to increase with scale (Rowe, 1972).

Appendix C. Constant parameter values used in the simulations

All the parameters listed below were kept constant throughout all simulations irrespectively of the scale.

Parameter	Symbol	Values used in the simulations
Langmuir coefficient	$a_{Langmuir}$	0.05 (Dimensionless)
Reactor wall thickness	d_w	0.003 m
Reactor wall thermal conductivity	$\lambda_{w,i}$	14.6 W/(m K)
Reactor wall emittance	θ_w	0.28 (Dimensionless)
Reactor wall specific heat capacity	$C_{p,w}$	500 J/(kg K)
Reactor wall density	ρ_w	$7850\,kg/m^3$
Wall mixing constant	κ_w	0.05 (Dimensionless)
Stefan–Boltzmann constant	σ	5.669×10^{-8} W/(m^2 K^4)
Particle diameter	d_p	250×10^{-6} m
Particle sphericity	ψ_p	0.86 (Dimensionless)
Particle density	ρ_p	$2600\,kg/m^3$
Particle specific heat capacity	$C_{p,p}$	837 J/(kg K)
Specific heat of dry air	$C_{p,dry\ air}$	1000 J/(kg K)
Particle thermal conductivity	λ_p	0.8 W/(m K)
Specific heat capacity of water	C_{p,H_2O}	4181.3 J/(kg K)
Specific heat capacity of cores	$C_{p,Core}$	902.537 J/(kg K)
Specific heat capacity of vapour	$C_{p,vapour}$	1850 J/(kg K)
Coating solution temperature	T_c	333.15 K
Atomisation air temperature	T_{at}	293.15 K
Absolute humidity of nozzle air	X_{at}	2.87×10^{-4} kg water/kg dry air
External air temperature	T_e	298.15 K
External atmospheric pressure	P_e	1.01×10^5 Pa
Gravity	g	$9.82\,m/s^2$
Thermal expansion coefficient of the fluidisation air	β_a	$3.0 \times 10^{-3}\,K^{-1}$

References

Akkermans, J.H.M., Edwards, M.F., Groot, A.T.J., Montanus, C.P.M., Van Pomeren, R.W.J., Yuregir, K.R., 1998. Production of detergent granulates. Patent WO98/58046.

Boerefijn, R., Hounslow, M.J., 2005. Studies of fluid bed granulation in an industrial R&D context. Chemical Engineering Science 60, 3879–3890.

Campbell, G.S., 1977. An Introduction to Environmental Biophysics. Springer, New York.

Cheresources.com. Visit at the homepage cheresources.com. March 2008.

Clement, K.H., Fangel, P., Jensen, A.D., Thomsen, K., 2004. Kemiske Enhedsoperationer, fifth ed. Polyteknisk Forlag.

Davidson, J.F., Harrison, D., 1963. Fluidised Particles. Cambridge University Press, New York.

Dewettinck, K., 1997. Fluidized bed coating in food technology: process and product quality. Ph.D. Thesis, University of Ghent.

Ennis, B.J., Tardos, G., Pfeffer, R., 1991. A microlevel-based characterization of granulation phenomena. Powder Technology 65, 257–272.

Hede, P.D., 2005. Fluidised bed coating and granulation. M.Sc. Thesis, Department of Chemical Engineering, CHEC Research Center, Technical University of Denmark, pp. 1–227.
Hede, P.D., 2006. Towards Mathesis Universalis: modern aspects of modelling batch fluidised bed agglomeration and coating systems—a review. CHEC Report R0605, Department of Chemical Engineering, Technical University of Denmark, pp. 1–101.
Hede, P.D., Jensen, A.D., Bach, P., 2007a. Top-spray fluidised bed coating: scale-up in terms of relative droplet size and drying force. Chemical Engineering Science 63 (14), 3821–3842.
Hede, P.D., Jensen, A.D., Bach, P., 2007b. Small-scale top-spray fluidised bed coating: granule impact strength, agglomeration tendency and coating layer morphology. Powder Technology 176, 156–167.
Hede, P.D., Jensen, A.D., Bach, P., 2007c. Validation of the flux number as scaling parameter for top-spray fluid bed systems. Chemical Engineering Science 63, 815–828.
Hede, P.D., Bach, P., Jensen, A.D., 2008a. Two-fluid spray atomisation and pneumatic nozzles for fluid bed coating/agglomeration purposes: a review. Chemical Engineering Science 63 (14), 3821–3842.
Hede, P.D., Bach, P., Jensen, A.D., 2008b. Fluidised bed coating with sodium sulphate and PVA/TiO_2. Part I: review and agglomeration regime maps. Industrial and Engineering Chemical Research, accepted for publication.
Hede, P.D., Bach, P., Jensen, A.D., 2008c. Fluidised bed coating with sodium sulphate and PVA/TiO_2. Part II: Influence of coating solution viscosity, stickiness, pH and droplet diameter on agglomeration. Industrial and Engineering Chemical Research, accepted for publication.
Hede, P.D., Bach, P., Jensen, A.D., 2008d. Fluidised bed coating with sodium sulphate and PVA/TiO_2. Part III: The role of tackiness and the tack Stokes number. Industrial and Engineering Chemical Research, accepted for publication.
Iveson, S.M., Litster, D.L., Hapgood, K., Ennis, B.J., 2001. Nucleation, growth and breakage phenomena in agitated wet granulation processes: a review. Powder Technology 117, 3–39.
Janna, W.S., 2000. Engineering Heat Transfer, second ed. CRC Press, Boca Raton, NY, pp. 1–683.
Kunii, D., Levenspiel, O., 1991. Fluidization Engineering. second ed. Butterworth-Heinemann, Stoneham.
Litster, J.D., Hapgood, K.P., Michaels, J.N., Sims, A., Roberts, M., Kameneni, S.K., 2002. Scale-up of mixer granulators for effective liquid distribution. Powder Technology 124, 272–280.
Maronga, S.J., Wnukowski, P., 1997a. Establishing temperature and humidity profiles in fluidized bed particulate coating. Powder Technology 94, 181–185.
Maronga, S.J., Wnukowski, P., 1997b. Modelling of the three-domain fluidized-bed particulate coating process. Chemical Engineering Science 17, 2915–2925.
Maronga, S.J., Wnukowski, P., 1998. The use of humidity and temperature profiles in optimising the size of fluidized bed in a coating process. Chemical Engineering and Processing 37, 423–432.
Mehta, A.M., 1988. Scale-up considerations in the fluid-bed process for controlled-release products. Pharmaceutical Technology 12, 46–52.
Mort, P.R., 2005. Scale-up of binder agglomeration processes. Powder Technology 150, 86–103.
Mostoufi, N., Chaouki, J., 2001. Local solid mixing drag coefficient in fluidized beds. Powder Technology 114, 23–31.
Omega.com, 2008. Visit at the website ⟨www.omega.com⟩, February 2008.
Rambali, B., Baert, L., Massart, D.L., 2003. Scaling up of the fluidized bed granulation process. International Journal of Pharmaceutics 252, 197–206.
Rhodes, M., 1998. Introduction to Particle Technology. Wiley, Chichester.
Ronsse, F., 2006. Modelling heat and mass transfer in fluidised bed coating processes. Ph.D. Thesis, Ghent University.
Ronsse, F., Pieters, J.G., Dewettinck, K., 2007a. Combined population balance and thermodynamic modelling of the batch top-spray fluidised bed coating process. Part I—model development and validation. Journal of Food Engineering 78, 296–307.
Ronsse, F., Pieters, J.G., Dewettinck, K., 2007b. Combined population balance and thermodynamic modelling of the batch top-spray fluidised bed coating process. Part II—model and process analysis. Journal of Food Engineering 78, 308–322.
Rowe, P.N., 1972. Estimation of solids circulation rate in bubbling fluidised bed. Chemical Engineering Science 28, 979–980.
Shampine, L.F., Reichelt, M.W., 1997. The Matlab ODE suite. SIAM Journal of Scientific Computation 18 (1), 1–22.
Stein, M., Ding, Y.L., Seville, J.P.K., 2002. Experimental verification of the scaling relationships for bubbling gas-fluidised beds using the PEPT technique. Chemical Engineering Science 57, 3649–3658.
Teunou, E., Poncelet, D., 2002. Batch and continuous fluid bed coating—review and state of the art. Journal of Food Engineering 53, 325–340.
van Ee, J.H., Misset, O., Baas, E.J., 1997. Enzymes in Detergency. Surfactant Science Series, vol. 69. Marcel Dekker, New York.
Werner, S.R.L., Jones, J.R., Paterson, A.H.J., Archer, R.H., Pearce, D.L., 2007a. Air-suspension particle coating in the food industry: part I—state of the art. Powder Technology 171, 25–33.
Werner, S.R.L., Jones, J.R., Paterson, A.H.J., Archer, R.H., Pearce, D.L., 2007b. Air-suspension particle coating in the food industry: part II—micro-level process approach. Powder Technology 171, 34–35.